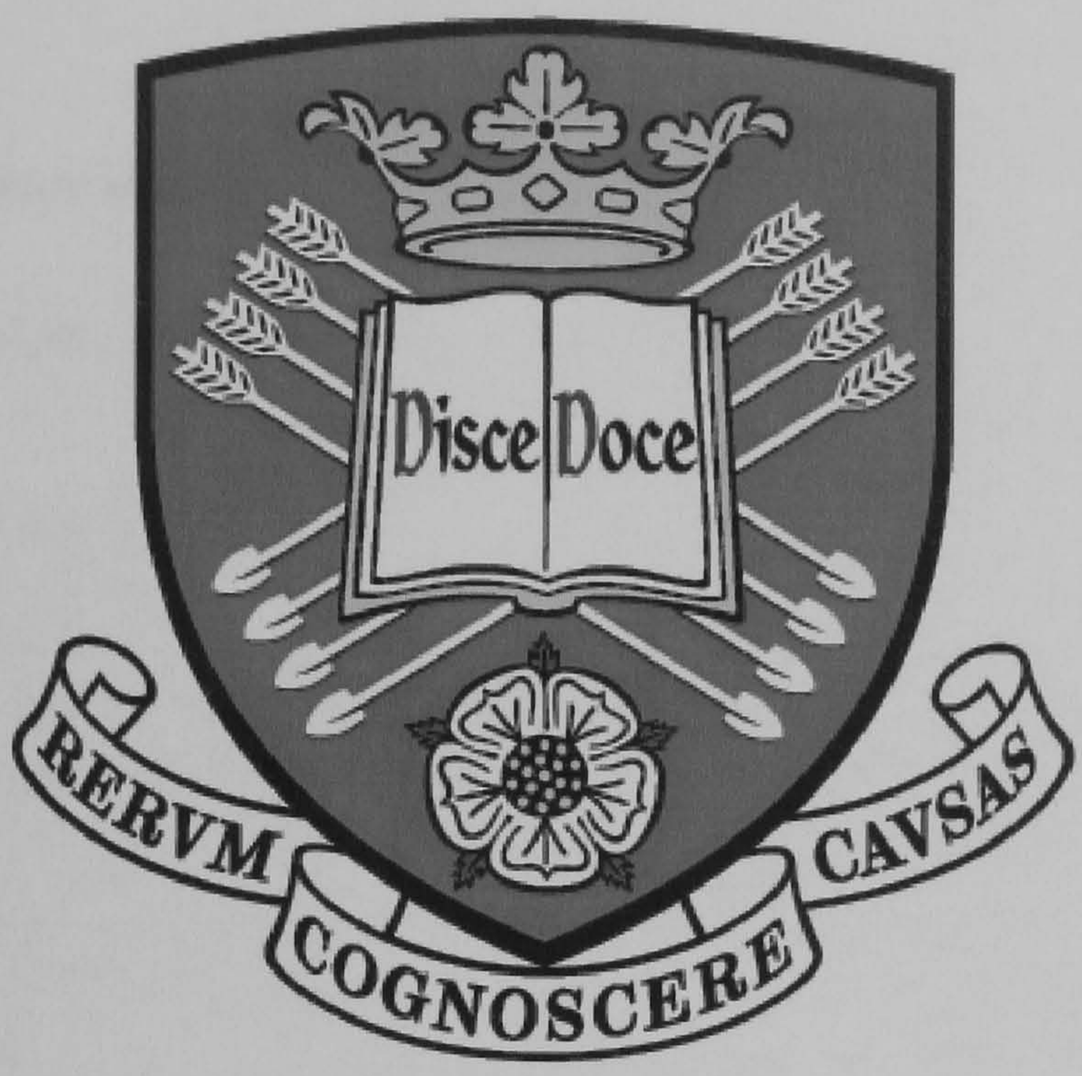

"Oxidation and wear behaviour of a work roll grade high speed steel"

by

Nelson Federico-Garza-Montes-de-Oca

Thesis submitted for the degree of Doctor of Philosophy

Department of Engineering Materials
The University of Sheffield
Sheffield, England May, 2008

Content

It is only in the mysterious equations of love that any logical reasons can be found

John Nash

Summary

The oxidation behaviour of high speed steel (1.55 % C, 7.70 % Cr, 4.90 %V, and 2.00% Mo) was studied isothermally at 550 and 615°C for three different environmental conditions, two of which consisted in a mixture of dry air and water vapour flowing at a rate of 0.45 or 1.45 cm^3/min respectively, compared to dry air conditions. At 615°C and for the maximum water vapour content, the oxidation behaviour was initially logarithmic followed by linear stage. In contrast, for a water vapour flow rate of 0.45 cm^3/min, the oxidation was parabolic, which resulted in a greater mass gain of the samples after 1 hour oxidation, even though there was a lower water content. This was believed to be related to the partial pressure of oxygen and therefore to the amount of oxygen available for oxidation. When exposed to dry air, logarithmic kinetics were observed, with much lower mass gain compared with the other two environmental conditions. Reducing the test temperature to 550°C only reduced the mass gain, with the same oxidation kinetics for each condition, suggesting the same oxidation mechanisms at both temperatures. For the humid conditions, an iron-chromium spinel $(Fe, Cr)_3O_4$ was formed along with magnetite Fe_3O_4 and hematite Fe_2O_3. In dry conditions the spinel and hematite were also present. In addition, a VO vanadium oxide layer was located at the top of the oxide layer, indicating oxidation of the MC vanadium rich carbides, promoted by the high partial pressure of oxygen of the environment.

The steel was also exposed to cyclic temperature fluctuations, of two different frequencies, in an attempt to more closely simulate the conditions found during operation of rolls in industry. For the high frequency tests, it was difficult to establish a mathematical relationship for the oxide growth, with the kinetics being rather stochastic. The cyclic oxidation produced a very thin granular layer which appeared to be the spinel $(Fe,Cr)_3O_4$. Local surface regions exhibited high plastic deformation associated with cracks that facilitated the oxygen dissolution within the steel. In the low frequency cyclic tests, the oxidation kinetics were parabolic at both test temperatures. Quenching in water, resulted in the preferential spallation of the hematite by a mechanism known as "buckling", generated from compressive thermal stresses. Material was removed at a rate of -0.13mg/cycle and -0.07mg/cycle at 615 and 550°C respectively, leaving the surface only protected by a layer of iron-chromium spinel.

The relationship between the wear of the high speed steel and oxidation was investigated at 600, 500 and 400°C in a rolling-sliding disc on disc configuration using a 2.5 kg load for a sliding distance of 111 km for two different environmental conditions (water, both gaseous and liquid, and laboratory dry air). The specific wear rate of the high speed steel discs was greater for the dry tests compared to the wet ones. However, the specific wear rate of the dry tests was strongly temperature dependent, while for the wet tests, the wear rate was insensitive to temperature. The dry tests exhibited a combination of metallic and oxidational wear, while the wet tests were almost entirely oxidational, with a different oxide phase constitution to the dry tests. Surprisingly, the wet tests exhibited higher friction compared to the wet tests. The reasons for this and the difference in wear rates are discussed and compared to the static oxidation tests.

Chapter 1

Introduction

1.1 Introduction

High speed steels (HSS) are highly alloyed steels whose microstructure normally contains vanadium, chromium and molybdenum rich carbides of high hardness dispersed in a martensitic matrix, resulting in a material with excellent wear properties at high temperatures as well as in operational conditions where abrasion and fatigue resistance are also important. These characteristics combined with the stability of the microstructure promote the use of this alloy as an ideal candidate for the manufacture of work rolls, the tools used to reduce the thickness of steel strips at high temperature (800~1200°C) in the finishing stands of hot strip mills. In these installations, the working conditions experienced by the work rolls are tough leading to a rapid degradation of the roll surface by mechanisms that include thermal fatigue, wear by abrasion and oxidation.

The study of the oxidation phenomena of work rolls is important for various reasons. Firstly, excellent surface quality of the laminated products in their final state is required as an advantage if they are competing against other metallic materials for specific applications, but acceptable quality levels can not be achieved if the surface of the work roll is altered by the presence of an oxide layer that inevitably grows onto them. Secondly, Caithness *et al.* (1999) commented that with the use of high speed steel work rolls the levels of friction and therefore the power consumption in the mills are greater than the values of these variables measured in mills that use work rolls of different materials like high chromium irons for example, but whether this increment in friction is or is not associated with the formation of oxides on the roll surface remains uncertain.

The reasons given in the above paragraph suggest that the study of work roll oxidation in hot strip mills and its relation with the friction values in the process and

surface quality of the steel strip is mandatory. Unfortunately, the knowledge of this phenomenon has been limited to only few works regarding the oxidation of work roll materials, particularly high chromium irons. A major concern is the way in which the available studies have used temperatures not realistic for the hot rolling process. In addition, studies have used either dry air or pure oxygen, which is a completely different regime to the environment in hot rolling, where water vapour is present. From the point of view of this work it is considered that water vapour is an important element that should be taken into account during the oxidation.

Factors that deserve special attention include the questions of how the oxide grows on the surface of the work roll during operation and, how the presence of water in the environment could affect the oxide formation during the process. Unfortunately it would be impossible to give an answer to these questions based on experiments carried out directly in the mill, given that these result expensive and dangerous.

The aim of this research was to study the oxidation behaviour of a work roll grade high speed steel under the action of various oxidant atmospheres some of them including water vapour, aiming to replicate the environmental conditions found in a hot strip mill, in order to observe if the presence of this gas modified the rate of oxide growth of this material. In addition to this, the oxidation behaviour of the material was also studied under conditions of temperature fluctuation in order to identify the preferred failure mechanism of the oxide layer in response to the presence of thermal stresses.

Finally, the behaviour of the oxide layer formed under the presence of ambient air or water vapour was studied under conditions of contact, load and motion aiming to clarify the role of the oxide layer grown on work rolls during the process and to relate the differences in the amount of oxide produced under dry and wet atmospheres with tribological variables of interest like the specific wear rate and the friction coefficient.

The outline of this work is described in the following manner: In Chapter 2, the results of a literature survey made on features including oxidation mechanisms and the

oxidation of iron and Fe-Cr alloys is presented together with aspects on oxide formation on work rolls in hot strip mills and the influence of these oxides during hot working processes. Chapter 3 contains information on the experimental methodology and the facilities developed to complete the objectives traced for this research. In Chapter 4, the most important results obtained from the experiments developed are presented and in Chapter 5 a discussion to these is made. And finally in Chapter 6 the most relevant conclusions obtained from the experiments are presented together with suggestions on some aspects that need to be taken into account for further investigations on the topics discussed in this thesis.

Chapter 2

Literature review

2.1 Introduction

In this chapter, the results of the literature survey carried out to understand the genesis and development of oxidation phenomena for metals and particularly of steel alloys are presented. The chapter contains a substantial amount of information on topics considered essential for the understanding of the high temperature oxidation reactions, covering subjects from a review to the characteristics of oxides as ionic compounds, to the role and the influence of oxides in metal forming operations at high temperature, focusing the attention on the formation of oxides on the surface of Fe-Cr alloys as well as on the surface of the work rolls materials used in hot strip mills.

2.2 Ionic nature of oxide layers

When a metal is exposed to atmospheres rich in oxygen, interactions between the metallic ions and oxygen occur at the atomic level in the from of chemical reactions that promote the development of physical and chemical changes that are normally represented by the growth of an oxide layer on the surface of the metal as the typical product of these reactions.

The crystal structure of the oxide layer formed is not a perfect arrangement of metallic and non metallic atoms, rather it contains defects like ion vacancies and ions located at interstitial positions, resulting in nonstoichiometry. This fact is important for the reason that the formation and subsequent growth of oxide layers is closely linked to the transport of metallic, non metallic ions and electrons across the oxide layer. This transport could only be possible by diffusion of ionic and electronic species through the

existent defects in the oxide, in a manner that always preserves the neutral character of the oxide compound, i.e. the addition of all the electrical charges contained in the oxide must be equal to zero.

As ionic and electronic conduction is believed to occur in an oxide layer, according to Wagner (Kubaschewski, 1953), oxides can be catalogued as semiconductors and therefore can be subdivide as n-type or p-type semiconductors depending on the type of defect present in their crystalline structure.

2.2.1 P-type oxide layers

These oxides are characterized by either a deficit in metallic ions or an excess of oxygen ions and are represented by the formulas $M_{1-\alpha}O$ or $MO_{1+\alpha}$ for each case, respectively, where α represents a small fraction of 1. In the first case, the oxide contains lattice positions with a positive charge deficit so that the electrical balance of the compound is preserved by means of alterations to the valence state of some cations that remain in normal lattice positions, maintaining the charge balance of the compound (Fig 2.1). If the partial pressure of oxygen is increased, the number of defects in the oxide increases and so the electrical conductivity within the compound increases and therefore it is expected that the rate at which cation deficient oxides layer grow also increases.

Oxides having an excess of oxygen located at interstitial positions are less likely to occur simply because oxygen ions are larger in size than most cations. Some uranium oxides are representative examples of this group (Kofstad, 1966).

2.2.2 N-type oxide layers

Oxides having either an excess of cations or a deficit in the amount of anions are representative of n-type semiconductors. Similar to the case of p-type oxides, the formulations used to represent the defects found in n-type oxides are $M_{1+\alpha}O$ and $MO_{1-\alpha}$ for defects involving cations or anions respectively. For the first case, which is the most

common, cations are located at interstitial positions in the oxide lattice and the total charge of the compound is balanced by the existence of electrons of the same magnitude as the valence state of the interstitial ions (Fig 2.2). The electrical conductivity in oxides having an excess of cations decreases as the partial pressure of oxygen is increased.

The anion deficit type oxide is not so well explained in some text books and comprehension of this kind of oxide is difficult, but basically this defect is present when anions are missing in their normal lattice positions and the electrical neutrality of compound is balanced by an amount of electrons of the same number as the valence state of the missing oxygen ions. The electrical conductivity in compounds showing anion vacancies is reduced as the partial pressure of oxygen increased.

2.3 Formation of oxides at high temperature

Oxide formation is considered a thermally activated process, this means that the formation of oxide and the rate at which this process occurs, i.e. the *kinetics,* is strongly linked to the temperature of the environment in which the metal is contained and the mathematical formulations that could represent the rate at which an oxide grows normally involves the dependence on temperature in the from of an Arrhenius expression such as:

$$k_p = Ae^{\left(\frac{-Q}{RT}\right)} \tag{2.1}$$

where, k_p is a constant, Q represents the activation energy needed to stimulate ionic motion for oxidation reactions to occur, T is the temperature in absolute units, R is the universal gas constant and A is a constant. The rate of oxide formation normally increases with temperature, but the rate of oxide growth is often influenced by the purity of the metal, the pressure of the system and the type and amount of defects present in the oxide layer.

Once a small amount of oxide is formed on the surface of the metal it represents a physical barrier for the metallic and non metallic ions to react and further growth of the layer will only be possible by the migration of the active species across the defects present in the oxide by solid state diffusion mechanisms (Fig.2.3). During the first stages of the oxidation process, the rate of reaction between the species and formation of oxide is expected to be high, because the barrier is relatively thin but as the oxide scale thickens, the distance that metallic ions and non metallic ions need to diffuse in order to react also increases and therefore a reduction in the reaction rate and in the oxide scale formation is likely to be observed.

2.4 Wagner's parabolic oxidation law

An idealized example of how an oxide scale grows on the surface of metals at high temperatures was given by Wagner in 1933 in his derivation of the parabolic oxidation theory. To develop this theory some assumptions were considered and are summarized as follows:

1. It is assumed that the oxide scale is free of physical defects (pores, cracks, blisters etc.) and it is perfectly adhered to the metallic substrate.

2. The rate controlling mechanism that influences the growth of the oxide layer is the diffusion of ionic and electronic species across the oxide layer.

3. Equilibrium is established at the metal-oxide and the gas-metal interfaces, this is, the rate at which the reactions occur at these interfaces are the same.

4. Oxygen is not soluble in the metal (a condition necessary to develop internal oxidation).

5. The driving force for the occurrence of oxidation reactions is the free energy change of oxide formation. This point suggests that gradients of chemical and

electrical potential determined by the activities of metal and the gas will be found across the scale Fig (2.4).

The sequence of Wagner's oxidation theory is complicated to follow with respect to the many variables and mathematical simplifications used to obtain the final expression that expresses the growth of the oxide as a function of the time, but as an alternative Birks and Meier (1986) presented a simplified approach to this theory based on the scheme shown in Fig 2.4. It can be seen that two reactions take place at each interface, the ionization of the reactive species (metal or oxygen) and the formation of the oxide. Once a small amount of oxide scale of thickness x has grown, cations and electrons travel towards the oxide-gas interface and oxygen in the opposite direction in order to continue with the reaction.

The electrical neutrality of the oxide lattice must be preserved; therefore the number of cations must be equal in number to the amount of vacancies in terms of flux as:

$$j_{M^+} + j_{V_M} = 0 \tag{2.2}$$

where j_{M^+} represents the flux of ions across the scale and j_{V_M} the flux of vacancies created at the oxide gas interface. This condition can be combined and represented mathematically using the first law of diffusion proposed by Fick applied to the vacancies concentration expressed as:

$$-j_{V_M} = D_{V_M} \frac{C^2{}_{V_M} - C^1{}_{V_M}}{x} \tag{2.3}$$

where D_{V_M} is the diffusion coefficient of metal vacancies, $C^2{}_{V_M}$ and $C^1{}_{V_M}$ the concentration of metal vacancies at the oxide-gas and metal oxide interfaces respectively.

It is important to note that the concentration of cation or anion vacancies are determined by the value of the partial pressure of oxygen found at each interface and in this case, the vacancies are generated in the oxide-gas interface and consumed at the opposite interface. As the equilibrium is fixed at the each interface, the term $D_{V_M}(C^2{}_{V_M} - C^1{}_{V_M})$ can be considered as a constant and included in a term namely k so that the change in thickness x with respect to the oxidation time t can be expressed as:

$$\frac{dx}{dt} = \frac{k}{x} \tag{2.4}$$

Arranging the terms of the equation equation 2.5 gives that:

$$\int x dx = k \int dt \tag{2.5}$$

After the integration of above equation, the final expression gives:

$$x^2 = 2k_p t \tag{2.6}$$

Equation 2.6 represents the mathematical expression of Wagner's theory of high temperature oxidation of metals, where x represents the thickness of the oxide layer measured throughout the oxidation time t and k_p is know as the parabolic rate constant a term that intrinsically includes the mobility of cations and electrons due to the gradients of chemical potential established across the oxide scale and the electrical conductivity of these species. The shape of the curve obtained by plotting equation 2.6 adopts the form of a parabola, but more important is the physical meaning of this theory, a feature that will be discussed during the next sections of this chapter.

2.5 Oxidation kinetics

Three oxidation kinetics modes have been proposed along the years as the basic behaviours that rule the oxidation of metals, these are:

a) Linear rate oxidation
b) Parabolic rate oxidation
c) Logarithmic rate oxidation.

The occurrence of one or another type depends on factors such as the nature of the metallic system (i.e. pure metal or an alloy of various species), temperature and oxygen partial pressure among others. However, in practice it is common that each mechanism may be present on its own or be a combination of mechanisms depending on the exact conditions. Although determination of the oxidation mechanisms based only on oxidation kinetics for metal or alloys is almost meaningless, these curves need to be combined with diffusion data, partial pressures data and results from previous works when the rate controlling mechanism for the oxidation of a metal or alloy is to be explained (Kofstad, 1966).

2.5.1 Linear rate of oxidation

For linear oxidation, the relationship between x and the time follows a proportional pattern (Fig 2.5 a). This rate is normally associated with the formation of non protective oxide scales or the oxidation of metals that form volatile oxides, because under these conditions, it could possible that bare metal will be always available to react with the oxygen contained in the atmosphere, being the supply of oxygen ions the rate controlling process that governs this oxidation rate. Mathematically, this behaviour is expressed as:

$$x = k_l t \tag{2.7}$$

where k_l is the linear oxidation constant and t is the exposure time to the oxidant atmosphere.

2.5.2 Parabolic rate of oxidation

The parabolic oxidation rate of metals has been normally associated with uniform diffusion of ionic species and electrons across a compact, defect free oxide scale. Fig.2.5 b) shows the graphical representation of this behaviour, characterized by a rapid initial oxidation rate followed by a progressive reduction as the oxide scale grows on the surface of the metal. Many metals and alloyed systems oxidize following a parabolic trend, although the attainment of this kind of behaviour depends strongly on conditions like the temperature of the system, the partial pressure of oxygen and the composition of the oxidant atmosphere. In equation 2.6, k_p is defined as the parabolic constant and has units of mg^2/cm^4-s, when the mass gain per unit of surface area is followed or $cm/s^{1/2}$ when the thickness of the oxide scale is measured.

2.5.3 Logarithmic rate of oxidation

This behaviour is represented by equations 2.8 and 2.9 for the direct and indirect logarithmic relations respectively. Logarithmic relations have been associated with the oxidation of metals and alloys at low temperature or with the development of thin oxide films and is graphically represented in Fig.2.5 c), characterized by a rapid initial stage sometimes greater than that observed for the parabolic behaviour in the same time interval, followed by an abrupt reduction in the rate of reaction.

The rate controlling mechanism for the reactions developed in this regime has been associated with the establishment of electrical fields across the oxide layer as a result of the tunnelling of electrons to maintain the electrical balance of the oxide lattice when oxygen ions are adsorbed in it. Evans, 1960 proposed another theory to explain the occurrence of the logarithmic rate based on the existence of cavities formed as result of vacancies concentration at the metal-oxide interface that reduce the surface area where

anion and cations are mobile, slowing the rate of reaction of metals. Two equations are normally proposed for describing this behaviour:

$$x = k_L \log(t + t_0) \tag{2.8}$$

$$\frac{1}{x} = A - k_L \log t \tag{2.9}$$

where A and k_L are constants, x is the variable used to quantify the oxidation phenomenon and t is the oxidation time.

2.6 Oxidation of iron

Not surprisingly, the oxidation of iron has been studied for many years given the extensive use of iron and steel under oxidative conditions. At one atmosphere pressure and for temperatures above 570°C, three oxide phases grow on the surface of pure iron namely Wüstite FeO, magnetite Fe_3O_4 and hematite Fe_2O_3, growing in this order from the metal oxide-interface in direction to the oxide-gas interface. Below 570° C, the Wüstite phase is not thermodynamically stable as indicated in the phase diagram of Fig.2.6 and therefore oxide scales formed at lower temperatures consist mainly of magnetite and hematite. Above this temperature, Wüstite becomes a stable constituent of the oxide layer normally increasing its thickness as the oxidation temperature of the metal in the system increases.

Although the mechanisms that describe the formation of the three iron oxide phases at high temperature can be found with fine detail in many text books (Kubaschewski, 1953, Kofstad, 1966, Birks and Meyers, 1983, Khanna, 2002) a brief explanation of the oxide formation process at temperatures above 570°C will be discussed in this section based on the diagram shown in Fig. 2.7.

At the metal-oxide interface, iron is ionized with the resultant release of cations and electrons, these constituents reduced magnetite at the Wüstite-magnetite interface to produce Wüstite FeO. Divalent $Fe^{2+}$and trivalent Fe^{3+} ions plus electrons move across the magnetite layer and react at the magnetite-hematite interface to form magnetite Fe_3O_4, the second constituent of the oxide layer. Finally the third constituent of the oxide layer, hematite Fe_2O_3, is produced in two ways; one implies the reaction of oxygen and iron ions at the magnetite-hematite interface due to the ionization of oxygen by the electrons released from Fe^{2+} ions and the other implies the reaction of excess trivalent Fe^{3+} ions and electrons with oxygen dissolved in the hematite layer. At temperatures above the instability point (570°C), the proportion of these components in the oxide layer is a ratio of about 95:4:1 (Birks and Meyers, 1983).

2.6.1 Oxidation of iron under the action of gaseous atmospheres

The formation of the three oxide layers on the surface of iron can be considered only as an idealized case because, under certain conditions, these layers are present on the surface iron or iron alloys in different proportions including modifications to their structure and properties due to the presence of certain chemical elements.

In practical applications such as high temperature forming processes, iron or its alloys are inevitably oxidized. Oxygen is rarely present as a pure gas, but usually in the oxidant atmosphere in the form of combustion products such as carbon monoxide (CO), carbon dioxide (CO_2), sulphur dioxide (SO_2), water vapour or simply air. Depending on the amount and type of the components of the oxidant atmosphere these gases alone or combined will influence the rate of oxidation, and accordingly the effects of the environment on oxidation have been studied for many years. In this section, the effect of oxygen, air and water vapour on the oxidation characteristics of iron are reviewed.

As a first example, Caplan and Cohen (1966) studied the oxidation of high purity iron in dry oxygen in order to identify the effects of the degree of cold work (Table 1) imposed on specimens on the oxidation rate and the oxide phases obtained in the

temperature interval between 400 and 650°C. Quasi parabolic kinetics were obtained for all the test conditions (Fig.2.8). They observed that annealing the specimens reduced the rate of oxidation, promoting the development of a porous oxide scale which had poor adherence to the substrate. The scale contained substantial amounts of hematite rather than magnetite up to 600°C. For the same test procedures and temperatures, but for conditions in which the specimens where only abraded prior the oxidation test, the rate of oxidation was greater when compared with the annealed specimens. This resulted in compact oxide layers of good adherence to the substrate, containing magnetite as the preferential phase obtained under this condition.

Caplan and Cohen explained the differences in the oxidation behaviour obtained based on the generation of vacancies for each condition. In the annealed specimens, the vacancy flux was established in the direction of the metal-oxide interface, which condensed at this interface, creating pores and cavities. The poor plasticity of magnetite resulted in separation of this layer from the substrate and preferential growth of hematite at the expense of the separated layer (Fig.2.9). In contrast, in the specimens that were abraded prior oxidation, the oxide microcrystallites formed in the abraded areas acted as a path for the diffusion of oxygen ions in the direction of the metal oxide interface. This compensated the loss of metal ions by filling the empty spaces, promoting the even development of an oxide layer of good adherence to the substrate. In addition to this mechanism, the existence of defects in the metal could also dissolve the vacancies generated. At 650°C, the oxidation rate and the development of oxide phases was similar for both specimens, and this was related to the existence of Wüstite FeO, a fairly plastic oxide layer that may suppressed the pores formed when expanded laterally.

In a different study, Caplan (1966) studied the effect of cold work on the oxidation resistance of pure iron and various Fe-Cr alloys ranging between 10 and 26 wt% Cr having water vapour as oxidant atmosphere at 600°C, based on the premise that the imposing a certain of degree cold work increased the oxidation resistance of stainless steels in water vapour. Caplan found that specimens of pure iron oxidized under the action of water vapour presented the same mass gain (Fig.2.10 a) regardless of their

preparation condition prior testing (abraded or annealed). This is contrary to the observations found in the previous study for specimens oxidized in dry oxygen, where the mass gain was higher in the abraded specimens. It was also found that for the alloys with chromium content between 10 and 16 %wt, the oxidation of rate, expressed by a parabolic relationship, was higher for mechanically worked specimens after 10 minutes and 20 hours exposure. However, for oxidation times of this order, the mass gained was almost the same for samples containing up to 14 %wt Cr either abraded of annealed (Fig.2.10 b). Increasing the chromium content of the alloys reduced the oxidation rate considerably for the specimens in the abraded condition whereas annealed specimens were oxidized considerably. Caplan explained these differences based on the suppression of the internal oxidation phenomenon due to the high diffusivity of chromium in the alloy in addition to the protection offered by an outer layer of $(Fe,Cr)_2O_3$ spinel formed in the specimens that received mechanical work.

According to Surman and Castle (1969), the oxidation products resulting from the exposure of pure iron and steel to atmospheres containing water vapour at 500°C consist of a double layer of magnetite, with the outermost layer formed by solid state diffusion of Fe cations across the oxide layer in the direction of the oxide-gas interface. Contrary to normal wisdom, Surman and Castle proposed that the diffusion coefficient of oxygen in magnetite was too low to promote the diffusion of this element across the scale in order to form the inner layer. Instead, they proposed that the transport of the cations across the scale could be determined by the formation of volatile hydroxides $Fe(OH)_2$. They based their hypothesis on observations made to the oxide microstructure in order to prove the existence of pores and micro channels in the oxide as well as using calculations of the oxidation rate k_p as a function of the partial pressure of water and oxygen. Another important aspect of this investigation is that for the oxidation of chromium containing steels, Cr ions remained as part of the innermost scale because of the impossibility of chromium to from volatile species.

Tuck *et al.* (1969) studied the effect of the addition of water vapour to oxygen on the oxidation characteristics of iron and mild steel at 950°C for samples having

geometries of rod or sheets and compared the results obtained against previous results for the same materials and geometries obtained under the presence of dry oxygen. In all cases, the addition of 12 % vol of water vapour to dry oxygen increased the oxidation rate of the specimens described by a parabolic relationship (Fig.2.11 a), regardless of whether the samples were preheated in argon or under the action of the oxidant mixture. In addition, depending on the oxidant atmosphere the specimens were exposed to, different oxide structures were identified by cross section analyses. For example, the materials oxidized in dry oxygen developed porous scales with bad adhesion to the metallic substrate having magnetite as the predominant phase, whereas the oxide scale obtained in the mixture oxygen-water vapour consisted of an adherent compact oxide layer containing no pores and whose growth was observed preferentially for specimens in the from of sheets.

Tuck *et al.* commented that the slope of the parabolic region in the oxidation rates observed for iron specimens exposed to oxygen with steam, steam, oxygen or, dry air atmospheres was nearly of the same order for all the testing conditions (Fig.2.11 b) so that the effect of water vapour on the oxidation rate was not so clear. Therefore they concluded that the effect of water vapour on the increment of the reaction rate was associated with the preservation of the compactness as well as the lack of the porosity of the oxide layer along the oxidation process. These characteristics were preserved by the presence of hydrogen in the oxide scale either as a diatomic molecule (H_2), hydroxide ions (OH^+) or as steam (H_2O). These molecules enhanced the activity and mobility of dislocations within the oxide layer promoting the creep and plastic flow of the oxide layer, improving the ability of the oxide to annihilate the pores created by condensation of vacancies, facilitating the diffusion of ionic species across the oxide.

Jansson and Vannerberg (1971) analyzed the effect of the oxygen pressure on the oxidation rate of iron samples (99.998%) with a certain degree of cold work. Cold working of the surface increased the oxidation rate. The parabolic oxidation rate of the cold worked material decreased when the oxygen pressure was increased from values varying from 0.02 to 1.0 atmospheres (Fig.2.12 a and b). This phenomenon was related to

the nucleation and growth of Fe_2O_3 whiskers parallel to the substrate that protected the surface of iron and made the oxidation phenomenon difficult to continue at temperatures between 500 and 625°C.

Baud *et al.* (1975) studied the influence of humidity additions to dry air on the oxidation behaviour and scaling characteristics of pure iron (99.998%) and iron alloyed with 5% wt carbon, oxidizing samples of these materials at 700°C in atmospheres containing dry air, ambient air with 1-2% water vapour and dry air saturated with 31 % water vapour. It was observed that the thickness of the oxide layer formed on the alloyed iron increased as water was added to dry air, whereas the thickness of the oxide layer that grew on pure iron remained practically the same values regardless the oxidant atmosphere (Fig.2.13).

It was also observed that the addition of water to the oxidant atmosphere also improved the adherence of the oxide to the surface of alloyed iron. This was attributed to the formation of a porous FeO layer next to the metallic substrate. However, water did not have a significant effect in the oxide layers that grew on pure iron because good adherence and low porosity was observed in all cases regardless the humidity content of the oxidant atmosphere. These findings were corroborated when the phase content of the oxides was measured in the alloyed iron, showing that for the samples oxidized in dry air + 31 % water vapour and 1-2 % water vapour, Wüstite comprised 90 % and 40 % of the oxide layer respectively, while in dry air Wüstite was not present at all and the layer comprised only of magnetite and hematite, which grew at the expense of Wüstite, suggesting separation of this layer from the substrate. The three iron oxides were present in all the oxidant conditions experienced by the samples of pure iron.

The oxidation rates observed for the alloyed iron increased marginally as the water vapour content of the oxidant mixture increased when compared to those of pure iron where the oxidation process occurred at a higher rate, with no visible differences whether the samples were oxidized in water or dry air. For all these cases parabolic oxidation kinetics were observed. It might be that in this work the effect of water vapour

on the oxidation of the materials studied was the same observed by Tuck *et al.* (1969) where the presence of hydrogen stimulated the plasticity of the oxide layer maintaining its compactness by increasing the disorder in the oxide structure due to the existence of hydrogen and water vapour molecules.

Taguchi and Suzuki (2006) analyzed the differences in the oxidation rate of three grades of iron that differed in the amount of oxygen dissolved within them prior the tests, and that were oxidized at 850°C in atmospheres containing dry or ambient air. The mass gained by the samples exposed to ambient air exhibited greater mass gain compared to the samples exposed only to dry air. For each test condition, the samples containing the minimum amount of dissolved oxygen resulted in the greatest mass gain compared to those containing more impurities (Fig.2.14). Taguchi and Suzuki also compared the results of oxidation experiments completed for pure iron at 700°C in both ambient air and dry air finding that the oxidation of iron was slightly higher in ambient air than that observed in dry air. This contradicts the results obtained by Baud *et al.* (1975) for pure iron where no significant variations were found for the experiments conducted in ambient air and dry air, as previously discussed. The justification for these variations was related to the differences in the amount of water vapour present in ambient air for both conditions that for the case of Taguchi was less than $6x10^{-3}$ g/m^3 and for Baud's conditions of about 14 g/m^3. They concluded that although the influence of humidity seemed small, small amounts of water can have a considerable effect on the oxidation of iron as suggested in the electron micrographs taken to the surface of the iron samples shown also in Fig.2.14.

2.6.2 Oxidation of Fe-Cr alloys and steels under the action of gaseous atmospheres

The oxidation in dry air at 800°C of a Fe-Cr alloy containing 3 %wt chromium was studied by Kahveci and Welsh (1986). They found that the oxidation kinetics of the alloy was characterized by an initial parabolic stage that was followed by inverse logarithmic behaviour (Fig.2.15 a). The development of the first oxidation stage was believed to be associated to the uniform diffusion of iron and oxygen ions across the

scale, promoted by the existence of abundant grain boundaries that acted as easy pathways for the migration of these species as well as a thin Wüstite layer formed next to the substrate due to a chromium depletion in this zones observed during the early oxidation stages up to 35 minutes.

The reduction in the oxidation kinetics found in the second stage characterized by a logarithmic trend was explained in terms of three factors: a) the development of a spinel next to the metallic substrate of the form M_3O_4 and M_2O_3 that exhibits low diffusion rates for Fe and Cr ions, b) the nucleation and growth of a columnar layer of α-Fe_2O_3 (Fig.2.15 b), that increased the thickness of the scale and therefore increased the diffusion distances and, c) the growth of coarse grains in the outer α-Fe_2O_3 that reduced the diffusion paths for oxygen ions.

Cory and Herrington (1987) pointed out that duplex scales grow by oxidation of metals in steam and oxygen and under this premise studied the influence of super heated steam on the oxidation behaviour of ferrous alloys containing chromium in amounts varying between 0 and 9 %wt with additions of molybdenum and niobium, at temperatures between 450 and 550°C under the action of various gas pressures. They found that the oxidation rate was parabolic and independent of the steam partial pressure, and increased when the temperature for oxidation increased, showing the opposite effect for reductions to the chromium content of the alloys.

The oxide layer formed on the alloy for all the experimental conditions was characterized by the formation a double oxide layer, comprised of an inner fine grained oxide layer of Fe-Cr spinel (M_3O_4) and magnetite as well as by an outer magnetite layer with columnar grains perpendicular to the alloy substrate. The spinel layer was formed by internal oxidation caused by inward diffusion of oxygen, possibly through pores or defects within the layer, and was deficient in iron but rich in chromium. Similar features were also observed for alloys with higher chromium content.

Cory and Herrington pointed out that during the oxidation process, pores were developed in the magnetite phase in the sample containing 2.25 %wt Cr suggesting that the oxide layer was permeable to hydrogen gas. The formation of hematite whiskers was found as a common phenomenon in samples that did not contain chromium and based on this they concluded that chromium may suppressed the formation of hematite structures in the alloys where this element was present.

Chang and Wei (1989) commented on the effect of water vapour, oxygen and air on the oxidation behaviour of steels and also summarized the effect of alloying elements in the scaling behaviour of the alloys. They pointed out that water vapour transports oxygen ions across the oxide scale in the direction of the metal surface. Once there, this molecule dissociates resulting in the production of oxygen that reacts with iron ions to produce more oxide but also liberating hydrogen, a reducing agent, resulting in a process that favours the production of more iron ions and water molecules, establishing a redundant cycle of reactions across the oxide scale. They also commented that in systems containing a mixture of water vapour and oxygen the oxidation rate increases with the water vapour content up to saturation values, and in systems that contain mixtures of water vapour and hydrogen, the rate of oxidation of the steel decreases as the amount of hydrogen increases. On the effect of alloying elements on the scaling behaviour of steel, they pointed out that alloying steel with chromium also results in the suppression of Wüstite at temperatures above 570°C when the chromium content exceeds 2.5 %wt, resulting in the growth of oxide layer that include only magnetite and hematite.

Simms and Little (1988) studied the oxidation rate and the oxide structures formed on the surface of a steel containing additions of chromium (2.5 %wt) and molybdenum (1% wt) under the presence of dry oxygen at 600 and 650°C for oxidation times up to 100 hours. The oxidation rate of the steel samples at these temperatures was parabolic (Fig.2.16 a), the greatest mass gain obtained at the highest temperature at which the steel was oxidized. Based on measurements made by EDX on fractures surfaces of the oxides, they found that in most cases the oxide layer as a whole was comprised of an inner fined grained structure of spinel M_3O_4, followed by an intermediate layer of

columnar magnetite Fe_3O_4 grains which was thicker than the outer layer of hematite Fe_2O_3 (Fig.2.16 b and c). Simms and Little pointed out that the growth of these oxide structures depended on the flux of cations and anions through the oxide scale. They also explained that the growth of the intermediate magnetite layer was caused by a deficit in oxygen observed in the hematite layer that fails to complete the oxidation process, giving the opportunity for magnetite to nucleate and grow at specific sites between hematite and the spinel layer.

Walter *et al.* (1993) analyzed the isothermal and cyclic oxidation behaviours of a steel alloyed with chromium (12 %wt), molybdenum (1 %wt) and vanadium (0.25 %wt) under the action of air, air with sulphur dioxide SO_2 and a mixture of argon, hydrogen and 50 % water. By comparison with the results obtained from isothermal oxidation tests in dry air and the tests carried out under the presence of water, they found that under both conditions the steel was oxidized following parabolic kinetics, the thickness of the oxide layer developed under conditions containing moisture considerably greater than that formed in dry air. The oxide phases present in the oxide layers obtained were also different depending on the oxidant atmosphere (Fig.2.17 b) and c). The oxide scale formed in the environment containing water vapour was similar to that observed by Simms and Little (1988), comprising a layer of spinel M_3O_4, an intermediate layer of magnetite Fe_3O_4 and an outer layer of hematite Fe_2O_3, whereas the samples oxidized in dry air and dry air mixed with sulphur dioxide only a thin layer of spinel M_2O_3 was present on the surface of the steel.

Laverde *et al.* (2004) studied the isothermal oxidation behaviour of a T91 steel containing 8.51 %wt chromium and small amounts of alloying elements similar to those found in the composition of a high speed steel (typically vanadium, molybdenum tungsten). They conducted isothermal oxidation experiments at temperature intervals between 575 and 650°C under the presence of a mixture of argon and steam produced at 90°C to give a relative humidity of 70 %. The oxidation kinetics of the samples quantified by both mass gain and thickness resulted in parabolic relationships for all the test temperatures, the values of the variables used to measure the oxidation rate increasing

with the temperature of the tests. For all the temperatures, the scale comprised an outer compact hematite layer (Fe_2O_3), a porous intermediate Fe_3O_4 and an inner layer of $(Fe,Cr)_3O_4$ spinel. The magnetite layer seemed porous being attributed to the release and presence of gaseous products and reactants through the scale that exist in the reaction established between magnetite and water vapour to form hematite represented as:

$$2Fe_3O_4 + H_2O \rightarrow 3Fe_2O_3 + H_2 \qquad (2.10)$$

Laverde *et al.* pointed out that at 600°C and for long exposure times, hematite was the dominant phase present on the surface of the steel and concluded that the development of the oxides structures obtained under the presence of water vapour give a protective character to the steel that at some point could diminish the reaction rate of oxidation.

Ehlers *et al.* (2006) studied the influence of additions of water vapour up to 7 % vol to a mixture of nitrogen and oxygen on the oxidation rate and the characteristics of the oxide scale formed on a P91 heat resistant steel containing 9 % Cr oxidized at 650°C. By comparison with tests carried out using the dry mixture and the mixture containing water vapour additions (Fig.2.18 a), they found that the oxidation of the steel increased as the water vapour content in the environment increased and that small additions of water to environments with low oxygen content promoted considerable changes in the oxidation rate as the water vapour content in the mixture was increased.

The differences found in the compositions and morphologies of the oxide layer were also remarkable. The oxide layer developed on the steel exposed to dry conditions developed a compact structure containing a chromium rich spinel formed next to the steel substrate and a thick hematite layer. The oxide layer grown on the samples of the steel exposed to the conditions containing moisture revealed the presence of several layers that included the development of an internal oxidation zone, a zone containing a mixture of

magnetite and a chromium rich spinel M_3O_4 followed by a porous layer of magnetite and finally a thin outer hematite layer (Fig.2.18 b).

Ehlers *et al.* explained the differences of these phenomena based on the permeation of water molecules into the oxide layer that were responsible for the acceleration of the mass intake as well as the development of porosity in the magnetite layer observed in the samples exposed to water vapour. These pores were created by the formation of volatile species of iron hydroxide from the reaction of magnetite and hematite with water molecules at sites where the dissociation of water molecules to produce oxygen and hydrogen was established. The establishment of these reactions was considered the main mechanism that promoted the ionic transport across the scale and that resulted in the pronounced increments of the oxidation rate observed under the presence of water vapour. This clearly contrasts with the mechanisms observed in dry conditions where oxygen was the only oxidant molecule existent in the environment available to oxidize the steel. They concluded that the oxide scales formed in water vapour are more permeable to water molecules rather than to oxygen molecules, therefore a competition between the molecules to oxidized the steel is established, competition where water molecules are preferred and that is controlled by the ratio of partial pressures pH_2O/pO_2.

2.7 Energy for oxidation in hot strip mills: heat transfer processes

High temperature oxidation is a common phenomenon found in the finishing stands in hot strip mills. The oxide develops in both strip and rolls as a result of the high temperature gradients experienced by the strip whose temperature normally varies between 800 and 1200°C. Particularly, the heat flux transferred from the strip to the work rolls is of great importance because it determines the temperature field experienced by the work rolls and to a certain point it could define the amount of oxide that could grow on their surface. Values of heat transferred to the work rolls between 5 and 12.5 MW were calculated by Colás (1994) depending on the thickness of the steel strip laminated in a compact steel mill.

2.7.1 Heat transferred to the work rolls

In the finishing stands of hot steel strip mills, the work rolls are heated mainly by conduction caused by the contact with the high temperature strip normally found in the temperature interval between 800 to 1200°C depending on the position of the stand. Investigations focused on determining the heat transferred to the work rolls and the values of thermal gradient imposed on their surface in hot strip mills are varied. Devadas and Samarasekera (1986) studied the heat transfer phenomena in the finishing stands in hot strip mills based on calculations made by means of a one dimensional mathematical model of the process. They found that the temperature on the surface of work rolls varied when different lubricants were used and calculated maximum and minimum temperatures reached by the work rolls giving values comprised between 620 and 250°C when the rolls were in contact with the strip whose temperature was 1100°C. Reductions in temperature comprised between 50 and 90°C where observed during the simulation of the cooling practices of the rolls (Fig.2.19).

Huan *et al.* (1995) developed an iterative bi dimensional mathematical model to predict the heat flux transferred to the work rolls as well as to calculate the distribution of temperatures on the surface based on the premise that these calculations are important to understand wear and friction phenomena as well as to improve cooling practices. The model took into account the temperature fluctuations measured on the surface of the work rolls during real operation conditions and that were in the order of 500°C to 50°C for heating and cooling stages respectively. Using this model, temperatures on the roll surface between 400 and 450°C (Fig.2.20) were predicted during the heating stage finding good agreement between measured and predicted values.

Guerrero *et al.* (1999) simulated the heat transferred from the strip to the work rolls located in the finishing stands of a hot strip mill, based on the development of four mathematical models that considered gains and losses of heat occurring in the roll depending on angular positions. Depending on the model and the initial temperature of the strip, maximum temperatures reached by the surface of the rolls were predicted

between 315 and 550°C (Fig.2.21 a and b). The variations found in the temperature values were related to the accuracy of the model used to compute the calculations in each case. The minimum temperature values of the roll surface during the cooling stage were computed between 20 and 85°C and it was also appreciated that the thermal cycles imposed on the surface of the rolls were repeated at intervals of 20 *m*s.

Pérez *et al.* (2004) studied the thermal behaviour of high chromium (Hi-Cr) iron and indefinite chilled work rolls using an analytical mathematical model of the heat transferred from the strip to the roll. The model took into account the variation of the strip temperature and the roll temperature profile along a complete rolling campaign. They predicted a maximum temperature of the roll surface of 650°C for the heating stage and a minimum temperature of about 90°C when cooling was applied by means of spayed water on their surface, the thermal cycle being repeated for time intervals of almost 1 second (Fig.2.22).

Sikdar and John (2006) pointed out that variations in the roll profile resulting from thermal expansion have a direct impact on the surface quality and dimensions of the rolled strip and solved a two dimensional mathematical model of the contact strip-roll in order to study the temperature fluctuations of the work rolls along the finishing stands. Dividing the work roll diameter in different characteristics zones depending on the nature of the heat transfer mechanism, they calculated the temperature profile of the roll surface finding that it follows a cyclic path increasing up to 620°C when in contact with the strip but being rapidly reduced down to 25°C as water was applied onto the surface (Fig.2.23).

2.8 Oxidation of work roll grade materials

As noted earlier, the work rolls are exposed to an aggressive oxidative environment that includes features such as the high temperature of the stock, the cooling water sprayed onto their surface and the water vapour generated as a product of the cooling practices. These features provide the necessary conditions to promote the growth of an oxide scale on the surface of the rolls as a layer that could alter the working

conditions of the subsequent stands but more importantly the final surface quality of the strip.

Work roll oxidation is also enhanced by the development of cracks generated on the roll surface, as a result of thermal fatigue commonly named "fire cracks" and that are propagated internally in the radial direction through the net of carbides present in the microstructure. These cracks act as oxygen pathways that promote the development of internal oxidation processes causing further loss of roll material, particularly where the cracks coalesce, as reported by Colás *et al.* (1999).

Although different metallurgical strategies and processes have been developed along the years to manufacture work rolls that withstand the severe working conditions found in hot strip mills, the oxidation phenomena remains present. A major concern is that the growth characteristics, behaviour and influence of this layer on the processes have been barely studied, and only a few studies have been undertaken in order to characterize the oxide layers, accordingly the existing knowledge is reviewed in the following sections.

Molinari *et al.* (2000) studied the isothermal oxidation of two high-speed steel work rolls with different chromium content (3 and 5 %wt), conducting thermo-gravimetric analysis (TGA) experiments in dry air at 500, 600 and 700°C for oxidation times up to 25 hours. They found that the oxidation processes initiated at the matrix-carbide interface, being the matrix more likely to oxidize rather than the carbides which presented a high resistance to oxidation. At all test temperatures the samples followed a parabolic behaviour except for the samples with the highest chromium content oxidized at 700°C where a transition from parabolic to a lower oxidation rate was observed (Fig.2.24). This reduction in oxidation rate was attributed the formation of an inner chromium rich spinel layer of the form M_3O_4 (M= Fe, Cr) next to the steel substrate.

In later work Molinari *et al.* (2001) studied the influence of the microstructure and the chromium content on the isothermal oxidation behaviour of high-speed steels (Table

2) in dry air at 700°C. They found that samples having chromium contents varying between 3-5 %wt presented low oxidation resistance. This was attributed to the high volume fraction of the carbides dissolved in the microstructure and that accounted for a reduction of the chromium content in the matrix reducing its resistance against oxidation expressed mathematically by a parabolic relationship (Fig.2.25 a).

They also commented that as a high content of carbides was present in the steels, the number of nucleation sites for oxidation defined as matrix-carbide interfaces were also a high factor that contributed to increase the oxidation phenomenon given that oxidation occurred preferably at these locations. In addition, they observed that samples containing greater amounts of chromium (between 10-12 %wt), developed a low carbide volume fraction and therefore a chromium rich matrix that improved its properties against oxidation expressed as a transition from a parabolic oxidation to a lower oxidation rate (Fig.2.25 b). They concluded that the oxidation rate of the steel was strongly related to the volume fraction of the carbides and the properties of the matrix as suggested in Fig.2.25.c).

In order to model the growth of the oxide scale on the surface of high-chromium iron work rolls (Hi-Cr) (Table 3), Gonzalez *et al.* (2001) conducted oxidation experiments in dry air using material taken from sections of real work rolls at temperatures between 400 and 600°C for oxidation times up to 32 hours. After completion of the experiments, the resultant oxide scale was comprised by layers of magnetite (Fe_3O_4) and hematite (Fe_2O_3), whereas Wüstite (FeO) was not detected during scan, feature attributed to the transformation of this phase to magnetite.

The oxidation kinetics of the roll samples was represented by parabolic relationships at all temperatures (Fig.2.26 a) having a time exponent of 0.2 rather than 0.5 (see equation 2.64 in Section 2.4) even though the plots look logarithmic at first instance. Based on these data, an apparent activation energy Q for the oxide growth was calculated and used for the development of a time compensation parameter used in order to simulate the growth of the oxide scale under thermal cycling conditions. Under these conditions,

they predicted the growth of the oxide scale as a function of the passage of several slabs taking into account the thermal cycling of the rolls (Fig.2.26 b).

Kim *et al.* (2003) investigated the influence of the oxidant atmosphere on the oxidation behaviour of various high-speed steels (Table 4), conducting isothermal thermo-gravimetric experiments at 600°C for exposure times up to 1 hour. In the presence of dry oxygen, the steel matrix was oxidized together with MC-type carbides, forming oxide structures that were described as parallelepiped shaped oxide crystallites that presented a weak adhesion to the substrate. In the experiments conducted for samples exposed to a moist atmosphere (created by mixing argon and water vapour), only the matrix was oxidized, this was attributed to the low vapour pressure of oxygen in the environment that was not enough to favour the oxidation of the carbides present in the microstructure.

During the early oxidation stages, the growth kinetics of the samples oxidized in the dry atmosphere followed a parabolic oxidation rate that progressively changed into a linear one as the oxidation time increased. This trend was observed for the samples containing about 5.6 %wt Cr, whereas for the samples with about 9.4 %wt Cr, a complete parabolic behaviour was present (Fig.2.27 a) associated to the formation of a protective oxide layer of iron-chromium spinel. The oxidation behaviour of the experiments conducted in the wet atmosphere was parabolic; in all cases no transition to a lower or higher oxidation rate was reported (Fig.2.27 b).

The oxide layer in both experimental conditions comprised an inner layer of magnetite (Fe_3O_4) and an outer layer containing a mixture of magnetite (Fe_3O_4) and haematite (Fe_2O_3). The only difference related to the oxide layer obtained for each experimental condition was that through scale cracks appeared in the oxide scale formed in dry conditions that maybe were responsible of enhancing the diffusion of oxygen through the scale and therefore increased the oxidation rate. This feature was not observed for the oxides obtained in wet conditions, and was explained based on the relief of stresses as result of the formation of voids within the scale.

Monteiro and Rizzo (2003) studied the oxidation behaviour of three different high-speed steels (Table 5) exposed to dry and moist atmospheres, oxidizing samples at 750°C up to 240 minutes using a thermo balance of controlled atmosphere. For the experiments conducted in the dry atmosphere, a gaseous mixture of nitrogen and oxygen (N_2 – 20%O_2) was used, finding that the oxidation kinetics of the steels exposed to it followed a parabolic trend in most cases, except for the sample with the highest chromium content in which a linear behaviour was observed (Fig.2.28).

The moist atmosphere had the composition N_2-17.5 %O_2 -12.5 % H_2O and the oxidation kinetics resulted in a combination of the parabolic and linear behaviours for the sample with 4.4 %wt Cr, parabolic for the samples with 3.5 %wt Cr whereas for the samples with 7.5%wt Cr the rate was characterized a combination of various oxidation laws (Fig.2.28). In all cases the mass gained by the samples was greater under this condition.

The morphology and composition of the oxide scale was completely different depending on the oxidation conditions and the chromium content of the alloy. For the samples oxidized in a dry environment, the oxide scale had an irregular morphology, suggesting that selective oxidation of steel took place in zones close to high chromium concentrations in the scale (zones with carbides). The samples with a high chromium content exposed to the moist atmosphere showed the formation of a porous oxide scale rich in vanadium and chromium, related to the internal oxidation of vanadium and chromium-rich carbides. These layers were possibly responsible for decreasing the oxidation rate, acting as protective layers. Monteiro and Rizzo concluded that the chromium content and the composition of the atmosphere influence the oxidation behaviour of these steels, whereas the presence of tungsten in the steels did not affect the oxidation kinetics of the steel nor the composition of the oxide layer.

Ziadi *et al.* (2005) noted that the oxidation behavior of alloyed white cast irons work rolls (Table 6) in dry air is affected by the previous heat treatment applied to the material. The oxidation of samples in the interval of temperatures comprised between 500 and 600°C followed a parabolic trend (Fig.2.29.). The oxide layer produced contained

two main components hematite and spinel $FeCr_2O_4$, and its growth was also characterized by the selective oxidation of MC vanadium rich carbides. More importantly, Ziadi *et al.* pointed out that the oxidation phenomenon observed for this material accounts for the increments to the values of friction observed in the stands of hot strip mills using this kind of work rolls.

2.9 Influence of oxides on the tribology of forming processes

2.9.1 General approach

The growth of oxides on the surface of the tools used in high temperature forming processes particularly in the hot rolling of steel strip is almost inevitable and for this reason it is proposed that they can assume an active role when tribological aspects of the process like friction and wear are analysed.

The role of the oxides found in a particular process could be ambiguous. Whilst in some processes they can be considered as a solid lubricant that reduces friction, in other cases they could act as an abrasive particle that increases the wear rate of the material. In this section a brief review of some works that were focused on defining the role of oxide scales in forming processes are discussed.

Under the premise that a significant amount of the energy used in the forging of metals is required to overcome friction, Luong and Heijkoop (1981) studied the influence of thickness and composition of the oxide scale formed in the process on the value of the friction coefficient developed in the forging of steel. By means of ring compression tests at high temperature under controlled atmosphere, they found that the value of the friction factor decreased as the oxide thickness increased also noting a decreasing trend when the oxide scale was comprised mainly of Wüstite (FeO) (Fig.2.30). In contrast, friction increased when a considerable amount of hematite (Fe_2O_3) was present in the oxide and when the oxide scale was thin. They concluded that the friction behaviour is strongly influenced by the thickness of the scales rather than their composition, but remarked that

both factors have to be taken into account when friction dependant parameters in the process are to be analyzed.

Batchelor *et al.* (1986) commented that the wear mechanisms experienced by the components of tribosystems are strongly influenced by the properties and structure of the oxide layers present in the system. For this reason, different contact properties are expected for systems in which thin or thick oxide layers are present. They pointed out that the rate of growth of oxides depends on the oxygen source present in the system resulting in different growth rates if, for example, the source is the atmospheric air or a compound like water of carbon dioxide (Figure 2.31). They also pointed out that for iron and its alloys, the oxides formed in tribosystems have a protective character, being the grade of protection a function of the kind of oxide present and its ability to remain attached to the substrate. They commented that most of the experiments used to study the oxidation kinetics of the metals that participate in tribosystems are not representative of the real system because these frequently exclude important features intrinsic of the system like the presence of water, for example.

Tu *et al.* (1998) pointed out that wear of the dies used in the high temperature forging process can be related to a combination of various mechanisms including adhesion, abrasion but most importantly oxidation. In order to understand these mechanisms, they carried out high temperature low-sliding speed experiments between 400 and 600°C using a block on ring rig in which the block was manufactured of 5CrNiMo steel, the same material used as die in the real process. They found that the wear rate of the block decreased from 400°C down to a minimum value reached at 500°C and beyond this temperature value the wear rate increased again being a similar trend observed for the values of the friction coefficient (Fig 2.32 a and b).

Tu *et al.* noted the presence of ploughed grooves and wear debris when the temperature of the test was 400 °C, but a smooth and even oxidized surface was observed for the tests carried out at 500 °C whereas at 550 and 600 °C cracking of the oxide scale formed on the surface of the samples was observed. The X-ray diffraction analysis of the samples revealed the presence of Wüstite (FeO) magnetite (Fe_3O_4) and hematite (Fe_2O_3)

on the worn surfaces at temperatures higher than 500°C while no oxides were detected for the samples tested at 400 °C. They explained that for the samples exposed at 400 °C, the temperature was too low to promote the growth of oxide layer and abrasion by wear debris and hard asperities were the cause of damage on the surface of the ring, but as the temperature increased, the formation of oxide scale had a positive influence on the protection of the block surface and in the low value of friction coefficient observed.

A similar study to that of Luong and Heijkoop (1981) was developed by Munther and Lenard (1999) in which the influence of the oxide scale formed on the surface of low carbon steels was related to the variations of friction coefficient in the hot rolling process. They pre oxidized steel samples in various oxidant atmospheres to produce different thicknesses and immediately after the samples were deformed in an experimental rolling mill in order to measure the value of the friction coefficient.

An important finding is shown in Fig.2.33 where they represented the variation of the friction coefficient as a function of the temperature for a fixed oxide thickness. It is shown that for the samples with the thickest oxide scale, the friction coefficient had the lowest value compared with the samples that developed a relatively thin oxide layer, where the friction coefficient was high. They concluded that although thick scales have a significant influence on the reduction to the value of the friction coefficient in the processes, this oxide is not industrially desirable given the poor surface quality of the final product. Most importantly, they commented that it is necessary to develop a more accurate model to describe the friction conditions found in the hot rolling process of steel including the wear phenomenon of the work rolls.

2.9.2 The role of oxides on the wear of work roll materials

In hot strip mills, most of the attention related to oxidation phenomena has been dedicated to the study of oxides formed on the surface of the strip. The contribution and the impact of the oxides that grow on the surface of the work rolls to the tribology of the hot rolling process as well as to their tribological behaviour has been barely studied and

not well understood (Beynon, 2002). In this section the most important contributions of some works that analysed the effects of oxides on the wear properties of work roll materials are reviewed.

Kato *et al.* (1992) commented that features like the temperature and the Hertzian stresses produced by the contact work roll-back up roll are the main features that induce wear on the surface of work rolls. To study these features, they carried out experiments using a disc on disc configuration rig (Fig.2.34) in order to identify the wear mechanisms of high chromium iron (Hi-Cr) work rolls. Observations of the worn surfaces after the experiments revealed abrasion of the roll surface as the most common wear mechanism but quantification of the size, morphology and composition of the abrasive particles responsible for this, was not defined. They also stated that wear of work rolls was more severe near to the edges of the strip than at the centre because at this location a dark oxide layer protected the surface of the roll giving no information on the composition of such oxide layer.

Erickson *et al.* (1993) highlighted the protective character of the oxide scale formed on the surface of high chromium work rolls against wear, when they studied the banding process (excessive groove formation by abrasive particles) of high chromium iron work rolls. First they conducted oxidation tests on mechanically polished samples obtained from these rolls heating them up in a furnace up to 500°C for exposure times of about to 5 hrs in order to compare the composition of the oxide layer formed in this heat treatment against the composition of the oxide found on the surface of the real rolls. By means of glow discharge optical emission spectrometry (GDOES), it was found that the oxide layer on the heat treated samples had a higher chromium content than that observed for the samples taken directly from the roll surface. The composition of the oxide layer formed on the rolls during the process was determined by the analysis of X-ray diffraction patterns, showing that the predominant oxide was magnetite (Fe_3O_4).

Erickson *et al.* (1993) pointed out that roll wear can be strongly correlated to the adhesion and strength of the oxide scale that builds up on the roll surface and proposed

that this oxide layer results from the transfer of oxide from the stock surface to the roll surface, based on the lack of chromium found in the oxide layer formed on the surface of the work roll as well as the presence of the phase Wüstite (FeO).

Spuzic *et al.* (1994) commented that a considerable percentage of the final cost of rolled products in shape mills is credited to the performance of work rolls during operation and based on this statement summarized the main factors that contribute to the wear of work rolls used in the hot rolling process of steel sections (Fig.2.35). They pointed out that the selection of the appropriate work rolls for a certain application depends strongly on the wear mechanisms experienced by the rolls. These mechanisms are normally associated with the mechanical and environmental interactions found in a particularly rolling process, being abrasion, thermal fatigue and corrosion attack the principal causes for the rapid reduction in active life of work rolls. They also commented that oxide formation on the surface of work roll has a protective character, its properties established depending on the temperature reached by the rolls at their surface. They proposed that the formation of a black adherent magnetite (Fe_3O_4) oxide layer is a common feature in the oxidation of cast steel rolls at temperatures above 400°C and this layer is responsible for the reduction of friction as well as the wear of work roll in the process.

The interaction of the work roll surface with the oxides formed on the surface of the stock also plays an important role in decreasing the active life of the roll. Depending on the temperature of the stock, Wüstite, magnetite and hematite will coexist in different proportions having hardness values of 300, 450 and 1050 HV respectively. Hematite, as Spuzic *et al.* (1994) mentioned, is the principal source of abrasion of rolls followed in order by magnetite, both responsible of third body abrasion wear mechanisms as they form hard quasi-spherical particles. These two oxides affect greatly the surface of the roll contrary to Wüstite, which is protective in nature and considered to have lubricious properties.

Choi and Kim (1999) analysed the wear mechanisms present in high nickel grain work rolls using a high temperature disc on disc wear configuration, where a disc of this

material was brought into contact against a counter face of low carbon steel heated up to 850°C. By means of observations in the scanning electron microscope, they found that the degradation process of the roll surface started with the formation of a black oxide layer created due to the high temperature reached at the surface of the roll. The process continued and cracks resulting from thermal fatigue appeared on the surface of the roll disc causing the failure of the oxide layer and leaving exposed carbides on the surface. These carbides were responsible for picking oxide up from the counter disc at every revolution of roll disc increasing the thickness of the layer formed on the rolls. Choi and Kim concluded that the wear of the roll surface is entirely dependent on the formation of the protective black oxide layer and the sticking phenomenon developed by the carbides.

Colás *et al.* (1999) studied the surface of high chromium work rolls used in the finishing stands of a rolling mill in order to analyze the mechanisms that stimulated their deterioration during normal operational conditions. Samples of two different work rolls subjected to different rolling conditions and which failed at some stage during the processing of a rolling schedule were prepared for observation and analysed using scanning electron microscopy and X-ray diffraction. It was found that cracks nucleated on the surface of the roll due to thermal stresses resulting from heating and cooling practices and propagated in the radial direction of the roll through the net of the primary carbides existent in the microstructure of the material. These cracks also enhanced the subsurface oxidation process of the work roll material by the development of internal oxidation zones containing mainly hematite and some traces of magnetite (Fig.2.36). These oxides increased the wear processes in work rolls, when different cracks coincided and surrounded good non oxidized roll zones causing their further spallation (Fig.2.37).

Li *et al.* (2002) recreated the mechanical and thermal conditions found in a hot strip mill in order to investigate the wear evolution of high speed steel work rolls under the action of different loads and slippage ratios using a disc on disc configuration rig. They found that increments in the wear rate experienced by the steel coincided with increments in the values of load and slippage ratio. After analysis of the surface evolution of the roll materials after different cycles, they concluded that the loads applied are more

important because they determine the wear mechanisms that account for the deterioration of the roll surface, although these mechanisms were not clearly explained. It was also pointed out by Li *et al.* that the wear rate of the steel had minimum values during the early stages of the test due to the formation of a protective thin black layer of oxide on the surface of the rolls.

Hanlon and Rainforth (2003) studied the differences in the wear behaviour of conventionally cast and spray formed high speed steels using a rolling-sliding disc on disc configuration rig at different temperatures ranging between room temperature and 650 °C. The wear rate of the discs was higher in the conventionally cast material due to softening at temperatures above 300°C for conventionally cast, in contrast to the spray formed steel where a good resistance was offered by its fine microstructure. The wear mechanisms observed for both materials were a combination of subsurface preferential oxidation nucleated at the carbide-matrix interface and extended along grain boundaries, as well as the propagation of cracks nucleated in carbides due to the Hertzian stresses generated in the experimental conditions (Fig.2.38).

Pellizzari *et al.* (2005) analysed the wear mechanisms of work rolls using a high temperature disc on disc rig in which a low carbon disc simulating the stock at high temperature was brought into contact with a disc which simulated the roll, in conditions of no lubrication between the components. The materials for the manufacture of the roll disc components of the rig were high-speed steel and a high chromium iron.

Examination of roll discs after the wear tests revealed that the main wear mechanism of the work roll disc was abrasion attributed to the oxide scale formed on the disc that simulated the stock. Two characteristics zones were easily distinguished on the surface of the roll discs, judging by the amount of scratches present on the surface and by energy dispersive analysis EDX carried out in these distinctive zones. It was found that in the zones where fewer scratches were present, a hard oxide scale protected the surface of the roll disc. This layer was believed to have a positive influence on the wear rate of the samples by reducing its value, its formation attributed to the preferential oxidation of the

martensitic matrix the extent of which was less for high speed steels than for cast irons (Fig.2.39).

Milan *et al.* (2005) evaluated the friction and wear of high speed steel and white cast irons by means of reciprocating wear tests conducted at different temperatures, choosing this test mode based on the premise that it could recreate the mechanical stresses found at the work roll-stock interface. For both materials, they found that the friction coefficient had high values at low temperatures and at the early stages of the test followed by a stabilisation period prolonged to the end of the test. The value of the friction coefficient decreased as the testing temperature increased (Fig.2.40), and the samples exposed to high temperature showed mass gain rather than mass losses certainly due to oxide formation.

It was also found that the friction coefficient increased as the value of the normal load increased, phenomenon attributed to the increase of the contact area, and again, all the samples tested under this condition showed mass gain rather than mass lost. This phenomenon was justified based on the fact that increments to the value of the load increased the volume of the protective layer formed during the process, although no explanation about the physical meaning of this mechanism was given.

Experiments using pre-oxidized samples in air at 200, 400 and 600 °C revealed that the existent oxide layer did not influence the value of the friction coefficient nor the wear rate. The dominant wear mechanism identified by examination of the samples was abrasion, maybe by the combination of hard oxide particles and the carbides detached from the matrix both mechanically mixed at some point during the tests. Milan *et al.* (2005) commented that the protective layer formed at the interface could be formed of oxidized metallic debris spalled from the roll materials, layer that was sintered and compacted during the process.

In an attempt to clarify the effects of oxides formed on the surface of the roll and the stock in the hot rolling process of steel, Vergne *et al.* (2006) carried out high

temperature tests on a pin on disc configuration rig using alloyed white cast iron as pin material faced against a disc made of mild steel, under various loads and speeds. The aim of the tests was to identify the mechanisms that caused the variation of the friction coefficient at specific stages during the sliding tests (Fig.2.41) and relate them to the oxide formation on the surface of the work roll material, in order to provide a more accurate knowledge of friction and the wear mechanisms of work rolls during rolling.

Based on electron microscopy observations and microanalyses using EDX, they explained the friction behaviour in the following manner. The initial increment in the friction coefficient was due to the increase in the value of the shear force needed to break the junctions formed when the pin entered into contact with the oxide layer (Fig.2.41 and 2.42). The second stage, in which a reduction in the values of friction was observed, was due to the formation of a lubricant oxide layer on the surface of work roll material that included oxides from the matrix and oxides produced by the oxidation of MC niobium rich carbides. And finally, the increase in the value of friction shown in stage three was attributed to the failure of the oxide layer and wear debris generation responsible of increasing the superficial area. As the contact area increased, more junctions where created subsequently increasing the value of shear stress needed to break the new junctions formed.

While studying the effect of carbide size and distribution of high speed steel, Rodenburg and Rainforth (2007) agreed with previous studies done by Vardavoulias (1994) and proposed that the critical oxide thickness formed on the surface the high speed steel as well as the size of the carbides are the main factors that influence the resistance of steel against wear. They concluded that the high wear rates experienced by the steels at high temperatures obeyed to a relatively rapid oxidation of the carbide matrix interface as well as the static oxidation of MC vanadium rich carbides.

It can be summarized from the information presented in this literature survey, that there is a limited knowledge on the effects of the composition of the oxidant atmosphere on the oxidation rate and the microstructure of the oxide layer that grows on the surface

of high speed steel work rolls. It can be also identified that influence of the composition of the atmosphere present in a hot strip mill on the values of tribological variables that have a direct impact on the active life of high speed steel work rolls, like the wear rate and the friction coefficient has not been studied extensively. The study of these points represents the main objective of this investigation and accordingly, the experimental procedure designed for the analysis of these features and the results obtained from it are reviewed and discussed in the next chapters of this work.

Chapter 3

Experimental work

3.1 Introduction

In this chapter the experimental work developed to achieve the objectives stated in Chapter 1 is reviewed. This includes all the experimental information on the facilities that were created and used in order to study the isothermal and cyclic growth of oxides on the surface of the material and also describes the modifications that were made to other experimental facilities to fulfil the requirements of this investigation. The way in which the experiments were realized is reviewed.

3.2 Material of study

A work roll grade high speed steel whose composition is shown in Table 7 was selected as the material to be used in all the experiments. The material was in the form of roll discs specially created by Sheffield Forgemasters as test samples for earlier roll projects that involved the creation of a special rig designed to study features associated with the wear and thermal fatigue of the work rolls used in the stands of hot strip mills (Goodchild, 2001 and Mercado, 2003 respectively). The material was therefore as close to real roll material as is possible, without sectioning a full sized roll.

3.3 Microstructural characterization

Insufficient information on the metallurgy and the components of the high speed steel was available from the previous works, and therefore a comprehensive characterization of its microstructure was undertaken.

The roll discs selected for the manufacture of the test pieces were cut by spark erosion as they were too hard and large for conventional cutting methods. 1.5 cm cube shaped samples were produced by this technique directly from the discs. Metallographic analysis of the samples was carried out in the normal fashion by grinding one face of the specimens using various passes of abrasive silicon carbide (SiC) paper followed by a final hand polishing using diamond paste of 6 and 1 μm on hard and soft polishing cloths respectively. After the polishing procedure, the samples were etched by immersion in a solution of 5 % Nital (5% nitric acid HNO_3 and 95% ethylic alcohol CH_3-CH_2-OH) for 8 seconds.

Alternatively, in order to differentiate the components of the microstructure some samples were etched by an oxidation technique (Vandervoort, 1986) especially created for this material. The procedure consisted of etching the specimens with 5% Nital followed by induction heating to 600°C under the protection of an inert atmosphere of argon gas. After heating for 10 minutes, the argon flow was interrupted and replaced by compressed dry air injected at 500 cm^3/min for 3 minutes, sufficient to stimulate the growth of a very thin layer of oxide whose colour depended on the microstructural phase the oxide layer grew on.

After the oxidative etching, the samples were inspected using a POLYVAR optical microscope, with images taken digitally and analysed using the software Image Grabber PCI Ink. Samples were also examined by scanning electron microscopy (SEM) on a JEOL 6400 with energy dispersive X-rays detector (Oxford Instruments, ISIS software) for chemical analysis. Quantification in weight percentage of the composition of carbides and matrix was also carried out using an EDAX Pegasus EDX detector of a FEI Sirion field emission gun SEM.

The area percentage that the carbides occupied in the microstructure of the steel was measured by image analysis using the software Sigma Scan Pro 5. This analysis consisted of taking images of the microstructure of the steel at 250X using a backscattered electron imaging on a CAMSCAN S2 SEM and converting them to a black

and white image using Corel Draw, yielding black carbides and a white matrix. The area that the carbides covered in the image was one of the variables given by a sub-routine in the Sigma Scan software, being this number divided by to the total area of the picture the measure of area fraction these phases occupied in the steel.

3.4 Isothermal oxidation experiments

The first experimental approach to this research was to study the isothermal growth of oxide layers formed on the surface of high speed steel under environmental conditions similar to those found in a hot strip mill in order to determine:

1) The rate of growth of the oxides and to analyze if this was dependant on the composition of the oxidant atmosphere.

2) The composition of the oxide layer formed on the surface of the steel.

3) The morphology of the oxides as well as the influence of the microstructure on the oxidation phenomenon of the high speed steel.

It was considered that water vapour, present in the atmosphere of a hot strip mill, could have an influence on the oxidation rate of the work rolls and therefore it was selected as one of the main components to be present in the oxidant atmosphere of the tests together with air, a component that is inevitable present in a hot strip mill.

Unfortunately, the thermo gravimetric (TG) analysers available in the department to study the oxidation phenomenon did not support the presence of water during oxidation experiments and, since this was fundamental to the study, TG was discounted. It was therefore necessary to design and assemble an experimental facility that allowed the introduction of water vapour as a component of the oxidant atmosphere in which the tests were to be developed.

3.4.1 The isothermal oxidation reactor

The isothermal oxidation phenomenon was studied after the design and development of an oxidation rig. Fig. 3.1 gives a schematic representation of the reactor as well as showing the real installation. This installation consisted of a high temperature induction furnace with a mullite ($3Al_2O_3.2SiO_2$) tube for the chamber in which the samples were heated to the desired temperature. Both extremes of the tube were sealed by means of glass fibre ceramic blanket placed between the end of the tube and the end caps that were used as the entrance and exit of the gas.

The oxidant atmosphere comprised of a mixture of air and water vapour was produced when compressed air was bubbled into a laboratory flask that contained the water vapour generated by heating distilled water with an electric mantle. By controlling the temperature of the water with the heating mantle, the amount of water vapour present in the mixture could be regulated. Before injecting the mixture in the reaction chamber, the pipe that contained the gas was passed through a small induction furnace in order to preserve the temperature of the mixture and avoid condensation in the pipe. With this installation it was possible to carry out oxidation experiments under any controlled atmosphere up to a maximum temperature up to 1100 °C, also offering the possibility of introducing argon gas to create an inert atmosphere during preheating stages to avoid oxidation at this point, as was the routine in this research.

Before the oxidation tests, the temperature profile of the tube furnace was measured and the highest temperature point within the tube was determined by mapping the temperature every centimetre along its length using a k-type mineral insulated thermocouple fitted to a PICO technology data acquisition system. As in the real tests the samples were heated up to the testing temperature under inert conditions, the profile of the furnace was obtained under the presence of argon. Fig.3.2 represents the temperature profile of the oxidation reactor for two calibrations.

The time required for one 1.5 cm cube shaped sample of the high speed steel to be uniformly heated up to 615°C under inert conditions was measured using a k-type thermocouple inserted at the geometric centre of a sample. It was found that a time of 25 minutes was needed for the whole sample to reach the temperature of the chamber. The initial and final mass of the sample was measured to prove the performance of the inert atmosphere to inhibit oxidation during the heating stage finding a difference of ±1mg.

3.5 Isothermal oxidation tests

After calibration of the oxidation reactor, the oxidation behaviour of the high speed steel was studied under isothermal conditions at two different temperatures under the action of three different environmental conditions summarized in Table 8, in order to achieve the objectives previously stated in Section 3.4.

3.5.1 Sample morphology and preparation procedures

Cube shaped samples of 1.5 cm side were machined directly from the roll discs by the spark erosion technique, as discussed previously. The size of the samples was chosen in order to analyse the oxidation phenomenon on as large volume of material as possible within the constraints of the uniform temperature region of the furnace. This sample size was certainly much larger than is used in conventional TGA experiments, which is important given the heterogeneities present in high speed steels. Five faces of each sample were ground using silicon carbide (SiC) papers of 120, 240, 400 and 800 grit while the remaining face was further ground using 1200 grit and then polished with diamond paste to a 1 μm finish. This differs from the industrial practice where the work rolls are not polished to a mirror finish. However, the idea of this polishing procedure was to produce samples of a slightly rough surface finish similar to that of a new work roll, but also with one polished face where it would be easier to follow the oxidation phenomena. The samples were then cleaned using a degreasing solution in an ultrasound bath for three minutes, dried and etched with 5% Nital for 8 seconds.

3.5.2 Oxidation tests

Before the oxidation tests, the mass of the samples was measured using a PRECISA 92SM precision balance having an accuracy of $\pm 1 \times 10^{-4}$ g. Prior to the introduction of the test sample into the reactor, the air inside the tube was purged with 1200 cm^3/min of argon, maintained while the sample was introduced. The sample was placed on a mullite boat and pushed exactly to hottest point within the reaction chamber, immediately after this the tube was sealed with a fibre glass patch and an end cap and then after one minute the argon flow was reduced to 600 cm^3 /min. This procedure was carried out in order to preheat (25 minutes) the sample up to the testing temperature under inert conditions. Two temperatures were chosen based on those reported in the literature (Guerrero *et al.* 1999, Pérez *et al.*, 2004) to reflect the upper limit and more normal operation values experienced by the work rolls during industrial rolling of steel, namely 615 and 550°C respectively.

After 25 minutes, the argon atmosphere was replaced by the oxidant gaseous mixture; which was created when compressed dry air was injected into the water vapour generator at a rate of 600 cm^3/min in order to mix it with the water vapour produced at 85 or 95 °C resulting in flow rates of water of 0.45 and 1.45 cm^3/min respectively.

Each sample was exposed to the gas for a fixed time and after completion, they were carefully removed from the furnace and cooled down by natural convection to room temperature. Once cooled, the samples were weighed again to establish the mass change due to oxidation. The analysis of the oxidized samples was followed using a new sample for each test for times up to 6 hours for the various environmental conditions and temperatures. These tests were compared to isothermal oxidation of the material for the same oxidation times but using a flow of 600 cm^3/min of dry air only. The oxygen partial pressure was calculated for each condition having values of 0.06, 0.11 and 0.21 atm for environmental conditions 1 to 3 respectively (Table 8).

The oxidation kinetics curves were obtained when the mass change of the samples divided by their average area obtained from the faces of the cubes was plotted against the respective oxidation time for each sample.

3.6 Cyclic oxidation experiments

Cyclic oxidation experiments were performed to analyse the growth and behaviour of the oxide scale under the presence of thermal cycles imposed to the surface of the steel as result of repetitive heating and cooling cycles, trying to recreate the thermal cycles experienced by the work rolls in a hot strip mill. As experimental facilities did not exist to perform these experiments in the laboratory, an installation that would allow such thermal cycles had to be designed and built, as in the case of the isothermal experiments.

3.6.1 High frequency cycling tests

3.6.1.1 Cyclic oxidation reactor

The real installation and the schematic diagram are shown in Fig.3.3 a) and b) respectively. The main idea of this installation was to induce the thermal cycles by the simple principle of heating the sample up to 615°C and cooling it down to 25°C as quickly as possible, repeating the thermal cycle as many times as required. This installation was built using a vertical induction tube furnace with a mullite chamber in which the specimens were heated up to the desired temperature. The hottest zone inside the furnace was estimated by means of mapping the temperature distribution along the length of the tube using a k-type thermocouple. A mixture of 600 cm^3/min dry air and water vapour produced at 85°C was injected into the furnace using a vitreous silica nozzle placed at the lower end of the tube furnace that accelerated the oxidant mixture through the chamber. A laboratory flask full of distilled water was located at the bottom of the tube furnace to quench the samples. The sample was loaded in the bottom part of the tube furnace holding by a platinum hook fastened to a nickel-chrome alloy wire wound to the pulley of an DC electric step motor placed above the induction furnace. This allowed the sample to be moved reproducibly between heating and quenching.

3.6.1.2 Temperature calibration for the tests

Prior to the tests, experiments to define the duration of the heating cycle aiming to define the time that the sample needed to remain inside the furnace to achieve 615°C on its surface were carried out. In order to impose a rapid heating cycle to the sample, the temperature of the furnace was set up to the maximum value allowed by the control of the furnace that was 1100°C. A k-type thermocouple connected to a data acquisition system was attached to a sample in a hole drilled at half the thickness of the sample at a depth of 0.5 cm. The sample was placed in the hot zone and the temperature readings were followed and recorded by the data logger. A temperature of 615°C was registered by the thermocouple after about 46 seconds of exposure to the hot zone and after this time the sample was moved down to the quenching pit and cooled to the water temperature of 25°C.

These thermal cycles were repeated several times (Fig.3.4 a) but the temperature values measured with the thermocouple represented the temperature of a point located at 0.5cm inside the sample and not the temperature value at surface that was presumably higher than the measured value. Using the measured temperature and considering the sample as a semi-infinite solid (Holman, 1986) the temperature on the surface after 46 seconds was estimated by means of the equation:

$$\frac{T_{(x,t)} - T_0}{T_i - T_0} = fer\left(\frac{x}{2\sqrt{\alpha t}}\right) \tag{3.1}$$

where $T_{(x,t)}$ is the temperature measured by the thermocouple at the distance x inside the sample measured at the time t, T_0 is the surface temperature at the same instant and T_i is the initial surface temperature measured in 25°C and α the thermal diffusivity of the steel. Giving values to the above expression and considering an exposure time of 46 seconds, the temperature on the surface of the steel T_0 was 655.6°C. By means of iterations to the time for equation 3.1 it was predicted that the sample needed an exposure

time of 42 seconds to reach 617.9°C on its surface. This temperature was corroborated by measuring the temperature of the sample prior entrance to the quenching pit using an optical pyrometer for different retention times inside the furnace and finding a good agreement between the predicted and measured values as shown in Fig.3.4 b).

3.6.1.3 Cyclic oxidation tests

Square shape high speed steel samples of 1.5 x 1.5 x 0.5 cm were used as the test piece for the cyclic oxidation tests. Prior to the tests, the surface of the samples was prepared following the same procedure as for the isothermal oxidation tests except that in this case the two faces of the square were polished to a 1μm diamond finish, while the remaining four lateral faces were finished using 800 grit SiC paper. After preparation, the Vickers micro and macro hardness values of the samples were also measured using loads of 0.5 kg and 2.5 kg respectively.

Following the thermal calibration, the thermal cycle chosen was 38 seconds in the hot zone and a 5 seconds quench. While this is not representative of the real industrial situation where the temperature rise and fall occurs during a single roll rotation, it was the most rapid cycle that could be achieved with the designed experimental system.

The difference between the initial and final mass of the sample, measured at the beginning and at the end of the each test using a precision balance was used to follow the oxidation kinetics for samples exposed for between 20 and 300 cycles, which represented ~ 6.5 hours testing. A new sample was used for each test.

3.6.2 Low frequency cycling tests

In order to study the mechanical behaviour of thick oxide scales formed on the surface of high speed steel under the action of thermal stresses, a low frequency cyclic test procedure was introduced. The testing principle was the same as for the high frequency testing; but in this case using the same rig as in the static oxidation tests and considering a heating phase of 1 hour followed by the same quenching cycle into distilled

water (Fig.3.5). All the experiments used an oxidant atmosphere created by mixing a flow 600 cm^3/min of dry with water vapour created at 85°C.

The specimens were prepared using the same metallographic procedure as in the case of the high frequency cycles before their introduction to the chamber. A small platinum ring was fitted to the hole drilled across the specimens in order to facilitate their handling during the cooling stage and avoid touching the sample. Before the tests, the mass of each specimen was weighed with a precision balance and recorded. After this, the specimen was soaked in distilled water, placed on a mullite boat and placed in the hottest zone inside the reaction chamber. The tests were carried out without the presence of a preheating stage under a protective inert atmosphere. The tube was sealed after introduction of the sample to the chamber and after 1 hour the sample was removed from the chamber, quenched in distilled water for 5 seconds, and placed back into the chamber, repeating this cycle on the samples as many times as required. A number of cycles comprised between 2 and 40 cycles were imposed to different steel samples up to 25 cycles; from this point the variation in mass was followed for the same sample at every 5 cycles until 40 were obtained. The difference in mass due to oxidation was used to follow the oxidation kinetics of the samples. Tests at temperatures of 615°C and 550°C were studied under this condition.

3.7 Growth of the oxide under contact, load and motion conditions

Clearly oxide scales that grow in real rolling mill applications grow under a combination of static and loaded contact conditions. Following the static and cyclic oxidations tests, further tests were undertaken to investigate the effect of a load and sliding motion conditions in order to study:

a) The growth characteristics and mechanical behaviour of the oxide layer on the surface of a work roll.

b) The wear mechanism of work rolls associated to the formation of an oxide layer.

c) The interaction of the oxide layer with a counter body.

3.7.1 General testing conditions and methodology

Because it was extremely difficult to study the growth characteristics and behaviour of the oxide layer formed on the surface of work rolls directly in the real process, the development of a physical model that included most of the elements representative to this process and that are involved in the generation of the oxide layer was required. Wear tests using a disc on disc configuration have been developed along the years in order to analyze features associated with the wear of work rolls under conditions found in hot strip mill and therefore a similar configuration was selected in this investigation to achieve the objectives established in the former section.

A Cameron-Plint multi purpose wear test machine was used to perform wear tests using a disc on disc configuration in rolling-sliding mode. The schematic representation of the rig is shown in Fig.3.6. The discs had 6 cm external diameter, and the test load was applied to the upper disc via a cantilever arrangement. Both shafts were driven by the 1.5kW DC motor that provided a maximum angular speed ω of 600 rpm. The lower disc was driven directly, while the upper disc was driven via a gear that allowed control of the relative slip between upper and lower discs. The friction coefficient was measured and recorded by a transducer located in the shaft that holds the upper disc, by measuring the lateral force of the system.

A 1.5 kW induction coil was also integrated into the rig to heat the lower disc by RF heating. A maximum temperature of 680°C could be reached in the high speed steel discs when the voltage of induction in the coil was set to 1.1 kV. The temperature on the surface of the disc was measured by means of a Rytek LT infrared optical pyrometer connected to a data acquisition system that compares the value of the aimed temperature entered in the software that controls the rig against the instantaneous reading taken by the pyrometer, providing a feedback loop to give dynamic temperature control. The precision of temperature control was ±15°C.

3.7.2 Materials and manufacture of the discs

The material for the manufacture of the lower test disc was the same high speed steel used in the isothermal and cyclic oxidation tests while the materials chosen for the manufacture of the counter body was a conventional M2 high speed steel. Due to the high hardness of the disc and the relative complexity of its shape, the work roll grade high speed steel test pieces were cut directly from a real work roll by the spark erosion technique in order to produce the final shape (Appendix 1) followed by a final grinding operation in order to remove the rough finish produced during the spark erosion process. Care was taken that the contact track of the all the test discs was ground using the same machining parameters. The test disc was chosen to have a flat contacting profile across its thickness in order to give a desired contact pressure when in contact with the counter disc.

The counter face discs were produced directly from a M2 high speed steel commercial bar, cutting and machining the discs to the final shape, followed by a heat treatment operation to obtain a hardness of 800 HV and finally grinded to remove the oxides product of the heat treatment operations. As these discs were bought from stock, a detailed explanation on their manufacture process is not offered here but if needed, is available in Rodenburg and Rainforth (2007). These discs were designed having a crowned profile across the disc thickness, as indicated in the diagram shown in Appendix 1, to define the contact position and to make Hertzian contact stress calculations more straight forward.

3.7.3 Testing procedure

The growth of the oxide layer was studied for the rolling sliding tests at 400, 500 and 600°C and two different environmental conditions namely dry air and water vapour. The ideal would have been to use true wet conditions, i.e. copious water applied directly to test disc, but this was obviously dangerous given the proximity of the induction coil. Therefore, water was applied drop-wise to the surface at the opposite side to the induction coil and had evaporated before rotation to the induction coil. In addition, water vapour

was also directed onto the test disc (Fig.3.7). A flow of 600 cm^3/min of dry air was mixed with water vapour at 85°C and applied directly to the surface of the test disc using a vitreous silica nozzle located close to the wear track of the lower test disc. The condensation of water vapour in the line of the nozzle acted as another source of water for the system. The kinetic energy of the mixture accelerated condensation water through the pipe establishing a stream at the exit of the nozzle that impacted the surface of the lower disc approximately at every minute during the tests, simulating the cooling water applied to a work roll in a real practice.

For the dry conditions the air was applied directly to the surface of the test disc through a vitreous silica nozzle at a flow rate of 600 cm^3/min.

Before all the tests, test discs and counter faces were washed with a solution of neutral detergent, dried with alcohol and cleaned with acetone in an ultrasound bath for 3 minutes. Immediately afterwards, the initial roughness of a pair of discs was measured by means of Surtronic 3+ stylus profilometer using a height resolution of 10 μm for an analysis distance 2.5 mm of across the wear track of the disc. The roughness measurements were taken using the software Taly profile levelling the first roughness profile taken and applying a Gaussian filter with a value of 0.8. Representative roughness profiles taken after the tests are shown in Appendix 2.

After the roughness analysis, Vickers macro hardness measurements were taken from the discs using a load of 30 kgf load for 15 seconds, these measurements were also taken at the end of a complete test. The mass of each disc was measured using a precision balance with and accuracy of ±1mg.

The operational conditions for the rig were selected to be as close as possible to the contact conditions found in a hot strip mill. A load of 2.5 kg was applied to the upper M2 disc to produce an initial contact pressure of 694 MPa calculated using the Hertzain theory of elastic contact applied to the case of an elliptical point contact (Appendix 3). This geometry best describes the contact between the flat lower disc and crowned upper disc profiles. The angular speed of the disc for all the test conditions was set to 250 rpm

in the motor giving a lineal speed of 0.8 m/s, a value close to that experienced by real work rolls in the first finishing stand in hot strip mills. A slippage of 5% was selected for all the test conditions. This is slightly higher than normal operation in a hot strip mill (although values vary from plant to plant and stand to stand), but is below the upper limits that are experienced.

At the beginning of the tests, the motor was set up to a low speed at the time that the induction coil was turned on, to allow rapid heating of the test disc. The temperature readings given by the optical pyrometer fixed to the rig were compared with readings taken with a portable optical pyrometer in which a value of emissivity for oxidized steel of 0.74 was selected to take into account the change of the steel emissivity as result of oxidation in order to have certainty in the temperature values. Once the test disc reached the test temperature the upper disc was brought into contact and the load applied to the system at the same time that the gaseous mixture and water droplets or dry air were applied to the surface of the test disc for humid or dry conditions respectively. The temperature readings as well as the evolution of the friction coefficient were recorded along the test using the control of the rig at a rate of 2 Hertz.

The duration of the test was 6 hours running continuously to complete a sliding distance of about 21 km. At the end of the tests the load was removed and the upper disc lifted up to allow the test disc to cool down using the gaseous mixture or dry air under conditions of no contact. The test disc was removed from the rig and weighed immediately, followed by roughness measurements across the wear track to evaluate the change of the surface topography as the test was developed. After this procedure, the test disc was placed back in position and the test continued under the same conditions of the former test. This procedure was repeated for each disc over five consecutive days to give a total test time 30 hours.

The dimensional wear coefficient K was calculated from the data measured along the rolling-sliding test using the relationship:

$$K = \frac{V}{SP} \tag{3.2}$$

where V is the volume of material removed in mm^3 calculated using the mass change, S is the instantaneous sliding distance in meters and P is the applied load in Newtons (Hutchings, 1992).

3.8 Characterization techniques

3.8.1 X-ray diffraction

To identify the oxide phases formed during the isothermal and cyclic tests, X-ray diffraction analysis was carried out in a Philips PW 1730 diffractometer using cobalt (Co) $K\alpha$ as radiation source, produced at 40kV and 30mA. High definition analyses were run to analyze the oxide layer that grew on the polished face of samples selected from specific positions in the oxidation kinetic plots scanning with diffraction angles 2θ from 20 to 80°, at a rate 0.1° 2θ/min, yielding ~12 h scans. The possible oxide phases relative to each diffraction peak were compared with the data contained in the JPDS diffraction cards generated by the ICDD (International Centre for Diffraction Data) via the software STOE Win XPOW.

Additionally, the wear debris produced during the sliding tests was collected and prepared for inspection as a powder on a STOE PSD X-ray transmission diffractometer with molybdenum $K\alpha$ as radiation source, produced at 50 kV and 30 mA. The powder was pasted on a transparent film using a special adhesive and then fitted to the diffractometer in order to perform high definition scans comprising 2θ angles from 5 to 40° scanned at a rate of 0.48 °2θ/min. The reflections detected during the scans were analyzed by the same method as in the case of the previous analysis.

3.8.2 Cross sectioning of the specimens after the tests

Samples selected at specific stages in the isothermal and cyclic test as well as at the end of the sliding tests were sectioned in all cases using a cubic boron nitride (CBN) wheel (specially designed for cutting operations of high speed and tool steels) in a Struers Accutom-5 precision cutting machine. Overheating was avoided by setting the angular speed of the wheel to 1500 rpm, a sample feed rate 0.025 mm/sec, medium pushing force and copious quantities of coolant, which gave no evidence of heating. After cutting, the samples were mounted in conductive bakelite, ground and polished by standard metallographic procedures and etched in 2% Nital.

In the case of the samples oxidized isothermally metallographic preparation of oxides inevitably leads to damage of the friable oxide, thereby not reproducing the oxide structure with absolute accuracy. Therefore, in an attempt to obtain a more accurate view of the true oxide structure, fracture surfaces of the oxidized steel were prepared. Coupons of 0.75 x 0.75 x 1.5 cm were cut from the steel cubes, prepared following the same metallographic procedure and then oxidized under exactly the same conditions experienced in the isothermal oxidation test. Prior to the oxidation of the specimens, a notch was cut through half the sample towards the polished face leaving a gap of 1.5 mm between the inspection surface and the end of the notch (Fig.3.8). After the oxidation test, the sample was immersed in nitrogen for 3 minutes to induce a transition to a brittle state and was broken thereafter using an impact load.

3.8.3 Surface and cross section characterization using SEM

The characteristic zones and features found on the surface of the cube shaped samples, cross sections, fractures surfaces and test discs were studied on the SEM (JEOL 6400 and FEI Sirion field emission gun) using the secondary and backscattered electrons detectors as well as energy dispersive x-rays (EDX) for chemical analysis. For the inspection of the test surfaces and fractures, the specimens were mounted on an aluminium holder using conductive silver paint as an adhesive and coated with a thin film of evaporated carbon. In the case of the mounted cross sections, the samples were only

dyed with silver paint to facilitate the dissipation of the charge. Values of acceleration voltage of 15 or 20 KV were used as standard during the analysis having a working distance between the lens and the specimen of 5 mm.

Chapter 4

Results

4.1 Microstructure of the steel

Following the oxidation etch, the carbides in the microstructure were coloured according to the effect that oxidation had on them (Fig.4.1). The most abundant carbide phase in the steel developed a red violet colour, the second most abundant was white and the least abundant was coloured in dark blue.

Fig.4.2 shows a backscattered electrons image of the microstructure, where the most abundant carbide appears in black, the second in dark grey and the third in white. The EDX analysis of these zones (Fig.4.3) revealed that the black carbides contained vanadium, chromium and iron, characteristic elements found in MC type carbides. Fig.4.3 b) gives the analysis of the carbides in dark grey revealing traces of chromium and iron, elements present in M_7C_3 carbides. Fig 4.3 c) shows a substantial amount of molybdenum and chromium, elements normally present in M_6C type carbides. Fig.4.3 d) shows the analysis of the matrix. The amount of each element in the carbides expressed in weight percent is presented in Table 10. Carbides covered and area of 11.07 ±2.5% in the microstructure.

4.2 Isothermal oxidation tests

Figs.4.4 and 4.5 show the oxidation kinetics curves obtained for both test temperatures. At both temperatures under condition 1 (dry air + vapour at 95°C) the mass gain was initially rapid, followed by a reduction with increase in oxidation time, following a logarithmic relationship. A transition from logarithmic to a linear relationship was observed at around 10,000s for the tests at 615°C under condition 1.

The tests developed under condition 2 (dry air + vapour at 85°C) followed a parabolic relationship at both temperatures. The mass gain during the early oxidation times was less than the mass of the samples tested under condition 1, but after an oxidation time of about 7500s the mass gain was greater than condition 1. The oxidation kinetics of the experiments under condition 3 followed a logarithmic relationship at both test temperatures, with the mass gain notably less than that in the other two cases.

The oxidation kinetics curves were corroborated in a similar manner to the method suggested by Kofstad (1986), namely a plot of Δx vs $\log(t)$ to verify logarithmic behaviour and Δx^2 vs $\log(t)$ for parabolic behaviour. The results from this analysis from the curves at 615°C are shown in Fig.4.6, where Fig.4.6 a) and b) demonstrate the logarithmic and linear stages of condition 1, Fig 4.6 c) the parabolic relation for condition 2 and, Fig.4.6 d) shows the logarithmic behaviour for condition 3. In the same way, Fig.4.7 a) to c) show the trends for the test carried out in conditions 1 to 3 at 550°C. A good linear fit was found in most cases using confidence intervals of 95%. The oxidation rate constants (obtained from the slope of these graphs) are summarized in Table 9. The logarithm of the oxidation constants were plotted against the inverse of the absolute temperature (Fig.4.8). While there is significant error associated with only using two data points, the slope of these plots gives an estimate of the apparent activation energy Q for each environmental condition. The behaviour of the activation energy with respect to the partial pressure of oxygen of each condition is shown in Fig.4.9.

4.2.1 Surface phenomena present in the steel

For all the environmental conditions and temperatures, the oxidation of the steel started with the development "coral" like oxide structures, as shown in Fig.4.10 a) but as the oxidation time proceeded (600s), this structure changed and adopted the shape of distinct oxide crystals (Fig.4.10 b). These oxide crystals could be related to the presence of magnetite and were always found in the steel surface as dark areas. From these crystals, fine oxide whiskers and platelets of hematite grew as it is shown in Fig.4.10 c) after ~900s, which was the dominant oxide phase morphology for longer oxidation times.

The evolution of the oxide morphology on the samples exposed to the three conditions was compared for similar time intervals. Fig.4.11 a) and b) show the surface of the samples oxidized under condition 1 at 615°C for 10 minutes and 3 hours respectively. After 10 minutes, the matrix was completely covered by a uniform layer of hematite platelets, but the carbides were free from oxide. However, after 3 hours oxidation of the carbides was also apparent.

Samples analyzed for the same time intervals under condition 2 showed a different behaviour. After 10 minutes (Fig.4.12) it was possible to appreciate considerable amounts of zones containing magnetite crystals, whose growth was presumably slow and even after 3 hours the carbides were not completely covered by the oxide layer as it was the case in condition 1. The analysis of the samples exposed to condition 3 after 10 minutes and 3 hours shown in Fig.4.13 a) and b) respectively, revealed a substantial amount of areas containing magnetite crystals present at both time intervals that suggested that the oxidation process under this environmental condition was quite slow.

The surface of the samples oxidized at 550°C exhibited similar features. The sample exposed for 10 minutes to condition 1 was covered by the uniform light grey layer of hematite platelets as shown in Fig.4.14 a), but there was no oxidation of the carbides. The carbides were covered by the lateral expansion of the oxide layer after 4 hours (Fig.4.14 b). After 15 minutes and 4 hours exposure to condition 2 the sample presented the same features as in the case of the sample in condition 1, the surface aspect was the same and areas with magnetite crystals were not identified (Fig.4.15 a and b). The samples oxidized under condition 3 exhibited a similar amount of zones containing magnetite after 15 minutes and 4 hours respectively (Fig 4.16 a and b), indicating that the oxidation phenomenon occurred slowly under this condition.

In the tests developed at 615°C under conditions 1 and 2, MC and M_7C_3 carbides were not oxidized although oxygen dissolved in, or on the surface of the carbide, was detected in the EDX patterns (Fig.4.17). In contrast, oxidation of carbides was present in

the samples exposed to condition 3 but only for MC carbides as suggested in Fig.4.18 where considerable amounts of vanadium, iron and oxygen were detected. M_7C_3 carbides did not show significant oxidation (Fig.4.19) although oxygen was dissolved in them as in the previous conditions.

The same behaviour was observed for the samples tested at 550°C, where MC and M_7C_3 were not oxidized under the presence of water vapour, as indicated in Fig.4.20 for condition 1, and Fig 4.21 and Fig.4.22 for condition 2 showing the MC and M_7C_3 carbides. The samples oxidized under condition 3 showed the formation of oxide structures on the surface of MC vanadium rich carbides as indicated in Fig.4.23 a) while M_7C_3 carbides only contained oxygen dissolved within them (Fig.4.23 b).

As noted before, throughout these experiments the oxide layer grew on the steel developing different morphologies that could have an influence on the oxidation kinetics of the steel. During the early oxidation stages in atmospheres containing water vapour, zones with markedly different oxide morphology were identified. This is shown in Fig.4.24 where the growth of hematite platelets from iron oxide crystals that contained vanadium and chromium is visible. This oxide structure was formed during the early oxidation stages, but homogeneity in the whole surface oxide structure was reached after 2 hours (Fig.4.25). After 3 hours oxidation, the hematite platelets adopted a structure similar to maple tree leaves shown in Fig.4.26, with a denser arrangement of oxides.

Under dry conditions for both temperatures, the oxide that grew on the surface of the steel adopted only two different morphologies. These included fine whiskers rich in iron and vanadium together with hematite platelets containing only iron (Fig.4.27). Whiskers as those shown in Fig 4.28 were easily found after 1 hour under this condition and significant changes to the oxide structures found on the surface of the steel were not present as the oxidation time increased.

4.2.2 Phase identification by X-ray diffraction

The analysis of the steel samples at different stages in the oxidation kinetics plots effectively revealed peaks that indicated the presence of magnetite Fe_3O_4 and hematite Fe_2O_3. Peaks indicating the presence of wustite FeO were not detected under any condition. The intensity of the peaks relative to the abundance of one or another phase depended on the oxidation time and the oxidant atmosphere. Fig.4.29 a) and b) give the patterns obtained after 15 minutes and 3 hours respectively for oxidation at 615°C under condition 1. During the early oxidation stages magnetite was present with more intensity than hematite and it is also possible to identify peaks indicating the presence of martensite. As the oxidation time increased hematite was detected with more intensity than magnetite and peaks related to the matrix were not observed.

A similar behaviour was found during the analysis of samples after 15 minutes and 2 hours oxidation under condition 2 at the same temperature (Fig.4.30 a and b) but the peaks relative to martensite remained present even after 2 hours.

Under condition 3 (Fig.4.31 a and b), martensite peaks together with reflections that indicated the presence of M_7C_3 and MC carbides were detected after 15 minutes oxidation, with few evidence of iron oxides. After 3 hours oxidation, oxide peaks of hematite and magnetite were observed, while the martensite peaks were still present, although with less intensity compared with the sample oxidized for 15 minutes. In addition, peaks that indicate the existence of a vanadium oxide VO were also detected.

The samples oxidized at 550°C under the three conditions presented similar results. Fig.4.32 a) and b) show the diffraction traces of the samples oxidized for 15 minutes and 6 hours under condition 1. These revealed peaks from the matrix and magnetite as the most abundant phases found during the early oxidation stages. After 6 hours the intensity of the martensite peaks diminished considerably and hematite became the most abundant phase detected.

The samples analyzed for condition 2 after 15 minutes and 2 hours (Fig.4.33 a and b respectively) presented similar reflections as the samples analyzed under condition 1. The difference was that the martensite peaks were not detected under this condition, contrary to what happened to the sample analyzed under condition 1 for 6 hours in which martensite peaks were detected even after this long exposure time. The sample after 10 minutes under condition 3 (Fig.4.34 a) revealed hematite as the main oxide detected as well as reflections of MC carbides and martensite. After 4 hours (Fig.4.34 b), vanadium oxide was detected as the most intense reflection together with hematite and magnetite reflections.

4.2.3 Cross sectioning of the oxide layer

The cross sectioning of the oxide layer was successful despite the brittle nature of the oxide. Fig.4.35 a) and b) show cross sections after 15 minutes and 2 hours exposure to condition 1 at 615°C respectively. In the first case, the oxide looks as a compact layer with good adherence to the substrate; and it is also possible to note zones in the steel substrate where the oxidation process occurred internally. The sample after 2 hours shows separation of the top layer, which may have occurred during the preparation process, but nevertheless, this image demonstrates that the oxide layer under this condition comprised two single layers, an inner layer with good adherence to the substrate that grew by oxygen dissolution in the steel (Fig.4.35 b) and outer layer with poor adherence to the layer formed next to the substrate.

EDX dot map analysis revealed the distribution of the elements present in the oxides (Fig.4.36 a and b). Three interesting features were identified from this analysis namely, the oxide layer formed next to the substrate shows iron deficiency but chromium enrichment as suggested by the intensity of the colours of each element in the respective dot maps. In addition, the outer layer only contains iron and oxygen and vanadium rich carbides were not oxidized under this condition and were covered by the oxide layer.

The samples oxidized at the same temperature under condition 2 presented oxide layers that had exactly the same characteristics as that of the oxide layers formed under condition 1 for the same oxidation times, as it is appreciated in Fig.4.37 a) and b) and in the EDX mapping shown in Fig.4.38 for the sample oxidized for 2 hours.

The cross sections of the oxide formed under condition 3 presented similar characteristics as in the previous cases. Fig.4.39 b) clearly shows that the growth of the oxide layer formed next to the substrate implied the dissolution of oxygen in the steel. The difference found in this condition is that apart from the existence of the zones mentioned earlier, a high concentration of vanadium was found located at both the outermost part of the top layer and in the zone formed next to the substrate (Fig.4.40).

The cross sections of the samples oxidized at 550°C, presented similar characteristics as those obtained at 615°C, except that the samples exhibited thinner oxides. Fig.4.41 a) and b) are micrographs of the oxide layer after 1 and 4 hours oxidation under condition 1. These show an oxide layer comprised of two single layers with poor adherence between them, and also show that the layer formed next to the substrate exhibited poor adherence. The X-ray dot maps of the layer after 4 hours (Fig.4.42) revealed the existence of the same two zones found in the tests carried out at 615°C and also revealed that the carbides were not oxidized under this experimental condition.

Fig.4.43 a) and b) show micrographs of the oxide layer formed under condition 2 after 15 minutes and 4 hours respectively. A porous outer layer is apparent together with the formation the inner layer by oxygen dissolution in the steel. Once more, the X-ray dot mapping of the oxide (Fig.4.44 a and b) revealed the same characteristics found in the tests at 615°C.

The cross section of a sample oxidized after 4 hours under condition 3 was slightly different with respect to the features observed at 615°C. Although in Fig.4.45 the formation of an oxide structure comprised by two single layers is suggested, in this case it

was difficult to establish the limits between the iron deficient zones and the outer layer. MC carbides were oxidized under this condition as indicated in the map of Fig.4.46.

The process to obtain fracture surfaces from the oxidized samples was carried out without any problems. Fig.4.47 a) shows the fracture surface of the oxide formed after 4 hours at 615°C under condition 1. Contrary to the suggestions given by the X-ray diffraction and cross sections analyses, the fracture of the oxide layer revealed the existence of three different microstructural components.

A fine grained structure deficient in iron and rich in chromium (Fig.4.48 a) was found next to the substrate, thought to be an M_3O_4 spinel (M= Fe, Cr). Following this, a second component contained an arrangement of oxide crystals of a shape similar to parallelepiped crystals containing iron and traces of chromium and vanadium, which was believed to be magnetite Fe_3O_4. Finally, an arrangement of a dense and closed structure, similar to the roots of a tree were found containing only iron and oxygen, which was believed to be the outer layer of hematite Fe_2O_3.

Similar structures were found for the same temperature after 1 hour under condition 2. The fined grained inner spinel and the compact outer hematite layer were defined clearly (Fig.4.47 b), but the parallelepiped crystal structure was not evident, however, the characteristic zone (iron depleted and chromium rich) was revealed in the EDX analysis of the oxide layer under this condition (Fig.4.48 b).

Fig.4.49 shows the microstructure of the oxide layer after 4 hours at 615°C under condition 3. Only two oxide structures were identified, comprising a fine grained layer formed next to the substrate thought to be magnetite and an outer hematite layer that had a shape similar to compact crystals. The X-ray dot mapping of Fig.4.50 revealed that it was difficult to establish the limits between the iron depleted zone and the outer layer, but most interesting was that a vanadium concentration in the outer part was revealed.

Fig 4.51 a) shows the microstructure of the layer obtained at 550°C after 15 minutes under condition 1. As in the previous cases, the fine grained magnetite layer, the crystal shaped magnetite and the outer hematite layer were also present at this temperature. The characteristic zones of iron and chromium were revealed by the EDX analysis of the layer after 4 hours exposure to this condition (Fig.4.51 b) shown in Fig.4.52. The same oxide microstructure was obtained for 4 hours at 550°C under condition 2, as it is shown in the micrograph of Fig.4.53 a) and b) and the element mapping of Fig.4.54.

Fig.4.55 shows the microstructure of the oxide layer formed under condition 3 after 4 hours at 550°C that not surprisingly is similar to that found under the same condition at 615°C. Contrary to what was previously shown in the micrograph of the cross section in Fig.4.42, the X-ray dot mapping of the elements revealed a concentration of vanadium located at the top of the outer oxide layer (Fig.4.56).

The concentration (%wt) of the chemical elements measured across the oxide layer after 4 hours of exposure to each oxidation condition revealed the following results. At 615°C for conditions 1 and 2 (Fig.4.57 a and b), oxygen was dissolved in the substrate and its content increased across the oxide layer in direction to the steel substrate. For both conditions chromium was measured in similar amounts in the steel substrate and its concentration increased in the zone of the fine grained oxide structure and then reduced again in the zones where different oxide microstructures were present (crystal magnetite and the 'tree roots' hematite). The concentration of vanadium measured for both conditions remained constant across the thickness of the oxide with low values.

For condition 3 (Fig.4.57 c), oxygen behaved in the same way as in the previous conditions but the trend observed for the chromium concentration always decreased in a direction towards the outer layer. The establishment of a vanadium gradient across the oxide layer in the direction from the substrate to the outer part of the oxide layer was registered.

The behaviour of iron across the scale in condition 1 and condition 2 is in agreement with the features previously observed during the cross section analysis of the oxides and the fracture surfaces. The concentration of iron decays from the steel substrate to a point located in the centre of the fine grained layer, (Fig.4.57 d), and then increased in the direction to the outer layer. The trend of iron in condition 3 is to increase from the metallic substrate in direction to the outer layer being reduced at the outermost part of the oxide layer where vanadium had a high concentration.

For the tests at 550°C under condition 1 and 2, Fig.4.58 a) and b) respectively, the trend of the oxygen content was to increase progressively from the substrate in the direction to the outer part of the oxide layer. A high concentration of oxygen was measured at this location for the samples exposed to condition 1 but in condition 2 the value of oxygen concentration was below measurable values. The trend observed for chromium was analogue to those previously analyzed for the same conditions at 615°C. The chromium concentration had a high value in the zones where magnetite was found and then the value decayed down to zero in the zone where hematite was present. The vanadium concentration remained practically constant across the scale with low values.

The trend for oxygen under condition 3, was to increase from a high value measured in the substrate, in direction to the outer part of the oxide layer. The chromium concentration increased slightly from the substrate to the magnetite zone and then decayed in direction to the outer oxide layer but not down to zero, suggesting the presence of this element in the outer layer, as in the case of conditions 1 and 2. A vanadium gradient was established across the oxide layer but with less vanadium dissolved at these locations compared with the amount dissolved at 615°C.

In the same way as at 615°C, a depletion of iron was observed for conditions 1 and 2 in the region where the spinel was formed (Fig.4.58 d) the content increasing in direction to the outer oxide layer as the fine grained spinel magnetite zone was left behind. The behaviour of iron in condition 3 at this temperature contrasts the same condition at 615°C (Fig.4.58 d). In this case the iron concentration decreased

progressively from the substrate in direction to the outer part of the oxide layer registering a partial increment in this region.

4.3 Cyclic oxidation of the steel

4.3.1 High frequency cycles

Fig.4.59 gives the mass change of the samples as a function of the number of thermal cycles. Two trend lines are shown, one corresponds to the bulk mass change of the samples measured before and after each individual test, and the other corresponds to the addition of the values of bulk mass changes from consecutive cycles. It can be seen that mass losses were present even after a few thermal cycles but as the number of cycles increased the behaviour was somehow stochastic, registering mass gains and losses between 60 and 90 thermal cycles, mass increments between 90 and 240 cycles, and mass losses after the development of 300 thermal cycles.

The accumulated mass gained (red line in Fig.4.59) was obtained from the addition of the mass values between consecutive cycles as if this value was measured only in one sample. This trend was to lose mass up to 120 thermal cycles and after this stage, the samples gained mass until the end of the test. The mass change registered was too small at this temperature and therefore; reducing the temperature to see the effect of this reduction on the production of oxide was discarded.

The surface analysis revealed a thin oxide layer after 90 cycles, which limited the characterisation of the oxide from this and previous stages. Moreover, the oxide layer grew only at specific regions on the steel surface and not as a uniform layer. These regions of preferential growth were located at the edge of the sample that first entered into contact with water during the quenching stage.

After 120 thermal cycles the samples developed a fine granulated structure on the surface of the steel (Fig.4.60 a and b) the EDX analysis revealing this as rich in oxygen,

iron and chromium, with traces of vanadium and manganese (Fig.4.61). The change in the colour intensity observed in the iron map suggests that a depletion of this element existed in the oxide, as in the case of the depletion observed in the layer formed next to the substrate in the isothermal oxidation tests.

Fig.4.62 a) and b) show the morphology of the oxide after 240 and 300 cycles respectively. The oxide layer was denser compared to the fine agglomerate formed after 120 cycles but retained its granulated nature (Fig.4.63 b). Spallation of a MC carbide is also apparent (Fig.4.63 a). Fig.4.64 gives the EDX mapping of the oxide after 240 cycles. This layer was rich in oxygen and iron, the latter element in deficit judging by the lower intensity observed in the map. A considerable amount of silicon was also detected as a component of this layer (Fig.4.65), which also contained iron, chromium and silicon, and a trace of vanadium.

The X-ray diffraction analysis of the samples was not successful for the detection and analysis of the oxides. Fig.4.66 gives the diffraction pattern obtained for the sample oxidized after 300 cycles where only the microstructural elements of the steel are identified.

Apart from oxidation, zones that revealed plastic deformation were found on the surface of some samples. Fig.4.67 shows a damaged zone that was found near the surface that first entered the quench water of a sample exposed to 240 thermal cycles. Plastic deformation resulted in distortion of the matrix as well as the formation of microcracks. Fracture of carbides under this condition was also evident and as the number of thermal cycles increased, the plastic deformation of the steel and the generation and propagation of micro cracks resulted in shear of large sections of the steel (Fig.4.68).

Cross sections revealed the propagation of micro cracks within the carbides or in zones near to them for samples exposed to 240 and 300 thermal cycles (Fig.4.69 a and b respectively). The EDX maps (Fig.4.70) taken from Fig.4.69 a) revealed the presence of chromium, iron and vanadium suggesting a M_7C_3 carbide. Although oxygen

concentrations were not easily detected at first sight in the micrograph, the dot map of this element revealed a small concentration of this element dissolved in the steel and also denoted the propagation path of this element through the carbide structure. Fig.4.71 a) and b) are other examples of typical failure zones found in the samples after 240 and 300 thermal cycles, formed near to areas were carbides are present.

Fig.4.72 shows the results of the hardness change of the samples as a function of the number thermal cycles. An increment in the hardness of the samples was registered between 30 and 60 thermal cycles for both tests and after this stage, the hardness decreased in a linear fashion with the amount of cycles registering a difference of 100 numbers between the initial and the final values of hardness.

4.3.2 Low frequency cycles

Fig.4.73 and Fig.4.74 show that the oxidation kinetics of the samples was represented by parabolic behaviours at both temperatures and as in the case of the isothermal oxidation tests. The difference between the tests was in the amount of mass gained at each temperature.

Spallation of oxide was expected because the oxide layer under these conditions was subject to the action of thermal stresses. These losses were identified when the values of mass between consecutive cycles were subtracted assuming that this difference would represent the real value of mass at the cycle. Fig.4.75 a) shows the curve resulting from this procedure for the data obtained at 615°C where an arrangement of maximum and minimums following a decreasing trend is observed. The maximums were fitted to a lineal relationship whose slope gave an estimate of the amount of spalled material per cycle (Fig.4.75 b). The curves for the data obtained at 550°C are shown in Fig.4.76 and comparison between both tests revealed that the rate of oxide spallation was higher at the highest temperature.

The X-ray diffraction patterns of the samples with 2 and 40 cycles presented interesting results. After 2 thermal cycles at 615°C, hematite and martensite were detected with more intensity than magnetite (Fig.4.77 a). After 40 cycles, magnetite became the predominant phase present on the steel surface and reflections of the hematite and martensite were detected with low intensity (Fig.4.77 b). At 550°C (Fig.4.78 a and b) similar behaviour was found, the only difference was related to the peaks corresponding to martensite, present with low intensity after 2 cycles and with a high intensity after 40. The strong peak intensity of magnetite and the intensity reduction in hematite observed for both temperatures after 40 cycles suggests the preferential spallation of the latter phase as the thermal cycling increased.

The surface of the samples at 615°C after 2 cycles contained elevations of the hematite layer forming convex zones (Fig.4.79 a) as well as zones where hematite had spalled leaving quasi circular zones where magnetite was exposed (Fig.4.79 b). Early stages of oxide formation were observed at the interface created between these zones (Fig.4.80 a) and the EDX mapping of the oxide (Fig.4.80 b) only revealed iron and oxygen as the main constituents, with a few traces of vanadium and chromium.

The comparison between the surface states after 2 and 40 cycles at 615°C is shown in Fig.4.81. After 2 cycles the surface was covered with hematite that was only removed in few zones where new oxide was growing rapidly. After 40 cycles, the proportion of the surface covered with oxide exhibiting darker contrast, which was believed to be magnetite, was greater, as was the extent of spalling. However, the spalled regions contained new oxide growth.

The spallation of the hematite layer was evident, but the mechanisms by which this process occurred were not clearly defined. Fig.4.82 a) shows a convex zone found in the sample after 40 thermal cycles. This zone exhibited brighter contrast than its surrounding regions because the oxide region had become detached and electrons would have escaped from below the surface as well as above, and from probable charging effects. The spalling had led to lifting of the oxide, presumably a result of the relief of the

residual stresses within the oxide layer, developed during quenching. Fig.4.82 b) shows the propagation of a crack in the hematite layer, whose development could also be related to the existence of thermal stresses.

The oxide layer formed below hematite also developed micro cracks (Fig.4.83 a). This layer did not spall, suggesting that the cracks were mainly generated by tensile thermal stresses during the heating stage. The analysis of elements present in this layer (Fig.4.83 b) revealed the same elements present in the oxide layer formed next to the substrate as in the isothermal oxidation tests. A high vanadium content was also detected during the analysis in a zone found next to a crack suggesting the oxidation of small MC carbides (Fig.4.83 d).

At 550°C the same failure mechanisms were observed as it is shown in Fig.4.84 a) and b) for samples oxidized after 2 and 40 cycles respectively. Fig.4.85 a) shows a magnification of a zone that presents the failure mechanisms where the elevation of the outer oxide layer is evident. Another interesting phenomenon found during the analysis was the spallation of complete carbides (Fig.4.85 b).

The amount of spalled area as a function of the number of thermal cycles obtained from the surface analysis (Fig.4.86), shows an increment in the amount of oxide spallation when the testing temperature and the number of cycles are increased.

4.4 Results on the rolling contact tests of the steel discs

4.4.1 General results

Fig.4.87 shows the final surface state of the discs tested in dry conditions. Under any environmental condition the discs were covered by a black-red oxide layer at 600 and 500°C and by a thin black layer at 400°C. The only variation found was the sample tested

at 600°C in dry air where a bright glaze covered the surface of the disc as shown in Fig.4.87 a).

Fig.4.88 gives the comparison of the weight change of the samples as a function of the sliding distance. The mass losses were greater in dry conditions and these increased with the temperature. This trend was not observed for the tests that contained water, and in fact the greatest mass lost was obtained at the lowest testing temperature whilst similar amounts of mass were lost at 500 and 600°C.

The wear coefficient *K* exhibited similar behaviour. Fig.4.89 shows that the wear of the discs in the test that included water increased with the sliding distance, giving similar values at 500 and 600°C, but resulting in greater wear at 400°C after 60 km. Fig.4.90 shows that for the tests in dry air the wear of the discs increased in a linear fashion with the sliding distance and the values also increased with the temperature of the tests. Fig.4.91 makes clear that the presence of water during the trials influenced all aspects of the sliding contact, in particular the wear coefficient.

The presence of water also had an impact on the surface roughness of the discs, with the dry samples generally having rougher surfaces than the water lubricated surfaces. Fig.4.92 shows the variation of the Ra parameter measured in the wear track with the sliding distance. The discs tested in dry air presented the most substantial changes in surface roughness. The Ra values increased considerable during the early stages of the test (about 20 km), but at 600 and 500°C the surface Ra changed comparatively little, with some surfaces becoming smoother, others staying the same and some showing further small increases in roughness. A considerable difference was established between these values when compared to those at 400°C. The surface roughness of the discs in the tests containing water exhibited lower Ra values than those in dry air, giving similar values at 500 and 600°C after 20 km being these considerably higher than those measured in the disc tested at 400°C.

The average values of friction coefficient μ recorded throughout the test are presented in Fig.4.93 a). High friction values (between 0.51 and 0.70) resulted from the test conducted with water. For these tests, friction was similar for the tests at 500 and 600°C, but was significantly higher than the values obtained at 400°C. Notable differences were also found for the dry conditions that comprised values between 0.50 and 0.62. The overall trend of the friction coefficient was to increase when increasing the test temperature for all the conditions (Fig.4.93 b).

4.4.2 Oxidation phenomena during the tests

The surface analysis of the samples in the presence of water at 600°C revealed regions that appeared to exhibit oxide spallation in the zones that were not in contact with counter disc located near to the wear track (Fig.4.94).

Fig.4.95 shows the surface topography of the discs at the end of the water lubricated tests. The back scattered electron images (right hand side of Fig. 4.95 show the distribution of oxide, which appears darker than the metallic regions). At 400°C (Fig.4.95 a and d) the disc contained a small area fraction of discrete oxide islands. The majority of the surface comprised deformed steel, with ploughed grooves of similar dimensions to the oxide particle size

The extent of oxide on the worn surface increased substantially in going from 400 to 500°C, compare Fig. 4.95 d and e, with a further increase in the size of the oxide islands at 600°C (Fig. 4.95 f). The extent of grooving in the metallic regions also increased with temperature, such that the surface was much rougher at 600 than it was at 400°C. As with the test at 400°C, the groove width generally corresponded to the size of the oxide islands.

The surfaces of the dry tests followed a similar trend to that for the water lubricated tests (Fig. 4.96 d to f), except some small, but important differences. The amount of oxide increased with temperature. The grooving in the metal also increased

with temperature in a similar manner, and as with the water lubricated tests the groove width was around the same size as the size of the oxide islands. However, one important difference was seen. In the water lubricated tests, the grooved metallic matrix inbetween the oxide islands was largely clear of oxide (e.g. Fig. 4.95 f). In contrast, the metallic regions in the dry test also included oxide particles that appeared to have been mechanically mixed in with the metal (Figs. 4.96 e, f). Smaller amounts of oxide were obtained in the tests conducted in dry air (Fig.4.96 a to f).

4.2.2.1 Characteristic zones formed under the presence of water

A detailed analysis of the characteristic zones formed on the surfaces of discs was made in order to identify features that could be related to the behaviour of tribological variables. Fig.4.97 shows the typical zones found on the surface of the disc at 600°C. One of these zones showed oxide platelets growing inside grooves created by abrasion, and that contained iron and oxygen as the most significant elements present in the structure (Fig.4.97 d). Fig.4.97 c) shows higher magnification details of the second distinctive feature shown as a dense black oxide layer that contained cracks. The chemical composition of this zone showed the dominance of iron, chromium and vanadium and oxygen and traces of Si, V and Mo from the steel. Fig.4.98 and Fig.4.99 show that the carbides in the steel had also oxidised as suggested by the considerable amount of oxygen contained within the zones. High manganese content was detected in the pattern that corresponds to the MC carbide.

The cross section of the disc revealed interesting features. Fig.4.100 a) and b) are secondary and backscattered electrons images that show three distinctive zones, one of these showing a thick oxide layer covering the steel substrate that contains steel fragments dissolved in it (Fig.4.100 b). The second zone shows the presence of a subsurface oxide layer, whilst a third zone reveals the partial oxidation of a MC vanadium rich carbide. The EDX analysis of these zones (Fig.4.101 and Fig.4.102 a to e) confirmed that the oxide layer was comprised by a chromium rich inner layer formed next to the substrate and by an iron rich outer layer that only contained traces of

chromium and vanadium. The subsurface layer had the same characteristics of inner oxide layer and MC carbides were oxidized as indicated by the patterns of vanadium and oxygen.

Significant changes in the surface features were not observed in the disc tested at 500°C. Fig.103 presents the distinctive features found in this condition and that effectively were not dissimilar to those previously studied at 600°C. The grooves formed on the steel contained the growth of new oxide platelets as well as the accumulation of wear debris (Fig.4.103 b). The black oxide islands were more abundant than at 600°C and also presented the development of cracks on the surface (Fig.4.103 c). Both zones presented similar elemental composition as revealed in the EDX area analysis shown in Fig.4.103 d) and Fig.4.103 e).

The cross section of the disc (Fig.4.104 a and b) showed the existence of the same three zones found in the previous test done at 600°C whose existence was again proven by the EDX analysis of this section (Fig.4.105 and Fig.4.106). In this case the outermost layer was thicker than the outer layer formed at 600°C. The oxidation of MC carbides was not as prominent as at 600°C, but they did become entrained in the oxide layer as shown in Fig.4.104 b). The subsurface oxide formation in this test condition included the presence of a high vanadium concentration and the steel substrate contained a considerable amount of oxygen dissolved near to the inner oxide layer (Fig.4.106 e).

Contrary to the features observed in the previous tests, at 400°C plastic deformation of the surface by abrasion and ploughing was the distinctive feature found on the disc (Fig.4.107). Oxide debris was accumulated in the grooves as granulated particles that did not protect the disc during this condition (Fig.4.107 c). The EDX analysis of the deformed zones revealed these containing a considerable amount of dissolved oxygen. The wear debris contained the typical reflections associated with iron and oxygen, although chromium and vanadium also had a significant presence.

It was a difficult process to find a cross section of the disc that included the oxide layer that grew on it, even though this represented a complicated task; a zone that contained both elements was found showing the oxide layer as agglomerate particles of round shape with poor adhesion to the substrate (Fig.4.108). The EDX analysis of the elements present in the oxide layer (Fig.4.109 and 4.110 respectively) revealed that the oxide layer contained iron, chromium and oxygen as main components, similar composition as that observed for the oxide layer formed next to the substrate in the previous tests.

4.2.2.2 Characteristic zones formed under dry conditions

The test at 600°C exhibited surface features that were observed in the previous condition. Oxide clusters of a considerable larger area than that observed in the tests containing water were abundant on the surface of the steel, which could be referred to as a glaze layer that was appreciated on the wear track of the roll disc shown in Fig.4.87. These clusters (Fig.4.111 b) constituted a smooth and compact layer that also presented cracks and a similar composition like that observed for the equivalent structures formed at 600 and 500°C in water conditions (Fig.4.111 d). The growth of oxide platelets inside grooves was not common in this case, and only few zones showing these elements were appreciated (Fig.4.111 c).

The cross section of the disc showed two different layers formed under this condition. One of them constituted the original oxide layer whilst the other was present on the surface in the form of a mechanically mixed oxide (Fig.4.112 a and b), both layers were rich in iron and chromium (Fig.4.113 and Fig.4.114 a). Subsurface oxide formation was also observed in this test and this was responsible of the detachment of steel slivers of considerable size (Fig.4.115 a and b).

At 500°C the amount of oxide clusters was lower and the presence of oxide platelets that indicated the growth of fresh oxide was not apparent. However, some oxide clusters were found (Fig.4.116 b) together with abundant zones that contained wear

debris of a round shape (Fig.4.116 c). The EDX analysis of elements present in the zones of Fig.4.116 a) revealed the oxide clusters as rich in iron, chromium and oxygen (Fig.4.117 a to c). Zones containing iron without oxygen were also found on the surface in the EDX map for iron in Fig.4.117, and the point EDX analysis of Fig.4.117 e) confirmed the existence of non oxidized steel zones. A zone where a considerable amount of vanadium was detected suggests that MC vanadium rich carbide participated during the degradation process of the surface (Fig.4.117 d).

Cross sections of the discs showed the oxide layer comprised compacted fine oxide particles of round shape and confirmed the presence of chromium and iron in it as indicated in Fig.4.119. Subsurface oxide formation was also responsible in this condition for the detachment of fresh steel (Fig.4.118 b). Fig.4.120 shows the EDX analysis made to different zones of Fig.4.118 b) showing that the oxide layer and all the zones studied during this analysis had the same features and characteristics of that studied at 600°C.

The characteristic zones found at 400°C only included deep grooves created by ploughing and abrasion (Fig.4.121 a). Pieces of steel separated from the surface were a common phenomenon together with zones that presented accumulation of fine oxide particles (Fig.4.121 b) where iron depletion was evident (Fig.4.121 g). The EDX analysis of the surface proved that oxide generation was not favoured under this condition and therefore traces of the original alloy were revealed (Fig.4.122 b). Oxidized MC carbides were also found as indicated by the EDX pattern of Fig.4.122 d).

The cross section of the disc showed the oxide layer as an arrangement of agglomerated oxide particles (Fig.4.123 a). The detachment of steel from the surface was also identified during this analysis and is shown in Fig.4.123 b), where it is also possible to see the fracture of a MC carbide below the surface of the steel. Fig.4.124 gives the element mapping of Fig.4.123 b), revealing the detached steel surrounded by a high concentration of vanadium. Fracture of MC carbides was a common phenomenon in this test and was linked with the detachment of steel zones of considerable size as indicated in Fig.4.125. This process did not occur for the other kind of carbides.

4.4.3 Wear debris analysis

The x-ray diffraction analysis of the wear debris gave suggestions on the nature of the abrasive particles that accounted for the wear of the discs during the tests. Fig.4.126 shows the diffraction patterns of the debris collected in the tests developed with water. In all cases hematite was the main component of the wear debris having some traces of magnetite. Reflections that indicated the presence of martensite in the wear debris were obtained only at 600 and 400°C having a greater intensity at the lowest temperature.

In dry conditions (Fig.4.127), at 600 and 500°C, martensite and hematite peaks were the most intense peaks detected in the diffraction patterns while reflections of magnetite were not detected. Peaks revealing vanadium carbide MC as a component of the wear debris were found at these temperatures. The intensity of the martensite peak reduced considerably at 400°C and reflections of MC carbides were not found, leaving hematite as the main component of the wear debris at this temperature.

4.4.4 Final observations obtained from the tests

Even though it was difficult to obtain cross sections of the test discs that contained the whole oxide layer attached to the surface of the disc, some sections showing a compact oxide layer were obtained and their thicknesses measured. Fig.4.128 represents the rate at which the oxide layer tended to accumulate on the surface of the roll disc as a function of the testing temperature, represented by logarithmic relationships for both environmental conditions, the thickness of the oxide was measured in two cross sections of the roll disc for each experimental condition.

The effect of the oxide thickness on the value of the friction coefficient of the tests is given in Fig.4.129 showing that value of μ was considerably higher for conditions in which water was present than for dry conditions.

The difference between the hardness values measured at the beginning and at the end of the tests revealed that this property was affected by both temperature and environmental conditions. The softening effect of the roll disc increased in a linear fashion with the testing temperature as indicated in Fig.4.130, where it is also possible to identify that the effect of hardness lost of the discs was greater for the conditions that included water than for those including only dry air.

Chapter 5

Discussion of results

5.1 Introduction

In this chapter an explanation of the results is given, aiming to answer the most important questions that could be formulated regarding the oxidation kinetics of the steel in both isothermal and cyclic modes, as well as to define the role of the oxide formed during the rolling-sliding experiments.

5.2 Microstructure of the steel

The characterization of the microstructural components of the steel revealed three different carbide phases based on the data presented in Table 10, which are expected constituents of a typical alloy used in the work rolls of the finishing stands of hot steel strip mills. The composition of the carbides and microstructure of the steel is in agreement with the typical composition of high speed steels suggested by Hoyle (1988), and Boccalini and Goldstein (2001) and is also similar to the compositions of the steels used in the works mentioned in Chapter 2 regarding the study of the isothermal oxidation of these alloys.

5.3 Effect of the oxidant atmosphere and temperature on the rate of oxidation of the high speed steel

5.3.1 The effect of the oxidant atmosphere

As shown in Figs.4.4 and 4.5 the oxidation kinetics of the steel are strongly influenced by the presence of water vapour in the atmosphere inside the oxidation reactor. The simplest explanation that can be given to this phenomenon is that the rate of

oxidation is higher for conditions in which water vapour is present because the water provides a second source of oxygen needed for the oxidation reactions, apart from the fraction of oxygen that is already contained in the dry air. Thus, in addition to the simple oxidation reactions that involve the iron of the steel matrix to form magnetite (Fe_3O_4) and hematite (Fe_2O_3) expressed as:

$$3Fe + 2O_2 \rightarrow Fe_3O_4 \tag{5.1}$$

and as:

$$4Fe + 3O_2 \rightarrow 2Fe_2O_3 \tag{5.2}$$

another oxidation reaction involving water vapour and iron to form magnetite was also present during the oxidation process expressed as:

$$3Fe + 4H_2O \rightarrow Fe_3O_4 + 4H_2 \tag{5.3}$$

The value of the Gibbs free energy for each one of the reactions proposed was calculated at the temperatures of the experiments using thermo chemical data obtained from tables (JANAF, 1971) and introducing these in the terms of the Gibbs relation expressed as:

$$\Delta G = \Delta H - T\Delta S \tag{5.4}$$

where ΔG is the Gibbs free energy change for the oxidation reaction, ΔH is the enthalpic change of the system, ΔS the entropic change and T is the temperature of the system in absolute units. The values of free energy resulting from the calculations are presented in Table 11 and for all the equations proposed gave negative values, suggesting that the oxidation process of the steel by the reactions proposed is thermodynamically feasible at the temperatures studied.

Laverde *et al.* (2004) proposed another oxidation reaction that involved the formation of hematite at the expense of the oxidation of magnetite by water vapour expressed as:

$$2Fe_3O_4 + H_2O \rightarrow 3Fe_2O_3 + H_2 \qquad (5.5)$$

Although this equation could potentially contribute to the oxidation of the steel, the free energy change is positive at the temperatures studied and therefore, the formation of hematite in this way was not believed to occur. Rather, only equations 5.1 to 5.3 are responsible for the development of oxidation at the temperatures studied.

Alternatively, Kofstad, (1995) suggested that by means of the reaction:

$$\frac{1}{2}H_2O + O_2 \rightarrow HO^+ + e^- + \frac{1}{4}O_2 \qquad (5.6)$$

the existence of positive HO^+ protons located at oxygen positions in the oxide scale is possible. If this was the case during the experiments, the production of more oxygen molecules inside the oxide scale was feasible giving an additional source of oxygen that promoted the continuity of the oxidation reactions.

5.3.2 Effect of oxide formation on the oxidation kinetics

The growth of oxide itself also influenced the way in which the oxidation processes occurred, for example, at both temperatures during the early stages of oxidation (up to times of about 5000 seconds), it was observed that oxidation occurred faster in condition 1 (water vapour 95°C+dry air) than in conditions 2 (water vapour 85°C+dry air) or 3 (only dry air). This premise is in agreement with the features observed during the surface inspection of the steel where it was noted that the surface of the steel exposed to condition 1 was completely covered with a grey oxide layer of hematite, that did not look as uniform in condition 2 for the same oxidation time. Instead, the surface of condition 2 contained zones (located near to carbides) where the oxidation process was in its first

stages of crystal formation (Fig.4.10 a). Combining the kinetic data and the observations made by electron microscopy, the only explanation for the slightly higher oxidation rate observed during the early oxidation stages in condition 1 can only be that the water vapour also reacts with the steel to produce oxide in addition to the reactions that involved the oxygen contained in the dry air.

With increased oxidation time the samples exposed to condition 2 gained more mass compared with the samples oxidized under conditions 1 and 3. In condition 1, the diffusion of metallic and non metallic ions across the scale was restricted by the rapid growth of hematite platelets on the matrix of the steel that also covered the carbides in the surface. This reduced the sites for fresh oxidation, i.e. the hematite introduced a passivation stage observed during condition 1. The oxidation continued when oxygen ions found across the scale or incorporated via the remaining carbides not covered by the layer reached the non oxidized steel in order to react and continue with the production of oxide.

The reduction in the oxidation rate observed in condition 1 is similar to the observations made by Jansson and Vannerberg, (1971) where the reduction in the oxidation rate of pure iron was attributed to the formation of hematite whiskers at similar temperatures. Khaveci and Welsh, (1986) also commented that the microstructure of hematite was responsible for the development of logarithmic oxidation kinetics in iron alloyed with 3%wt Cr. In fact the microstructure of the oxide layer obtained in their work is very similar if compared with the microstructure of the layer observed in this work (Fig.2.15 b and Fig.4.47 a) respectively. Molinari, (2001) also observed a reduction in the oxidation rate of high speed steel when oxidized in dry air at 700°C although in this case the reduction was related to the formation of a protective iron-chromium spinel.

The development of the parabolic oxidation stage found in condition 2 is explained based on the observation that even after 3 hours the surface of the steel contained zones where the early oxidation stages remained in the same form (Fig.4.12 b), i.e. a thin oxide layer covered the surface of the steel together with non oxidized carbides

that were not covered by lateral growth of the oxide layer. These sites acted as easy paths that allowed oxygen ions to reach the steel substrate, assuring the continuity of the oxidation process at both testing temperatures. The absence of voids in the oxide scale formed under this condition at 615°C and 550°C observed in Fig.4.37 and Fig.4.43 b) favoured the uniform diffusion of ions across the scale. Voids in the scale can be generated by the coalescence of metal vacancies within the scale (Caplan and Cohen, 1966). In the current case, the absence of such voids suggests that the presence of water vapour and the generation of hydrogen, as suggested in equation 5.3, could have increased the plasticity of the oxide layer, as proposed in Tuck *et al.* (1969).

The values of the parabolic constants obtained under this condition at both temperatures were 6.16×10^{-2} mg/cm^2-s$^{1/2}$ and 2.82×10^{-2} mg/cm^2-s$^{1/2}$ at 615 and 550°C respectively. These values can be compared to those obtained (in the same units) by Molinari *et al.* (2001) at a higher temperature (700°C) under dry air, namely 5.94×10^{-2} mg/cm^2-s$^{1/2}$ and 1.29×10^{-2} mg/cm^2-s$^{1/2}$ for high speed steels with 5% and 10% wt chromium respectively. It can be seen that even though the temperatures used in this investigation are lower than those studied by Molinari *et al.*, the parabolic constants were similar or had higher values than those obtained at higher temperatures where the mass gain of the samples is supposed to be also catalyzed by the temperature of the system. Therefore, it is proposed that the addition of water vapour effectively accounts for the increment in the oxidation rate of the steel.

The samples exposed to condition 3 experienced logarithmic oxidation kinetics. Presumably the adsorption of oxygen ions in the steel and across the oxide scale was limited due to the type and ionic characteristics of the oxides formed under this condition. This would affect the movement of ionic species across the oxide scale, hence reducing the intensity of the electrical fields that allow the transport of ions and electrons across the oxide layer needed to stimulate its growth, which are features normally associated with the development of logarithmic stages in oxide scales (Khanna, 2002).

5.3.3 Effect of oxygen partial pressure

Another explanation for the effect of water vapour on the oxidation kinetics of the steel can be related to the reduction of the partial pressure of oxygen as result of the addition of water vapour to dry air. If the oxidant mixture is considered as an ideal gas assuming that the volume of air is greater than the existent volume of water vapour, the equation that describes the behaviour of the gas gives that:

$$pO_2V = nRT \tag{5.7}$$

where pO_2 is the partial pressure of the gas, V is the volume, n is the number of moles, R the universal gas constant and T the temperature of the system in absolute units. If a constant k is used to group the ratio of gas volume with respect to the temperature and the gas constant, the number of oxygen moles in the system is given by:

$$n = kpO_2 \tag{5.8}$$

The values of n calculated from the values of the experimental variables from the tests for both conditions at 615°C gives the number of moles of oxygen present is 6.34×10^{-4} for condition 1 and 1.16×10^{-3} moles for condition 2. The greater oxygen supply for condition 2 is consistent with the more rapid oxidation kinetics observed.

In condition 2 oxygen ions will always be available to compensate the loss of oxygen due to their adsorption and reaction with iron simply because the amount of oxygen in the atmosphere is greater in this condition, ensuring the supply of these ions progressively with the oxidation process. In condition 3, the fact that only two oxidation reactions occur on the surface of the steel, combined with the ionic nature of the oxides affected by the partial pressure of oxygen, appears to be the only reasons that could explain the development of logarithmic behaviour, even though the amount of oxygen is greater than in the other two conditions.

The relationship between the values of pressure of the gas used in the experiments and the amount of mass gained by the samples of the high speed steel is in agreement with the behaviour observed by Jannson and Vannerberg, (1971) for the oxidation of pure iron under different oxygen partial pressures in which reductions to the partial pressure of the system increased the oxidation rate of the specimens (Fig.2.12).

The trend of the apparent activation energy with respect to the partial pressure of each condition shown in Fig.4.9 suggests that the minor amount of energy required to initiate the oxidation process in the steel is present when the partial pressure of the gas in the system had the lowest value, in other words when the amount of water vapour in the environment was a maximum. Therefore, it was easier to initiate the oxidation process when water vapour was present in the system in significant amounts simply because it required less energy compared with the greater amount of energy required to initiate the oxidation process when the amount of water vapour was reduced or not present.

5.3.4 The effect of temperature

The effect of temperature on the oxidation of the steel is shown in Figs.4.4 and 4.5. Irrespective of temperature, the same kinetic law is followed at both temperatures, except for condition 1, where a transition was observed. Moreover, the amount of mass gained in the experiments carried out at 615°C was almost twice the value of the mass gained under the same environmental conditions at 550°C. The answer to this is simple: the oxidation kinetics represented by k, is a strong function of temperature, as suggested in equation 2.1.

5.4 Oxide phases obtained and oxidation mechanisms

5.4.1 Oxide phases

Three oxide phases were identified in the X-ray diffraction analysis of the samples, namely magnetite Fe_3O_4, hematite Fe_2O_3 and vanadium oxide VO. The first two

phases were present in all environmental conditions while the remaining phase was obtained exclusively for oxidation in dry air. From the point of view of equilibrium, as represented in Ellingham diagrams, and considering the reactions of iron with oxygen to form magnetite and hematite, the partial pressure of oxygen required for the dissociation of the oxides at the test temperatures are between 10^{-18} and 10^{-25} for hematite and magnetite respectively at 615°C and between 10^{-22} and 10^{-28} for hematite and magnetite respectively at 550°C. As the partial pressures of oxygen for all the experiments were higher than the dissociation pressures, the production of these phases was thermodynamically favoured, in agreement with the data obtained by X-ray diffraction and by the calculation of the free energy of Gibbs for the oxidation reactions presented earlier in this chapter.

Wüstite (FeO) was not detected from X-ray diffraction analysis of the samples for two reasons. The first of these is that although Wüstite is stable at 615°C, as suggested in the iron-oxygen diagram of Fig.2.6, its formation was suppressed by the existence of chromium in the steel, an element that increases the number of defects in the crystal structure of Wüstite and favours its transformation to magnetite or chromium rich spinel structures as noted by Chang and Wei, (1989) and Khanna, (2002). The second reason is just a matter of thermodynamic equilibrium and is proposed that at 550°C Wüstite is not formed because this temperature is below the stability point of this phase (570°C). The absence of Wüstite in the oxide layer is in agreement with the observations found in the oxidation studies of work rolls developed by Gonzalez *et al.* (2001) and Kim *et al.* (2003) for high chromium and high speed steel work rolls and it is also is in agreement with the observations made during the study of the oxidation characteristics of iron-chromium alloys presented in Chapter 2.

A doubt remained with respect to the equilibrium conditions of the vanadium oxide VO (as detected by XRD) as the required Ellingham diagram that allowed the calculation of the equilibrium pressure for this compound could not be found. However, the presence of this element in the oxide layer indicates that it was favoured by the thermodynamics of the system.

Thermodynamic calculations of the Gibbs free energy that involved the reaction of vanadium carbide ($VC_{0.88}$) with oxygen or water vapour to form vanadium oxide (VO) or vanadium oxide (V_2O_5) showed in equations 5.9 to 5.11 as:

$$VC + O_2 \rightarrow VO + CO \quad (5.9)$$

$$VC + 2H_2O \rightarrow VO + CO + 2H_2 \quad (5.10)$$

$$4VC + 7O_2 \rightarrow 2V_2O_5 + 4CO \quad (5.11)$$

show that the formation of VO is energetically more favoured than the formation of V_2O_5 in oxygen and in water vapour (Table 11). Zhou *et al.* (2004) showed that the formation of V_2O_5 from the oxidation of TiAlN/VN at temperatures similar to those studied in this work is a feasible process resulting in the production of large crystals of V_2O_5 with a morphology similar to the oxide crystals observed during the oxidation of vanadium rich MC carbides (Figs.4.18 and 4.23). However, although the morphology of the oxide crystals is similar, the presence of VO in the oxide layers studied in this work was confirmed by X-ray diffraction of the oxides instead of V_2O_5, and is favoured by the equilibrium conditions. This contrasts with the work of Zhou *et al.* (2004), probably because the oxidation properties and chemical composition of the vanadium nitrides and vanadium rich carbides are different. Nevertheless, the presence of V_2O_5 cannot be discarded completely and should be taken into consideration because even though this phase was not detected during the X-ray diffraction analysis, it could have been present in small quantities given that its production is also favoured by thermodynamics and its omission could be associated with the instability offered by the vanadium oxides as indicated by Kofstad, 1953.

5.4.2 Oxidation mechanisms

A schematic representation of the oxidation mechanisms is given in Figs. 5.1 to 5.3. The basis for these proposed mechanisms is given in the following discussion.

At 615°C and 550°C for the conditions in which water vapour was present in oxidant atmosphere, the oxidation process started with the formation of the magnetite layer by a mechanism that implied the oxygen adsorption into the steel and the establishment of oxidation reactions between iron and water vapour and between iron and the oxygen contained in the dry air, as shown in equations 5.1, 5.2 and 5.3.

The dissolution of oxygen into the steel was a common phenomenon developed along the oxidation process studied under all the conditions and was evident during the cross section analysis of the oxide layer (Fig.4.35, Fig.4.37 and Fig.4.39) and by EDX measurements (Fig.4.57 and Fig.4.58). Therefore, it is suggested that this process controlled the formation of the magnetite layer. Once magnetite was formed, iron ions from the metallic substrate and from magnetite travelled in the direction to the gas-oxide interface in order to react at this location to produce hematite by means of the reaction between iron and oxygen shown in equation 5.2. As iron ions left their normal positions in the magnetite lattice to form hematite, these positions were occupied by chromium Cr^{+} ions present in the steel matrix and that did not participated directly in the oxidation process maybe because of their low mobility in magnetite (Chang and Wei, 1989). The substitution of iron ions by chromium ions initiated the development of the M_3O_4 spinel (where M= (Fe,Cr)) layer formed next to the substrate found during the EDX characterization of fracture surfaces and cross sections, instead of magnetite.

The intermediate magnetite layer found between the spinel and hematite layers could have been formed in the way suggested by Robertson and Manning, (1988). According to their investigation the duplex oxide layer formed in chromium steels normally consists of an inner fine grained spinel oxide rich in chromium, followed by a layer of columnar grains of magnetite formed from the parent spinel structure. They suggested that the formation of the top layer is only possible if space is available over the fine grained spinel layer to allow the nucleation of the oxide structure with columnar grains. At the same time, they commented that the fine grained spinel layer corresponded to the original surface of the metal.

In this investigation two routes for the creation of the intermediate magnetite layer are proposed. Firstly, space could have been created between the spinel and the hematite layer originated by local increments of pressure at the spinel-hematite interface caused by the accumulation of water vapour molecules that created micro voids that allowed the nucleation of the magnetite phase that grew at expenses of the spinel layer. The other possible route is that the intermediate magnetite was formed directly at the expense of the spinel layer during the early oxidation stages and that hematite was formed after the formation of the columnar magnetite phase.

Although both suggestions are logical, the second seems more appropriate from the features observed in the fracture surfaces of the specimens, where it was clearly noted that the intermediate layer of magnetite represented a continuous layer suggesting that the formation of this layer effectively started after the formation of the spinel phase. The morphological characteristics and stoichiometry of the phases obtained in this work are in agreement with the oxide layers studied in the works of Cory and Herrington (1987), Simms and Little (1988) and Laverde *et al.* (2004) that were mentioned in the literature review for Fe-Cr alloys.

The oxidation mechanism in dry air was different because vanadium formed an oxide phase which was located at the outer side of the whole scale, as indicated by EDX analyses of the cross sections. The formation of the outer vanadium rich layer observed during condition 3 was believed to be associated with the oxidation of MC vanadium rich carbides observed only under this condition. However, before considering this condition, the absence of this layer in conditions 1 and 2 will be explained. According to Santafé and Borgianni (1985) vanadium carbide ($VC_{0.98}$) has a great affinity for oxygen at high oxygen partial pressure and, in the interval of temperature comprised between 500 and 580°C its oxidation produces vanadium oxide V_2O_5 at a rate dependent on the partial pressure of oxygen. Based on this argument, it is possible that the reduction of the partial pressure of oxygen caused by the addition of water vapour to dry air suppressed the oxidation of MC vanadium rich carbides during the exposure of the steel to conditions 1 and 2 respectively where water vapour is present. In addition to this, a positive value of

Gibbs free energy exists for the reaction of VC with water vapour, indicating that the development of this reaction is not thermodynamically favoured (Table 11).

Instead of pronounced oxidation, the MC carbides together with M_7C_3 and M_6C dissolved oxygen within them as suggested by the EDX area analyses shown in Fig.4.17 and Fig.4.19 to Fig.4.22. This observation is also in agreement with the observations made by Santafe and Borgianni (1985), at least for the vanadium carbide studied in their work. The absence of oxidation of the carbides caused by the reduction of partial pressure of oxygen is also in agreement with the observations of Kim *et al.* (2003) on the oxidation of high speed steel when this was exposed to a mixture of argon and water vapour.

The oxidation of carbides could not be avoided in the experiments carried out under condition 3 (dry air only) where the value of partial pressure of oxygen was higher (0.20 atm) than in the other two conditions. In fact, the development of oxide crystals on MC carbides was observed at both test temperatures for dry air (Fig.4.18 and Fig.4.23). The oxidation of carbides under these conditions could be related to the great affinity of vanadium for oxygen, in agreement with the observations made by Kim *et al.* (2003).

The vanadium oxide was observed across the entire surface, not just local to the carbide particles. This raises the question as to whether this oxide was derived from just the vanadium rich carbides, with the vanadium being mobile across the surface, or whether the vanadium present in the steel matrix as small secondary carbides also contributed to the formation of this layer. No answer to this question can be found with certainty. However, even though since the majority of vanadium was tied up as carbides, the smaller fraction of vanadium present as secondary carbides in the steel matrix also contributed significantly to the oxidation process to provide a uniform top layer.

The reason for the presence of VO rather than V_2O_5 apart from the instability of the vanadium oxides discussed earlier, could be related to the purity of the MC carbides. In the present work for the alloy used, the MC carbides were far from pure VC

(vanadium 63%wt and carbon 15 %wt), but contained iron (4.44 %wt) and chromium (6.94 wt%) as indicated in Table 10. This suggests that these elements would also favour the growth of VO instead of V_2O_5 if they performed as doping particles.

Avoiding the formation of V_2O_5 is considered to be a positive observation in these steels because during the rolling process, temperature values as high as 675°C can be achieved on the surface of the rolls, which would lead to the volatilization of this oxide (Kubaschewski, 1953). The oxide would not therefore be able to contribute to the abrasion resistance, with the likely result of increasing work roll wear.

The oxidation mechanism of the high speed steel under dry conditions (condition 3) can be deduced from the observations made during the analysis of surface morphology, cross sectioning and fracture surfaces under this condition and it is relatively simple. The oxidation process started with the dissolution of oxygen in the matrix and within the MC carbides. Oxidation reactions similar to those presented in equation 5.1 and 5.2 presumably were established inside the metal to transform the steel into magnetite, while the hematite layer was formed at the oxide-gas interface by diffusion of iron ions from the substrate in the direction to this interface, at the same time that vanadium oxide was formed on the surface of carbides. As the oxidation of the steel surface was not accelerated by the presence of water vapour in this condition, the oxide layer formed was thin enough to allow the diffusion of vanadium ions (driven by the high partial pressure of oxygen) from the matrix and carbides across the scale to feed the oxide layer formed on the outer layer. The development of vanadium rich oxide needles as those shown in Fig.4.28 can be considered as evidence of the diffusion of vanadium ions for the formation of the external oxide layer supported by the vanadium gradient measured across the scale Figs.4.57 and Fig.4.58 c.

Monteiro and Rizzo, (2004) observed the presence of vanadium rich layers in experiments conducted under the presence of humidity. However, in their work, the humidity content was lower than in the present work and was probably not high enough

to produce a significant reduction to the partial pressure of oxygen and therefore carbide structures as well as the matrix were oxidized.

5.4.2.1 Influence of oxide stoichiometry on the oxidation phenomena

The question can be posed: how do the oxide phases found in each oxidation condition influence the oxidation kinetics of the steel? To answer this, one has to look at the ionic nature of the compounds. If the simplest reactions for iron oxide formation are considered (equations 5.1 and 5.2), from the point of view of thermodynamics at the temperatures of the tests the formation of hematite is energetically more favoured than magnetite, although the difference between the values of free energy of formation is not considerable (Table 11). Thus, it is not surprising that the formation of both compounds was observed at the same time.

Hematite is defined as a n-type metal excess semiconductor (Kubaschweski, 1953 and Khanna, 2002) in which the ionic conductivity within the oxide and hence its growth increases if a reduction to the partial pressure of the oxygen in the system is experienced. It is proposed that throughout the oxidation of the steel in the presence of water vapour, Fe ions were always available to support the growth of hematite because these were released by spinel as a part of its equilibrium process to keep its stoichiometry M_3O_4 as observed in the EDX maps of the oxide layers. If this condition is combined with the fact that the pressure of oxygen is lowered by the existence of water vapour in the atmosphere, the ionic conductivity within hematite increases favouring the mobility of cations and anions across the layer and therefore its growth, and the growth of the oxide layer as a whole.

Hematite was detected in the X-ray diffraction patterns as the predominant phase rather than the spinel M_3O_4 or magnetite for longer exposure times. However, the proportion of each oxide phase changed with time and the condition as indicated by micrographs of the fracture surfaces shown in Fig.4.47 and 4.51 for test at 615 and 550°C. In contrast, during the early oxidation stages, the formation of the spinel or

magnetite was the critical stage, while the formation of hematite was thermodynamically unlikely, consistent with the X-ray diffraction analysis of the early stages of oxidation.

Although the ionic nature of magnetite as a semiconductor is not considered within the standard theories of high temperature oxidation, Chen *et al.* (2006) in their investigation on the high temperature corrosion of a ferritic steel by water, considered magnetite as p-type semiconductor with a metal deficit (where the ionic conductivity within the oxide is increased by means of increasing the value of oxygen pressure in the system). At first sight the proposal by Chen *et al.* seems valid and the M_3O_4 spinel could be considered as p-type semiconductor for the reason that a marked deficit in iron was observed in most of the EDX map analyses, Figs.4.48 and 4.52 for example. During the early oxidation stages, oxygen was initially dissolved in the steel to form the spinel M_3O_4. Although the partial pressure of oxygen in the system was lowered by the addition of water vapour (Table 8), the oxygen pressure was sufficiently high to promote the migration of iron ions from the spinel to form magnetite and hematite at the expense of the spinel layer. As the oxide layer thickened progressively with oxidation time, the pressure of oxygen in the areas where the spinel and magnetite layers were formed was locally reduced, affecting the ionic conductivity within the spinel and magnetite layers, giving a progressive reduction in the thickness of both layers. This condition was not observed and a balance of the thickness of the spinel and hematite layers was constant for long oxidation times.

Based on the evidence just discussed and the fact that magnetite is an inverse spinel that grows by diffusion of Fe^{2+} and Fe^{3+} as well as the fact that Cr ions take the position of missing iron ions to form the spinel, it is proposed that under these conditions the spinel layer and magnetite behaved as a n-type semiconductor with excess metal rather than a p-type one with metal deficit. Therefore the local reduction of the partial pressure of oxygen as the oxide layer grew, stimulated and ensured the conductivity of ionic species in this layer and hence the overall growth of the oxide layer.

Based on the observations of the oxidation tests performed under dry conditions in which the carbides where oxidized, there is not doubt that the rate of growth of the oxide layer is strongly influenced by the high pressure of oxygen inside the oxidation reactor. Vanadium oxide V_2O_5 is considered as a n-type semiconductor where increments to the partial pressure of oxygen decreases the conductivity within the oxide therefore its presence as a part of the whole layer contributed significantly to a reduction in the mobility of ions, resulting in the development of a logarithmic rate of reaction.

If the presence of vanadium oxide VO is considered, this semiconductor behaves either as n-type or p-type. In the present work it might be possible that the oxidation of vanadium carbide and the vanadium contained in the matrix lead to the growth of n-type vanadium oxide VO whose electrical conductivity is reduced in high partial pressure environments, as was the case in the dry conditions. If this compound acted as a p-type semiconductor, this would imply that for the existent oxygen partial pressure the electrical conductivity inside the oxide should be high. However, this seems unlikely given that the oxide kinetics were logarithmic and no alteration to a rapid oxidation rate was observed.

The growth of hematite, magnetite and the spinel phases was also limited by the high pressure of oxygen in dry conditions. These being n-type semiconductors show a limited conductivity of ionic species and electrons within them, consequently reducing the rate of reaction and hence the rate of oxide growth that was expressed by the development of the logarithmic oxidation rate at both temperatures.

5.5 Experiments carried out under cyclic conditions

5.5.1 High frequency cycles

The oxidation of the material under this condition was not as severe as is it was expected and only slight changes were observed. The mass change of the samples exposed to the action of various thermal cycles can be better explained if the

accumulation of mass is taken into account (Fig.4.59). This plot suggests that instead of a mass loss, as would normally be expected in cyclic oxidation conditions, the general trend was one of mass gain. This phenomenon can be explained if a relation to the morphology of the oxide, the chemical elements contained within it and the number of the cycles imposed to the samples is considered.

The oxide layer was too thin to measure up to 120 cycles. Between 120 and 300 cycles the oxide layer consisted of fine oxide nodules (Fig.4.60 a and Fig.4.62 b). Thus, during this stage, the early stages of oxidation were being observed, and therefore low values of mass gain were observed.

The second factor that supports the premise of the early stages of oxide formation is that in most of the EDX analyses of these oxides, the presence of iron, chromium and oxygen was a common finding (Fig.4.64). It is proposed that the oxide formation in these experiments also started with the dissolution of oxygen in steel and its reaction with oxygen to form magnetite, where Cr^{+} replaced the Fe^{+} to form a Cr rich spinel with a fine grained structure similar to the one shown in Fig.4.10 a) and b). Therefore, if fine nodules existed on the surface of the samples containing mainly iron, chromium and oxygen, this oxide structure can be associated with the early stages of formation of the spinel M_3O_4.

In some cases a significant amount of silicon was detected during the EDX analysis of the oxide layer (Fig.4.65). The silicon content of the steel was not enough to promote silicon based oxides, the iron silicate known as fayalite Fe_2SiO_4 (Chang and Wei, 1989) was considered as a possible oxide phase present on the steel. However, the growth of this phase can be discounted, as this phase is only found with the presence of Wüstite (FeO) whose formation was suppressed by the presence of chromium in the steel. Therefore, the presence of silicon in the oxide could be considered in the form of an isolated oxide phase of silicon dioxide SiO_2, probably a product of contamination from the reaction chamber. Unfortunately, the X-ray diffraction analysis of the steel was not successful as the phase was present in too small a quantity to be detected.

Finally, if the average time of exposure of each sample at 615°C was of about 1.5 seconds per cycle, this implies that this value multiplied by the total amount of cycles experienced for one sample (300) results in a total amount of exposure time of 450 seconds for the whole experiment (7.5 minutes in total). If the sample were to be exposed to isothermal conditions for this amount of time, the resultant oxide layer would have been thin and only showed the early oxidation stages of the steel. Therefore it can be concluded that the number of cycles the samples were exposed to were not enough to promote the growth of thick scales and the oxide grown under the conditions studied represented the early oxidation stages of the steel. As such, the oxide scale on the surface of the high frequency cyclic tests could not be directly compared with those from the isothermal tests.

During the surface inspection of the steel it was found that the samples subjected to around 240 thermal cycles experienced severe plastic deformation at the surface and microcracks in zones located near to the bottom edge of the samples (i.e the region where the sample impacted in the water quench each time). This can only be related to the thermal shock imposed to the samples when they were quenched after the heating stage. The plastic deformation was concentrated at the edge of the sample and occurred in zones locally to carbide clusters (Fig.4.67). This suggests that the thermal mismatch stresses between carbide and matrix were sufficient to cause plastic deformation. The cracks observed inside the carbides or in zones near to them are indicative of the high local strain that clearly exceeded the fracture strain of the carbides. The nucleation of cracks in carbides or in zones near to these sites is a feature that is in agreement with the observations made by Colás *et al.* (1999), although their test conditions were not pure cyclic oxidation tests. The microcracks generated in the steel and carbides acted as oxygen diffusion paths (Fig.4.67) promoting local oxidation within the steel (Figs.4.69 and 4.70). Such microcracking and oxidation leads to local spalling of the roll surface during hot rolling, which is a principal reason that the rolls have to be re-ground.

5.5.2 Low frequency cycles

Low frequency cycle testing was used to observe the causes of oxide failure and spallation from the surface of the steel. Thicker oxide scales were obtained under these conditions compared to those formed in the higher frequency cyclic tests.

Mass losses were expected from the spalled oxide, but this did not occur in the oxidation kinetics plots because the exposure time to the heating stage was long enough to produce the growth of new oxide in sites where oxide was previously removed during the cooling cycle, so that the mass lost in this action was rapidly replaced by the growth of new oxide. However, the procedure used to give an approximation of the rate at which oxide was lost (Fig.4.75 b) and Fig.4.76 b) can be considered as correct if the results from the X-ray diffraction analyses combined with the surface inspection of the samples are reviewed.

At both temperatures, the X-ray diffraction patterns of the samples after the action of 2 thermal cycles revealed hematite as the dominant oxide phase on the surface of the steel. Exposure to 2 heating cycles is equivalent to almost 2 hours of continuous oxidation under this environment, which promoted the development of a thick hematite layer whose growth was favoured by the low partial pressure of the environment, as discussed in Section 5.4.2.1.

In contrast, after 40 cycles XRD reflections corresponding to magnetite or spinel phases suggested these as the dominant phases present on the surface of the steels. The information obtained in the diffraction patterns agrees with the evidence found in the micrographs of the steel after 2 thermal cycles where the surface of the steel was covered by a dense grey hematite layer. Spallation only occurred in a few zones. After 40 cycles where the black zones of magnetite or spinel were the dominant phase found on the steel, the extent of spalling was greater than in the samples that experienced few oxide cycles (Fig.4.86).

Fig.4.79 shows an uplift of the oxide, which is a partially spalled region, as shown schematically in Fig.5.4.b). It is clear the failure of the oxide scale started with the formation of buckled zones normal to the surface of the steel preferentially in the hematite layer (Fig.4.79). These zones have similar characteristics to the zones described by Evans, (1995) during the analysis of failure mechanisms in oxide scales. According to this author the development of curved zones or "buckling" in oxide scales exposed to thermal cycles results from the existence of compressive thermal stresses acting on the relatively plastic oxide scales which have poor adherence to the substrate (Fig.5.4 a). The analysis of the fracture surfaces of the oxide layer obtained during the isothermal oxidation tests suggested that the adherence between the outer hematite layer and the intermediate magnetite is low (Fig.4.35 b) and Fig.4.37 a) and Fig.4.53 b) for example). In addition, according to Tuck *et al.* (1969) the presence of water vapour may increase the plasticity of the oxide scale as it was the case during the isothermal oxidation of the steel, where pore formation was not observed under the presence of water.

Based on these observations, the two basic conditions required for the development of the buckling mechanism in the oxide layer were satisfied at both test temperatures, these are: 1) the existence of a fairly plastic oxide layer with low adhesion to the substrate and 2) the presence of compressive stresses developed during quenching.

As the number of thermal cycles increased, hematite continued to grow in zones where spallation did not occur. The preferential spallation of hematite leads to the preferential growth of the spinel and magnetite phases therefore, as the number of thermal cycles increased; the surface steel at both test temperatures contained a considerable amount of spinel and magnetite, as shown by the X-ray diffraction patterns.

The trend in Fig.4.86 that gives the amount of oxide lost expressed as a percentage of the spalled area, shows that the amount of oxide spalled increased progressively with the number of cycles, a result of the preferential loss of hematite. The difference between the amounts of oxide spalled at both temperatures can be linked with the values of compression thermal stress that acted on the oxide layers and the steel

during each cooling stage and that was calculated according to the expression proposed by Walter and Schutze, (1992) as:

$$\sigma_{ox} = \frac{E_{ox}(\alpha_{ox} - \alpha_{me})\Delta T}{1 - \mu_{ox}} \tag{5.12}$$

where σ_{ox} represents the value stress acting on components of an oxide scale, E_{ox} the elasticity modulus of the oxide, α_{ox} and α_{me} are the linear expansion coefficients of the oxide and steel respectively, ΔT the thermal gradient of the experiments and μ_{ox} the Poisson ratio of the oxide.

Using data taken from the literature (Table 12), a value of compressive stress of -287 MPa was obtained for hematite when the temperature was reduced from 615 to 25°C whereas a value -226 MPa was obtained but when the temperature was reduced from 550 to 25°C. If the same equation is used for the calculation of compressive stress that acted on magnetite and the spinel layer, higher values of stress acting on these layers are obtained that are in the order of -484 MPa and -431 MPa for cooling from 615 and 550°C respectively.

Although the stress is higher for magnetite than for hematite, the columnar structure of magnetite and the fine grained structure of the spinel suppressed the deformation of these layers under compression. If during heating, the steel substrate expanded faster than the oxide scale, the stress becomes positive and a tensile stress is applied to the entire oxide layer. These stresses caused the transverse fracture observed in the hematite layer (Fig.4.82 b) and the development of cracks in the spinel (Fig.4.83 a) providing that the adherence of this phase to the steel substrate was good, as suggested by microstructural observations of the isothermal oxidation experiments. The development of cracks in the spinel layer is also in agreement with the second failure mechanisms proposed by Evans, (1995) denominated as wedging.

By comparison of the values of stress obtained for hematite, it is clear that a considerable difference between the absolute values of compressive stress present at each temperature exists (~62 MPa), therefore if higher compressive stresses are imposed on the oxide as result of the greater thermal gradient experienced when quenching from 615°C and if also the growth of the oxide layer is faster under this condition so that thick layers are obtained, the amount of hematite spalled is consequently higher at 615°C than at 550°C as it was suggested in Fig.4.86. Fig.5.4 b) shows a schematic diagram of the spallation mechanisms present in the steel.

If in a high speed steel work roll used in the hot rolling of steel strip, the spallation of hematite occurs at every cooling cycle, this oxide is not present on the surface leaving just an oxide layer covering the surface that is comprised of magnetite and spinel M_3O_4. In addition to this, if cracks are generated in the remaining layer, the presence of oxygen below the oxide layer in direction to the substrate zones is stimulated and so the formation of oxidation zones below the surface of steel.

5.6 Influence of the oxide growth on the evolution of the rolling contact experiments

In all the rolling-sliding tests, the formation of a red-black oxide layer on the surface of the disc was a common observation. The aspect of this layer was similar to that observed in the samples tested in the isothermal oxidation experiments. The formation of this oxide layer is in agreement with previous observations regarding the wear mechanisms of work rolls reviewed in Chapter 2, which suggested that these are strongly related to the formation of a black oxide layer on the surface of the work rolls (Kato *et al.* (1992), Erickson *et al.* (1993), Choi and Kim (1999) and Li *et al.* (2002)). The differences in the amount of oxide produced during the test as well as the influence of these layers on the values of tribological variables of interest observed during the tests are discussed in the following sections.

The worn surfaces all contained oxides (see Figs 4.95 and 4.96). In addition, the wear debris was almost entirely oxide for the water lubricated tests and a mixture of oxide and metal for the dry tests (Fig.4.126 and Fig.4.127 respectively). Therefore, oxidational wear was an important mechanism for all tests. Much is known about oxidational wear from numerous studies over many years, many of which focus on ferrous materials. It is clear that oxides play a major role in determining the wear rate of these materials, shown for example, by the classical work of Welsh, (1965), and Quinn and co-workers (see a comprehensive review in Quinn, (1983)). Thus, the friction and wear behaviour observed in the current study will be related to the role of the oxide formation and detachment, as well as the classic ploughing wear mechanism that was also evident.

In agreement with the investigations of Nield and Griffin (1961) and Lancaster (1962) who noted that the wear behaviour of metals is a strong function of the local environment, the wear rate of the high speed steel discs was higher for the test in dry conditions than in those that included water and water vapour. This difference was strongly linked to the amount and composition of the oxide layer that grew in each condition. The morphology of the worn surface under water lubricated conditions was different to that under dry conditions. For the dry tests, the oxide was clearly mechanically mixed into the surface. In contrast, for the water lubricated tests the oxide tended to stand proud of the surface, as oxide islands, which were chromium rich islands of the spinel M_3O_4. Thus, there appears to have been an important difference in the contacting asperities, which appeared to be oxide for the water lubricated tests and a mechanically mixed mixture of oxide and metal for the dry tests. Thus, the water and water vapour appeared to accelerate the oxidation rate (equation 5.3), as was observed for the static oxidation tests (Fig.4.4 and 4.5), leading to the formation a thick oxide scale on the surface of the test disc (Fig.4.128).

According to Hirst and Lancaster (1953), Bowden (1953), Sullivan and Athwal (1983) and Stott (1998) the growth of oxide layers on the surface of metals subject to sliding reduces the wear rate considerably. This was certainly the case for the tests at 500

and 600°C under the presence of water, where it was observed that relatively thick scales grew driven by the high temperature of the environment and the presence of water, completely covering the contacting asperities of the test disc, ensuring that virtually no contact was from the metal substrate (Fig.4.95 b to f), promoting the low values of wear observed at these temperatures.

Quinn (1971) and Stott (1998) pointed out that in the oxidative wear of metals subject to sliding; the wear rate is mainly determined by the rate of removal of the oxides formed. The X-ray diffraction analysis of the wear debris collected at 500 and 600°C revealed that the wear debris was almost entirely oxide. The main component was hematite, but traces of magnetite were also present, but no positive identification of metallic iron. Thus, from this and the observations of the surface state of the discs (Fig 4.95 b to f), it can be stated that the main wear mechanism at 500 and 600°C an under this condition is oxidational, consistent with the definitions by Quinn (1971) and Stott (1998). The oxide layer was presumably removed in the classical manner, namely detachment when it reached a critical thickness. Fragmentation and agglomeration of the oxide wear debris was apparent in the lower areas of the worn surface (i.e. the areas that were not in contact).

The dominant presence of hematite in the wear debris suggested its preferential removal leaving the surface of the test disc protected by a layer of compacted and agglomerated wear debris which was predominantly the spinel M_3O_4. According to the investigations of Bisson *et al.* (1957), Earles and Hayler (1972), Sullivan and Athwal (1983) and, Stott (1998), films of spinel magnetite Fe_3O_4 provide more protection against wear than any other iron oxide formed on steel surfaces subject to sliding, leading to the development of low wear rates because these films prevent successfully direct metal to metal contacts. This certainly was the case at 500 and 600°C where it was observed that iron and chromium rich oxide pads (Fig 4.97 a) and Fig.4.103 a)) protected the surface of the test disc and prevented the establishment of such contacts.

The wear rate at 400°C under the presence of water and water vapour was marginally higher than at 500 and 600°C under the same environmental condition. The extent of oxidational wear was less at this temperature, as shown by both plan view and cross section analyses of the test disc (Fig.4.107 and 4.108). The possibility of forming a protective oxide layer at this temperature was therefore reduced. This allowed the establishment of metal-metal contacts that resulted in the plastic deformation of the surface by the ploughing exerted by the hard asperities of the counter disc. Ploughing would certainly have been helped by the softening of the disc at this temperature. The considerable content of iron found during the X-ray diffraction analysis of the wear debris collected at this temperature (Fig.4.126 c) suggests that this mechanism is correct.

In contrast to the tests that included water, the dry tests yielded considerably higher wear rates, which were also a strong function of temperature. In this condition the wear of the test disc appeared to be associated with two mechanisms: oxidation and plastic deformation (i.e. ploughing). Both mechanisms are strongly linked to the temperature of the test and their combination has been observed before for work roll materials subject to sliding conditions (Rainforth *et al.* (2002)).

The level of oxidation of the surface increased with the temperature of the test, as shown by the surface state of the disc (Fig.4.96). However, at any temperature, the micrographs of the surface still revealed zones of the metallic substrate that confirmed that oxide production in this condition was not as pronounced as in the tests that included water. Thus, the increase in wear rate with temperature would simply have been a result of the decrease in surface hardness with temperature, suggesting that the metallic wear was dominant over the oxidational wear.

The oxide layer formed on the substrate of the test discs had a composition similar to that of hematite Fe_2O_3 as shown by X-ray diffraction analysis of the collected wear debris. No other iron oxides were present. The preferential development of this layer during the test is in agreement with the results obtained from the isothermal oxidation experiments at least at 600 and 500°C that revealed a considerable amount of this phase

(Fig.4.31 and 4.34). The growth of this layer clearly did not offer much benefit in reducing wear rate, and not as effective as magnetite Fe_3O_4 or better reported as the spinel M_3O_4. Bisson *et al.* (1957) noted that water and water vapour promoted lower wear rates as a result of magnetite formation. In addition, in this condition only few thin pads of oxide were formed on the surface as the temperature of the test was increased (Fig.4.96) but these were easily removed by mechanical damage offering no protection to the surface against both oxidation and plastic deformation. Further evidence that the oxide did not provide adequate protection is shown by the way in which oxide was mechanically mixed into the metallic regions of the surface. This also demonstrates the considerable plastic deformation that occurred at the surface, which would have become more pronounced as the temperature increased.

The increment in the wear rate with the temperature of the tests is also consistent with the increase in relative intensity of the iron peaks revealed in the X-ray diffraction patterns of the wear debris (Fig.4.127). This fact suggests the amount of metal present in the debris increased progressively with the temperature given that the removal of metal fragments was facilitated by the softening of the surface and therefore proves that the mechanism of plastic deformation of the substrate is the dominant mechanism and controls the amount of wear experienced by test disc in this testing condition.

The wear behaviour as a function of temperature was quite different under wet compared to dry conditions. For wet tests, the wear rate was largely insensitive to temperature, while for dry tests, the wear rate was strongly dependant on temperature. At first sight this is difficult to explain. However, as has been discussed already, under wet conditions, the wear mechanism was predominantly one of oxidational wear. The oxide structure did not change dramatically between the temperatures. The absence of a strong effect of temperature on wear rate suggests that the basic properties of the oxide (i.e. hardness and fracture strength) did not change enough to influence the wear rate between the temperatures of 400 and 600°C. In contrast, the wear rate in the dry tests appears to have been controlled by metallic wear and not oxidational wear. The strong influence of

temperature on substrate hardness would therefore explain the increase in wear rate with increase in temperature.

The behaviour of the friction coefficient was complex and difficult explain. The friction coefficient was higher for the water lubricated tests compared to the dry tests, (Fig. 4.93 b), which is the reverse of what would be intuitively expected. Both wet and dry tests exhibited an approximately linear increase with temperature, which is not surprising. However, the marked change in friction with temperature for the wet test is completely different behaviour to the wear rate, which was largely insensitive to temperature. Moreover, it is possible that the water had not entirely evaporated before entering into the contact region, which would also be expected to reduce the friction.

Before trying to explain this behaviour, the expected behaviour from the literature is discussed. According to investigations of Earles and Hayler (1972), Bisson *et al.* (1957), Lancaster (1962), Stott and Wood (1978), and, Stott (1998) the formation of oxides on the surface of metals subject to sliding, particularly steels, would generally be expected to reduce the value of the friction coefficient. This can be for several reasons: the oxide is harder than the substrate, it may act as a solid lubricant, and the interfacial shear strength between an oxide and metal (or another oxide) is lower than between a metal and metal as the adhesive forces are lower.

According to Bowden and Tabor (1964) the friction coefficient is defined as the ratio between the friction force and the normal load applied to the tribosystems as:

$$\mu = \frac{F}{P} \tag{5.13}$$

where μ is the friction coefficient, F the friction force and P the normal load. The friction force consists of two components related to the contacts formed or junctions. A component of adhesion associated to the attraction forces established between the

junctions formed and a component of deformation that involves the ploughing exerted by of the hard asperities of one body against the soft asperities of another body so that equation 5.13 can be better represented as:

$$\mu = \frac{F_{adhesion} + F_{ploughing}}{P} \tag{5.14}$$

Thus, for the wet case, where the oxide coverage was greater, the value of $F_{adhesion}$ should have been lower than for the dry tests. For example, So (1995) reported that for metallic surfaces sliding against oxides, the friction coefficient has low values because the adhesion component of the coefficient is low. It is certainly difficult to envisage a scenario where it is larger. This suggests that it is $F_{ploughing}$ that is higher for the wet case compared to the dry case. However, this is again the reverse of what would have been expected as it was the dry case that was dominated by metallic ploughing, while the wet tests were dominated by oxide contact. Of course, in all this argument it is assumed that the counterface did not change appreciably between wet and dry conditions. However, being a similar material, the counterface would have undergone the same changes as the test disc.

The friction coefficient increased linearly with the temperature presumably because the ploughing component of the friction coefficient increased as more oxide was found on the surface as in the case of the experiments conduced under the presence of water but with a lower value fixed by the brittle nature of hematite Fe_2O_3, the oxide layer found on the surface.

The surface roughness of the steel discs in wet conditions increased from the initial low value to relatively high values and remained practically constant for the rest of the test. However, the surface roughness was generally lower compared to those obtained in dry conditions (Fig.4.92). This behaviour is possibly associated with the formation of the abundant flat chromium rich oxide islands of the spinel M_3O_4 of compacted debris that gave the surface a smooth character even though ploughed zones were also a

common finding on the surface. In contrast, the roughness values measured from the surface of the test discs in dry conditions were higher than those measured in the wet experiments (Table 13 and Fig.4.92). This can be logical considering the strong topographical changes induced to the surface of the disc as result of the removal of non oxidized steel fragments by mechanisms that involved the ploughing of the soft steel matrix and that was not protected by a thick oxide layer. The change in surface roughness in this condition is consistent with the amount of steel fragments removed from the surface of the discs that increased as the temperature of the test was increased.

A feature that can be also associated to the relatively low values of friction measured in dry conditions deals with the penetration of oxide particles into the metallic matrix. If these hard particles of hematite were pushed into the matrix as was commonly observed at the end of the test (Fig.4.96 d and f) this formed small oxide pads that possibly acted as low shear strength layers thereby limiting the friction values.

One of the failings of equation 5.14 is believed to be that it does not take into account changes in asperity sizes, i.e. the junction size, that occur as a result of the frictional contact. The equation that describes the growth of a junction in the theory of friction presented in Hutchings (1992) is expressed as:

$$W^2 + 4F^2 = A^2 {p_0}^2 \qquad (5.15)$$

where W is the normal load, F the friction force, A is the true area of contact and p_0 is the yield stress in compression. Given that the normal load and the yield stress represent constant properties, the only term responsible to increase the value of the friction force F in equation 5.15 is by means of increasing the true area of contact of the interface formed by the discs. While the roughness of the wet tests was lower than the dry, this does not necessarily mean that the junction size was also smaller. It is proposed that in the experiments developed under the presence of water the production and incorporation of considerable amounts of debris at the contact zone formed by the discs increased the number of junctions formed and consequently the magnitude of the true area of contact of

the interface action reflected as an increment in the value of the friction force required to break the junctions formed. This effect is analogous to the investigation conducted by So (1995) where he pointed out that the incorporation of fragments of wear debris to the contact zone formed during the sliding of steel tend to increase the value of the friction coefficient. The friction coefficient is therefore higher in wet conditions than in dry conditions because of the greater amounts of wear debris produced in the former case given that the oxidation phenomenon of the surface is increased by the presence of water and water vapour being the extent of wear debris production controlled by the temperature of each test.

An additional factor that may account for the development of high friction values in the wet conditions is the presence of water either as a liquid or gaseous lubricant. Hirst and Lancaster, (1953) identified that high temperature oxidized stainless steel lubricated by stearic acid developed a high friction coefficient in sliding conditions of about 0.56 value higher than the one measured for non oxidized metal lubricated in the same liquid. In a different investigation, Bisson *et al.* (1957) found that in the presence of a lubricant film of cetane, the friction coefficient of steel sliding against steel had values as high as 1. The mechanisms that explain these high values of friction are not well established in these works but they maybe are related to increment to the value of shear strength of the interface as result of the existence of an extra layer of different physical properties (high viscosity for example). In the current work the presence of water either as a liquid or as a gas may represent another physical barrier that needed to be sheared additionally to the oxide layer that exists on the surface and that definitely accounted to increase the value of the shear strength of the interface. Undoubtedly this feature requires a more detailed investigation.

One last experimental observation that is difficult to explain, but would have had an effect on the friction and wear rate is the frictional heating. No direct measure of the frictional heating was made (as this is experimentally impossible), but there is an indirect measure. Fig.4.130 shows the hardness lost by the test material as a result of heating during the test. For both wet and dry conditions there is a near linear increase with test

temperature, which is not surprising. However, what is very odd is that the wet tests lost more hardness than the dry tests, despite having cold water dropped onto the specimen throughout the test. This can only mean that the substrate in the wet tests was hotter than in the dry tests. This implies that the thermal conductivity at the contacting asperities was lower for the wet tests than the dry tests. This is consistent with the microstructural observations that the wet test contacts were oxide, while the dry were a mixture of oxide and metal. Moreover, the oxides were different between the two conditions, with spinel being present for the wet tests, but not for the dry. Spinel M_3O_4 exhibits a low thermal conductivity ($k_{average} \approx 0.035$ W/m-°C between 400 and 25°C, Molgard and Smeltzer (1971)) that avoided a proper dissipation of the heat flux either to the atmosphere or to the counter disc, increasing the degree of softening of the surface.

The greater heat generation at the interface in the wet tests compared to the dry would have decreased the surface hardness more for the wet tests. This would have resulted in a higher value of $F_{ploughing}$ (equation 5.14), thus explaining why higher friction was found for the wet tests. It is interesting, however, that the higher substrate temperature did not result in greater wear rates.

Chapter 6

Conclusions and further work

6.1 Conclusions

1) A water vapour-air mixture accelerates the oxidation process of the work roll grade high speed steel, when compared to dry air only. This is because of the establishment of additional oxidation reactions on the steel, giving another source of oxygen ions to generate the oxide scale.

2) The oxidation rate depends on the amount of water vapour present in the oxidant atmosphere regardless the oxidation temperature. Logarithmic relations were observed for the maximum water vapour content, and for dry air although with considerable differences in the mass gain. Perfect parabolic kinetics were observed when the water saturation of the mixture was reduced to 70 %.

3) The rapid growth of the oxide layer during the early oxidation stages in the condition with maximum water vapour (condition 1), was associated with the low value of apparent activation energy required to initiate the oxidation process under this condition. The activation energy value increased as the amount of water vapour in the atmosphere was reduced.

4) The logarithmic oxidation rate found in condition 1 was associated with a reduction in the oxidation rate on the surface of the steel as a consequence of a rapid growth of a dense and compact layer of hematite platelets, with fine grained spinel oxide in the early oxidation stages. These structures reduced the diffusion of metallic and non metallic ions across the oxide layer.

5) The parabolic behaviour which was characteristic of condition 2 (0.45 cm^3/min water vapour) suggests that the oxidation phenomenon occurred progressively so that a continuous supply of oxygen ions were available during the whole process. Migration of oxygen was assisted by regions where the carbides were not covered by lateral growth of the oxide layer, acting as easy paths for oxygen to reach the non oxidized steel.

6) The logarithmic behaviour observed in dry conditions resulted from the absence of the additional oxidation reactions that were promoted by the water vapour.

7) A black-red oxide layer was formed on the high speed steel in wet conditions, consistent with the published literature. The composition of the oxide included a chromium rich spinel of the form M_3O_4 (M=Fe,Cr), an intermediate layer of magnetite Fe_3O_4, and an outer Fe_2O_3 hematite layer.

8) VO oxide was observed on the surface of the steel during exposure to dry conditions, but not in wet conditions. The formation of this oxide was favoured by the high partial pressure of oxygen in the environment that promotes the oxidation of MC vanadium rich carbides and the vanadium dissolved within the steel matrix. In environments of lower oxygen pressure, oxidation of MC carbides is not observed and the vanadium oxide layer is not formed.

9) The low partial pressure of oxygen present in environments containing water vapour favours the growth of the whole oxide layer by the individual contributions of the spinel, magnetite and hematite layers, which being n-type semiconductors promote the ionic and electrical conductivity across the oxide layer under these conditions. The increment in the partial pressure of oxygen in dry air reduced the ionic and electrical conductivity in the spinel and hematite layers and therefore the growth of the oxide layer. The electrical and ionic conductivity in the ampotheric conductor vanadium oxide VO is favoured under

these conditions, but the vanadium content in the steel is not enough to produced notable increments to the oxidation rate of high speed steel.

10) The number of thermal cycles imposed on the steel samples during the high frequency cycling oxidation experiments was not enough to promote significant mass gain. The thin oxide layer formed in this condition can be associated with the early stages of formation of the chromium rich spinel M_3O_4.

11) During the cyclic oxidational tests, severe plastic deformation and micro cracks were induced by the thermal shock on the sample as it was quenched in water. Plastic deformation was most prominent around the larger carbides and the associated stress concentration resulted in crack initiation and propagation. The microcracks effectively act as paths that promote the flow of oxygen in the steel.

12) During the low frequency cyclic oxidation tests, the spallation of hematite was favoured by: 1) The plasticity of the oxide scale associated with the presence of water vapour and 2) The compressive thermal stresses existent during quenching promoting the buckling failure mechanism, as well documented in the literature. The spallation of hematite increased with the number of thermal cycles, and the surface of the steel was only protected by magnetite and spinel, phases whose growth is favoured by the absence of hematite.

13) Cracks were observed in the spinel layer, but spallation of this phase was not observed, attributed to the strong adherence of this layer to the steel substrate, despite the compressive stresses that act on this layer are higher than those experienced by the hematite layer.

14) The rate of oxide spallation and therefore the amount of oxide removed from the surface of the steel is greater at 615°C than at 550°C, because of the greater compressive stresses associated with the greater temperature difference.

15) The wear mechanisms during the rolling-sliding tests involved oxidational wear under all conditions of temperature and the environment. However, under wet conditions, wear was predominantly oxidational, while under dry conditions, wear was a combination of oxidational and metallic (ploughing wear).

16) The wear rate was lower for all water lubricated tests compared to dry tests. The wear rate for the wet conditions was independent of temperature, while for dry conditions the temperature had a strong effect on wear rate. This suggests that for the wet conditions the mechanical properties of the oxide at the contacting asperities did not change appreciably with temperature. In contrast, for the dry tests the reduction in the hardness of the steel with temperature would have resulted in increased metallic wear and therefore a significant temperature dependence of wear rate.

17) The friction coefficient observed was higher for the water lubricated tests compared to the dry tests, an unexpected result. In both cases the friction coefficient increased almost linearly with temperature. There was no evidence that the water acted as a lubricant.

18) The contacting asperities on the test disc for water lubricated conditions were entirely oxide, while for the dry tests there was a mixture of oxide and metallic contact. The oxides observed were different between the two conditions, with spinel being present for the wet tests, but not for the dry.

19) Surprisingly, the steel lost more hardness with temperature in the wet test than for the dry tests. This indicates increased frictional heating for the water lubricated tests, which explains the higher friction coefficient. It is believed that the increased frictional heating was associated with the presence of spinel M_3O_4 in the water lubricated tests which exhibits a low thermal conductivity ($k_{average} \approx 0.035$ W/m-°C between 400 and 25°C).

20) The experimental facility used during the rolling-sliding experiments allowed the effective recreation of the oxidation and cracking processes of the steel developed during commercial practice.

6.2 Further work

1) The oxidation kinetics of the high speed steel should be studied at other temperatures as long as the temperature selected lies in the interval of those experienced by the work rolls in hot strip mills, in order to obtain more accurate values of apparent activation energies and oxidation rate constants with modelling purposes of interfacial phenomena found in the stands. Particularly at 650°C the effect of this temperature on the mass change of the high speed steel is interesting because this point is near to the temperature value where vanadium oxides are volatile.

2) The differences in the cooling practices of work rolls in hot strip mills could lead to differences in the rate of growth of the oxide layer and because of these, the effect of different amounts of water vapour in the oxidation rate of the high speed steel is also a matter of interest and should be studied.

3) It is also proposed that the oxidation behaviour and characteristics of alloyed white cast ions as another work roll materials should be studied, in order to map the differences with respect to the high speed steel and to see if their incorporation to the stands of the hot strip mill is feasible.

4) The problem in attaining a sufficient number of thermal cycles on the surface of the high speed steel could be addressed by the use of an induction coil rather than an induction furnace. A preliminary trial was conducted resulting in a heating time of 30 seconds to reach 600°C using the sample morphology proposed in this investigation.

5) As in the case of the isothermal tests, the comparison between the oxidation rate of high speed steel and alloyed white cast irons under cyclic oxidation conditions is also suggested.

6) The effect of different loads, speeds and slippage ratios on the behaviour of the oxide layer should be measured as only one condition was investigated in the current study. The study of the effect of these characteristic on the growth of the oxide layer is suggested in order to simulate the variations found along the different stands in hot strip mills.

7) The topographical changes of the test disc surface can be represented in three dimensions using the data obtained from the roughness measurements introducing them to mathematical algorithms available in the literature that can give an approximation of the actual state of the surface. This mathematical representation of the surface could be introduced to a finite element simulation code in order to study in a more direct way the interaction of the asperities of the surface when in contact with a second body for example the oxides found on the surface of the strip.

8) At the moment it is only possible to simulate the contribution of the back up roll to the change in the surface characteristics and wear of the high speed steel disc, but the direct integration of the third component present in hot strip mills, the strip, is mandatory. In order to have a more complete physical model and to study the effect to the oxides grown on the strip on the wear characteristics of work rolls, it is possible to modify the Cameron-Plint machine and adapt a third disc to it by means of a gear box. This disc can represent the steel stock if it is heated up to a desired temperature by changing the induction coil that is actually fitted to the machine by one that allows reaching temperatures up to 900°C. Unfortunately it will no be possible to apply a deformation load to the disc because deformation will lead to detachment of material from the surface resulting this in a dangerous

operation; but even tough a deformation load will not be present, oxide will be generated on the surface of the disc and this feature could produce interesting results in a more complete way, closer to the real process.

References

Batchelor, A. W., Stachowiak, G. W., Cameron, A. (1986). "The relationship between oxide films and the wear of steels". Wear Vol.113, no.2, pp. 203-223.

Baud, J., Ferrier, A., Manenc, J., Bénard, J. (1975). "The oxidation and decarburization of Fe-C alloys in air and the influence of relative humidity". Oxidation of Metals Vol.9, no.1, pp.69-97.

Bedolla, A. (2001). "The effect of silicon and mischmetal on the structure of high chromium cast irons for wear resistance applications" Ph.D Thesis. Department of Engineering Materials. The University of Sheffield, Sheffield, U.K

Belzunce, F.J. Ziadi, A., Rodriguez, C. (2004). "Structural integrity of hot strip mill rolling rolls". Engineering Failure Analysis Vol.11, pp.789-797.

Beynon, J.H. (1998). "Tribology of hot metal forming". Tribology International Vol.31, no.1-3, pp.73-77.

Birks, N. Meier,G.H. (1983). "Introduction to high temperature oxidation of metals". Edward Arnold, USA.

Bisson, E., Johnson, R.L, Swikert, M.A. (1957). "Friction, wear, and surface damage of metals as affected by solid surface films: A review of N.A.C.A" Proceedings on the conference of lubrication and wear, The Institution of Mechanical Engineers, paper 31, pp.385-395.

Boccalini, M., Goldenstein, H. (2001). "Solidification of high speed steels". International Materials Reviews, Vol.46, no. 2, pp. 92-115.

Bowden, F.P. (1962). "Introduction to the discussion: The mechanisms of friction". Proceedings of the Royals Society of London A273, pp.441-449.

Bowden, F.P., Tabor, D. (1964). "The friction and lubrication of solids. Part II". Oxford University Press

Caithness, L., Cox, S., Emery, S. (1999). "Surface behaviour of HSS in hot strip mills". Advances in Mill Roll Technology Rolls 2000+ Conference Papers, Birmingham UK.

Caplan, D., Cohen, M. (1966). "Effect of cold work on the oxidation of iron from 400-650°C". Corrosion Science Vol 6, pp.321-335.

Caplan, D. (1966). "Effect of cold work on the oxidation of Fe-Cr alloys in water vapour at 600°C".Corrosion Science, Vol.6, pp.509-515.

Chang, Y., Wei, F. (1989). "High temperature oxidation of low alloys steels". Journal of materials science Vol.24, pp.14-22.

Chen, Y. (2006). "Microstructural examinations formed on an oxide dispersion strengthened ferritic steel exposed to supercritical water".Journal of nuclear materials, Vol.359, pp.50-58.

Choi J., Kim, D. (1999). "Mechanisms of Surface Deterioration of High-Ni Grain Roll for Hot Strip Rolling". ISIJ Vol. 39, no. 8, pp. 823-828.

Colás, R. (1995). "Modelling heat transfer during hot rolling of steel strip". Modelling Simulation in Materials Science Engineering Vol. 3, pp. 437-453.

Colás, R., Ramírez, J., Sandoval, I., Morales, J.C., Leduc, L.A. (1999). "Damage in hot rolling work rolls". Wear Vol.230, no.1 pp.56-60.

Cory, N., Herrington, T. (1987). "Kinetics of oxidation of ferrous alloys by super heated steam". Oxidation of metalsVol.28, no.5-6, pp. 237-258.

Devadas, C., Samarasekera, I. V. (1986). "Heat transfer during hot rolling of steel strip". Ironmaking Steelmaking Vol. 13, no. 6, pp. 311-321.

Earles, S.W.E., Hayler, M.G. (1972). "Wear characteristics of some metals in relation to surface temperature". Wear 20, pp.51-57.

Ehlers, J., Young, D.J., Smaardijk, E.J., Tyagi, A.K., Penkalla, H.J., Singheiser, L., Quadakkers, W.J. (2006). "Enhanced oxidation of the 9%Cr steel in water vapour containing environments". Corrosion Science Vol.48, pp.3428-3454.

Erickson, L.C and Hogmark, S. (1993). "Analysis of banded hot rolling rolls". Wear Vol.165, no.2, pp.231-235.

Evans, H. E. (1989). "Stress effects in high temperature oxidation of metals". International materials review Vol.40, no.1, pp.1-40.

Evans, H. E. (1989). "Cracking and spalling of protective oxide layers." Materials Science and Engineering A120, pp.139-146.

González, V., Rodríguez, P., Haduck, Z., Colás, R. (2001). "Modelling oxidation of hot rolling work rolls". Ironmaking & Steelmaking Vol. 28, no. 6, pp. 470-473.

Goodchild, J. (2002). "The design of a laboratory test machine to simulate surface damage to work rolls for hot strip rolling". Ph.D Thesis Department of Mechanical Engineering, The University of Sheffield, Sheffield,U.K,.

Guerrero, M. P., Flores, C.R., Pérez, A., Colás, R. (1999). "Modelling heat transfer in hot rolling work rolls". Journal of Materials Processing Technology Vol.94, no.1, pp.52-59.

Hanlon, D.H, Rainforth, W.M. (2003). "The rolling sliding wear response of conventionally processed and spray formed high speed steel at ambient and elevated temperature". Wear Vol.225, no.7-12, pp.956-966.

Hirst, W., Lancaster, J.K. (1953). "The influence of oxide and lubricant films on the friction and surface damage of metals". Proceedings of the Royals Society of London A223, pp.324-337.

Hoyle, G. (1988). "High speed steels". London, U.K, Butterworths & Co.

Holmam, J.P. (1986). "Heat transfer". Mc Graw Hill Book Company.

Huang, C.H., Ju, T. M., Tseng, A. (1995). "The estimation of surface thermal behaviour of the working roll in hot rolling process". International Journal of heat and mass transfer Vol.38, no.6, pp.1019-1031.

Hutchings, I.M. (1992). "Tribology, friction and wear of engineering materials". Butterworth-Heinnemann publications, Oxford, U.K.

International Centre for Diffraction Data; "ICDD Powder Diffraction File", Swarthmore, USA, 1990.

JANAF. (1971). "Thermochemical tables". Office of standard reference data, Natural bureau of standards, Washington, D.C, USA.

Jansson, L., Vannerberg, N. (1971). "The effect of oxygen pressure and the growth of whiskers on the oxidation of pure Fe". Oxidation of metals Vol. 3, no.5, pp.453-461.

Kato, O., Yamamoto, H., Ataka, M., Nakajima, K. (1992). "Mechanisms of surface deterioration of roll for hot strip rolling". ISIJ International Vol. 32, no. 11, pp.1216-1220.

Kahveci, A.I., Welsch, G.E. (1986). "Oxidation of Fe-3%wt Cr Alloy". Oxidation of metals Vol.26, no.3-4, pp.213-230.

Kerr, E. J. (2000). "High speed steel work rolls at Dofasco". Iron and Steelmaker (USA) Vol. 27, no. 1, pp. 27-30.

Khanna, A.S. (2002). "Introduction to high temperature oxidation and corrosion". ASM International.

Kim, H., Lim, J.W., Lee, J.J. (2003). "Oxidation behaviour of high-speed steels in dry and wet atmospheres." ISIJ International Vol. 43, no.12, pp. 1983-1988.

Krzyzanowski, M., Beynon, J. H. (2002). "Measurement of oxide properties for numerical evaluation of their failure under hot rolling conditions". Journal of Materials Processing Technology (Netherlands) Vol. 125-126, pp. 398-404.

Kofstad, P. (1966). "High temperature oxidation of metals". John Wiley & Sons, Inc. USA.

Kofstad, P. (1995). "Defects and transport properties of metal oxides". Oxidation of metals Vol. 44, no. 1-2, pp. 3-27.

Kubaschewski, O. (1953). "Oxidation of metals and alloys". London: Butterworths.

Lancaster, J.K. (1962). "The formation of surface films at the transition between mild and severe wear". Proceedings of the Royals Society of London A273, pp.466-483.

Laverde, D., Gómez-Acebo, T., Castro, F. (2004). "Continuous and cyclic oxidation of T91 ferritic steel under steam". Corrosion Science Vol. 46, no.3, pp. 613-631.

Lewis. R, (2005). "Tribology of machine elements, lecture notes". Department of Mechanical Engineering, The University of Sheffield, Sheffield, UK.

Li, C.S., (2002). "Experimental investigation on thermal wear of high-speed steel rolls in hot strip rolling". Materials science and technology Vol.18, no.2, pp.1581-1584.

Luong, L. H., Heijkoop, T. (1981). "The influence of scale on friction in hot metal working". Wear Vol.71, no.1, pp.93-102.

Mercado-Solis, R. (2002). "Simulation of thermal fatigue in hot mill work rolls". Thesis (Ph.D.). Department of Mechanical Engineering, The University of Sheffield. Sheffield, U.K,

Milan, J.C.G., Carvalho, M.A., Xavier, R.R., Franco, S.D., De Mello, J.D.B. (2005). "Effect of temperature, normal load and pre-oxidation on the sliding wear of multi-component ferrous alloys". Wear Vol. 259, no.1-6 pp.412-423.

Molinari, A., Straffelini, G., Tomasi, A., Biggi, A., Corbo, G. (2000). "Oxidation behaviour of ledeburitic steels for hot rolls". Materials Science and Engineering A 280(2), pp. 255-262.

Molinari, A., Straffelini, G., Tomasi, A., Biggi, A., Corbo, G. (2001). "Influence of microstructure and chromium content on oxidation behaviour of spin cast high speed steels". Materials Science and Technology, Vol. 17, no.4, pp. 425-430.

Molgaard, J. S., Smeltzer, W.W. (1971). "Thermal conductivity of magnetite and hematite". Journal of applied physics, Vol.42, no.9, pp.3644-3647.

Monteiro, M. J., Rizzo, F.C. (2003). "Oxidation behaviour of high-speed steels under dry and moist air environments". Journal of Corrosion Science and Engineering, UMIST 2003 Vol. 6, Paper H040.

Munther, P. A., Lenard, J. G. (1999). "The effect of scaling on interfacial friction in hot rolling of steels". Journal of Materials Processing Technology Vol.88, no.1-3, pp.105-113.

Nield, B.J., Griffin, G. (1961). "Relation between wear rate and debris composition in wear of wrought iron and mild steel". Wear Vol.4, pp.111-122.

Nylen, T. (1999). "Development of carbide reinforced rolls for hot rolling". Advances in Mill Roll Technology Rolls 2000+ Conference Papers, Birmingham UK.

Perez, A., Corral, R.L., Fuentes, R., Colás, R. (2004). "Computer simulation of the thermal behaviour of a work roll during hot rolling of steel strip". Journal of Materials Processing Technology Vol.153-154, pp.894-899.

Pellizzari, M., Molinari, A., Straffelini, G. (2005). "Tribological behaviour of hot rolling rolls". Wear Vol.259, no. 7-12, pp.1281-1289.

Quinn, T.F.J. (1971). "Oxidational wear". Wear 18, pp.413-419.

Quinn, T.F.J. (1983). "Review of oxidational wear: Part I: The origins of oxidational wear". Tribology international Vol 16, no. 5, pp. 257-271.

Quinn, T.F.J (1983). "Review of oxidational wear Part II: Recent developments and future trends in oxidational wear research". Tribology international Vol 16, no. 6, pp. 305-315.

Rainforth, W.M. (2002). "High resolution observations of friction-induced oxide and its interaction with the worn surface". Tribology international Vol. 35, no. 11, pp. 731-748.

Rodenburg, C. Rainforth, W.M. (2007). "A quantitative analysis of the influence of carbides size distributions on wear behaviour of high-speed steel in dry rolling/sliding contact". Acta Materialia, Vol. 55, no. 7, pp. 2443-2454.

Santafé, C., Borgianni, C. (1975). "Study of the oxidation kinetics of vanadium carbide". Oxidation of metals Vol. 9, no. 5, pp.415-425.

Schütze. M., (1995). "Mechanical properties of oxide scales". Oxidation of metals, Vol. 44, no.1-2 pp.29-61.

Sikdar, S., John, S. (2006). "Simulation of thermal history of work rolls of finishing stand in hot strip mill; a numerical approach". Iron making and steel making Vol. 33, No.6, pp.493-499.

Simms, N.J., Little, J.A. (1988). "Scale growth on 2.25Cr-Mo steel". Materials science and technology Vol.4, pp.1133-1139.

So, H. (1995). "The mechanism of oxidational wear". Wear Vol.184, pp.161-167.

Spuzic, S., Strafford, K. N., Subramanian, C., Savage, G. (1994). "Wear of hot rolling mill rolls". Wear Vol.176, no.2, pp.261-271.

Stott, F.H., Wood, G.C. (1978). "The influence of oxides on the friction and wear of alloys". Tribology International Vol 11, no. 4, pp. 211-218.

Stott, F.H. (1998). "The role of oxidation in the wear of alloys". Tribology International Vol.31, no. 1-3, pp.61-71.

Sullivan, J.L., Athwal, S.S. (1983). "Mild wear of a low allow steel at temperatures up to 500°C". Tribology international Vol.16, no.3, pp.123-131.

Surman, P.L., Castle, J.E. (1969). "Gas phase transport in the oxidation of Fe and steel".CorrosionScience Vol.9,no.10, pp.771-777.

Taguchi, T. Suzuki, K. (2006). "Effect of oxygen content on the oxidation of pure iron". Oxidation of metals Vol.66, no 1-2, pp.107-114.

Tu, J. P., Jie, X. H., Mao, Z. Y., Matsumura, M. (1998). "The effect of temperature on the unlubricated sliding wear of 5 CrNiMo steel against 40 MnB steel in the range 400-600 °C". Tribology international Vol.31, no.7, pp.347-353.

Tuck, C., Odgers, W. M., Sachs, K. (1969). "The oxidation of iron at 950°C in oxygen water vapour mixtures". Corrosion Science Vol. 9, pp.271-285.

VanderVoort, G. F. (1984). "Metallography Principles and Practice". McGraw-Hill, New York.

Vardavoulias, M. (1994). "The role of hard second phases in the mild oxidational wear mechanism of high speed steel based materials". Wear Vol.173, no.1-2, pp.105-114.

Vergne, C., Boher,C., Gras, R., Levaillant, C., (2006). "Influence of oxides on friction in hot rolling: Experimental investigations and tribological modelling". Wear Vol.260, no. 9-10, pp.957-975.

Walter, M., Schütze, M., Rahmel, A. (1993). "Behaviour of oxide scales on 12 Cr-1Mo steel during thermal cycling". Oxidation of metals Vol.39, no.5-6, pp.389-410.

Welsh, N.C. (1965). "The dry wear of steels. Interpretation and special features". Philosophical transactions of the royal society of London Vol.257, no.1077, pp-51.70.

Zhou, Z., Rainforth, W.M., Tan,C.C., Zeng, P., Ojeda, J.J., Romero-Gonzalez, M.E., Hovsepian, P.Eh. (2007). "The role of the tribofilm and roll-like debris in the wear of nanoscale nitride PVD coatings". Wear Vol.263, pp.1328-1334.

Ziadi, A., Belzunce, F.J., Rodriguez, C., Riba, J. (2005). "Wear and oxidation behaviour of multicomponent white cast irons". Materials Science and Technology Vol. 21, no. 10, pp. 1181-1186.

Tables

Table 1. Working conditions imposed to the iron samples shown in Fig.2.8 oxidized in *Caplan and Cohen* (1966).

Sample	***Surface Condition***	***Oxidation Temperature (°C)***
1	Electropolished-annealed-electropolished	500
4	Electropolished and diamond abraded	500
11	Electropolished-annealed-electropolished	400
12	Electropolished and diamond abraded	400
13	Electropolished-annealed-electropolished	450
14	Electropolished and diamond abraded	450
15	Electropolished-annealed-electropolished	550
16	Electropolished and diamond abraded	550
17	Electropolished-annealed-electropolished	580
18	Electropolished and diamond abraded	580
19	Electropolished-annealed-electropolished	600
20	Electropolished and diamond abraded	600
21	Electropolished-annealed-electropolished	650
22	Electropolished and diamond abraded	650

*Annealed was carried out at 900°C and diamond abrasion was done with 8μm diamond.

Table 2. Chemical composition of the high speed steel studied by *Molinari et al.* (2001)

Alloying elements in %wt								
C	**Si**	**Mn**	**V**	**W**	**Cr**	**Mo**	**Ni**	**Fe**
0.8-2.0	0.6-0.1	0.5-0.9	0.5-5.5	0.0-4.0	3.8-12.0	1.5-4.0	0.7-1.2	Bal

Table 3. Chemical composition of the Hi-Cr work roll studied by *Gonzalez et al* (2001)

Alloying elements in %wt								
C	**Si**	**Mn**	**V**	**W**	**Cr**	**Mo**	**Ni**	**Fe**
2.77	0.6	0.93	-	-	16.08	1.1	1.31	Bal

Table 4. Chemical composition of the high speed steels studied by *Kim et al.* 2003.

Alloying elements in %wt							
Steel	C	W	Mo	Cr	V	Si	Mn
A	2.04	6.48	**4.13**	**5.58**	**4.28**	0.21	0.91
B	1.96	2.90	**1.05**	**5.55**	**5.05**	0.75	0.90
C	1.98	1.90	**2.90**	**9.40**	**3.60**	0.80	0.40

Table 5. Chemical composition of the high speed steels studied by *Monterio and Rizzo* (2003).

Alloying elements in %wt							
Steel	C	W	Mo	Cr	V	Si	Mn
A1	1.90	2.00	**2.00**	**3.50**	**5.10**	-	-
A2	1.80	2.00	**2.00**	**7.50**	**4.80**	-	-
A3	1.80	3.90	**2.30**	**4.40**	**4.80**	-	-

Table 6. Chemical composition of the white iron studied by Ziadi *et al.* (2005)

Alloying elements in %wt								
C	Si	Mn	V	W	Cr	Mo	Ni	Fe
1.5-1.9	0.6	0.5-0.7	**4.0-5.0**	**1.5-2.5**	**7.5-8.5**	1.1	0.7-0.9	Bal

Table 7. Chemical composition of the high speed steel used for the experiments. After Mercado (2001).

Alloying elements in %wt								
Steel	C	W	Mo	Cr	V	Si	Mn	Ni
HSS	1.55	0.49	**2.08**	7.70	**4.90**	0.66	0.54	0.52

Table 8. Experimental conditions studied in the isothermal oxidation tests

Test condition	*Vapour Temperature*	pH_20 *(atm)*	pO_2 *(atm)*	nO_2 *(mol)*		nH_2O *(mol)*	
				615°C	**550°C**	**615°C**	**550°C**
1	**95°C**	**0.83**	**0.06**	$6.34x10^{-4}$	$6.83x10^{-4}$	$8.76x10^{-3}$	$9.46x10^{-3}$
2	**85°C**	**0.57**	**0.11**	$1.16x10^{-3}$	$1.25x10^{-3}$	$6.02x10^{-3}$	$6.49x10^{-3}$
3	**25°C***	**0.32**	**0.21**	$2.11x10^{-3}$	$2.27x10^{-3}$	$3.38x10^{-3}$	$3.64x10^{-3}$

***This property is just mentioned as a mere reference assuming that some water was present in the compressed dry air**

Table 9. Rate constant and behaviours obtained for each oxidation condition.

Temp	*Apparent activation energy Q*	*Characteristic law*		*Rate constant k*	
600°C	Condition 1 23.32KJ/mol	Logarithmic	Linear	$k_L = 0.3940 \frac{mg}{cm^2 - s}$	$k_l = 1.31 \frac{mg}{cm^2 - s}$
	Condition 2 70.08KJ/mol	Parabolic		$k_p = 6.16x10^{-2} \frac{mg}{cm^2 - s^{1/2}}$	
	Condition 3 130.77KJ/mol	Logarithmic		$k_L = 1.83 \frac{mg}{cm^2 - s}$	
500°C	Condition 1 23.32KJ/mol	Logarithmic		$k_L = 1.32 \frac{mg}{cm^2 - s}$	
	Condition 2 70.08KJ/mol	Parabolic		$k_p = 2.82x10^{-2} \frac{mg}{cm^2 - s^{1/2}}$	
	Condition 3 130.77KJ/mol	Logarithmic		$k_L = 0.4432 \frac{mg}{cm^2 - s}$	

Table 10. Chemical composition of the high speed steel and its components obtained by EDX analysis.

Alloying elements in %wt						
	C	**Fe**	**Cr**	**V**	**Mo**	**Si**
Steel matrix	1.50	85.46	6.83	2.85	1.72	1.08
MC	15.32	4.44	6.94	63.03	8.90	1.37
M_7C_3	9.44	32.43	35.99	12.73	9.03	0.38
M_6C	7.50	35.32	8.52	11.41	33.31	3.94

Table 11. Free energy change values calculated for the oxidation reactions proposed.

Reaction proposed	**$\Delta G_{615°C}$ KJ/mol**	**$\Delta G_{550°C}$ KJ/mol**
$3Fe+2O_2 \rightarrow Fe_3O_4$	-813.33	-835.90
$4Fe+3O_2 \rightarrow 2Fe_2O_3$	-1163.34	-1199.18
$3Fe+4H_2O \rightarrow Fe_3O_4+4H_2$	-3.93	-14.40
$VC+O_2 \rightarrow VO+CO$	-446.102	-445.704
$VC+2H_2O \rightarrow VO+CO+2H_2$	-41.38	-73.87
$4VC+7O_2 \rightarrow 2V_2O_5+4CO$	-270.63	-273.78
$2VC+7H_2O \rightarrow V_2O_5+2CO+7H_2$	+64.33	+68.73

Table 12. Properties of the oxides considered for the calculation of the thermal stresses.

Material	Elasticity modulus E (GPA)	Expansion coefficient α(1/°C)	Poisson ratio ν
Fe_2O_3	219[(1)]	$13x10^{-6}$	0.19[(1)]
Fe_3O_4	208[(1)]	$12x10^{-6}$	0.29[(1)]
$Steel_{(615°C)}$	225[(2)]	$14.8x10^{-6}$[(2)]	0.30
$Steel_{(550°C)}$	225[(2)]	$14.0x10^{-6}$[(2)]	0.30

[(1)]Schütze. M., "Mechanical properties of oxide scales". Oxidation of metals Vol. 44, No1-2, 1995.

[(2)]Mercado-Solis. R,"Simulation of thermal fatigue of work rolls". PhD thesis, The University of Sheffield, 2002.

Table 13. Evolution of the roughness values measured from the surface of the test discs.

Test Conditions											
Water + Water vapour test						Dry tests					
400°C		500°C		600°C		400°C		500°C		600°C	
Sliding distance (m)	Ra (μm)	Sliding distance (m)	Ra (μm)	Sliding distance (m)	Ra (μm)	Sliding distance (m)	Ra (μm)	Sliding distance (m)	Ra (μm)	Sliding distance (m)	Ra (μm)
0	0.32	0	0.30	0	0.18	0	0.34	0	0.67	0	0.57
22210	0.94	22315	1.8	22145	2.41	22195	1.62	22230	3.07	22200	4.33
44545	1.40	44730	2.83	44315	2.64	44345	2.96	44375	3.05	44400	4.05
66895	1.05	67105	2.2	66490	3.001	66660	1.82	66525	3.01	66600	3.58
89195	1.18	89720	2.0	88665	2.32	88995	1.63	88675	3.6	88805	3.18
111600	1.35	112360	2.36	110890	2.56	111140	1.76	110910	3.17	111015	3.36

Figures

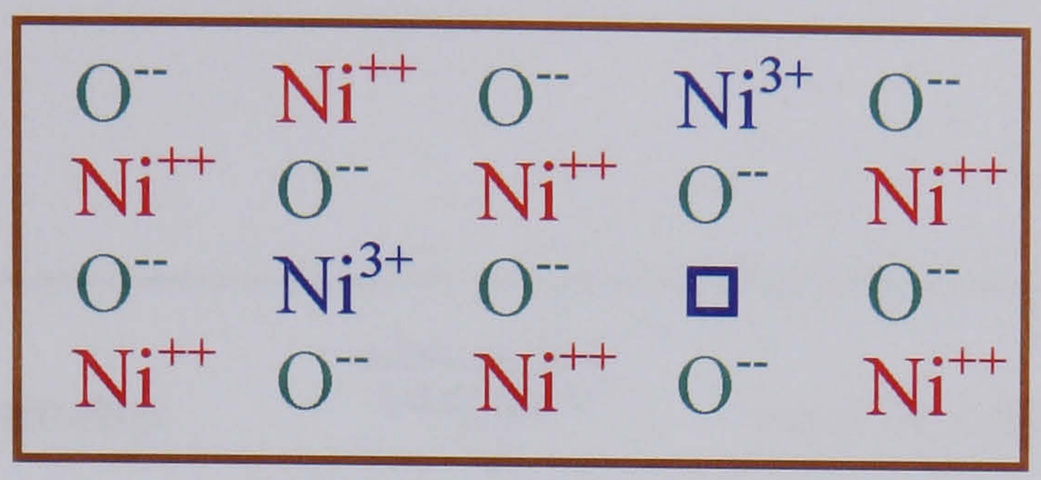

Fig.2.1. Oxide lattice of nickel oxide showing p-type cation deficit defects. The neutral character of the compound is preserved by the existence of nickel ions with a higher valence state that compensate the negative character of the created cation vacancy.

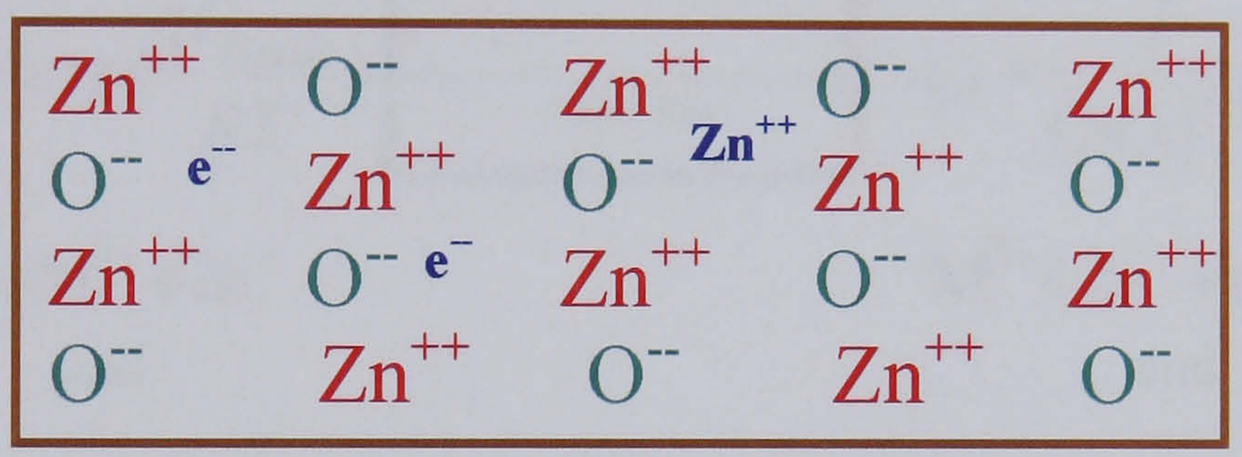

Fig.2.2. Oxide lattice of zinc oxide showing n-type cation excess defect. Excess zinc ions are located at interstitial sites so that the neutrality of the compound is balanced by the existence of electrons product of ionization reactions.

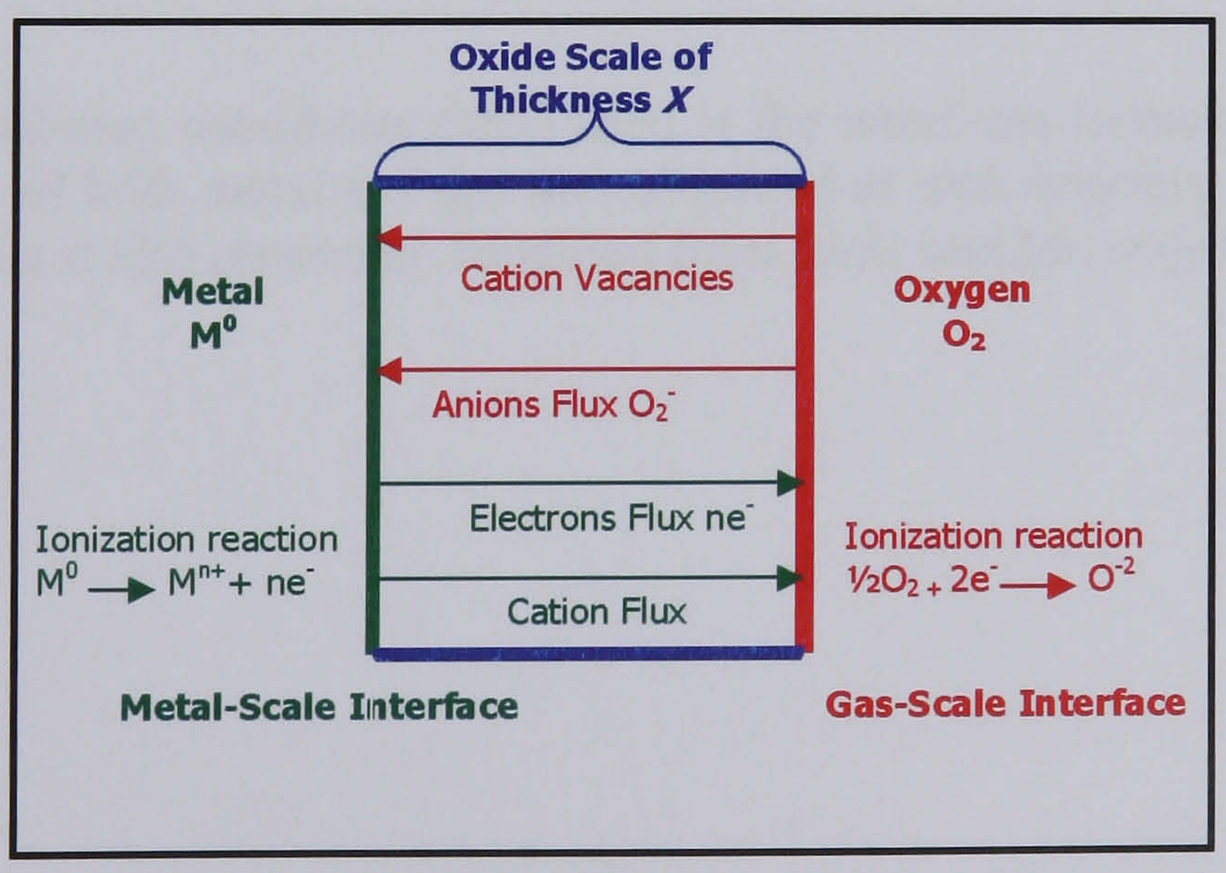

Fig.2.3. High temperature reactions established between a metal and the atmosphere in which it is contained. Schematic representation of ionic diffusion for oxide scale formation.

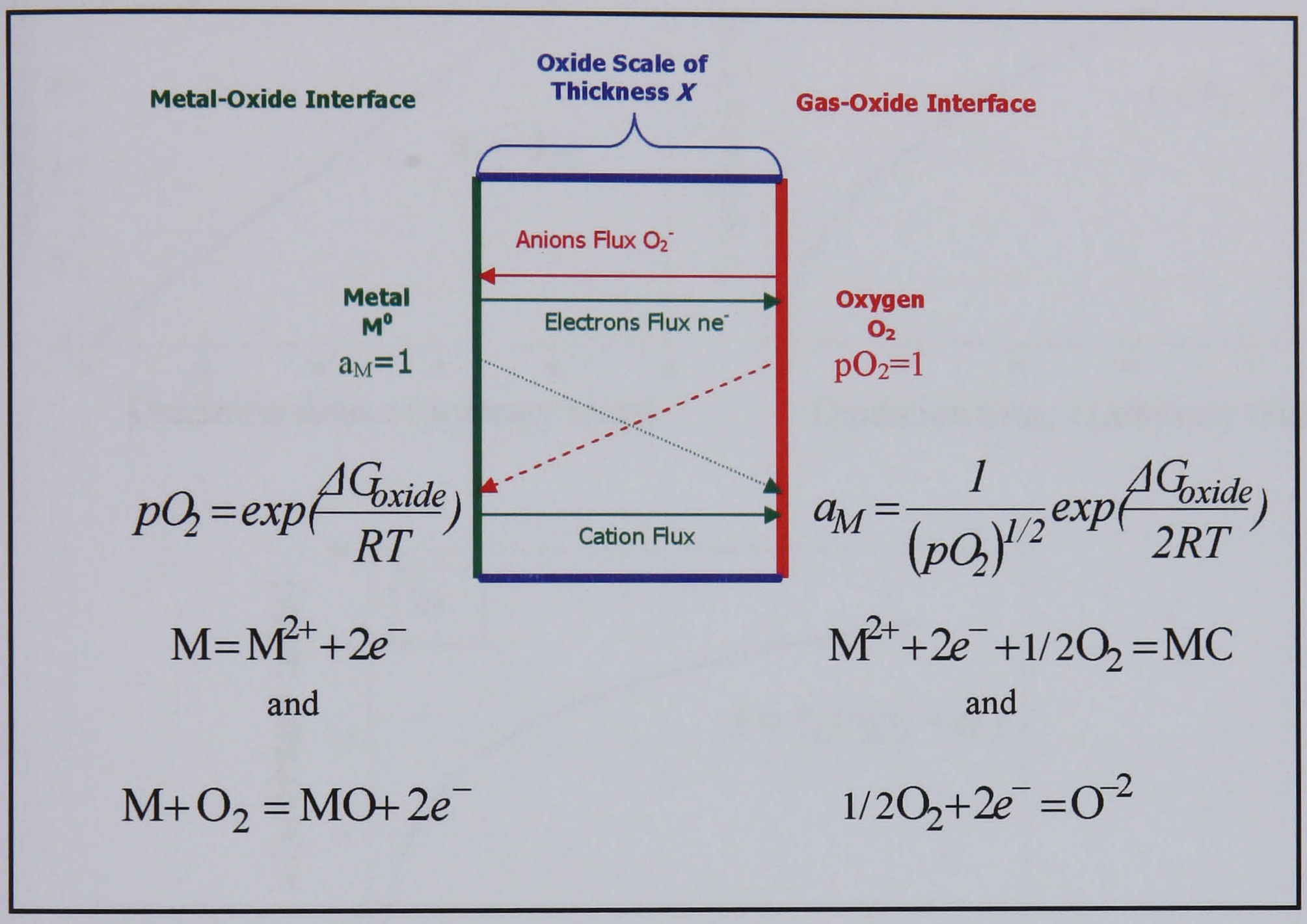

Fig.2.4. Equilibrium conditions established at the interfaces formed in an oxide layer. The activities of both metal and gas are calculated at each interface and their variation across the scale is also presented. Modified from *Birks and Meier* (1986).

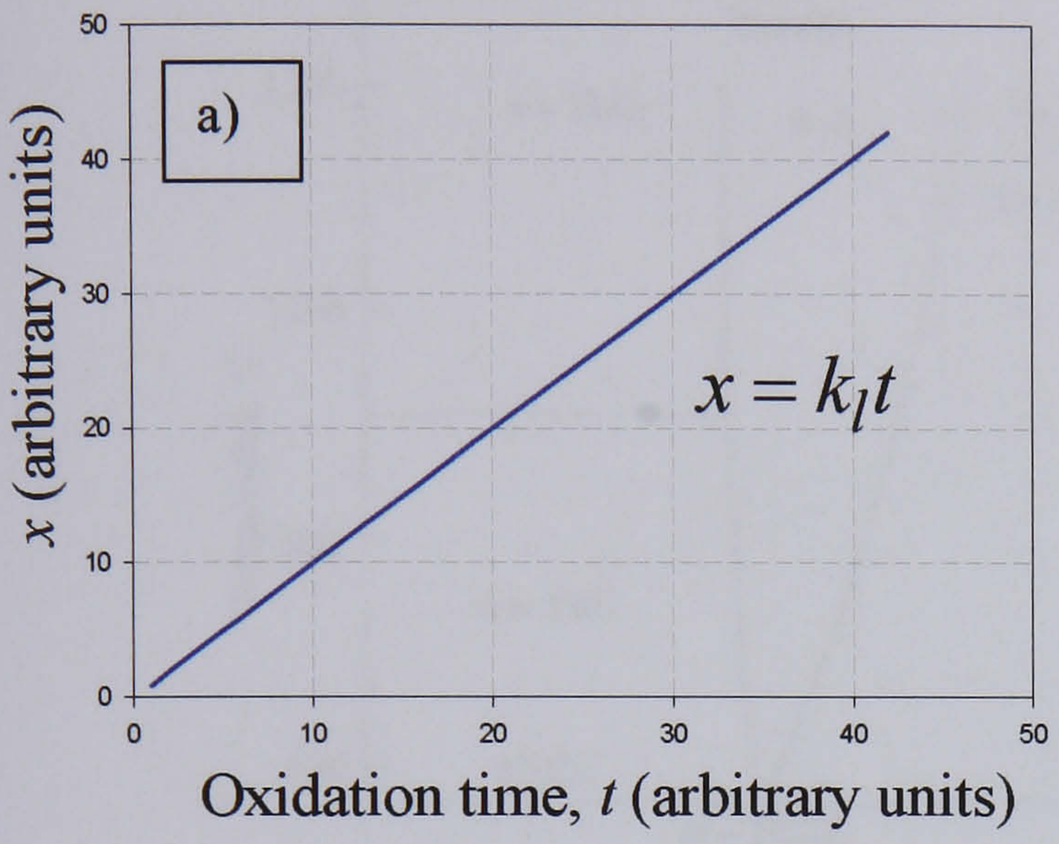

Fig.2.5. a) Plot representative of the linear oxidation rate, b) plot representative of the parabolic oxidation behaviour and in c) logarithmic oxidation rate.

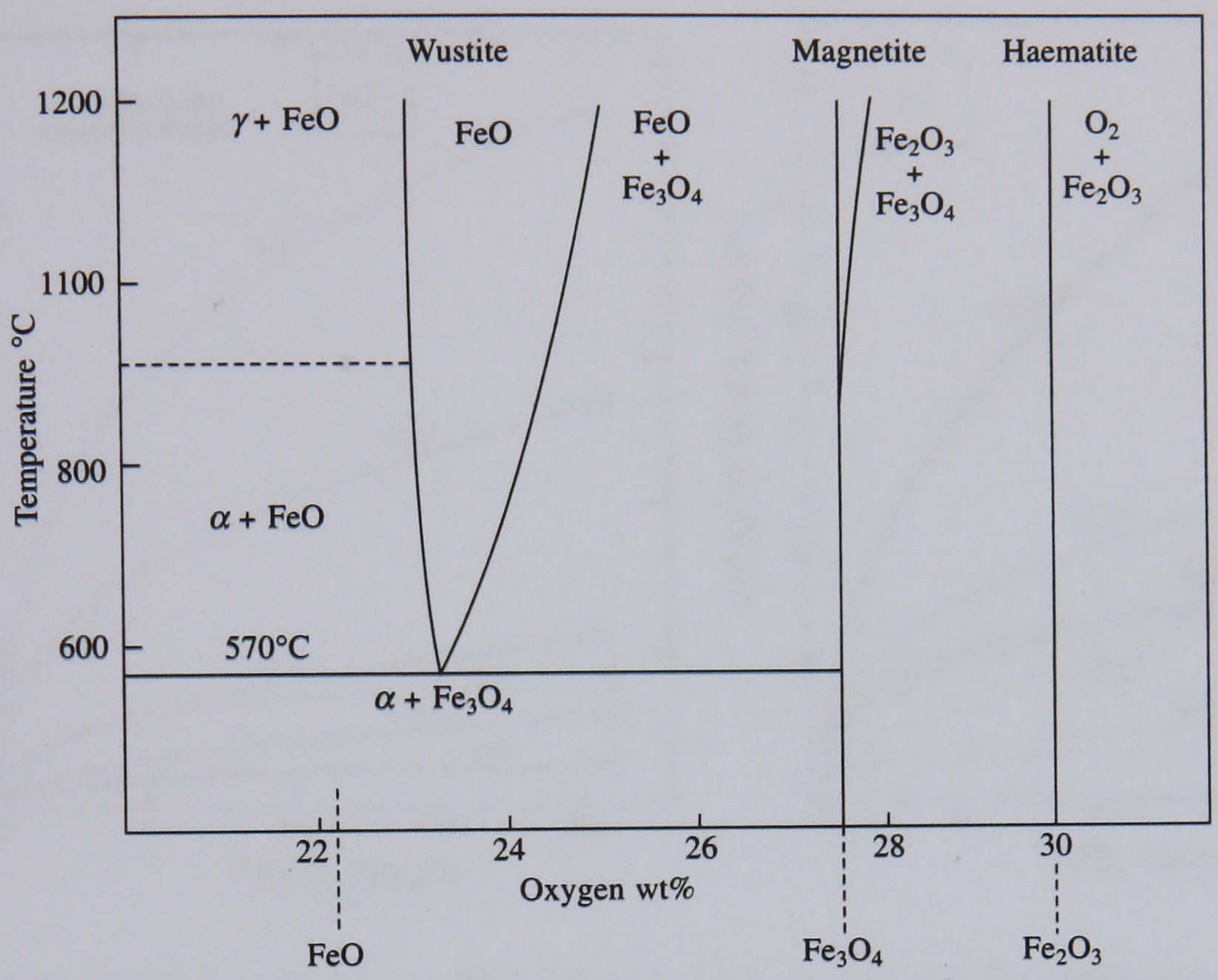

Fig.2.6. High temperature section of the Fe-O phase diagram. *After Khanna* (2002).

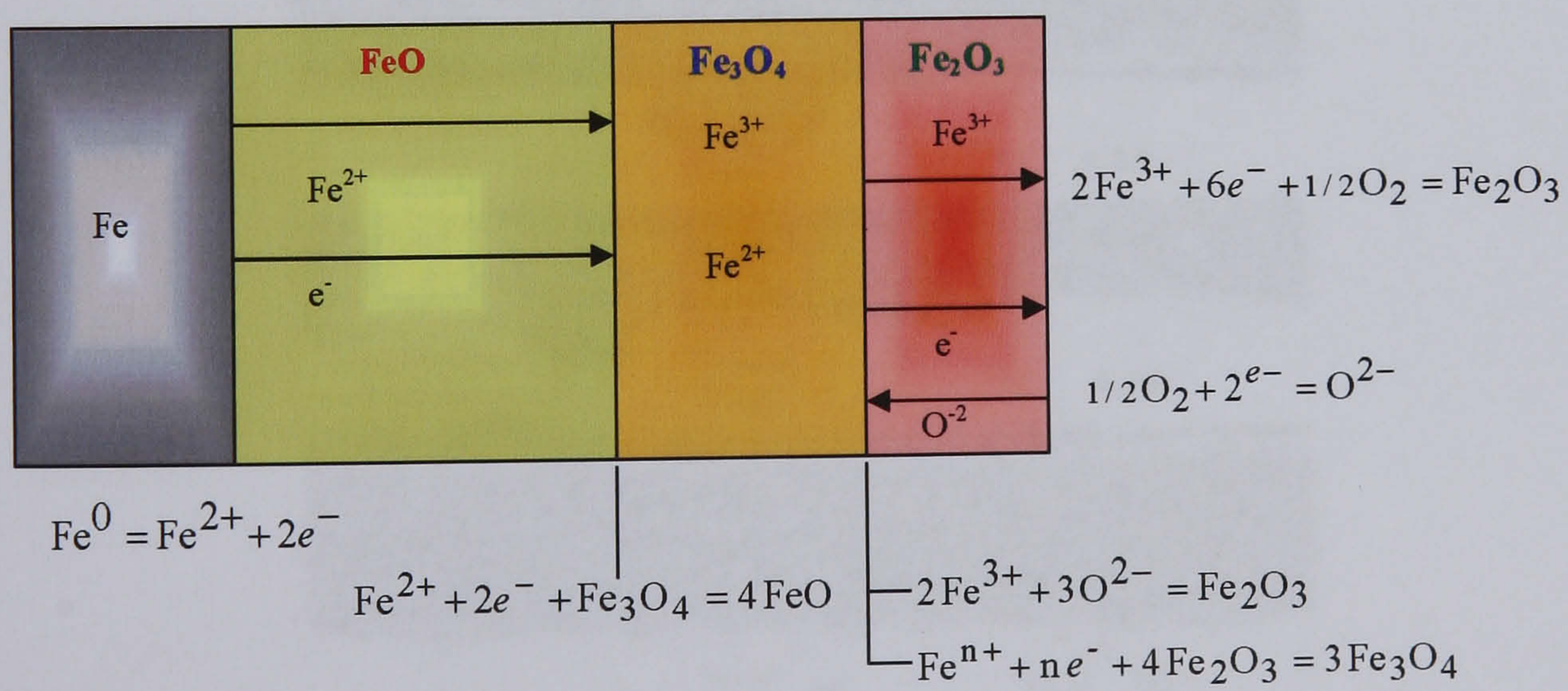

Fig.2.7. Oxidation of iron above 570°C. Modified from *Khanna* (2002).

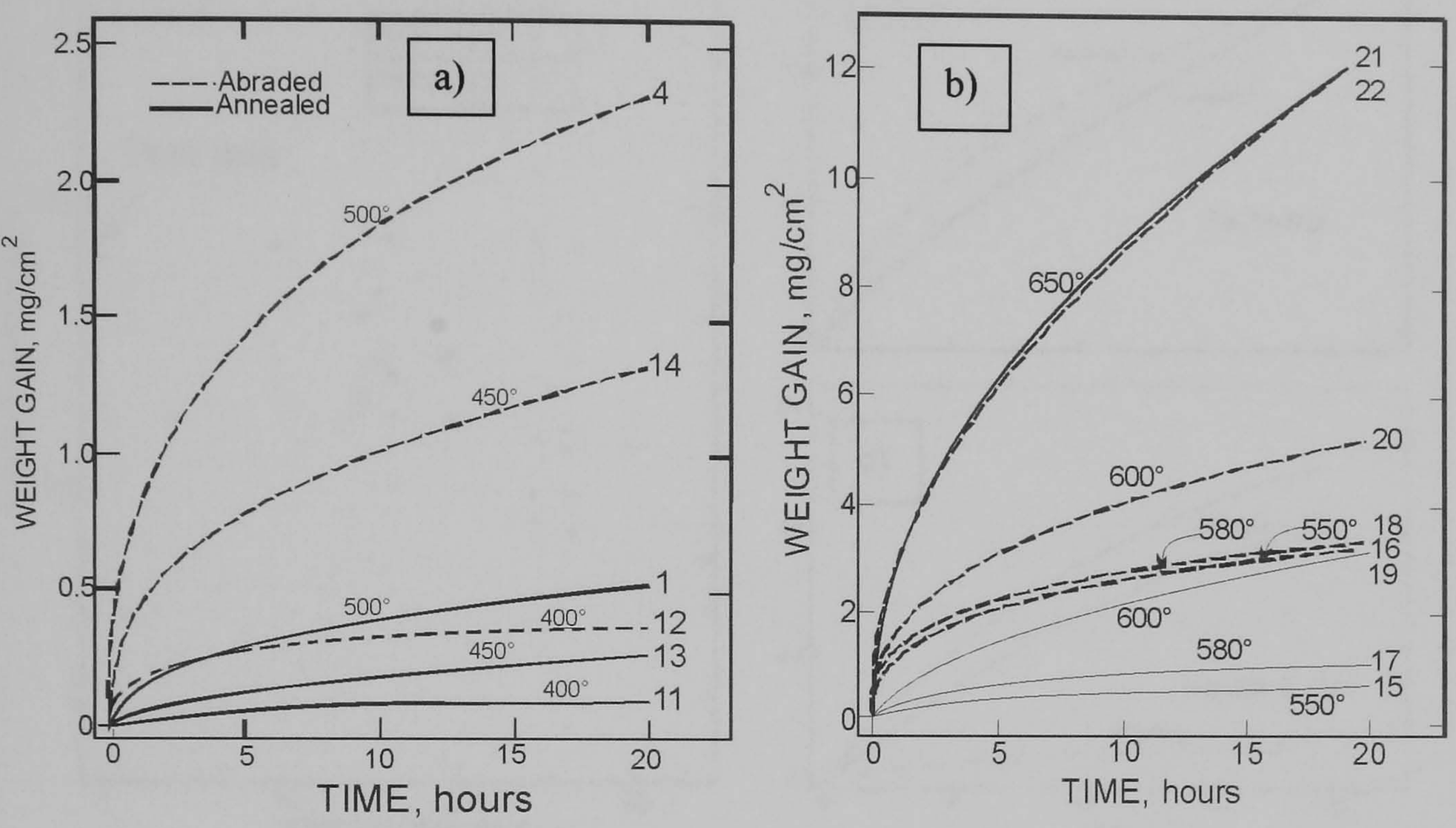

Fig.2.8. Oxidation kinetics plots of pure iron in dry air for different temperatures and preparation procedures. Abrading the samples prior oxidation resulted in greater oxidation for temperatures up to 600°C. *After Caplan and Cohen* (1966).

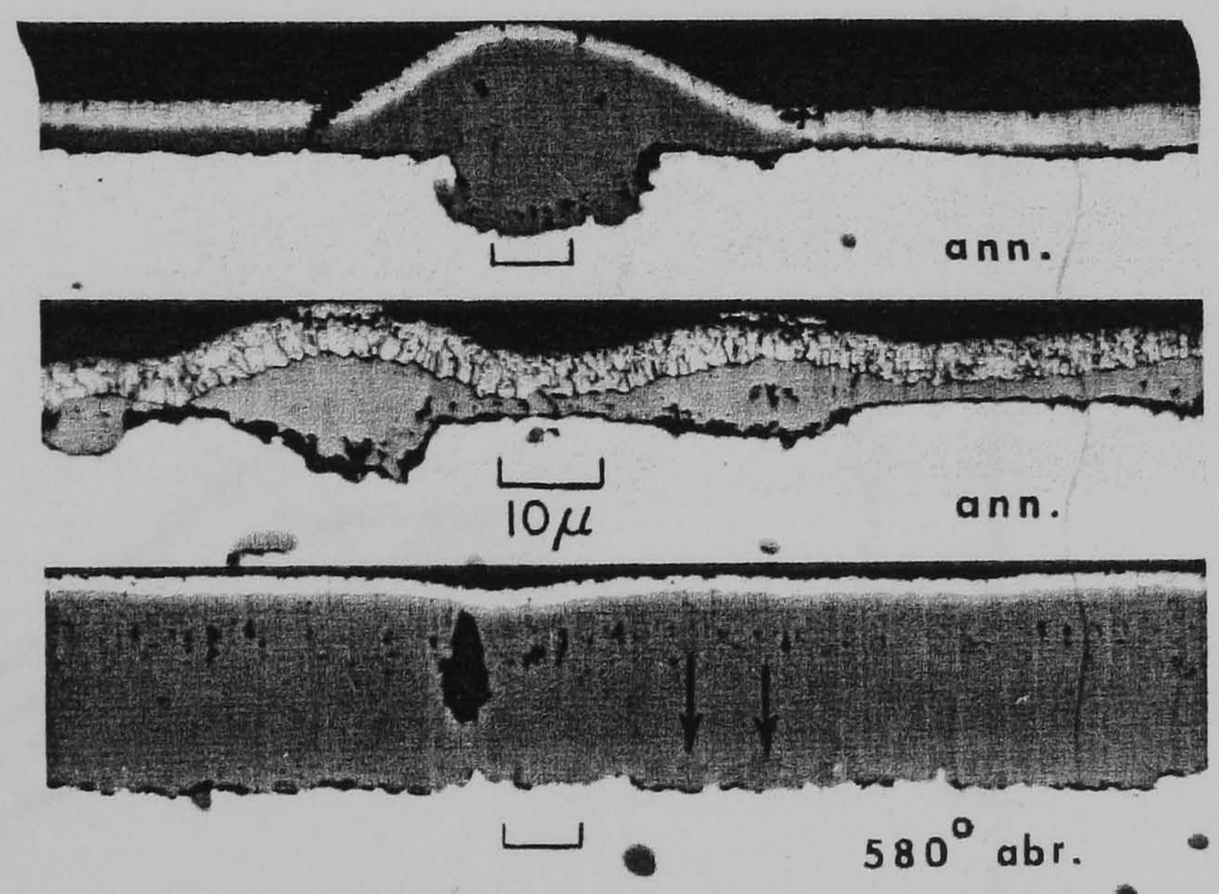

Fig.2.9. Microstructural differences found in an oxide layer grown on abraded and annealed pure iron at 580°C. *After Caplan and Cohen* (1965).

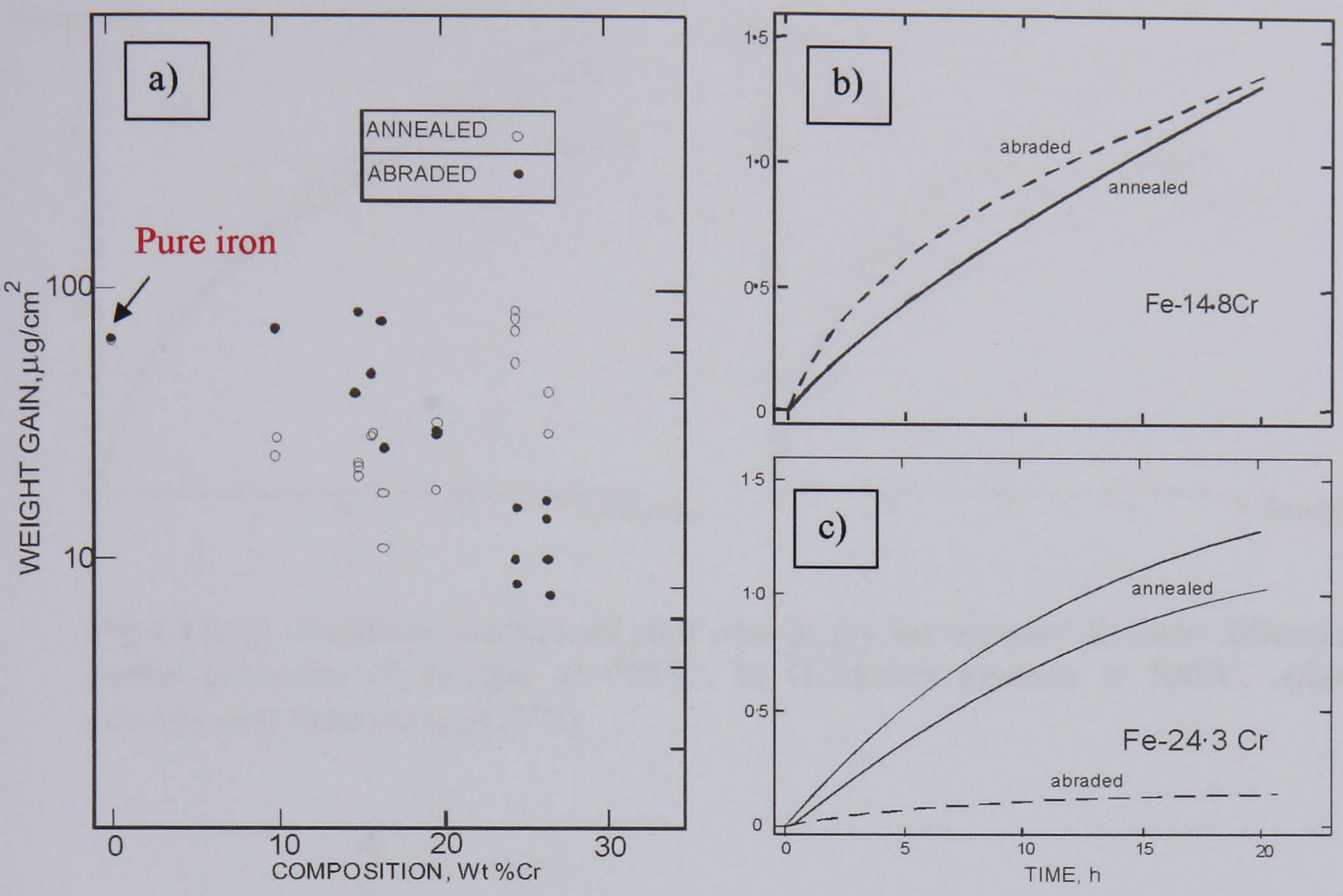

Fig.2.10. a) Mass gained as a function of the chromium content and condition. b) and c) show a comparison of the oxidation kinetics obtained in water vapour for alloys with two different chromium contents. *After Caplan* (1966).

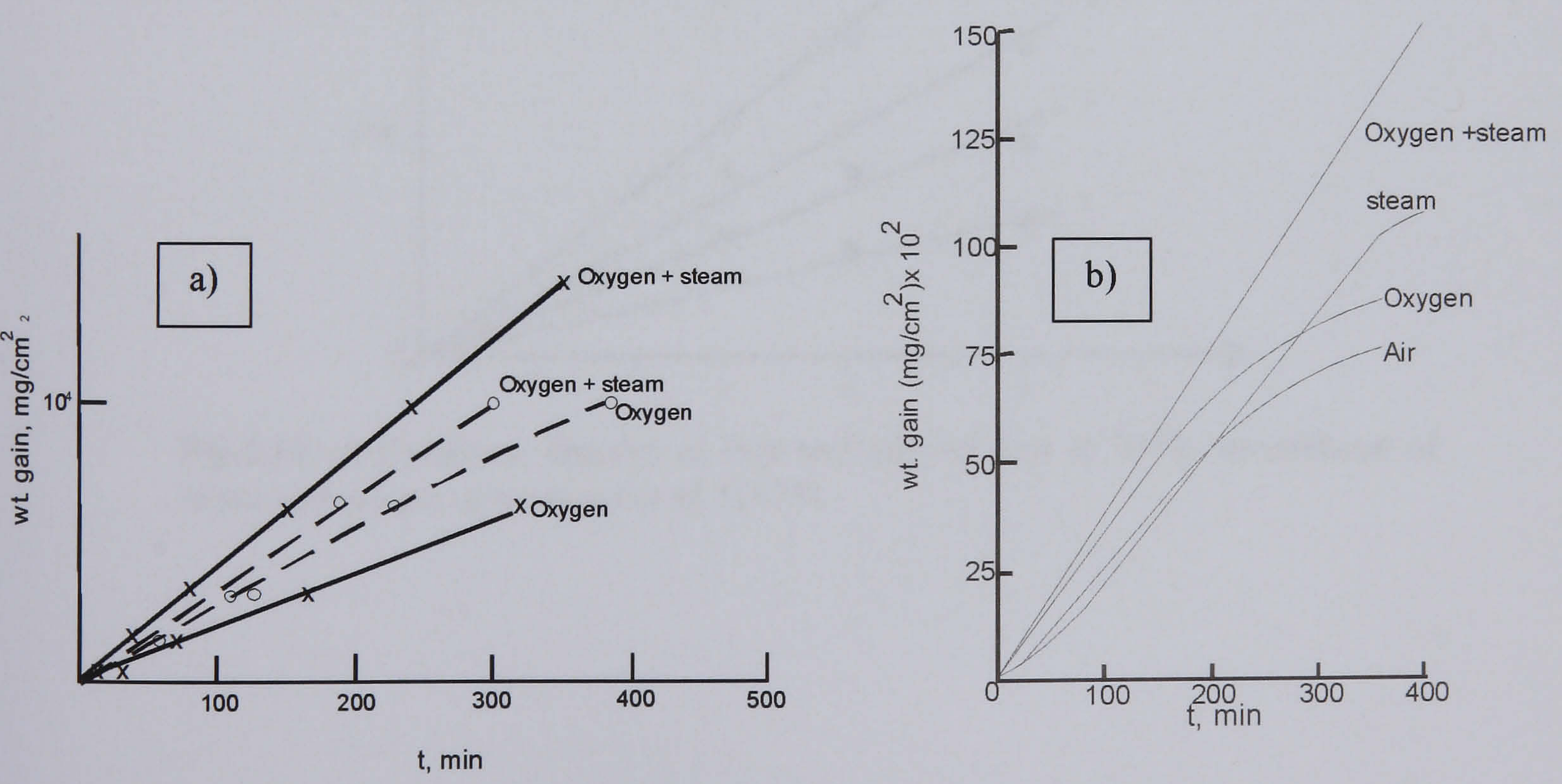

Fig.2.11. a) Oxidation kinetics of rods (x) and sheets (o) of pure iron in oxygen and oxygen with water vapour. b) Comparison of the oxidation of iron under various atmospheres. *After Tuck et al. (1969).*

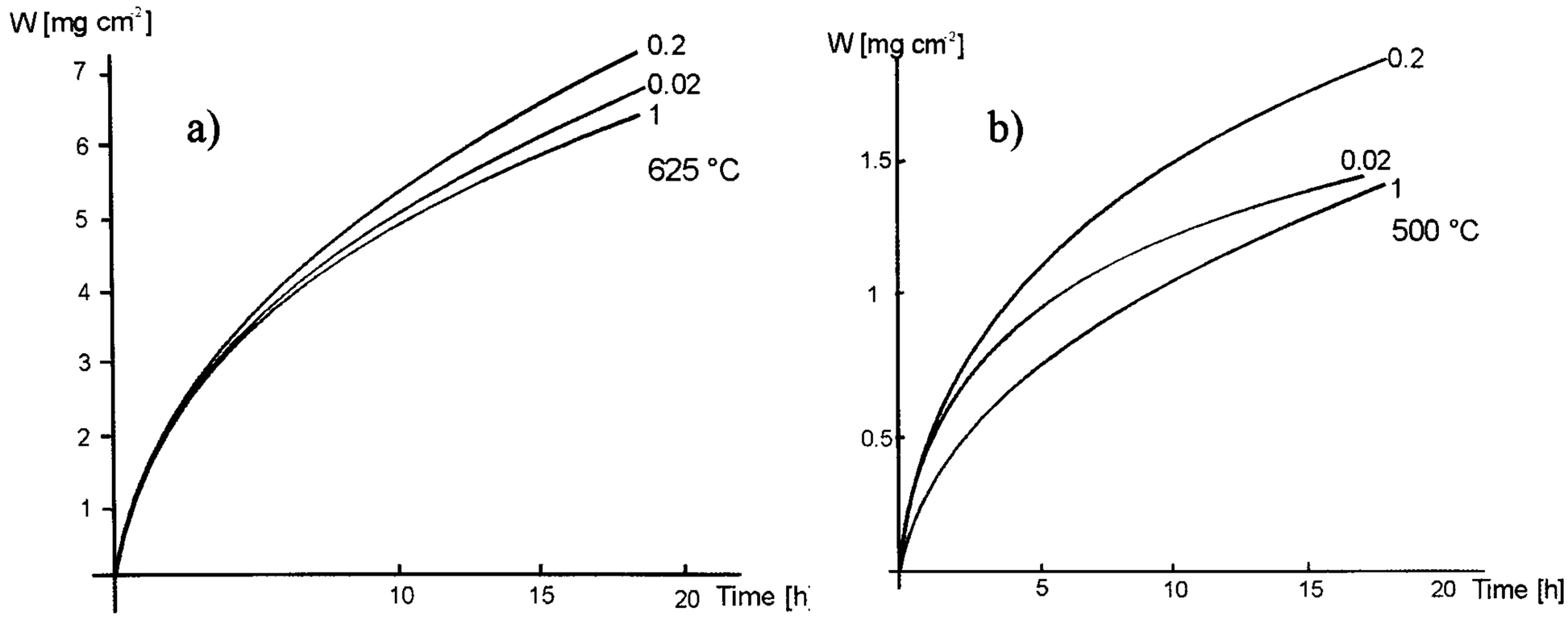

Fig.2.12. a) Oxidation kinetics of pure iron in dry air exposed to three different partial pressures of oxygen at 625°C. b) Oxidation kinetics at 500°C. *After Jansson and Vannerberg* (1971).

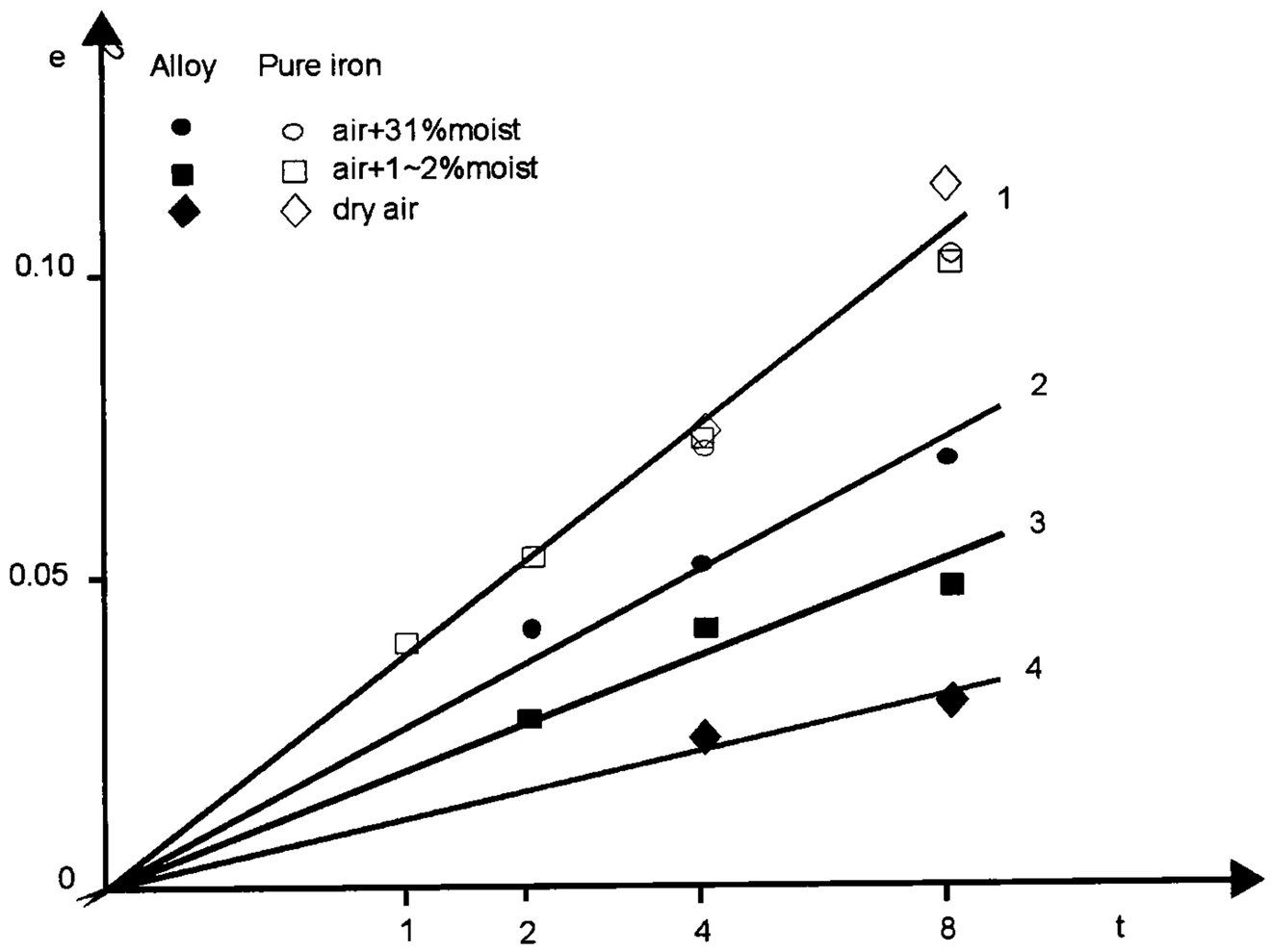

Fig.2.13. a) Oxidation kinetics of iron and alloyed iron at 700°C in mixtures of moist and dry air. *After Baud et al.* (1975).

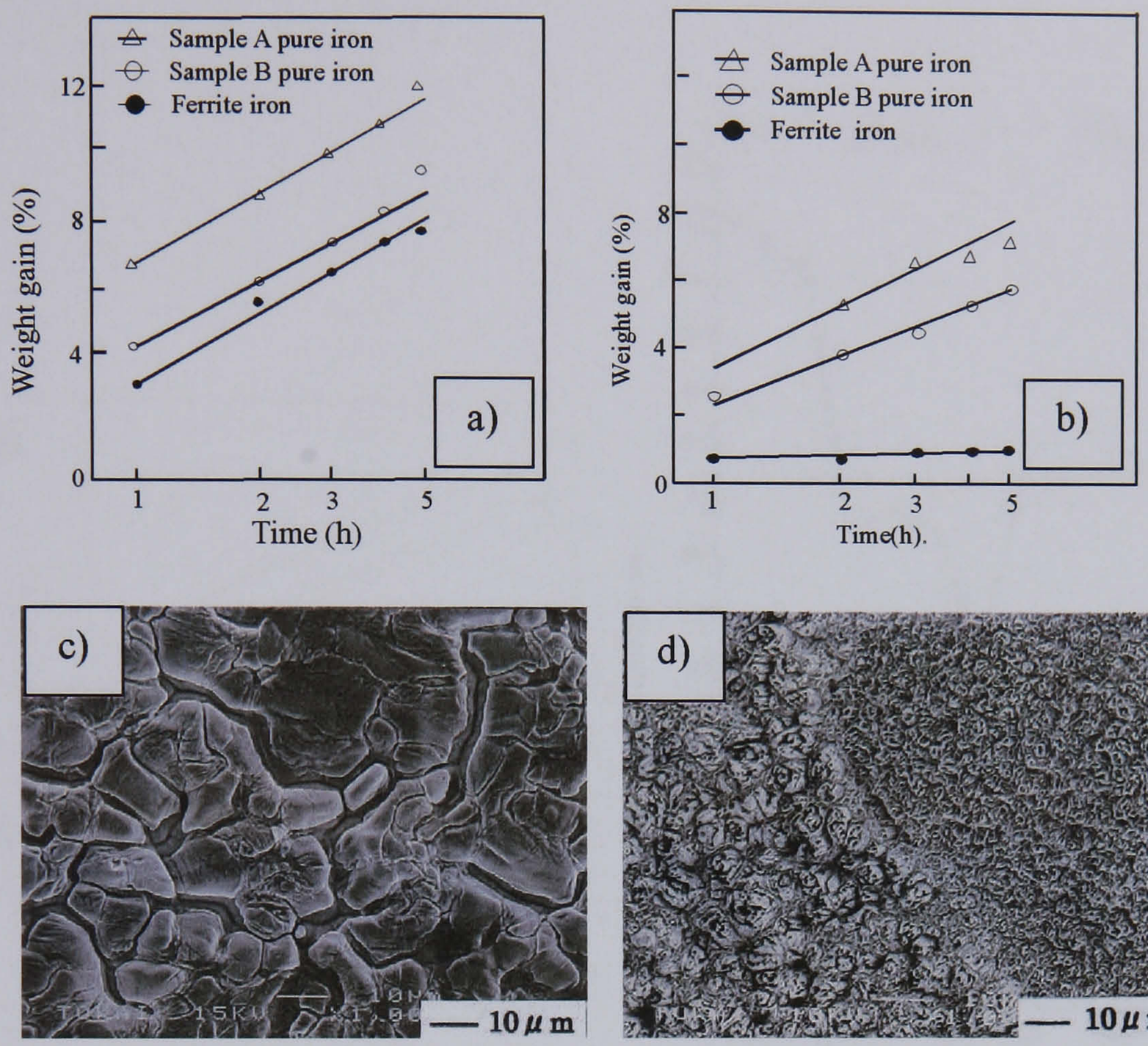

Fig.2.14. Oxidation of pure iron samples in moist a) and dry b) mixtures. The morphology of the oxides is also different depending on the oxidation atmosphere, c) moist atmosphere and d) dry atmosphere. *After Taguchi and Suzuki* (2006).

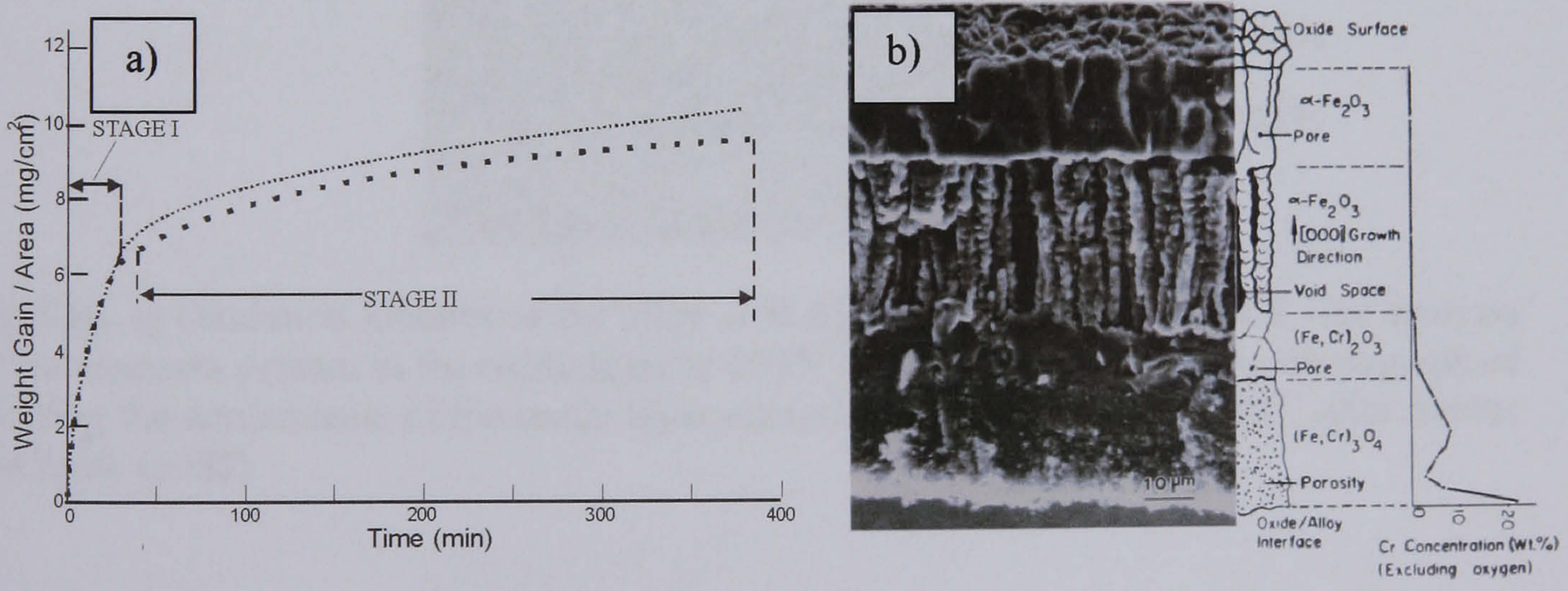

Fig.2.15. a) Oxidation kinetics of the Fe- 3% wt Cr alloy in dry air. b) Microstructure of the oxide layer taken from examination of samples in stage 2. *After Kahveci and Welsh* (1986).

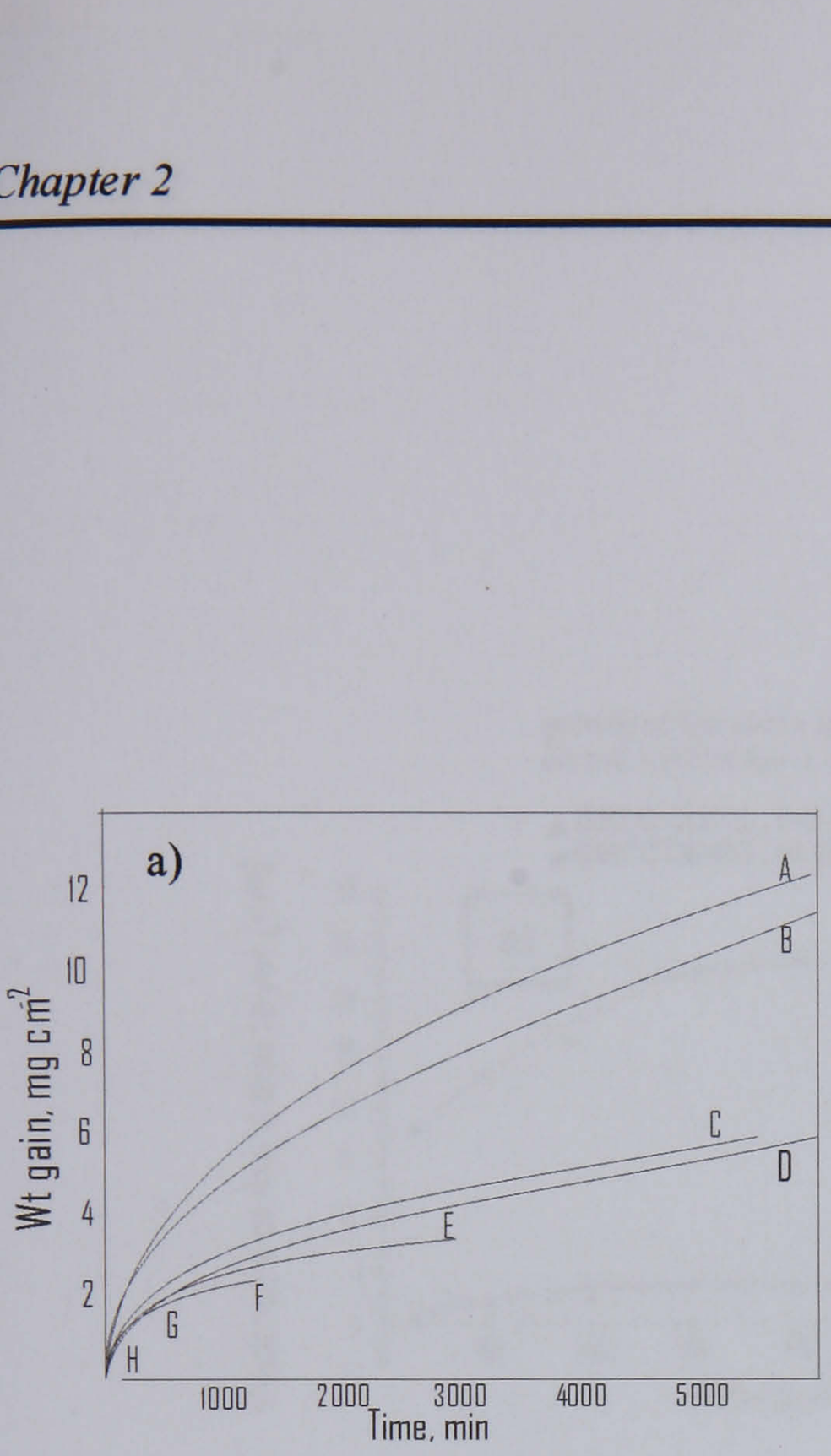

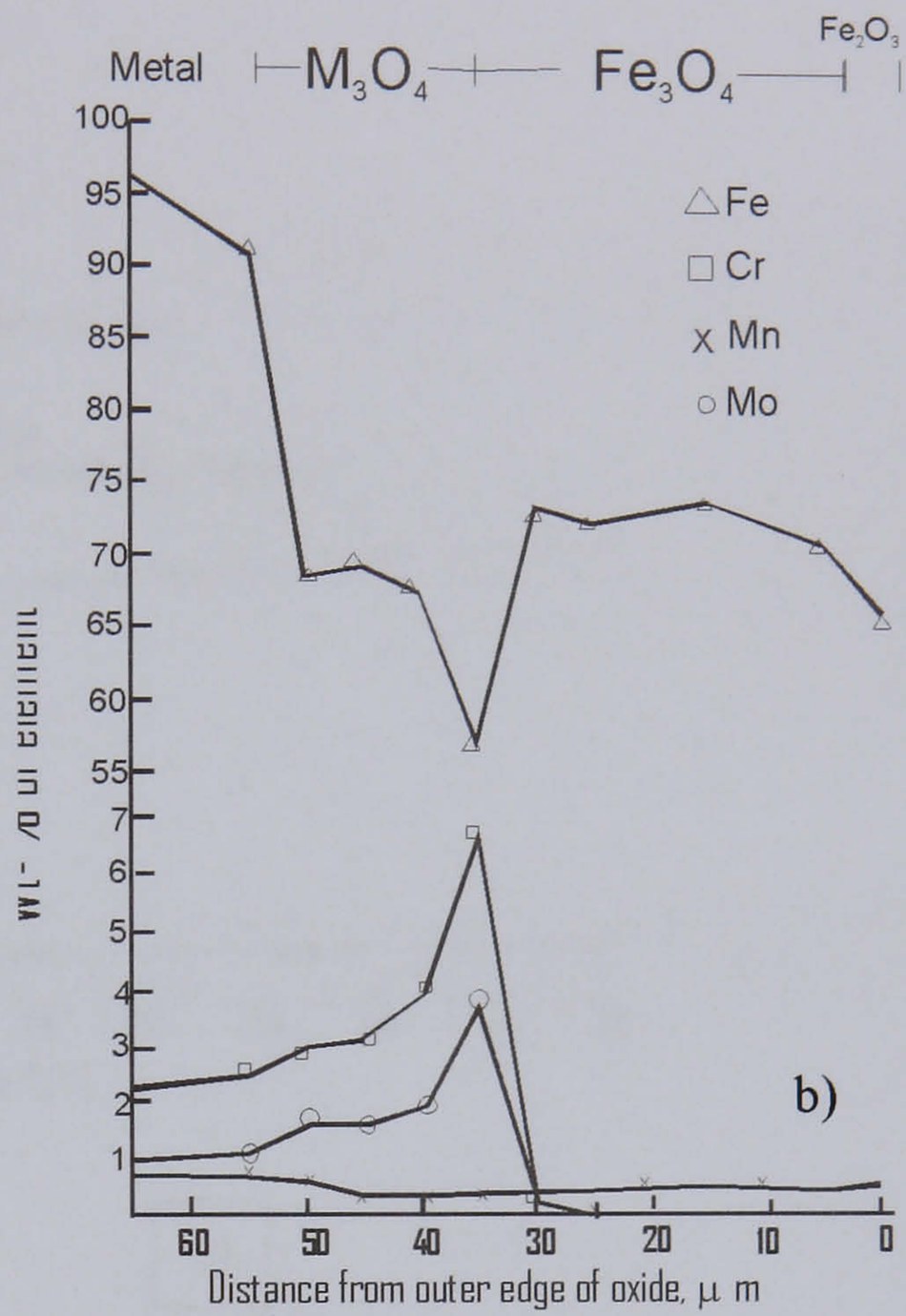

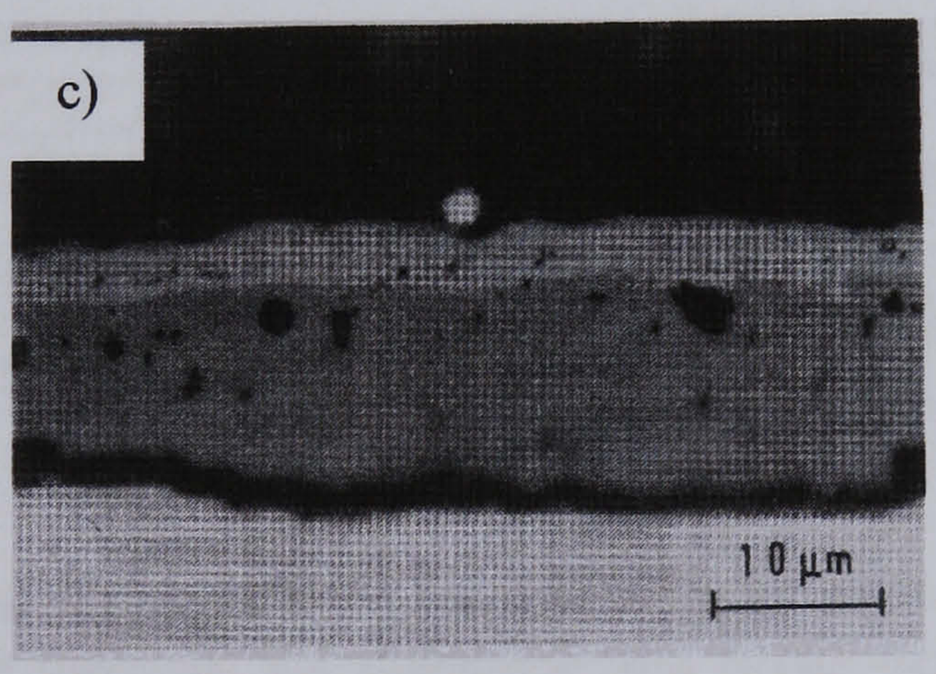

Fig.2.16. a) Oxidation kinetics of the alloy A-B 650°C, C-H 600°C. b) EDX line analysis of the elements present in the oxide layer at 600°C and c) Scanning electron micrograph of showing the constituents of the oxide layer obtained after 22 hours at 600°C. *After Simms and Little* (1988).

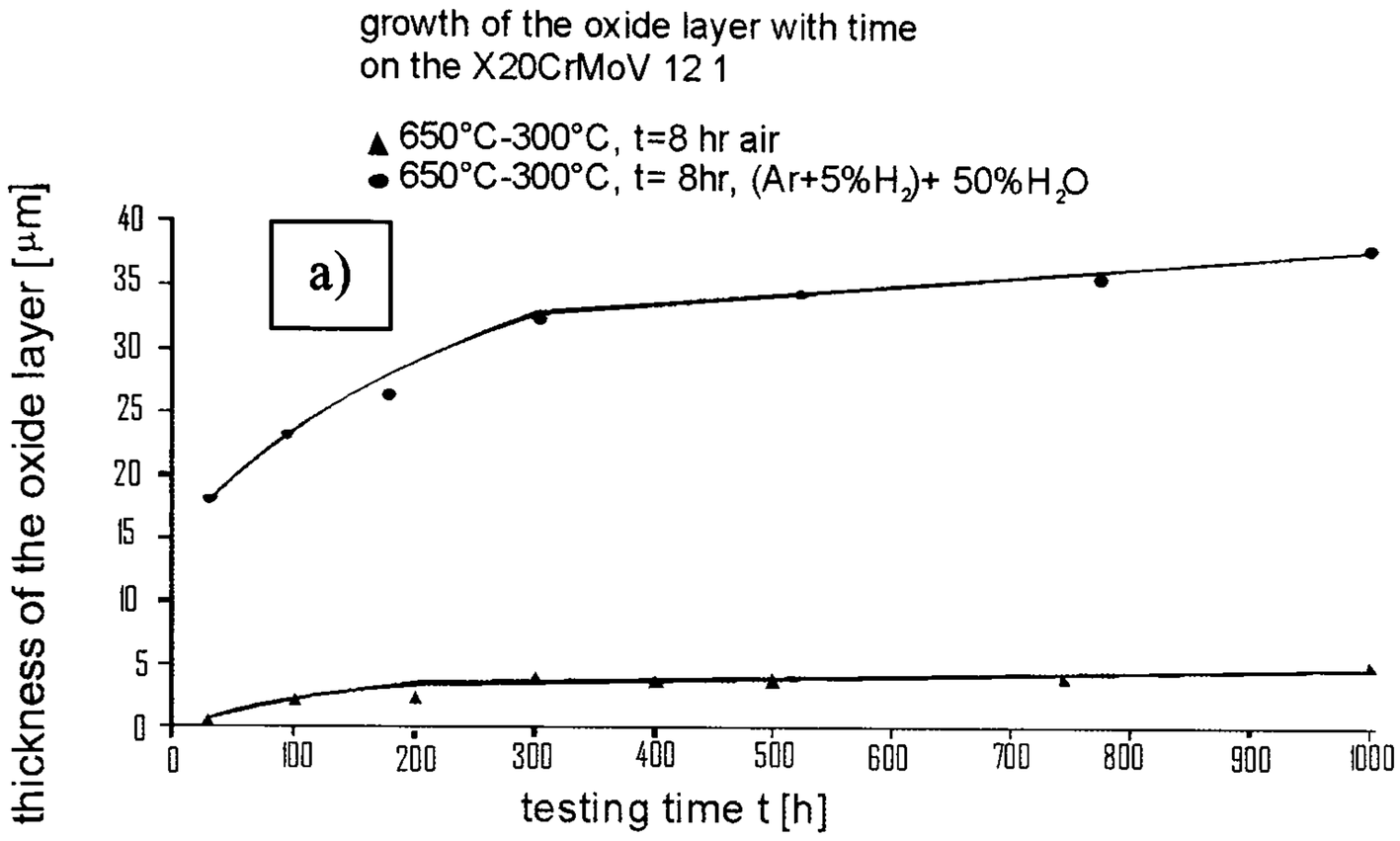

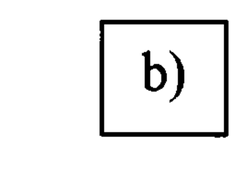

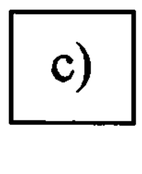

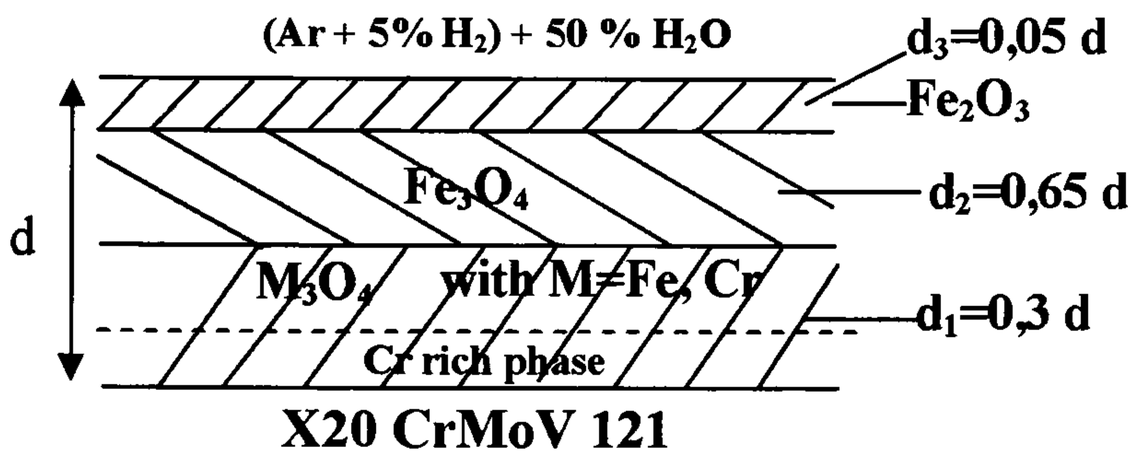

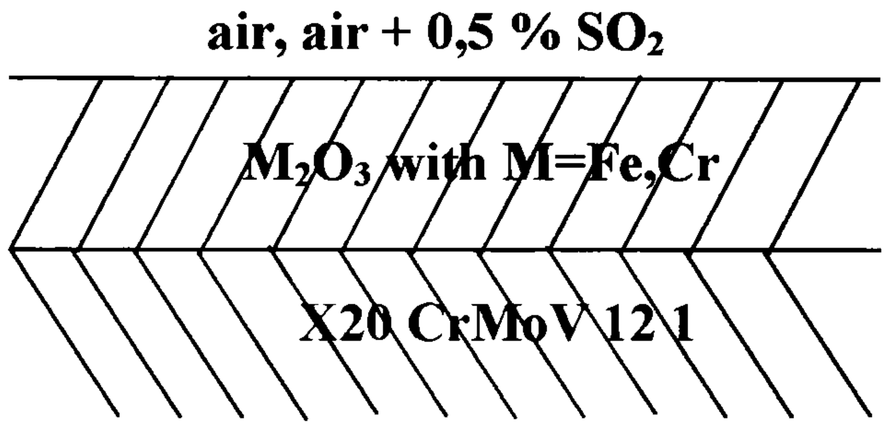

Fig.2.17. a) Comparison of the oxidation kinetics of the alloys in air and water containing mixtures observed for isothermal and cyclic oxidation experiments. b) schematic representation of the oxide layer developed in the mixture and c) oxide layer grown in air and air plus sulphur dioxide. *After Walter et al.* (1993).

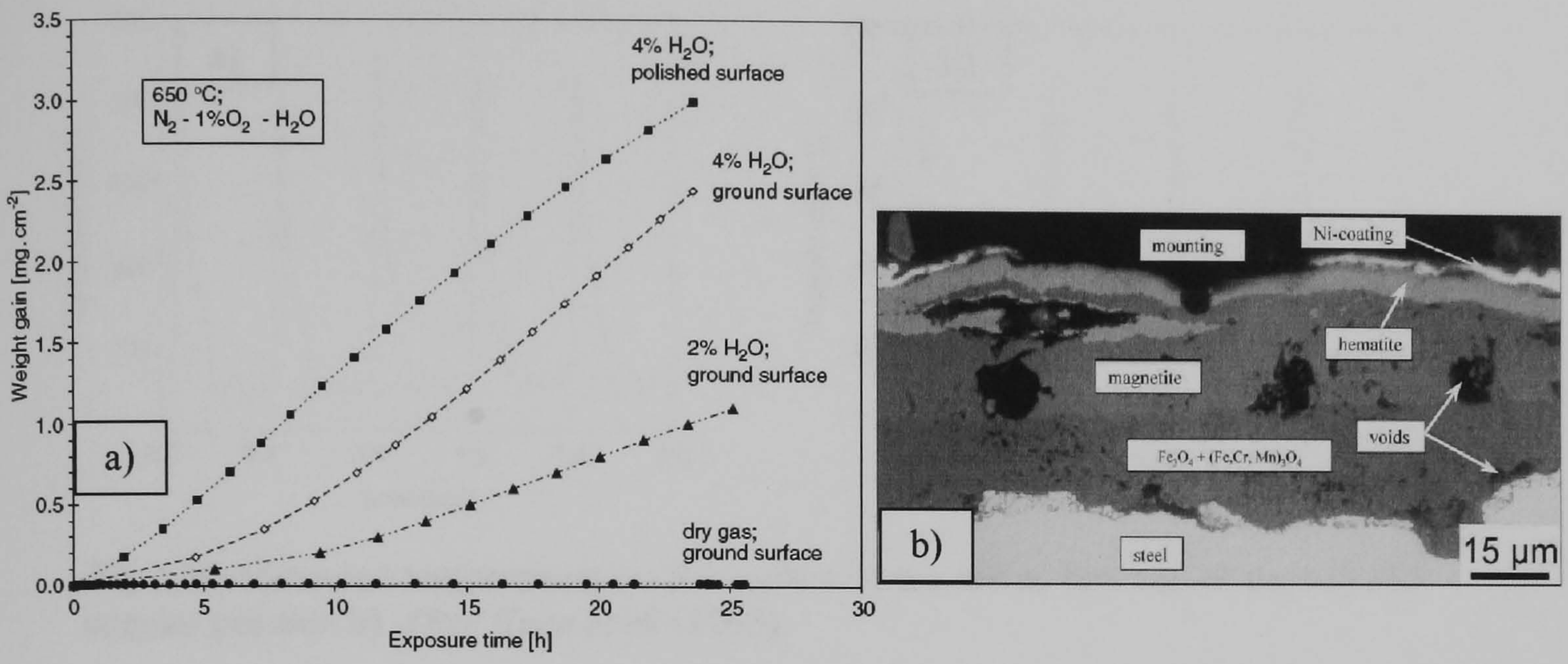

Fig.2.18. a) Oxidation kinetics plots of the steel obtained for dry and moist atmospheres. b) Oxide scale formed on the steel at 650°C under conditions containing water vapour . *After Ehlers et al.* (2006).

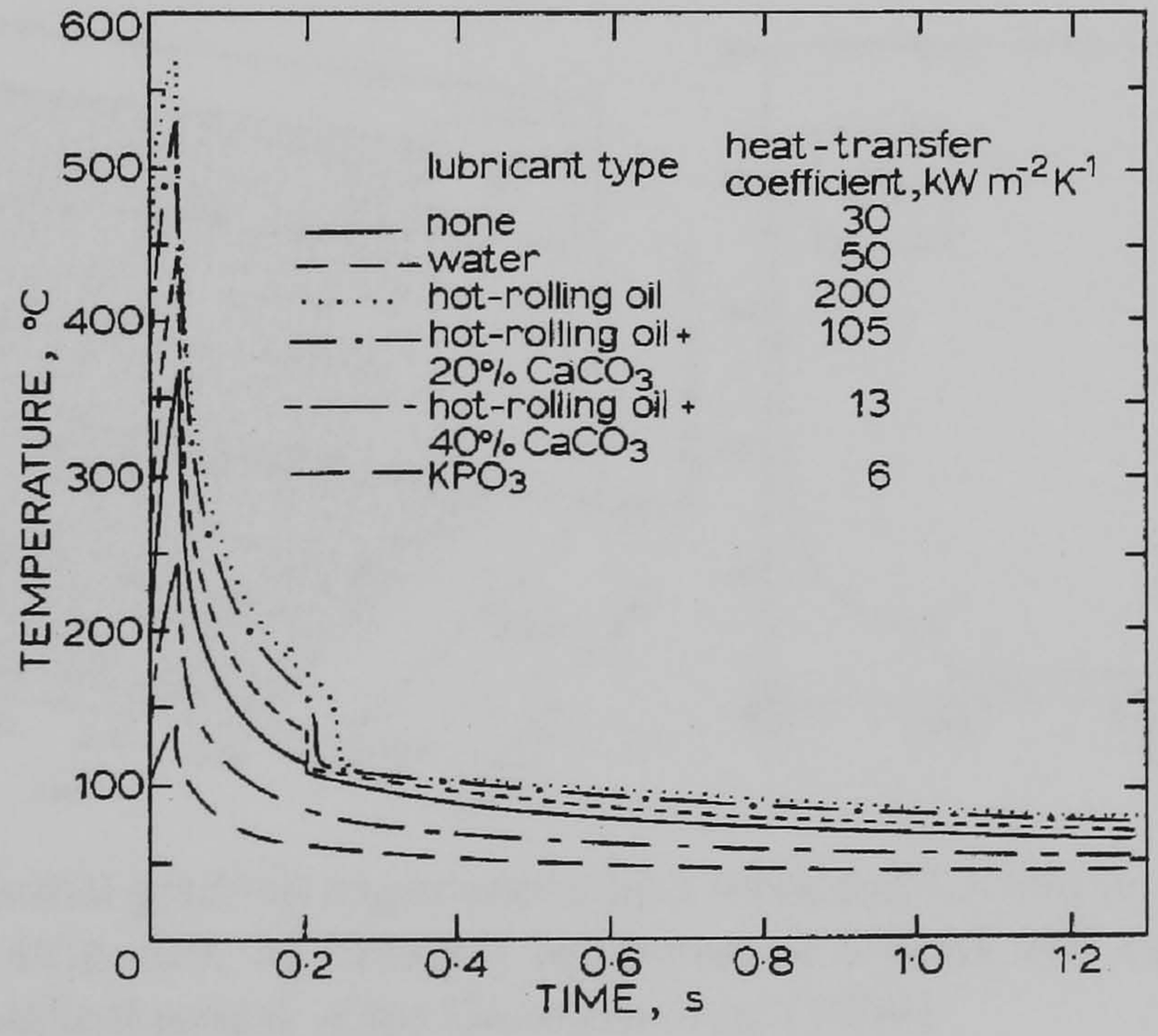

Fig.2.19. Temperature variations in the first stand of a hot strip mill as function of the lubricants used. *After Devadas and Samarasekera* (1986).

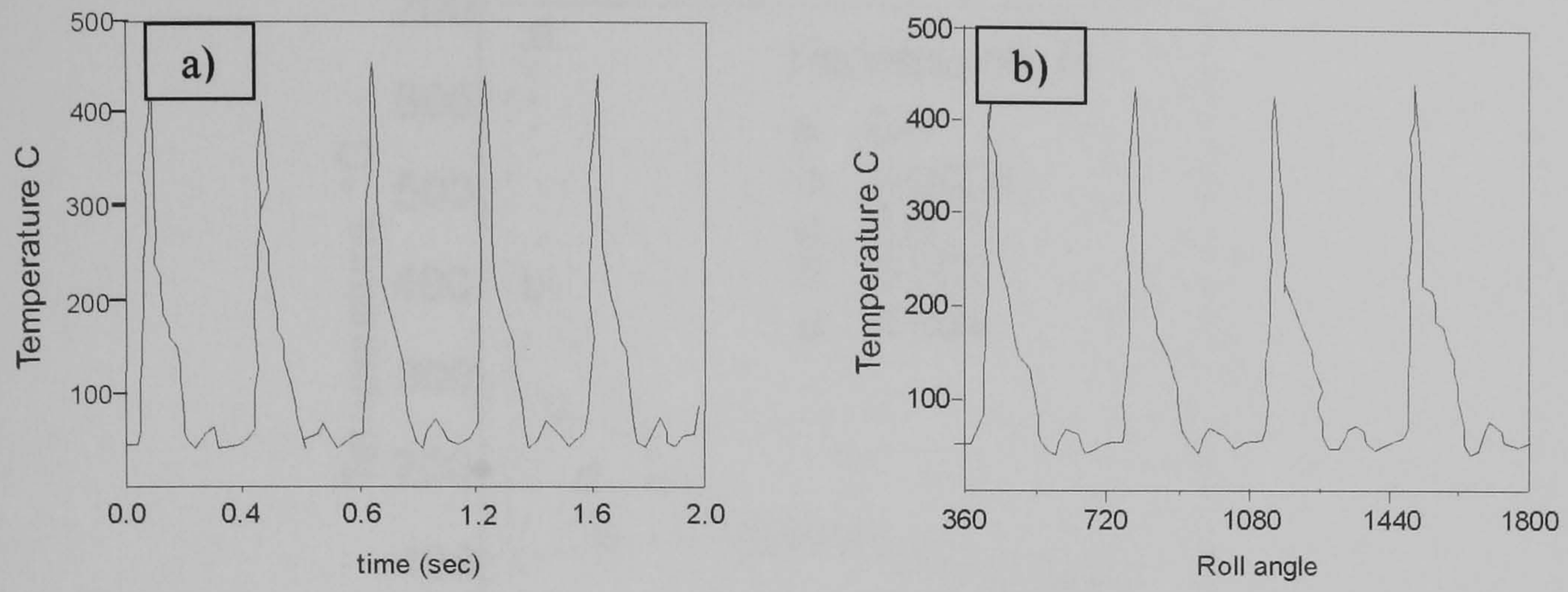

Fig.2.20. Measured temperatures on the surface of the roll as function of time a) and angular position b). *After Huan et al.* (1995).

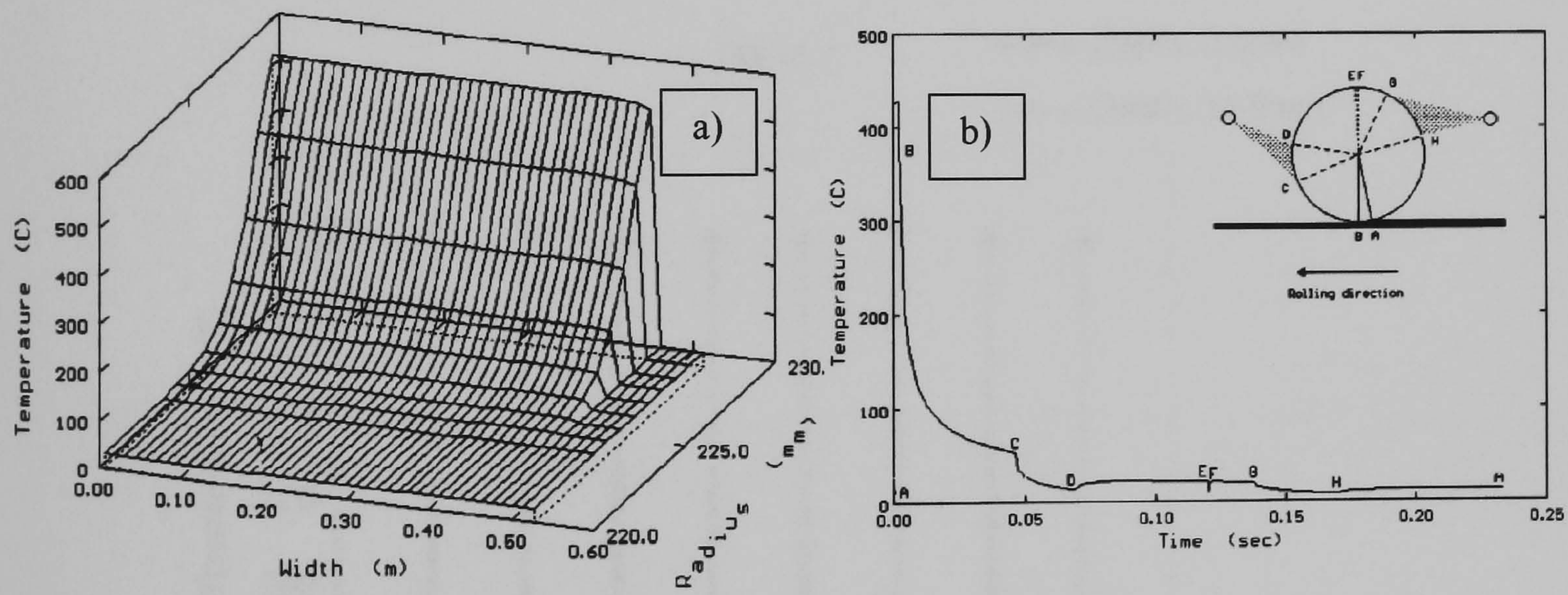

Fig.2.21. a) Thermal gradient experienced by a work roll located in the first finishing stand of a hot strip mill. b) Thermal behaviour of a work roll calculated using a specific mathematical model. *After Guerrero et al.* (1999).

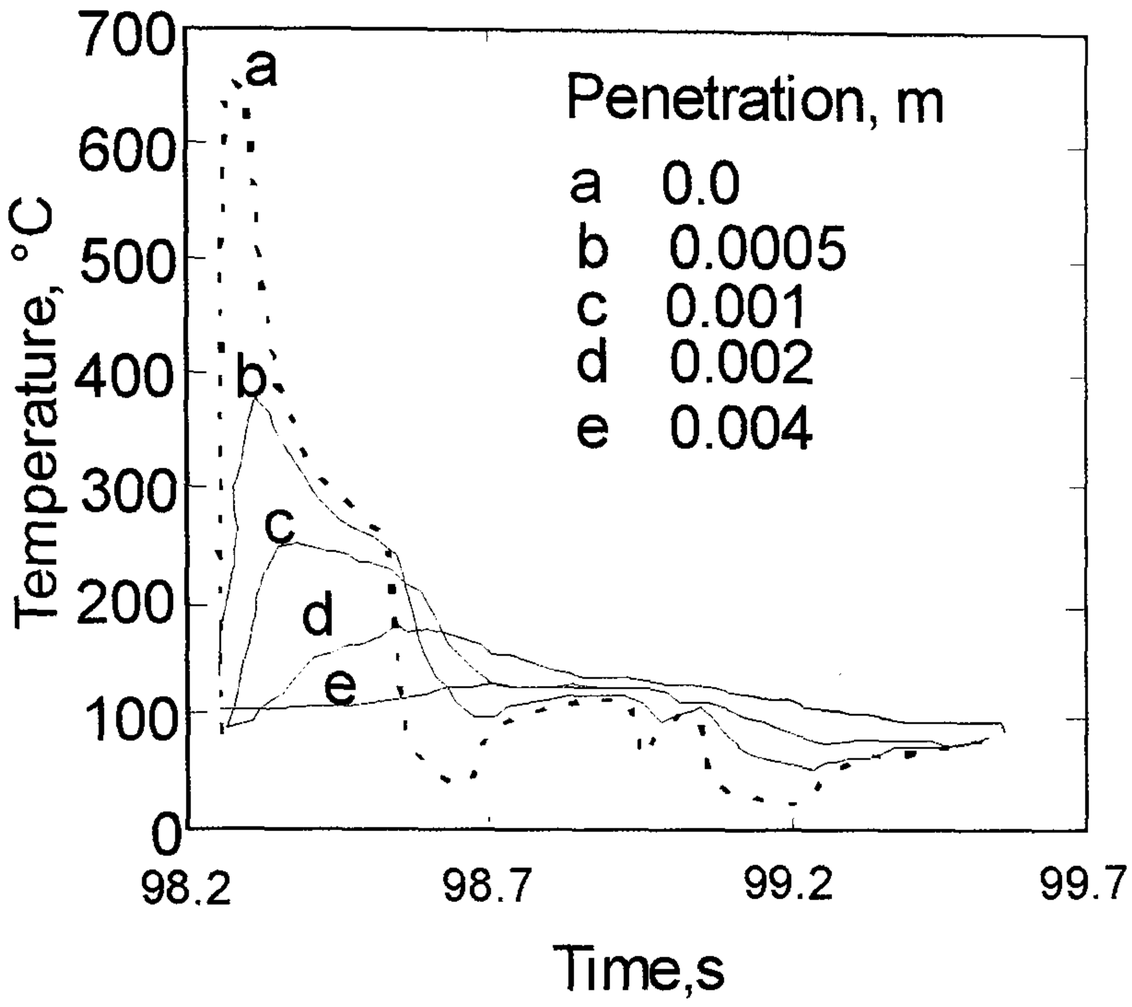

Fig.2.22. Calculation of the thermal cycles experienced on the surface of a High chromium iron work roll. *After Perez et al.* (2004).

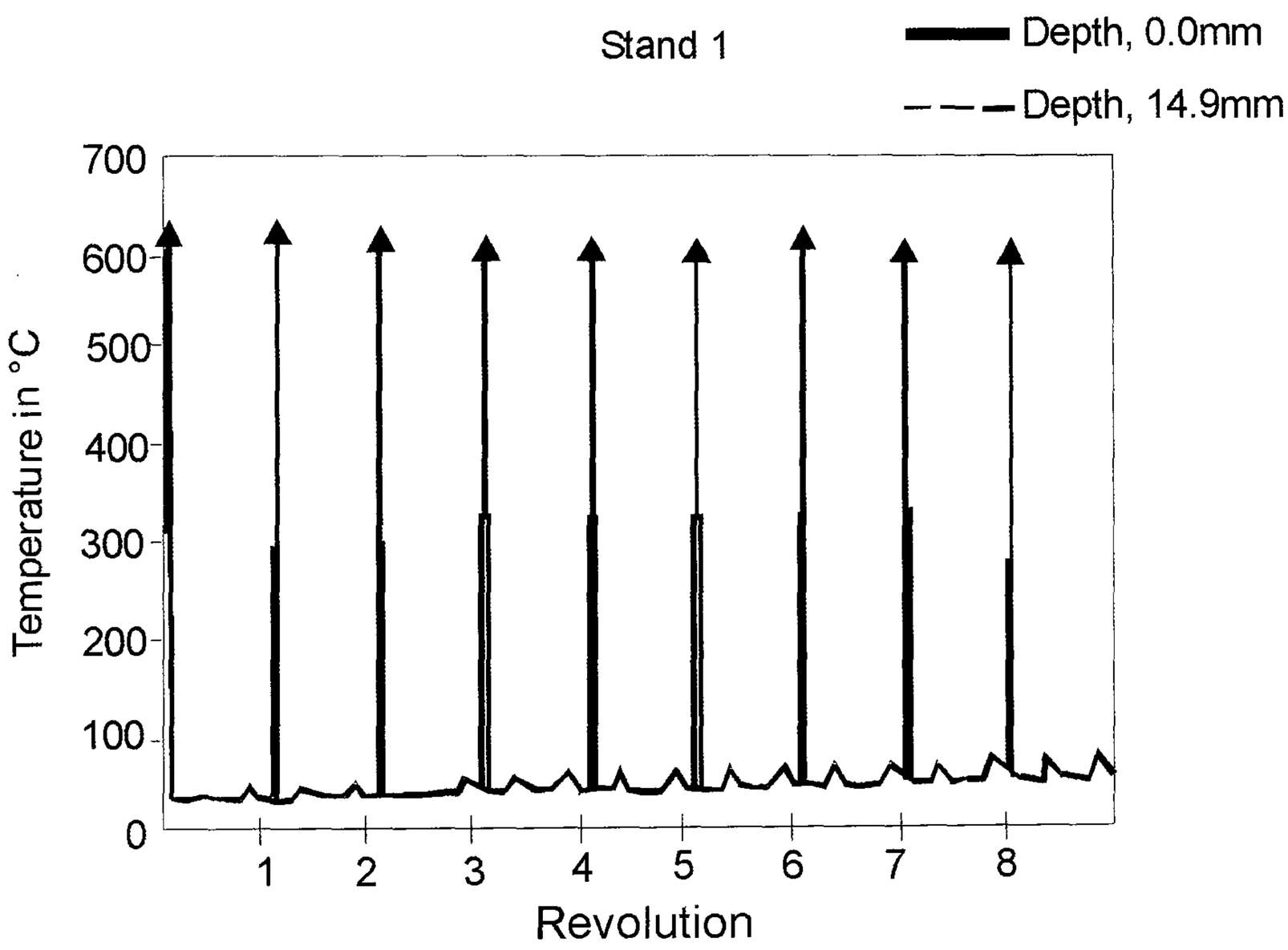

Fig.2.23. Thermal cycles imposed on the roll surface per roll revolution. *After Sikdar and John* (2006).

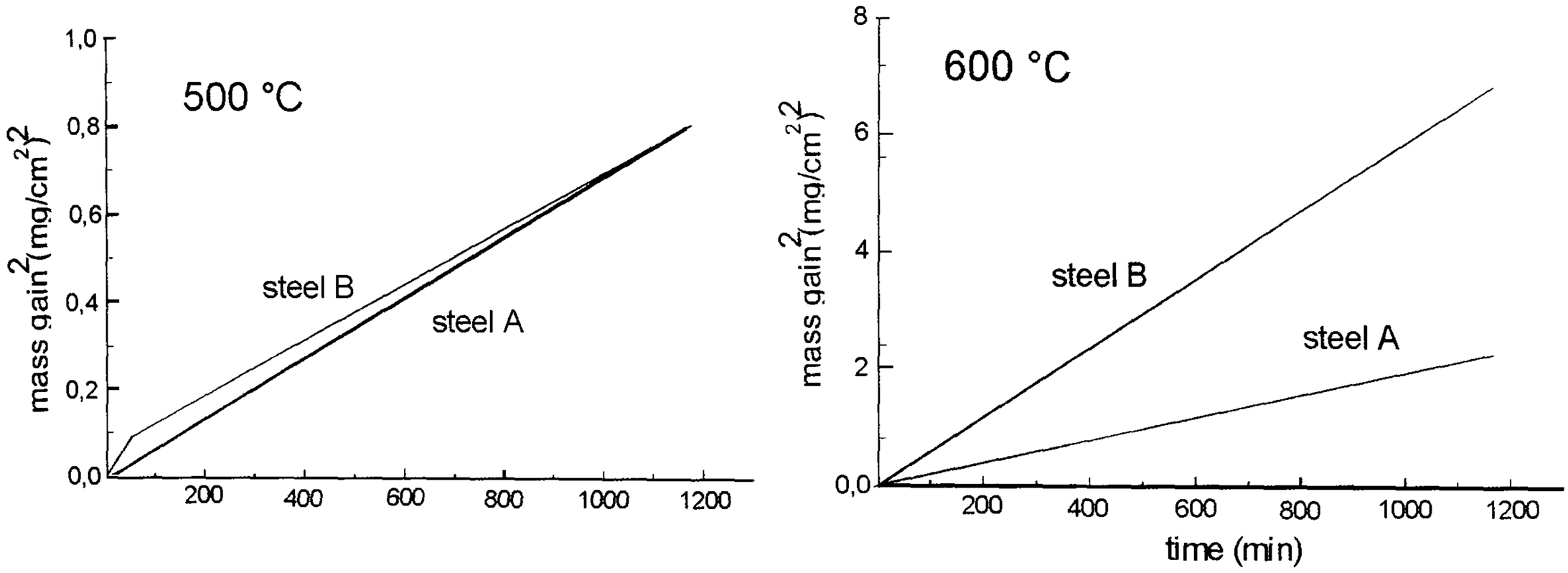

Fig.2.24. Quantification of the oxidation phenomenon obtained at three temperatures for two steels containing different amounts of chromium (%A>%B). Note the differences in the mass gained as a function of the testing temperature. *After Molinari et al.* (2000).

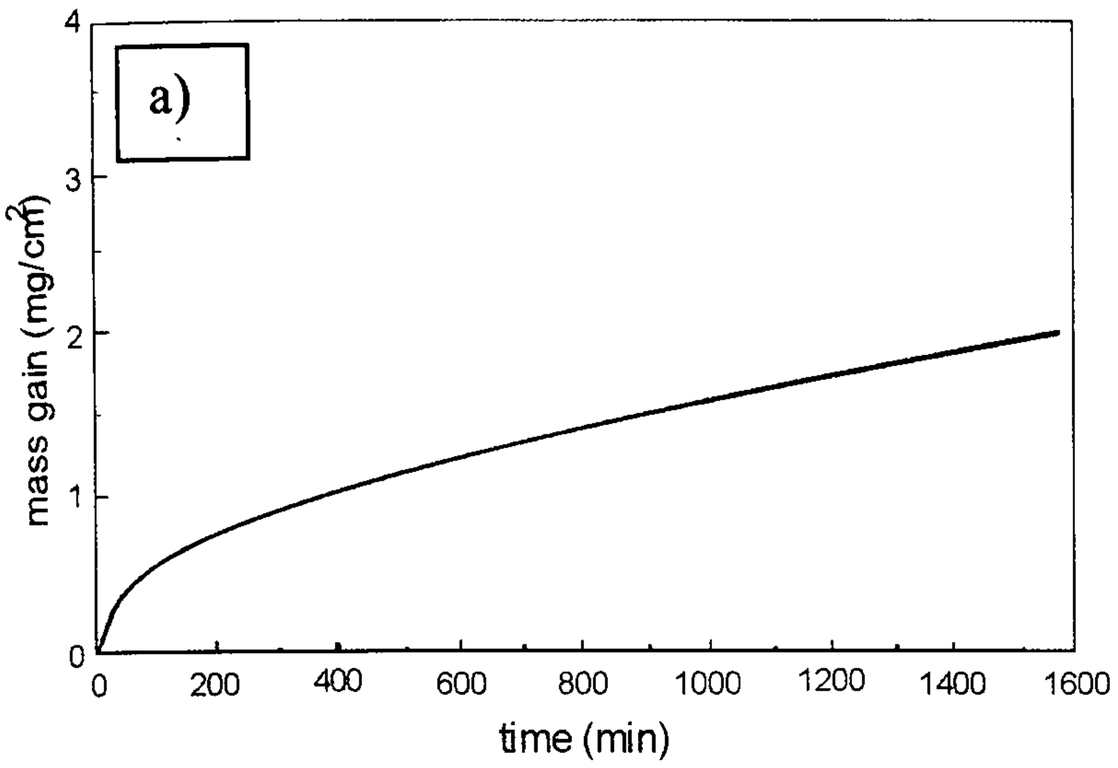

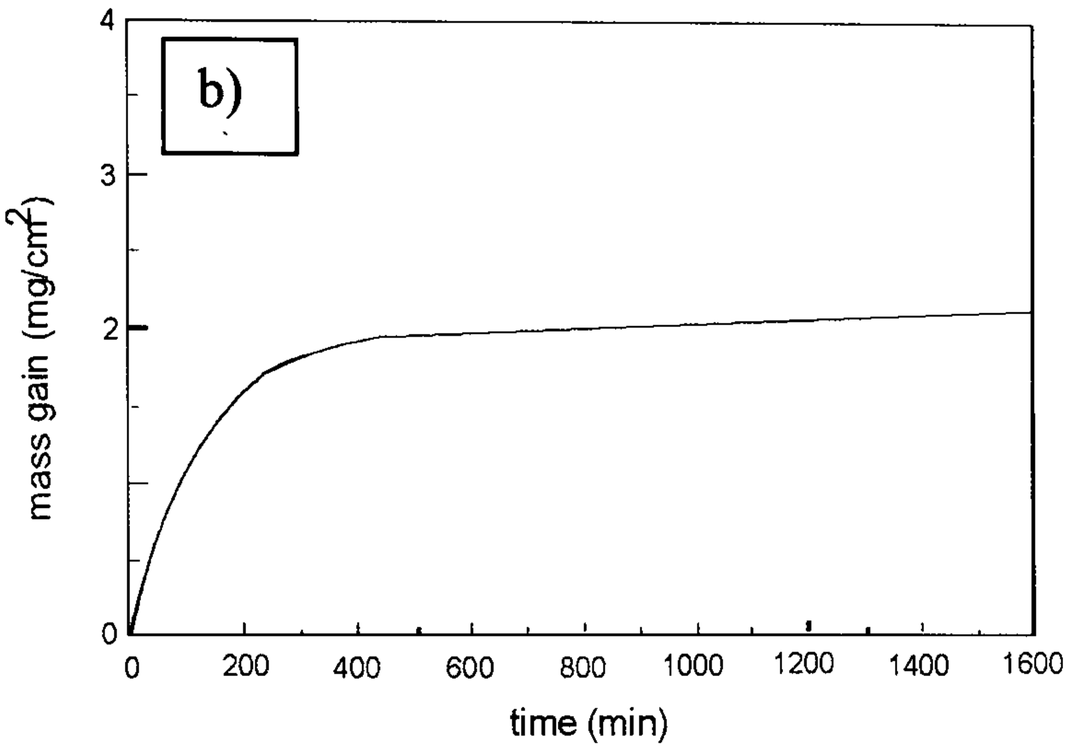

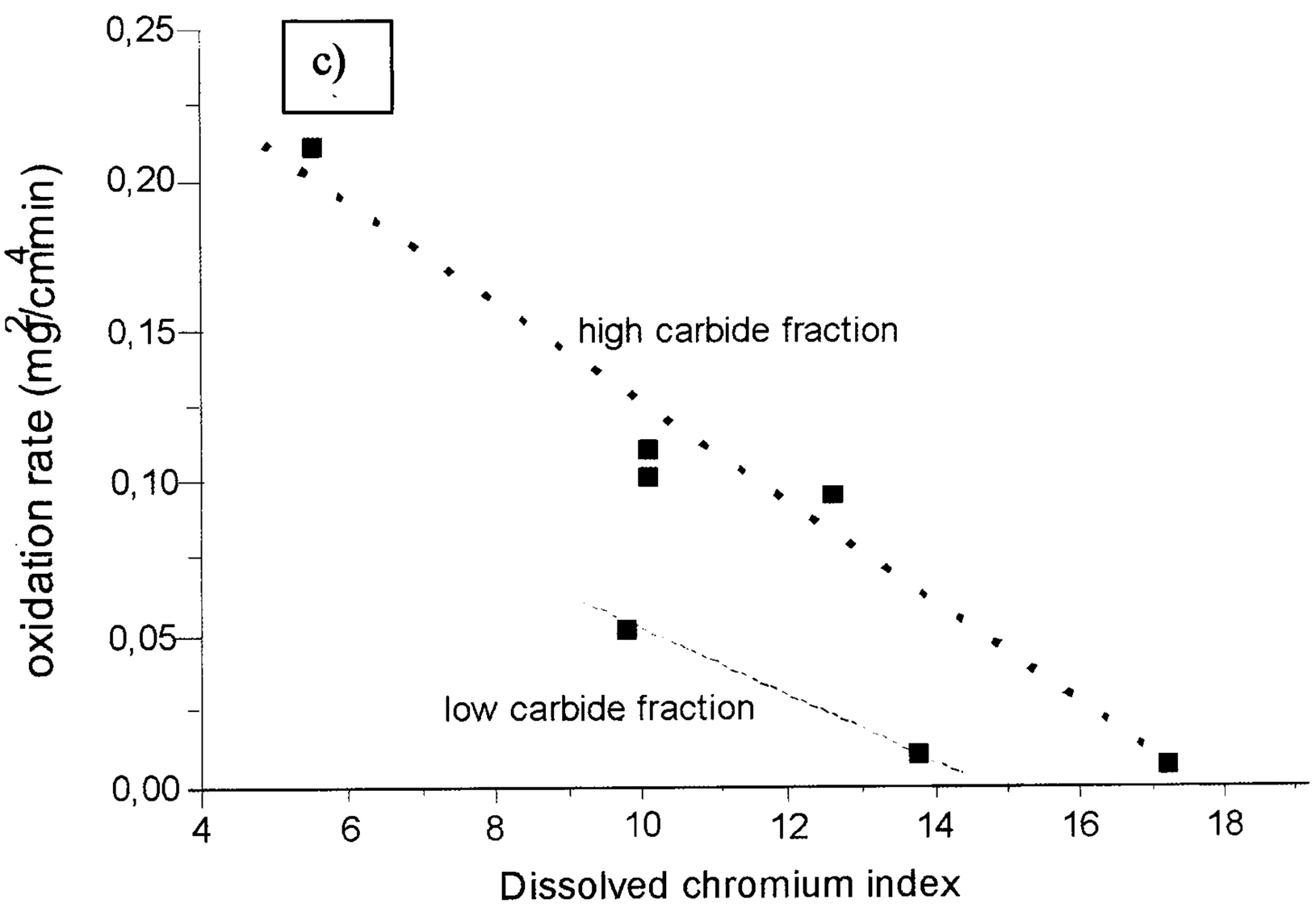

Fig.2.25. Oxidation kinetics plots obtained for different high speed steels. a) Parabolic oxidation rate obtained for a high speed steel with 5 %wt Cr. b) Transition from the parabolic to a logarithmic oxidation rate observed for a high speed steel with 12 %wt Cr. c) Oxidation rate of high speed steel as a function of the ratio Cr/Fe of the matrix. *After Molinari et al.* (2001).

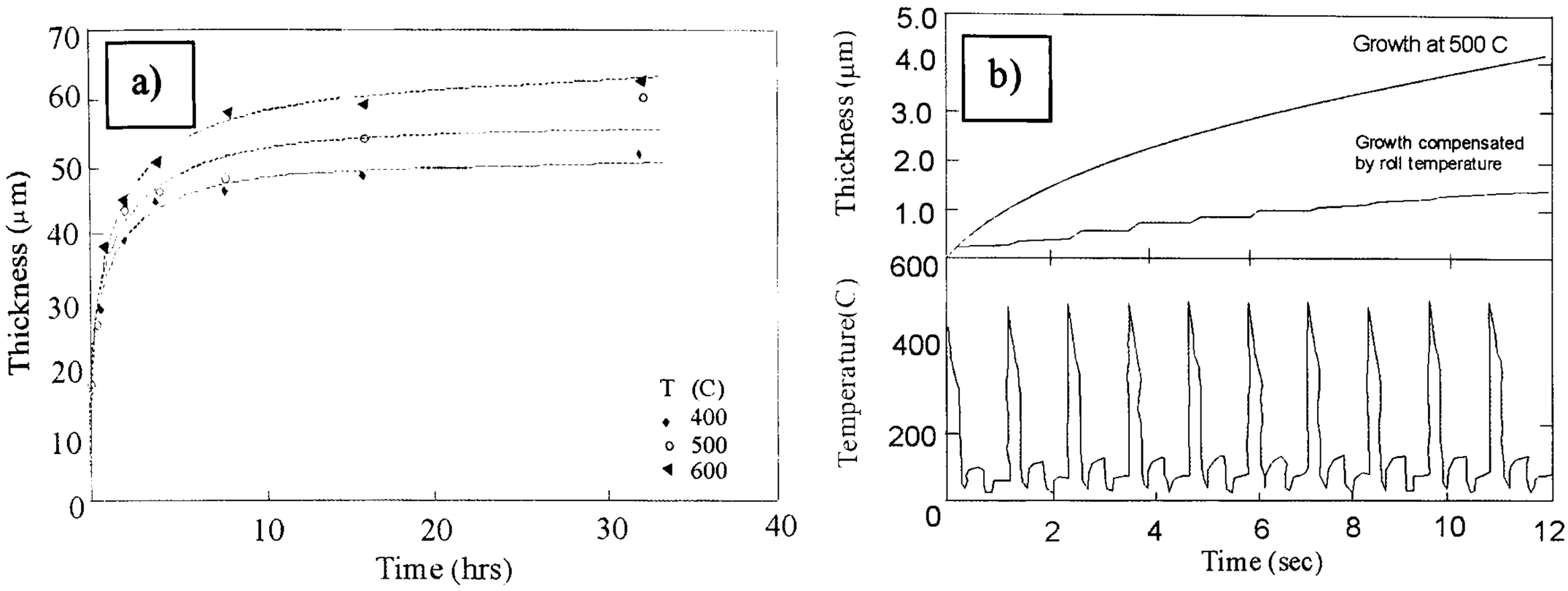

Fig.2.26. a) Variations in the isothermal oxidation behaviour of the Hi-Cr rolls with the oxidation temperature. b) Modelling and comparison between isothermal growth and growth under the action of thermal cycles at 500°C. *After Gonzalez et al.* (2001).

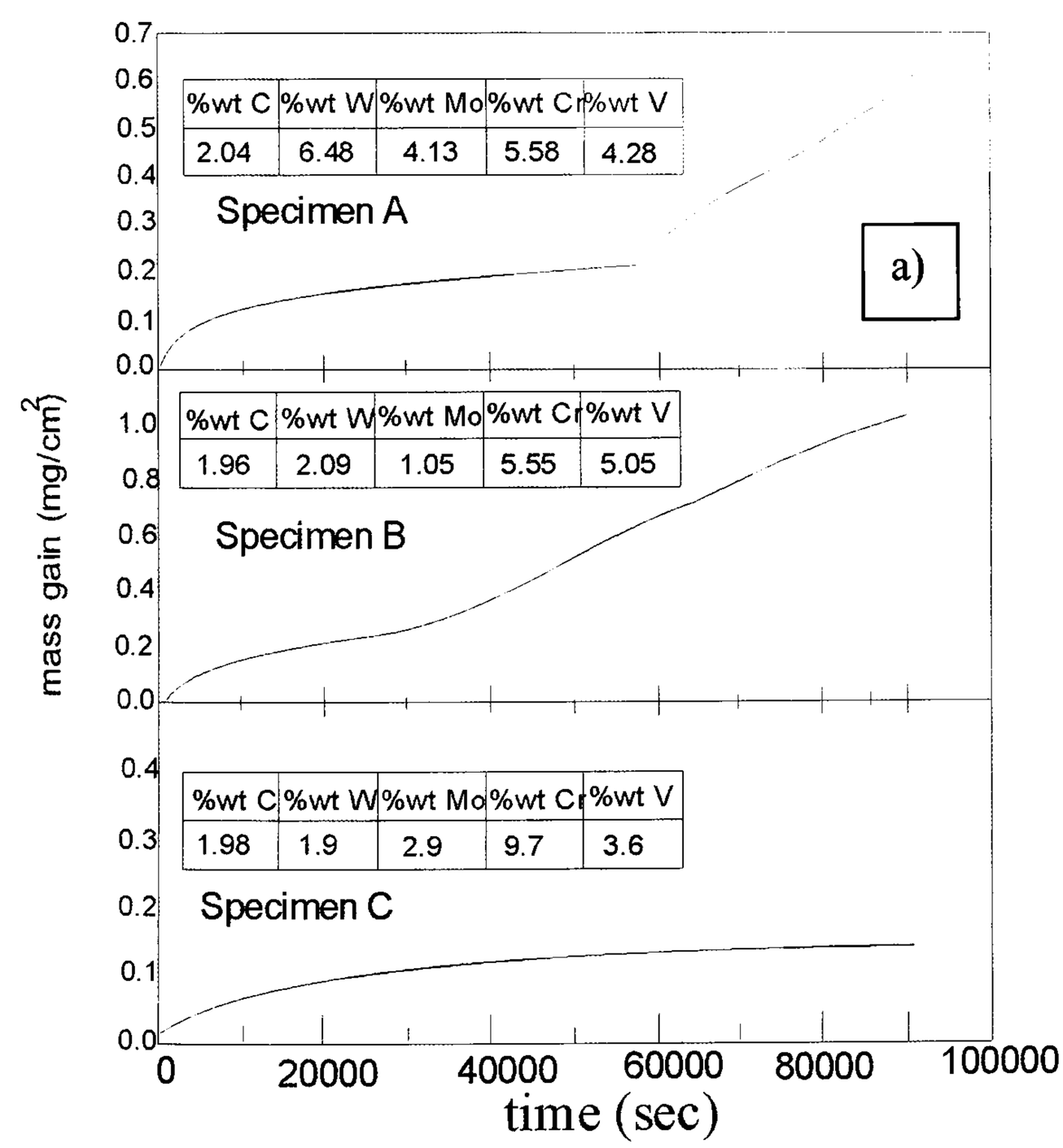

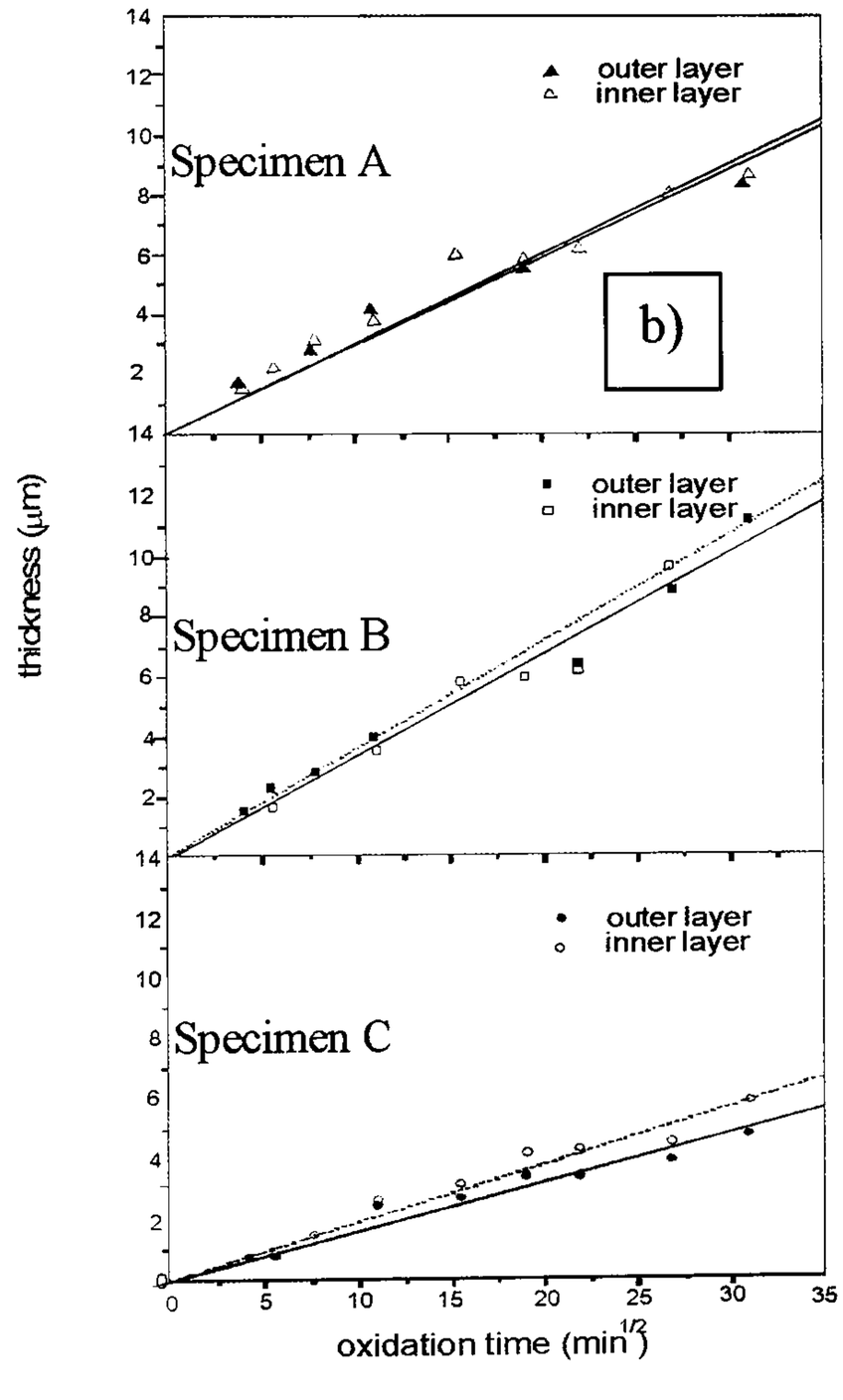

Fig.2.27. Oxidation kinetics of different compositions of high speed steels. a) Steels oxidized in dry oxygen. b) Steels oxidized in argon + water vapour. *Modified from Kim et al.* (2003).

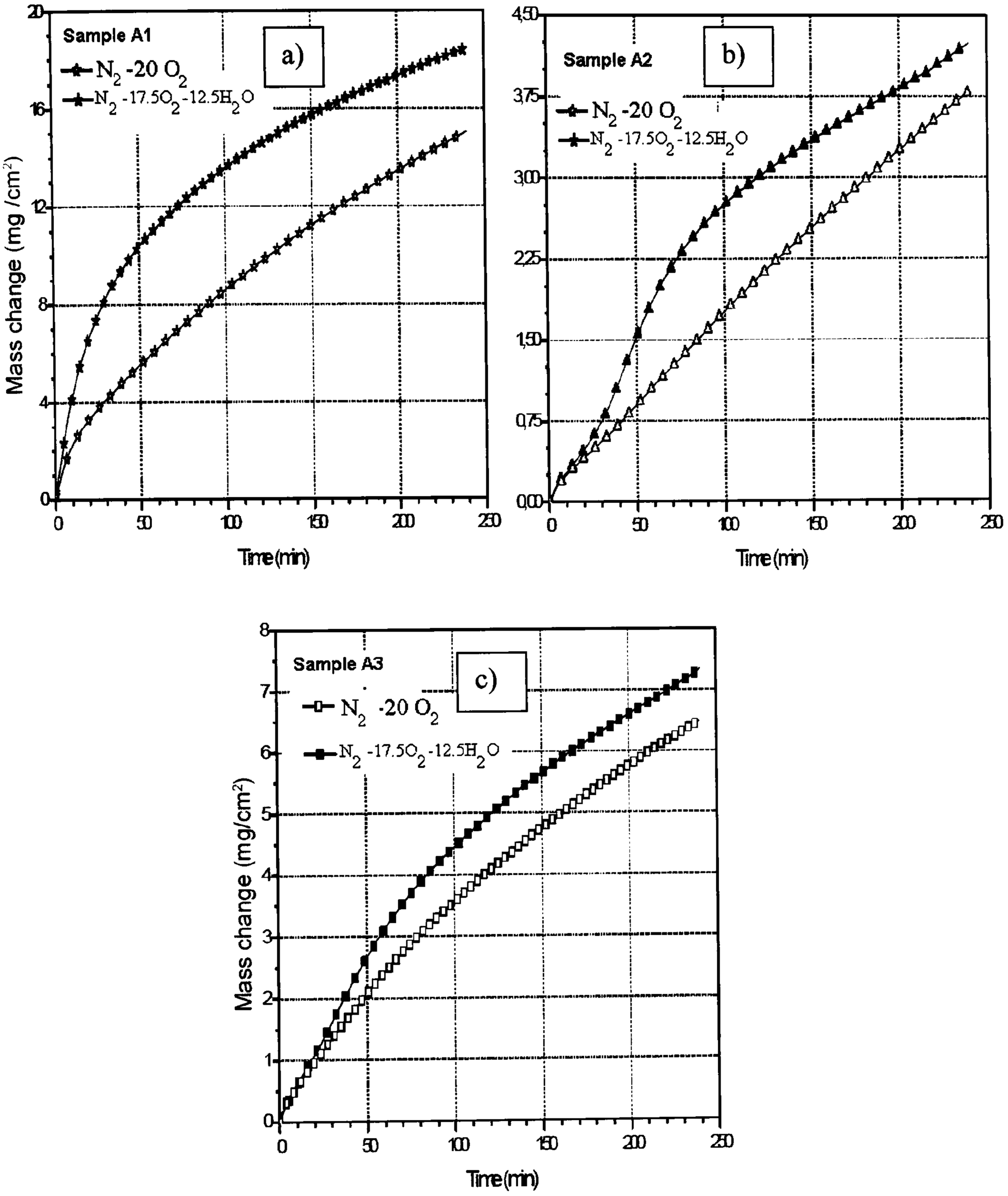

Fig.2.28. Comparison of the oxidation behaviour of different high speed steels samples in dry and moist atmospheres. a) 3.5 %wt Cr, b) 7.5 % wt Cr and c) 4.44 %wt Cr. *Modified from Monteiro and Rizzo* (2003).

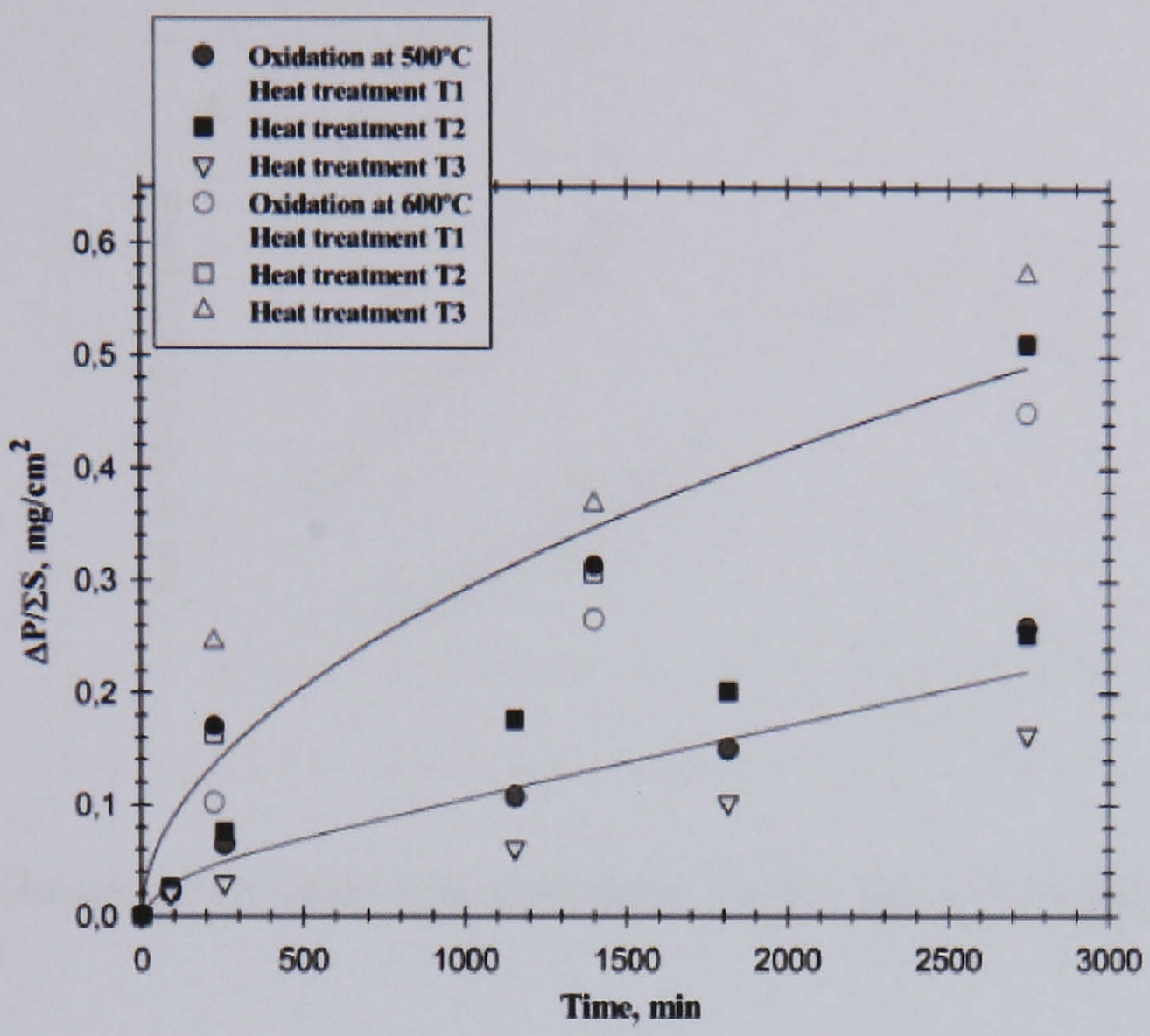

Fig.2.29. Oxidation behaviour of white cast irons as a function of the temperature and different tempering heat treatments. *After Ziadi et al.* (2005).

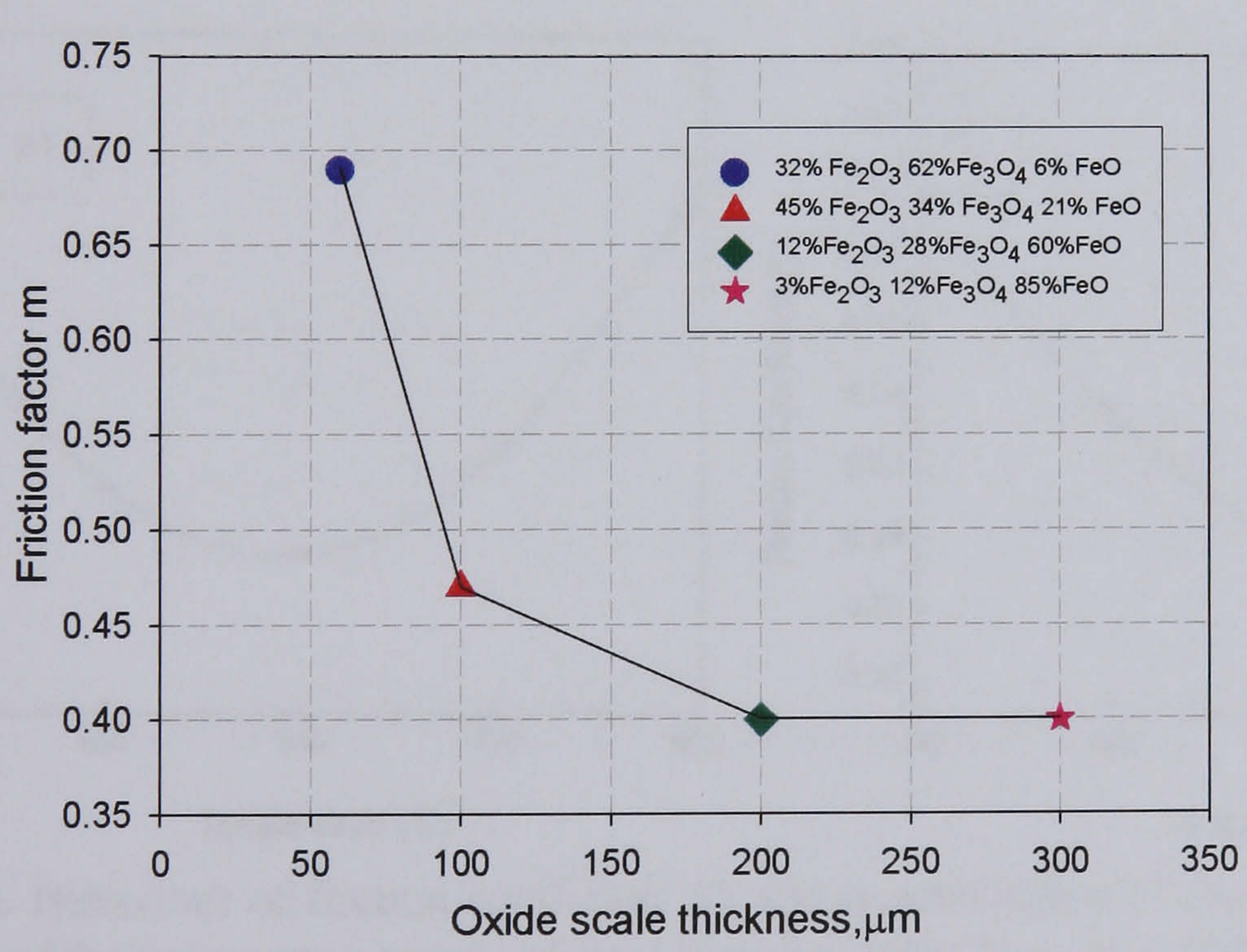

Fig.2.30. Variation of the friction factor as a function of the scale thickness obtained from ring compression tests of oxidized steel specimens in controlled atmosphere. The value of the friction factor decreases as the thickness of the oxide scale increases. Data taken from *Luong and Heijkoop*, (1981).

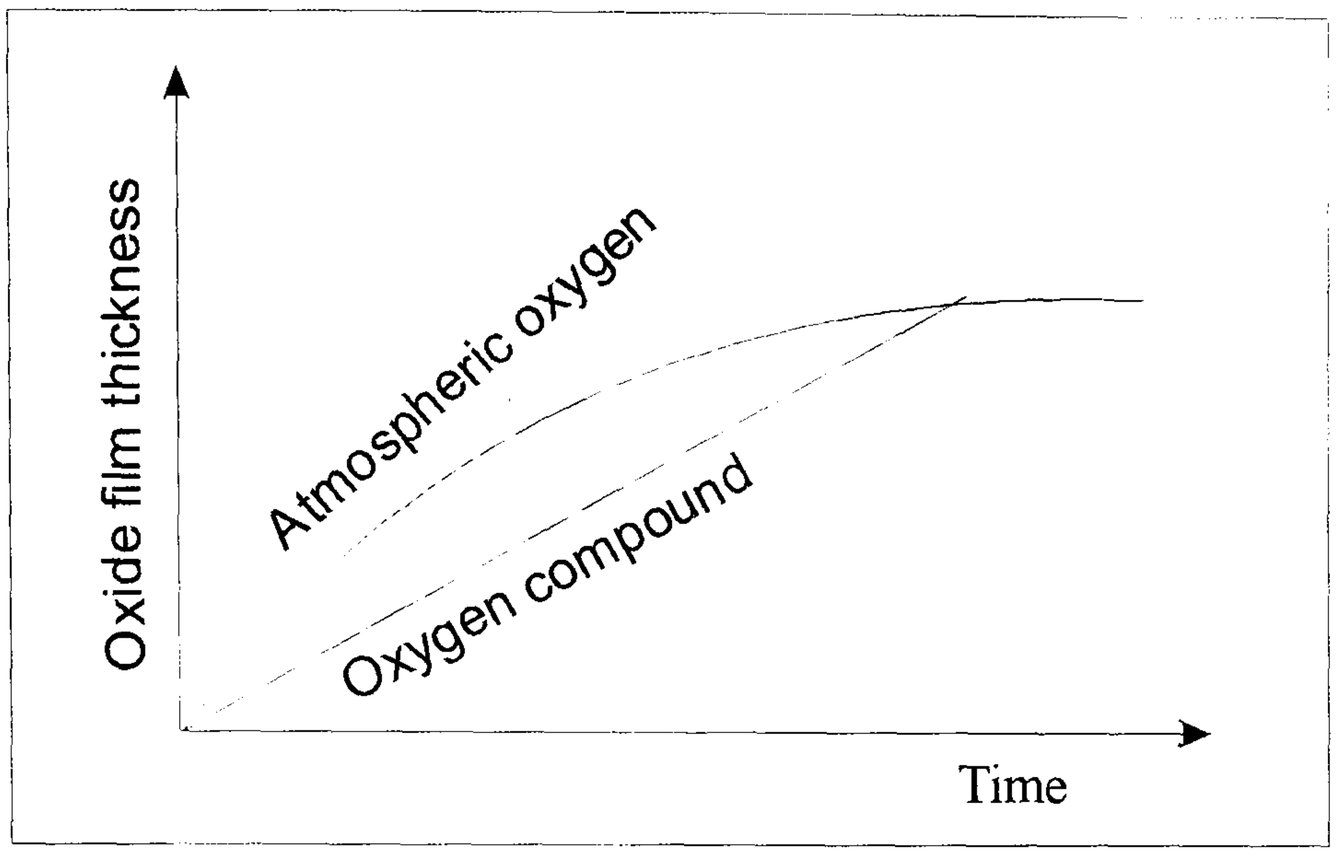

Fig.2.31. Growth of an oxide film depending on the source of oxygen. *After Batchelor et al.* (1986).

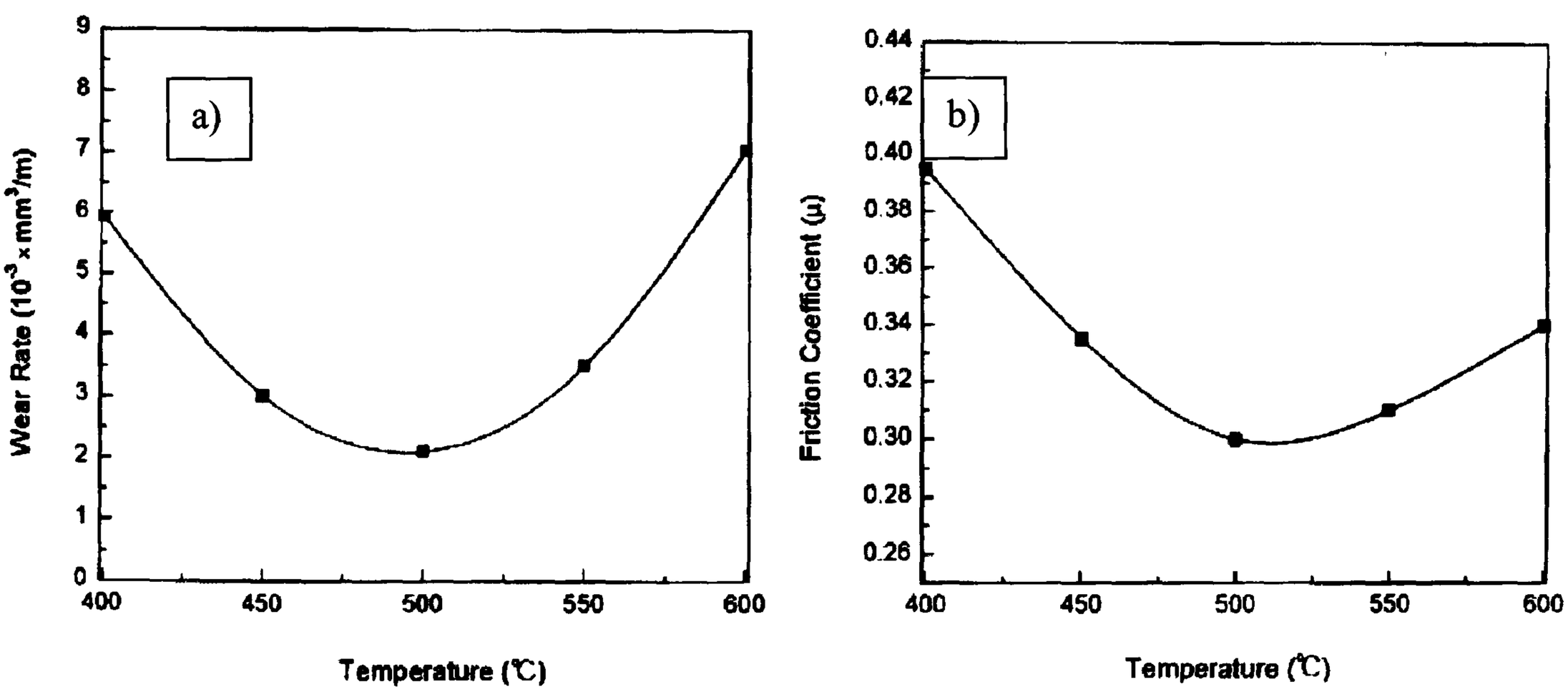

Fig.2.32. Behaviour of friction coefficient a), and quantification of the wear rate b) as a function of the testing temperature of steel samples. After *Tu et al.* (1998).

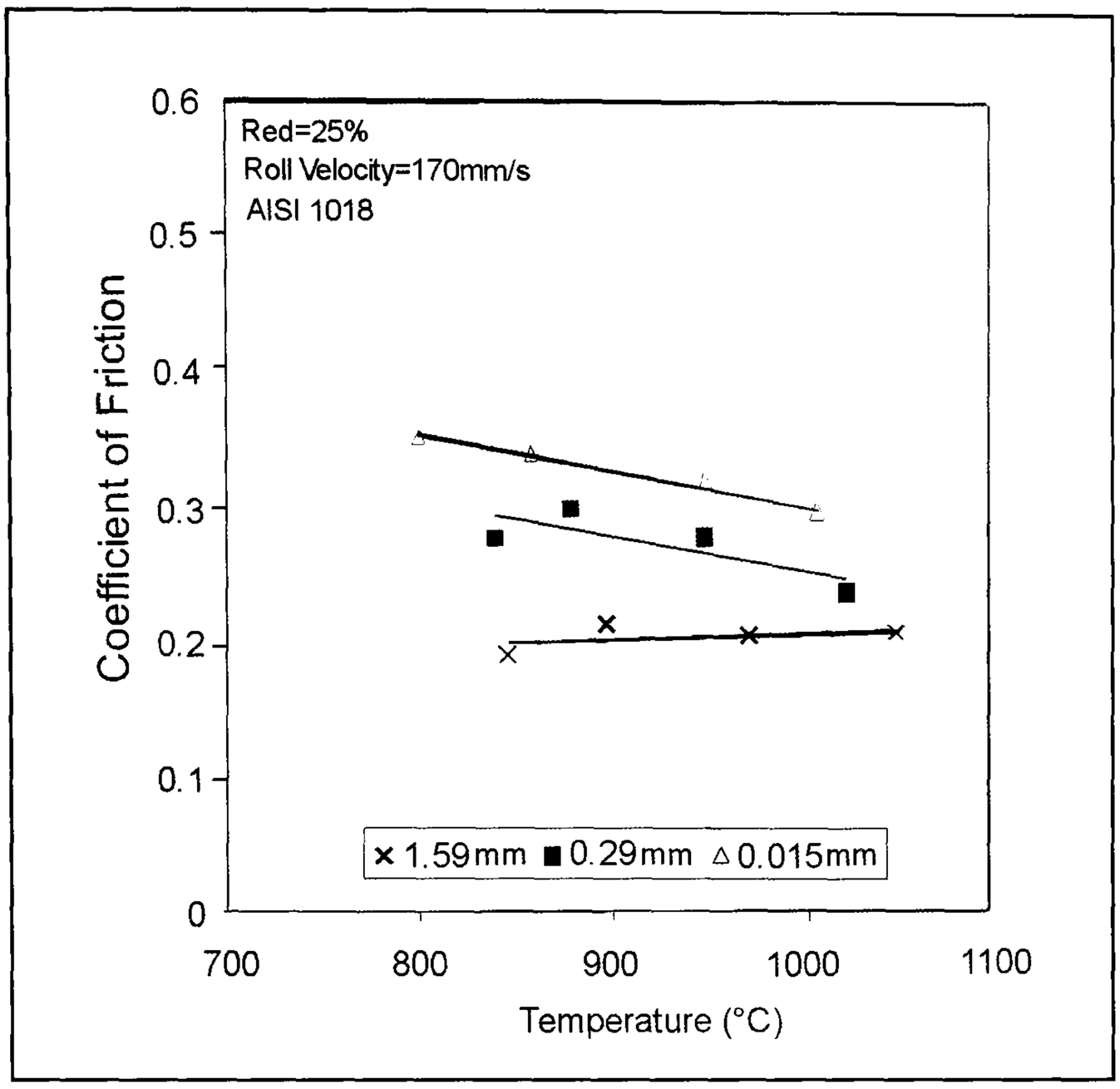

Fig.2.33. Friction coefficient variation with the test temperature and oxide scale produced for the rolling of low carbon steel. *After Munther and Lenard* (1999).

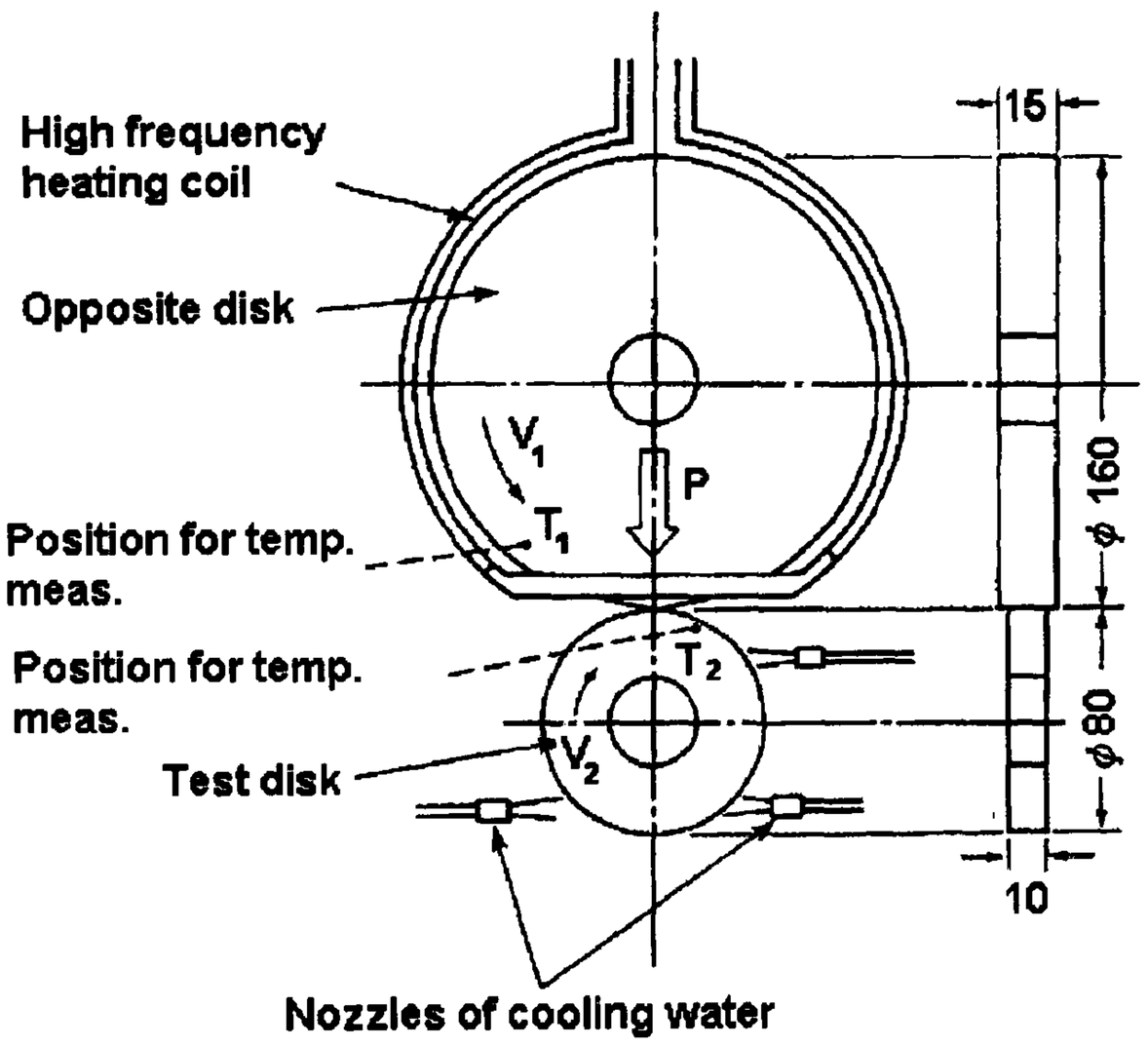

Fig.2.34. Experimental methodology used by Kato *et al.* to assess the wear of Hi Cr work rolls. *After Kato et al.* (1992).

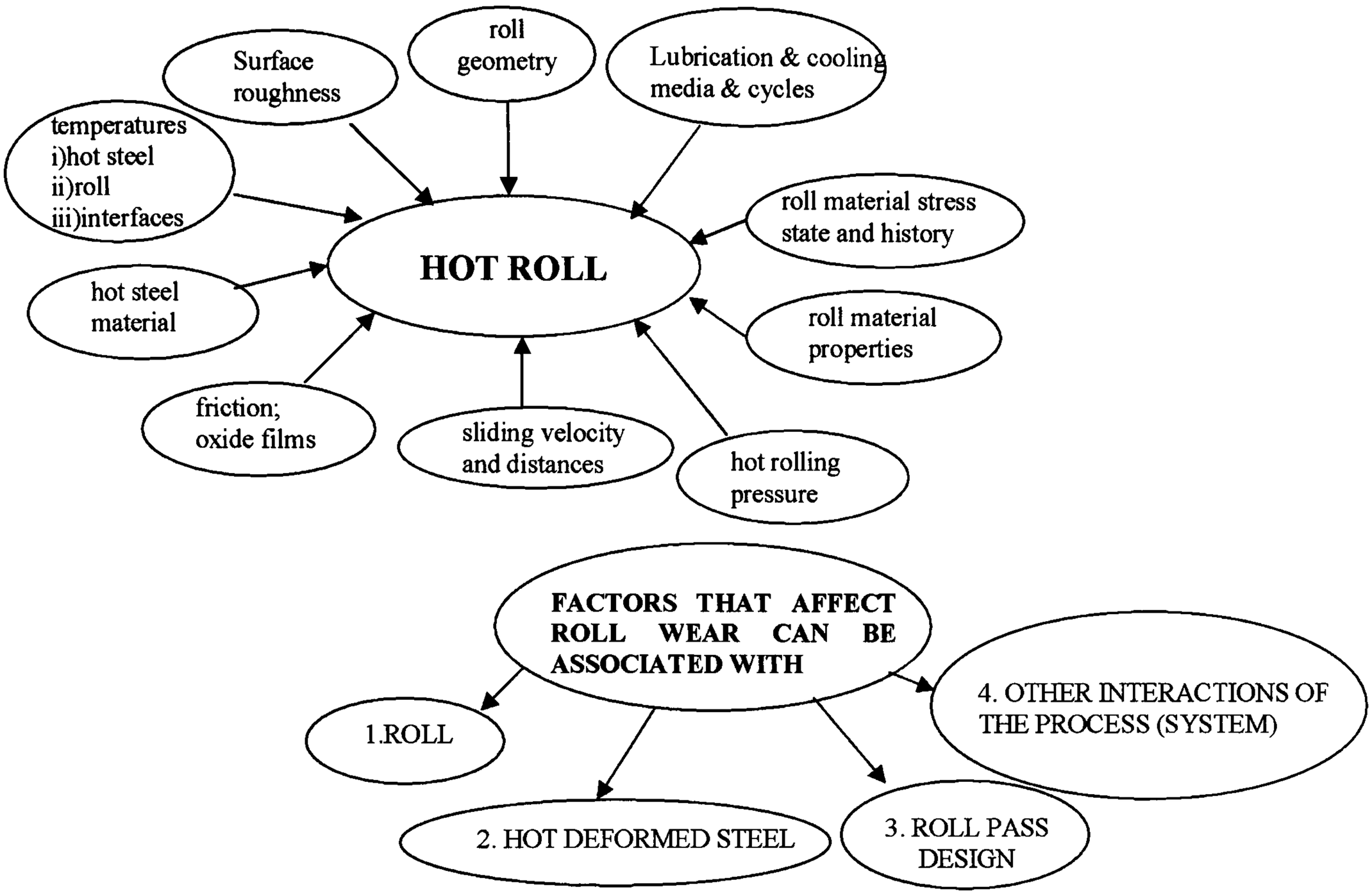

Fig.2.35. Variables affecting the wear of work rolls in hot steel mills. *After Spuzic et al.* (1999).

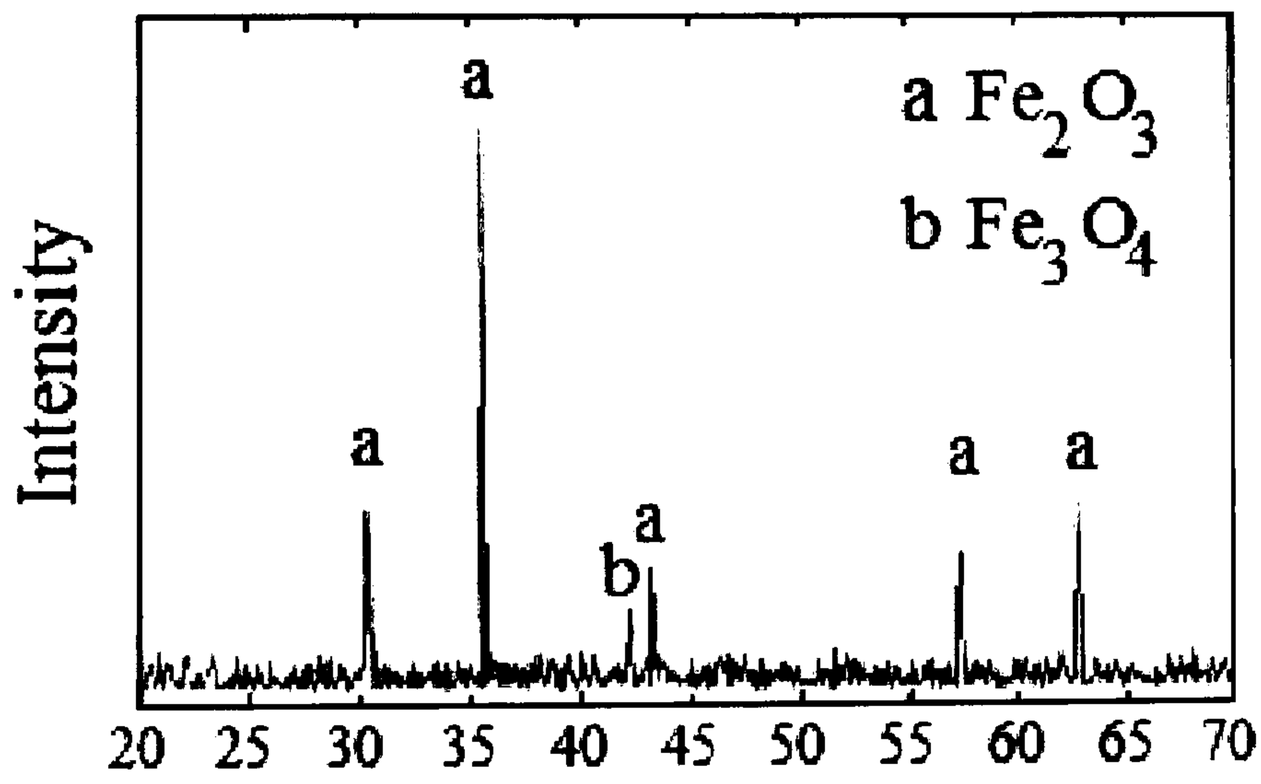

Fig.2.36. X-ray diffraction pattern of the oxide layer grown on the surface of high chromium iron work rolls. *After Colas et al.* (1999).

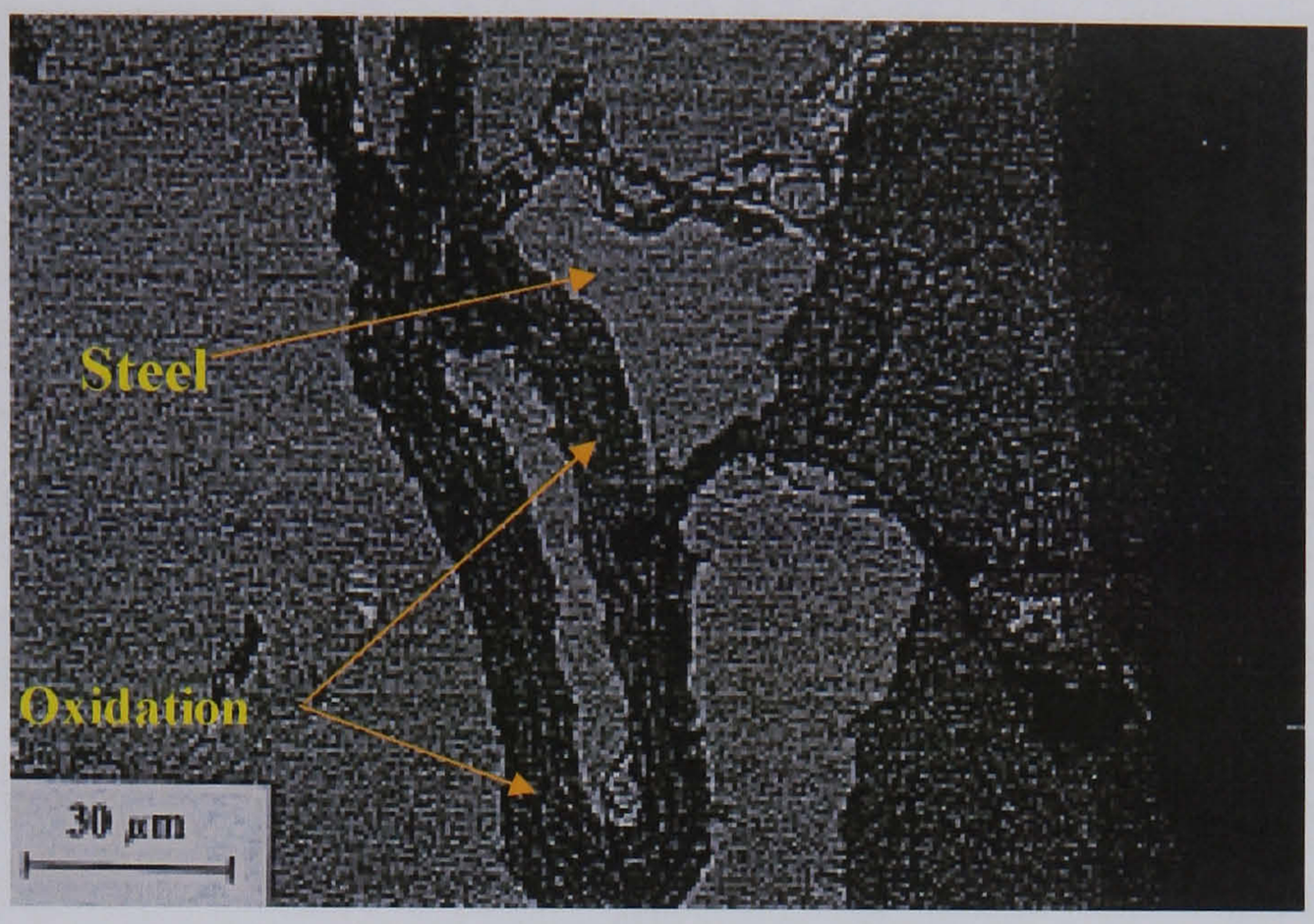

Fig.2.37. Cross section of a Hi-Cr steel after the rolling of steel. Propagation of cracks is observed as well as internal oxidation. *Modified from Colas et al.* (1999).

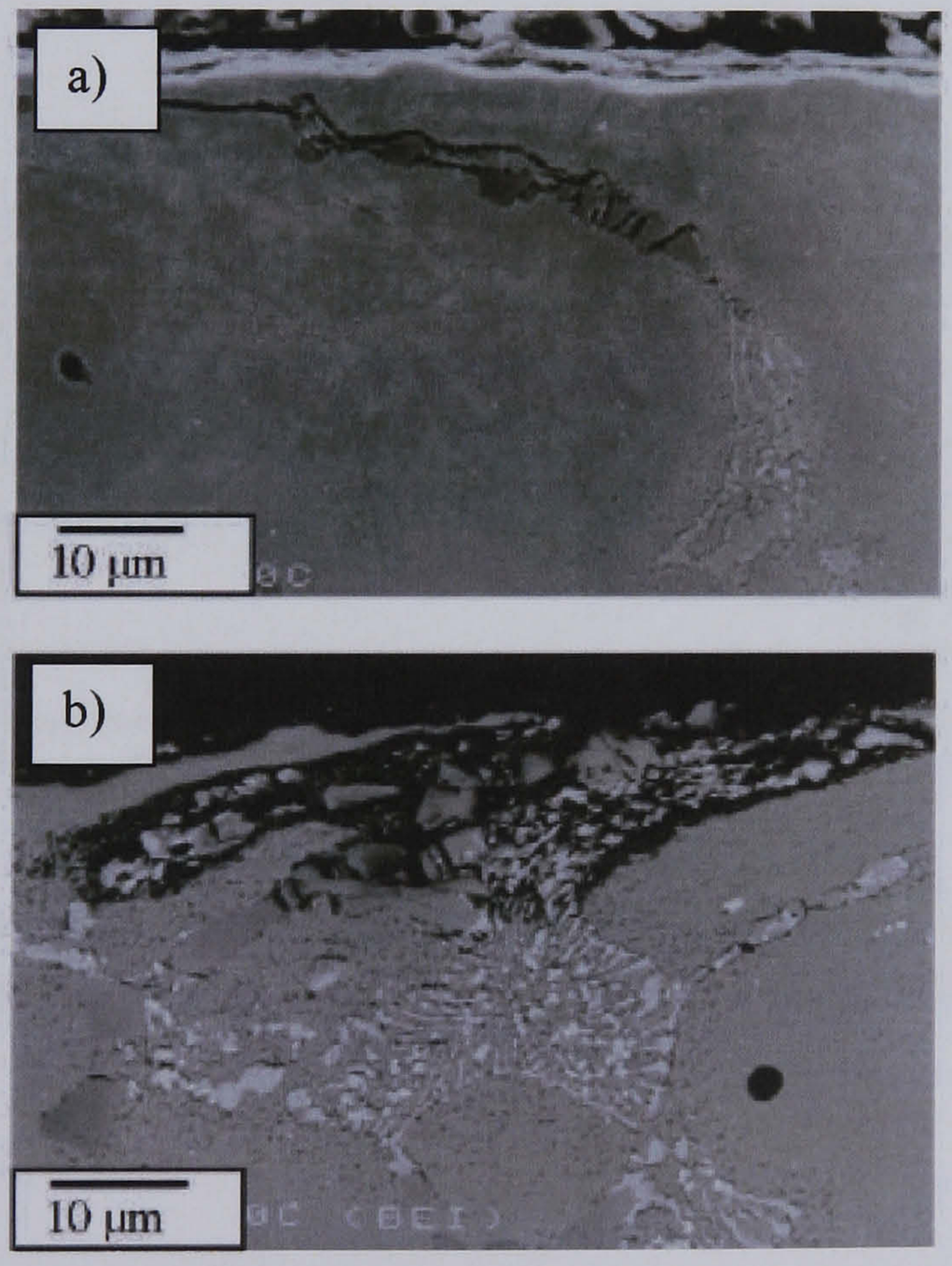

Fig.2.38. Failure mechanisms found in a conventionally cast high speed steel work rolls at 600°C a) Fracture of carbides due to Hertzian stresses. b) Preferential oxidation and deformation of the martensitic matrix. *After Hanlon and Rainforth* (2003).

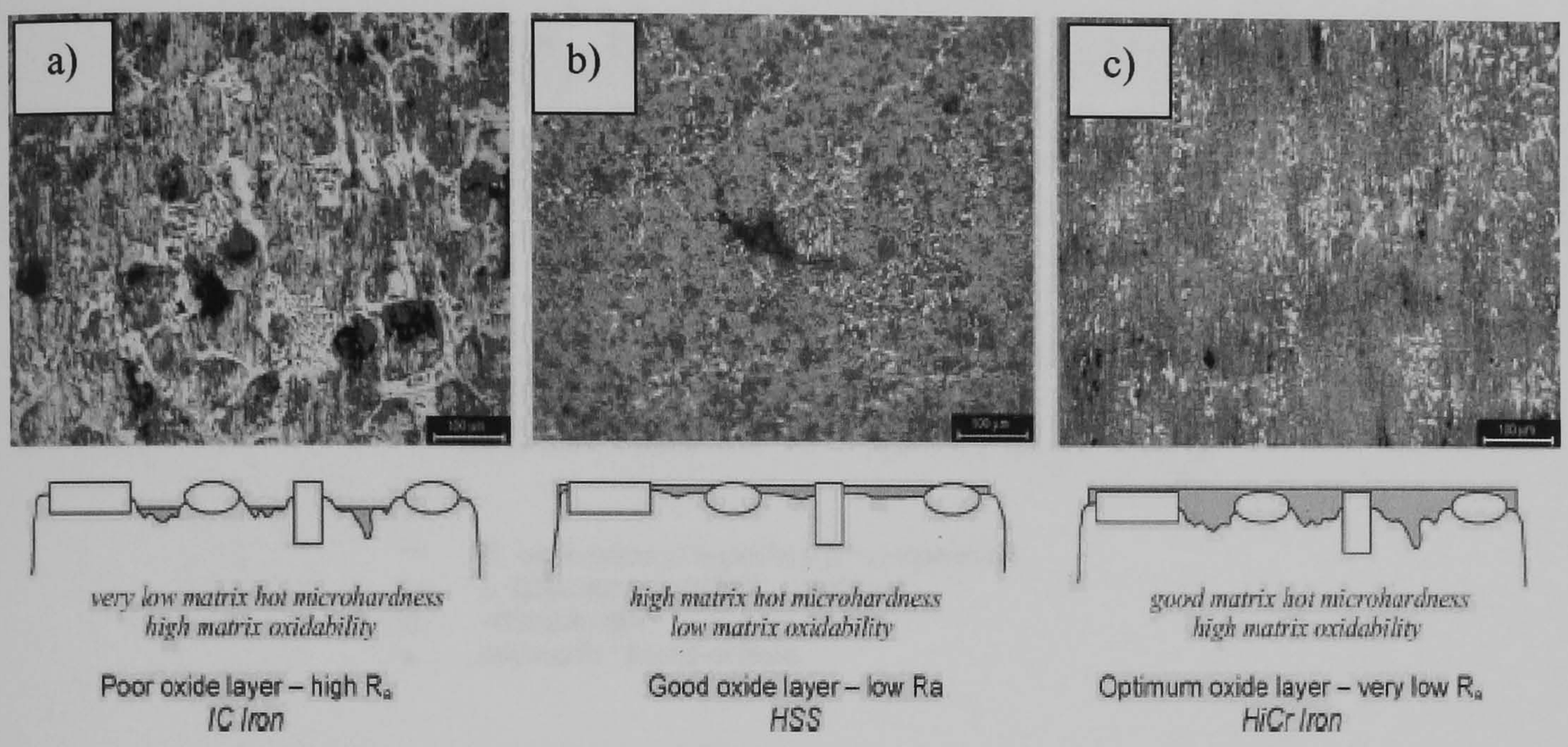

Fig.2.39. Comparison of the oxide layer formed in different work roll materials a) Indefinite chilled iron. b) High speed steel. c) High chromium iron Hi-Cr. *After Pellizzari et al.* (2005).

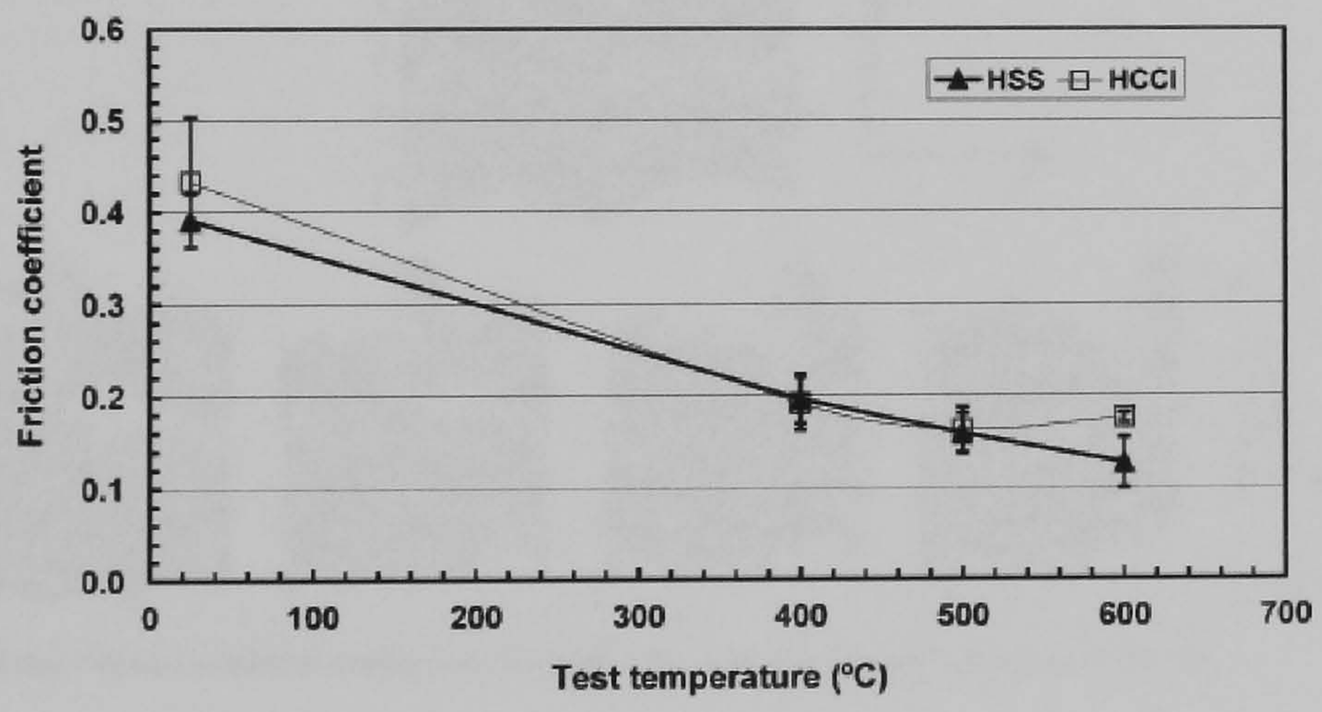

Fig.2.40. Variation of the friction coefficient as a function of the testing temperature observed for High speed steels and High chromium irons. *After Milan et al.* 2005.

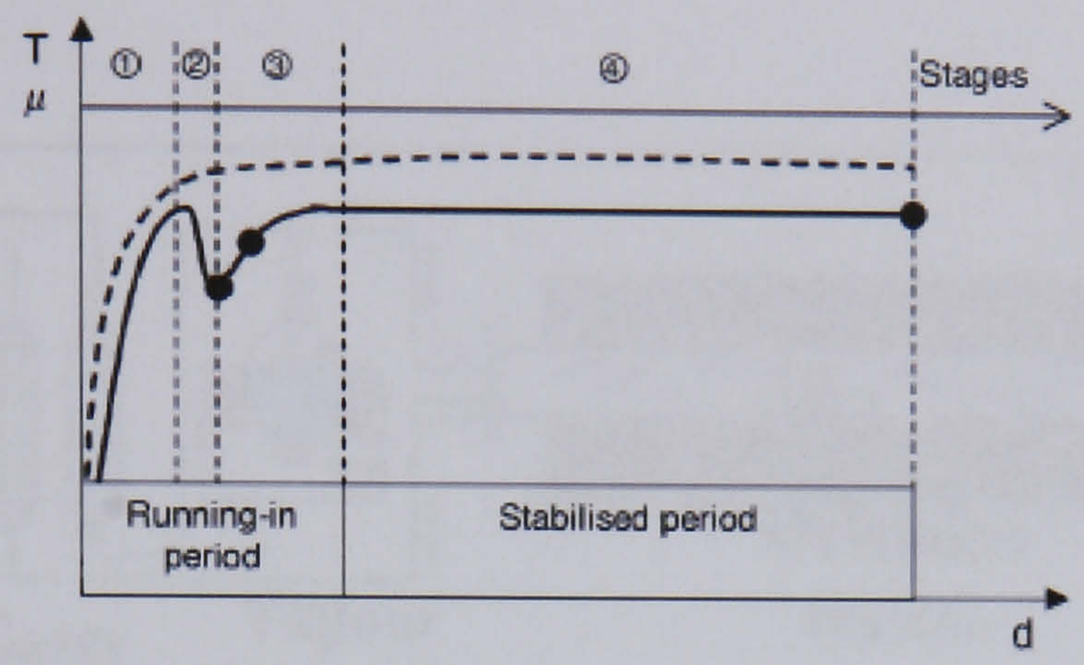

Fig.2.41. Variation of the friction coefficient obtained in pin on disk test of high chromium Hi-Cr iron. *After Vergne et al.* (2006).

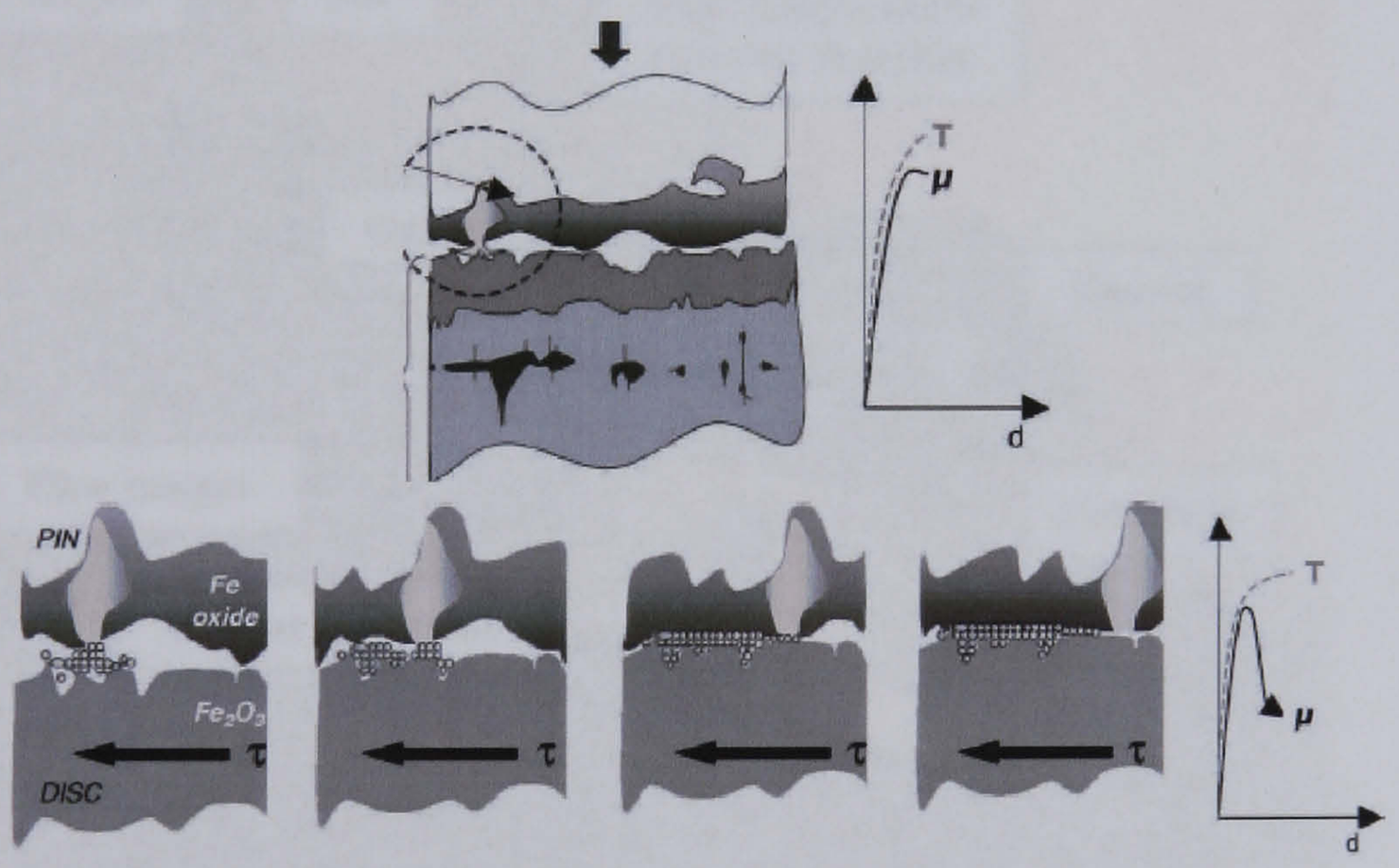

(a) Stage 2 Shear and attrition of oxide outgrowths rich in Nb-oxide grains transfer from the pin to the disc.

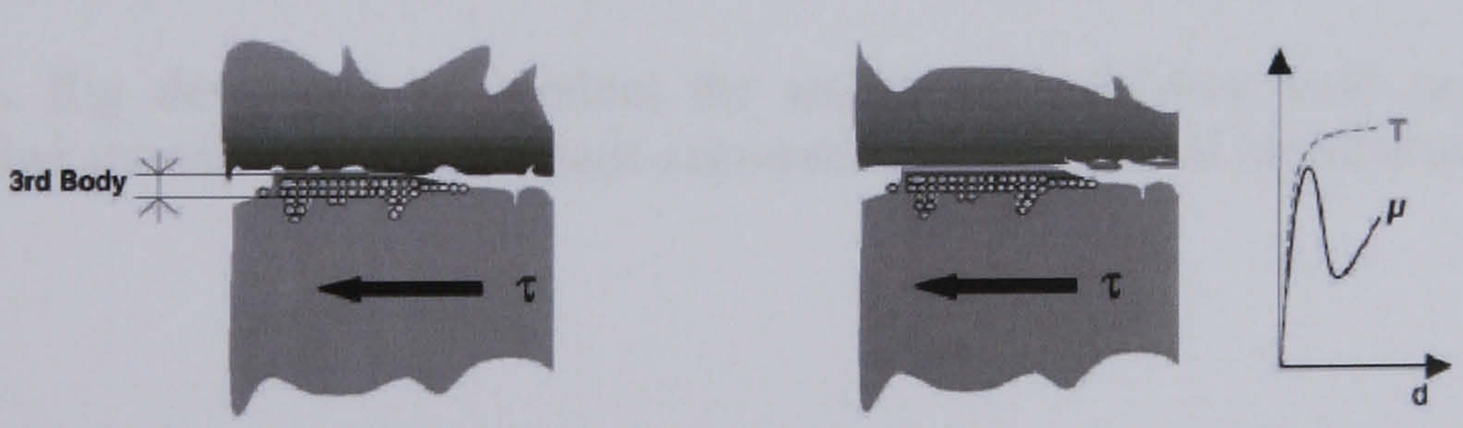

(b) Stage 3 Adhesion and plastic deformation of iron oxide scale at the disc surface on Nb- oxide agglomerated grains.

Fig.2.42. Stages that explain the variations in the value of the friction coefficient found by *Vergne et al.* (2006).

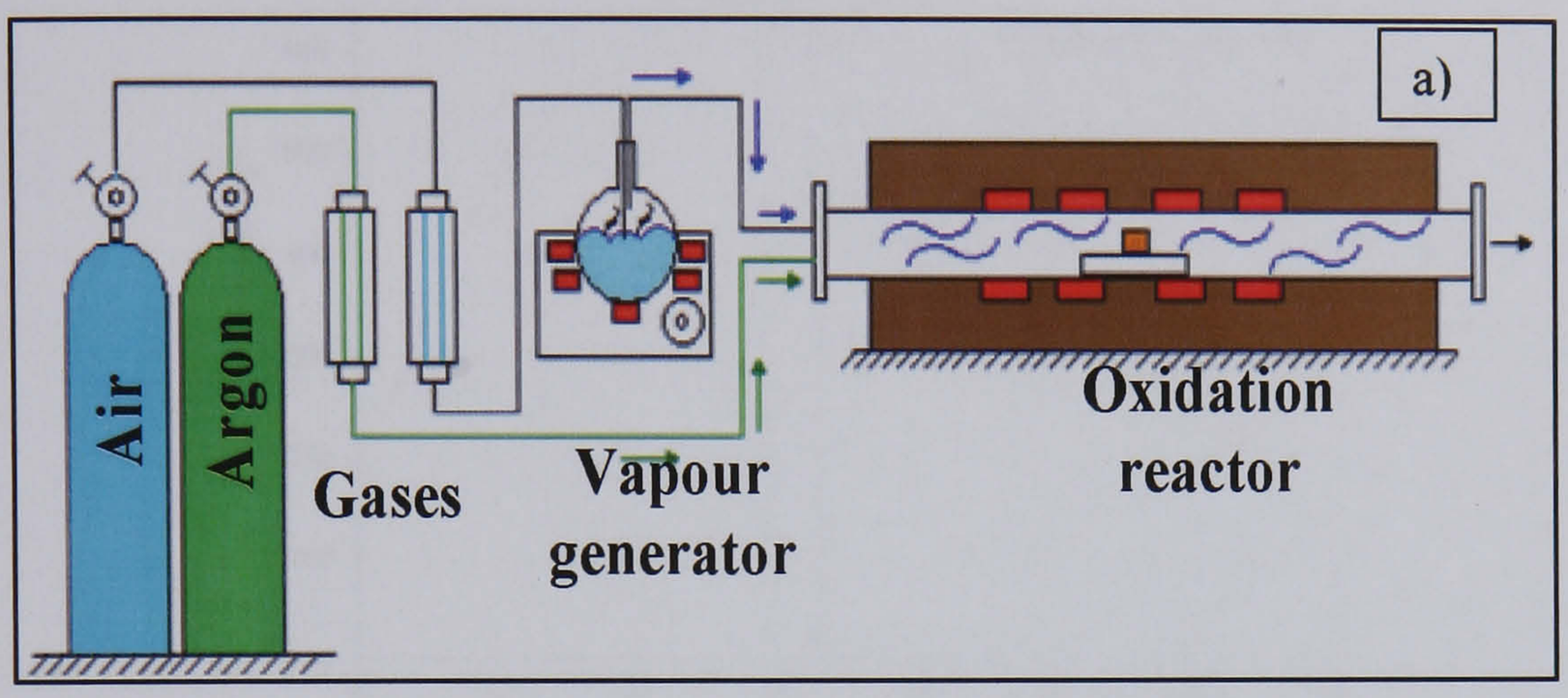

Fig.3.1. Rig developed to conduct the isothermal oxidation tests under controlled atmosphere. a) Schematic representation and b) real installation.

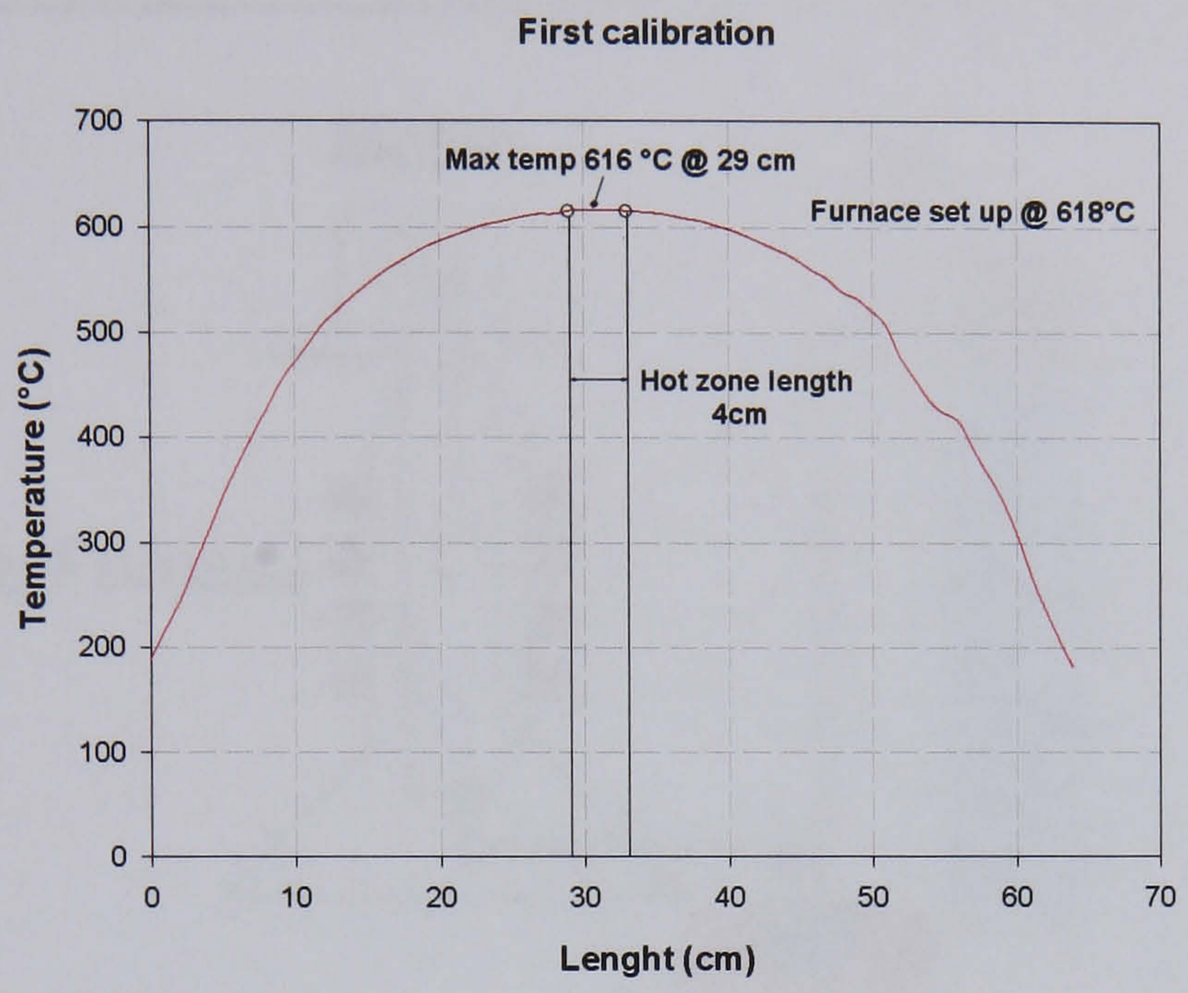

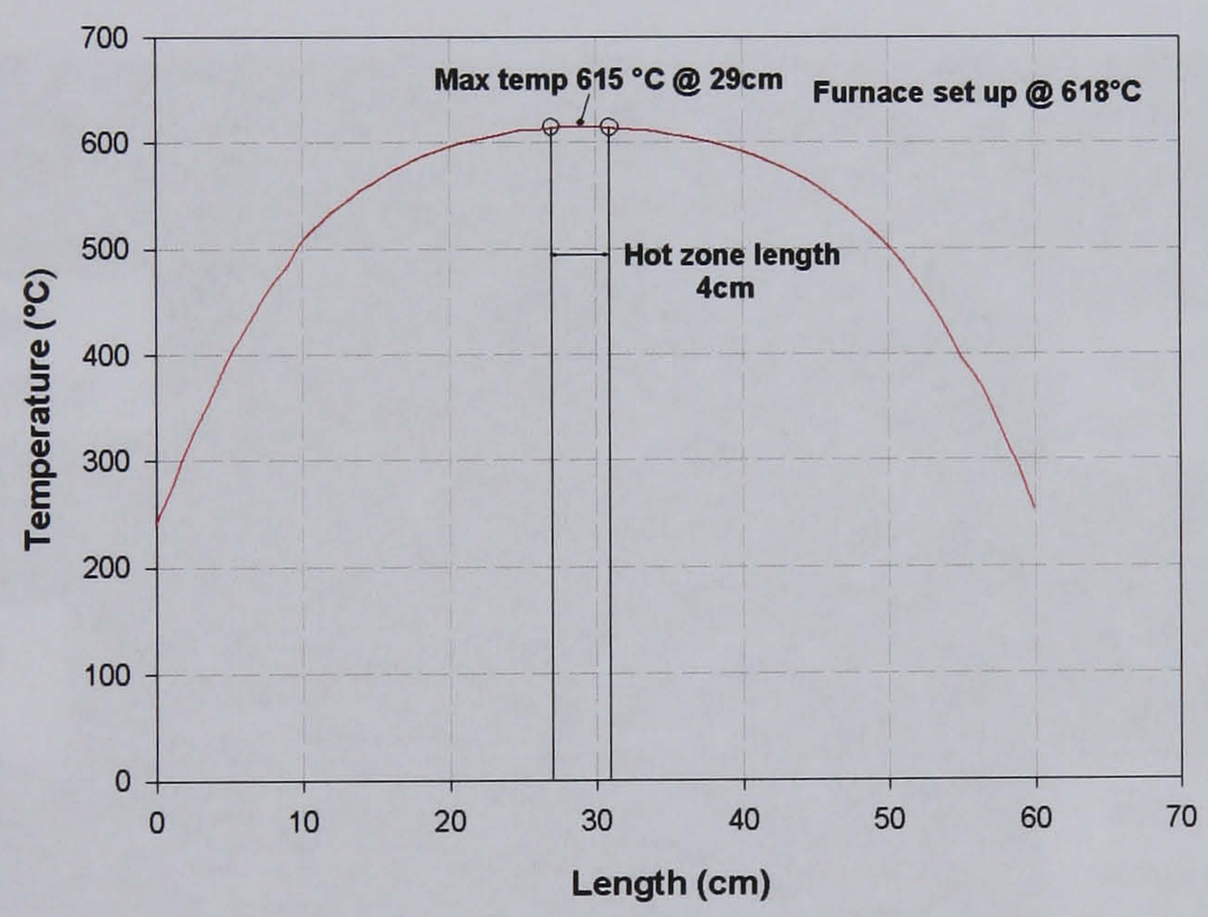

Fig.3.2. Temperature measurements inside the oxidation reactor. Determination of the hot zone.

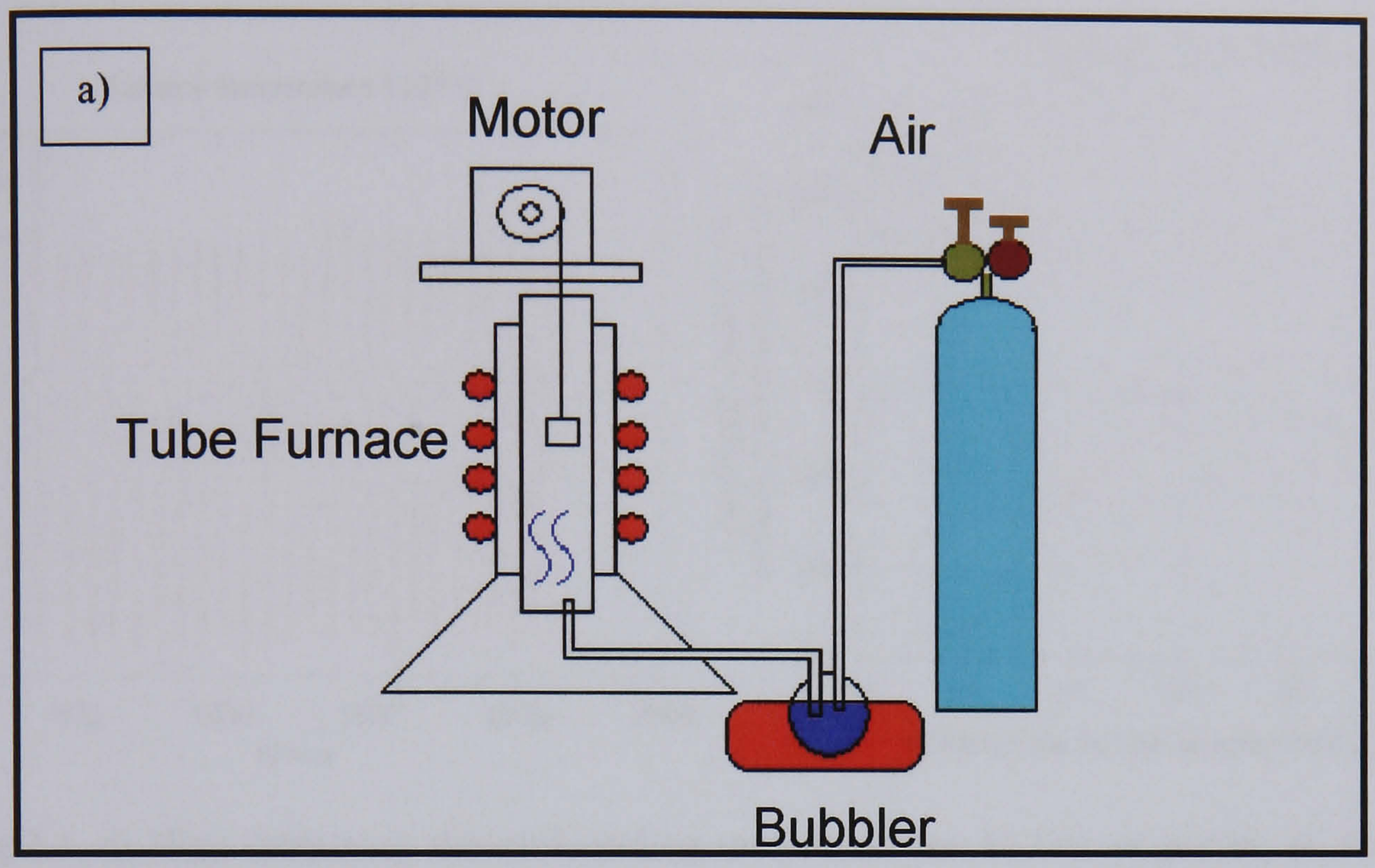

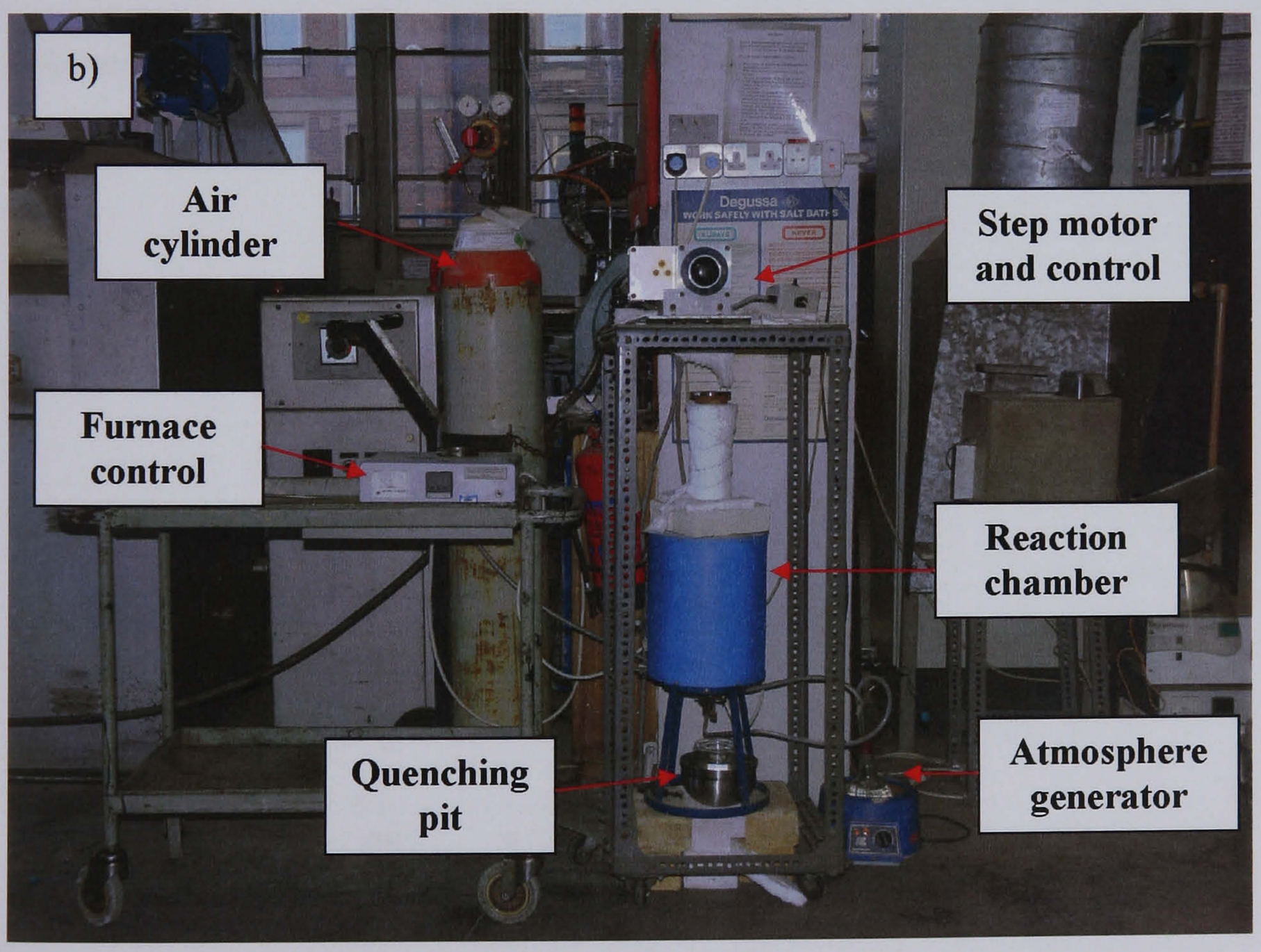

Fig.3.3. a) Schematic representation of the device built to develop the high frequency cyclic oxidation testing. b) The real rig.

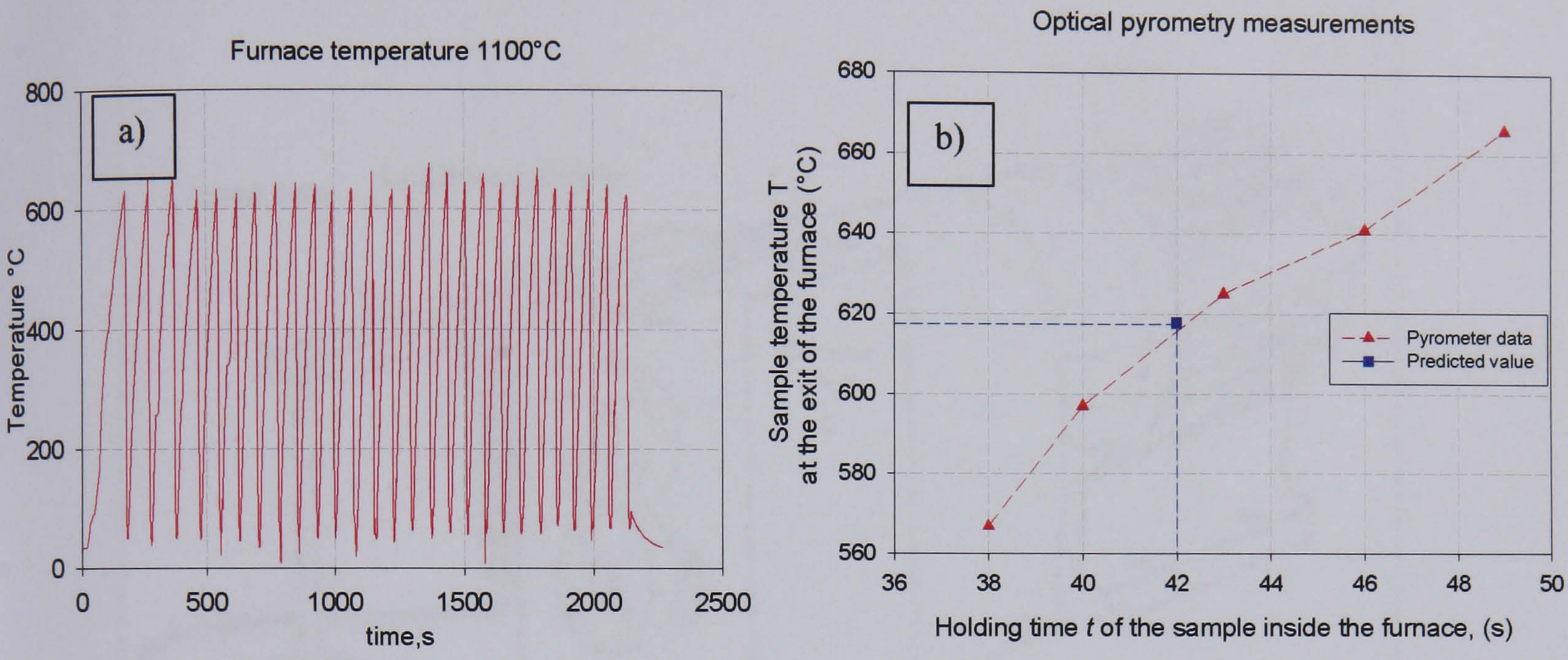

Fig.3.4. a) High frequency thermal cycling measurements. b) Determination of the maximum holding time of the sample inside the furnace during the thermal cycling. Comparison of the calculated temperature value against the measured temperature value of on the surface of the sample before quenching.

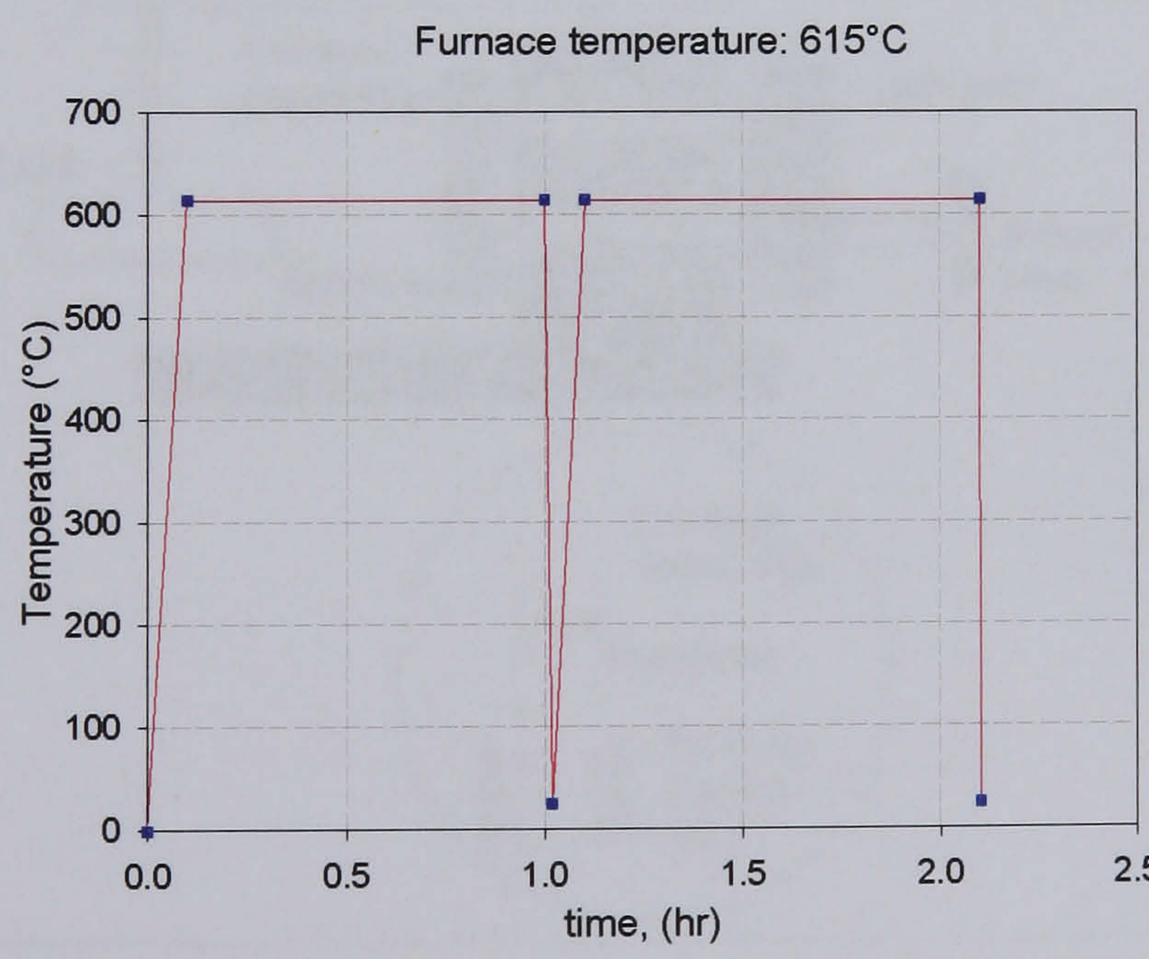

Fig.3.5. Low frequency thermal cycling of a high speed steel sample.

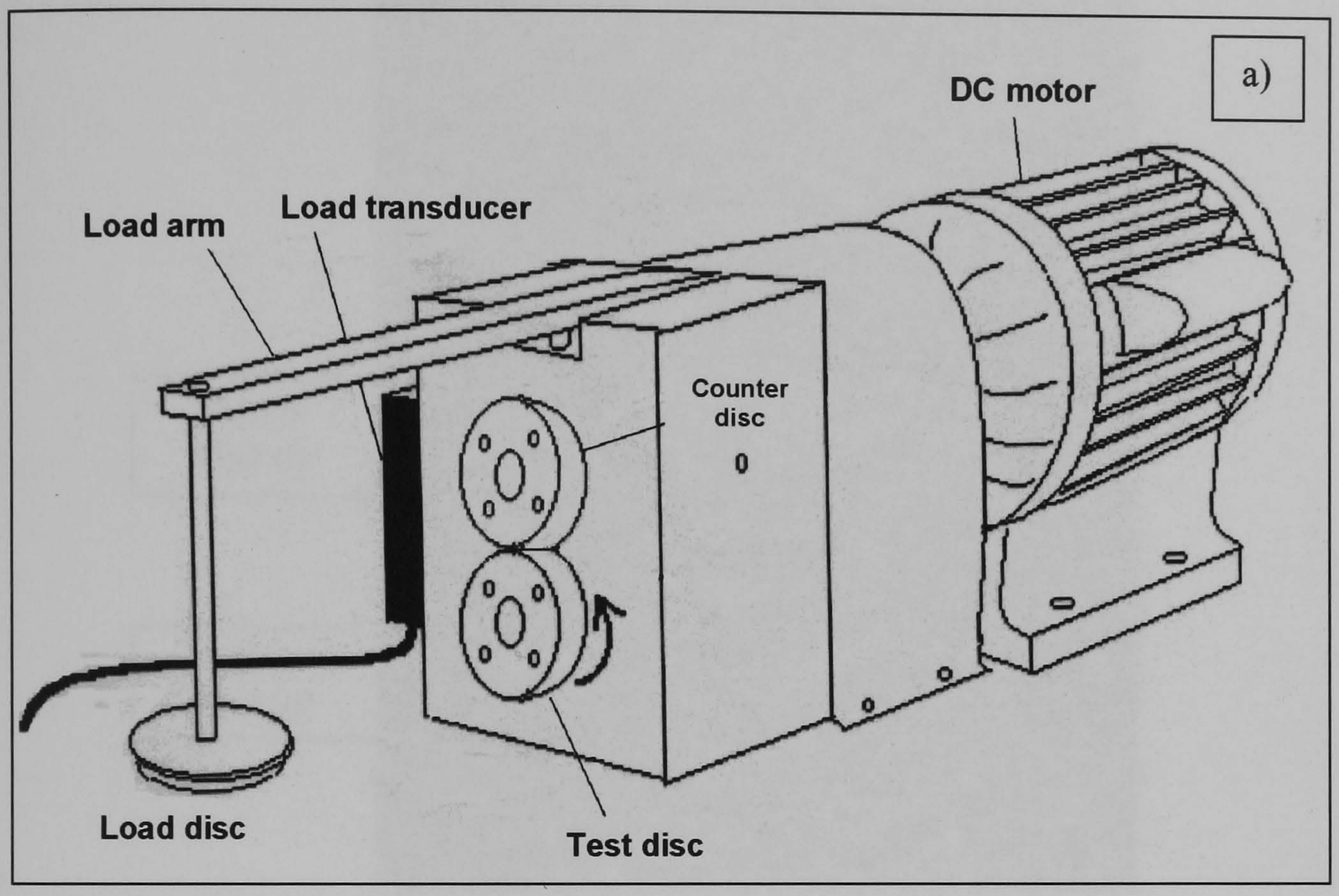

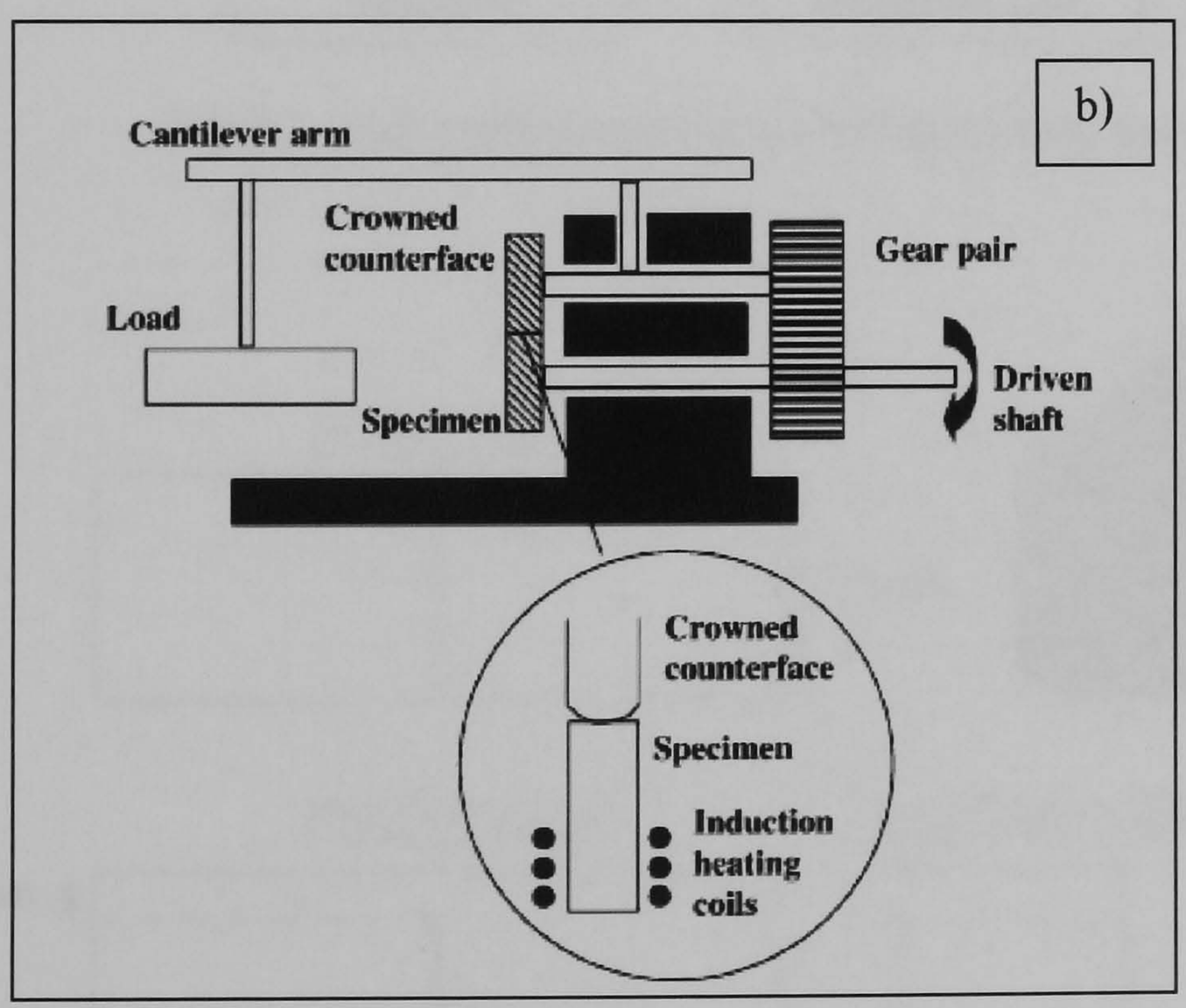

Fig.3.6. Schematic representation of the Cameron-Plint machine, the device used for the rolling-sliding tests. *After Bedolla, 2001.* b) Engineering drawing. *After Hanlon and Rainforth, 2003.*

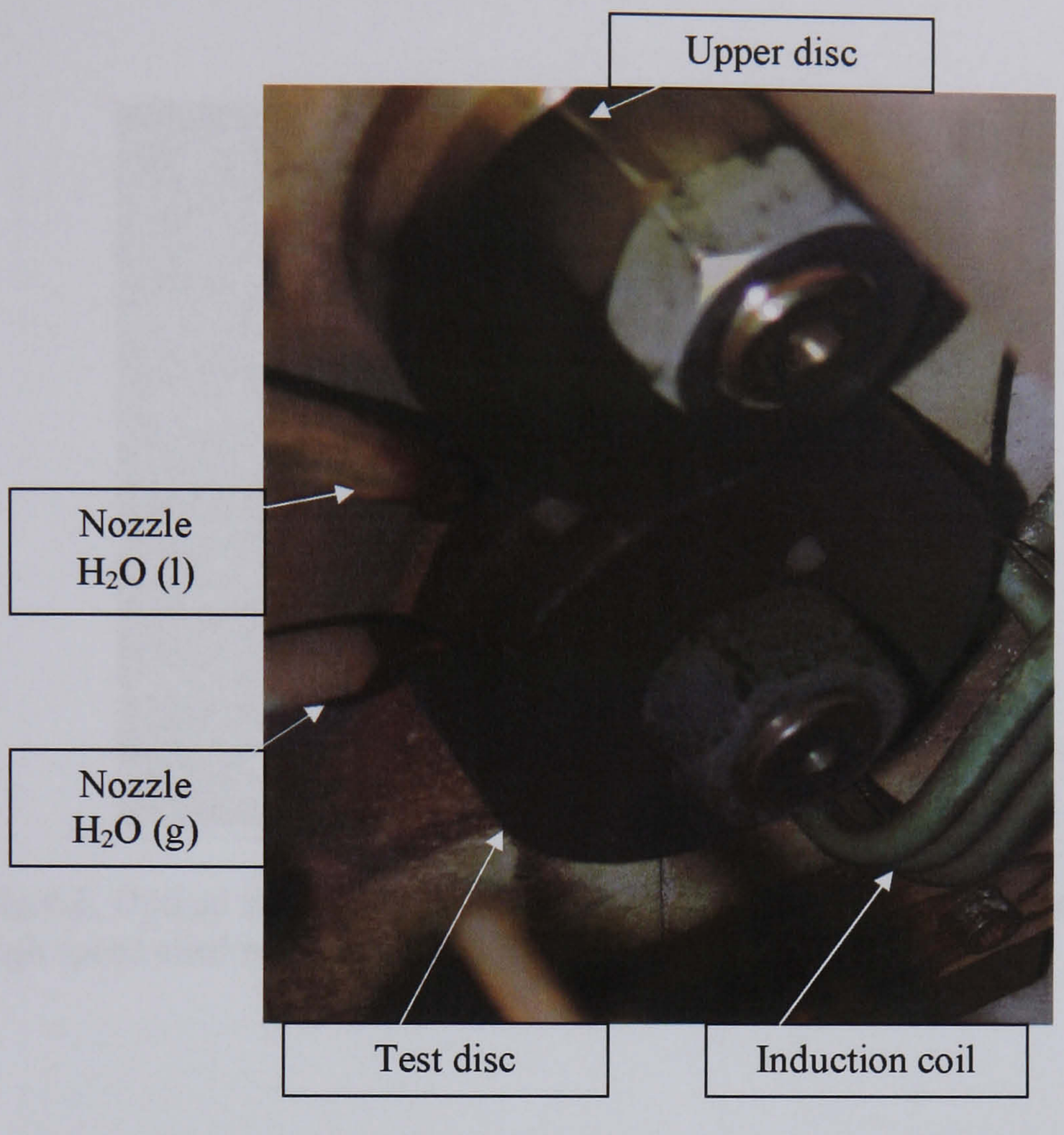

Fig.3.7. Real configuration of the rolling-sliding tests.

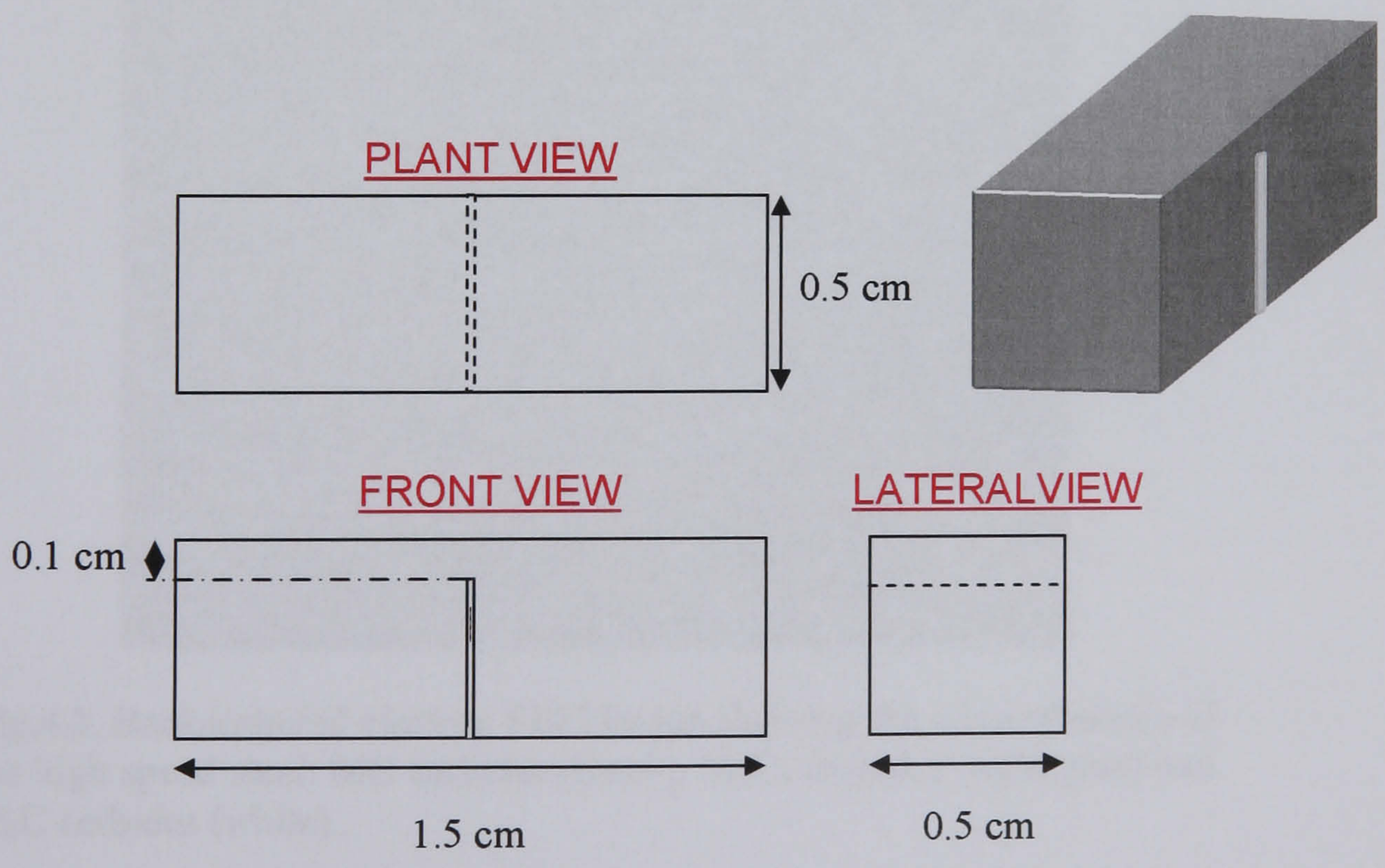

Fig.3.8. Notched specimen for the creation of fracture surfaces of the oxide layer.

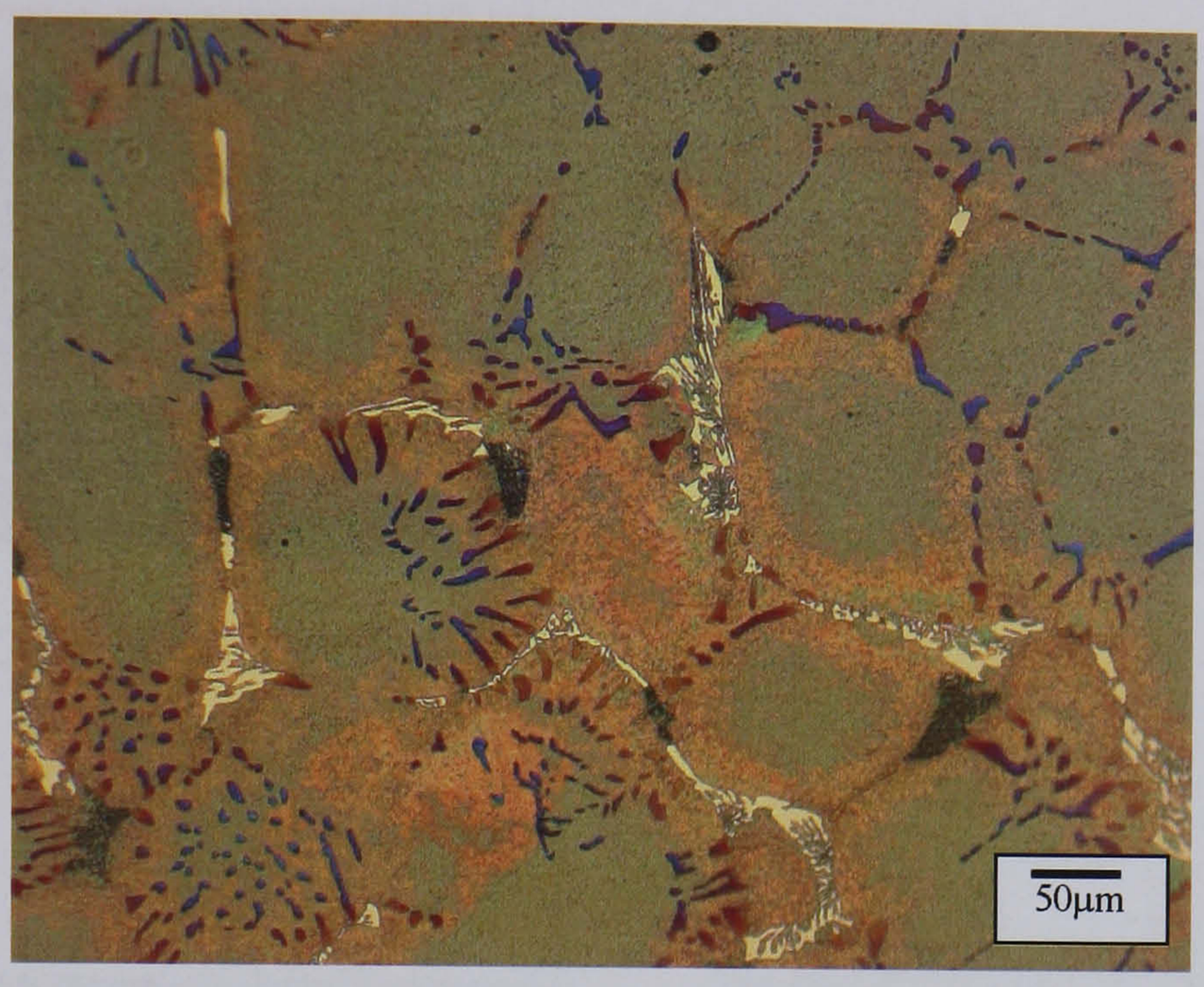

Fig.4.1. Optical micrograph showing the microstructural components of the high speed steel revealed after the oxidation etching.

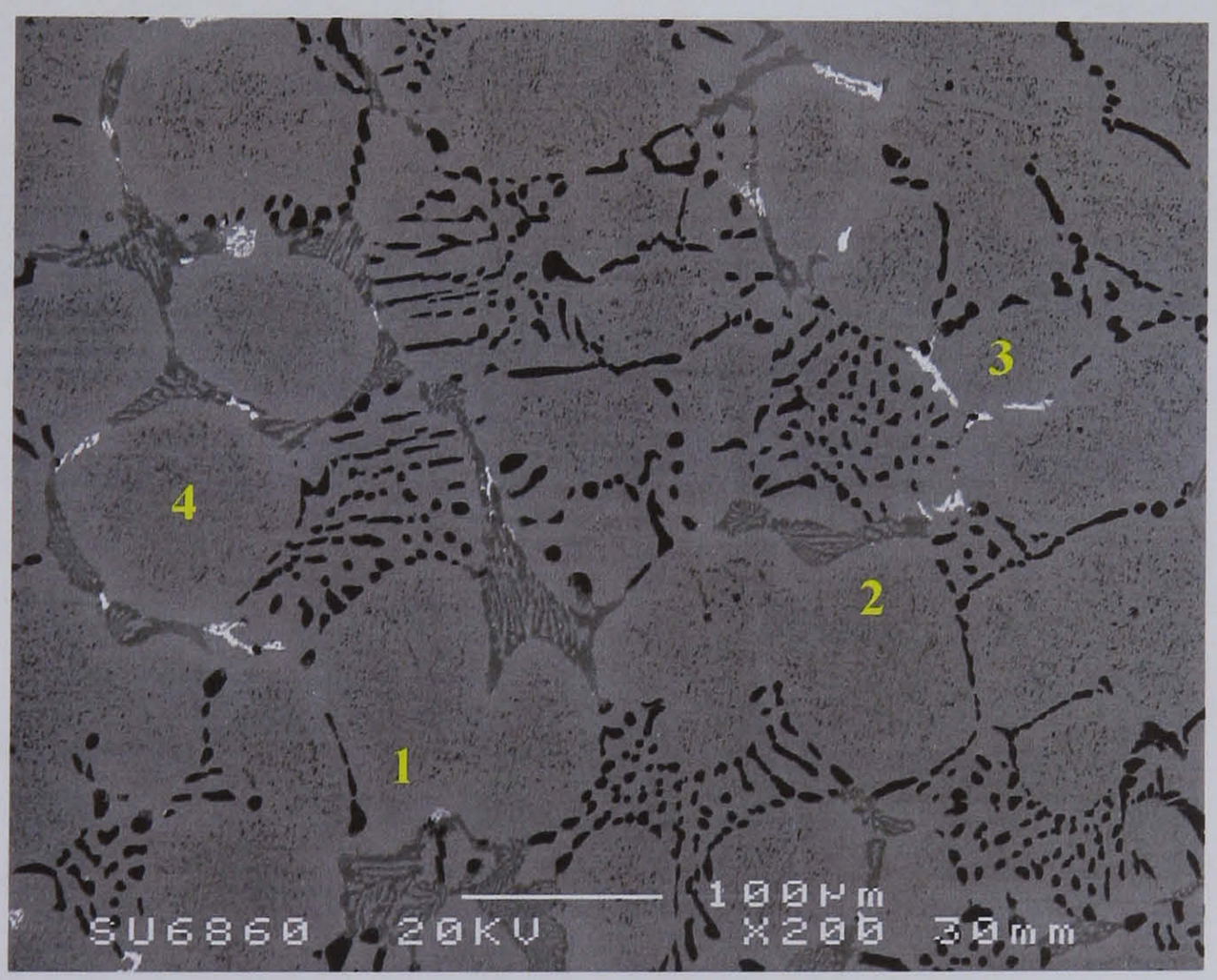

Fig.4.2. Backscattered electron SEM image showing the microstructure of the high speed steel. MC carbides (black), M_7C_3 carbides (light grey) and M_6C carbides (white).

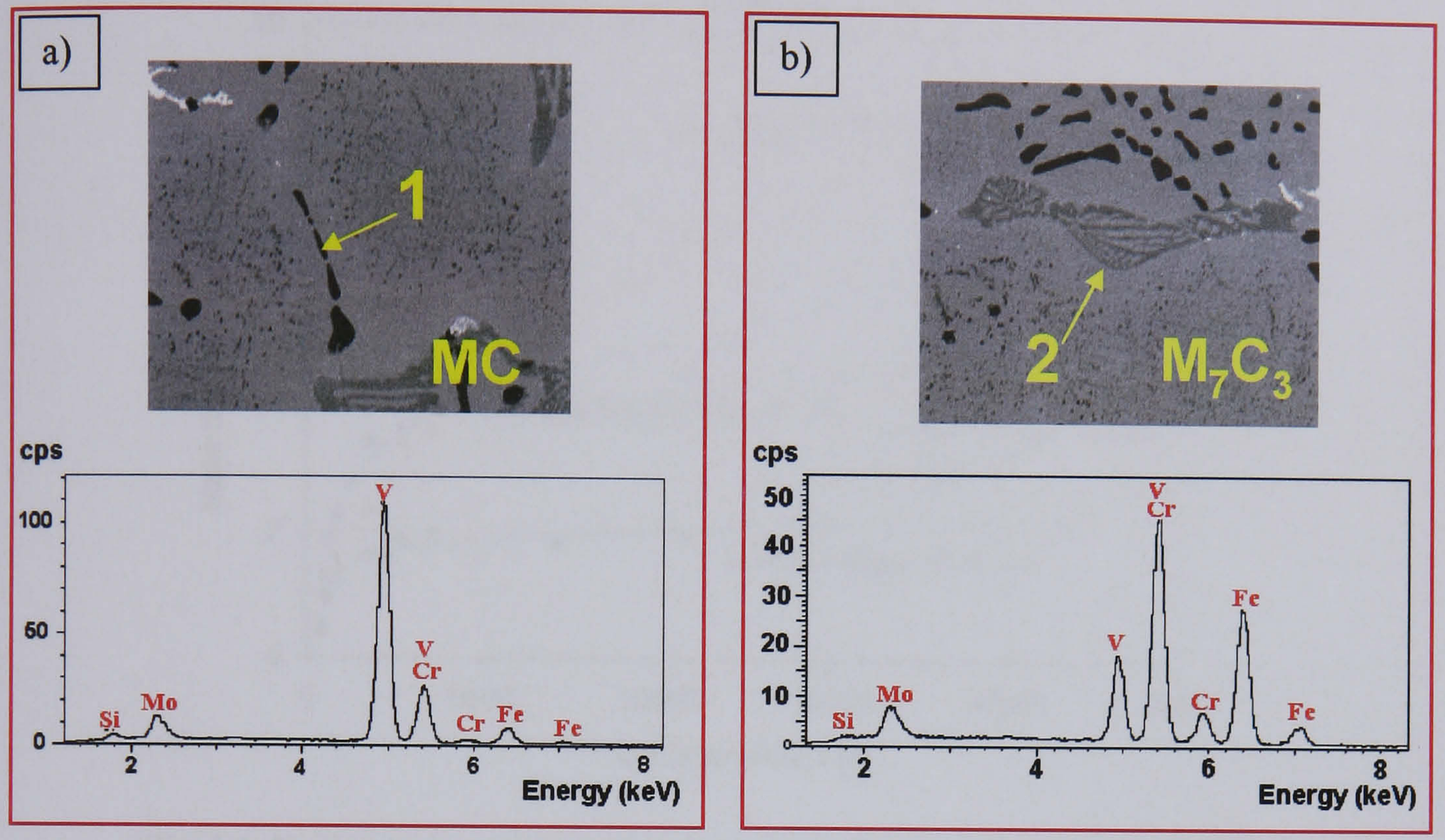

Fig.4.3. EDX analysis of the zones shown in Fig 4.2. a) MC vanadium rich carbide, b) M_7C_3 chromium and iron rich carbide, c) M_6C, Molybdenum rich carbide and d) Elements present in the matrix.

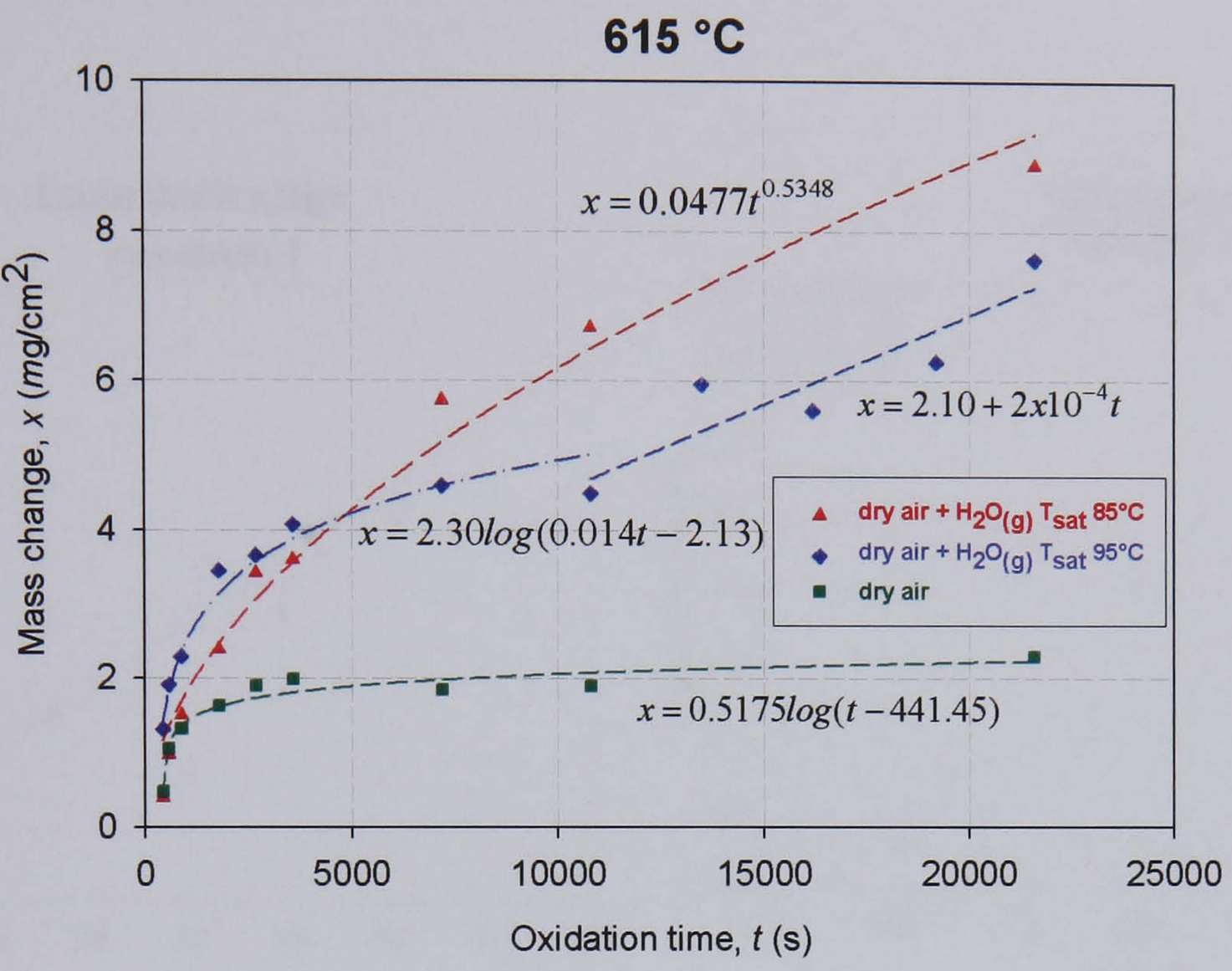

Fig.4.4. Isothermal oxidation kinetic curves obtained for tests at **615°C.**

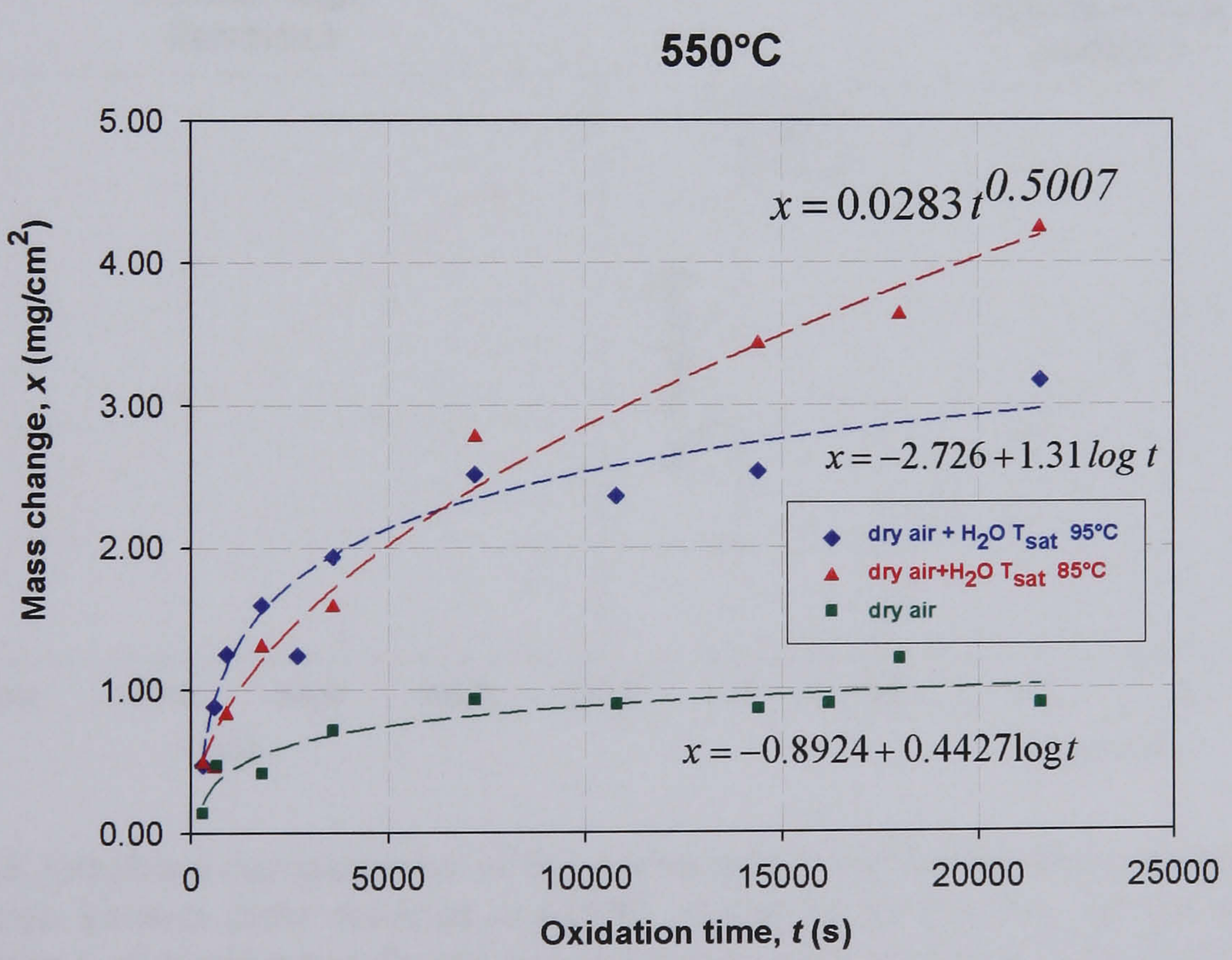

Fig.4.5. Isothermal oxidation kinetic curves obtained for tests at **550°C.**

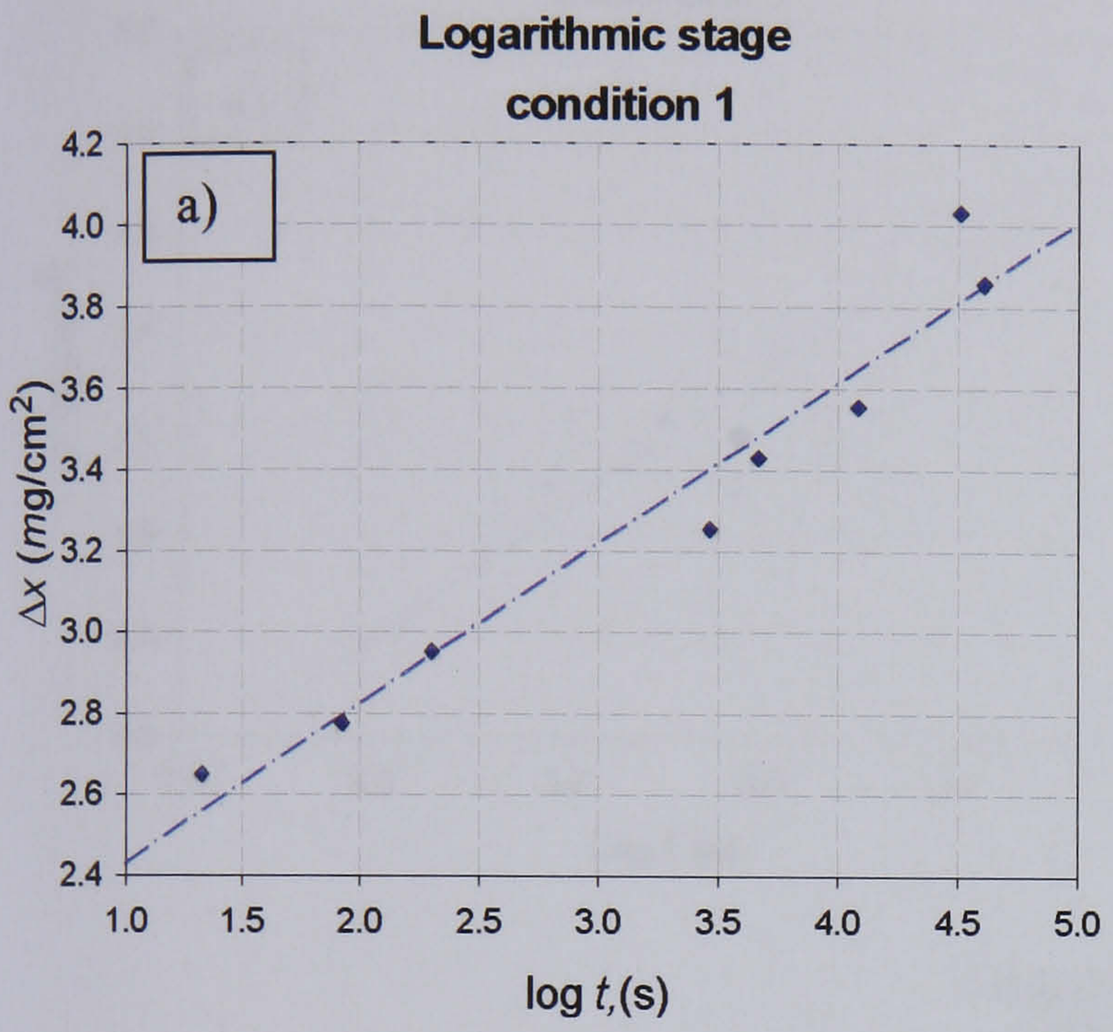

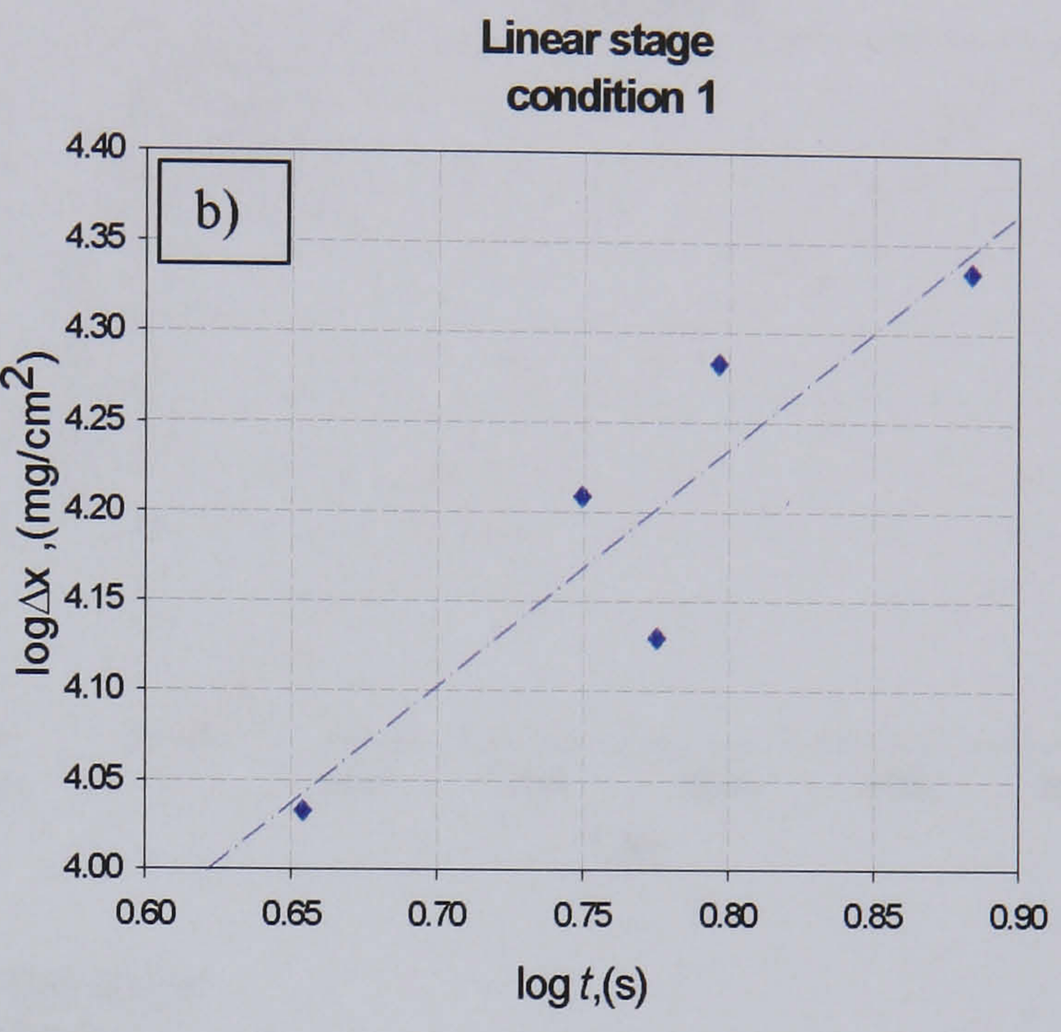

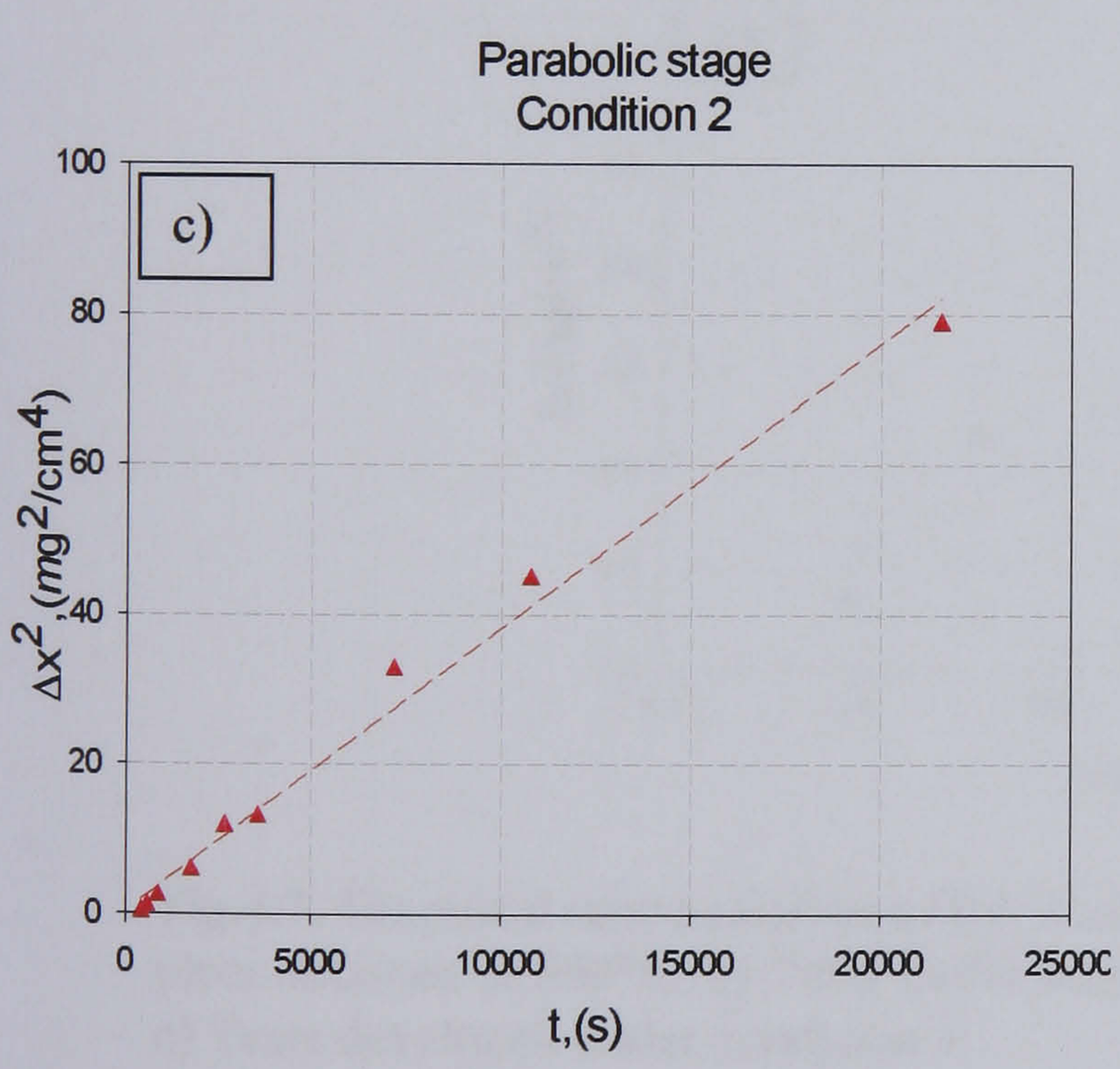

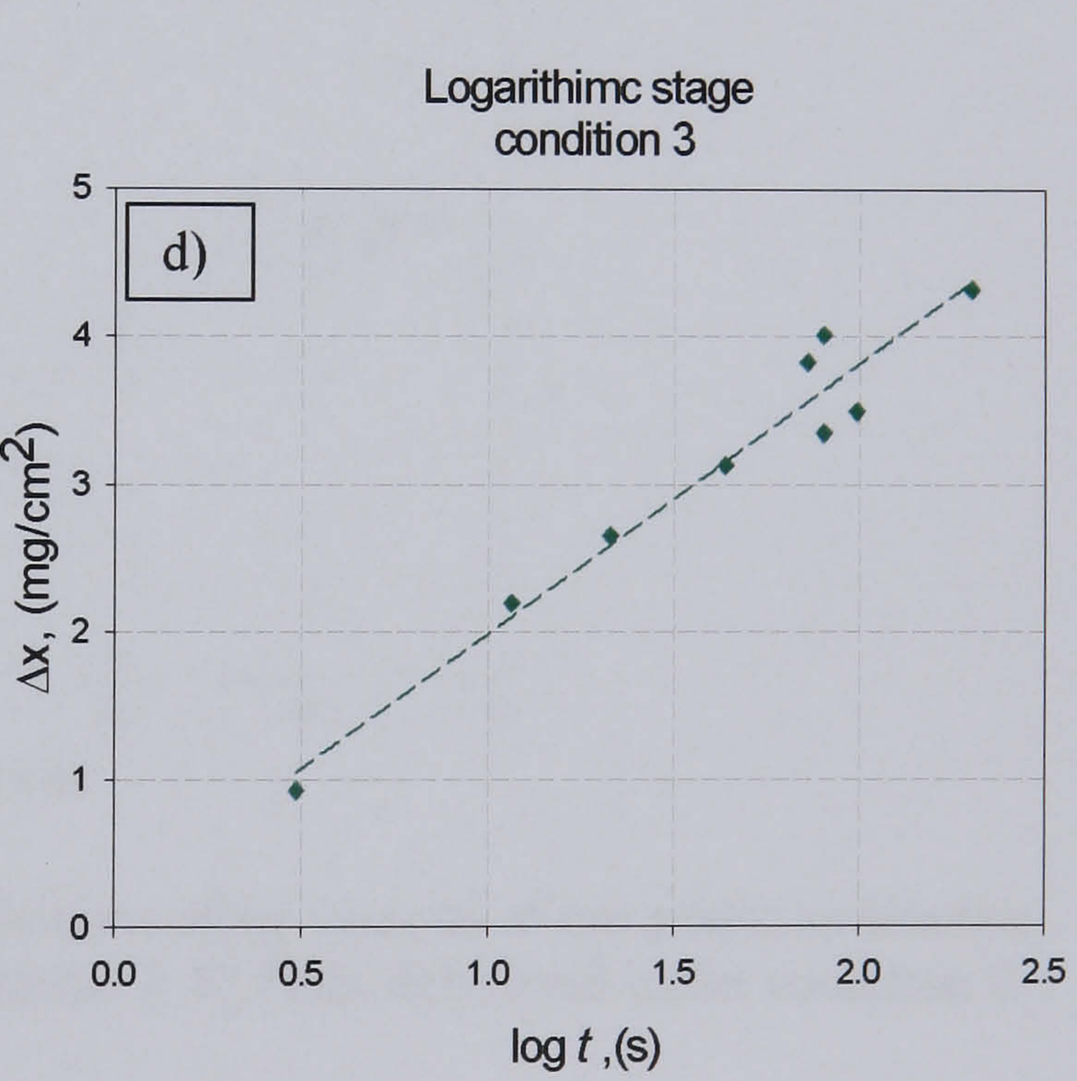

Fig.4.6. Graphical representation of the mathematical verification of the veracity of the oxidation kinetics plots obtained at **615°C**. a) and b) Verification for the test under condition 1. c) Verification for the test developed under condition 2. d) The tests under condition 3.

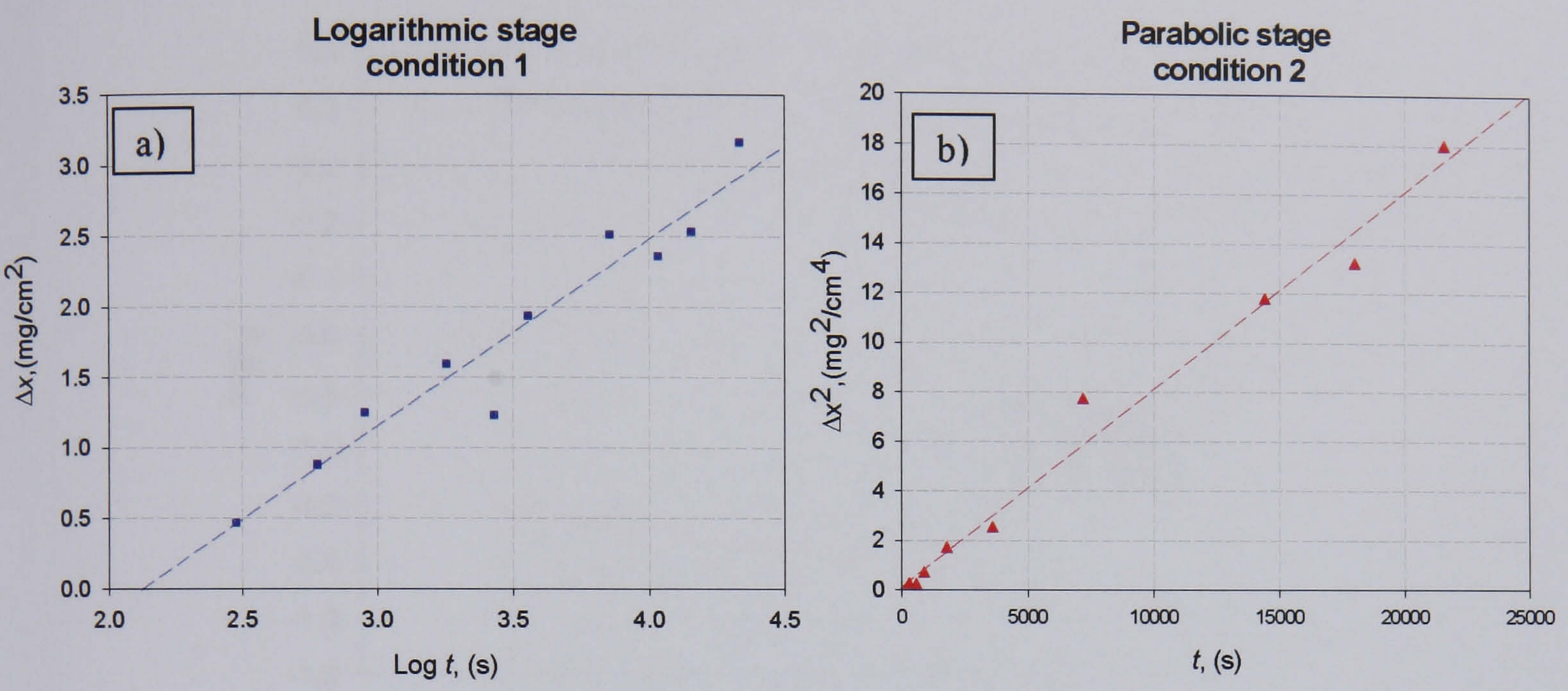

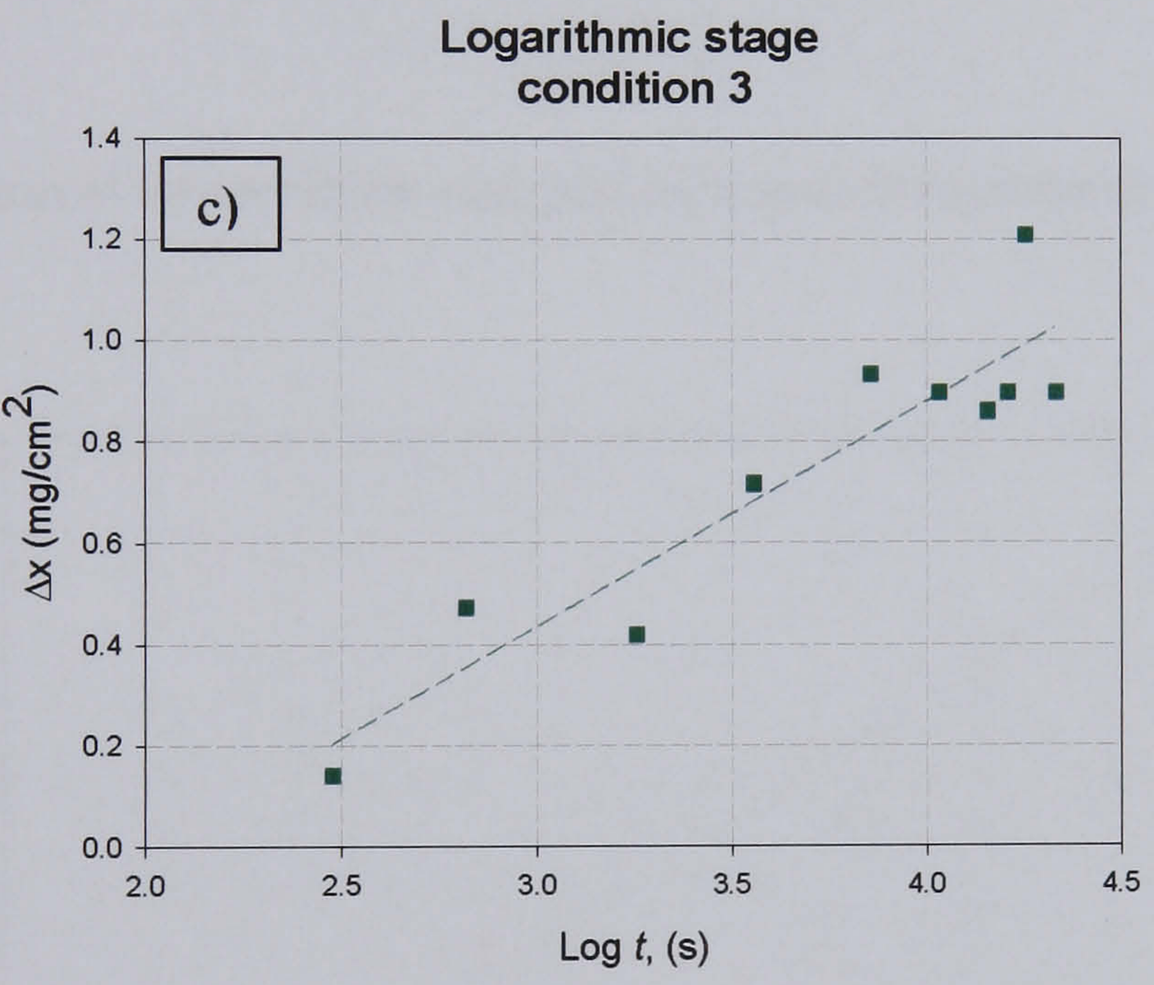

Fig.4.7. Graphical representation of the verification of the veracity of the oxidation kinetics plots obtained at **550°C**. a) Tests under condition 1. b) Tests developed under condition 2. c) Tests developed under condition 3.

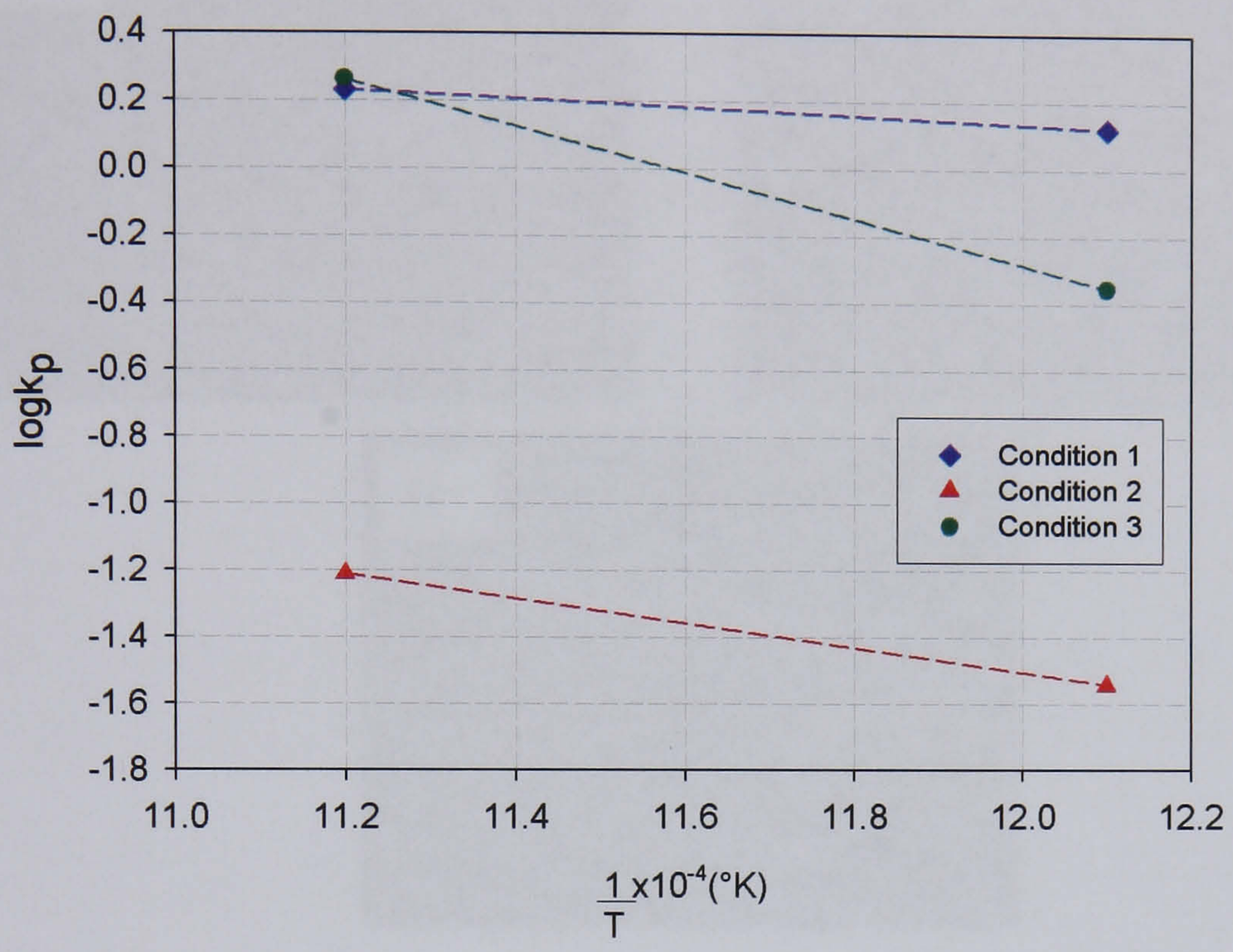

Fig.4.8. Variation of the oxidation rate constants with the temperature of the tests.

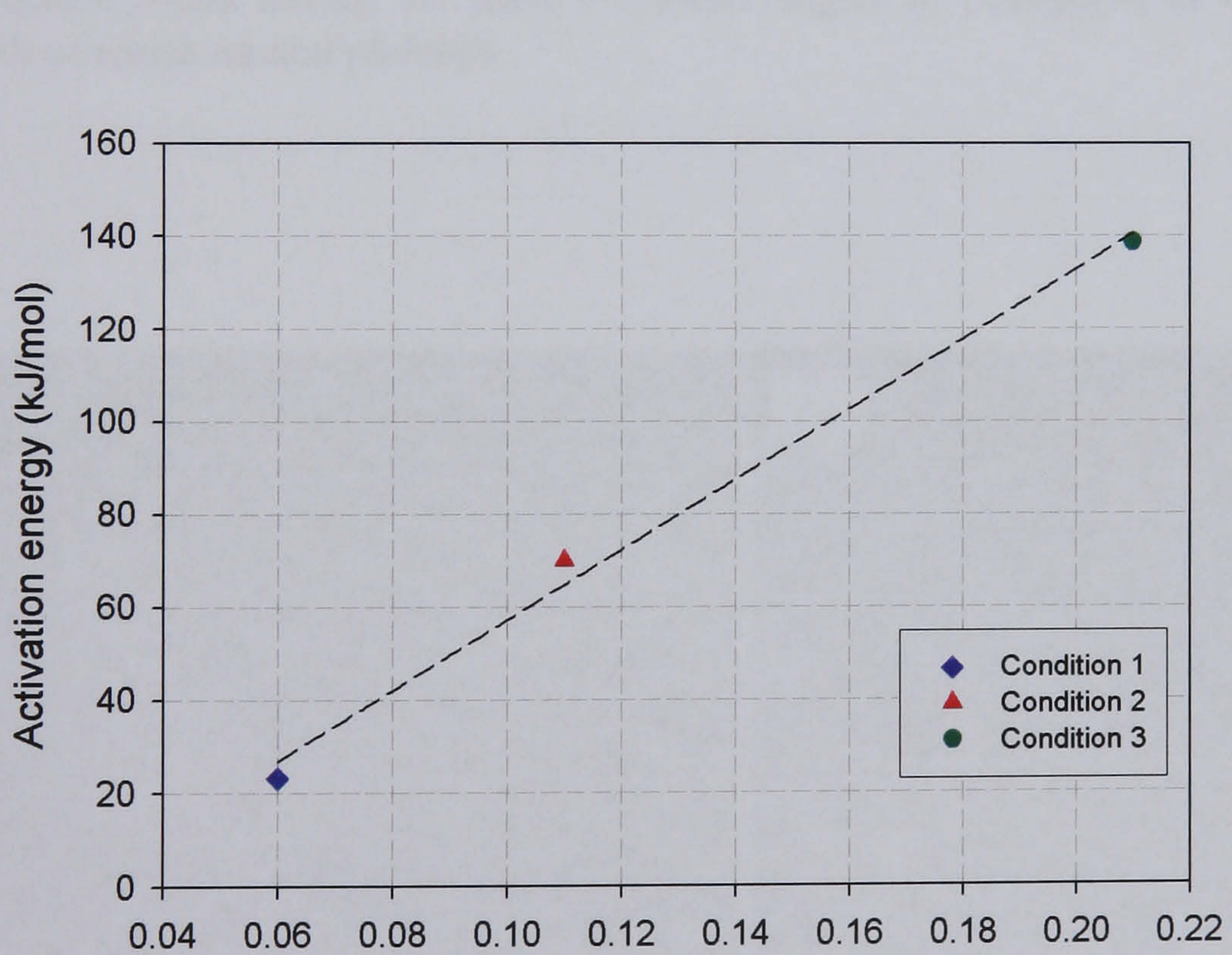

Fig.4.9. Activation energy variation with respect to the partial pressure of the tests.

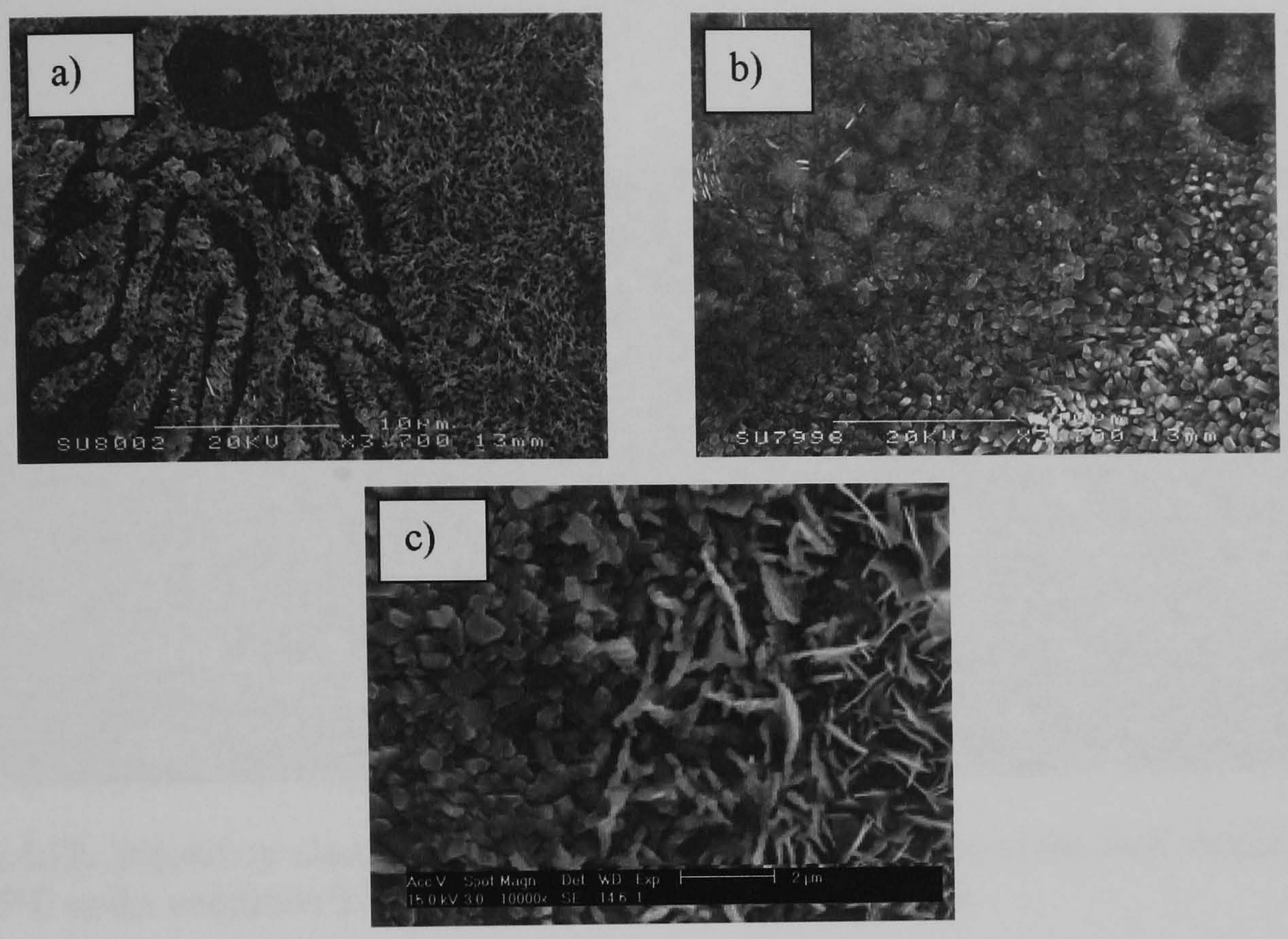

Fig.4.10. Secondary electron SEM images showing the stages of initial oxide formation. a) Structure found during the early oxidation stages. b) Formation of oxide crystals. c) Growth of whiskers and platelets.

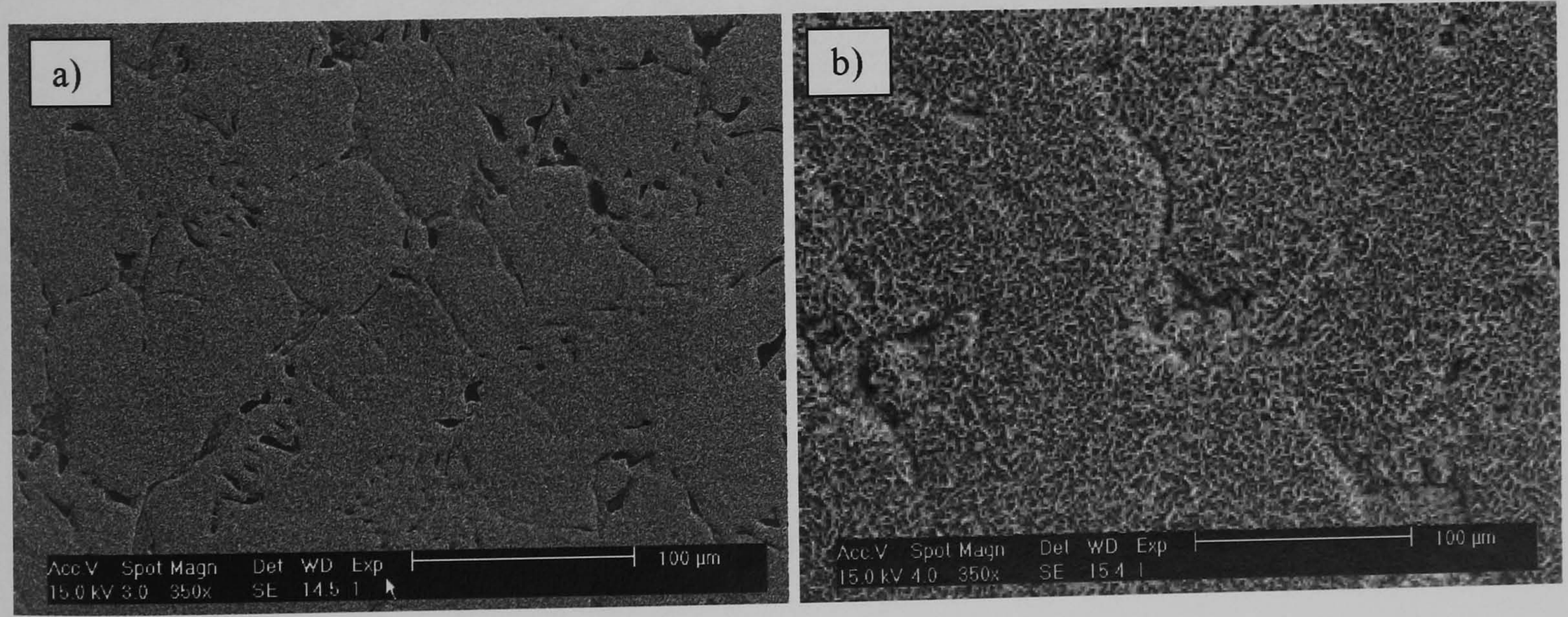

Fig.4.11. Secondary electron SEM images showing the surface of the steel oxidized at **615°C** under condition 1. a) After 10 minutes. b) After 3 hours.

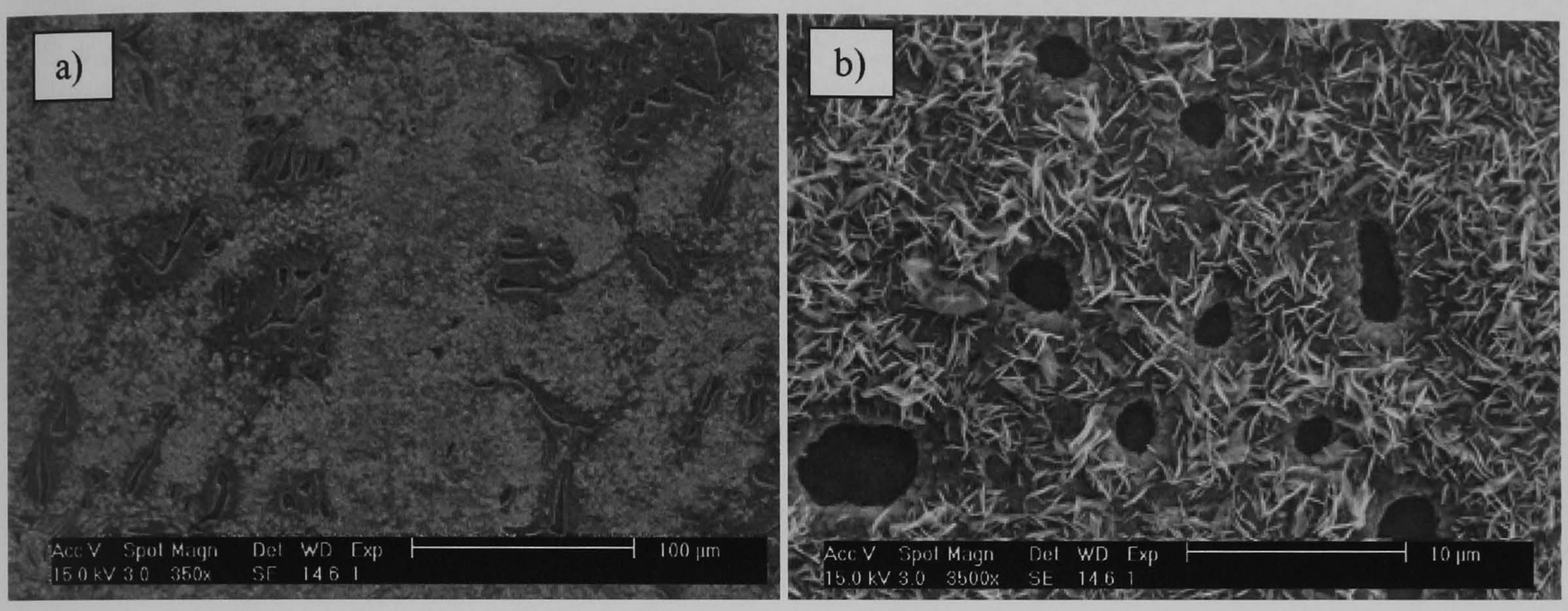

Fig.4.12. Secondary electron SEM images showing the surface of the steel oxidized at **615°C** under condition 2. a) After 10 minutes. b) After 3 hours.

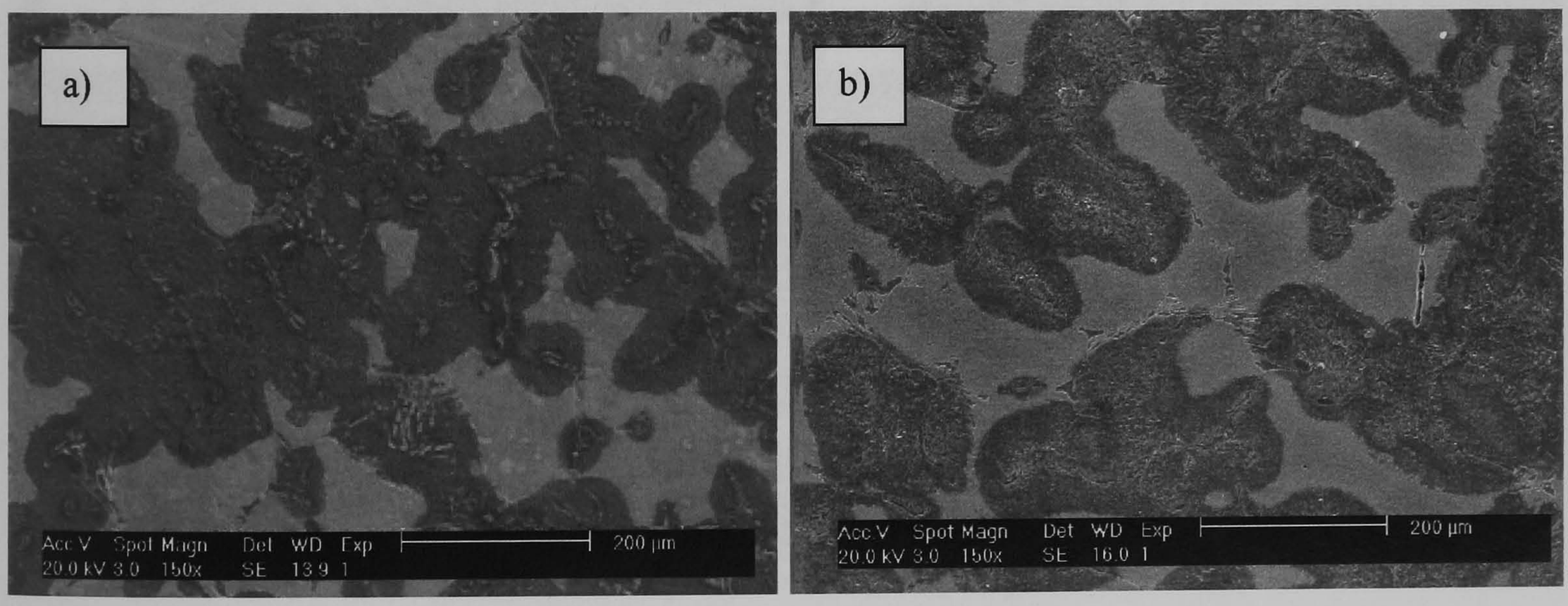

Fig.4.13. Secondary electron SEM images showing the surface of the steel oxidized at **615°C** under condition 3. a) After 10 minutes. b) After 3 hours.

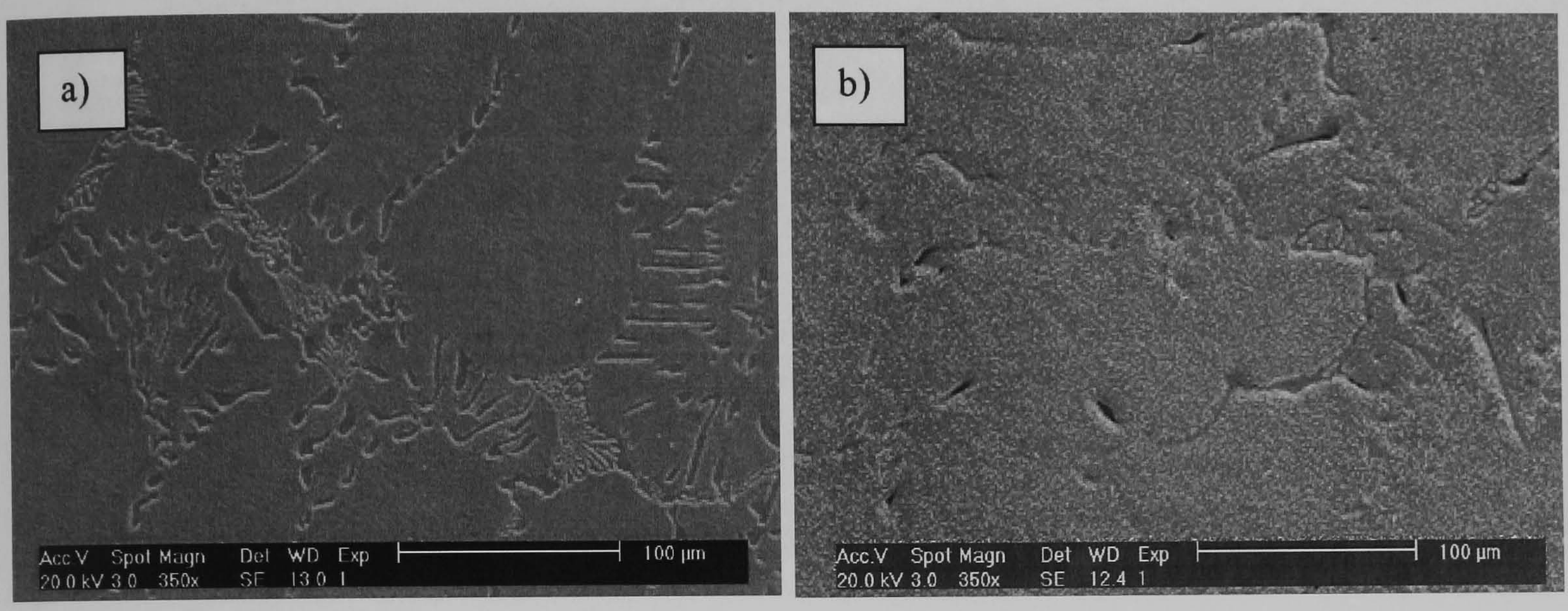

Fig.4.14. Secondary electron SEM images showing the surface of the steel oxidized at **550°C** under condition 1. a) After 10 minutes. b) After 4 hours.

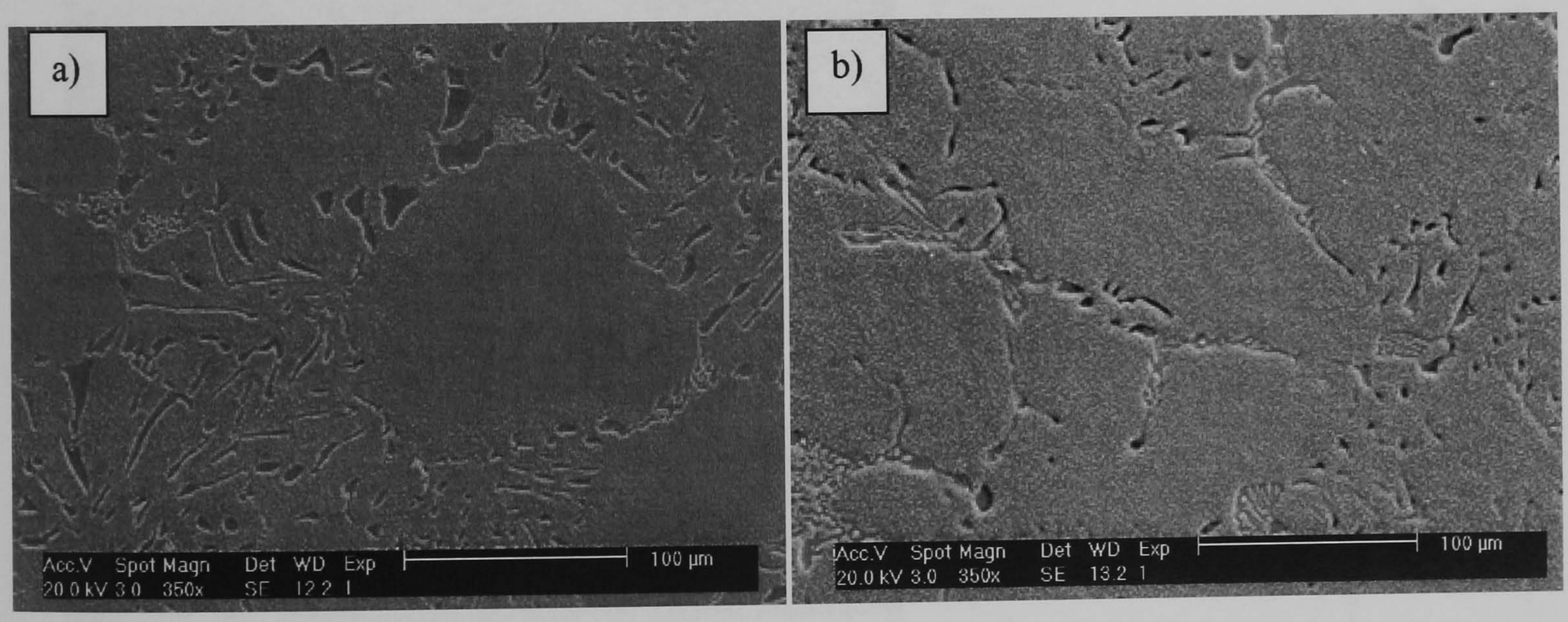

Fig.4.15. Secondary electron SEM images showing the surface of the steel oxidized at **550°C** under condition 2. a) After 15 minutes. b) After 4 hours.

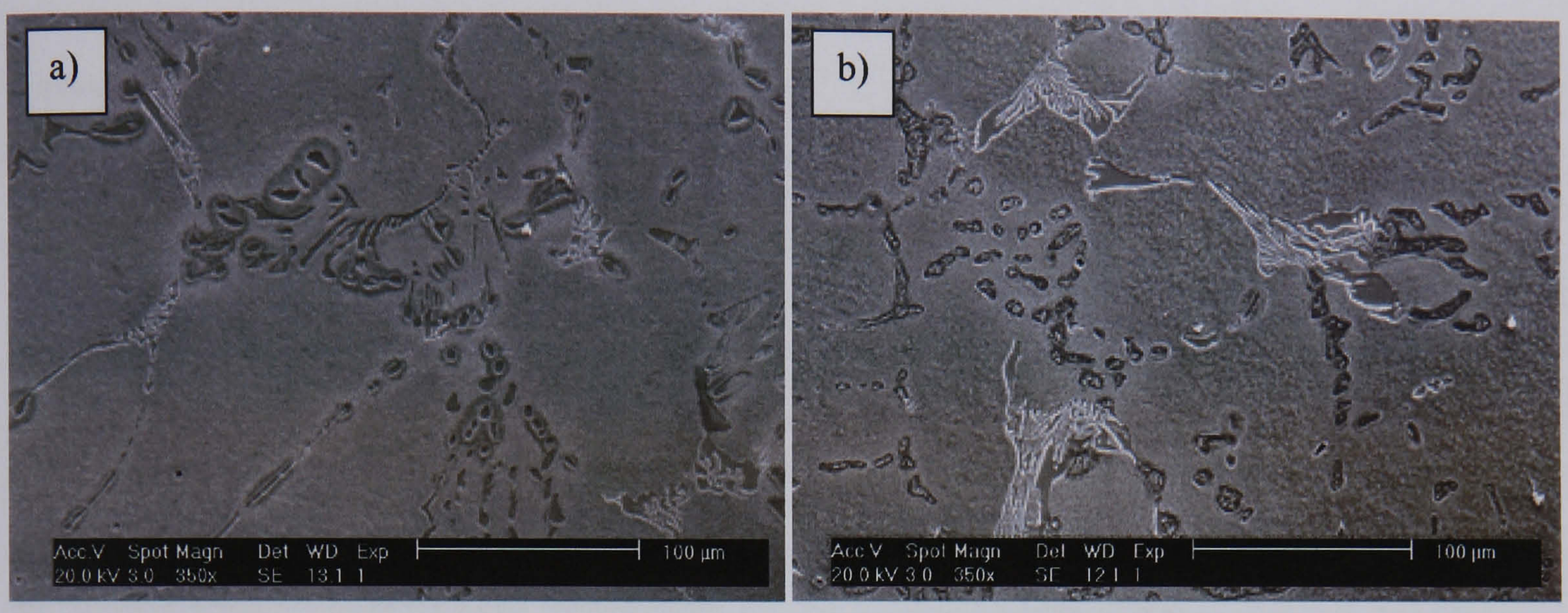

Fig.4.16. Secondary electron SEM images showing the surface of the steel oxidized at **550 °C** under condition 3. a) After 15 minutes b) After 4 hours.

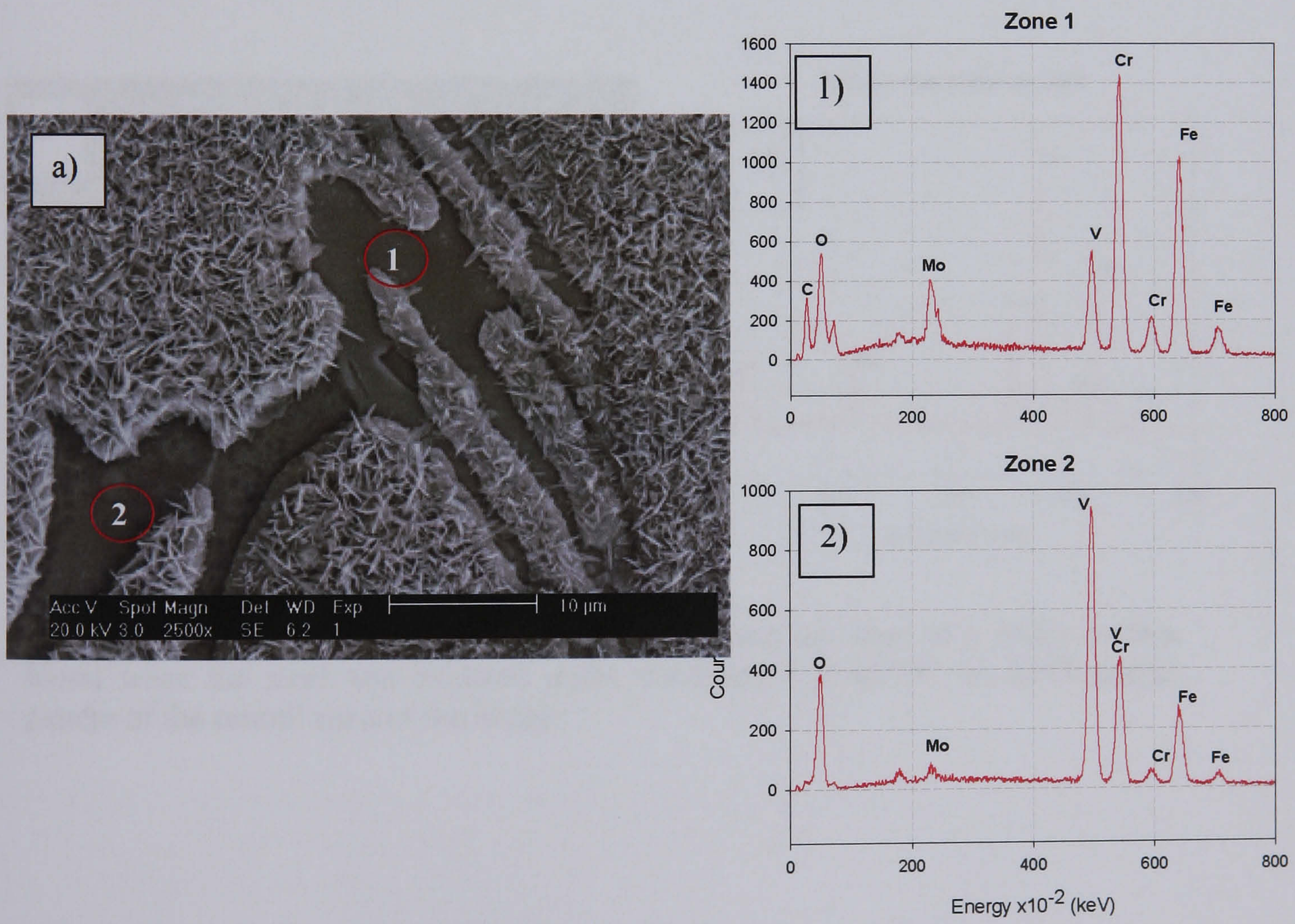

Fig.4.17. a) Secondary electron SEM image showing the condition of the carbides in a sample oxidized under condition 2 at **615°C**. 1) EDX pattern of a M_7C_3 carbide. 2) EDX pattern of a MC carbide.

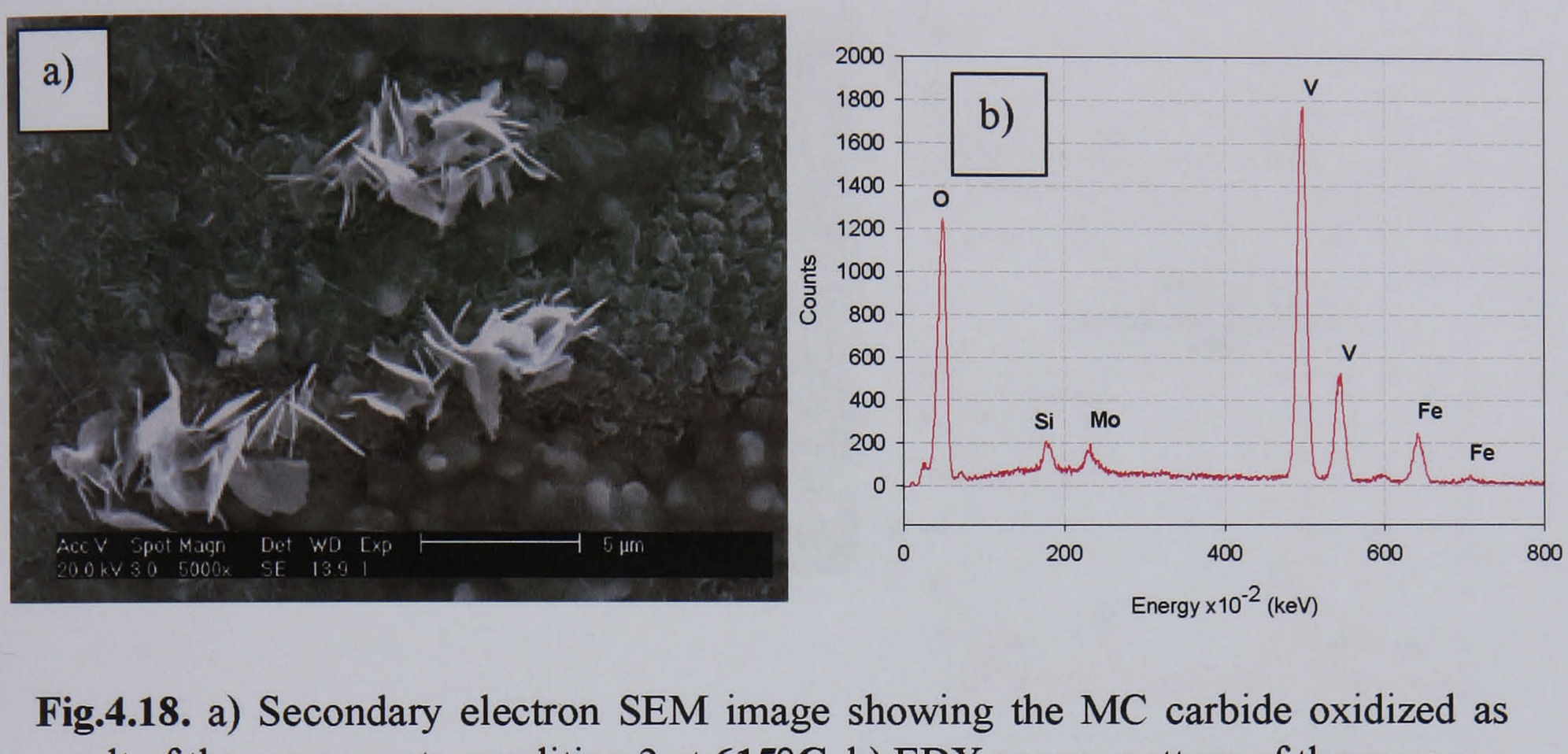

Fig.4.18. a) Secondary electron SEM image showing the MC carbide oxidized as result of the exposure to condition 3 at **615°C.** b) EDX energy pattern of the zone.

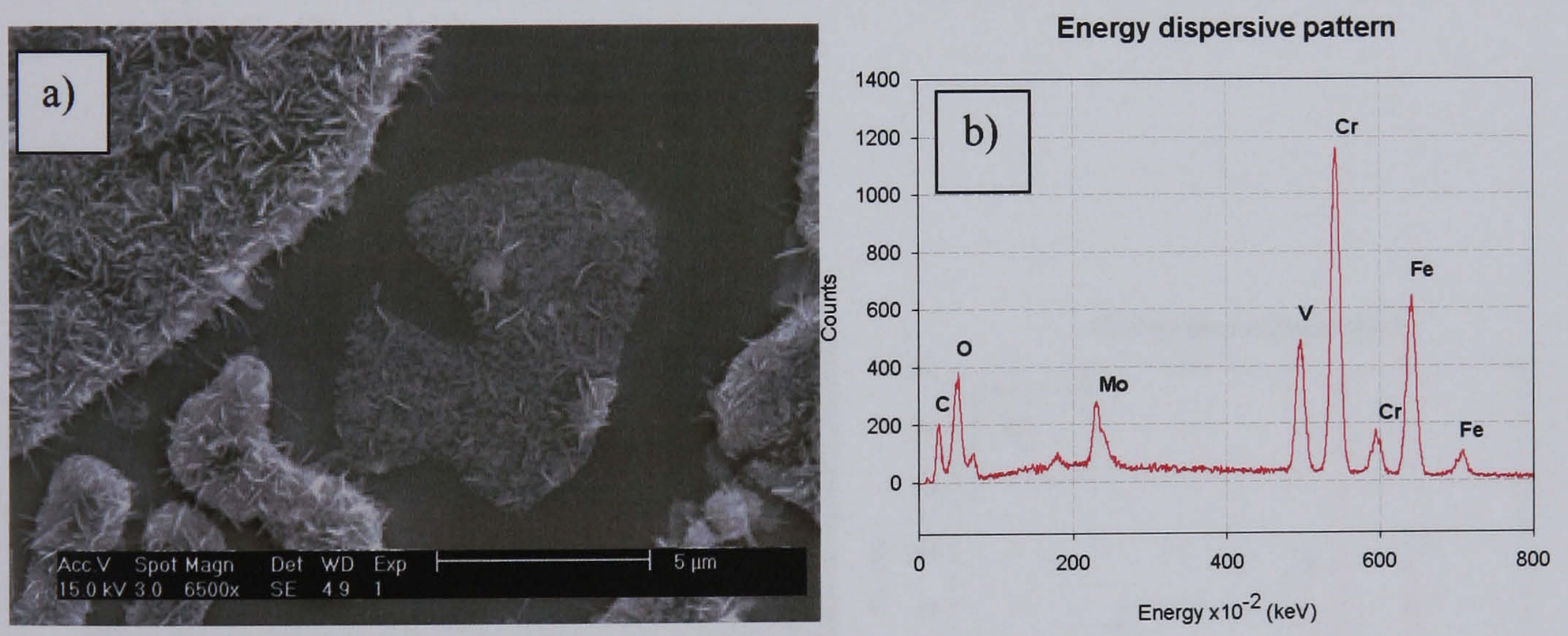

Fig.4.19. a) Secondary electron SEM image showing the state of a M_7C_3 carbide found when the steel was oxidized under condition 3 at **615°C**. b) EDX energy pattern of the central zone of the image.

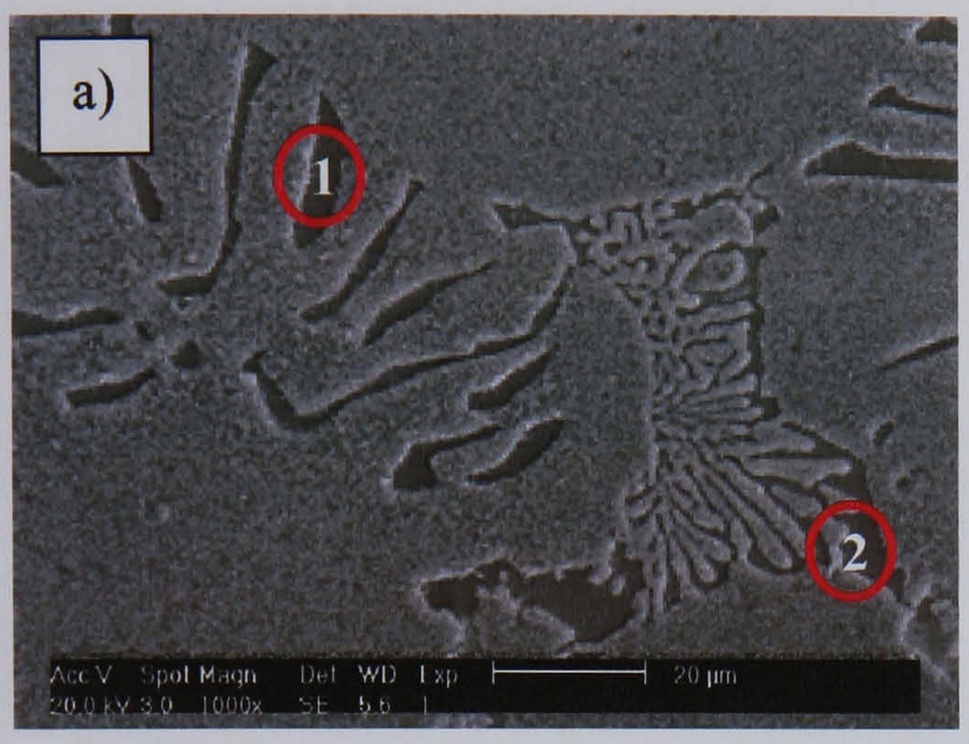

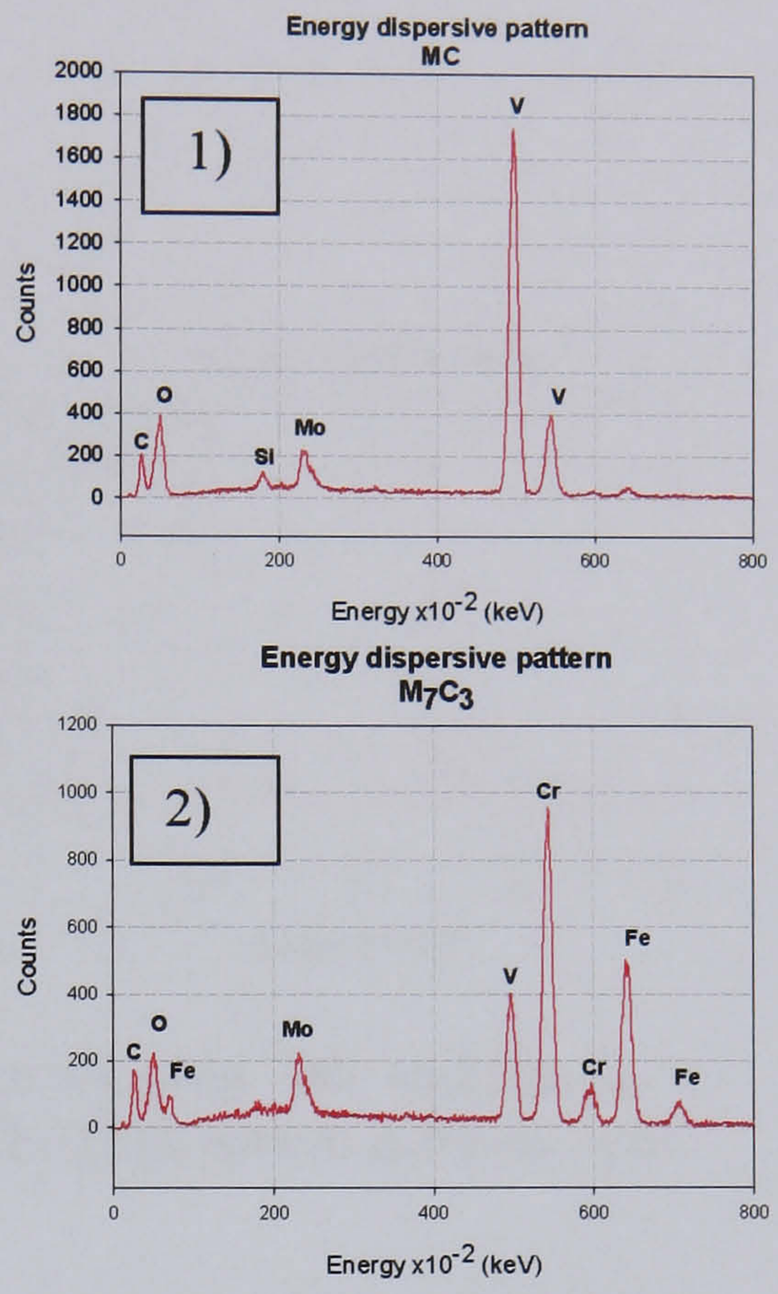

Fig.4.20. a) Secondary electron SEM image showing the carbides in a sample oxidized in condition 1 at **550°C**. EDX patterns obtained for MC (1) and M_7C_3 (2) carbides.

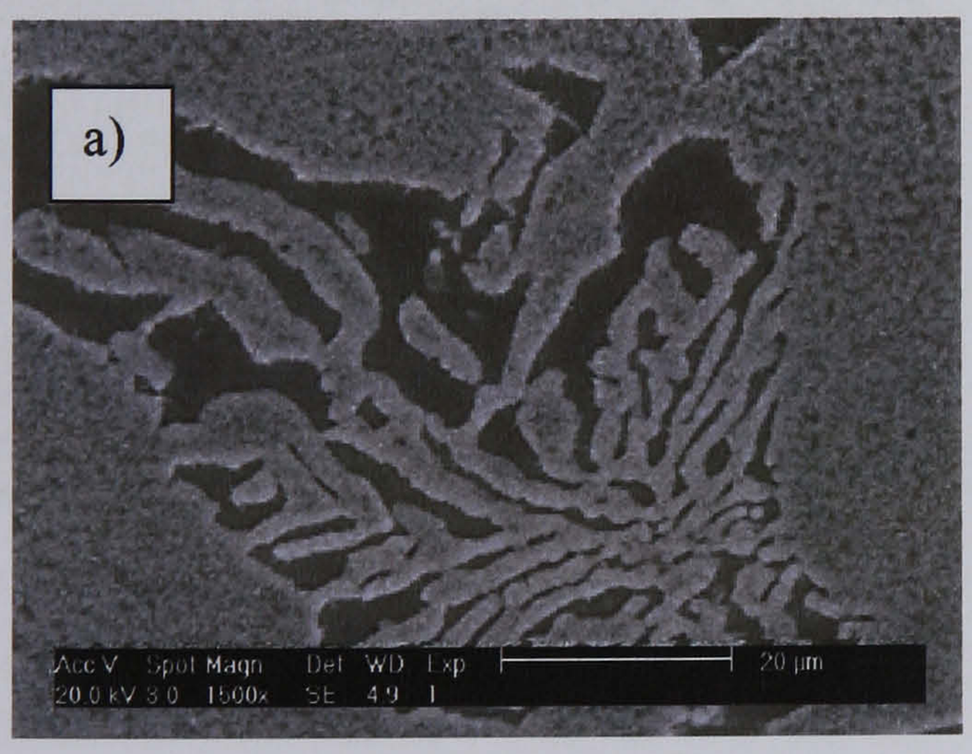

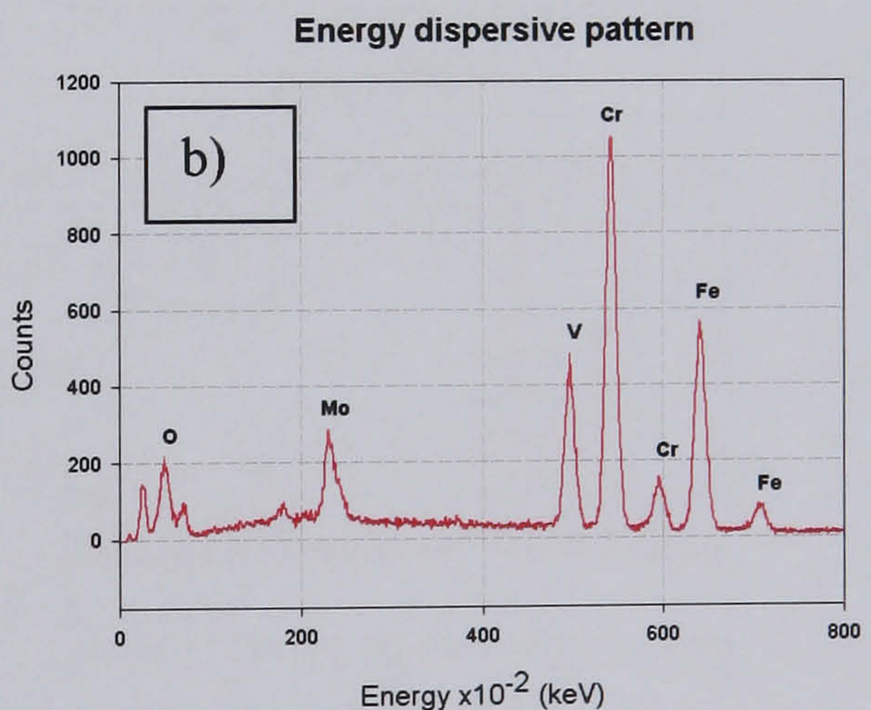

Fig.4.21. a) Secondary electron SEM images showing the M_7C_3 carbides in a sample oxidized under condition 2 at **550°C**. The EDX pattern obtained from the carbide is shown in b).

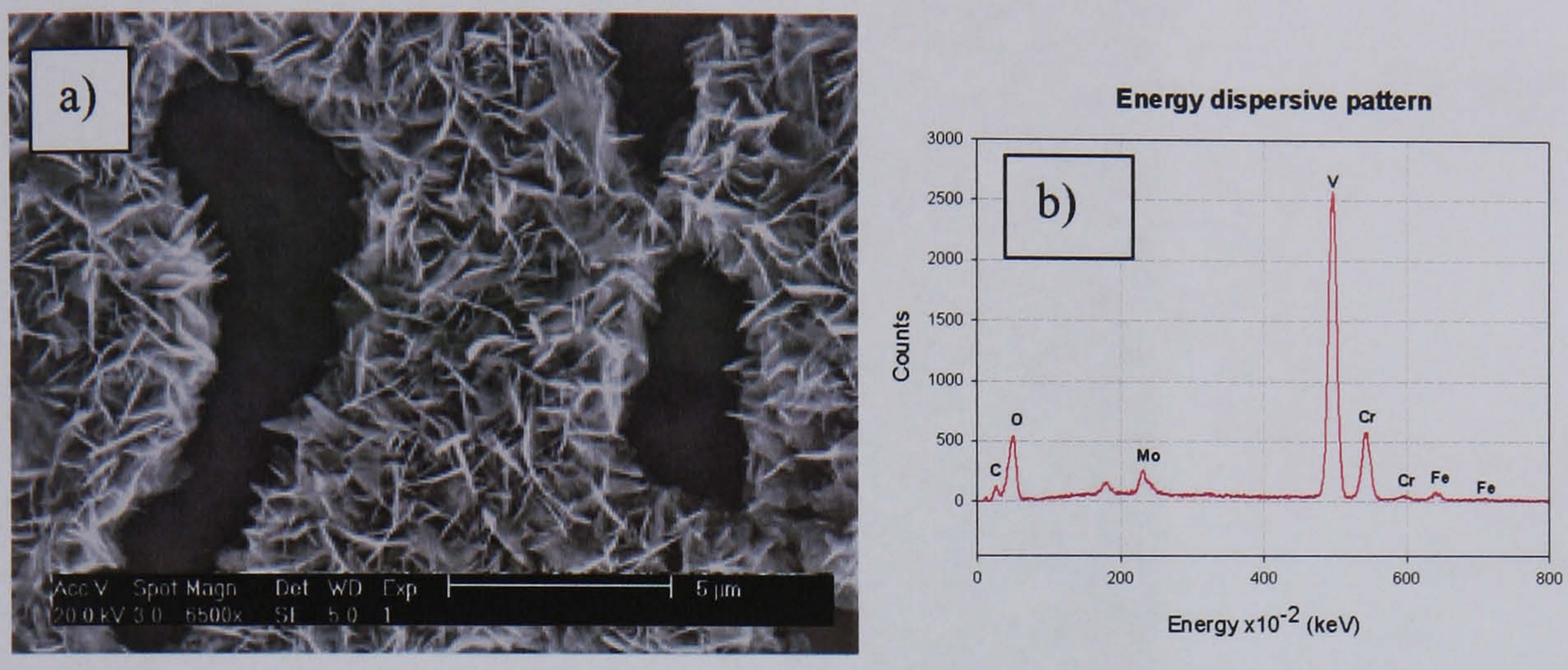

Fig.4.22. a) Secondary electron SEM image showing MC carbides in a sample oxidized under condition 2 at **550°C**. The EDX pattern is shown in b).

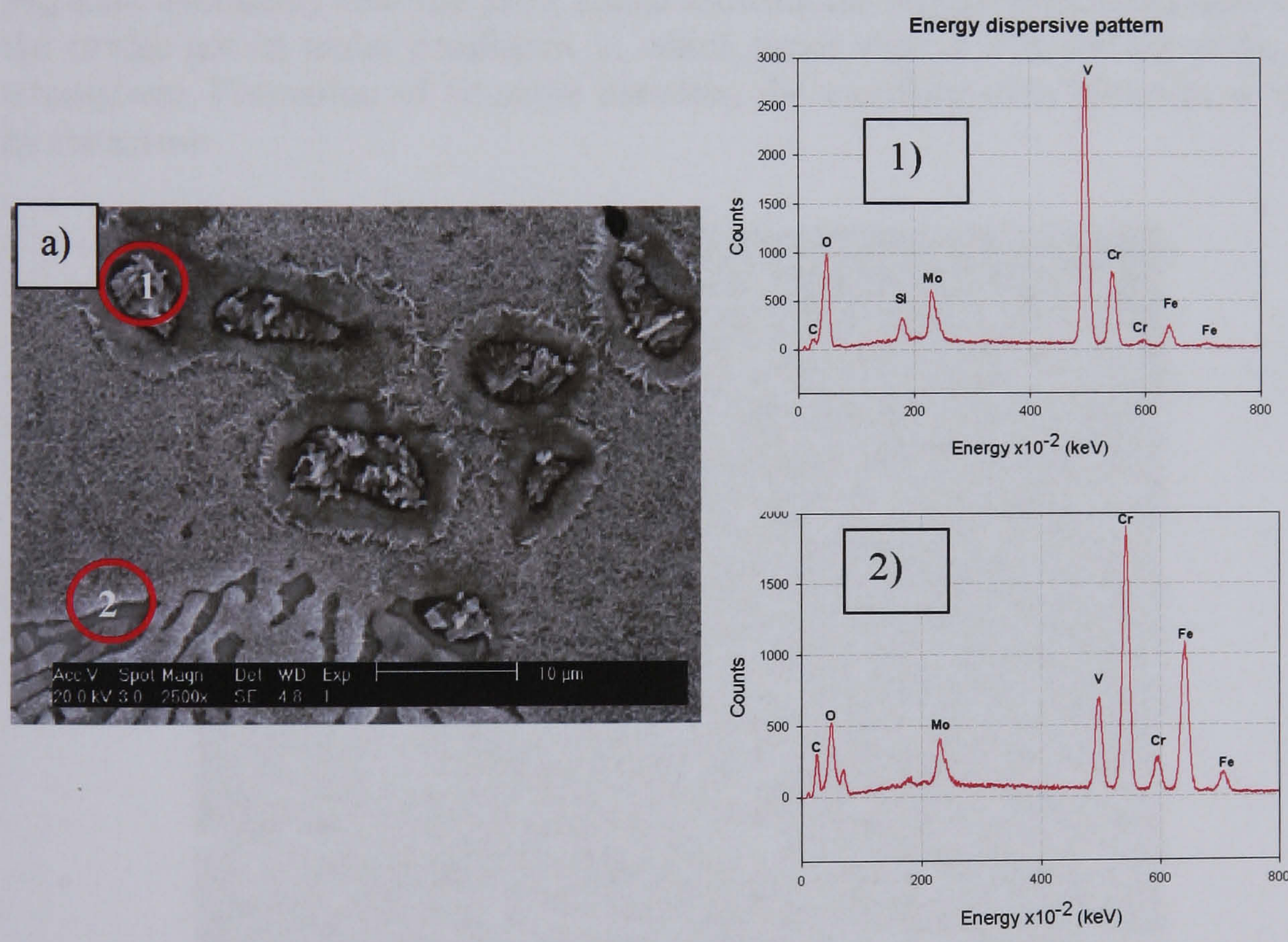

Fig.4.23. Secondary electron SEM image showing the carbides in a sample oxidized under condition 3 at **550°C**. The EDX patterns for MC (1) and M_7C_3 (2) carbides are shown.

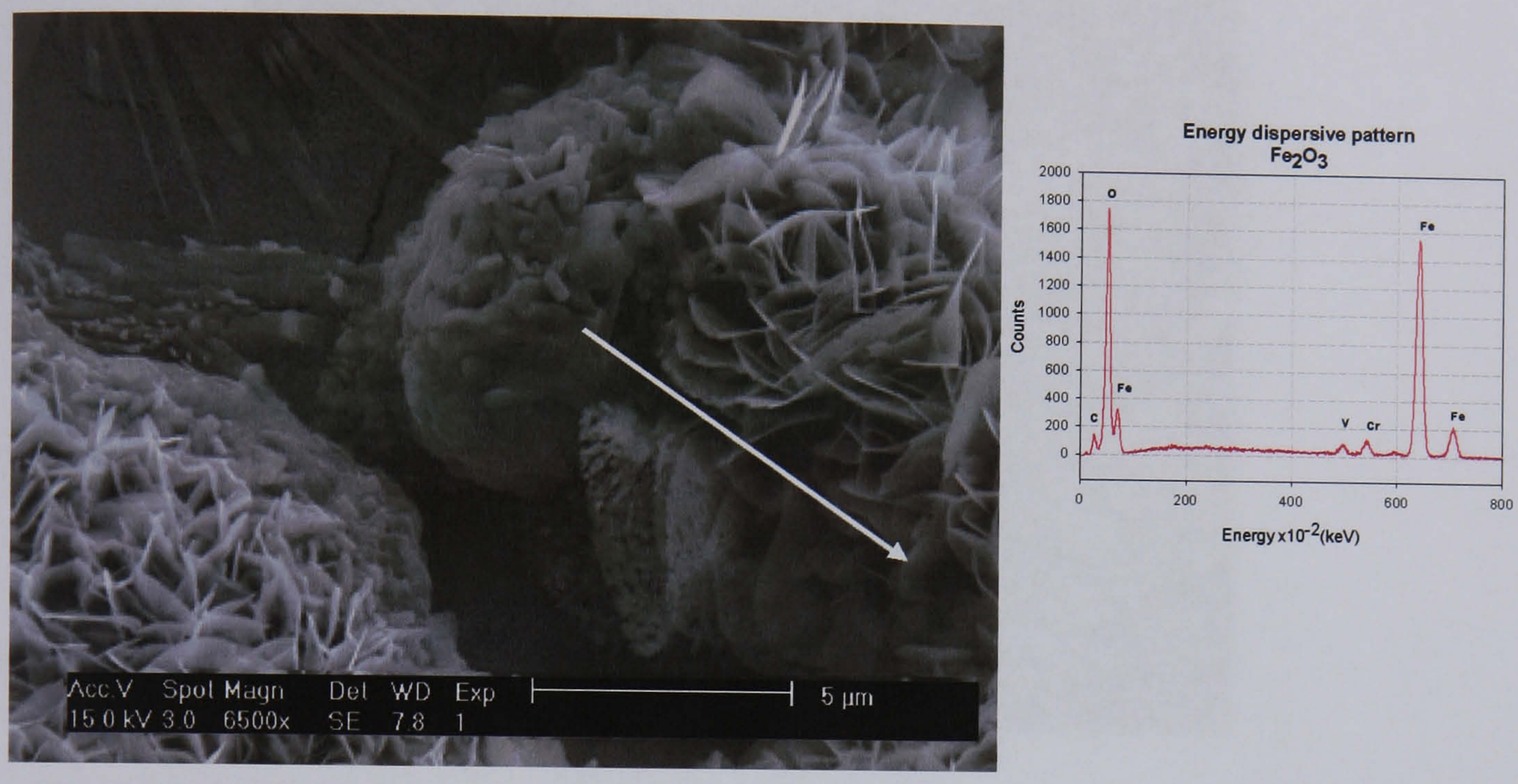

Fig.4.24. Secondary electron SEM image showing the morphological changes found for the oxides grown under conditions in which water vapour was present in the oxidant atmosphere. Formation of hematite platelets, the transformation direction is indicated by the arrow.

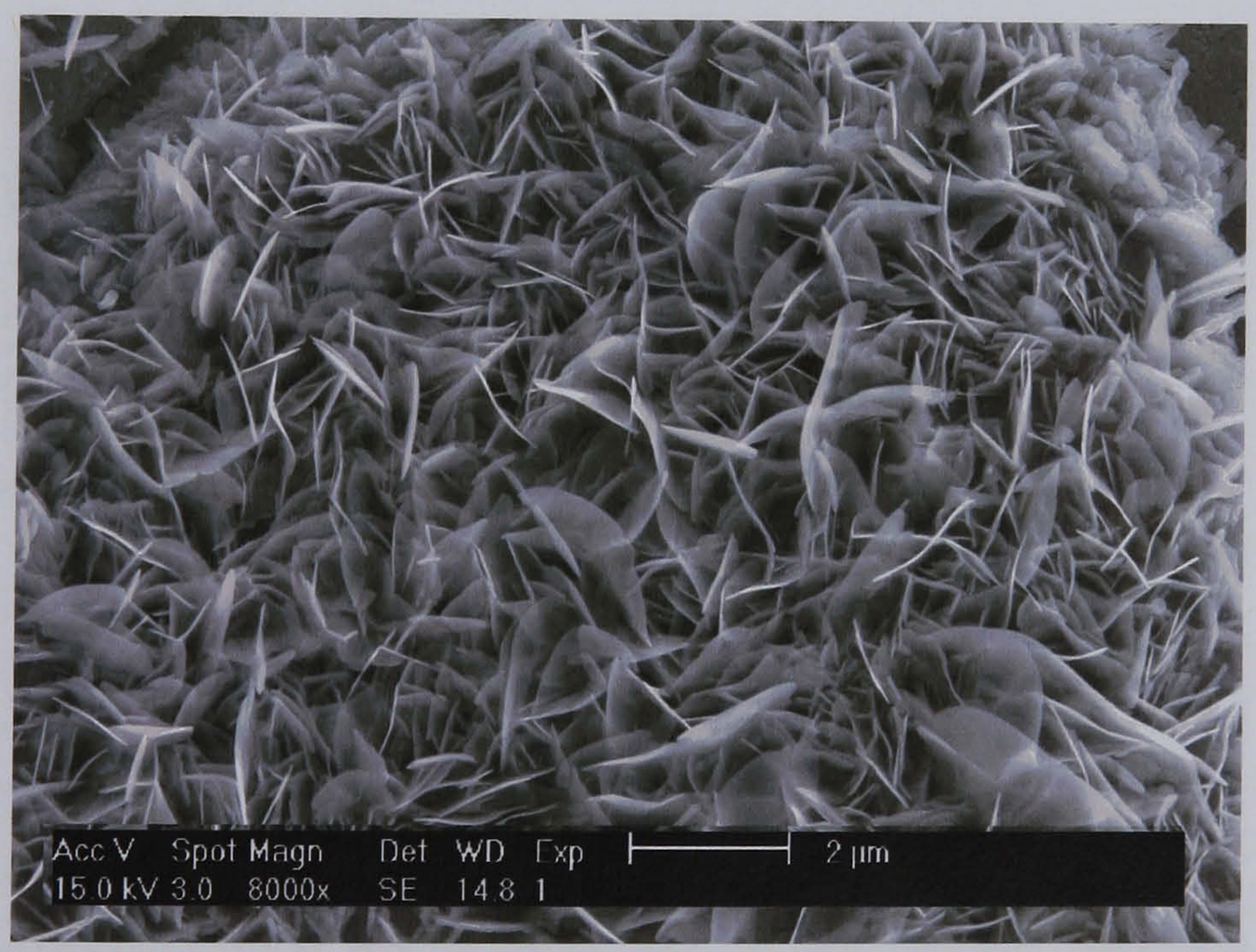

Fig.4.25. Secondary electron SEM image showing the morphology of the oxide layer grown on the matrix of the steel in the test containing water vapour as part the oxidant mixture for both temperatures. Fe_2O_3 platelets formed after 2 hours oxidation.

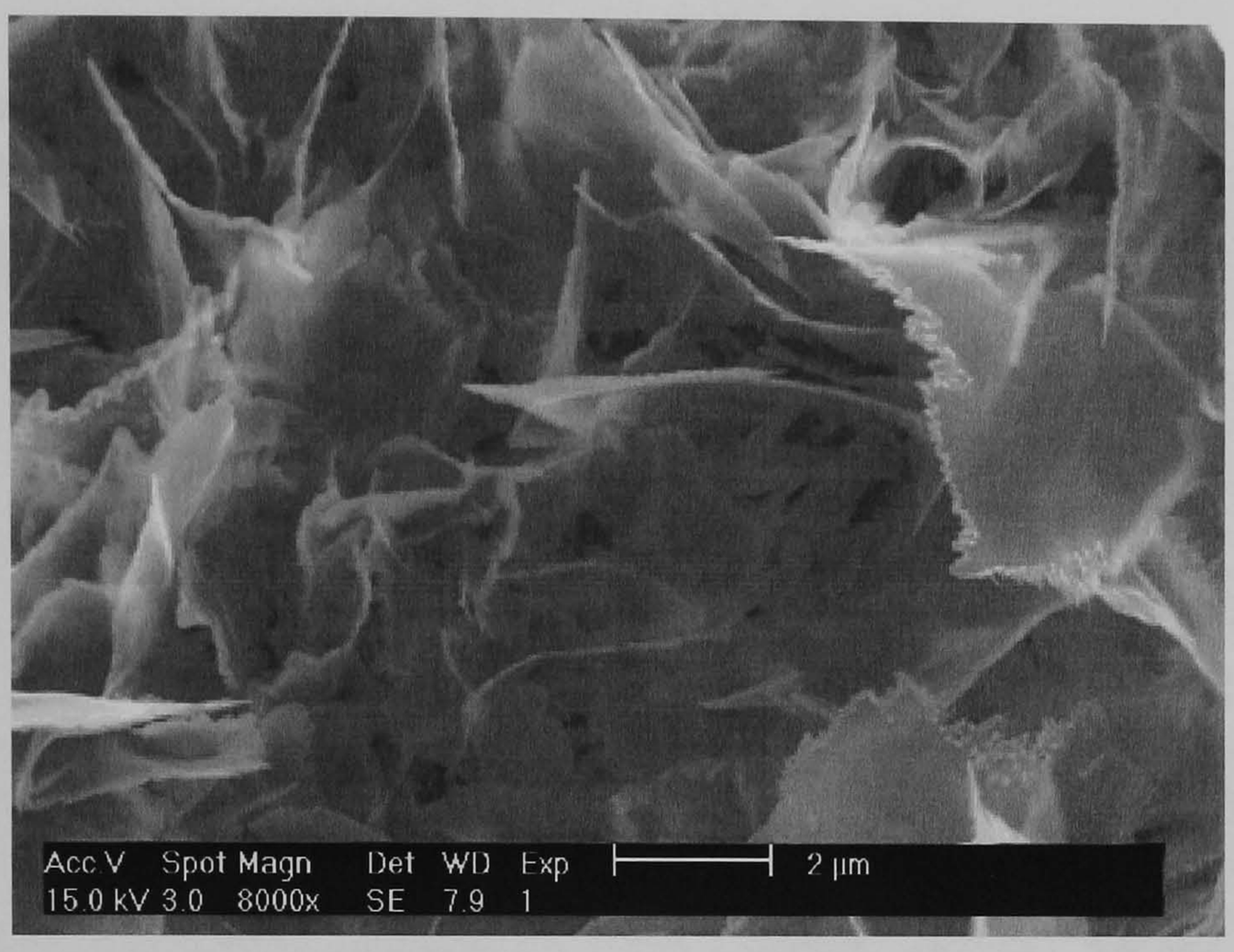

Fig.4.26. Secondary electron SEM image showing the morphology of the oxide layer grown on the matrix of the steel in tests containing water vapour. Transformation of Fe_2O_3 from platelets into leaves after 3 hours oxidation.

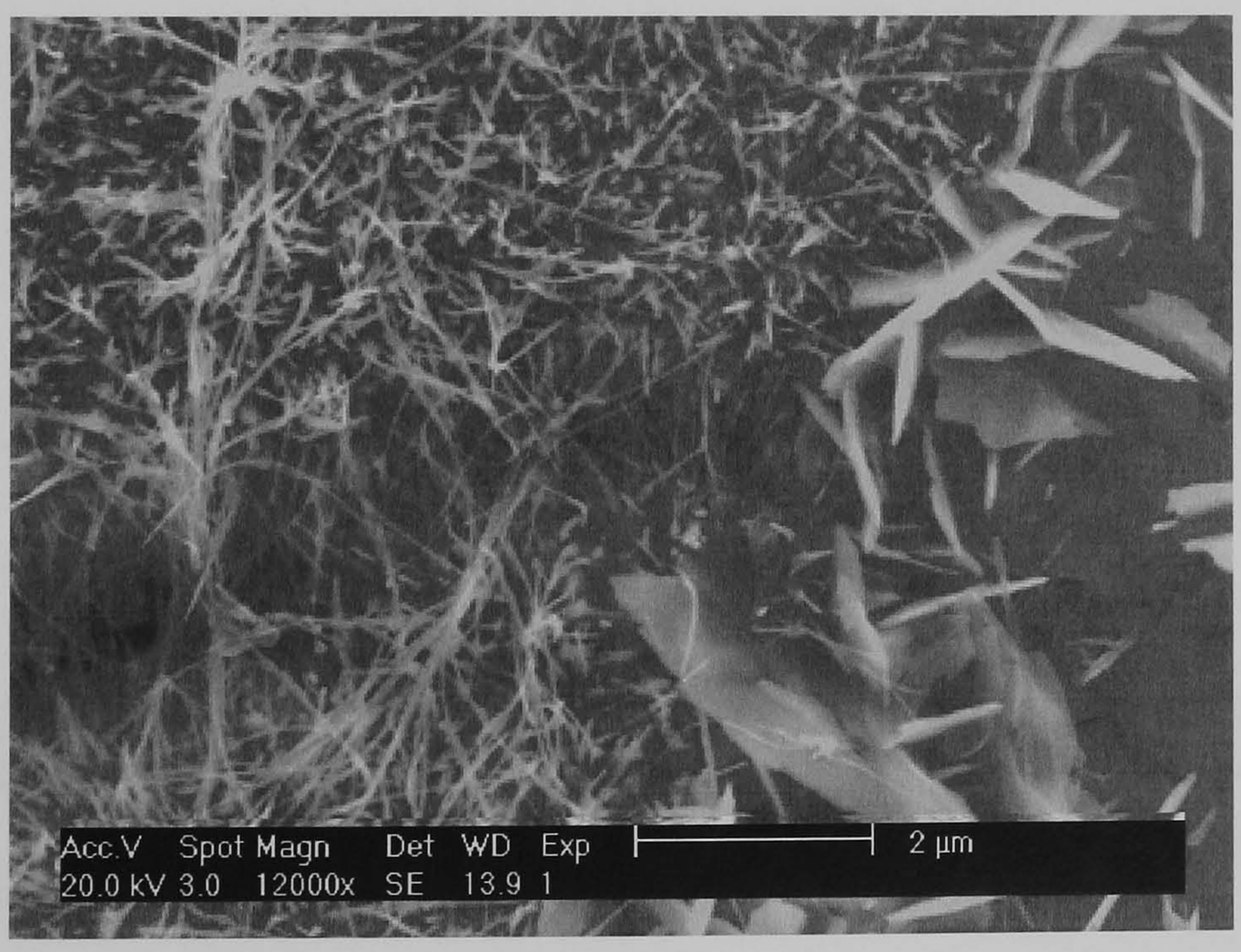

Fig.4.27. Secondary electron SEM image showing the formation of very fine oxide needles and oxide platelets characteristic morphology of the oxidation processes under condition 3 at both temperatures.

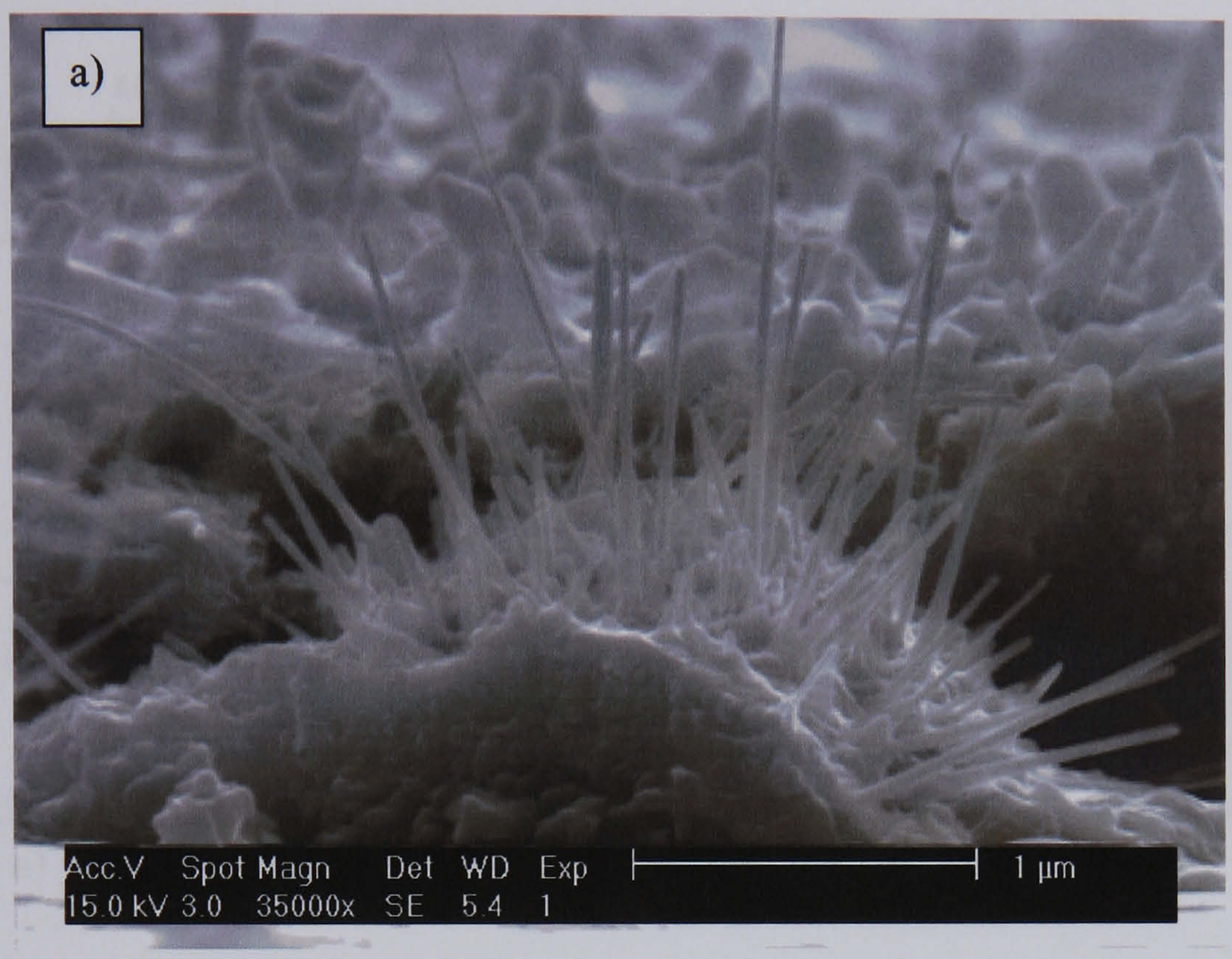

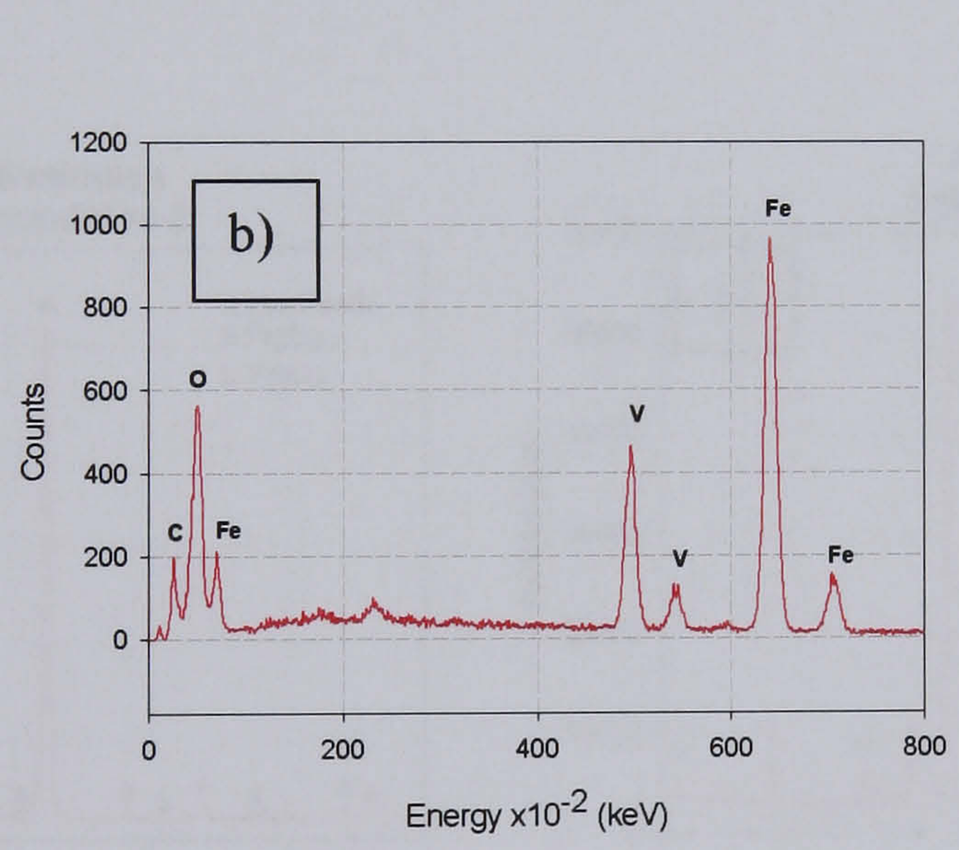

Fig.4.28. a) Secondary electrons SEM image showing Fe-V oxide whiskers. Similar structures like the one shown in this image were found in the samples oxidized under condition 3 at both temperatures. b) EDX point analysis taken at the centre of the oxide structure shown in b).

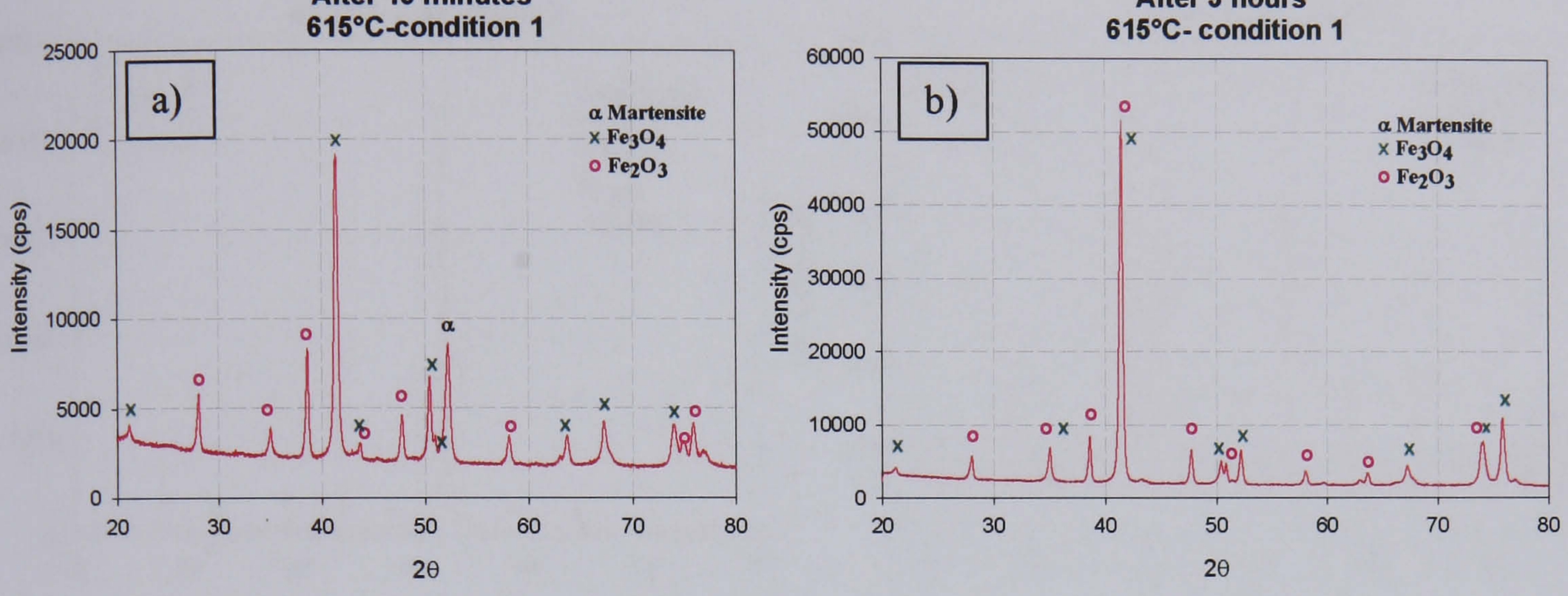

Fig.4.29. X-ray diffraction patterns of the samples oxidized under condition 1 at **615°C**. a) Phases obtained after 15 minutes. b) After 3 hours.

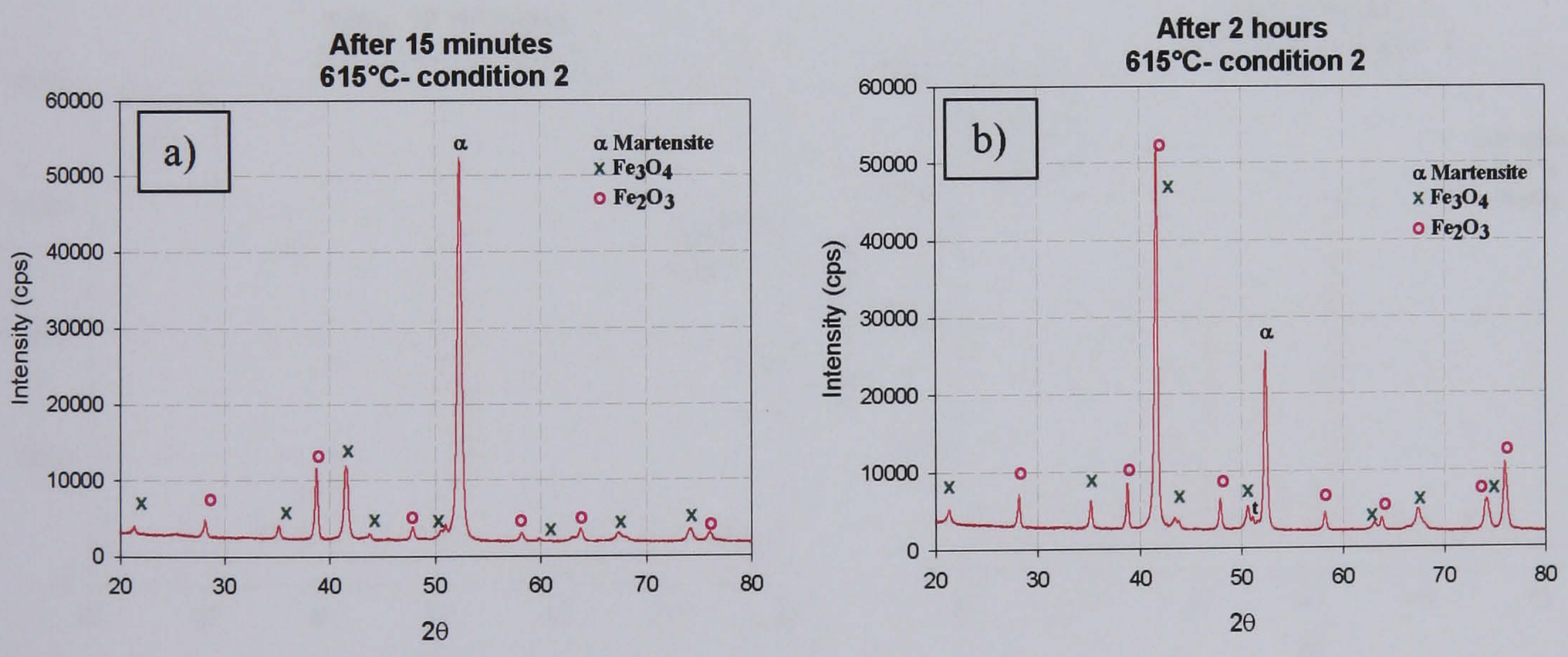

Fig.4.30. X-ray diffraction patterns of the samples oxidized at **615°C** under condition 2. a) Phases obtained after 15 minutes b) After 2 hours.

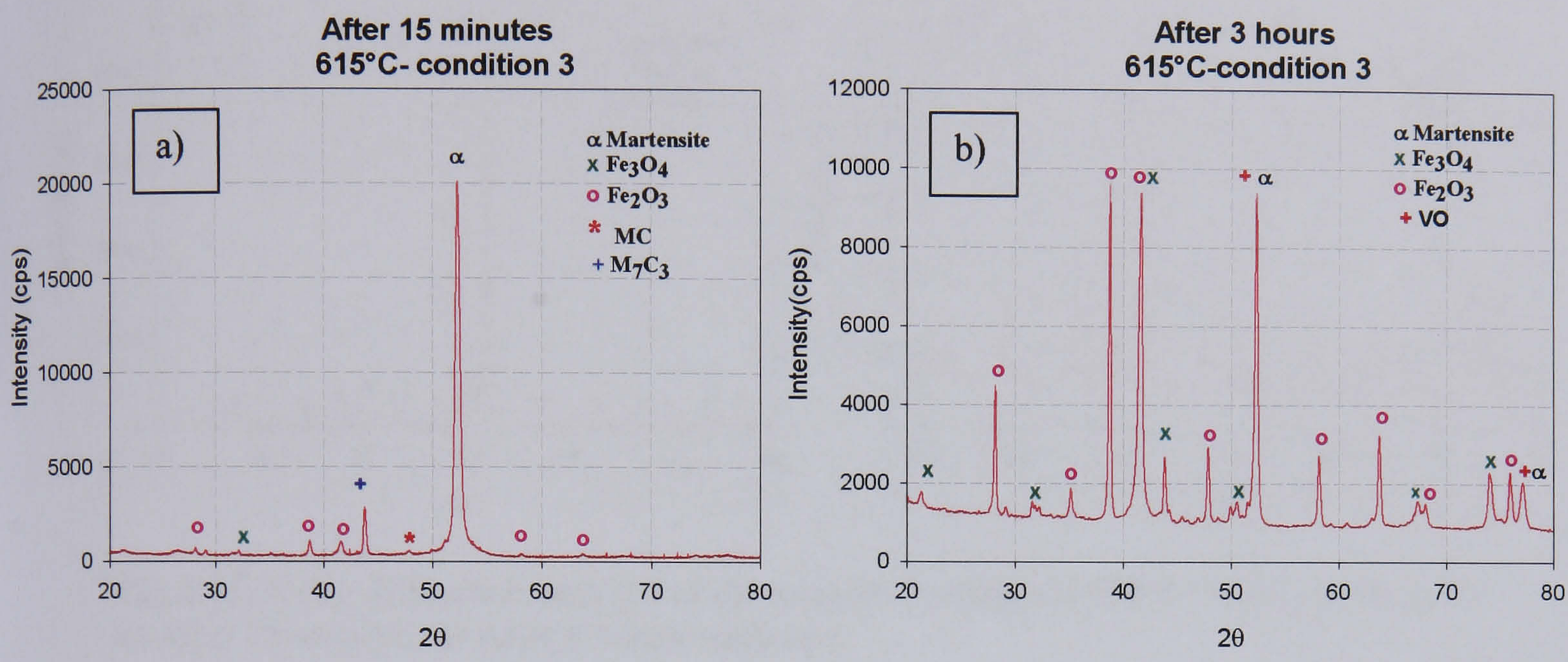

Fig.4.31. X-ray diffraction patterns of the samples oxidized at **615°C** under condition 3. a) After 15 minutes. b) After 3 hours oxidation.

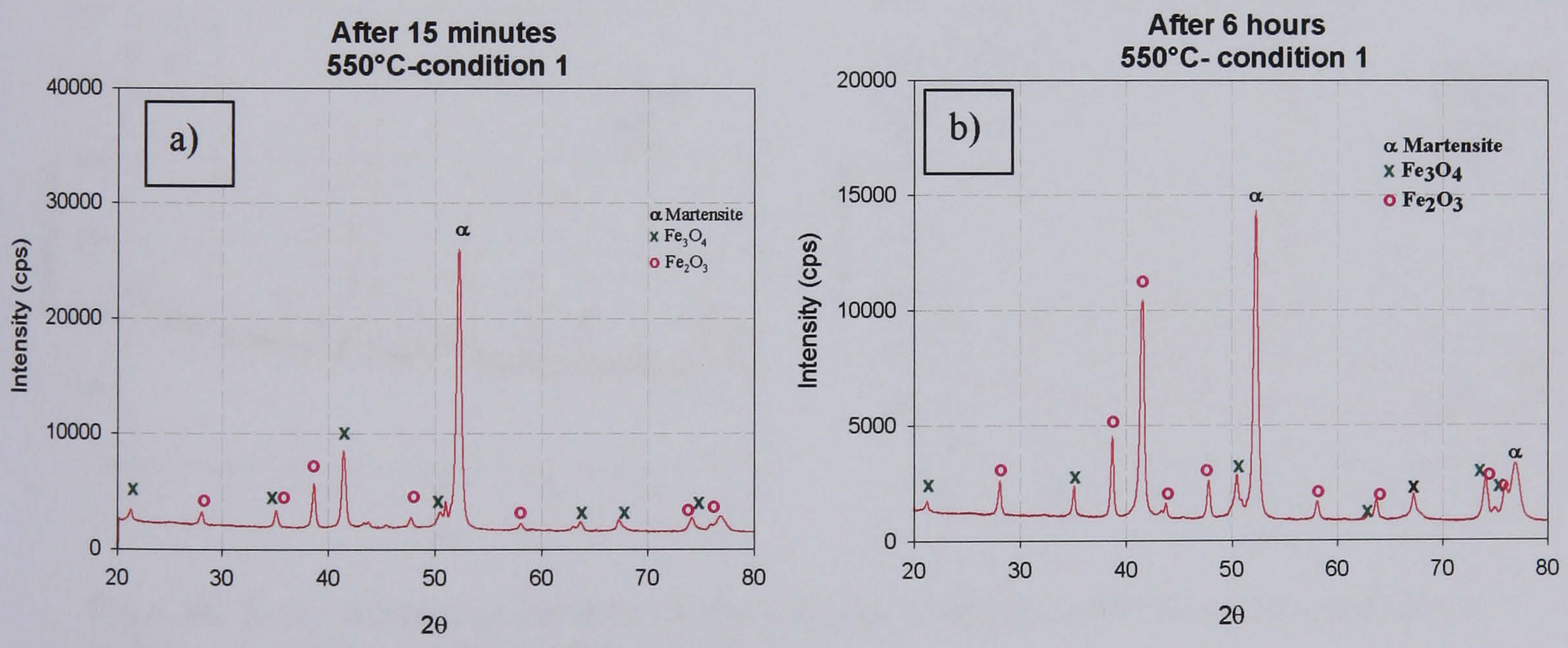

Fig.4.32. X-ray diffraction patterns of the samples oxidized at **550°C** under condition 1. a) After 15 minutes. b) After 6 hours oxidation.

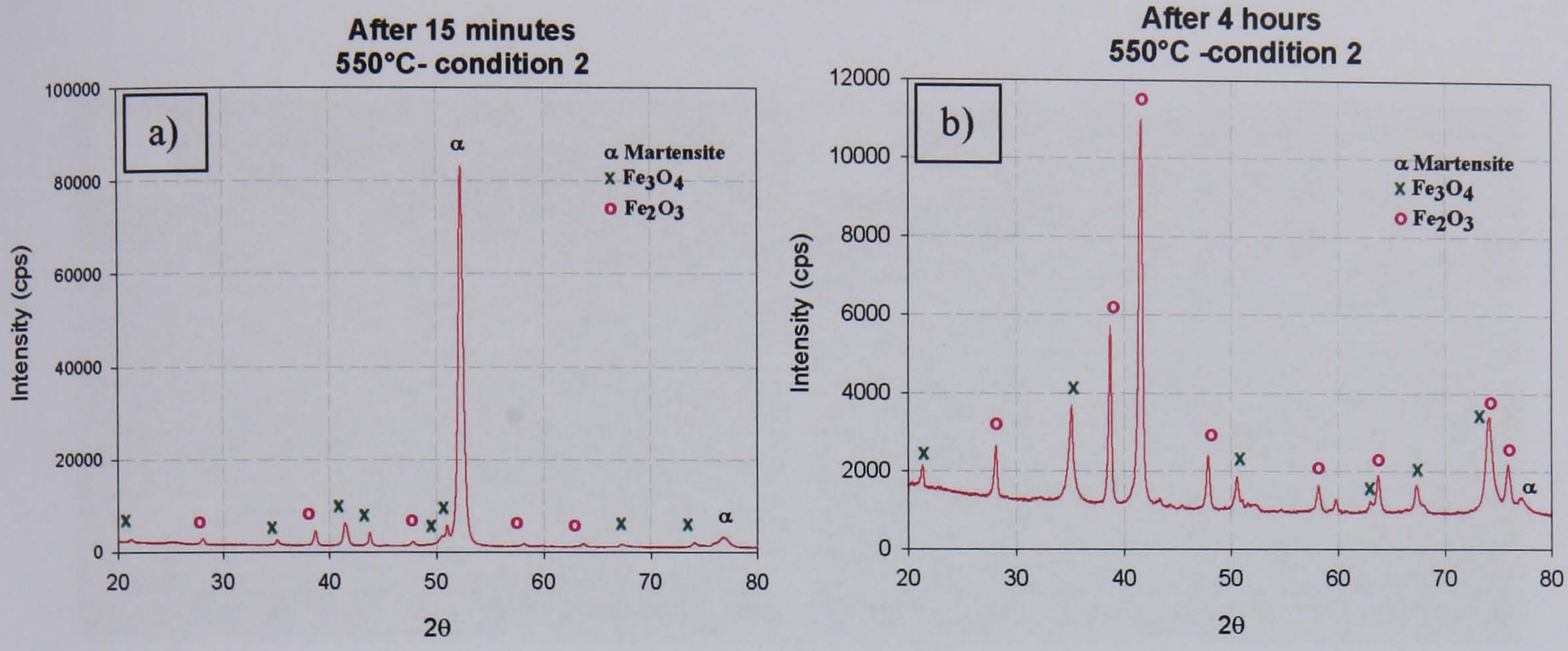

Fig.4.33. X-ray diffraction patterns of the samples oxidized at **550°C** under condition 2.
a) After 15 minutes. b) After 4 hours oxidation.

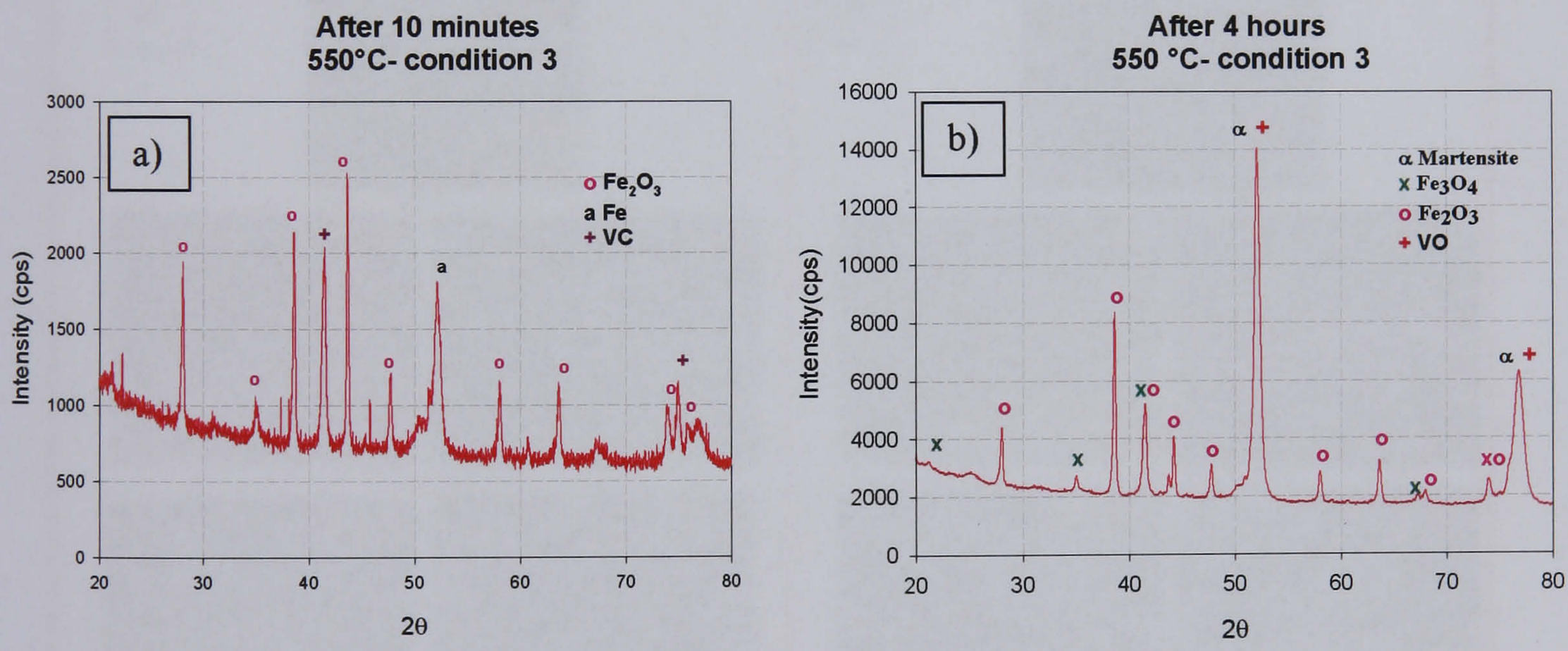

Fig.4.34. X-ray diffraction patterns of the samples oxidized at **550°C** under condition 3.
a) After 10 minutes .b) After 4 hours oxidation.

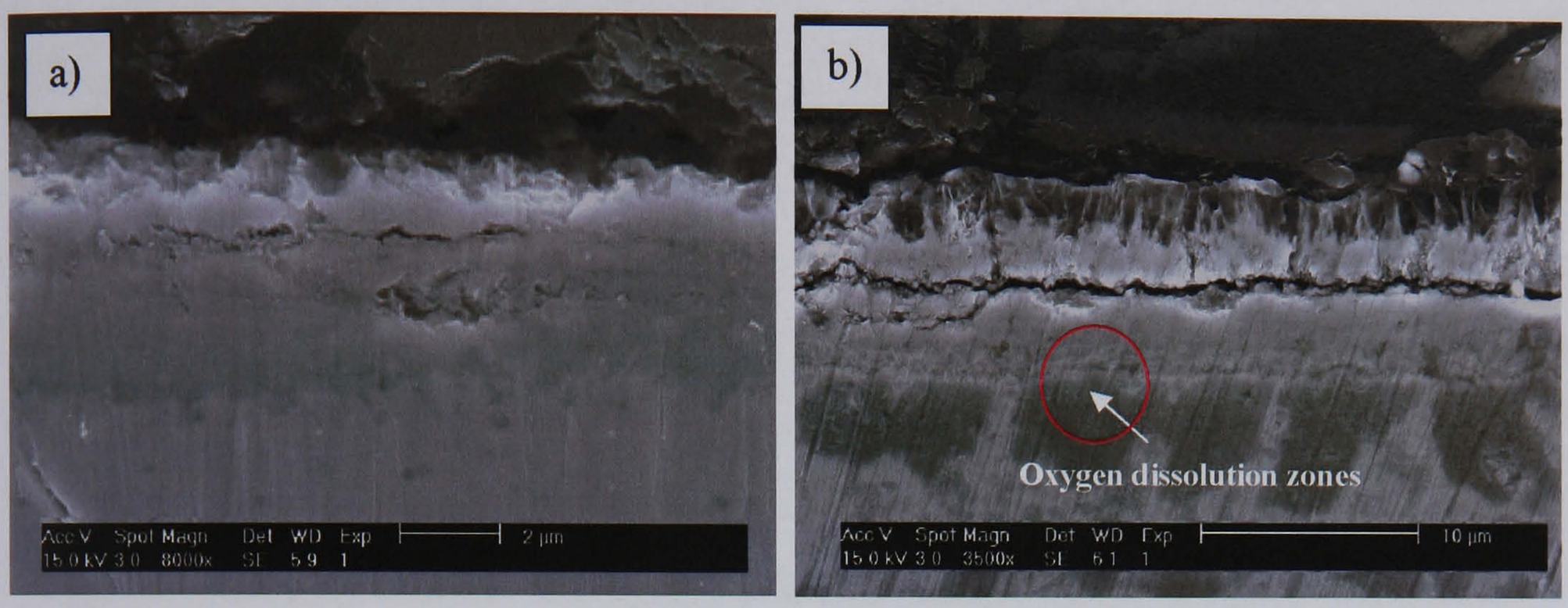

Fig.4.35. Secondary electron SEM micrographs of a cross section of the oxide layer obtained at **615°C** under condition 1. a) After 15 minutes. b) After 2 hours oxidation. Stages of internal oxidation are appreciated in b).

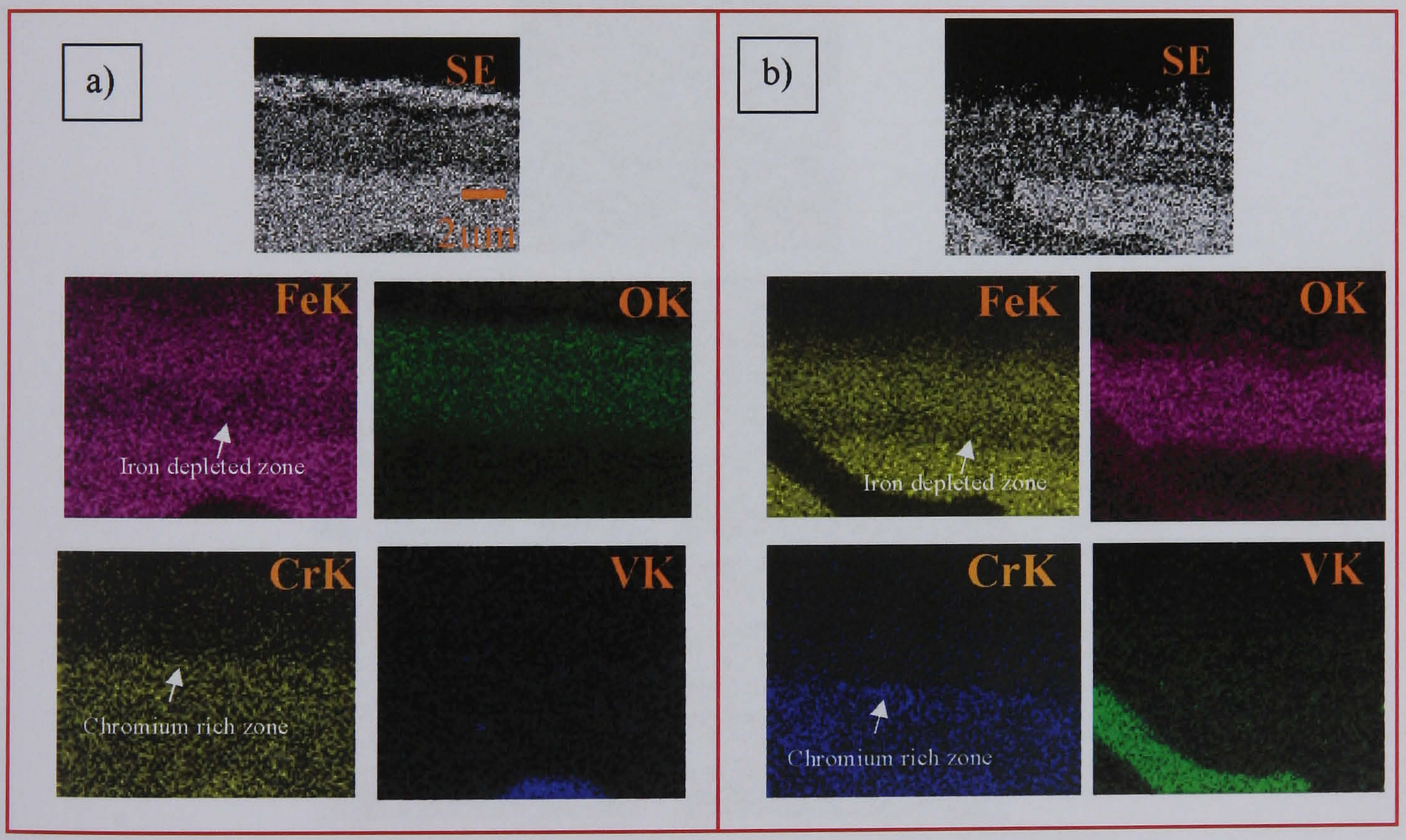

Fig.4.36. Energy dispersive x-ray dot mapping of the elements present in the oxide scale formed at **615°C** under condition 1. a) After 15 minutes. b) After 2 hours.

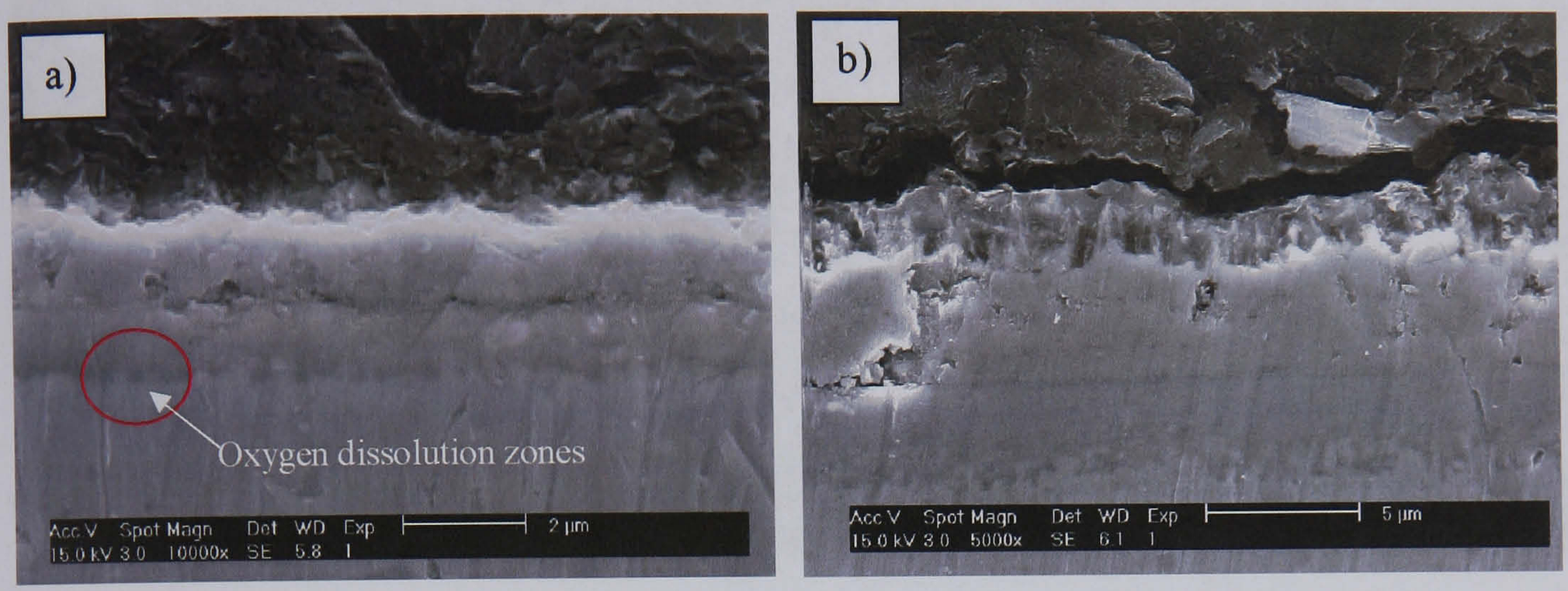

Fig.4.37. Scanning electron micrograph of a cross section of the oxide layer obtained at **615°C** under condition 2. a) After 15 minutes. b) After 2 hours.

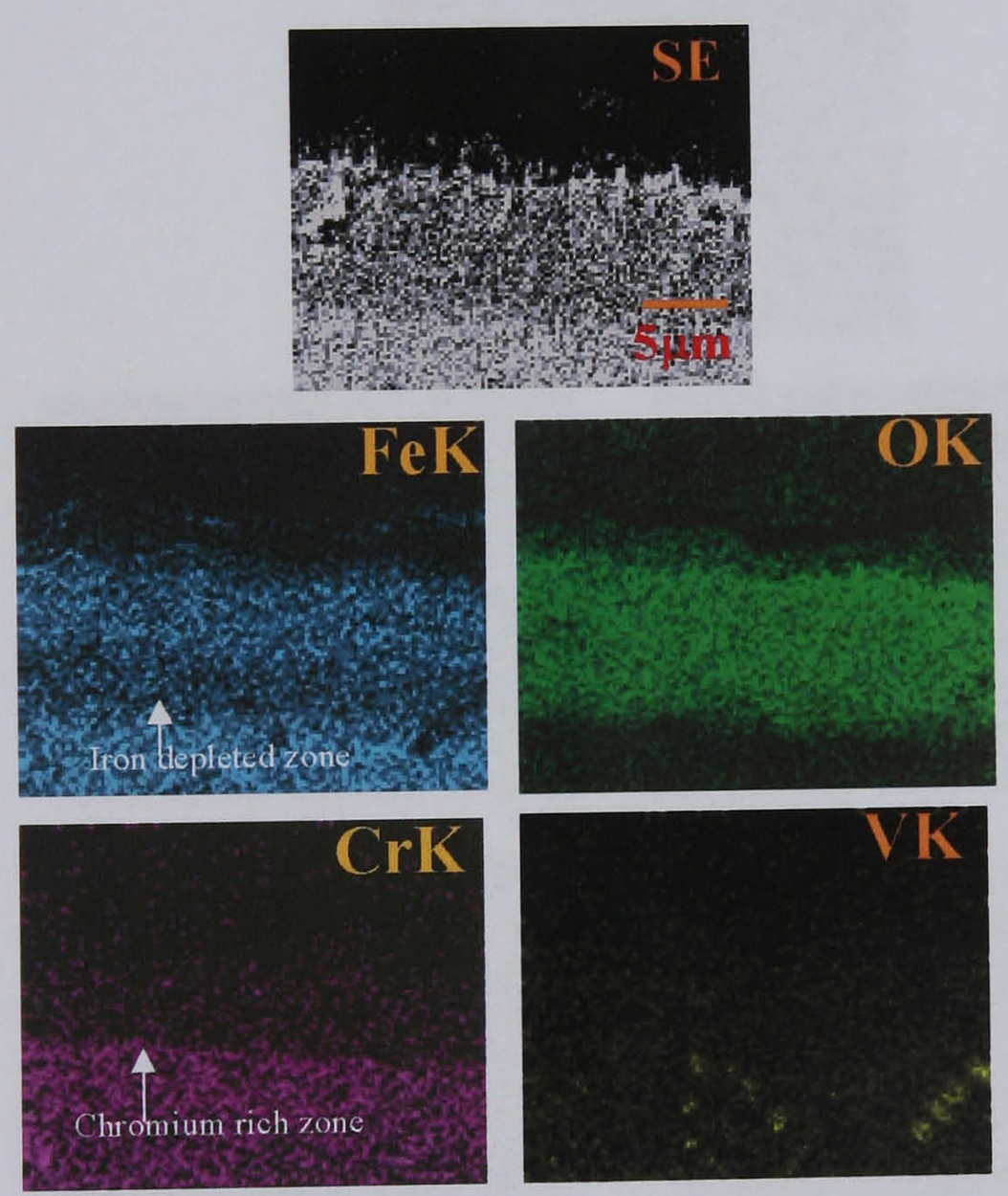

Fig.4.38. Energy dispersive x-ray dot mapping of the elements present in the oxide scale formed at **615°C** under condition 2 after 2 hours.

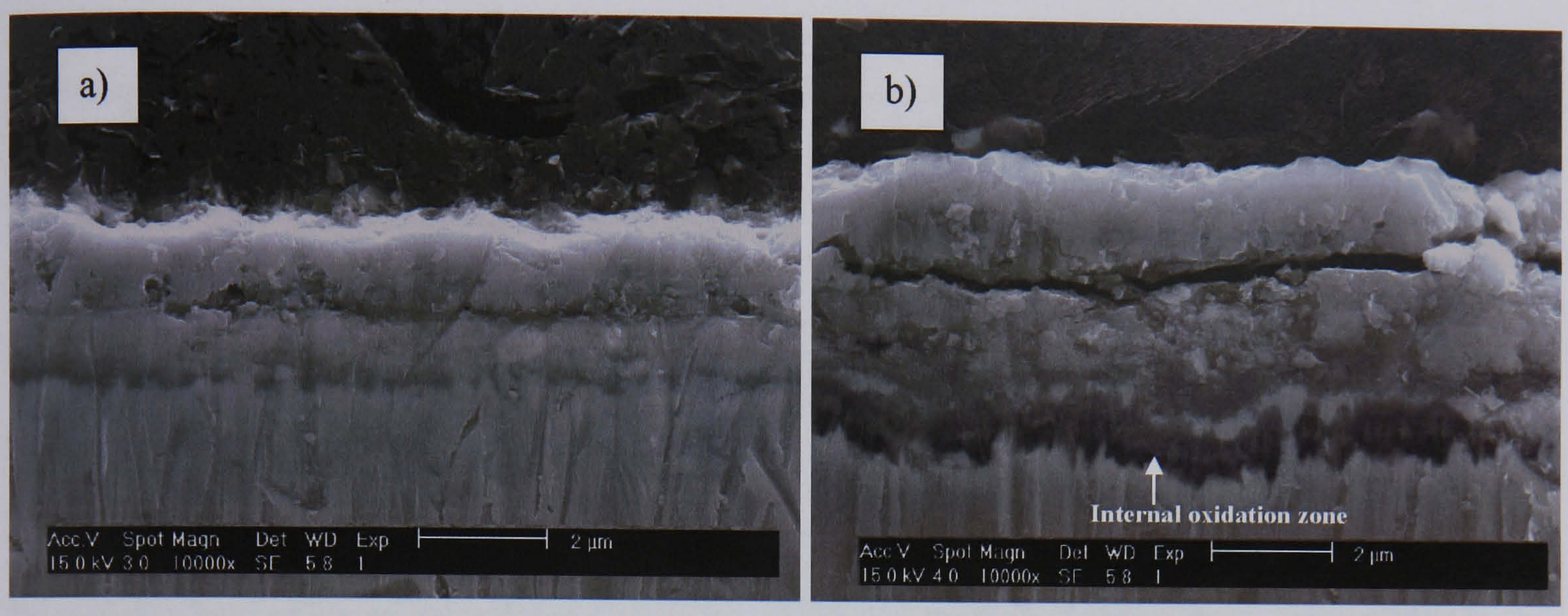

Fig.4.39. Cross section of the oxide layer obtained at **615°C** under condition 3. a) After 15 minutes. b) After 2 hours.

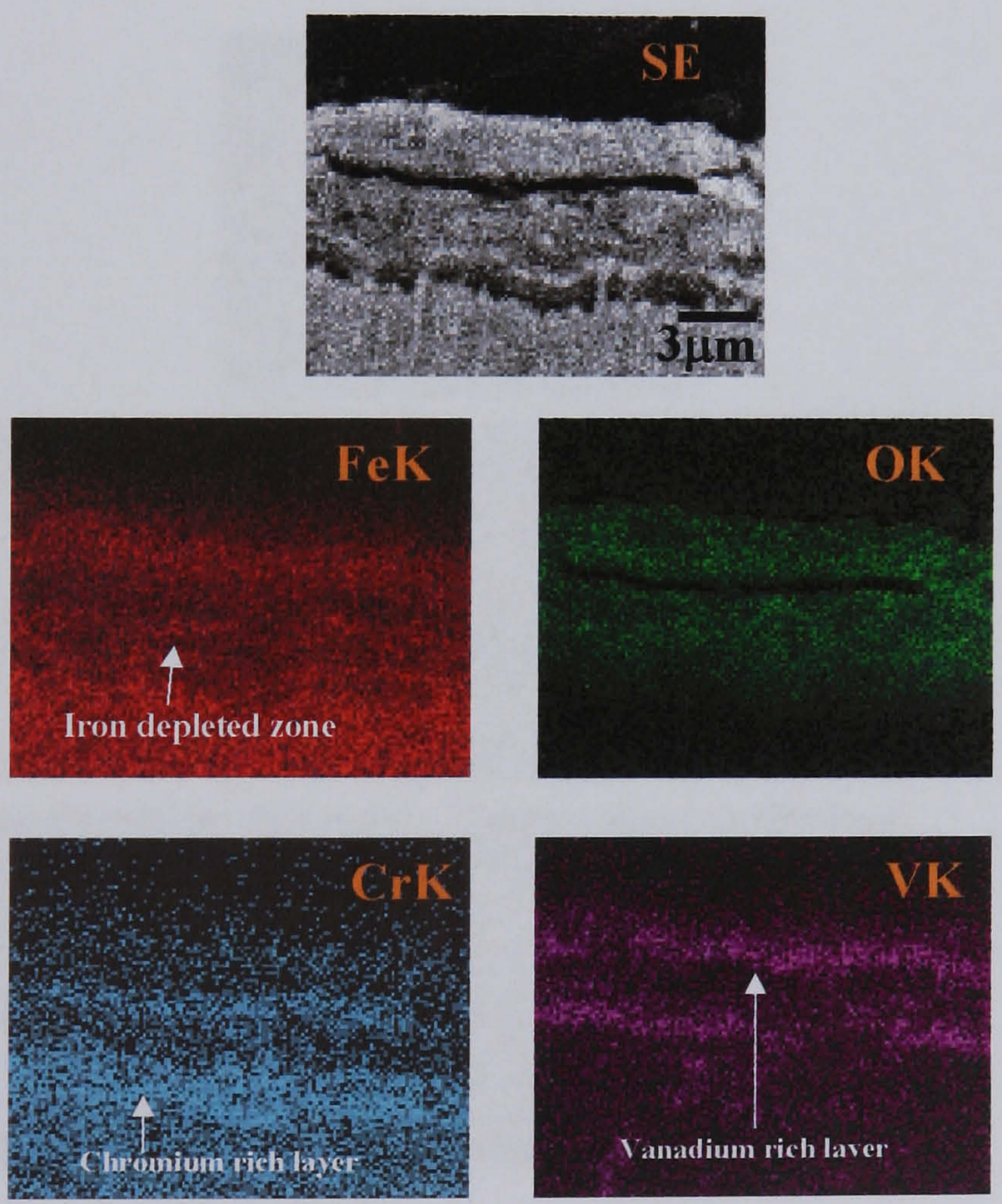

Fig.4.40. Energy dispersive x-ray dot mapping of the elements present in the oxide scale formed at 615°C under condition 3 after 2 hours.

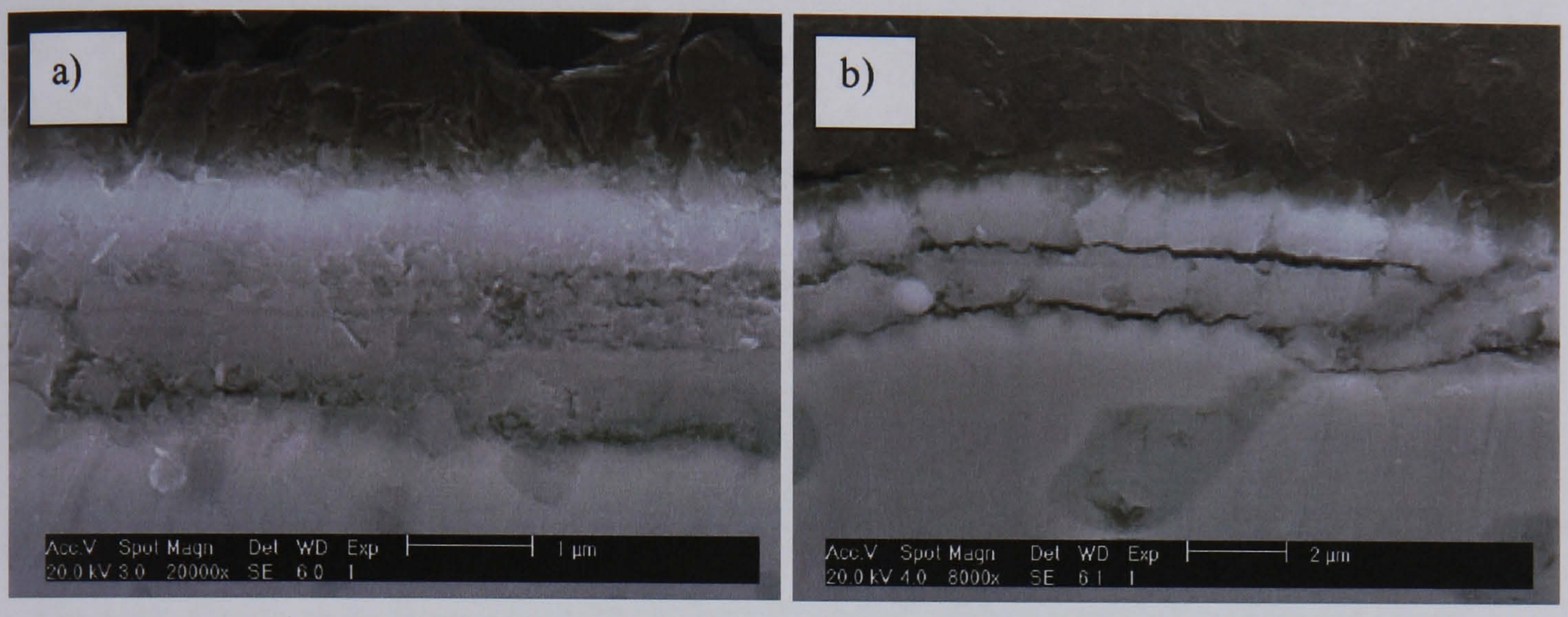

Fig.4.41. Oxide scale formed at **550 °C** under condition 1. a) After 1 hour. b) After 4 hours.

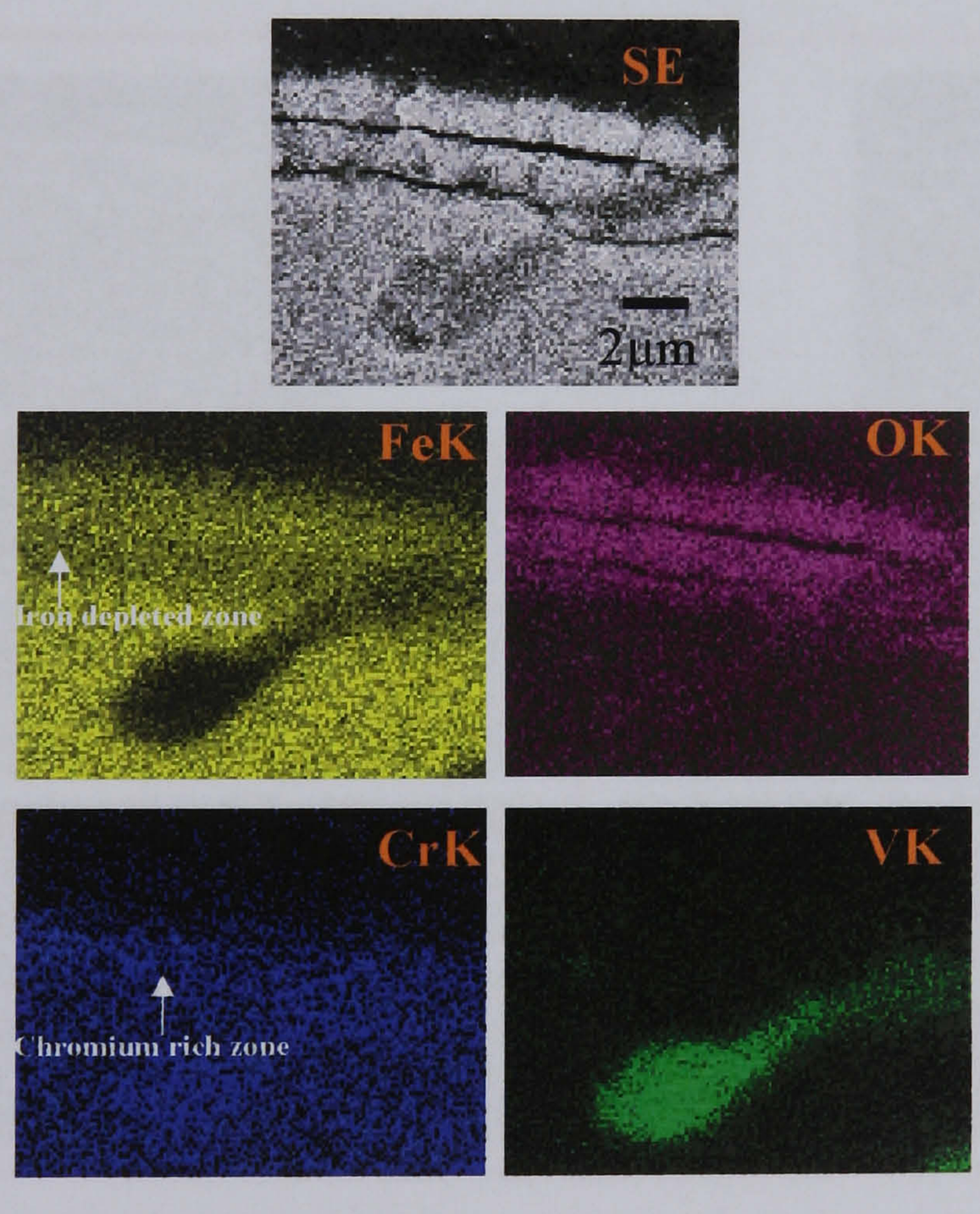

Fig.4.42. Energy dispersive x-ray dot mapping of the elements present in the oxide scale formed at **550°C** under condition 1 after 4 hours.

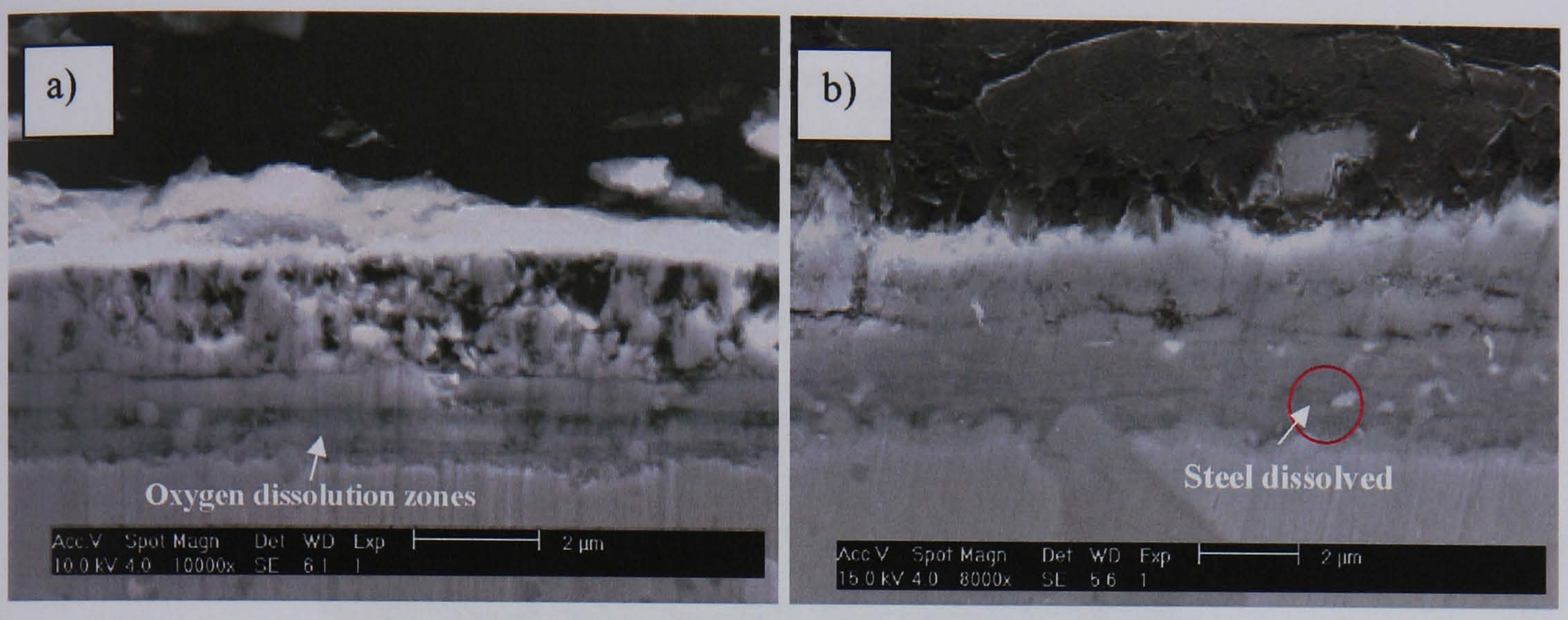

Fig.4.43. Oxide scale formed at **550 °C** under condition 2. a) After 15 minutes. b) After 4 hours.

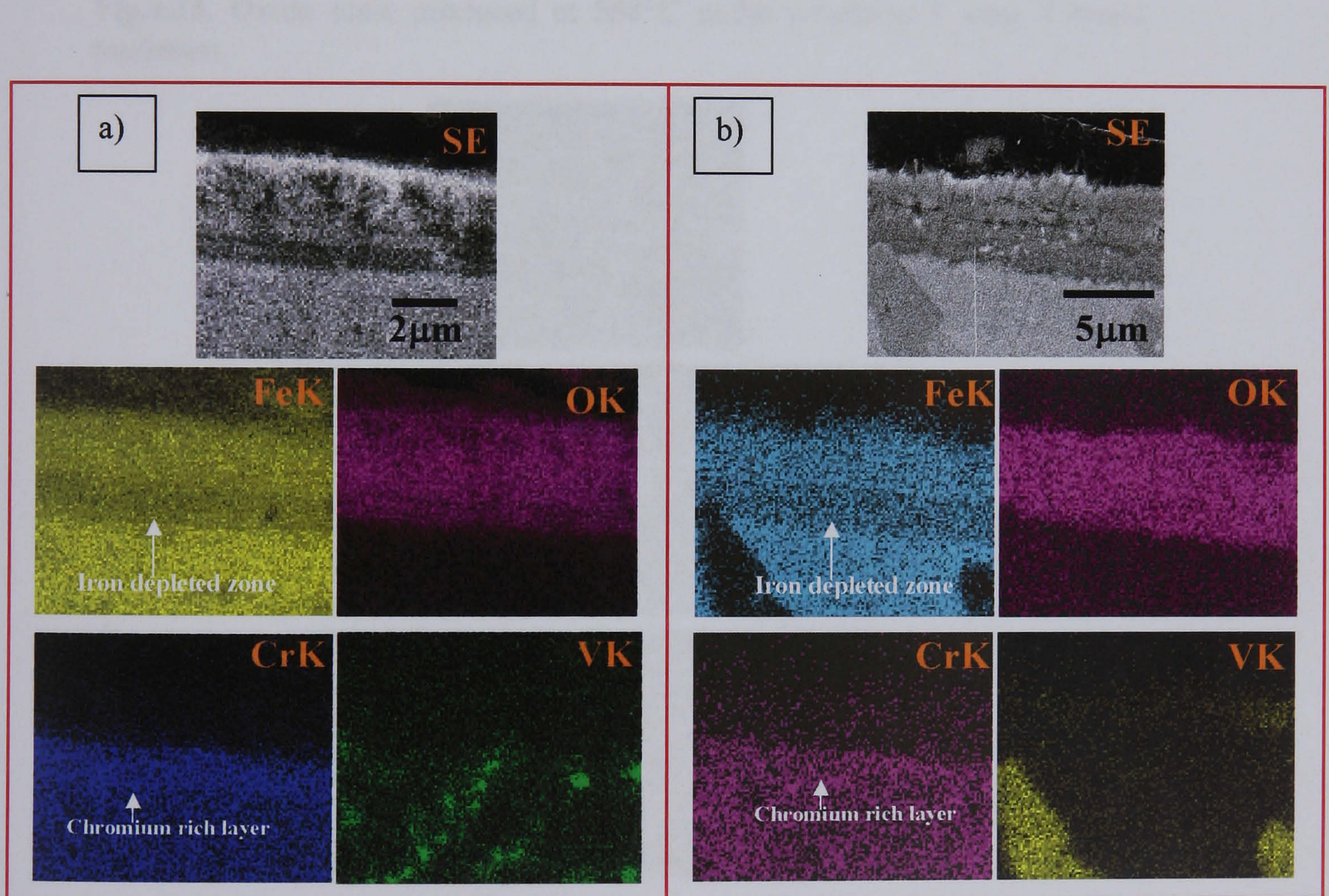

Fig.4.44. Energy dispersive x-ray dot mapping of the elements present in the oxide scale formed at **550°C** under condition 2. a) After 15 minutes. b) After 4 hours.

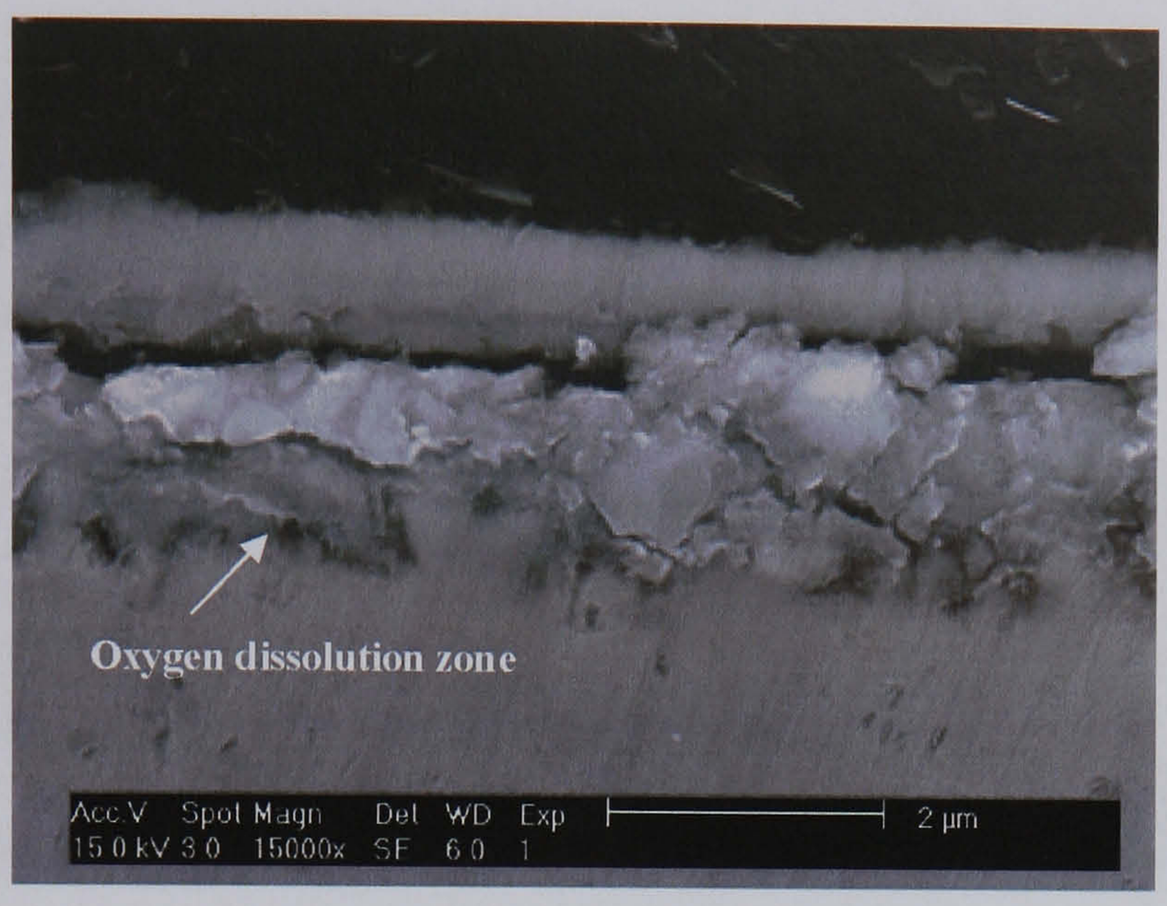

Fig.4.45. Oxide scale produced at **550°C** under condition 3 after 4 hours oxidation.

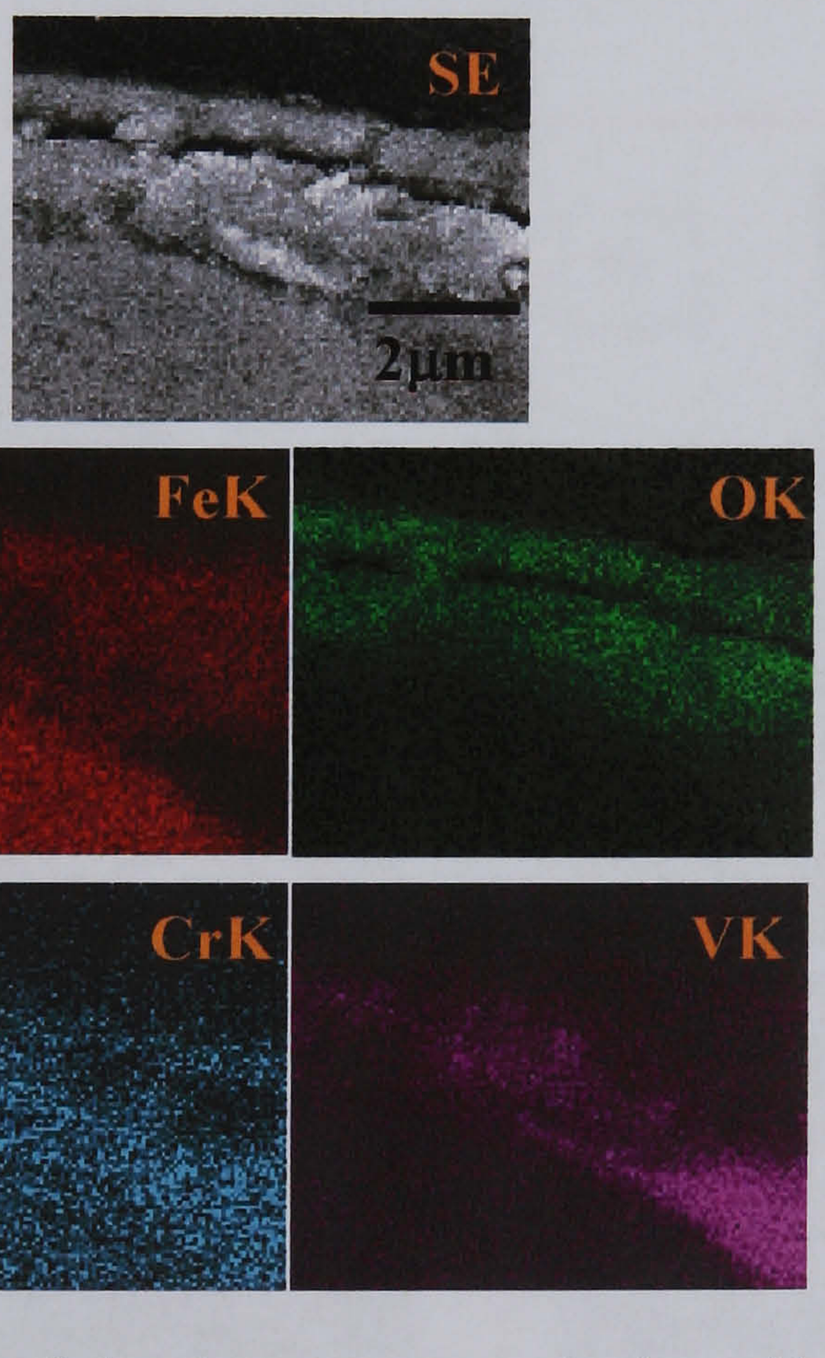

Fig.4.46. EDX dot maps of the elements present in the oxide scale shown in Fig.4.45.

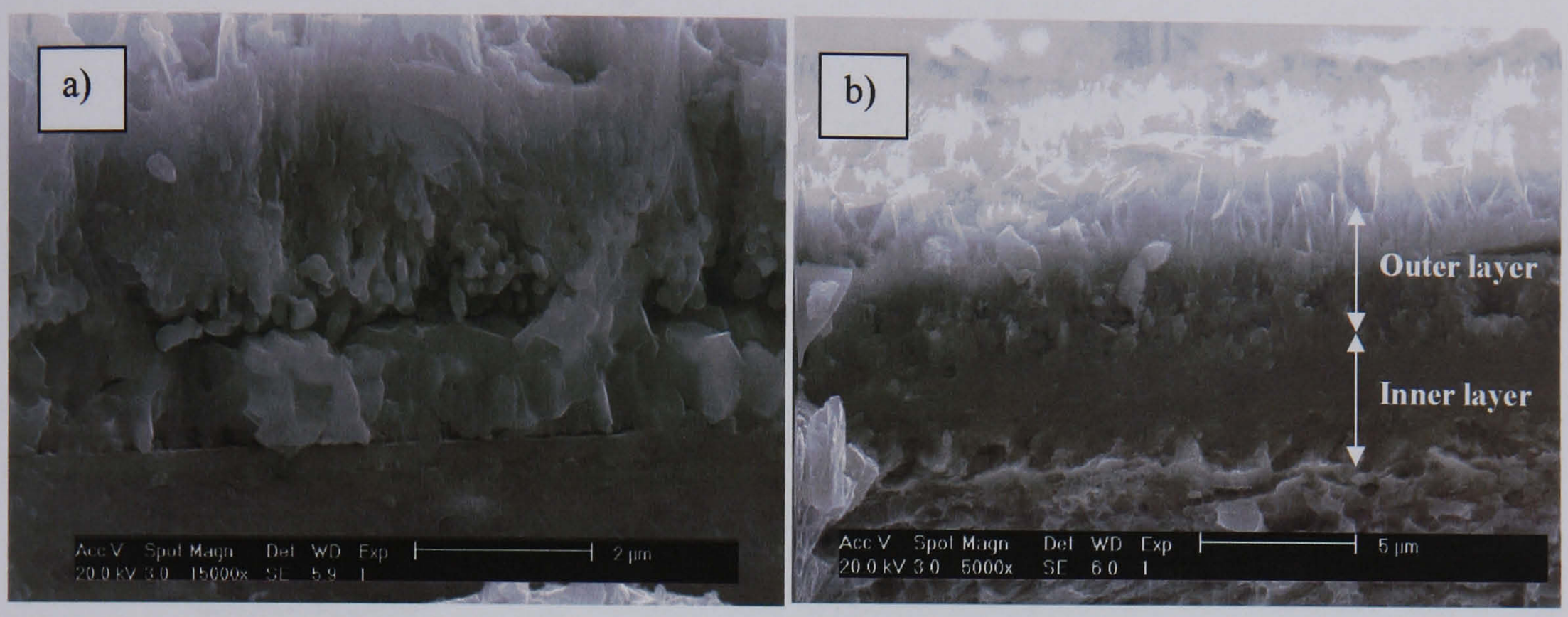

Fig.4.47. Fracture surfaces showing the microstructure of the samples oxidized at 615°C in wet conditions. a) After 4 hours under condition 1. b) After 1 hour under condition 2.

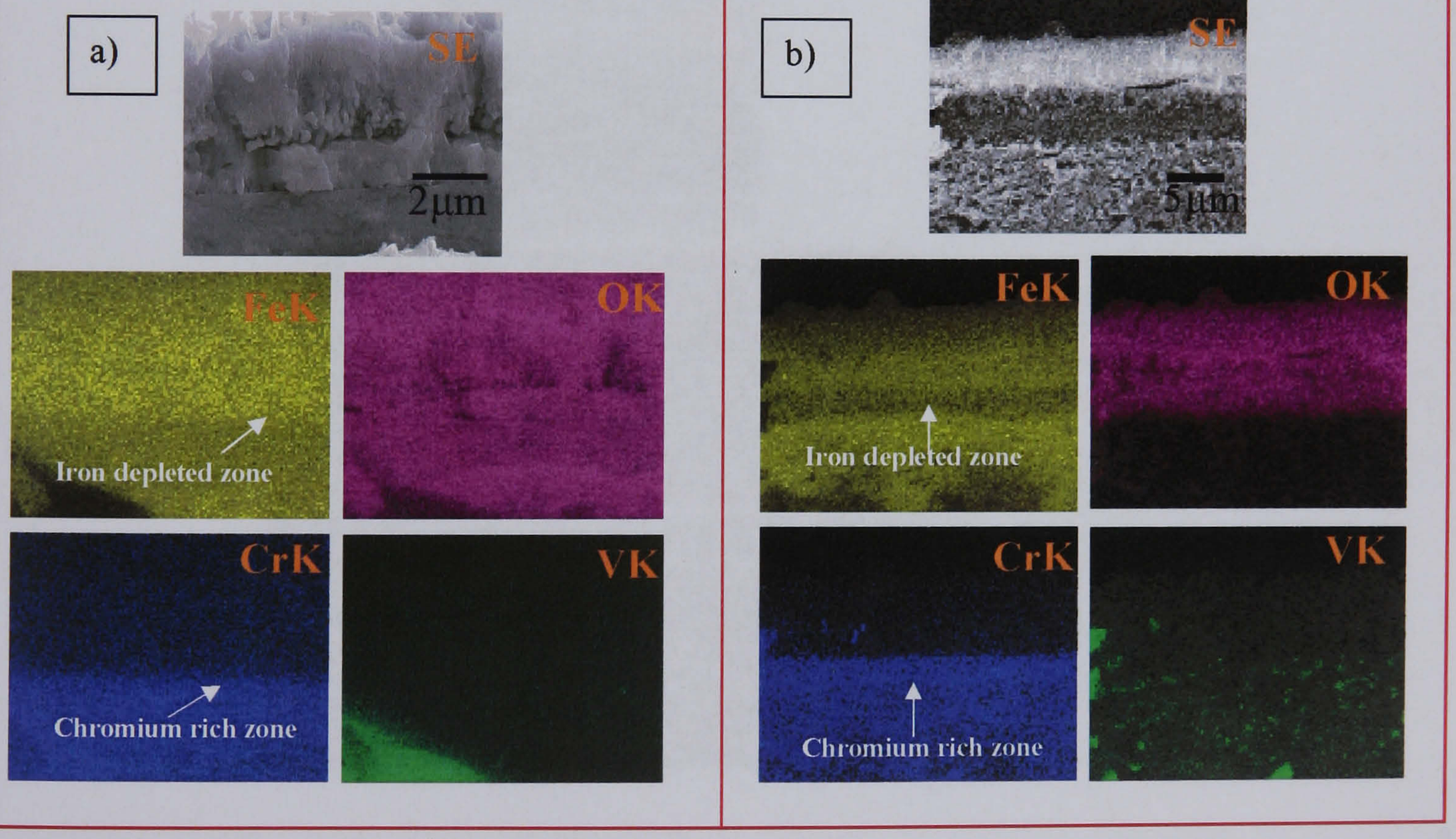

Fig.4.48. Energy dispersive x-ray dot maps of the images shown in Fig.4.47. a) After 4 hours under condition 1. b) After 1 hour under condition 2.

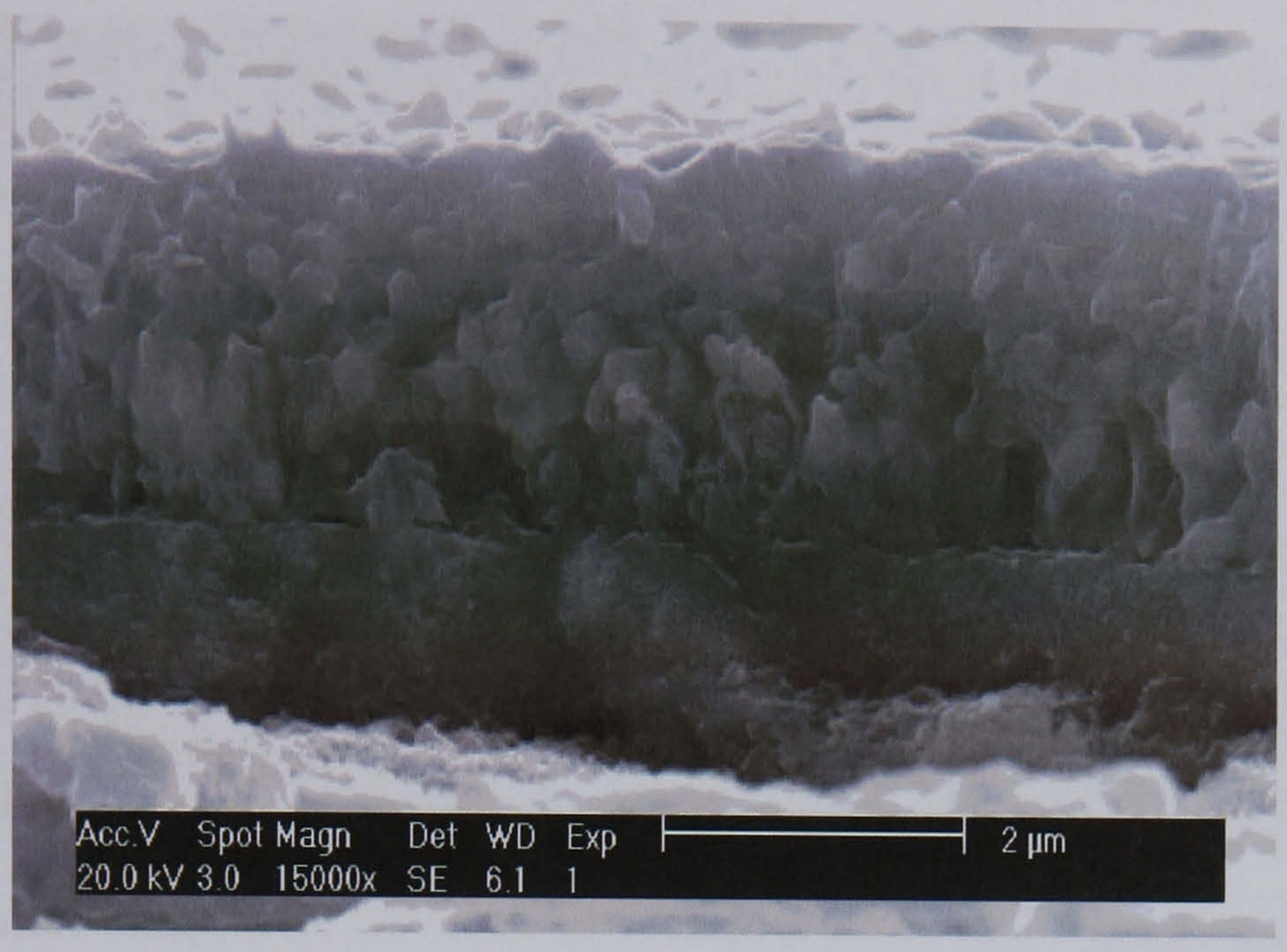

Fig.4.49. a) Fracture surface of the oxide layer grown at **615°C** under condition 3 after 4 hours.

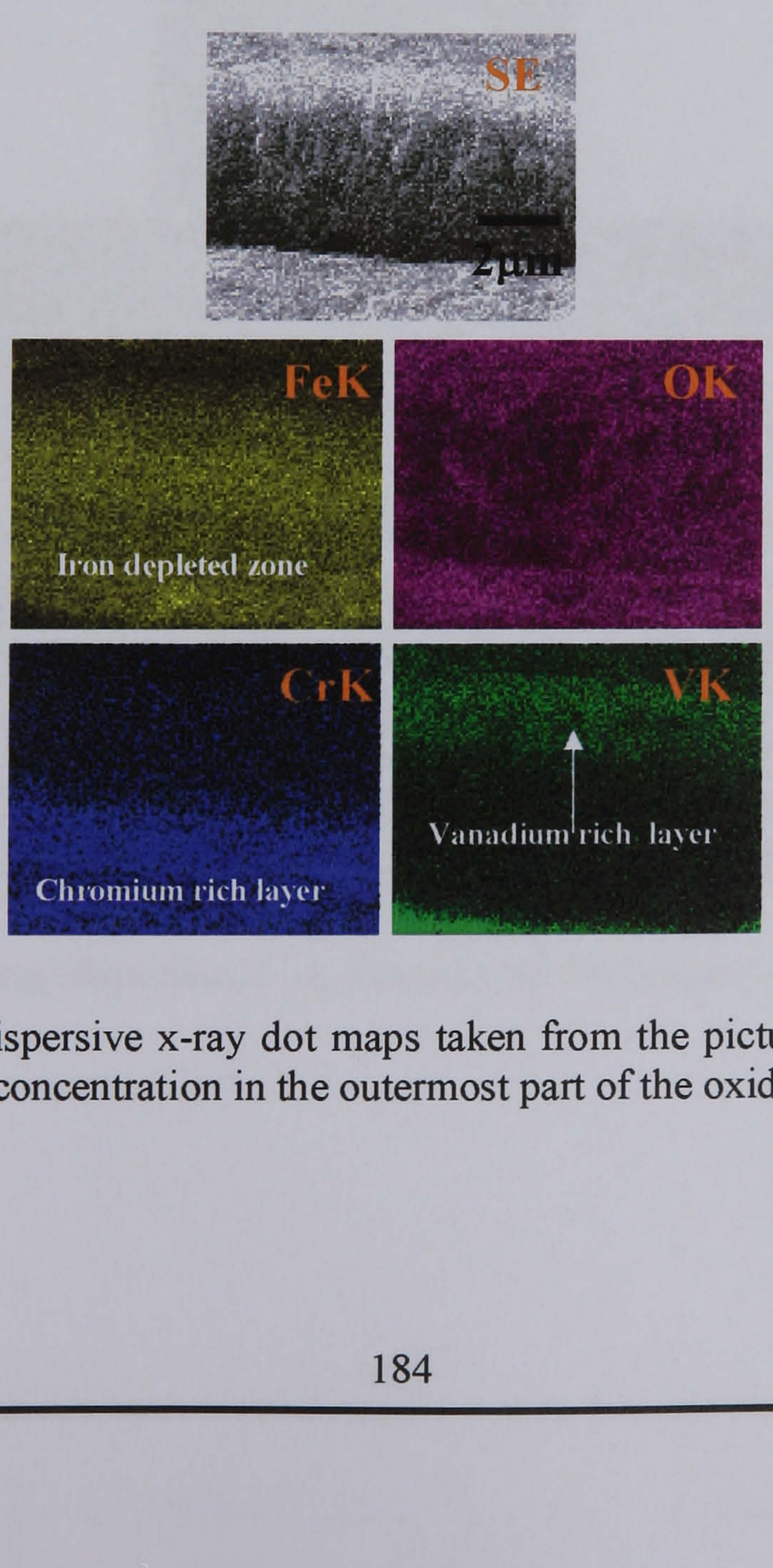

Fig.4.50. Energy dispersive x-ray dot maps taken from the picture in Fig.4.49. Note the high vanadium concentration in the outermost part of the oxide scale.

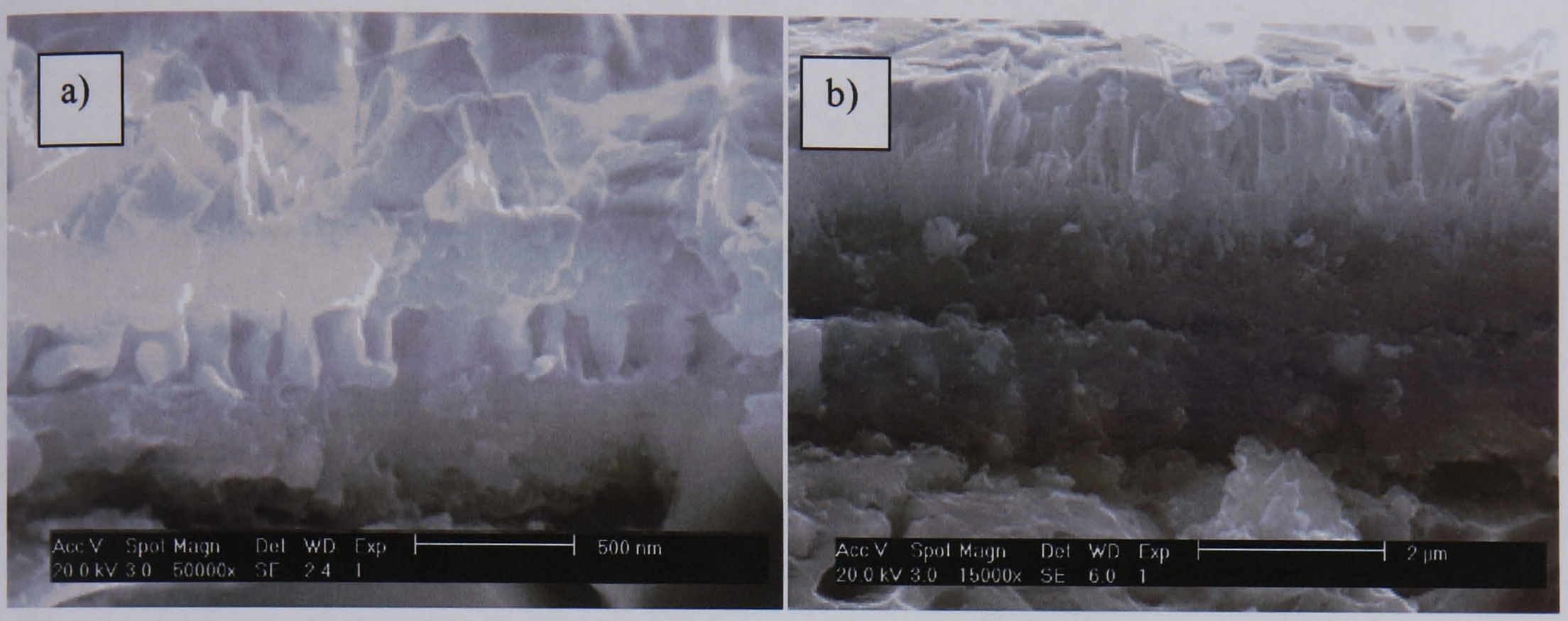

Fig.4.51. Fracture surfaces of the oxide layer obtained at **550°C** under condition 1.a) After 15 minutes b) After 4 hours.

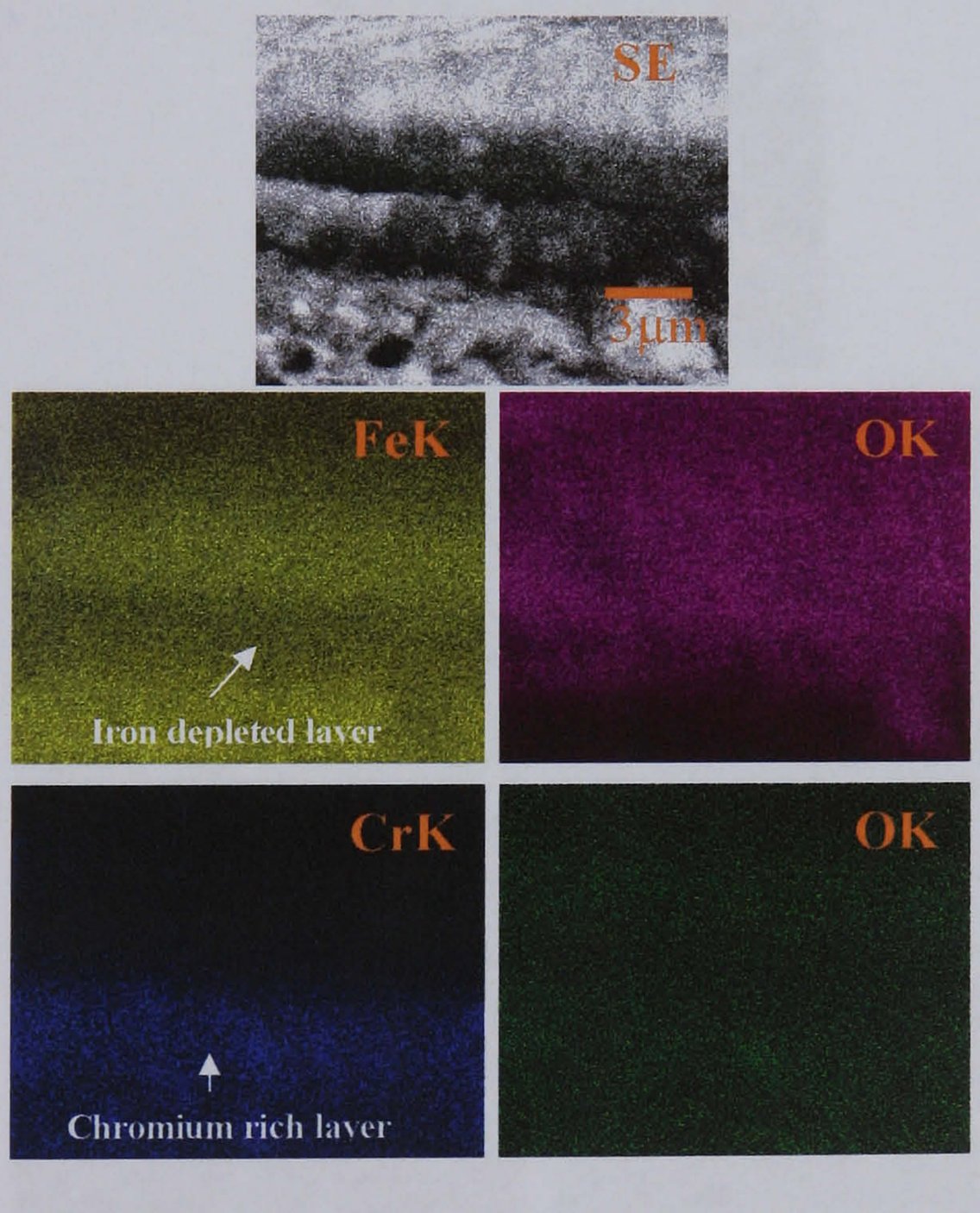

Fig.4.52. Energy dispersive x-ray dot maps of the sample of Fig .4.51 b) after 4 hours.

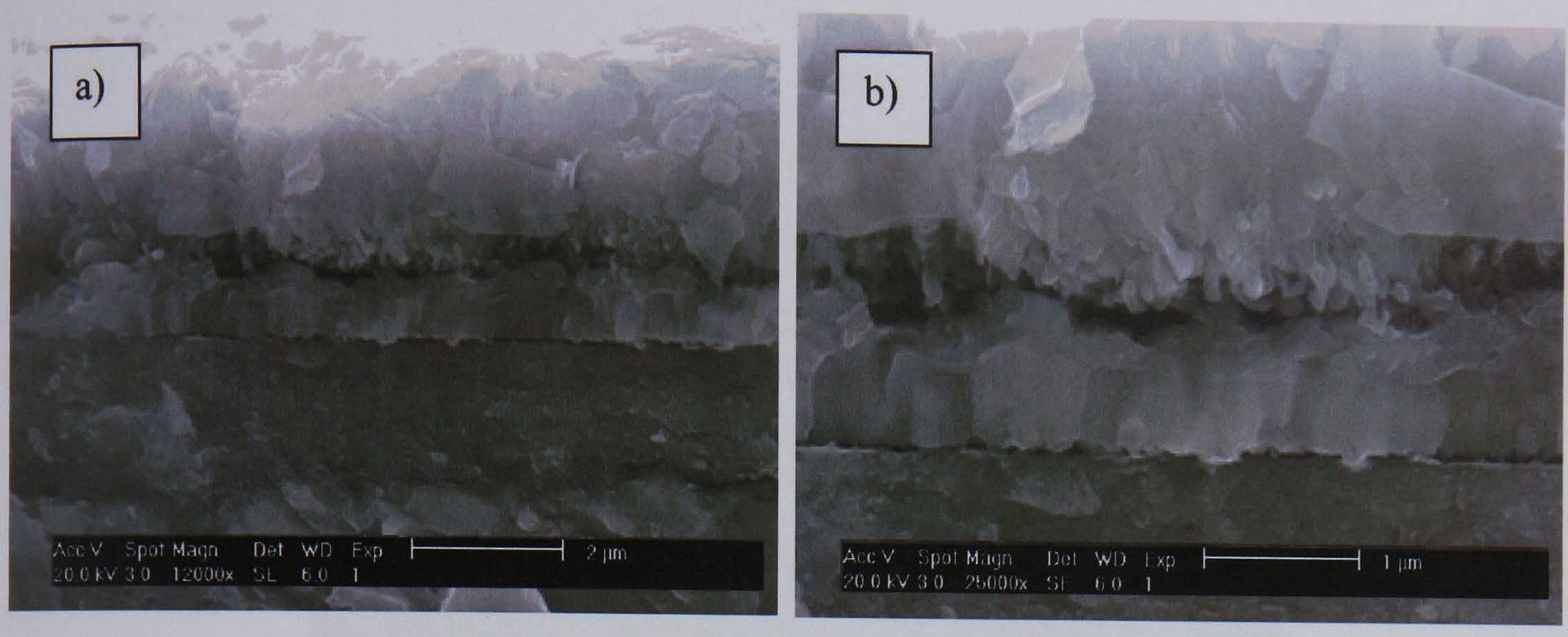

Fig.4.53. Fracture surfaces of the oxide layer obtained at **550°C** under condition 2. a) After 4 hours oxidation. b) Greater detail of the microstructure shown in a).

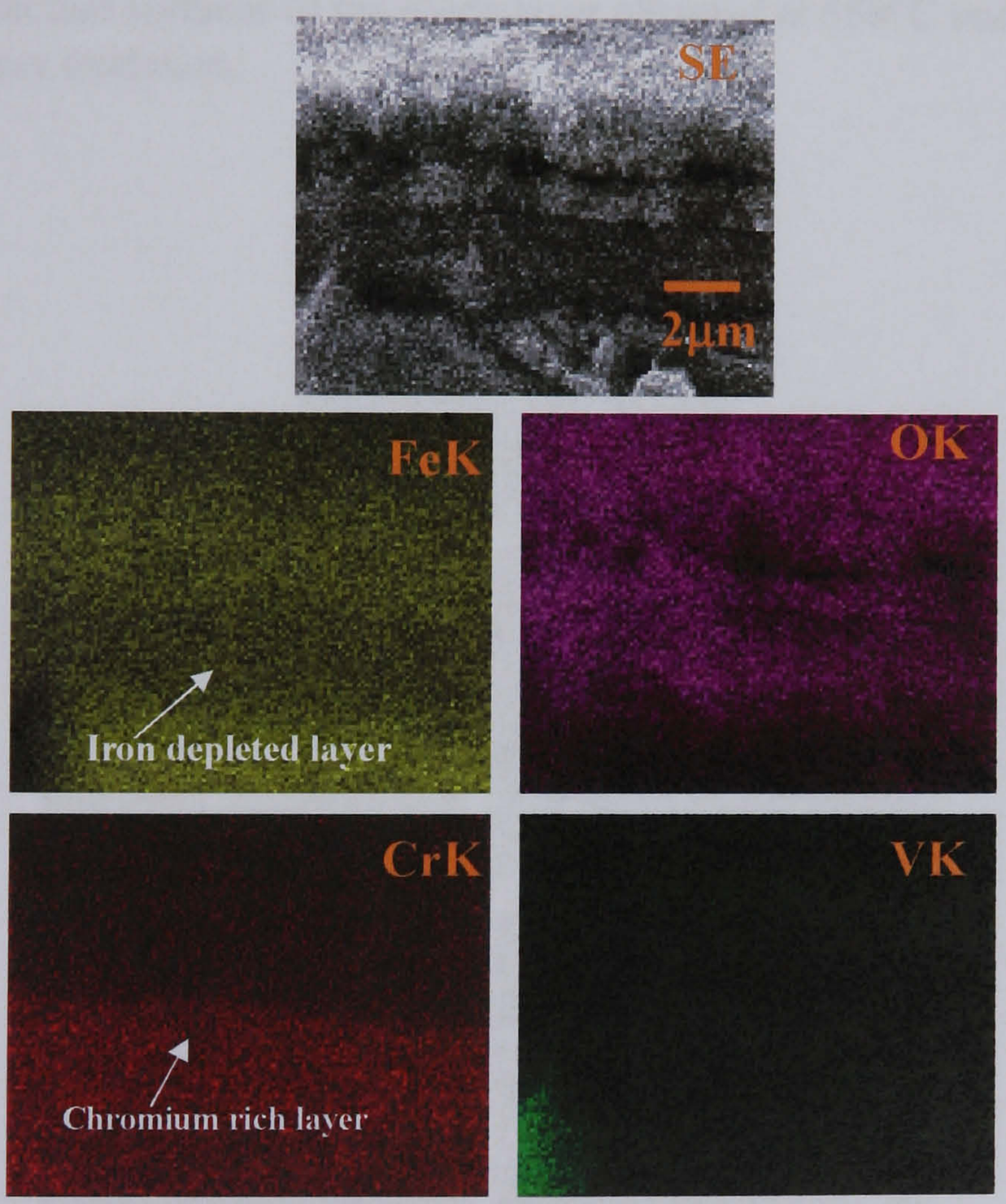

Fig.4.54. Energy dispersive x-ray dot maps of the microstructure shown in Fig.4.53 a).

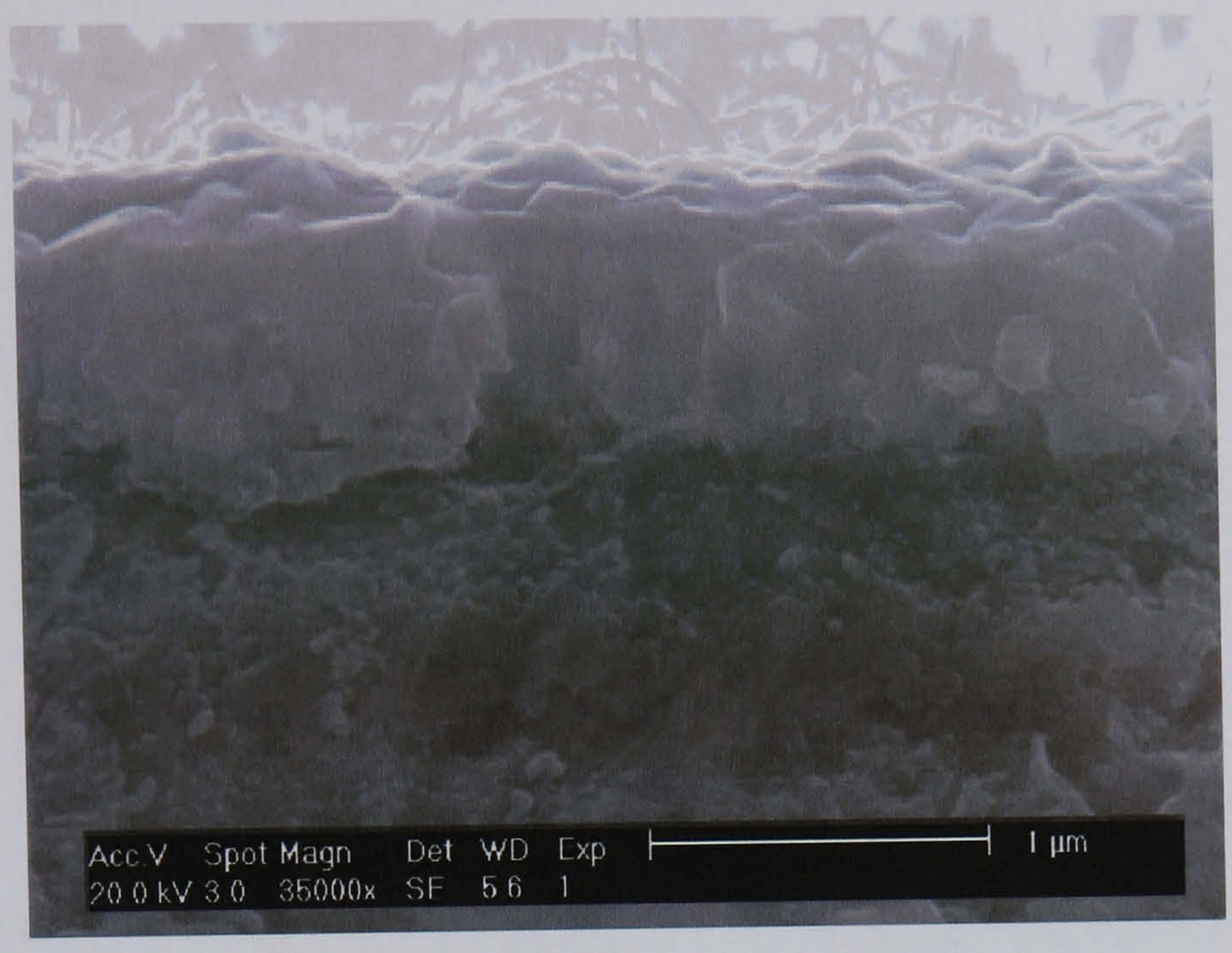

Fig.4.55. Fracture surfaces of the oxide layer obtained at **550°C** under condition 3 after 4 hours oxidation.

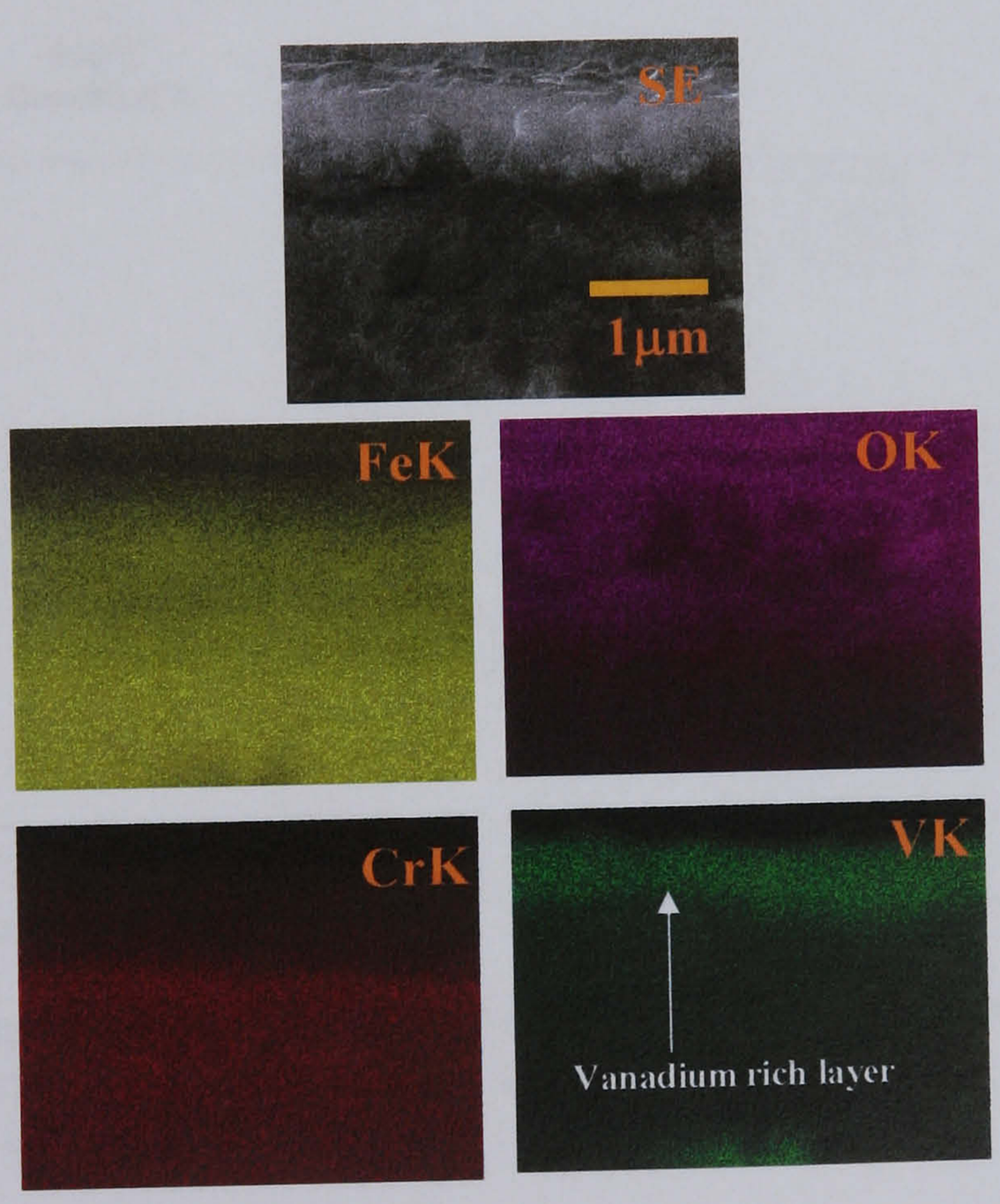

Fig.4.56. Energy dispersive x-ray dot maps of the fracture surface shown in Fig.4.55. Note the high vanadium concentration in the outermost layer.

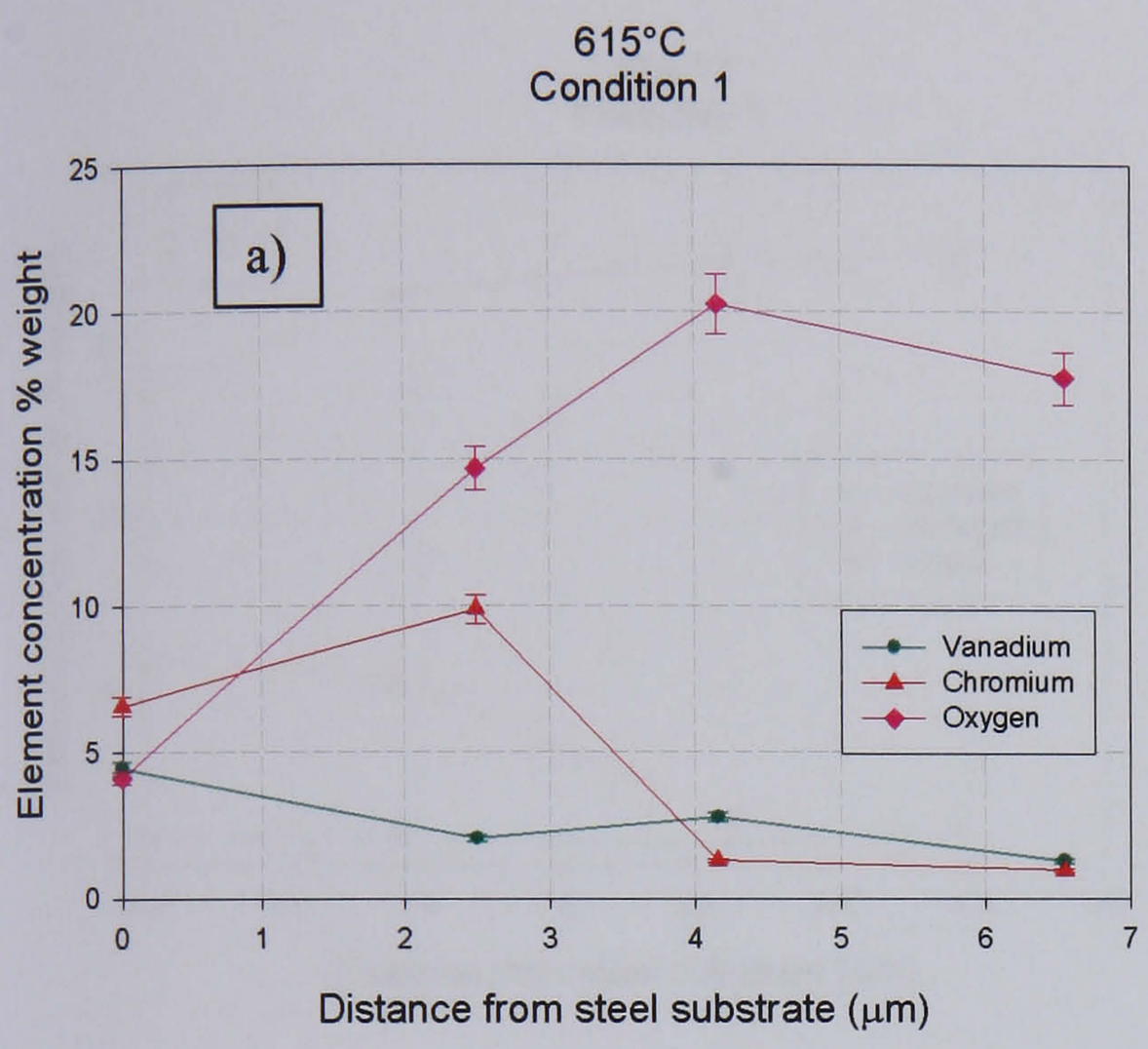

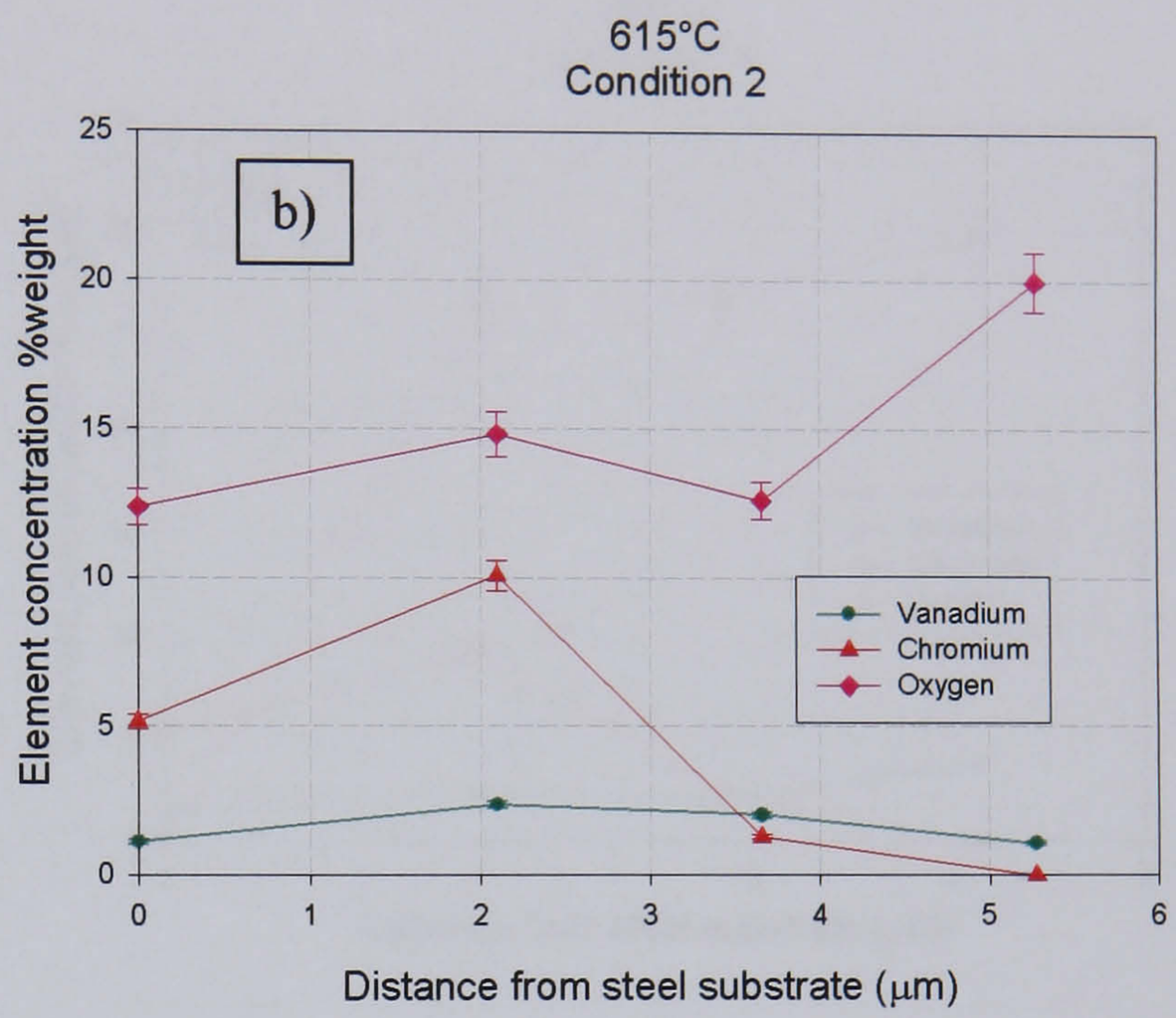

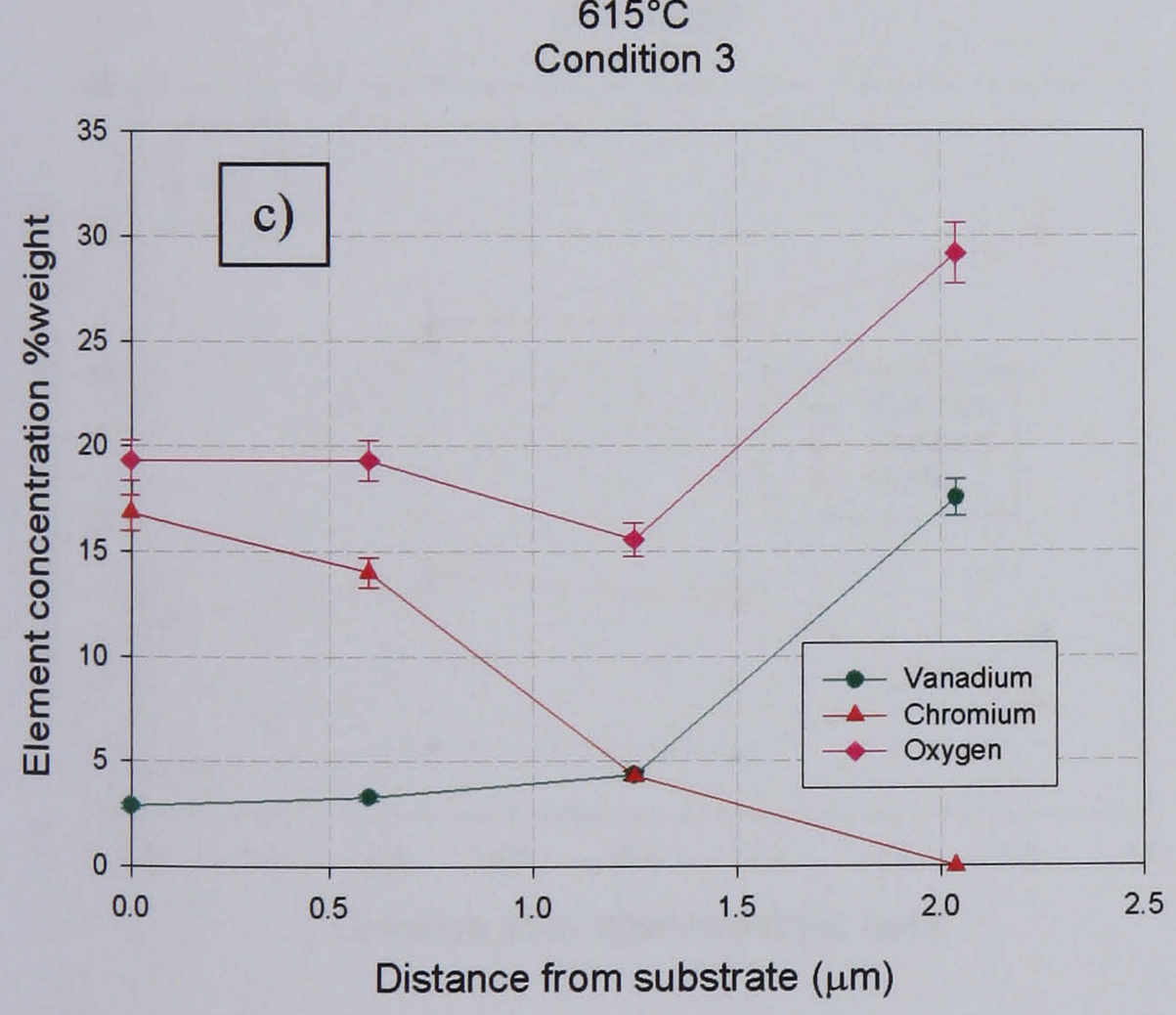

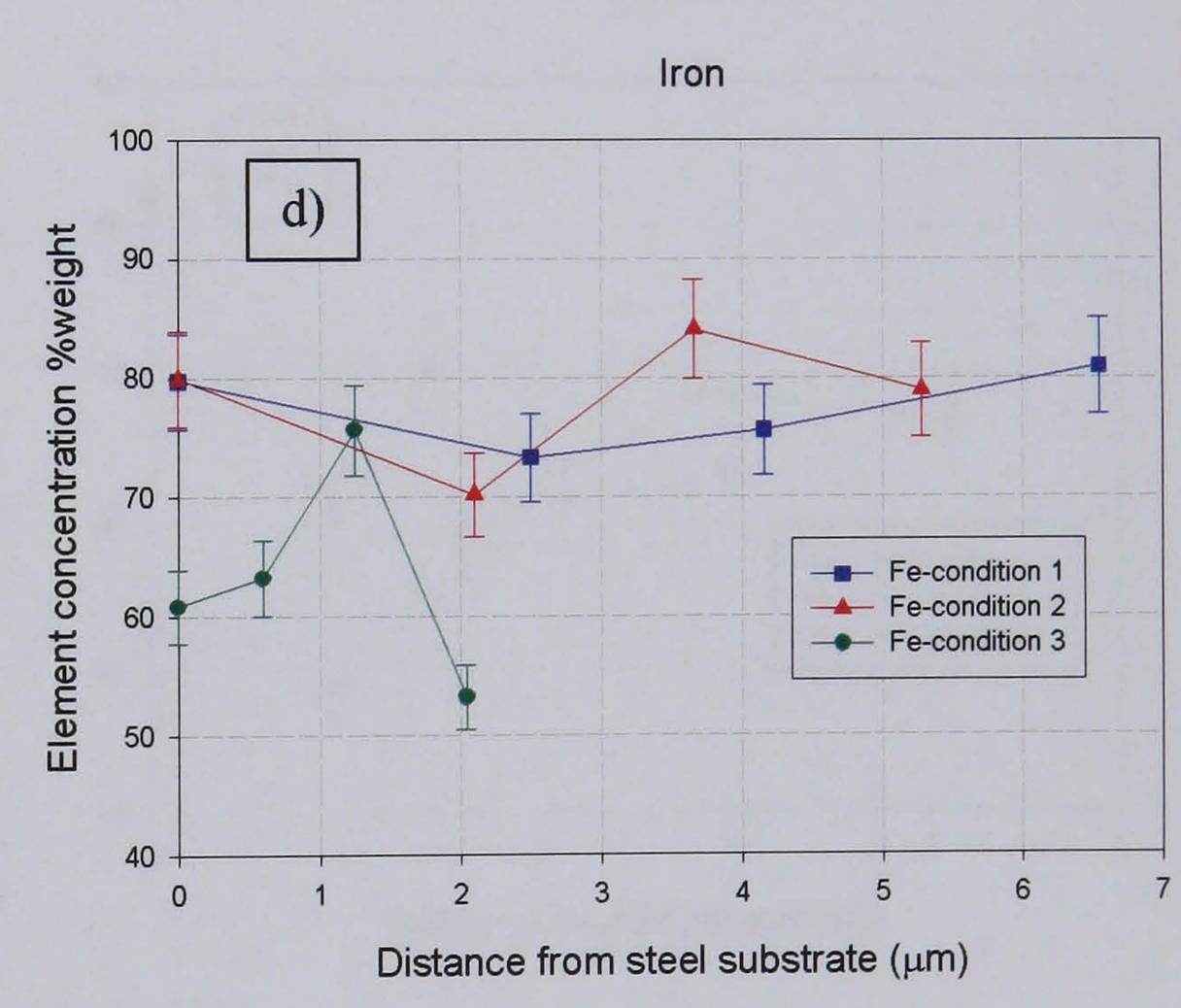

Fig.4.57. Element distribution across the oxide scale after 4 hours of exposure to the different atmospheres at **615°C**. a) Condition 1. b) Condition 2. c) Condition 3. d) Distribution of iron across the scale.

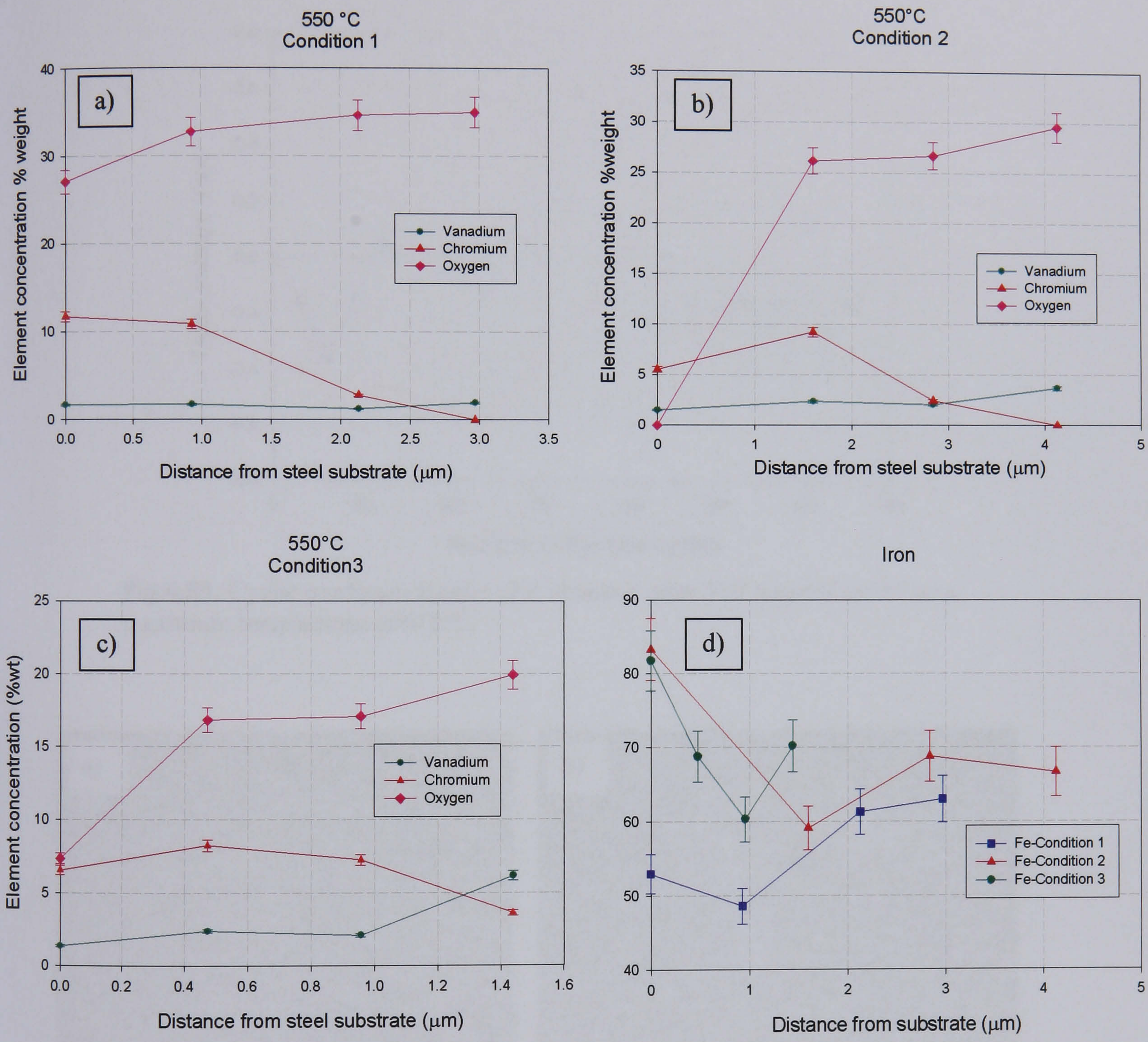

Fig.4.58. Element distribution across the oxide scale after an oxidation time of 4 hours at **550°C**. a) Condition 1. b) Condition 2 c) Condition 3. d) Distribution of iron across the scale.

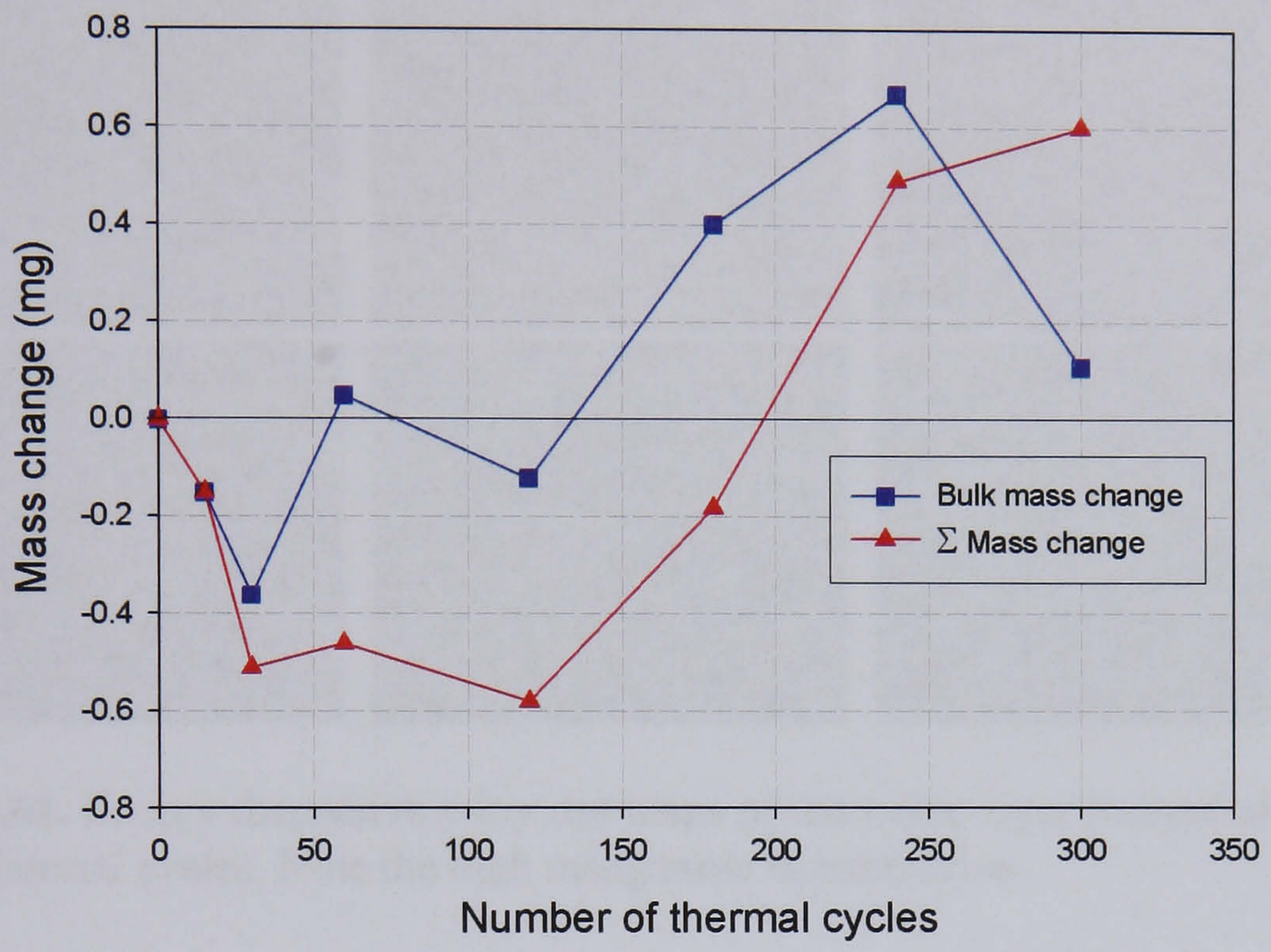

Fig.4.59. Cyclic oxidation kinetic plot obtained after 300 thermal cycles at a maximum temperature of 615°C.

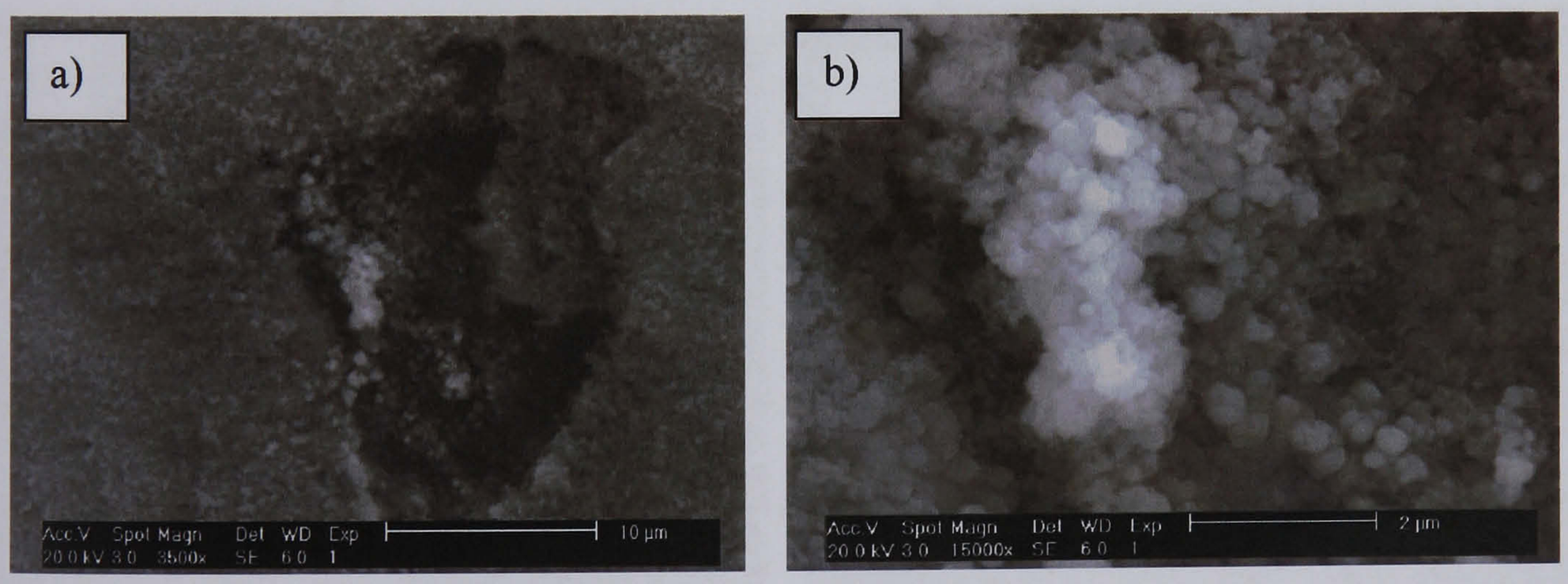

Fig.4.60. a) Surface morphology of the sample after the action of 120 thermal cycles.
b) Fine oxide granules.

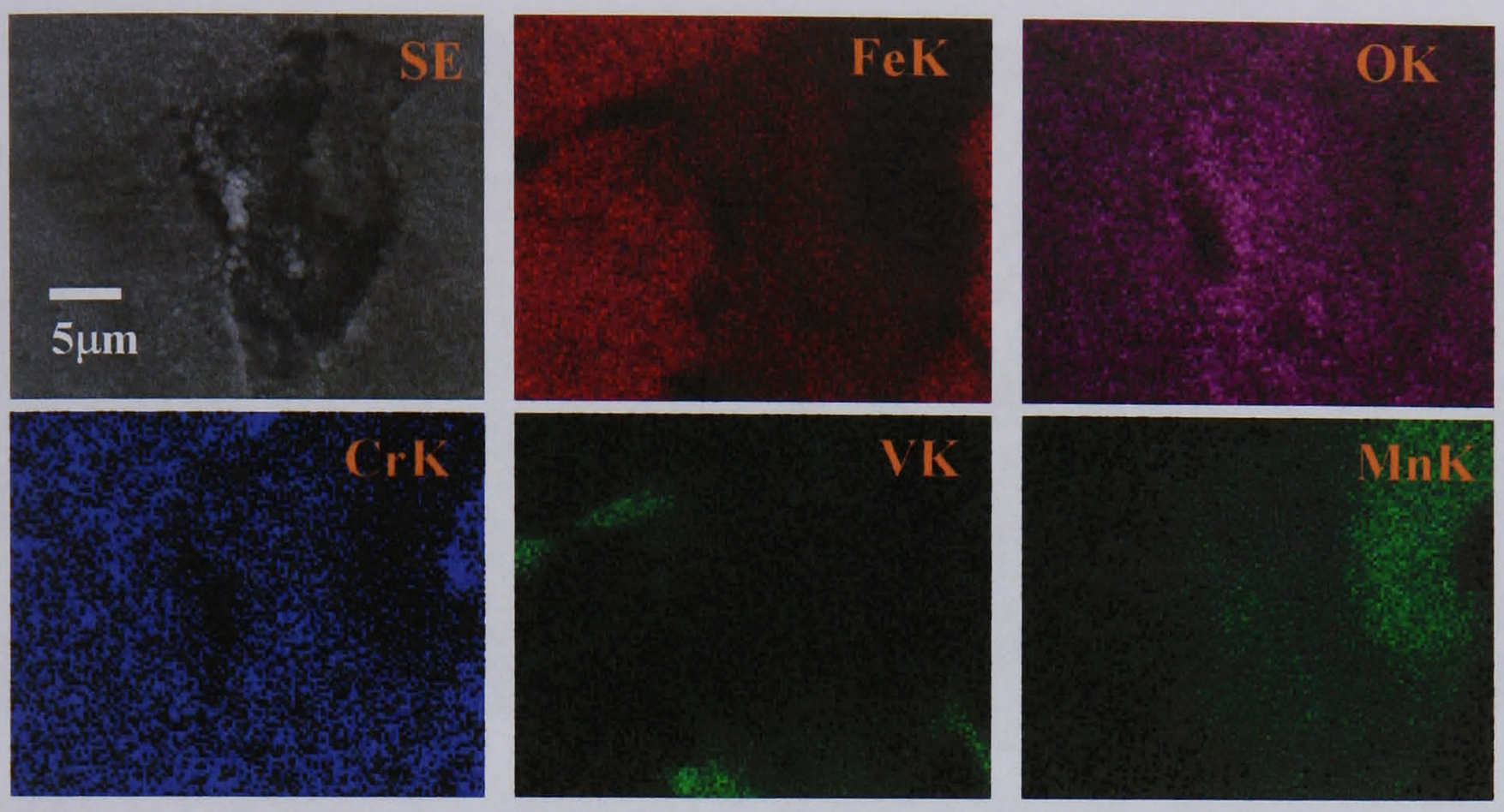

Fig.4.61. Energy dispersive x-ray dot maps of the oxide layer formed after 120 thermal cycles. Note the high manganese concentration.

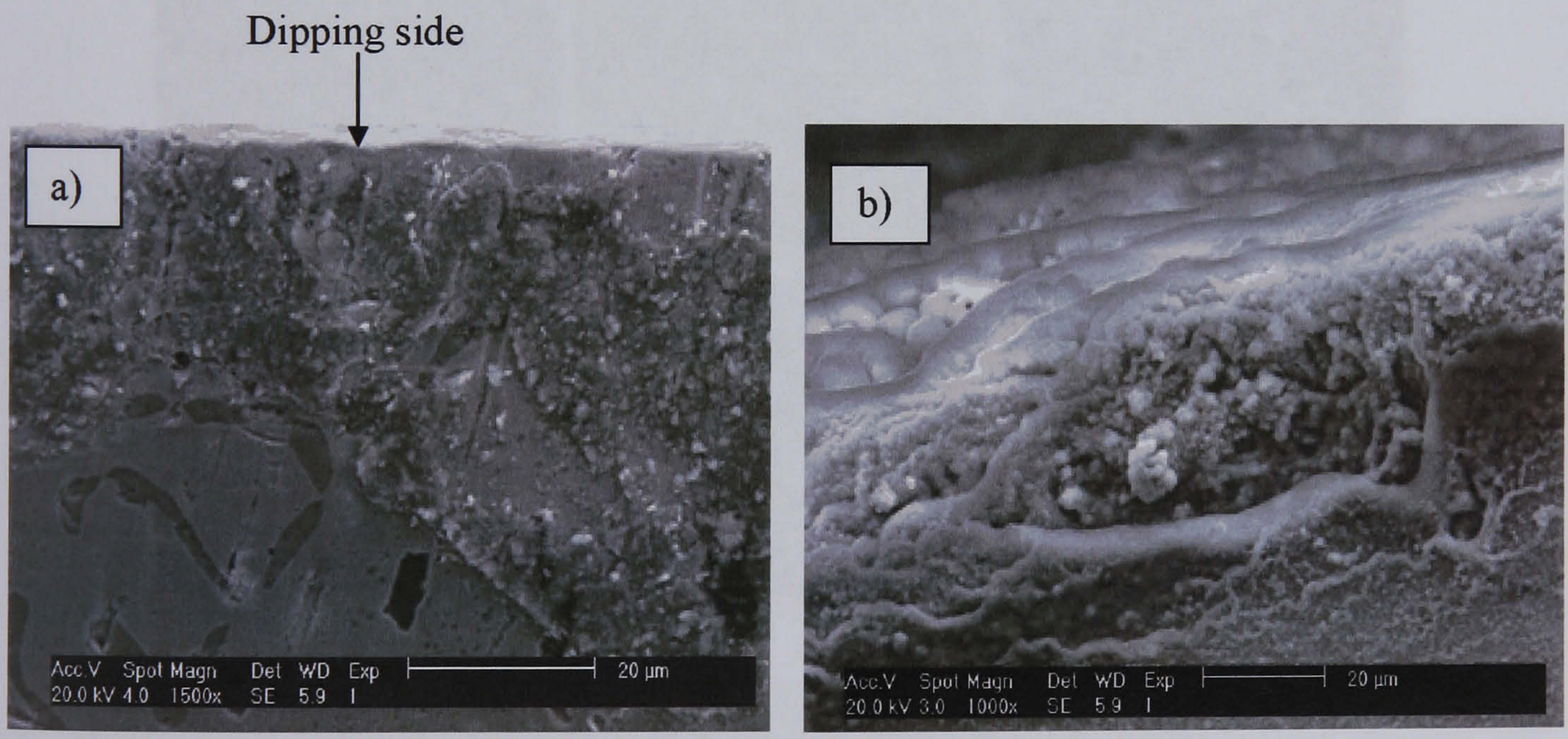

Fig.4.62. a) Oxide formation near to the zone that first entered into contact with the cooling water after the passage of 240 cycles b) Oxide formed after 300 thermal cycles.

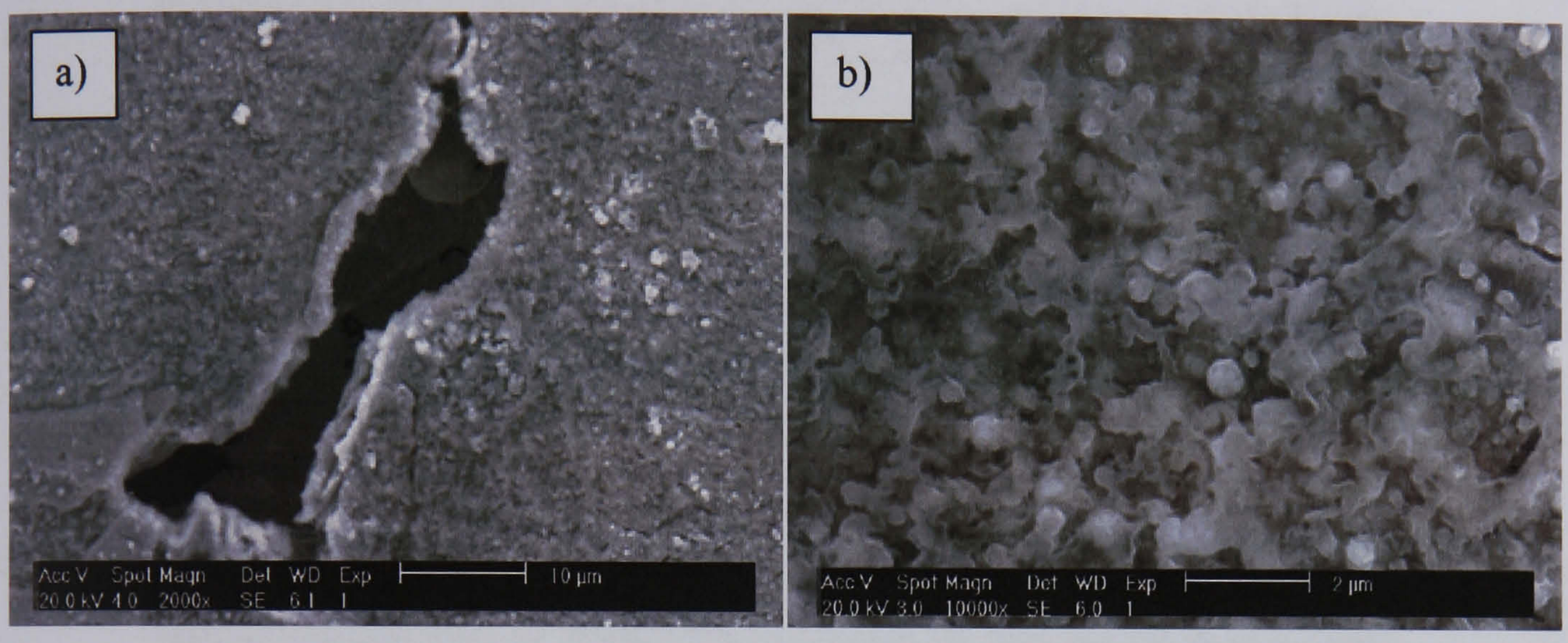

Fig.4.63. a) Formation of a very fine grained oxide layer and spallation of a carbide after 240 thermal cycles. b) Magnification to the fine oxide granules.

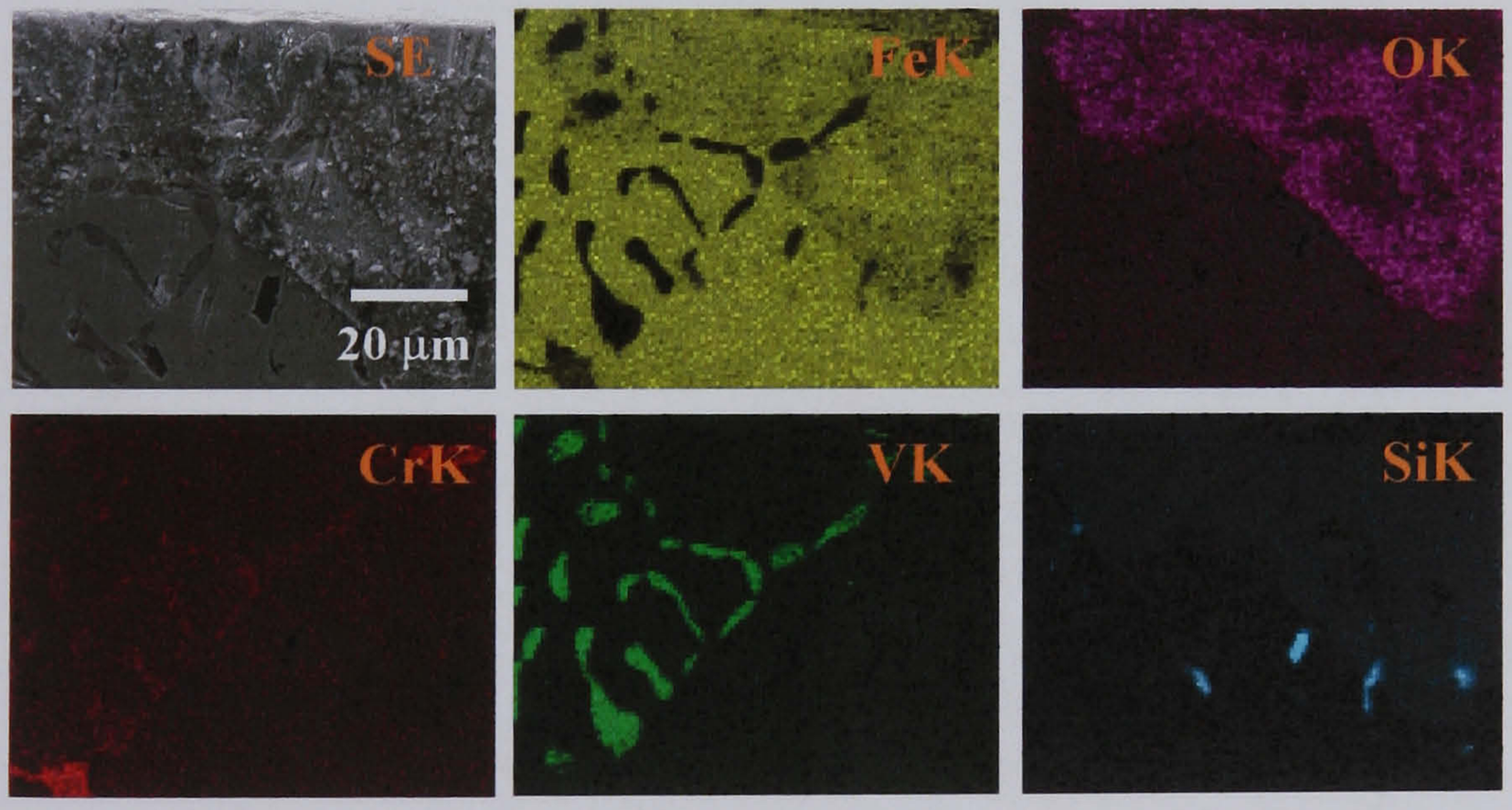

Fig.4.64 Energy dispersive x-ray dot maps taken from Fig.4.62.a) showing the elements present in the formation of the oxide layer after 240 cycles.

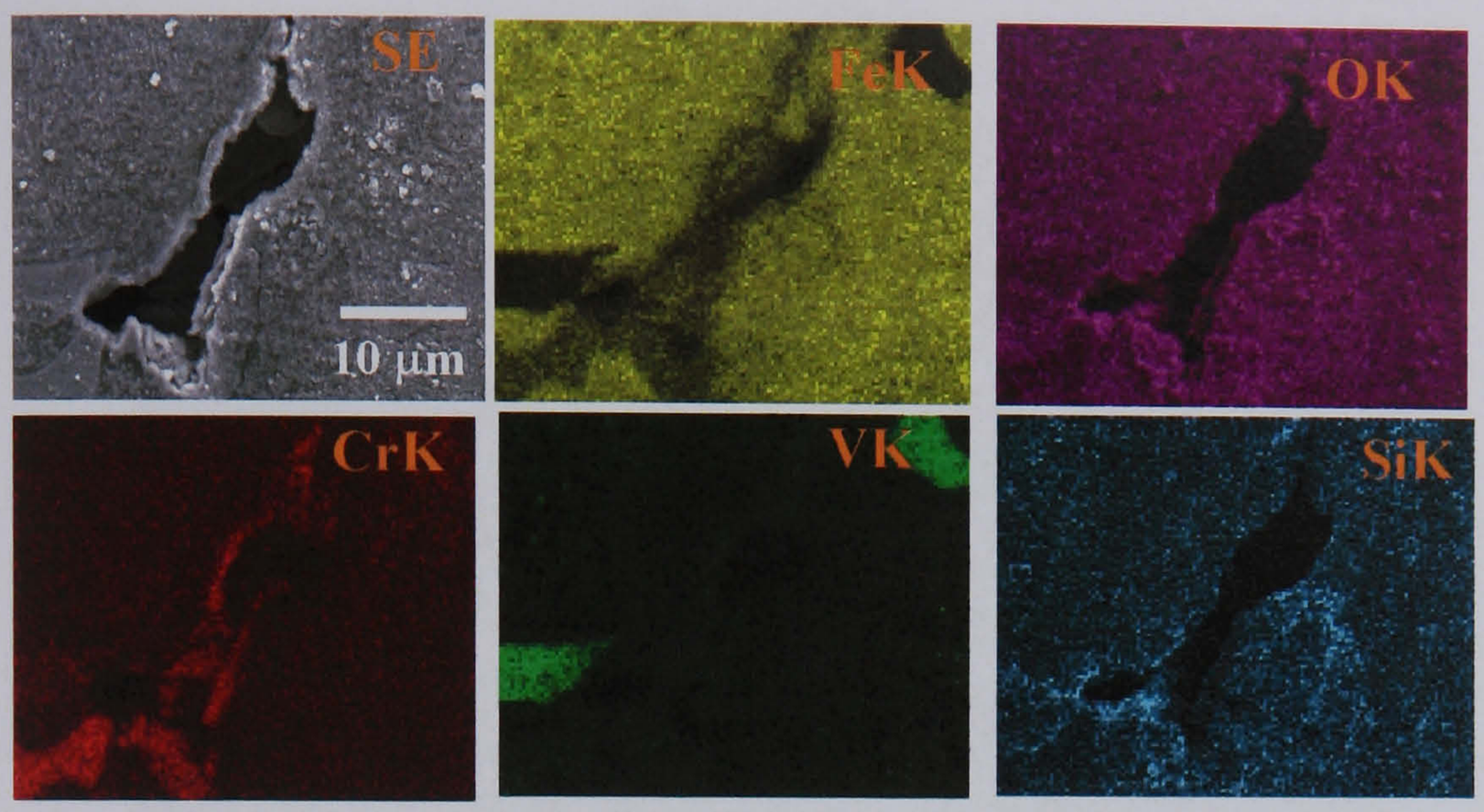

Fig.4.65. EDX dot map of the elements present in the oxide layer shown in Fig.4.63.a)

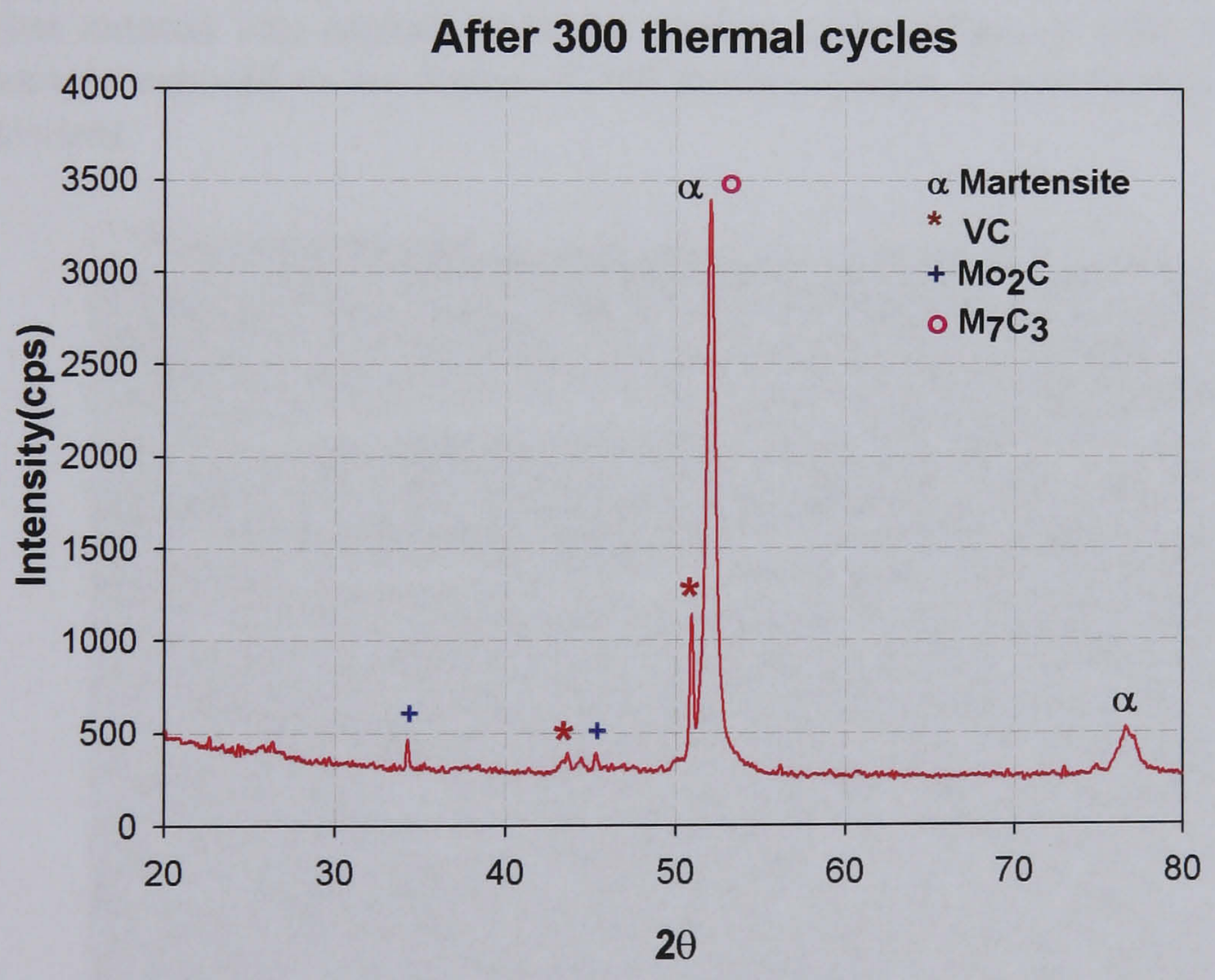

Fig.4.66. XRD diffraction pattern taken from the sample exposed to 300 thermal cycles. Oxides were not detected during the scan, only microstructural components were identified.

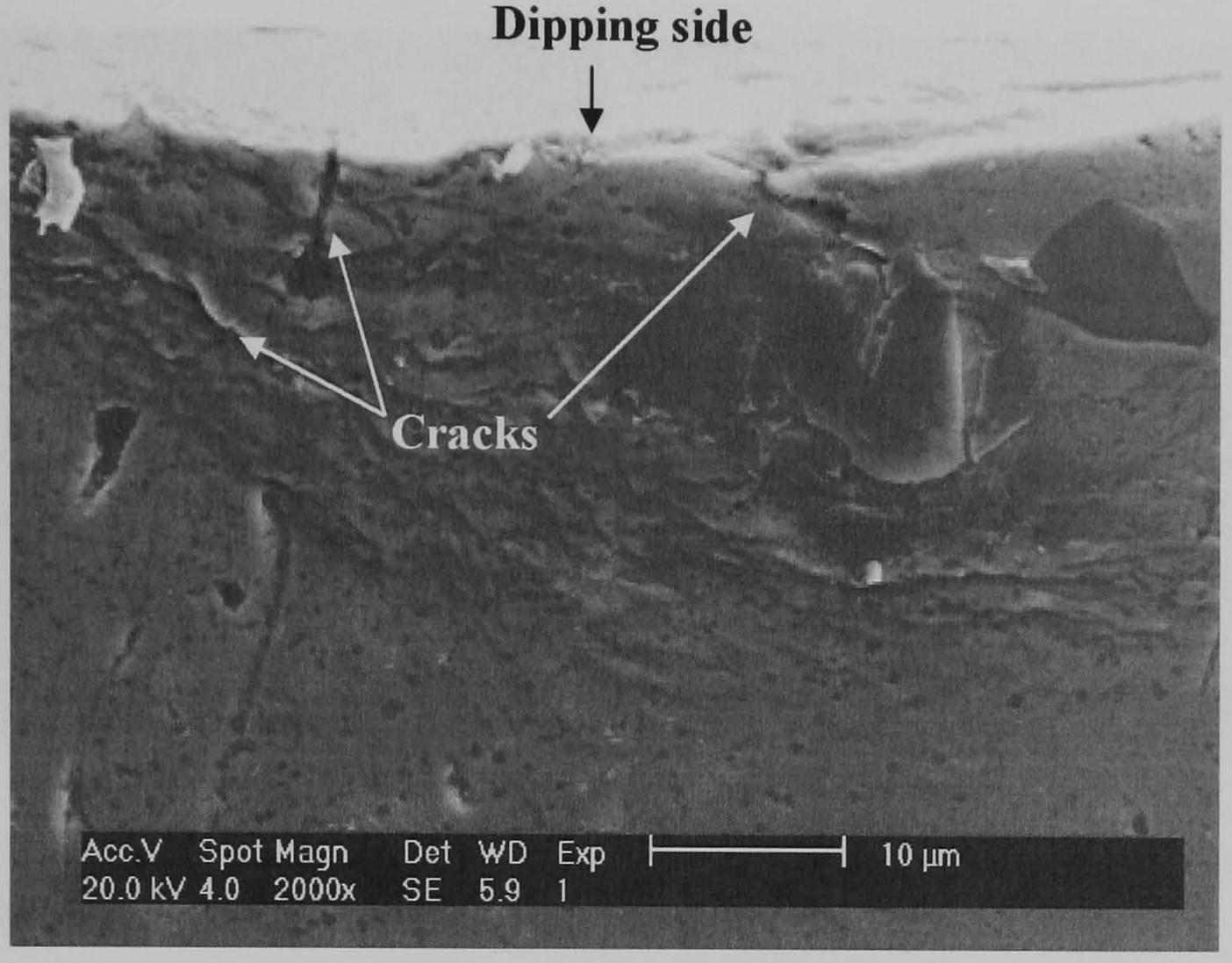

Fig.4.67. Severe plastic deformation zone found near to the zone that first entered into contact with the cooling water (dipping side) in the sample exposed to the action of 240 thermal cycles. Crack formation is evident.

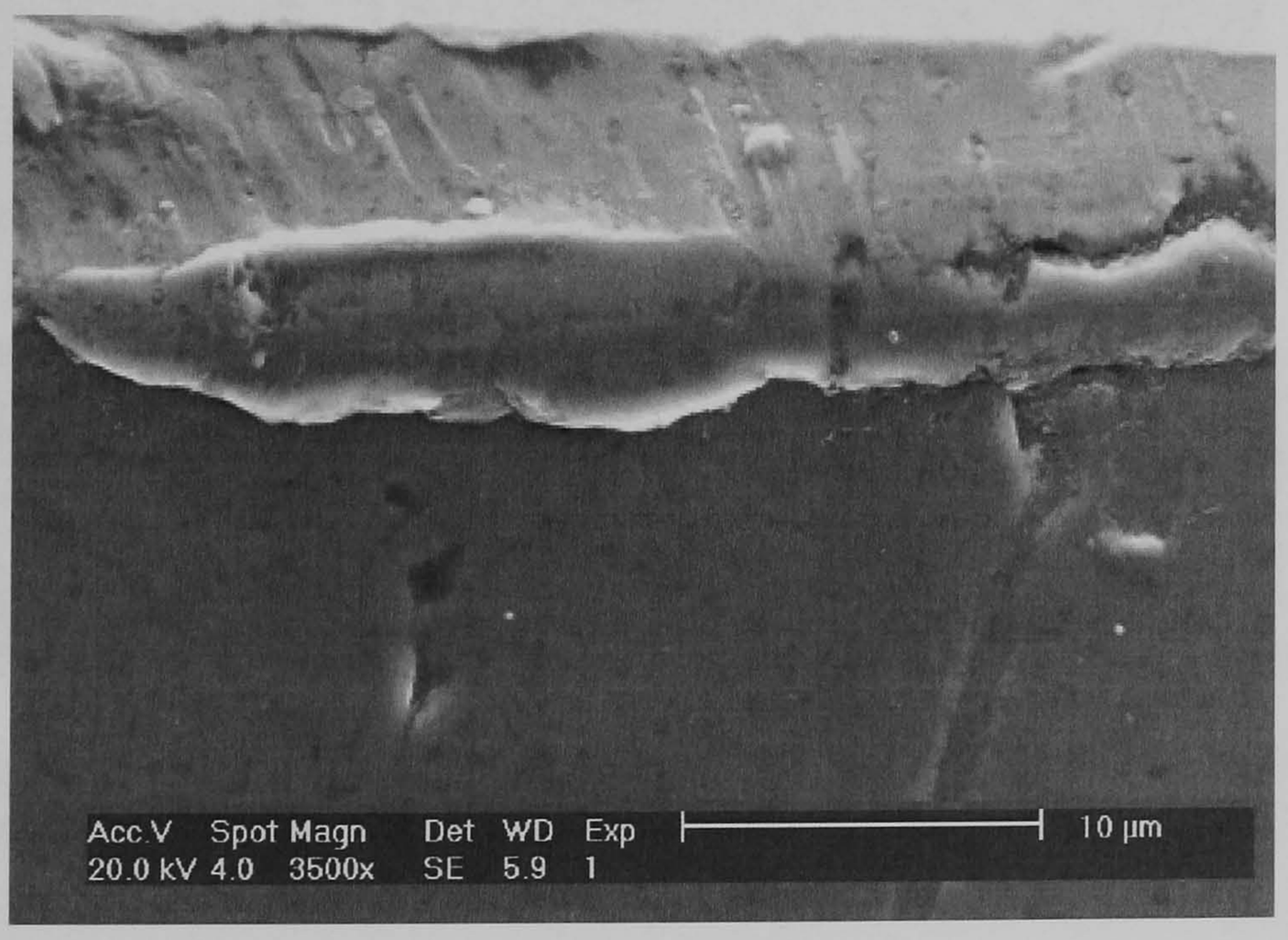

Fig.4.68. Zone containing a high degree of the plastic deformation and spallation of the steel in a sample exposed to the action of 300 thermal cycles.

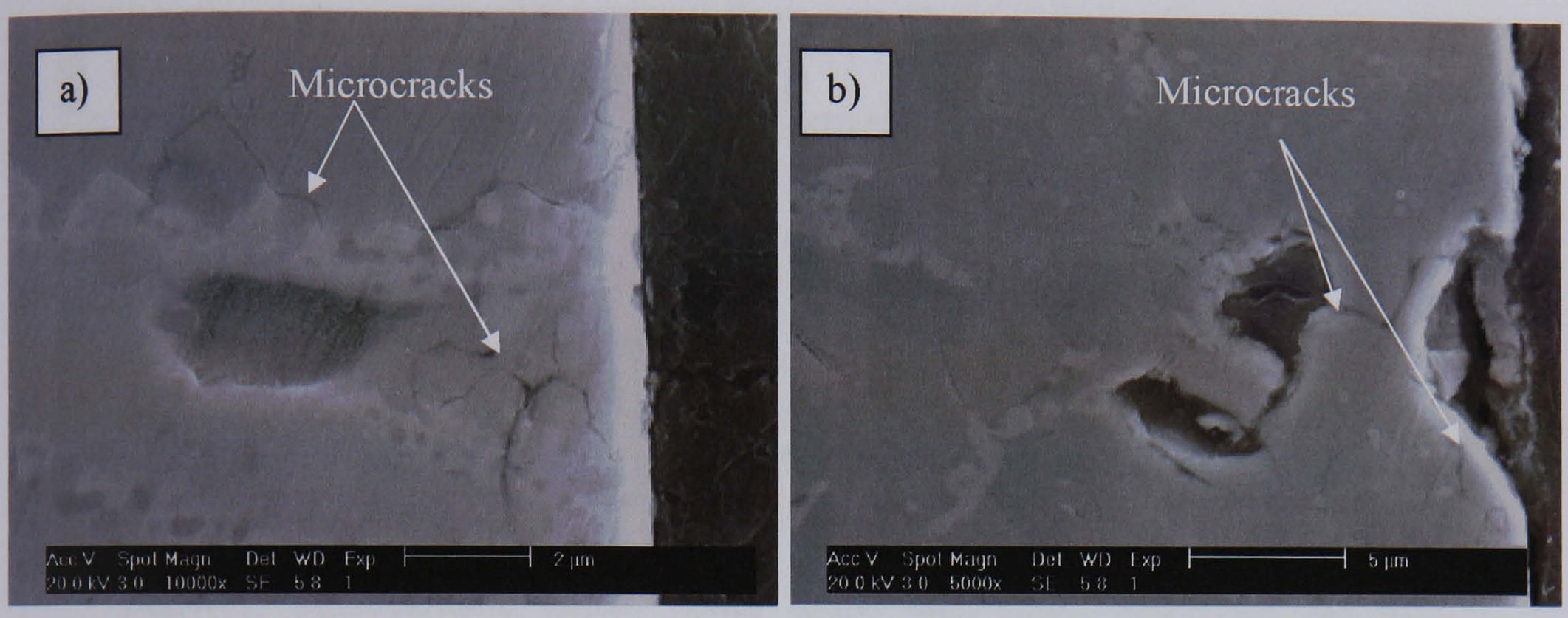

Fig.4.69. Cross sections of the steel showing propagation of micro cracks near carbides. a) After 240 cycles. b) After 300 cycles.

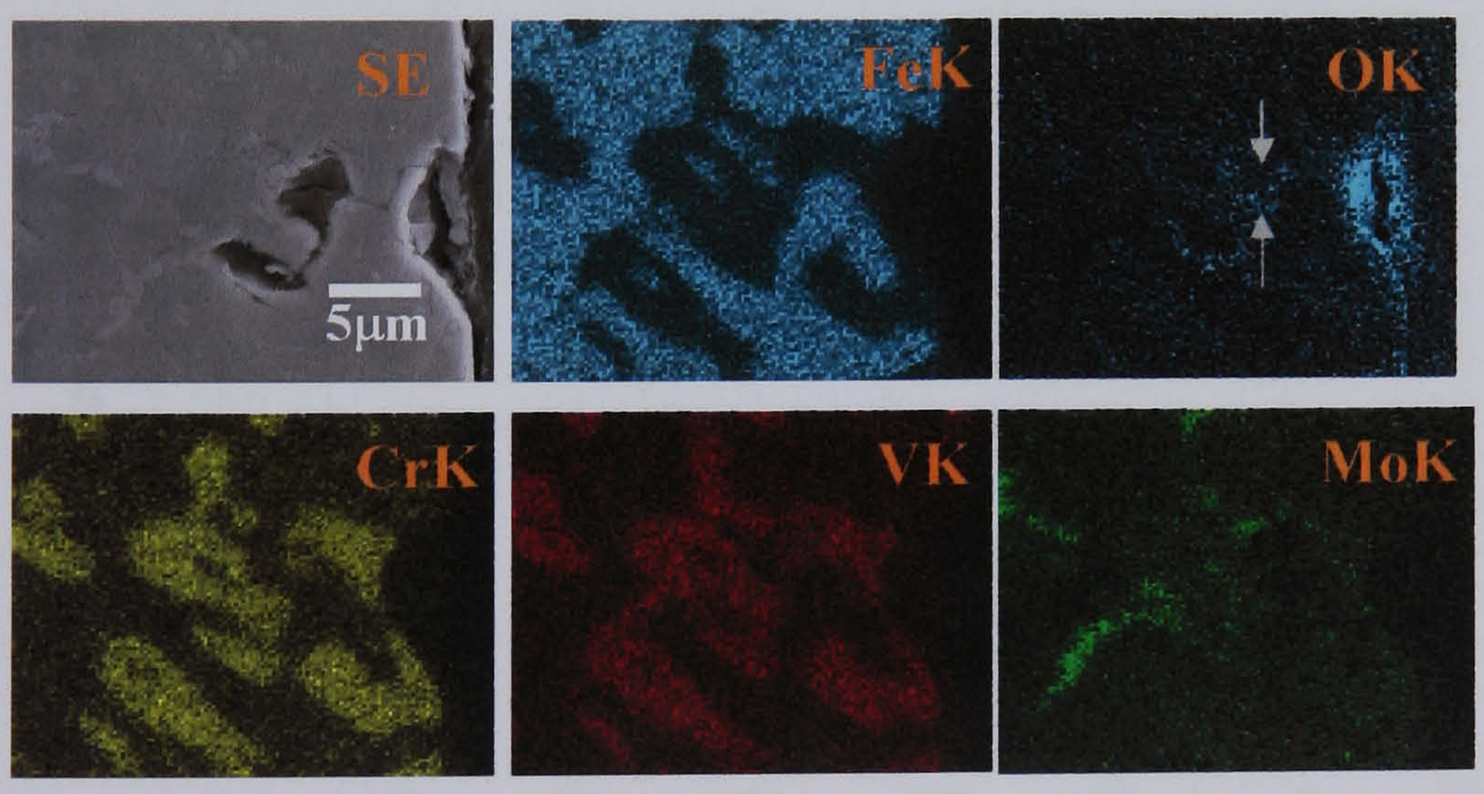

Fig.4.70. Energy dispersive x-ray dot maps taken from Fig.4.69.a). A small concentration of oxygen is observed as well as the propagation path of this element, as indicated by the arrows.

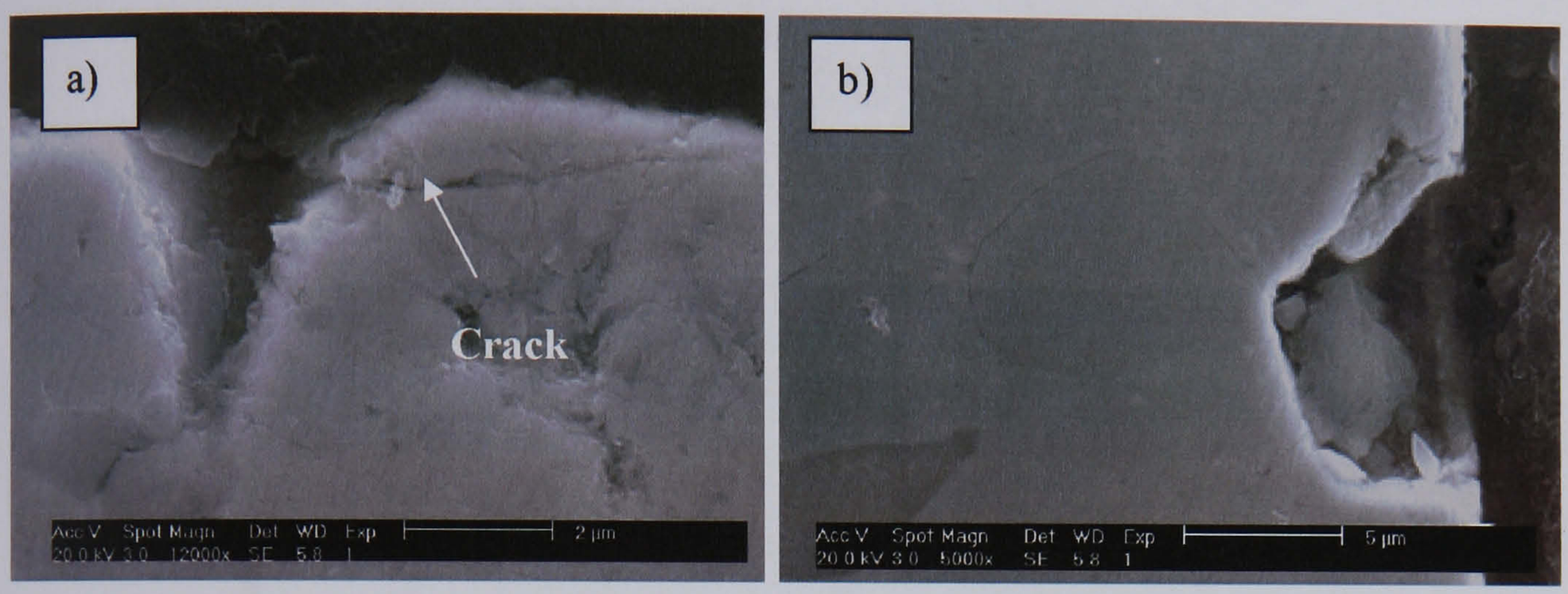

Fig.4.71. Characteristic failure zones found after cross sectioning the steel samples exposed to 300 thermal cycles a) Propagation of cracks b) Spalled section found in a sample.

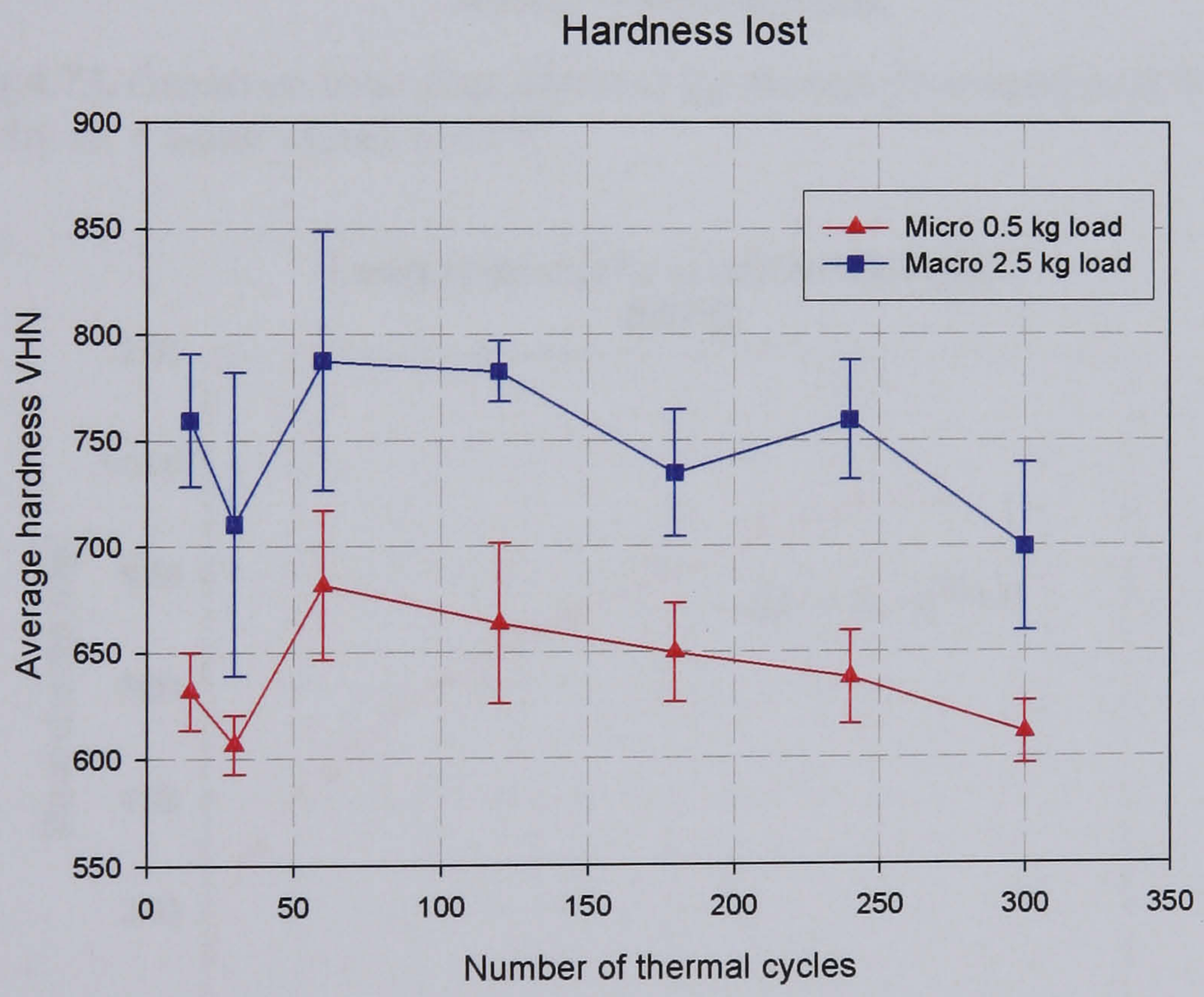

Fig.4.72. Macro and micro hardness evolution of the samples as a function of the number of thermal cycles.

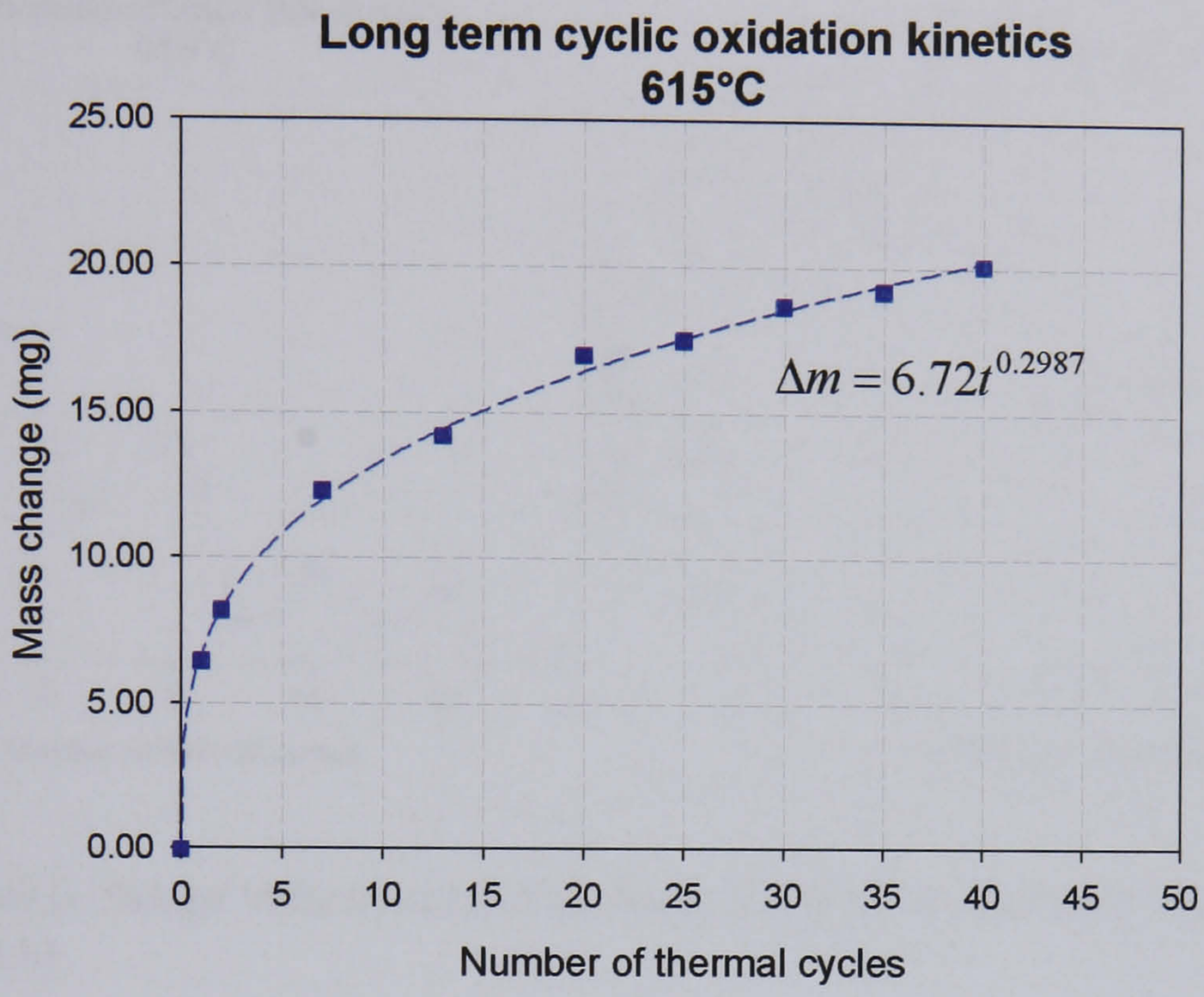

Fig.4.73. Oxidation behaviour obtained for the test developed at **615°C** in dry air + water vapour at 85°C.

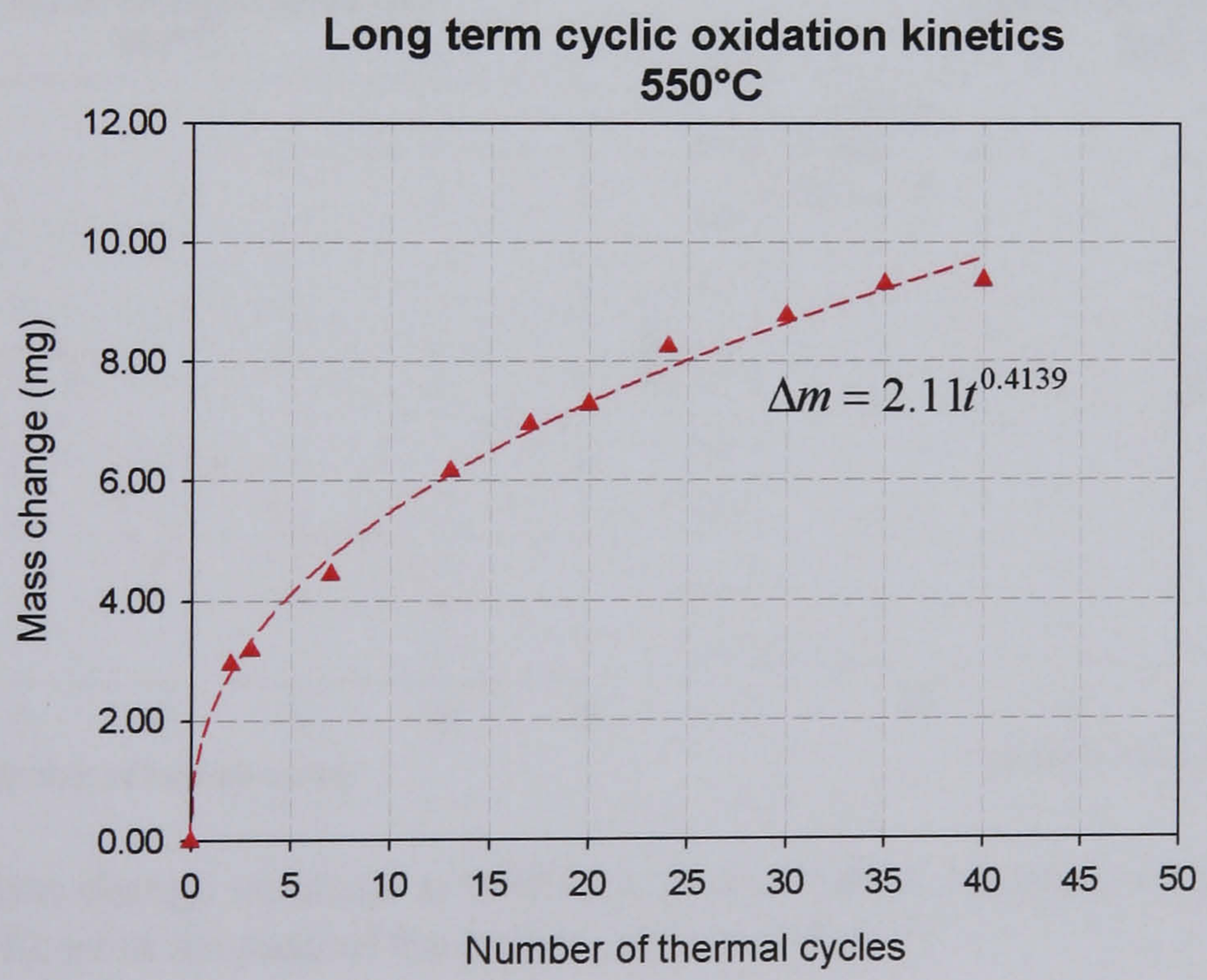

Fig.4.74. Oxidation behaviour obtained for the test developed at **550°C** in dry air + water vapour at 85°C.

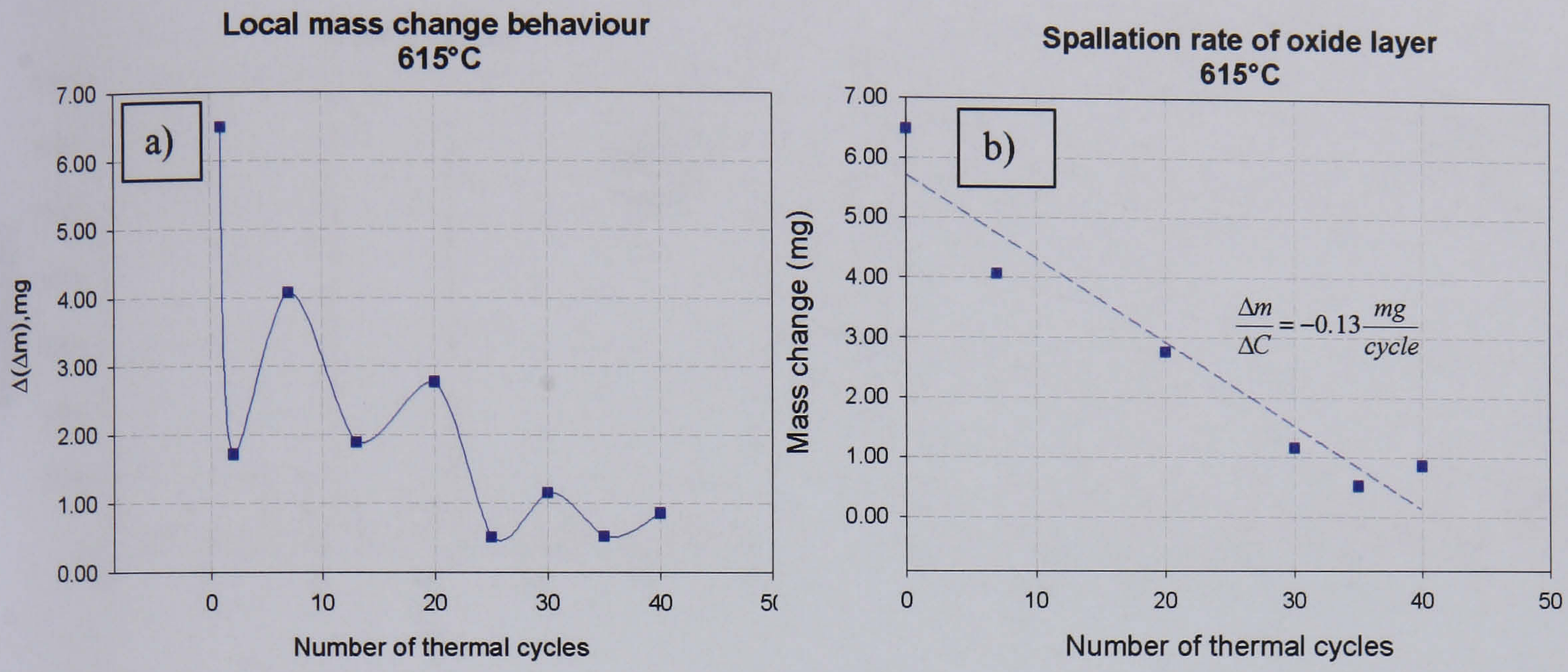

Fig.4.75. a) Mass change variation at **615°C,** from this plot the spallation trend is calculated and plotted in b).

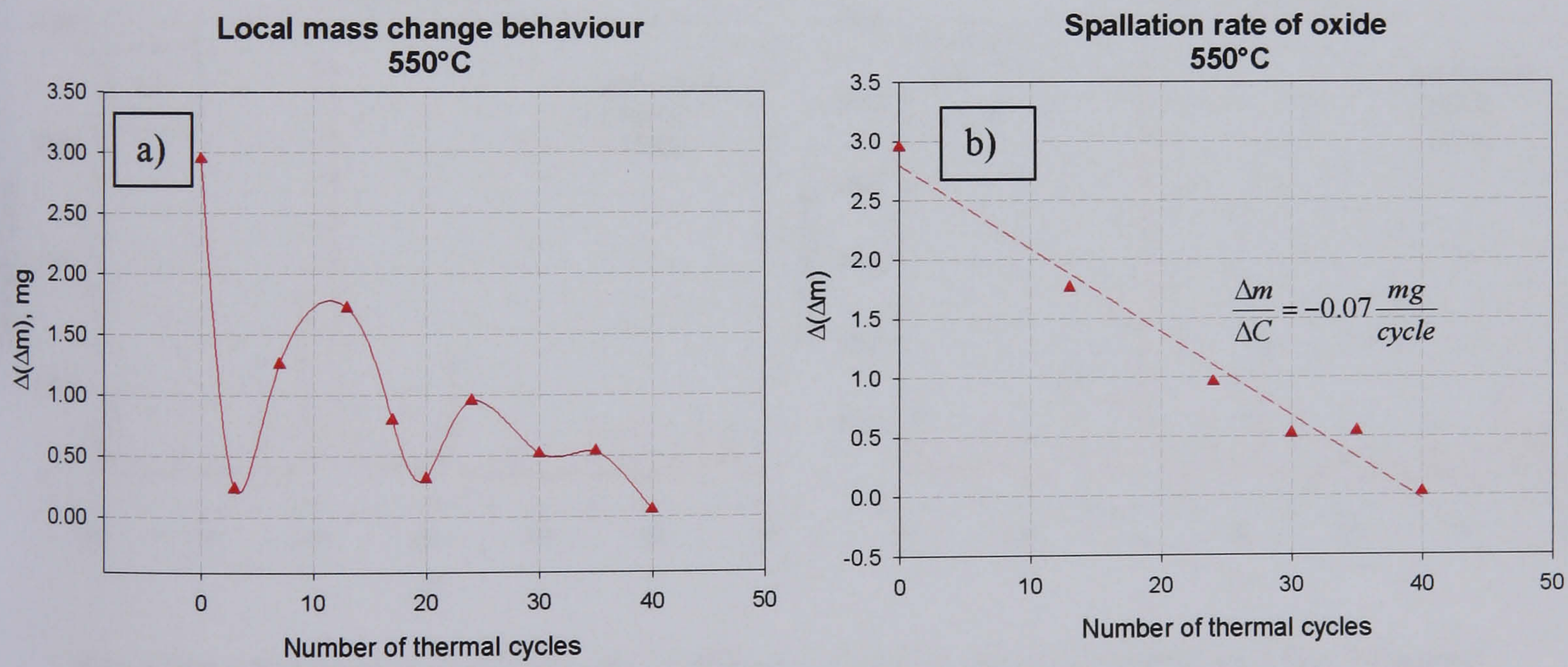

Fig.4.76. a) Mass change variation at **550°C,** from this plot the spallation trend is calculated and plotted in b), as in the case of the test developed at 615°C.

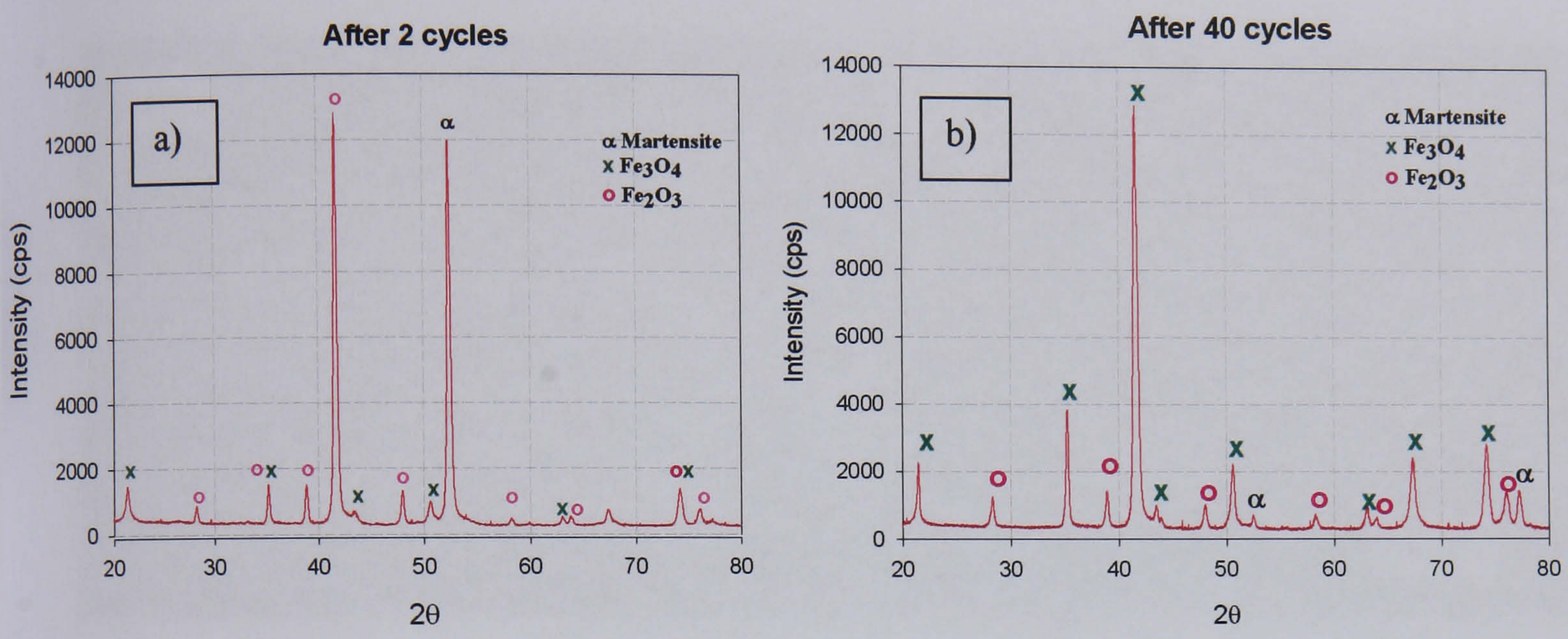

Fig.4.77. XRD patterns taken for two different oxidation stages at **615°C** a) After 2 thermal cycles. b) After 40 thermal cycles.

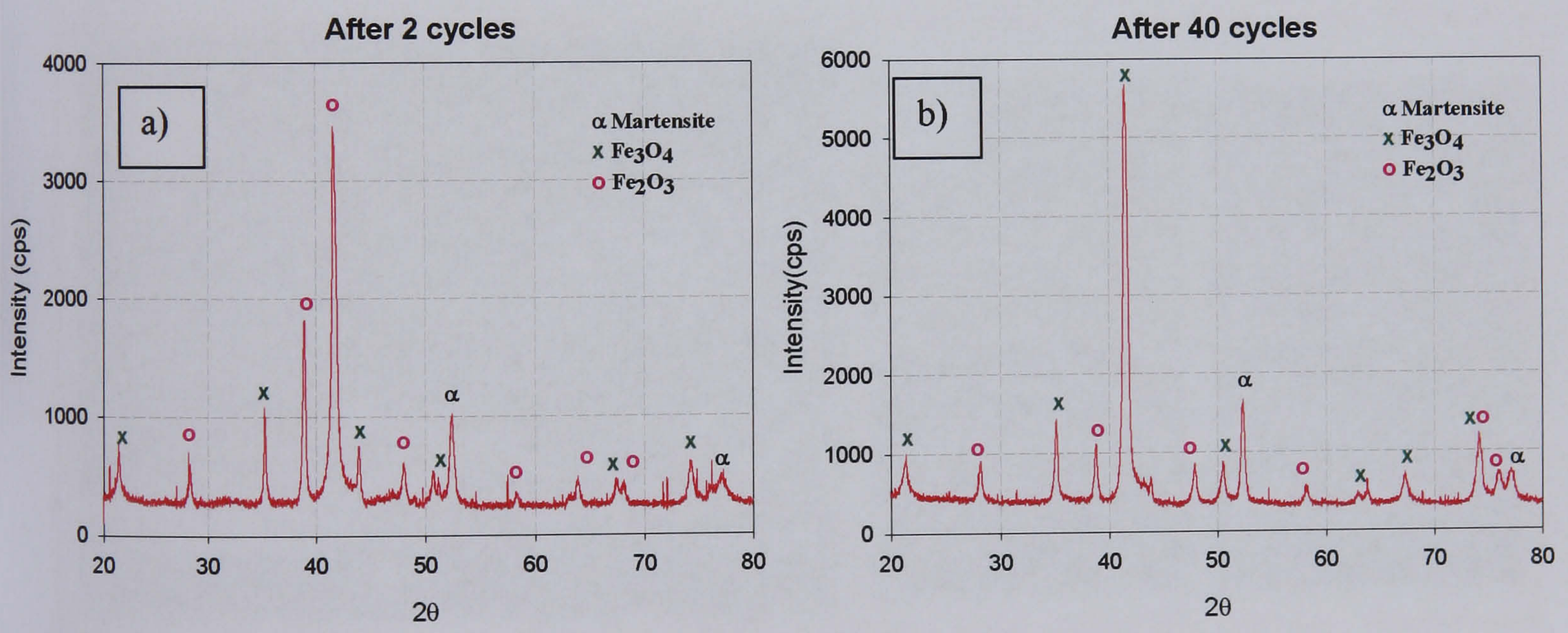

Fig.4.78. XRD patterns taken for two different oxidation stages at **550°C** a) After 2 thermal cycles. b) After 40 thermal cycles.

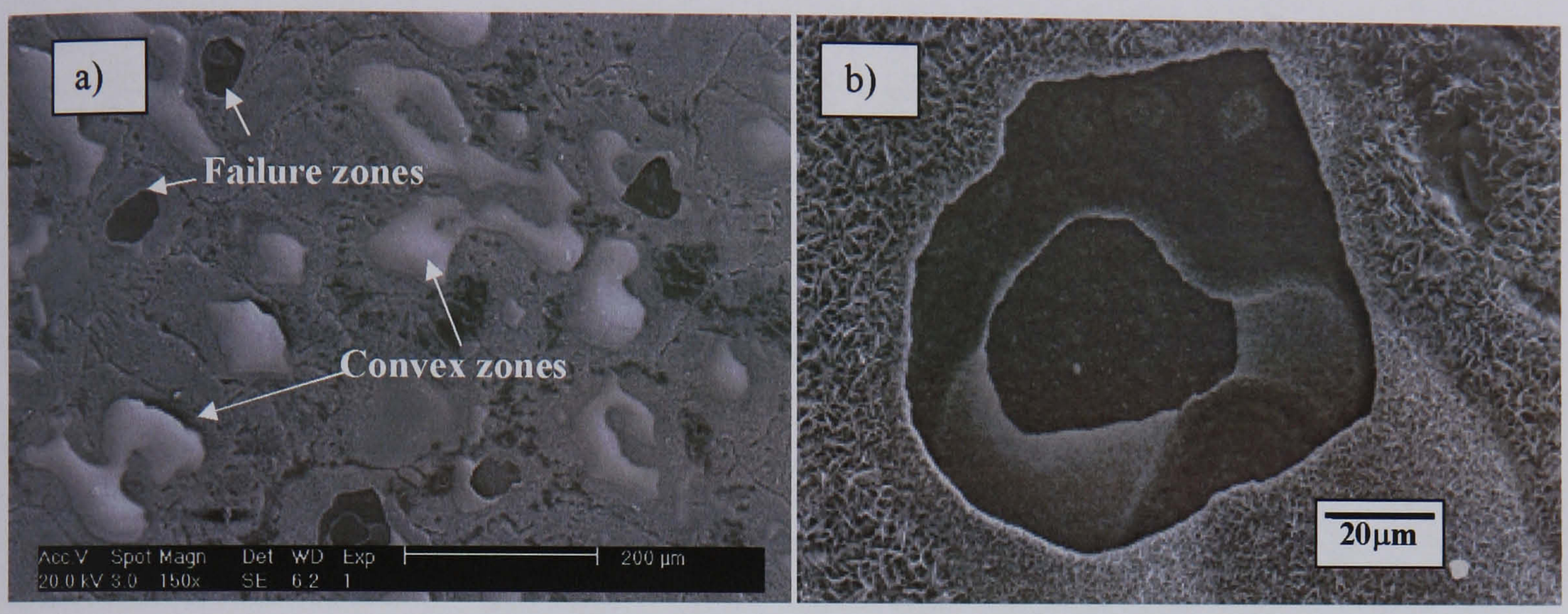

Fig.4.79. a) Surface state of the sample after the action of 2 thermal cycles. Buckled zones and spalled zone were found. b) Spallation of two oxide layers.

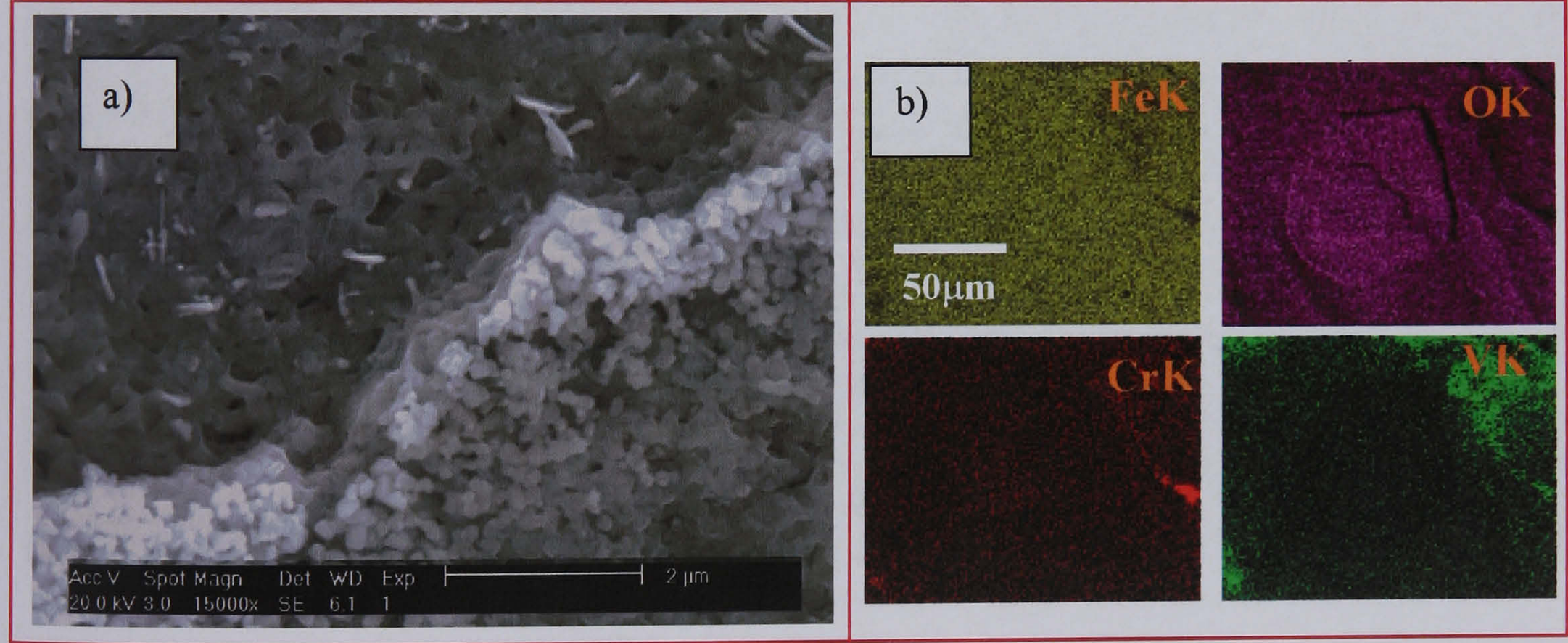

Fig.4.80. a) Interface formed inside of a double spalled zone, at the top left the initial stages of oxide formation are shown and bottom right advanced formation of oxide crystals. b) EDX maps of Fig.4.79.b).

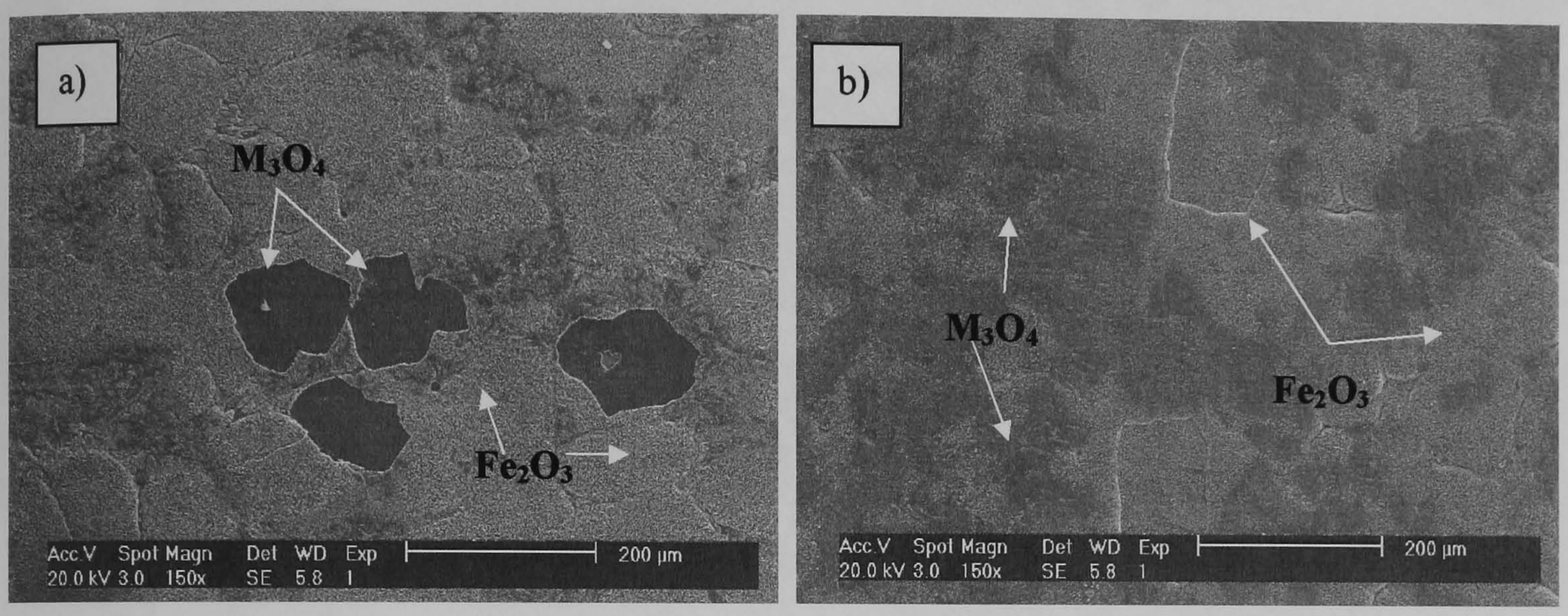

Fig.4.81. Comparison between two oxidation stages of the samples oxidized at **615°C** a) After 2 cycles. b) After 40 cycles. Note the differences in the phase content per stage.

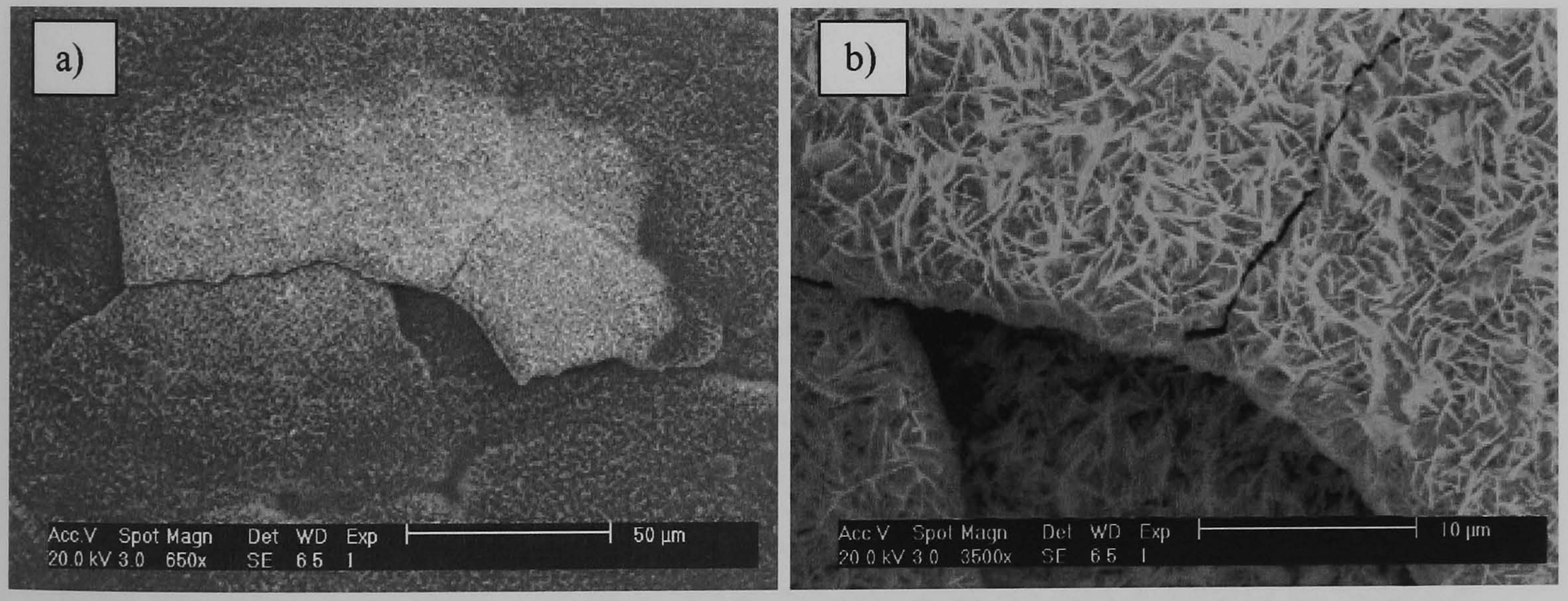

Fig.4.82. Failure mechanisms experienced by the Fe_2O_3 layer. a) Buckling of the layer is identified as the first stage followed by the sectioning or wedging of the oxide layer (b). Images taken after 40 thermal cycles.

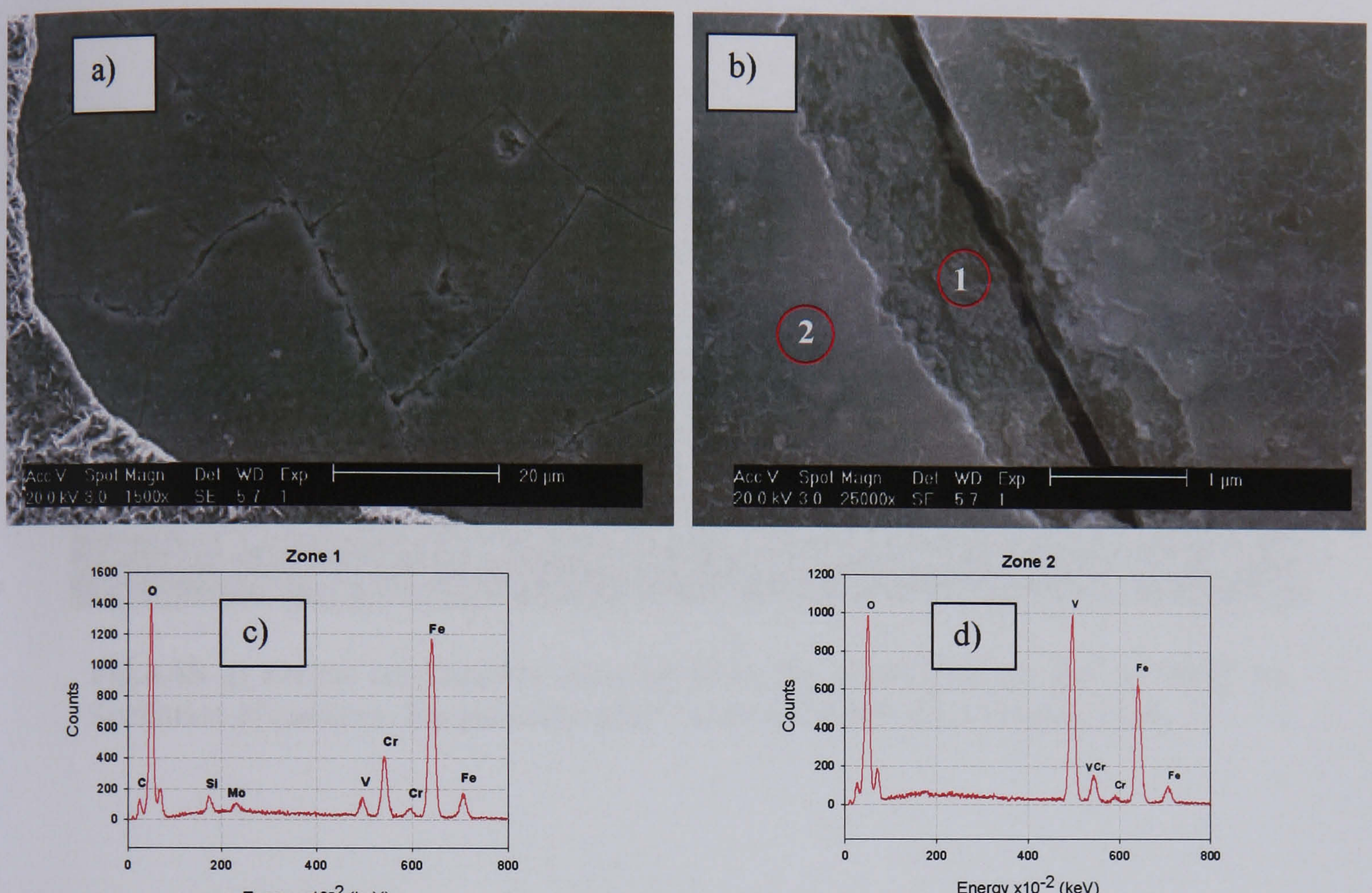

Fig.4.83. a) Micro crack formation observed for the internal oxide layer M_3O_4. b) Magnification to the oxide layer shown in a). c) and d) EDX point analysis of the zones shown in b).

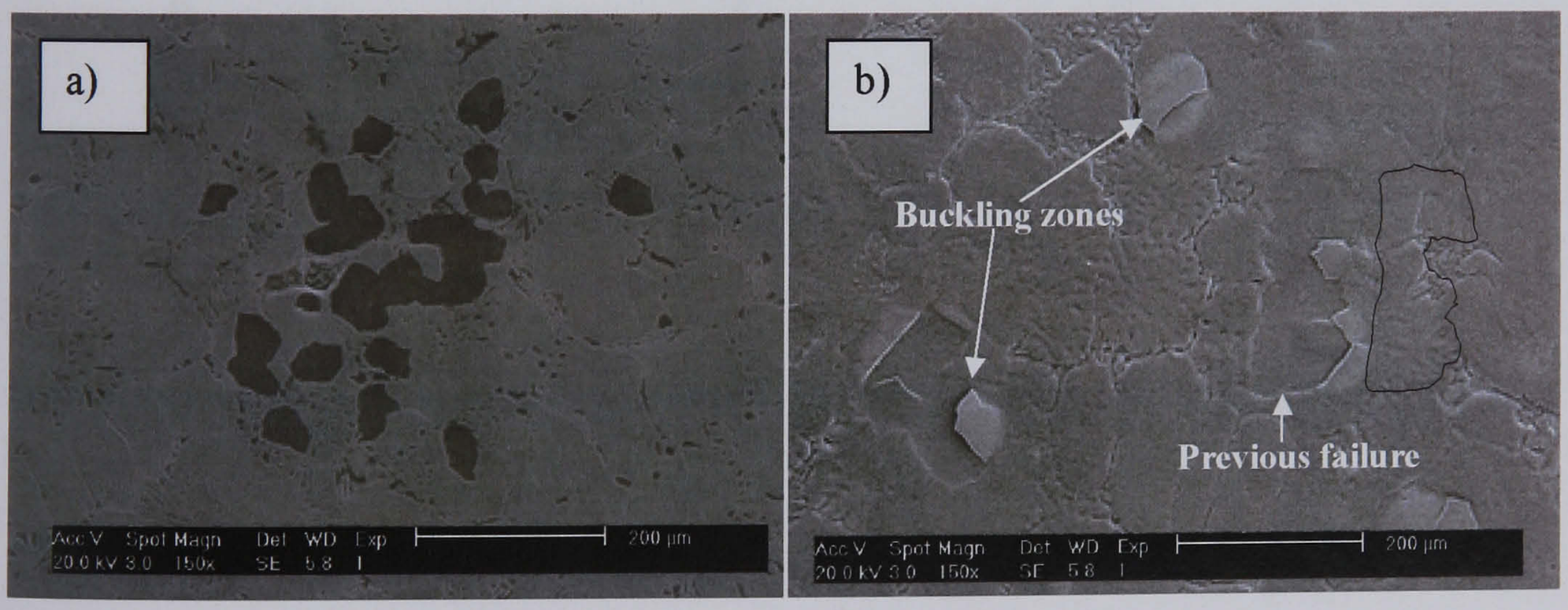

Fig.4.84. Similar failure mechanisms observed for the samples tested at **550°C** a) After 2 thermal cycles b) After 40 thermal cycles.

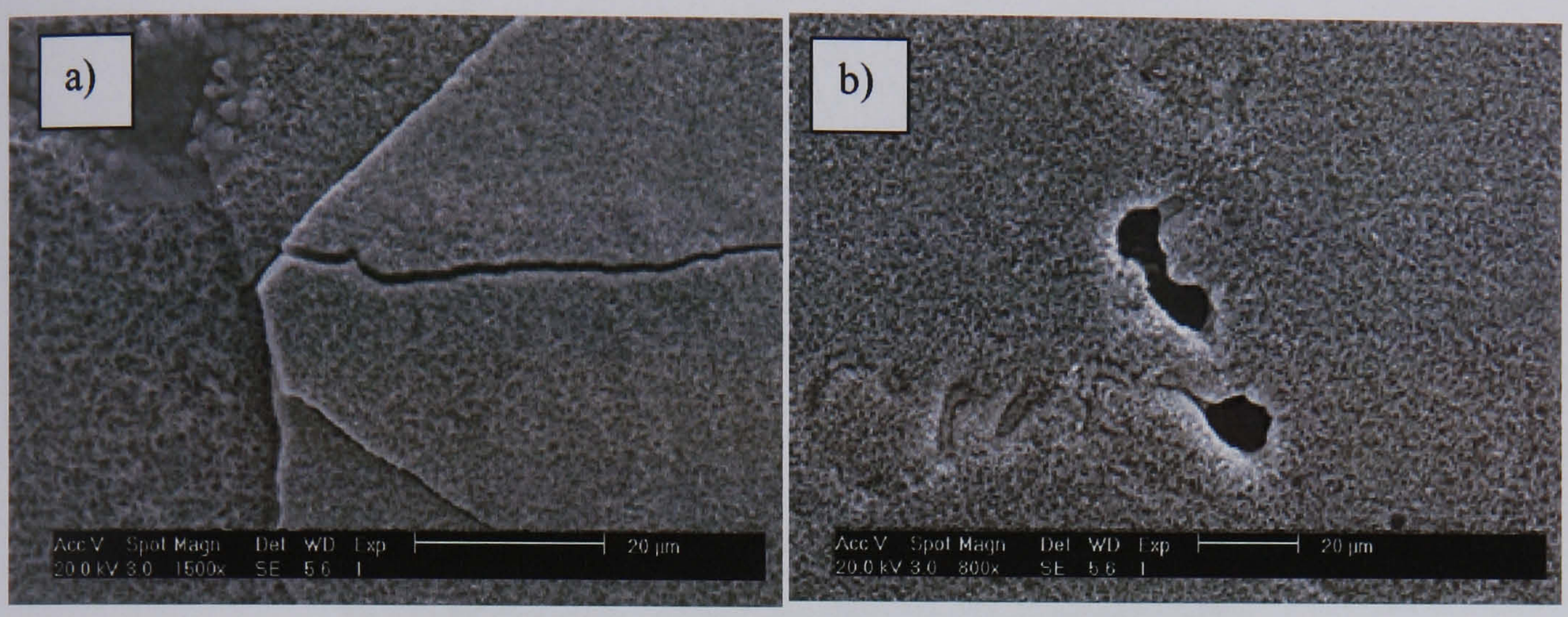

Fig.4.85. a) Failure mechanisms experienced by the oxide scale formed at **550°C**. b) Spallation of carbides. Images taken after 2 and 40 thermal cycles respectively.

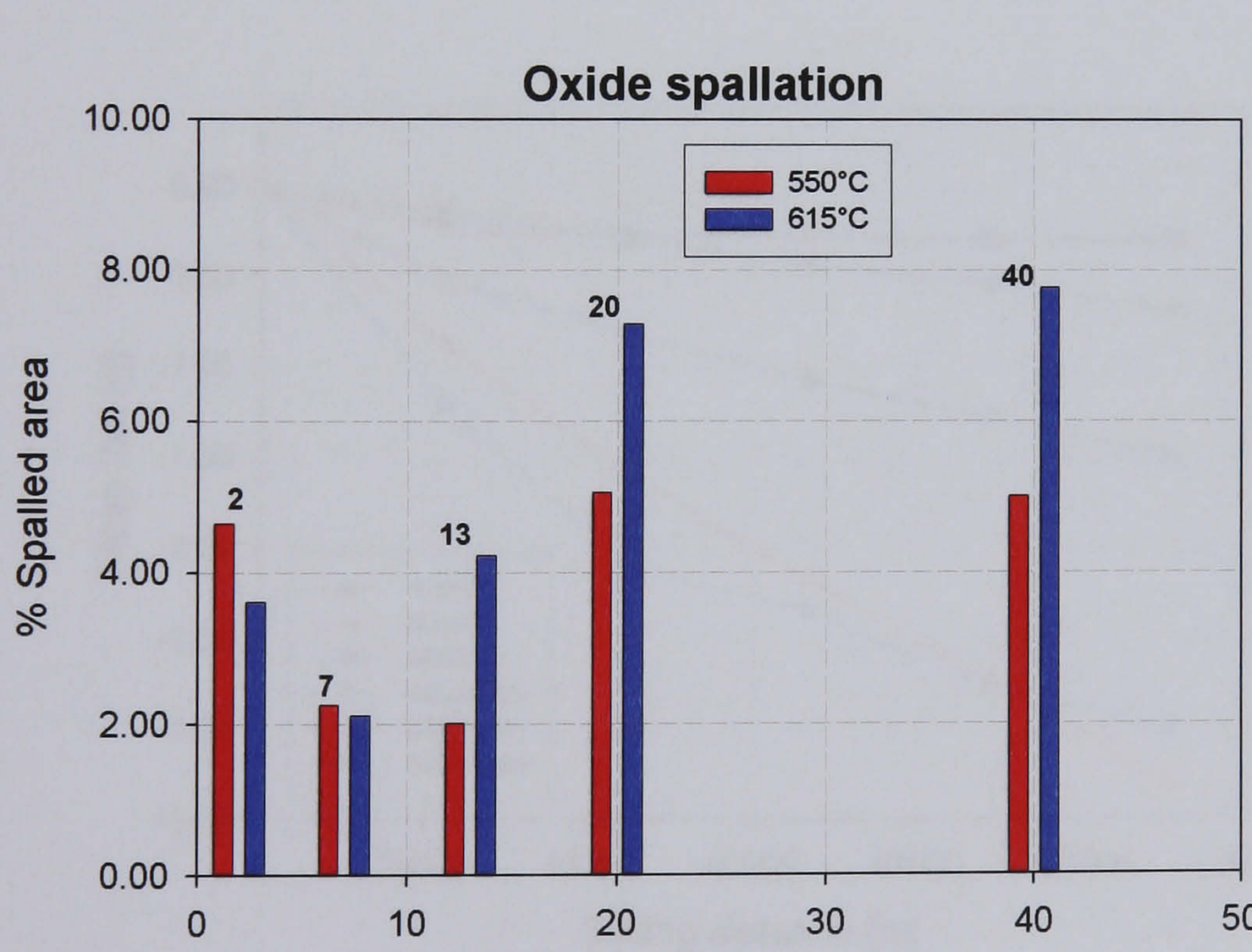

Fig.4.86. Percentage of spalled area as a function of the number of thermal cycles.

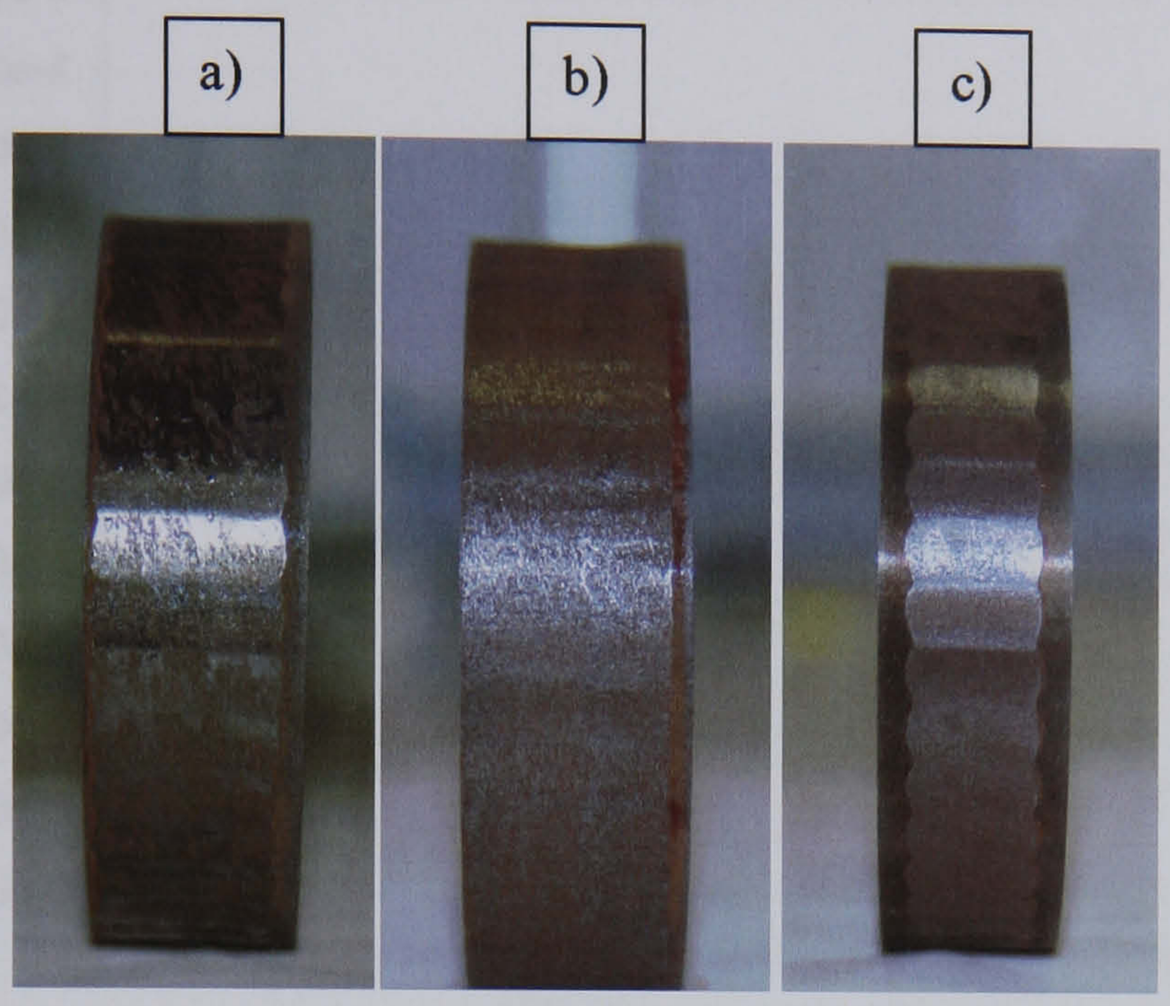

Fig.4.87. Appearance of the disc after the dry tests at a) 600°C b) 500°C c) 400°C.

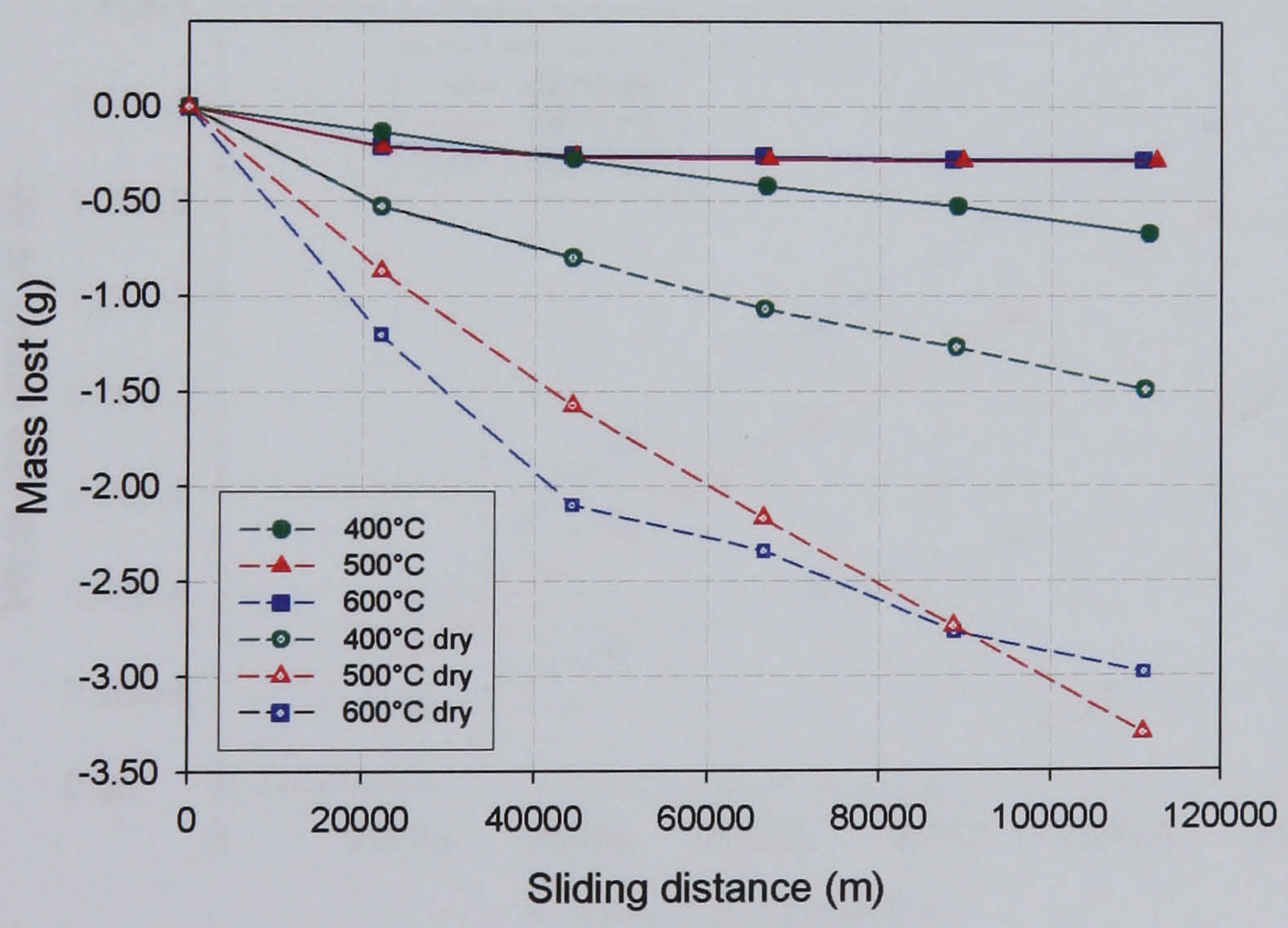

Fig.4.88. Comparison of the mass lost during all the test conditions.

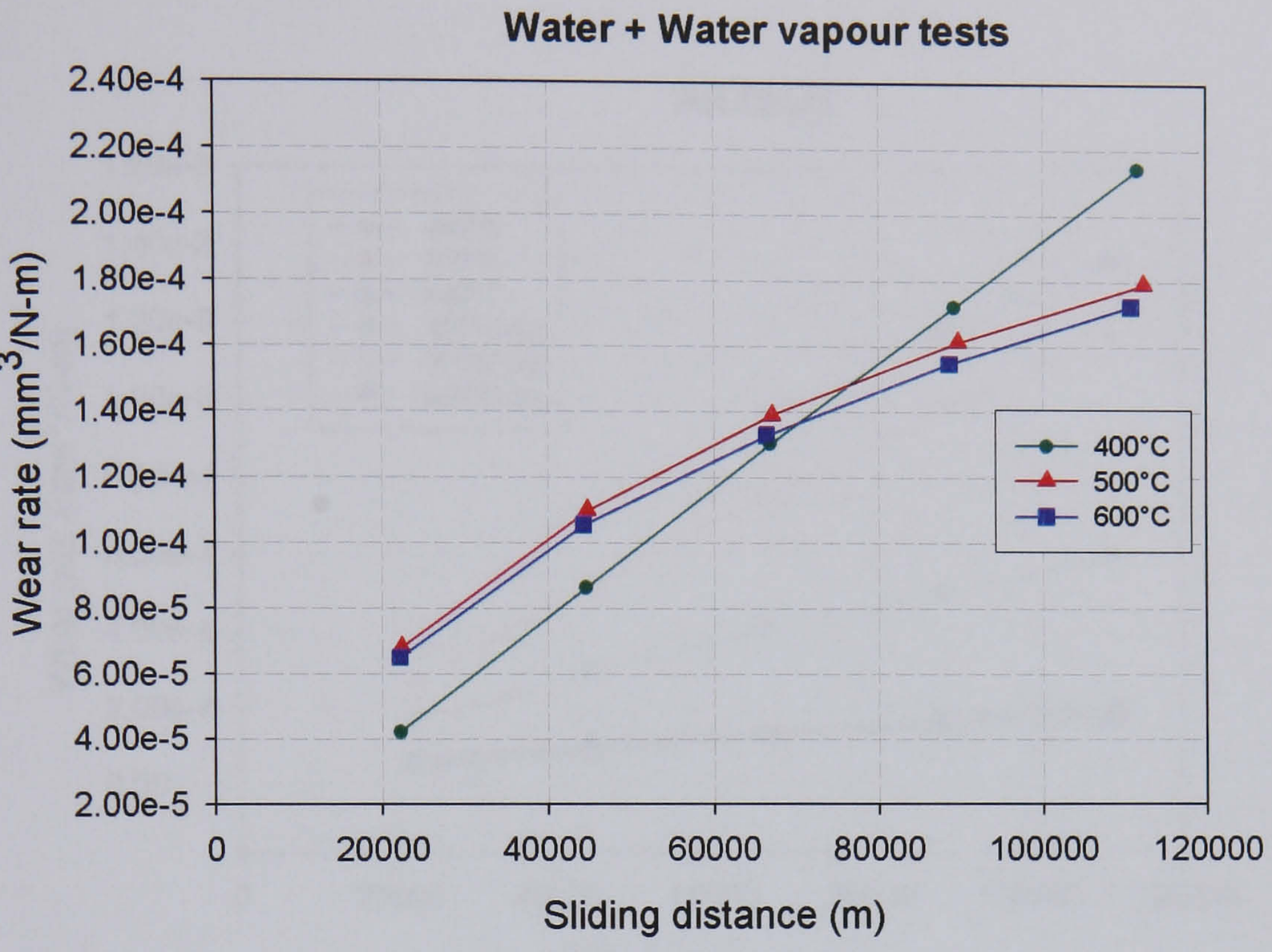

Fig.4.89. Specific wear rate obtained from the sliding tests developed under the presence of water.

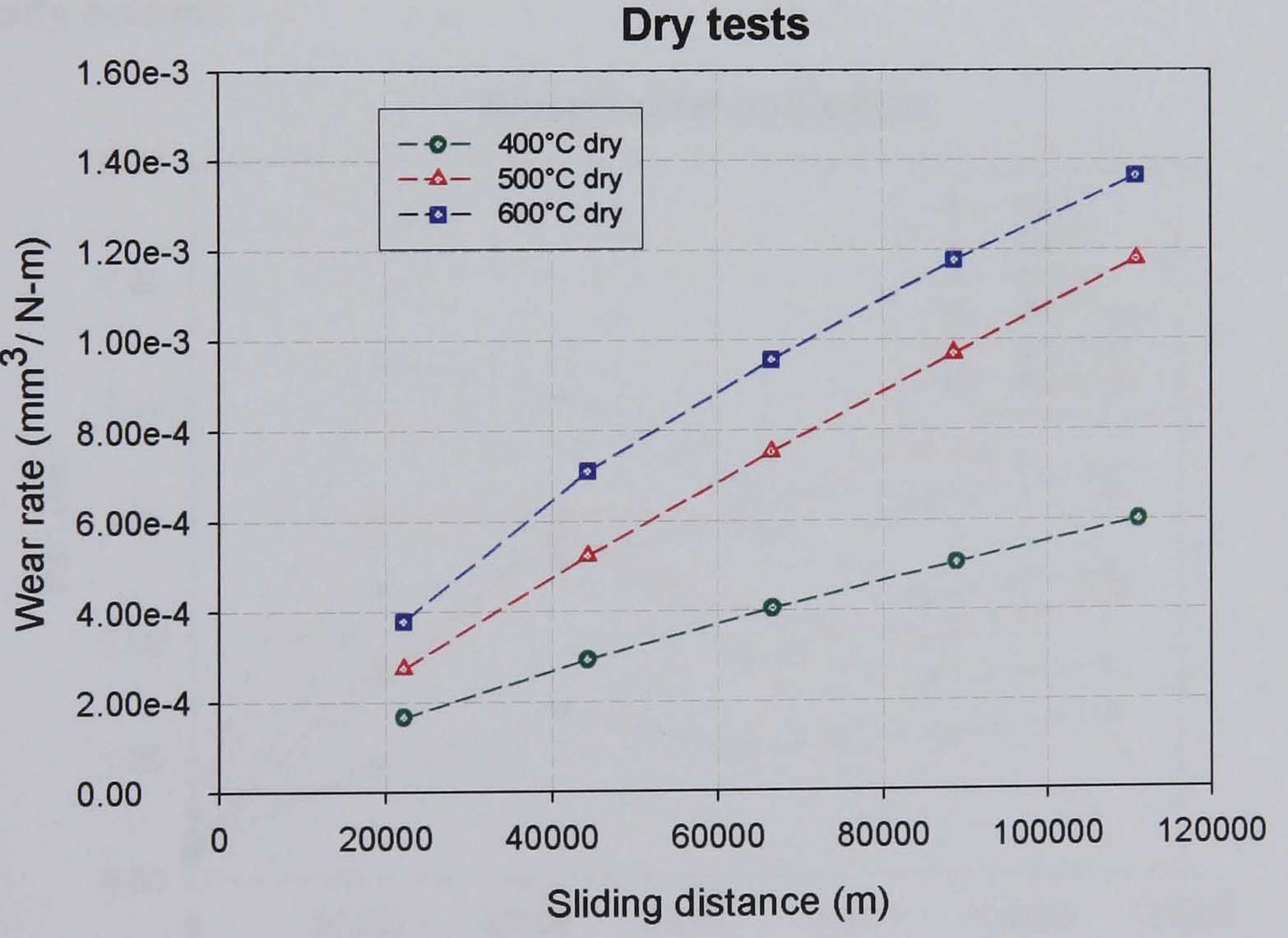

Fig.4.90. Specific wear rate obtained from the sliding tests developed under the presence dry ambient air.

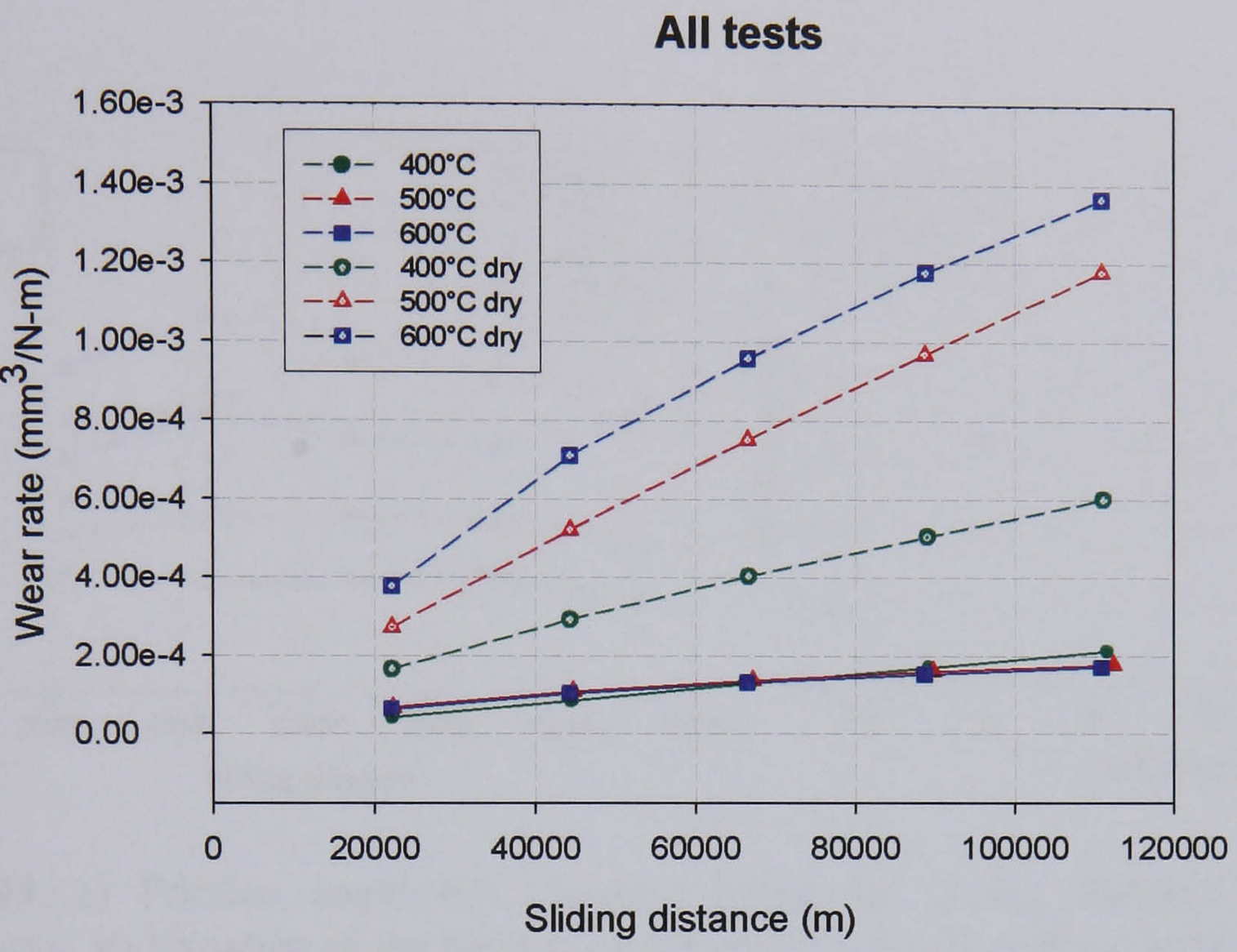

Fig.4.91. Comparison of the specific wear rates for all the testing conditions. The effect of water vapour on the values of this variable is clearly evident.

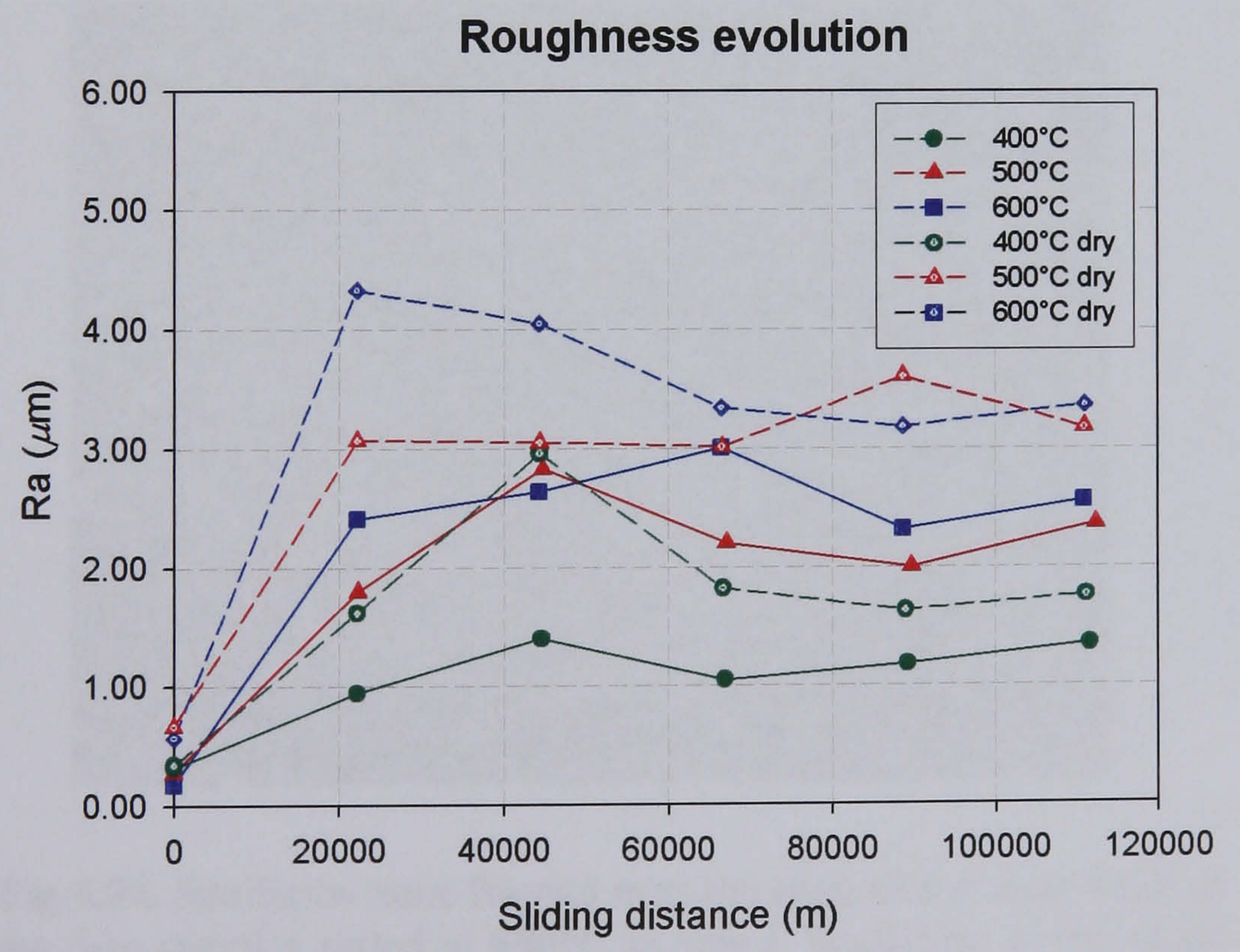

Fig.4.92. Roughness evolution of the roll discs measured for each testing condition.

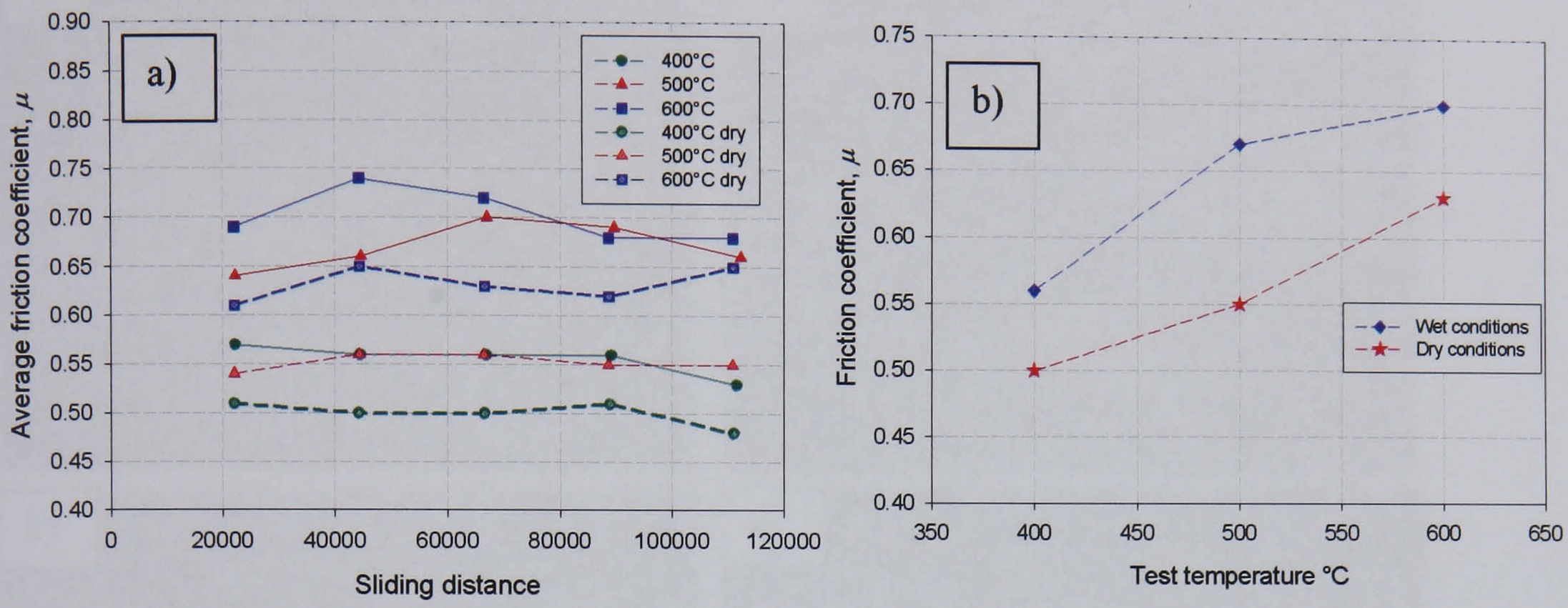

Fig.4.93. a) Friction coefficient variation along the sliding distance for all the test conditions. b) Variation of the friction coefficient as a function of the temperature.

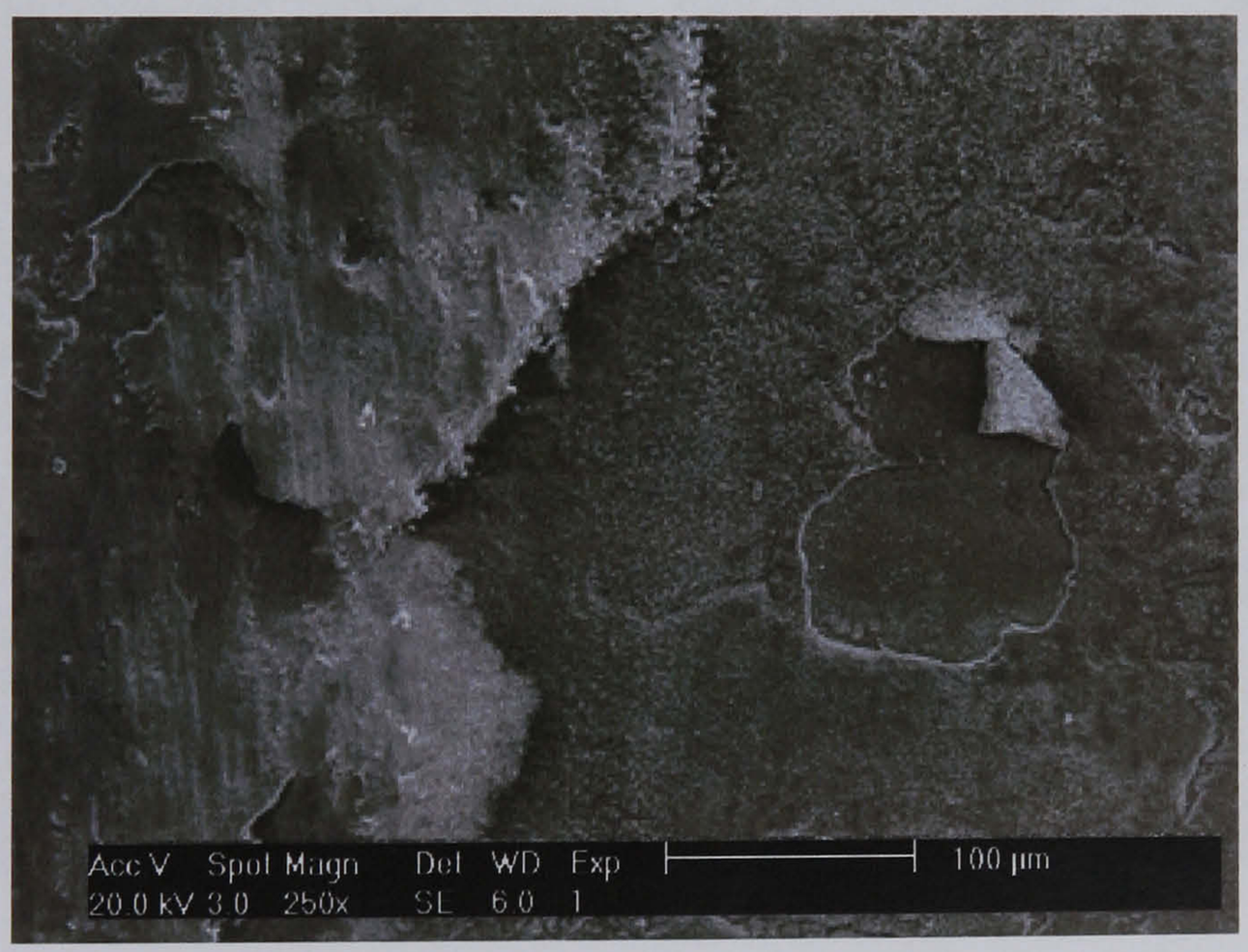

Fig.4.94. Spallation zone formed near the edge of the wear track of the disc samples tested at **600°C** in water. Spallation of the oxide scale was also observed during these conditions.

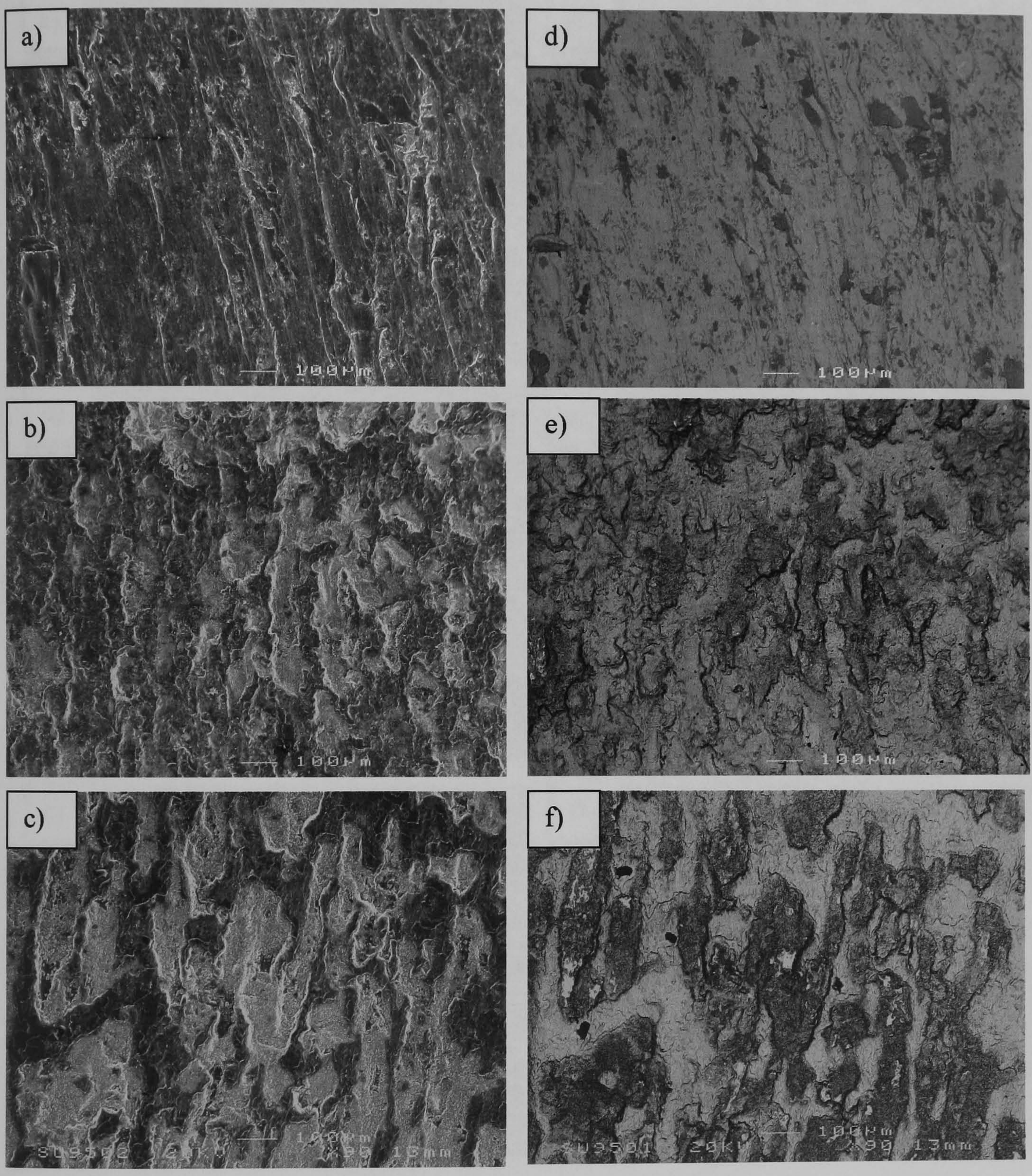

Fig.4.95. Surface state of the test samples after the sliding tests with water. The images on the left column a), b) and c) are secondary electrons images of the surface topography of the discs tested at 400, 500 and 600°C respectively. The column on the right are the backscattered electrons images of the same surfaces. The rolling direction points to the bottom of the page.

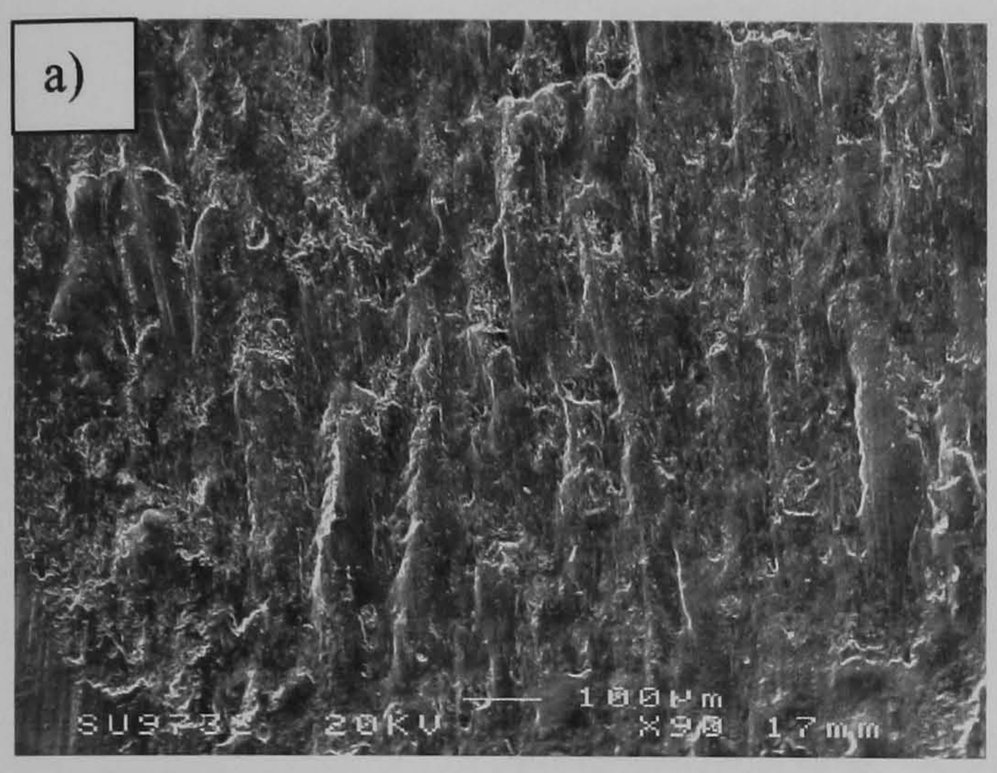

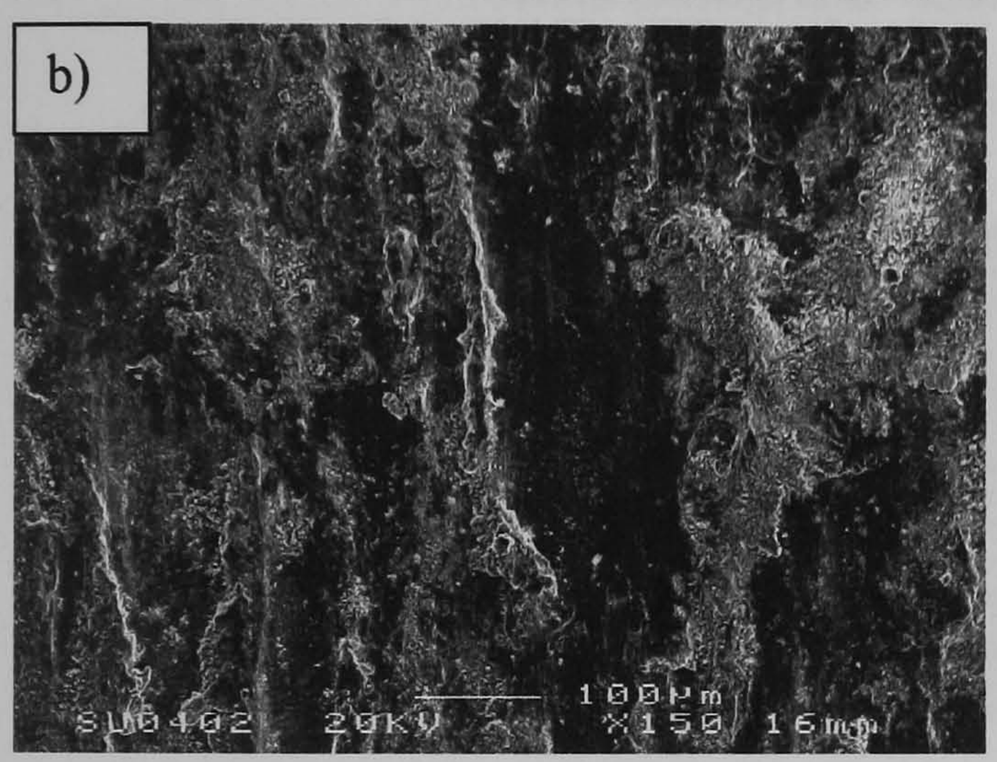

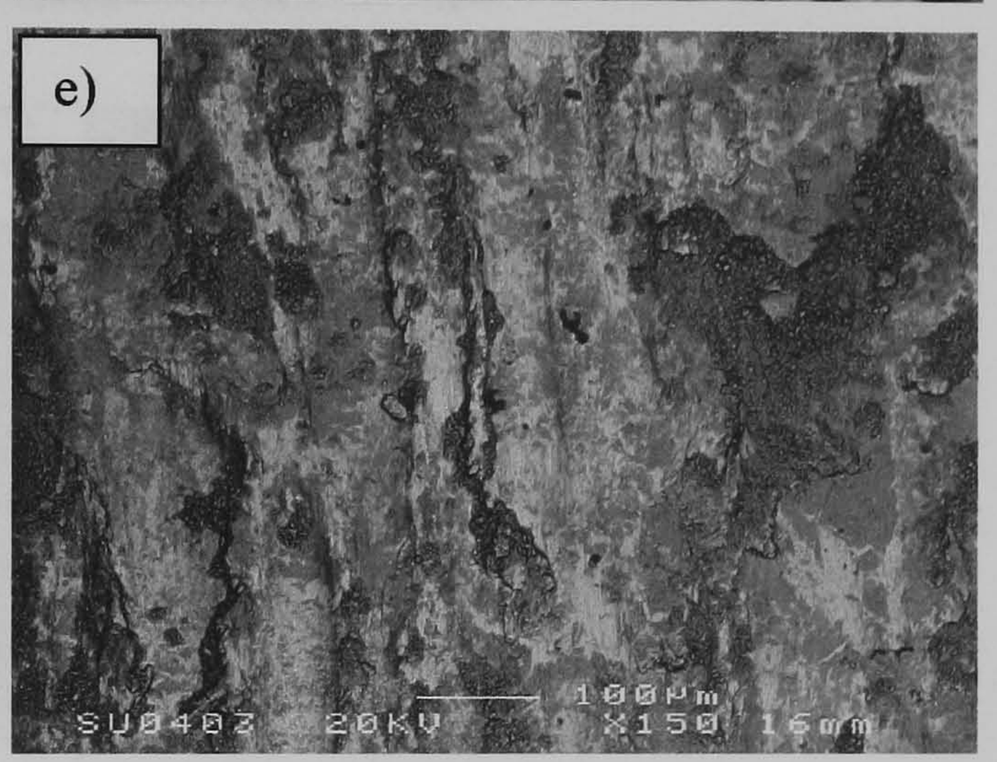

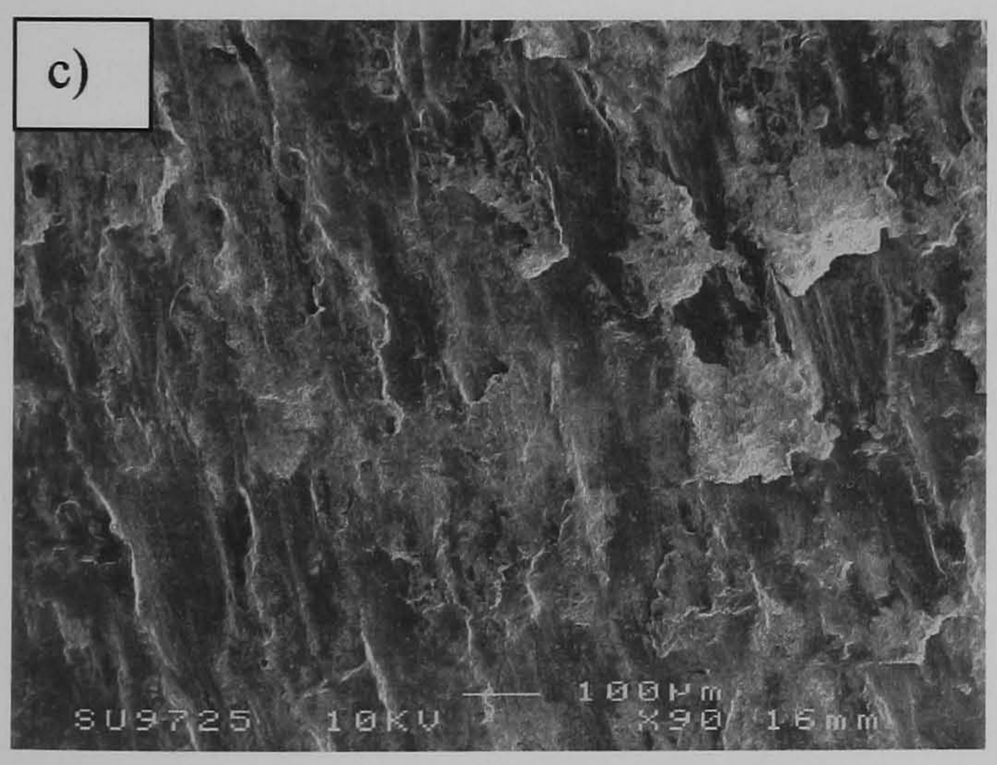

Fig.4.96. Surface state of the test samples after the sliding tests developed in dry conditions. The pictures on the left column a), b) and c) are secondary electrons images of the surface topography of the discs tested at 400, 500 and 600°C respectively. The column on the right are the backscattered electrons images of the same surfaces. The rolling direction points to the bottom of the page.

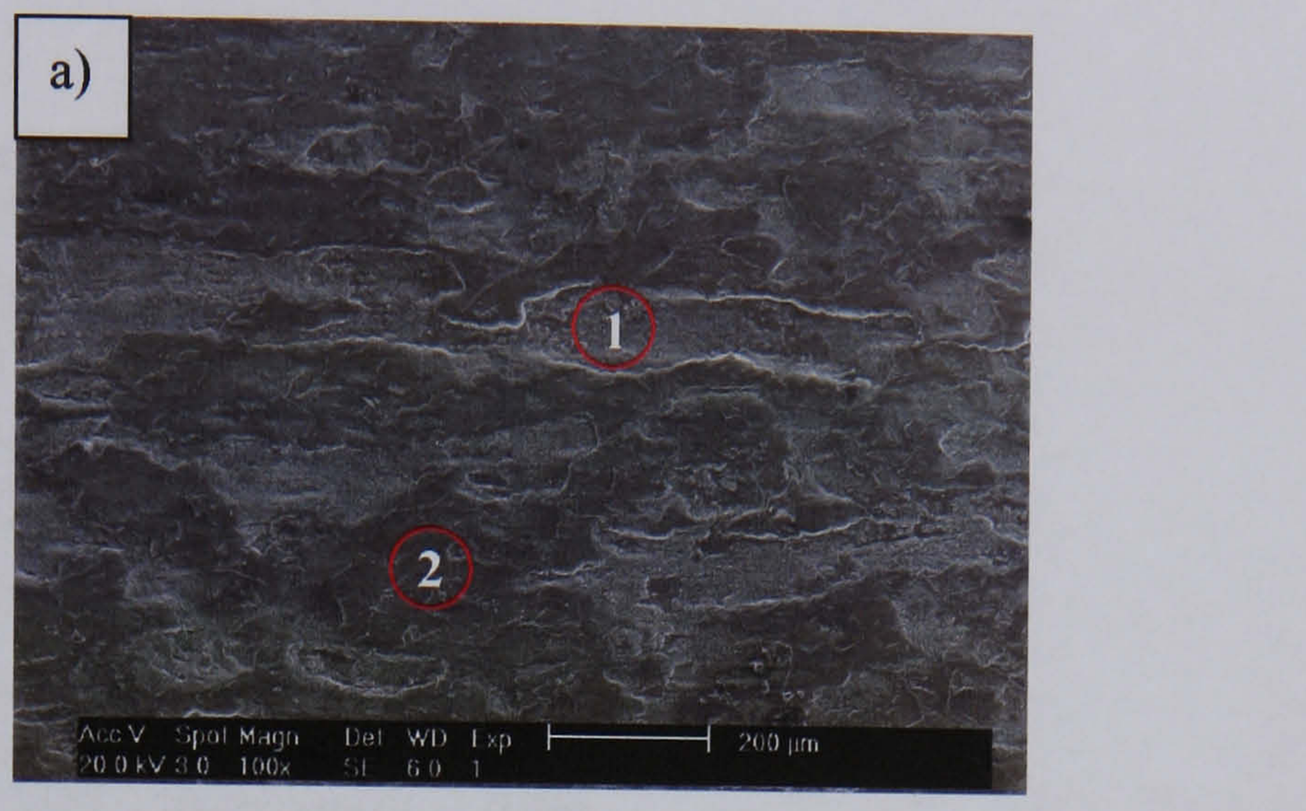

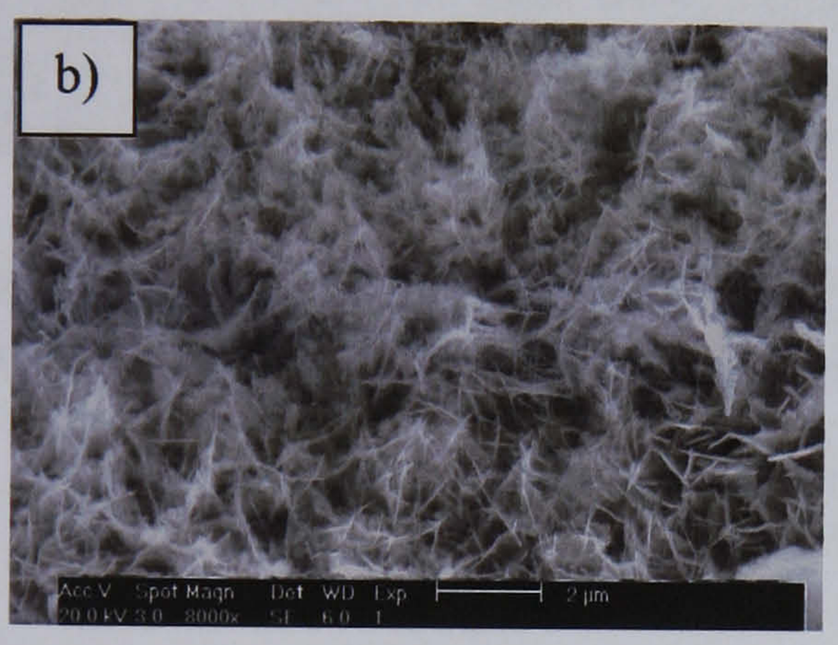

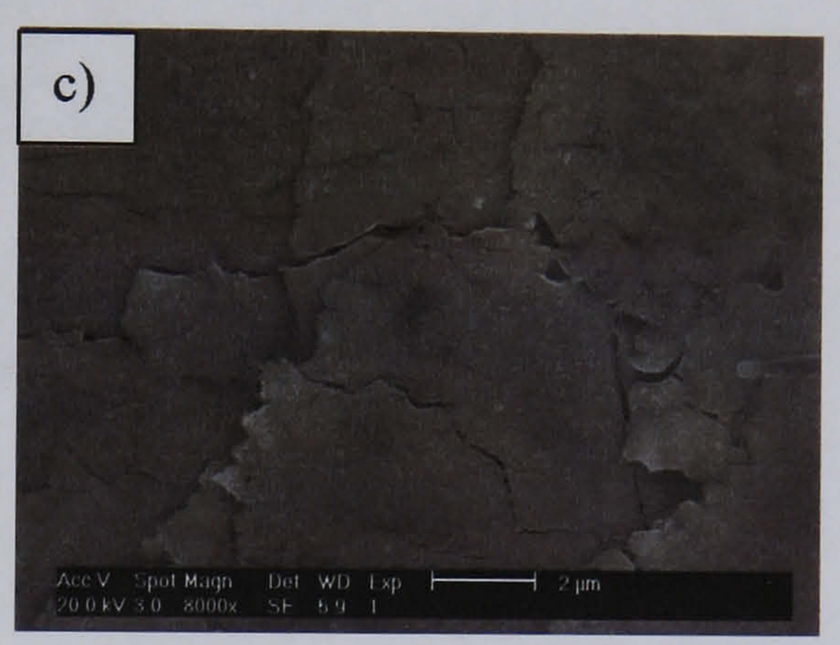

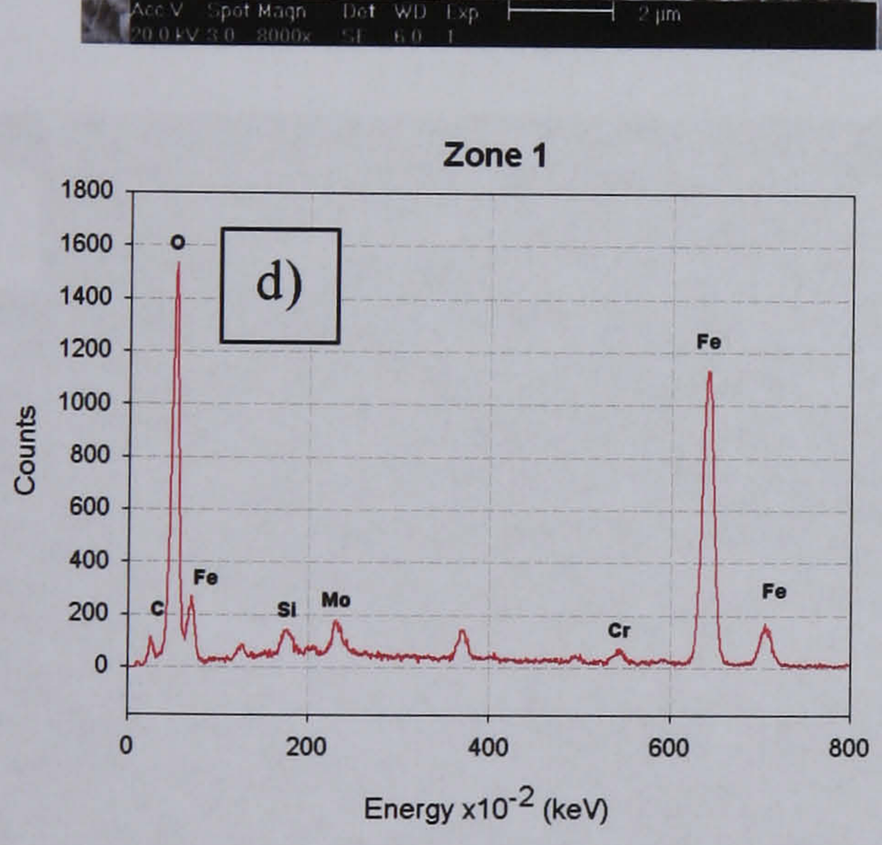

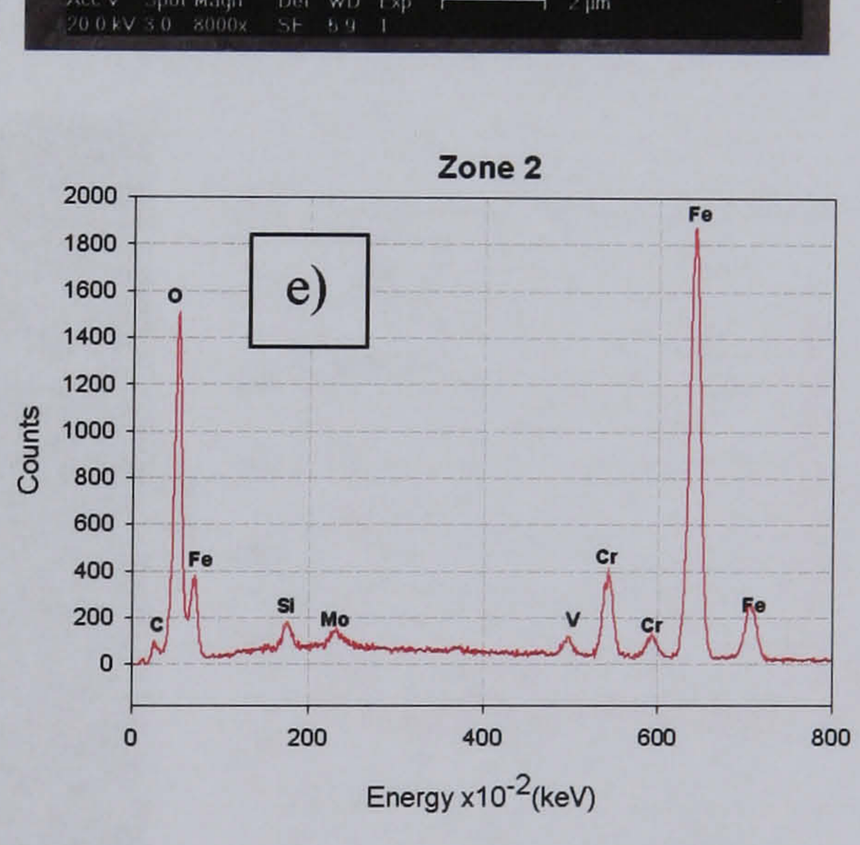

Fig.4.97. Secondary electron SEM images showing the characteristic zones found in the disc tested at 600°C under the presence of water. a) Surface topography. b) Zone 1 in picture a) showing Fe_2O_3 platelets. c) Zone 2 in picture a), showing fracture and crack propagation in the spinel layer. d) and e) EDX point analysis of zones 1 and 2 respectively.

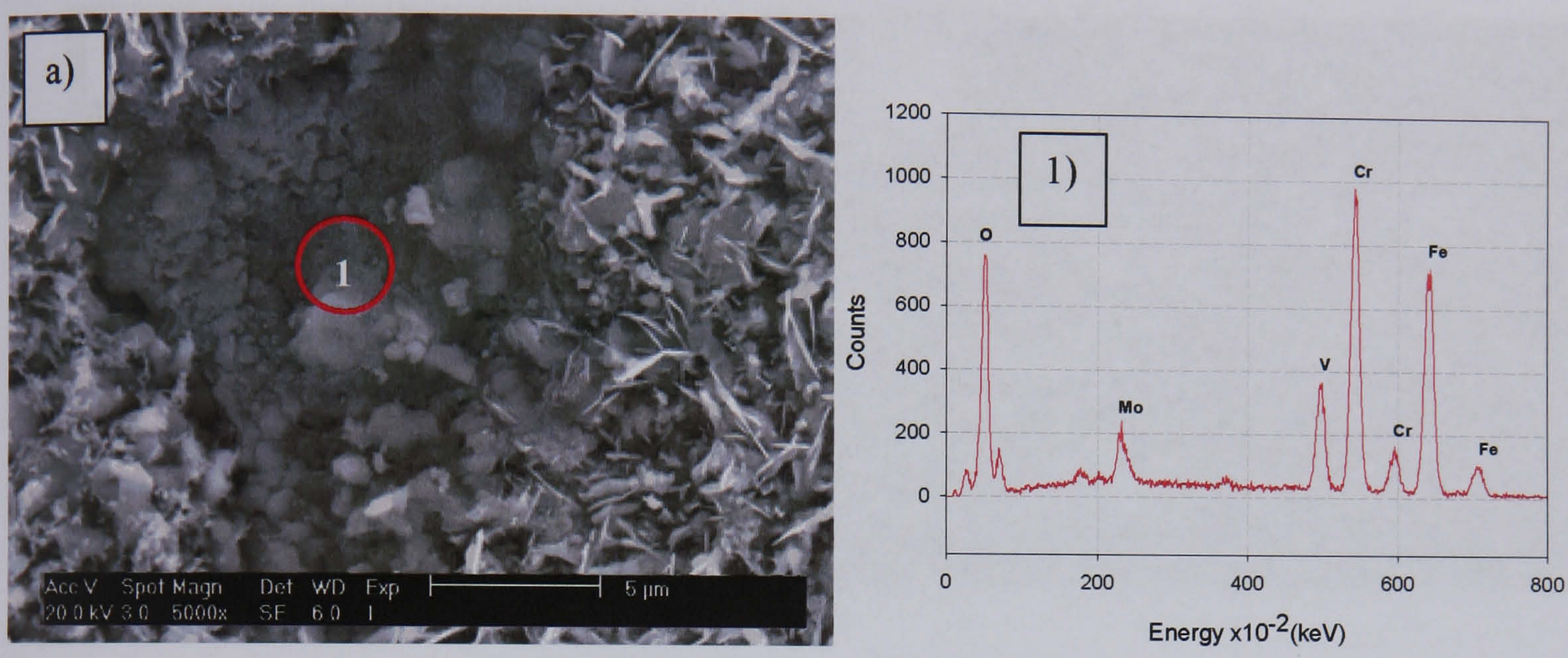

Fig.4.98. a) Oxide formation observed in a M_7C_3 carbide found in the sample tested at **600 °C** in water. 1) EDX area analysis of the oxidized zone.

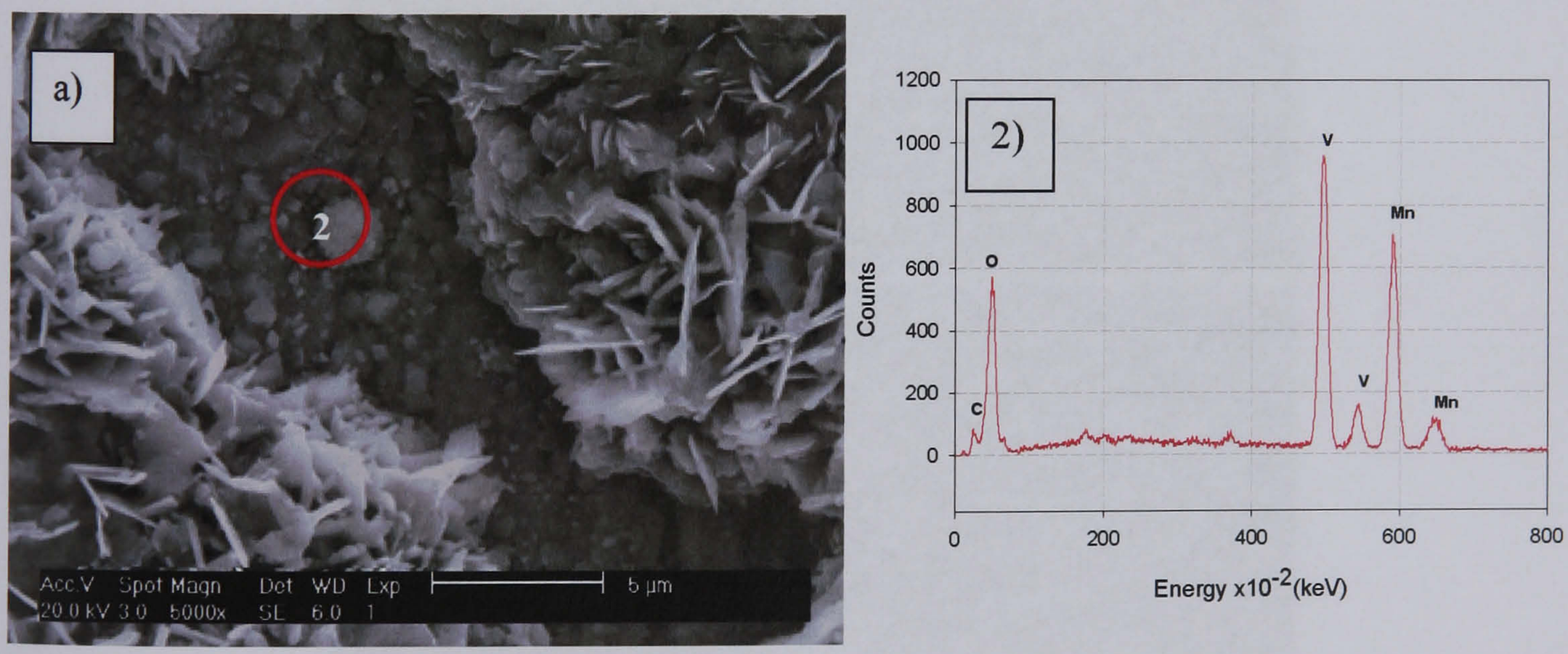

Fig.4.99. a) Oxide formation in a MC carbide found in the sample tested at **600°C** in water. 2) EDX analysis of the oxidized zone. Note the peaks relative to manganese content.

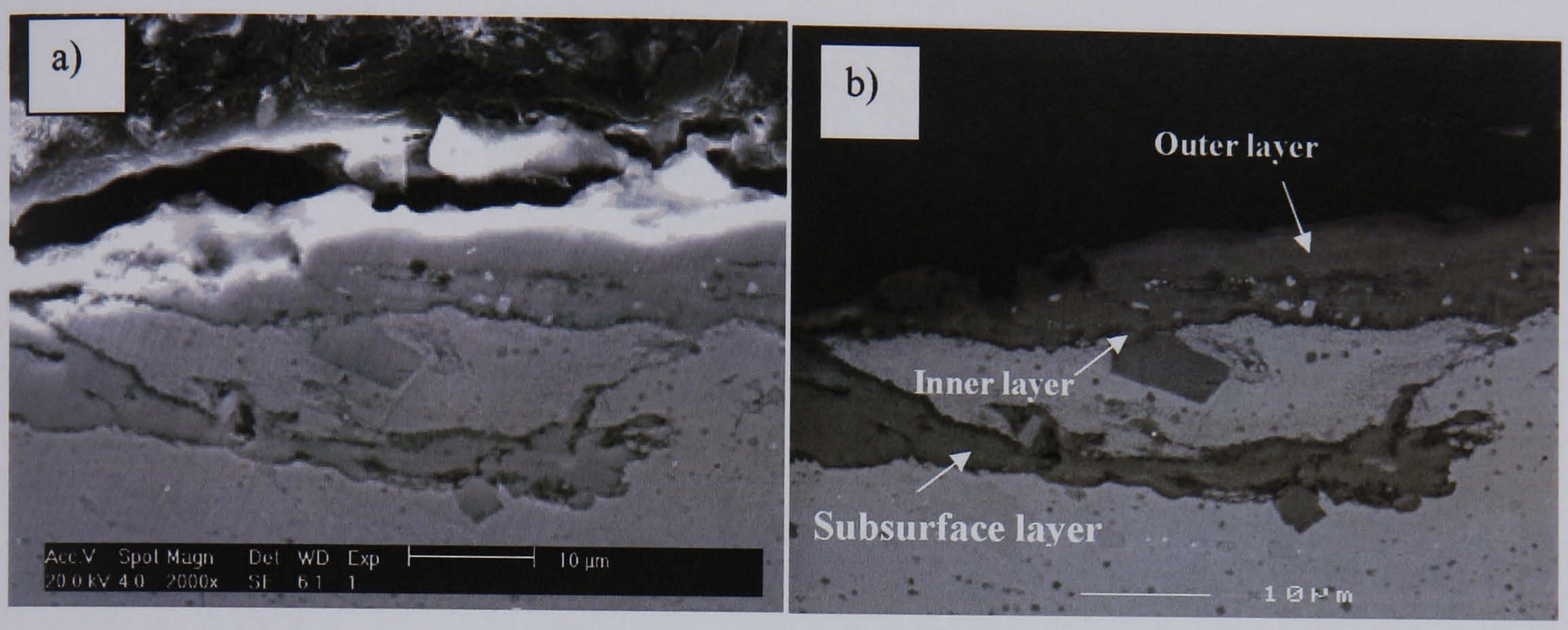

Fig.4.100. a) Secondary electrons image of a cross section of the test disc at **600°C** under water. Subsurface oxidation is evident. b) Backscattered electron image of a).

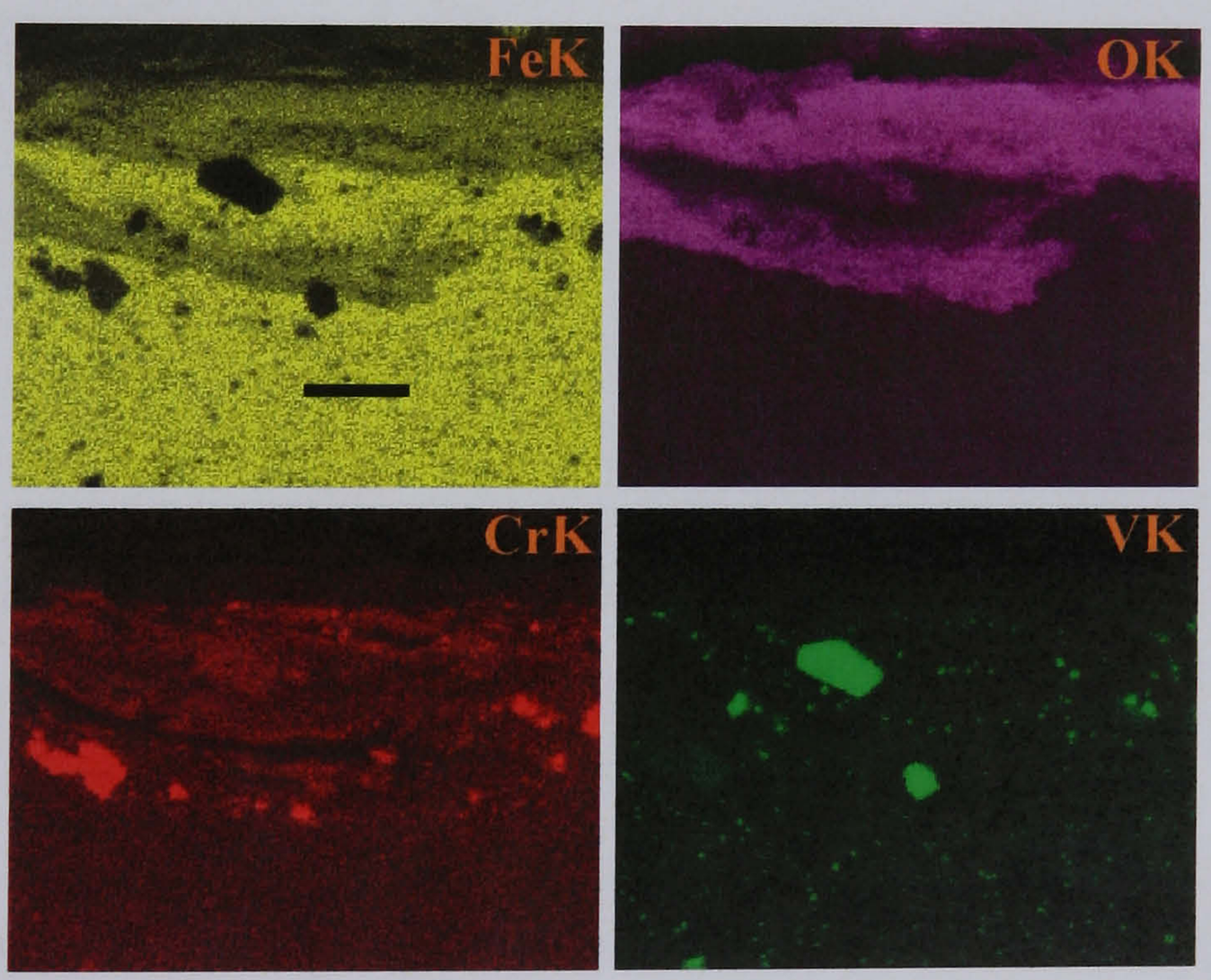

Fig.4.101. EDX maps taken from picture a) in Fig.4.100.a) the oxidation zones are revealed and defined clearly.

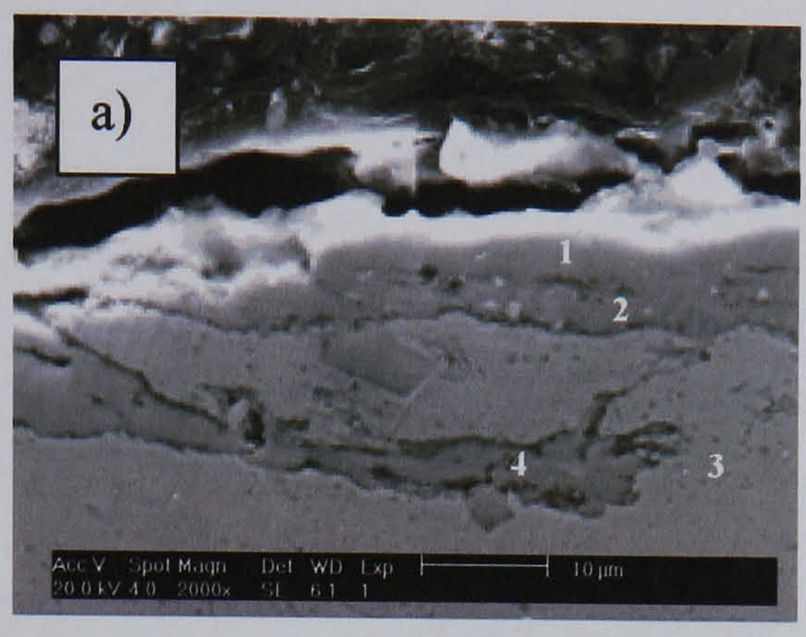

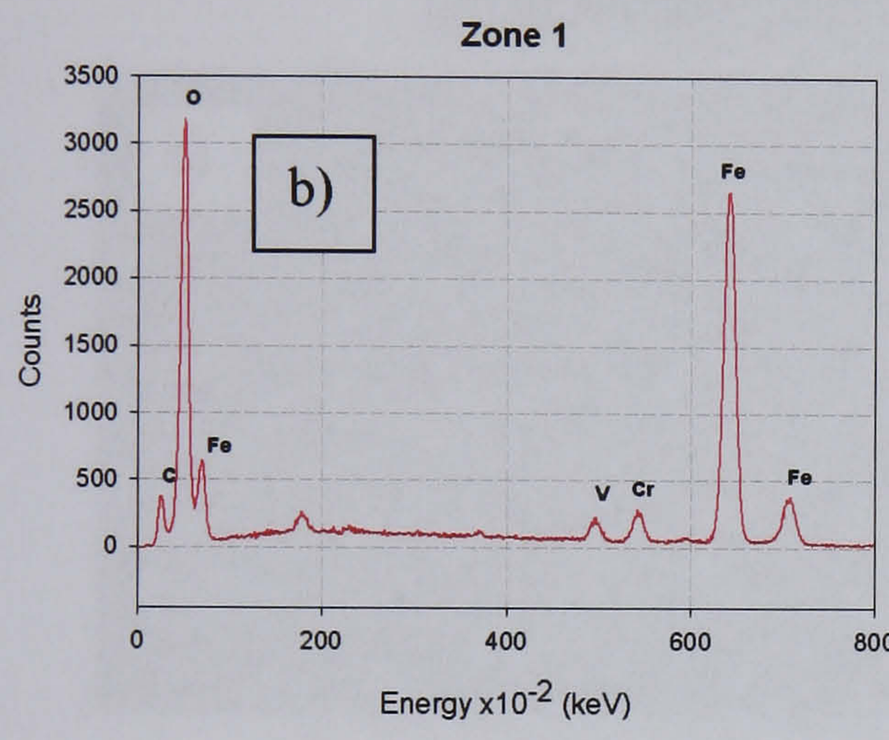

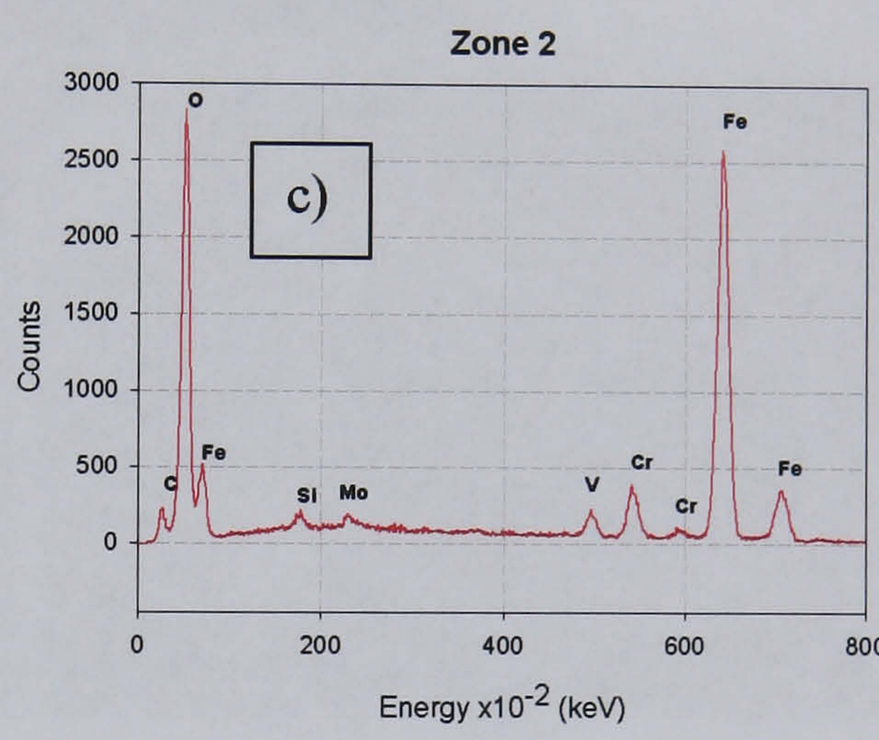

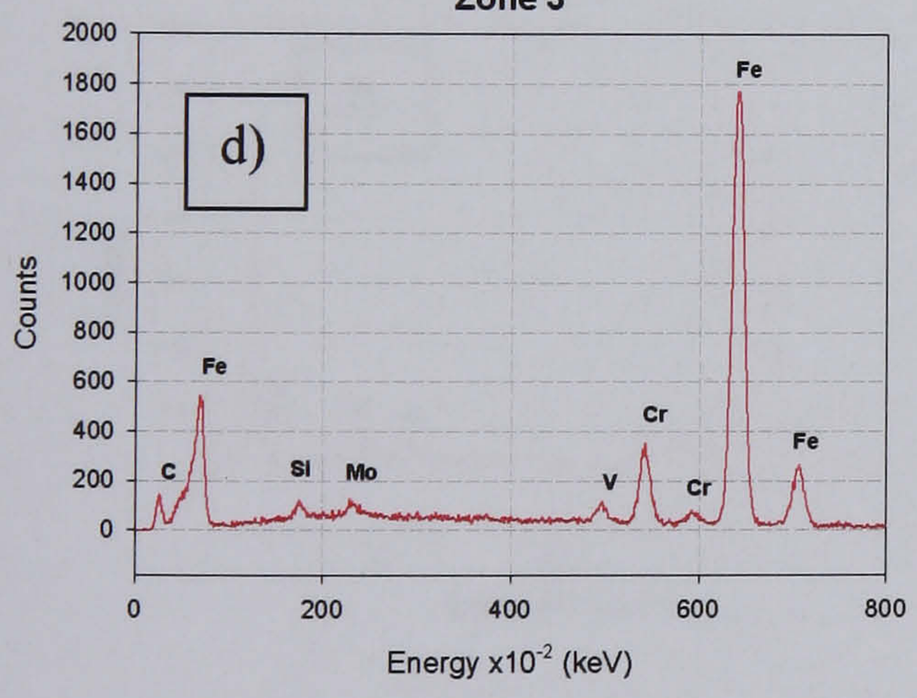

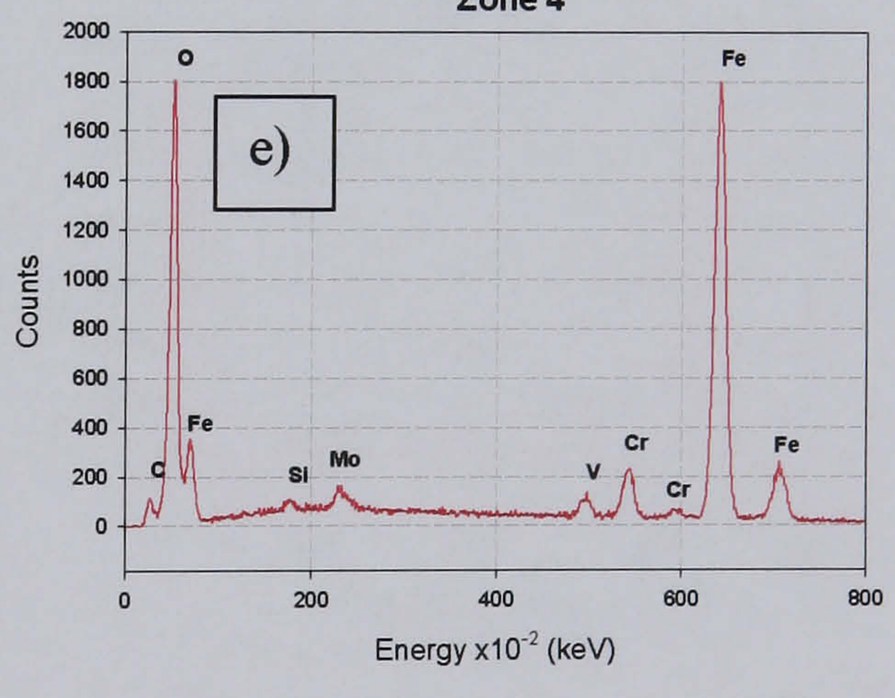

Fig.4.102. EDX point analyses of specific regions in the secondary electrons image shown in a). b) Elements present in zone 1, c) zone 2, d) zone 3, e) zone 4.

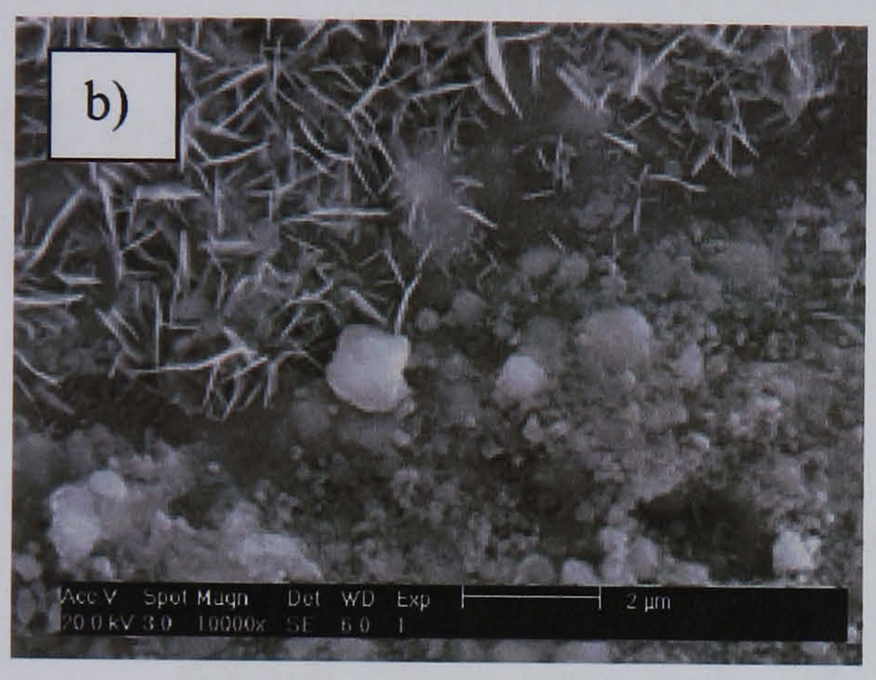

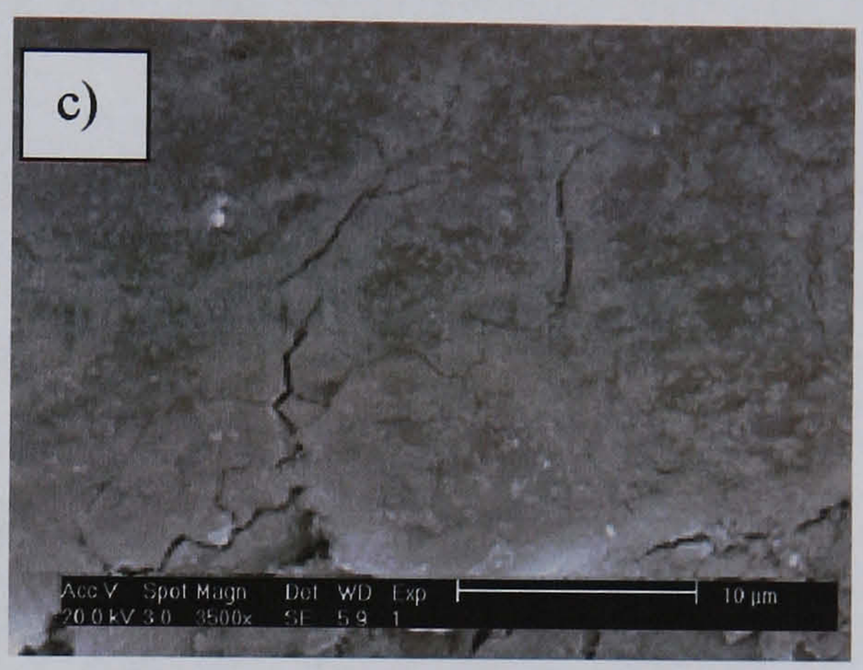

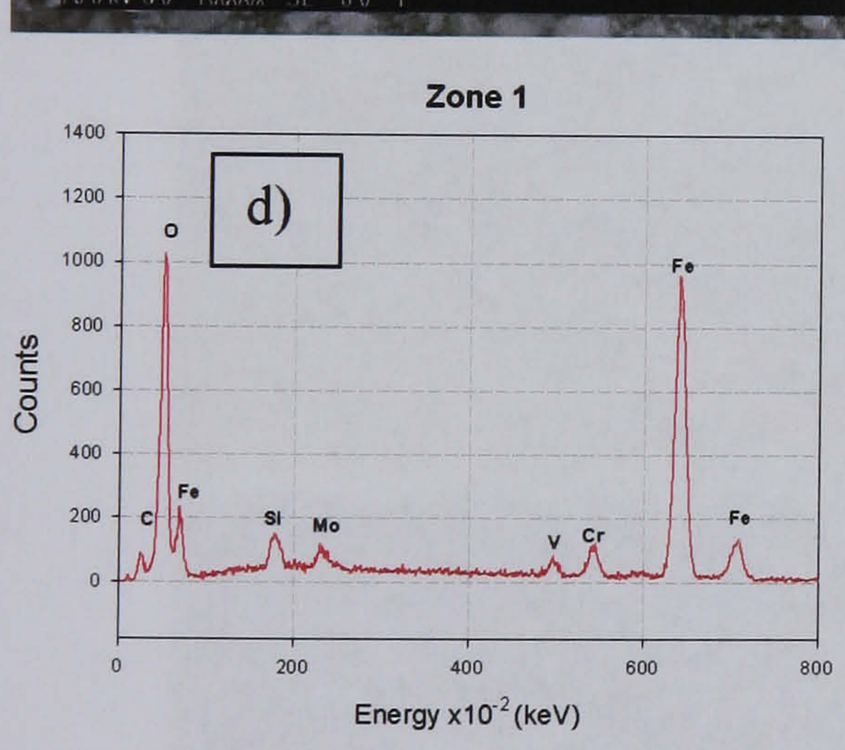

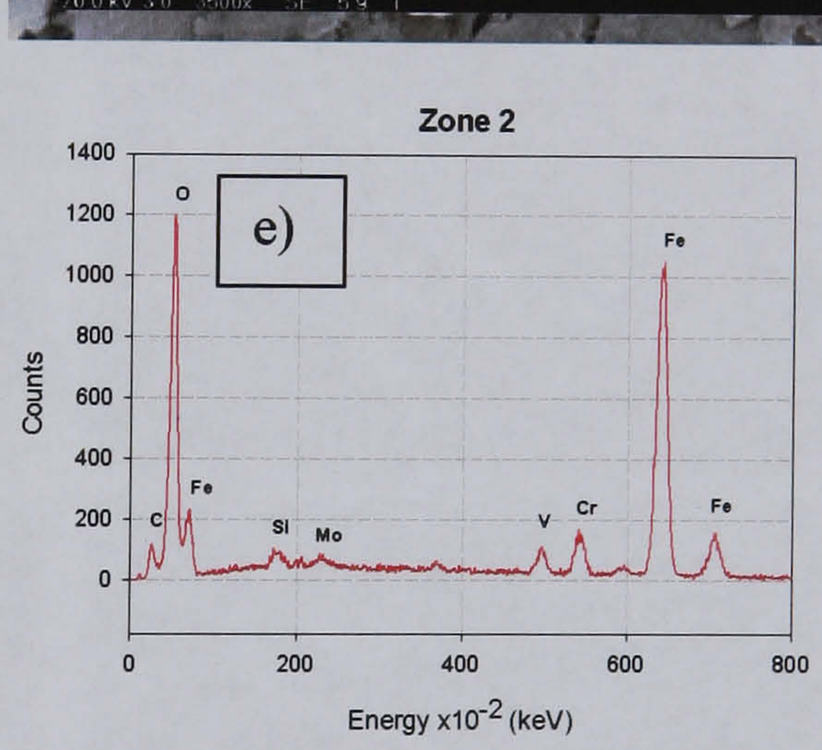

Fig.4.103. a) Characteristic zones found in the test disc after the test at **500 °C** in water. b) Zone 1 in a) showing the growth of Fe_2O_3 platelets as well as wear debris particles within the wear track. c) Zone 2 in a) showing fracture and crack propagation observed in the spinel layer. d) and e) EDX area analysis of zones 1 and 2 shown in a) respectively.

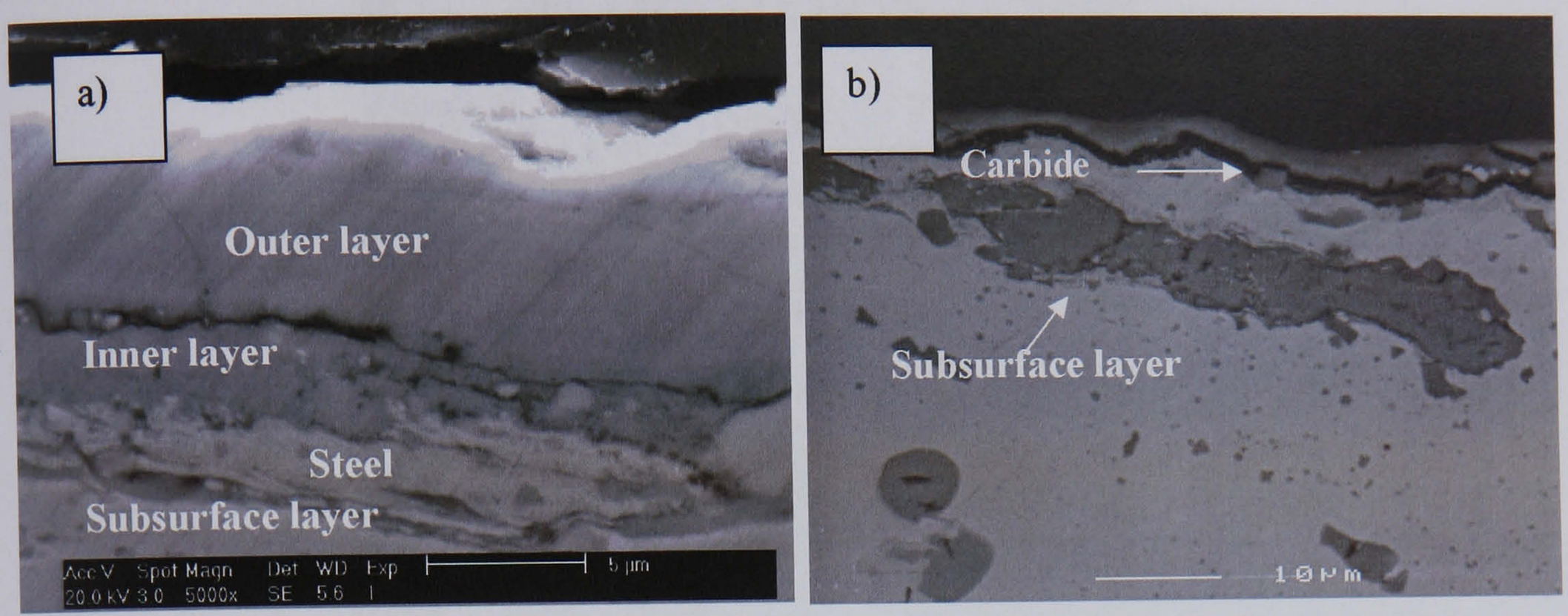

Fig.4.104. a) Secondary electrons image of a cross section of the test disc at **500°C** with water. b) Backscattered electrons image of a different zone in the sample showing subsurface oxidation of the steel.

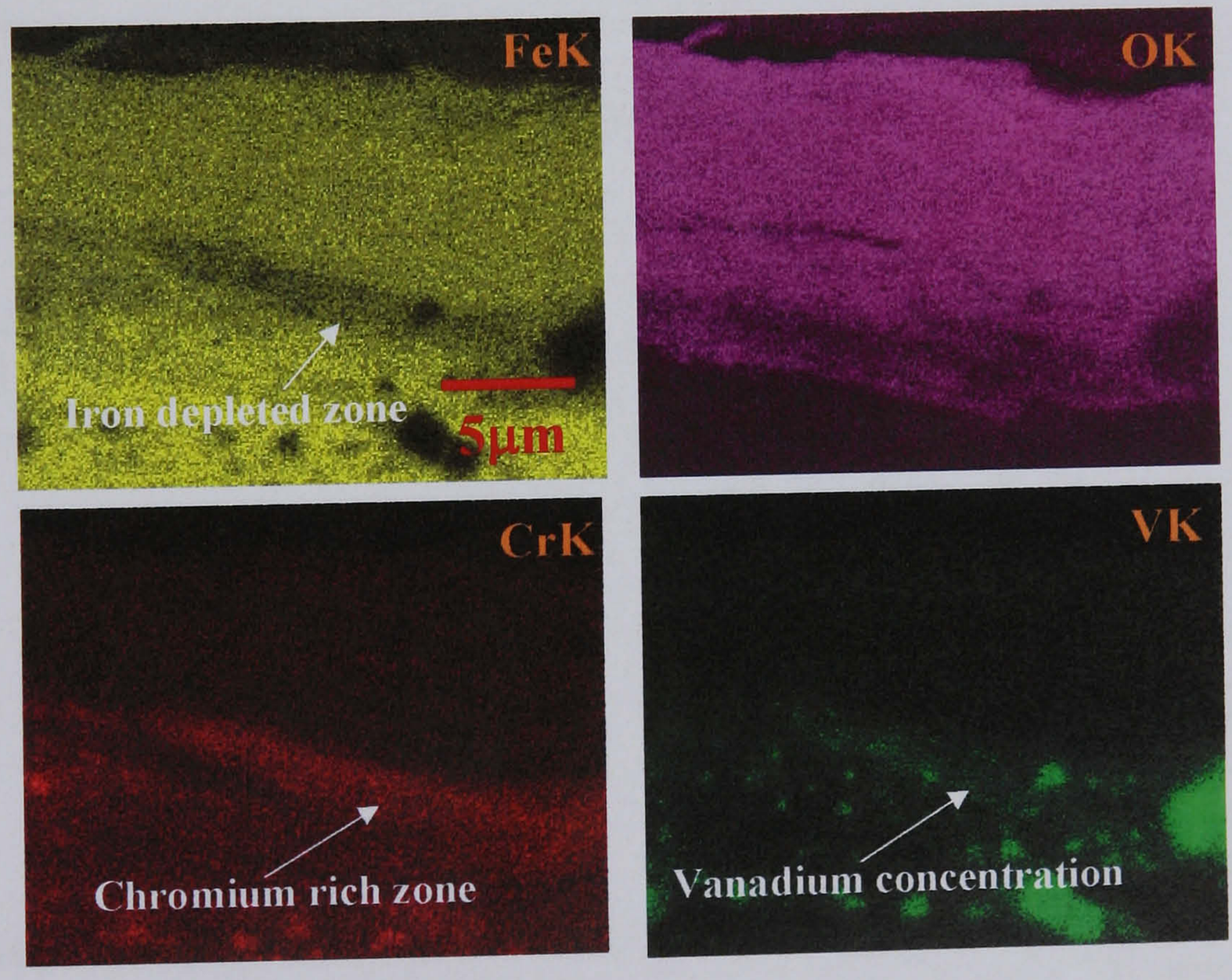

Fig.4.105. EDX dot maps of the picture a) in Fig.4.104.The oxide layer is clearly defined as well as the layer formed under the surface.

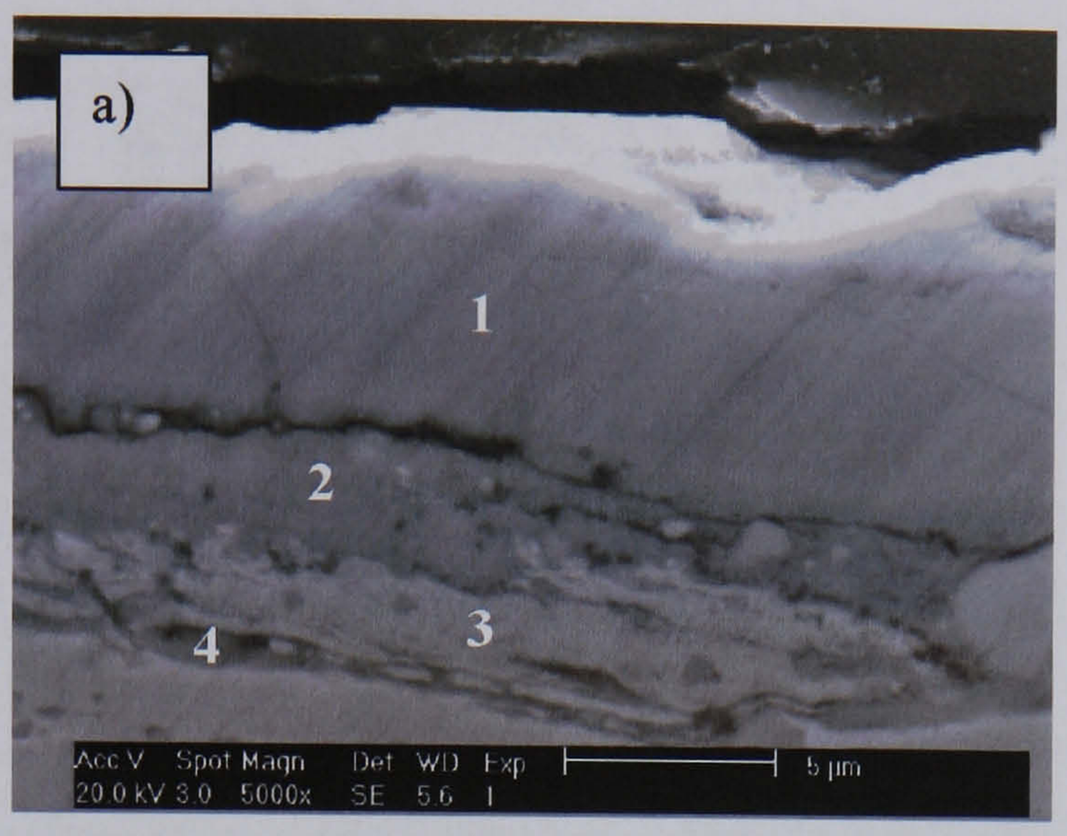

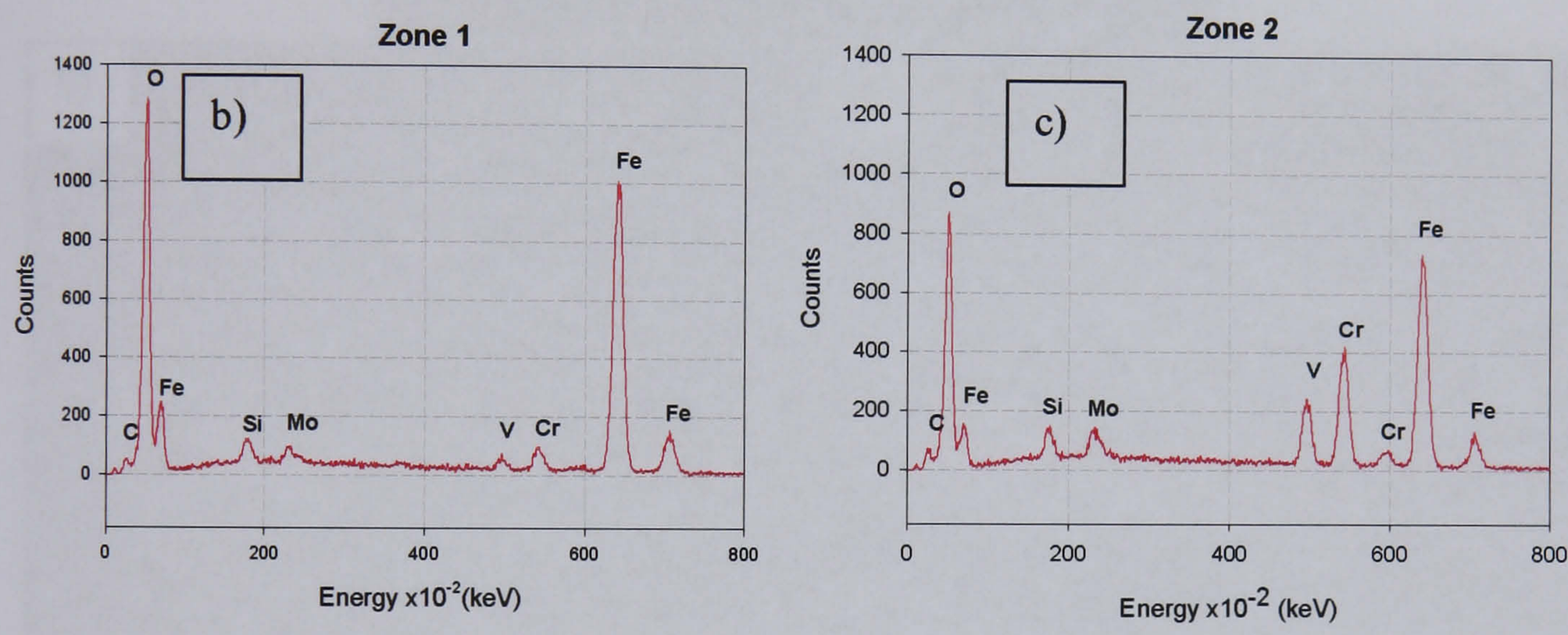

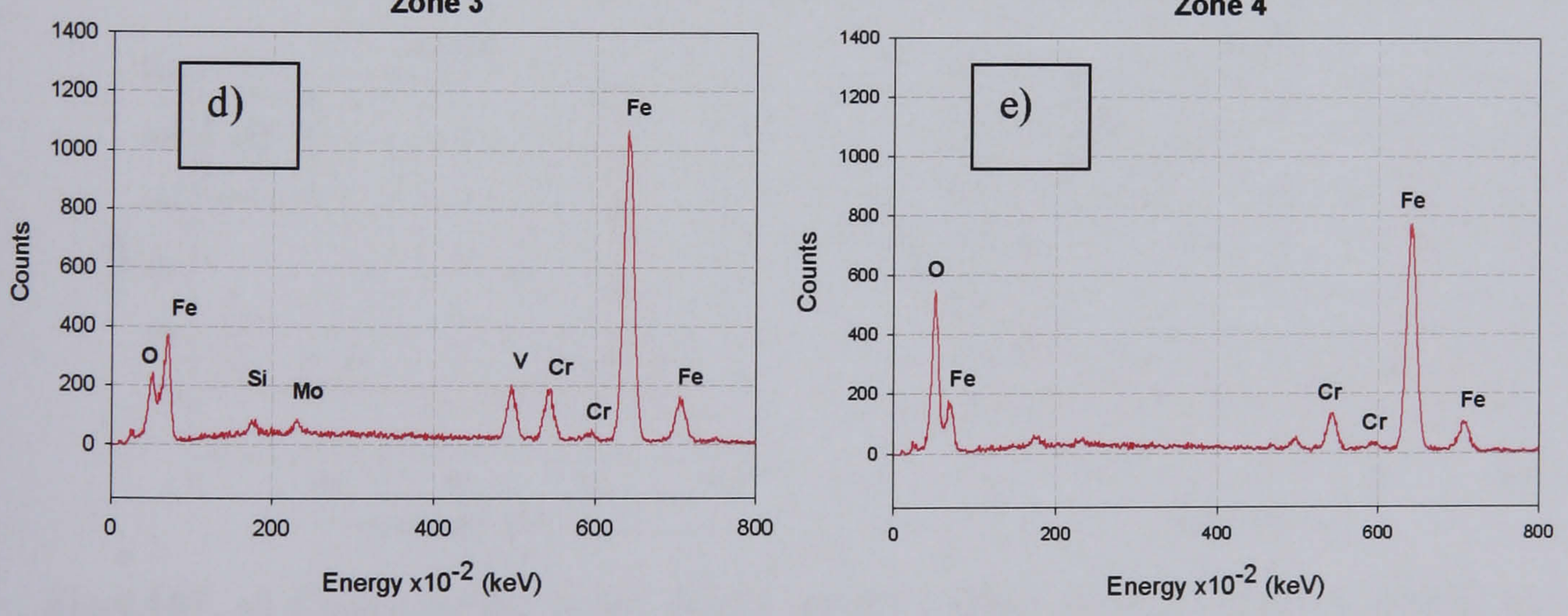

Fig.4.106. EDX point analyses of the specific regions marked in the secondary electrons image shown in a). b) Elements present in zone 1, c) zone 2, d) zone 3, e) zone 4.

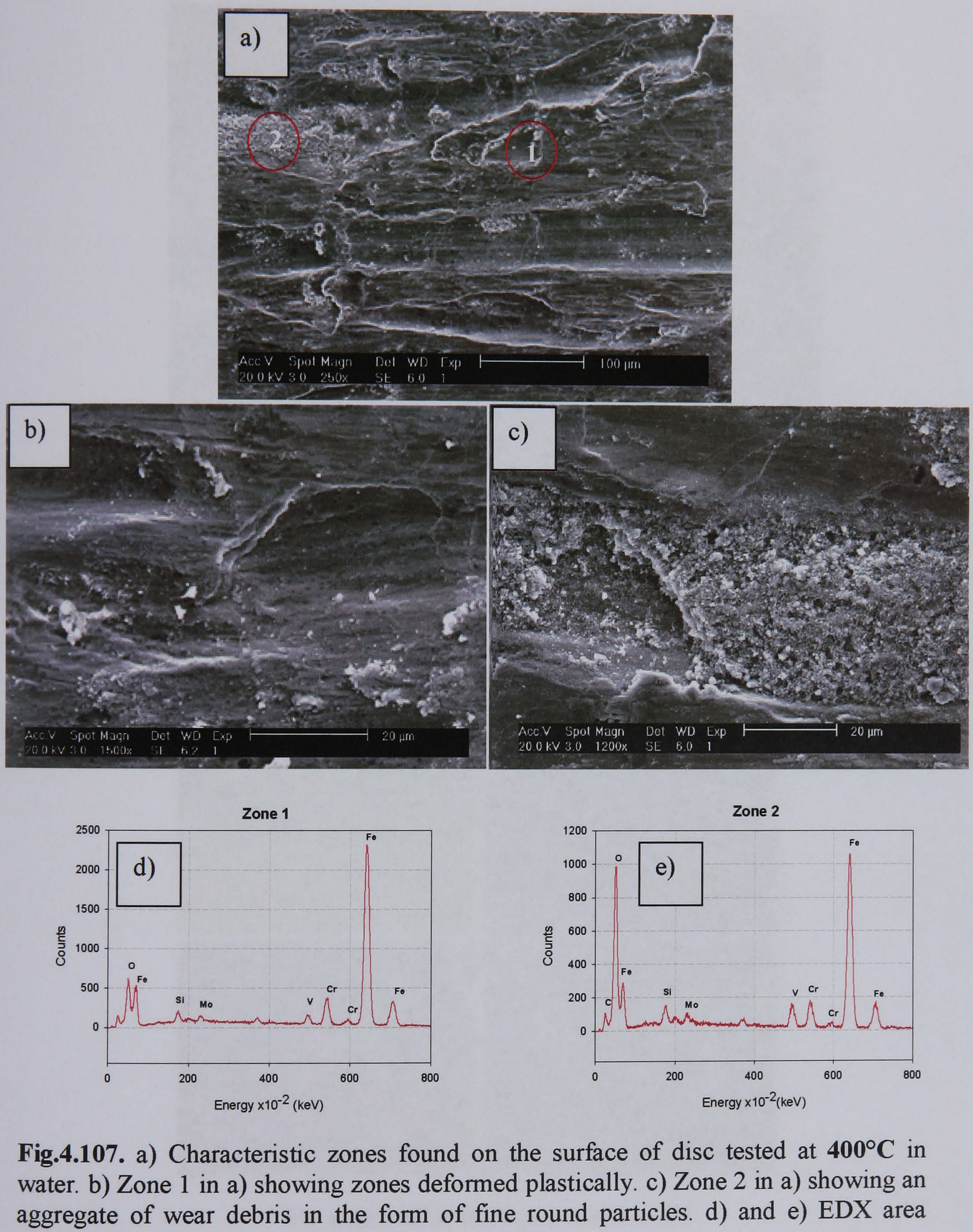

Fig.4.107. a) Characteristic zones found on the surface of disc tested at **400°C** in water. b) Zone 1 in a) showing zones deformed plastically. c) Zone 2 in a) showing an aggregate of wear debris in the form of fine round particles. d) and e) EDX area analysis of zones 1 and 2 shown in a) respectively.

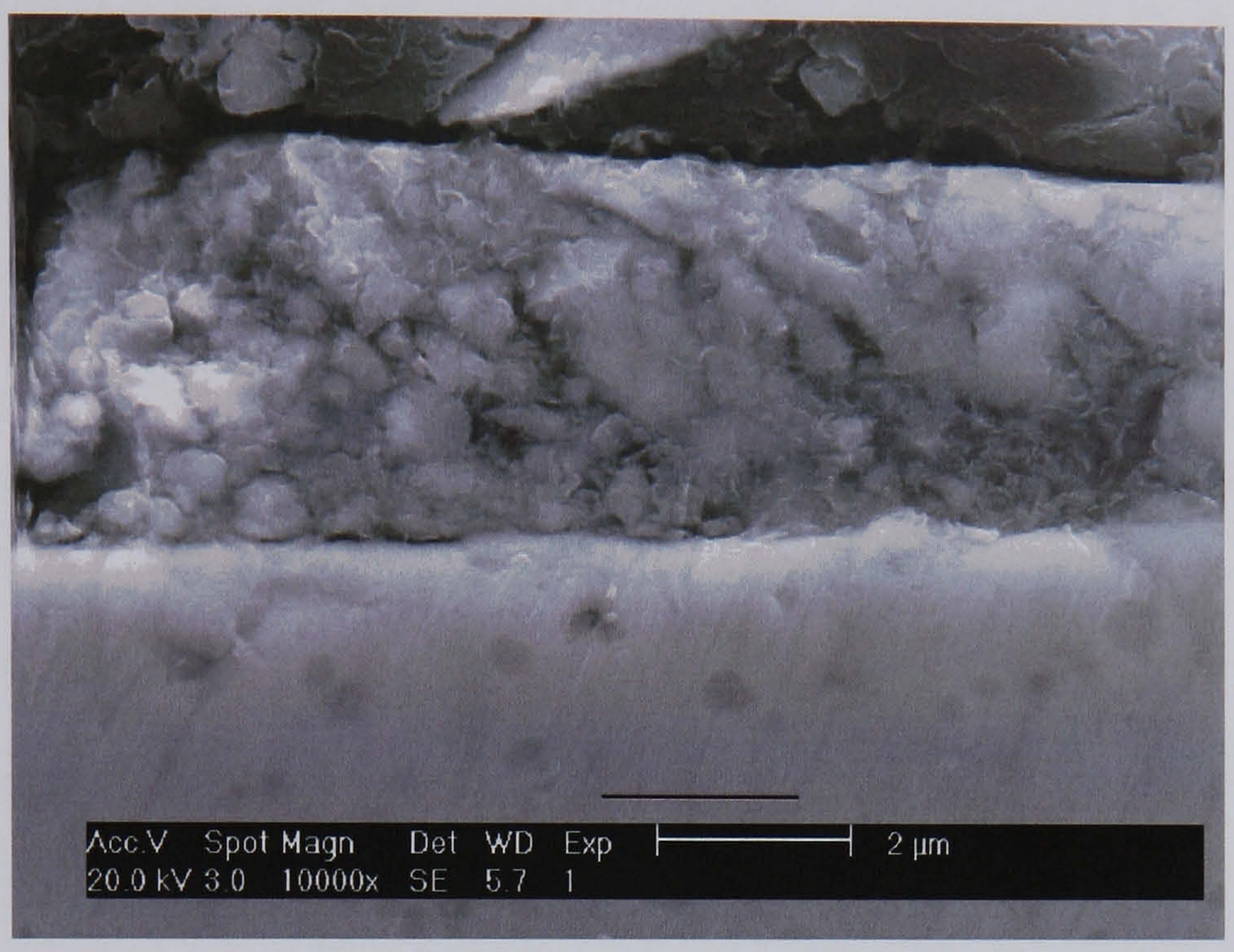

Fig.4.108. Cross section of the oxide layer formed on the surface of the test discs at **400°C** in water. It can be identified that the oxide layer is comprised by an aggregate of oxide particles.

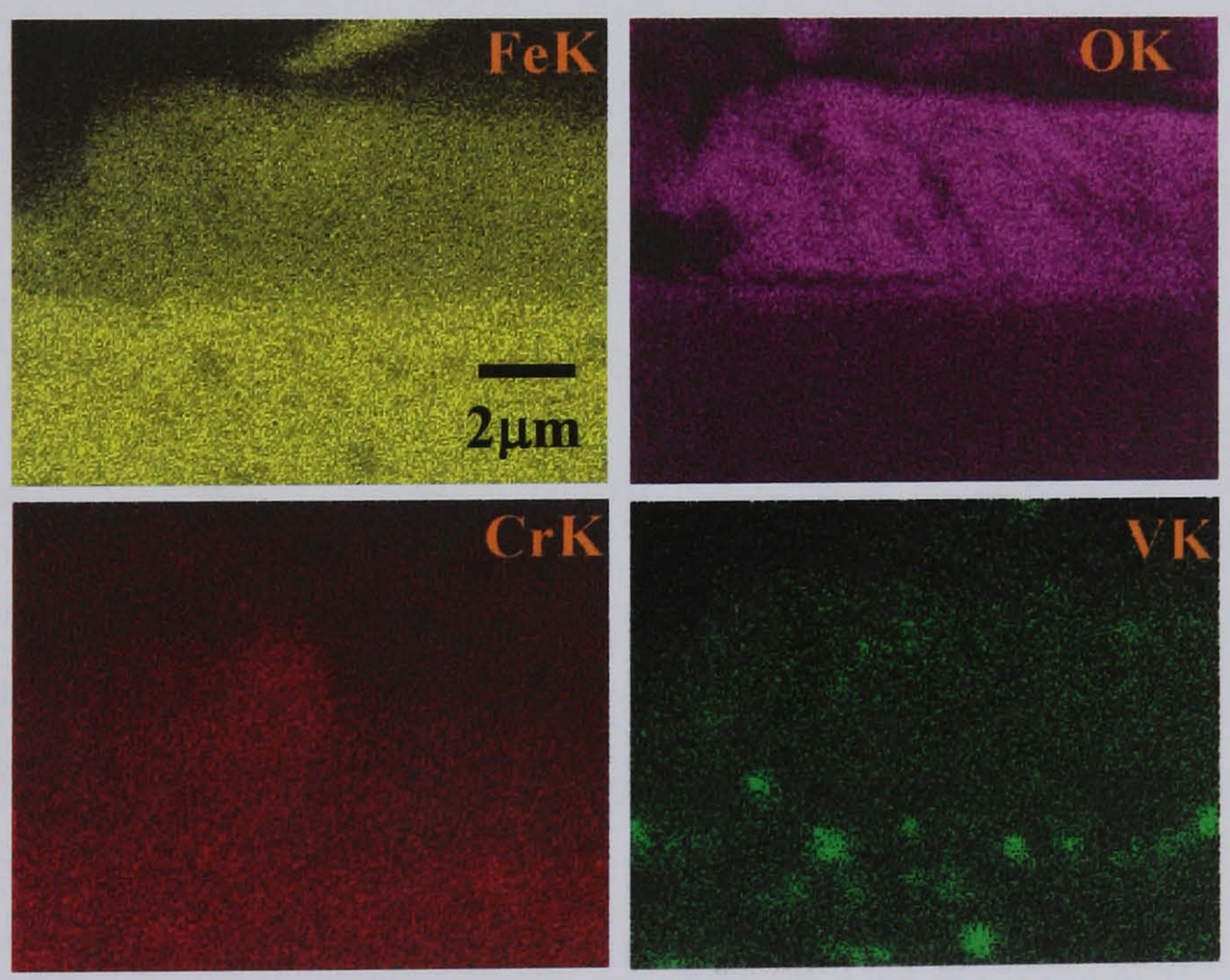

Fig.4.109. EDX dot maps of Fig.4.108..

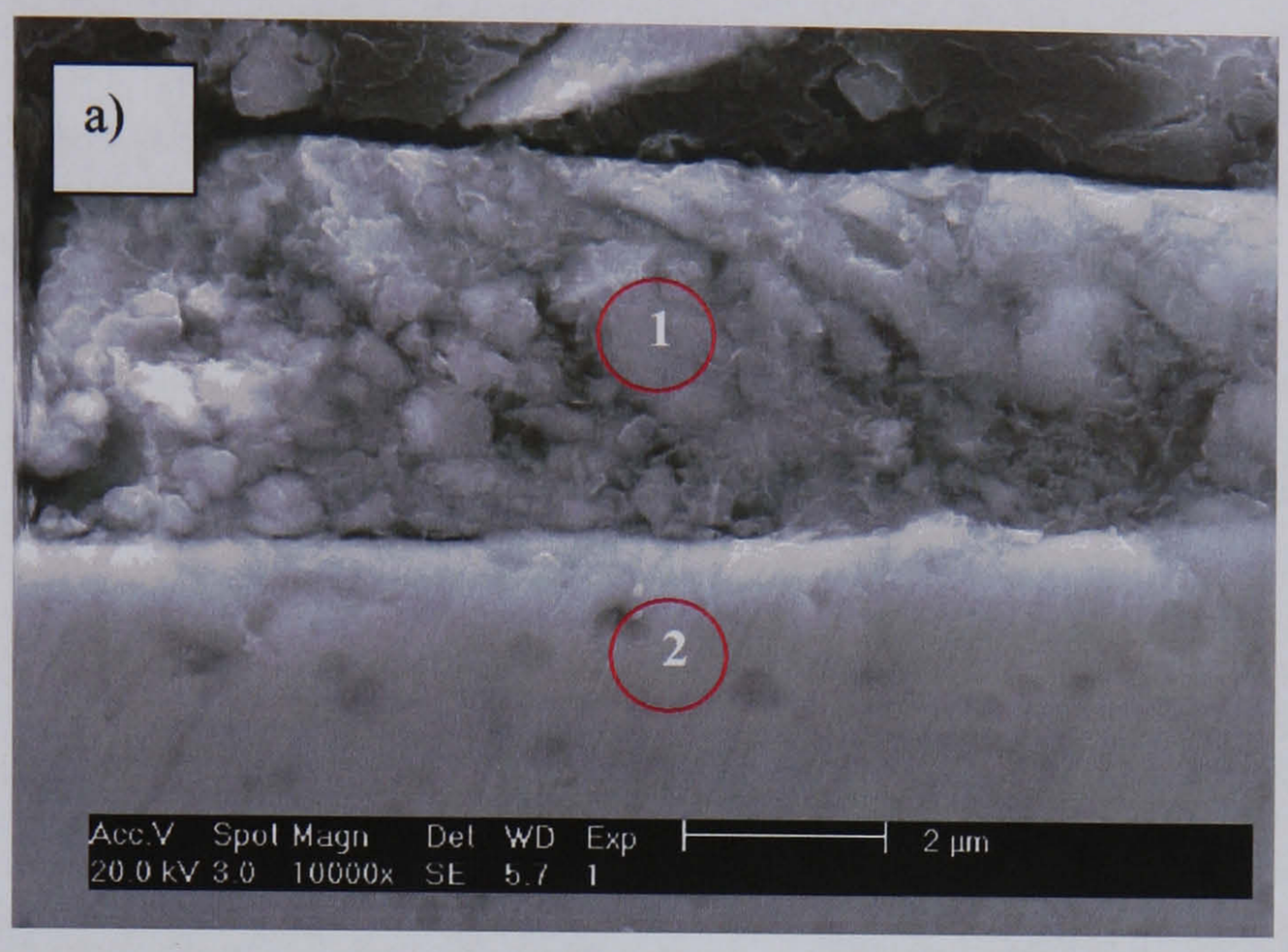

Fig.4.110. EDX area analysis of the zones shown in a). b) The oxide layer and c) the steel, no internal oxidation zones were found under this condition.

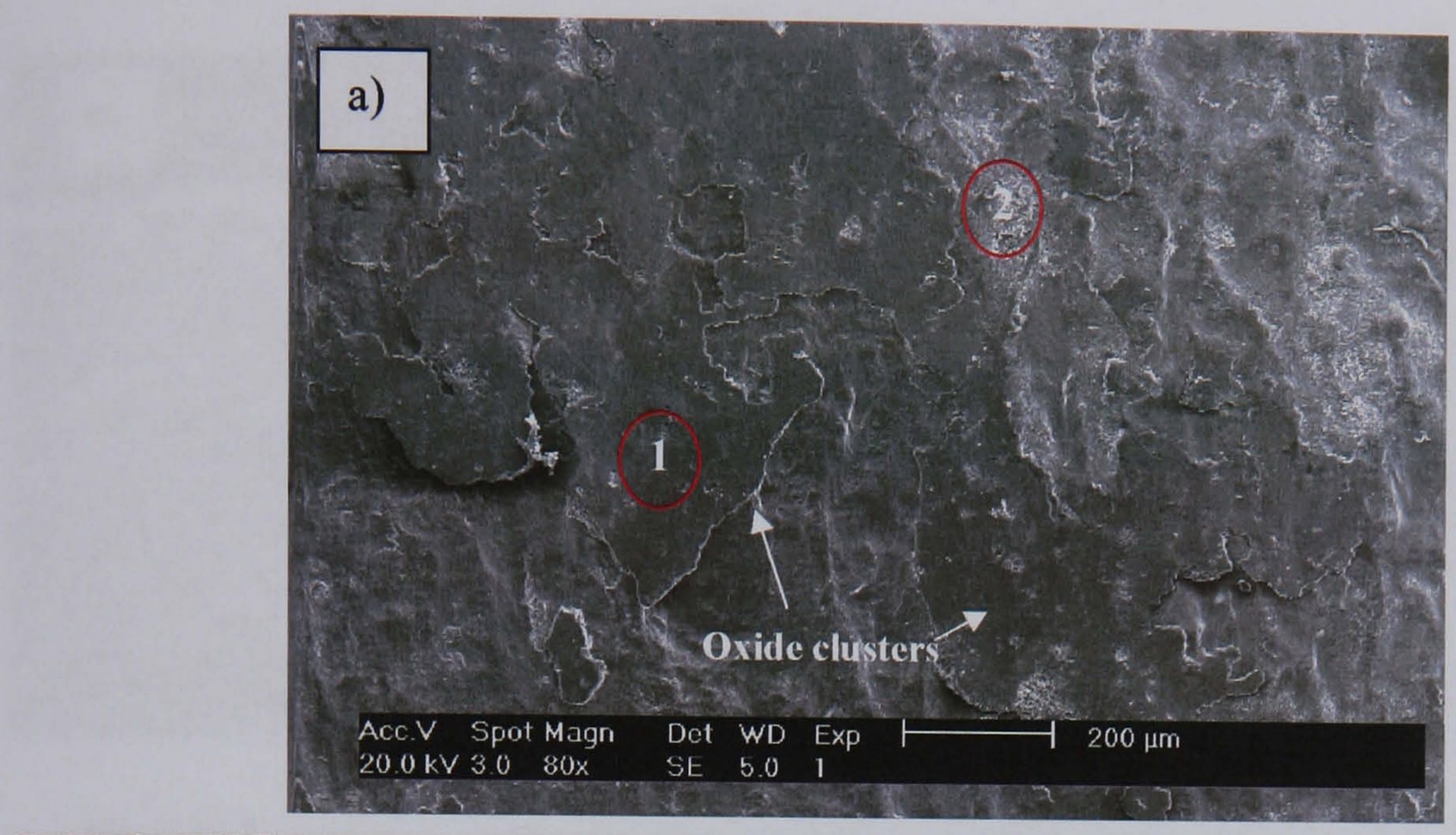

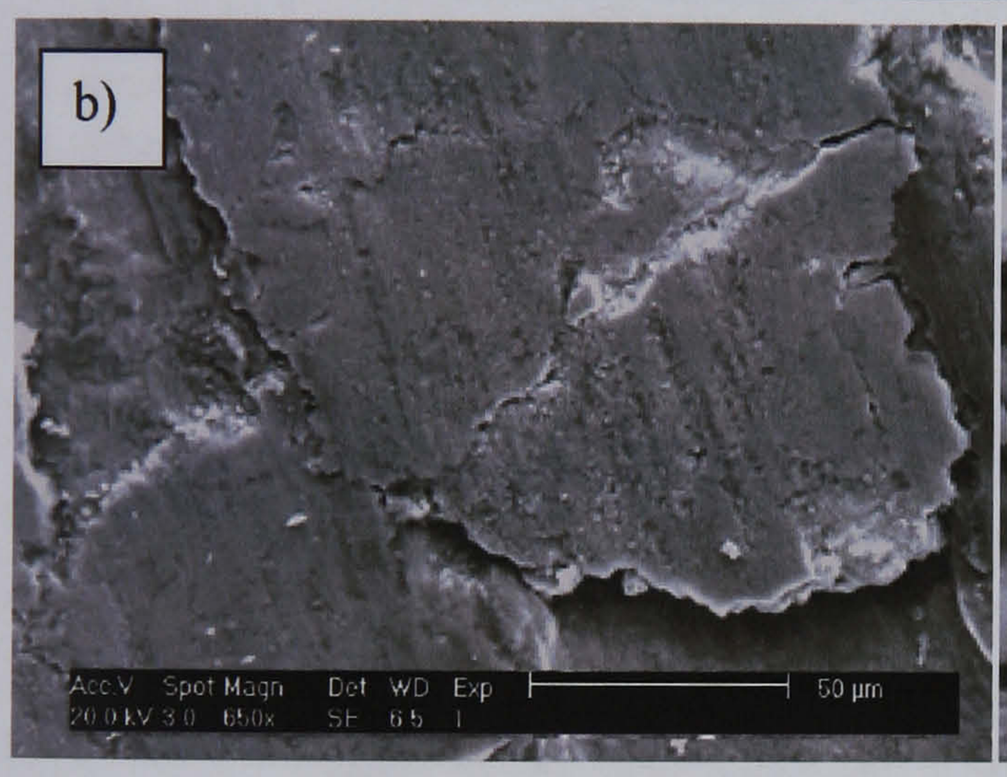

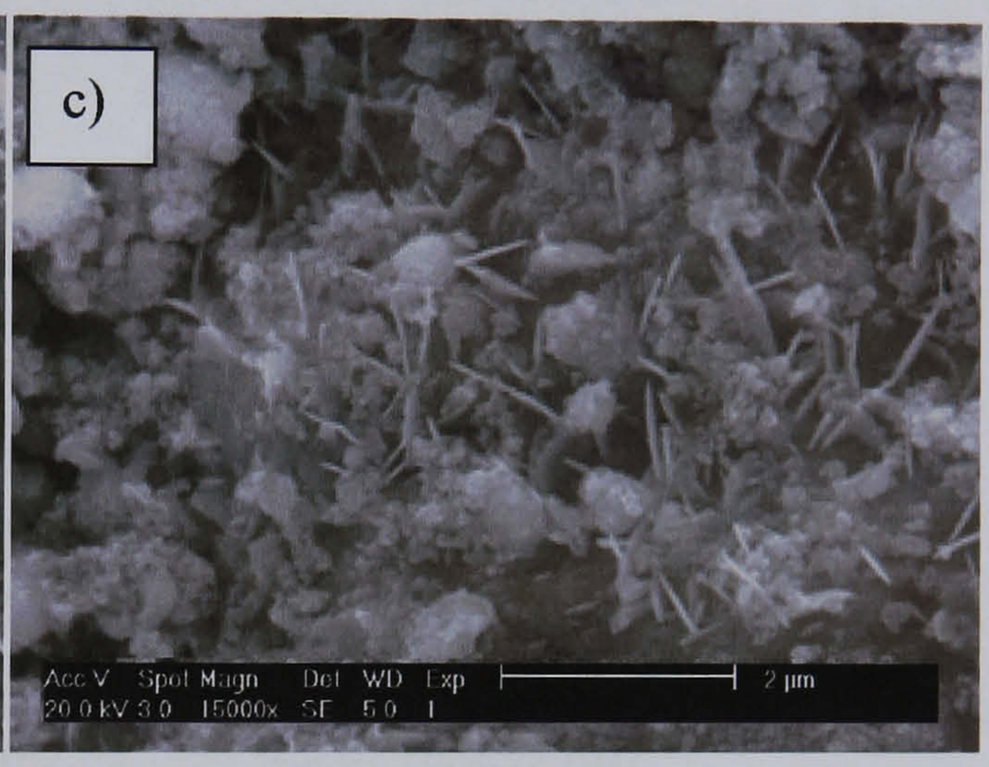

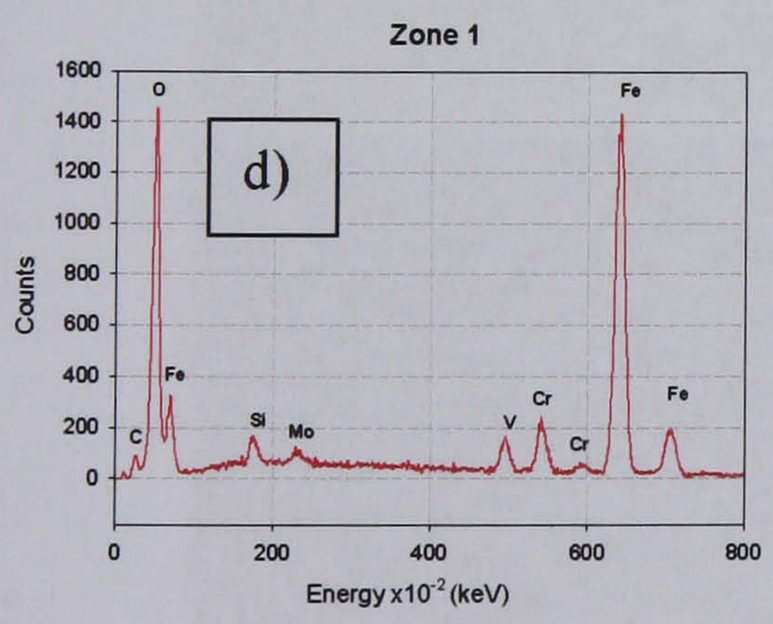

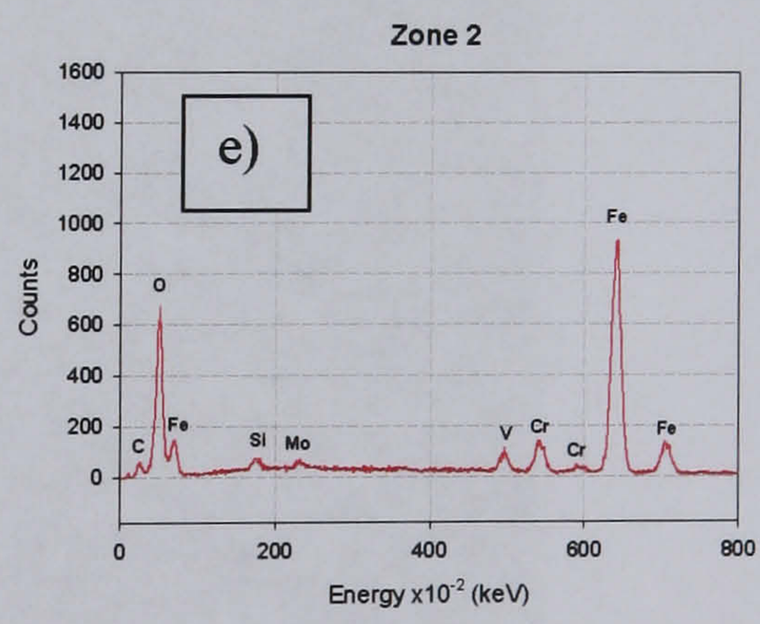

Fig.4.111. Characteristic zones found on the surface of the test disc at **600°C** in dry air b) Oxide cluster. c) Formation of hematite Fe_2O_3 platelets and the presence of wear debris. d) and e) EDX area analysis of b) and c) respectively.

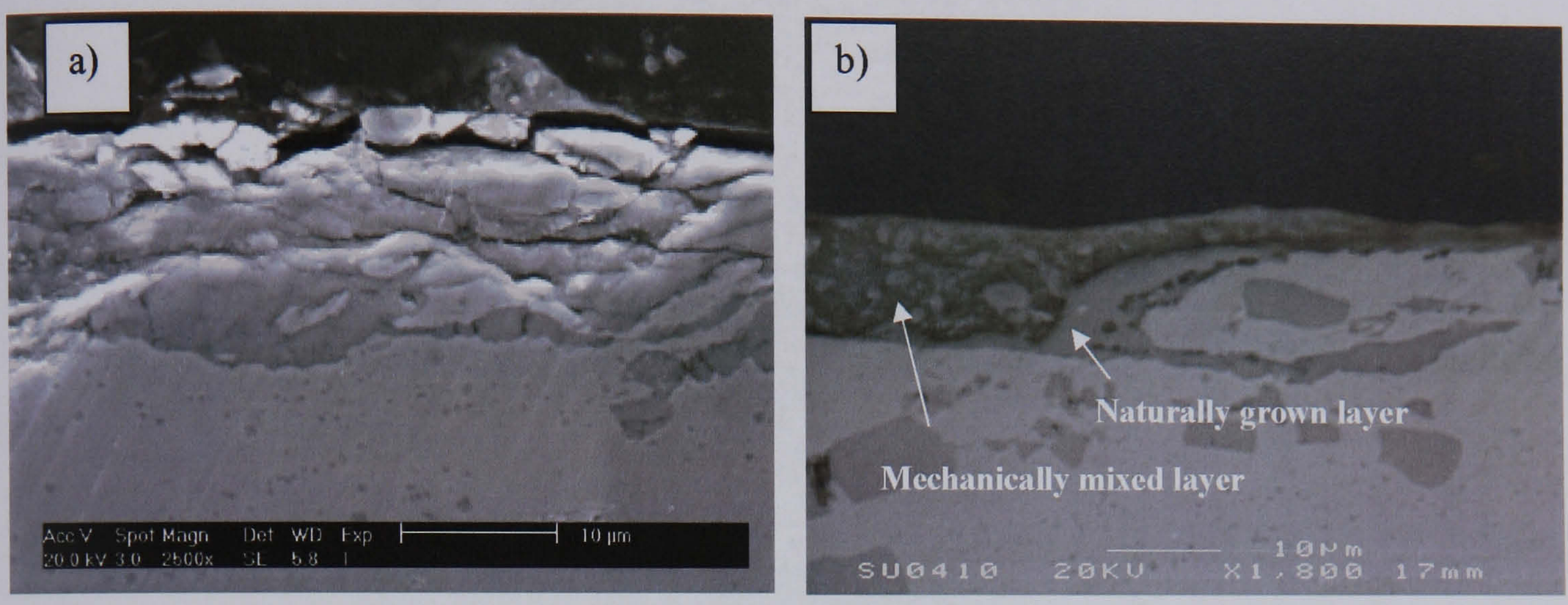

Fig.4.112. a) Cross section of the oxide layer formed in the tests at **600°C** in dry air. Formation of surface and subsurface layers with abundant cracks was a characteristic phenomenon of this experiment. b) Backscattered electron image of a different zone found in the same sample.

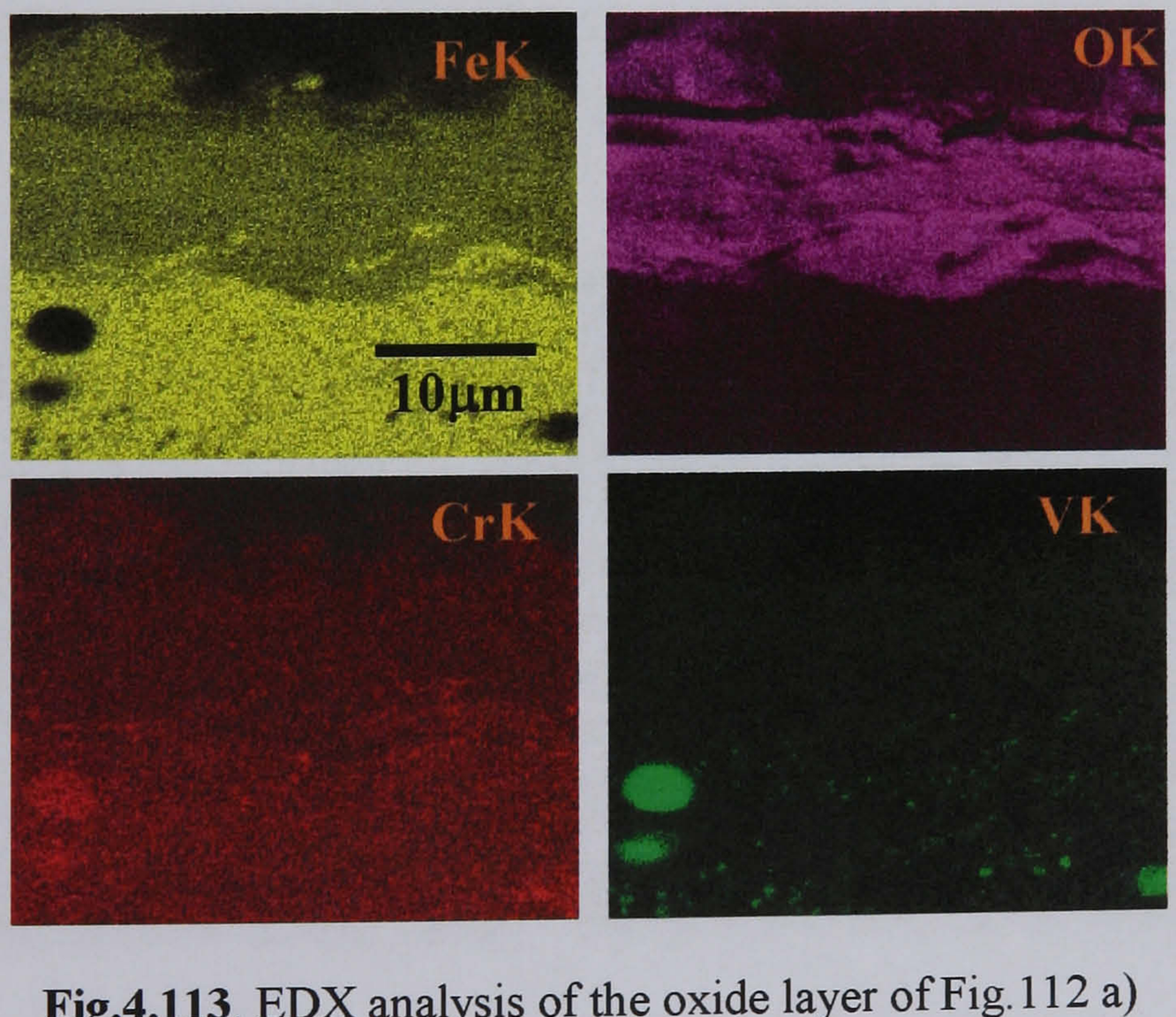

Fig.4.113. EDX analysis of the oxide layer of Fig.112 a)

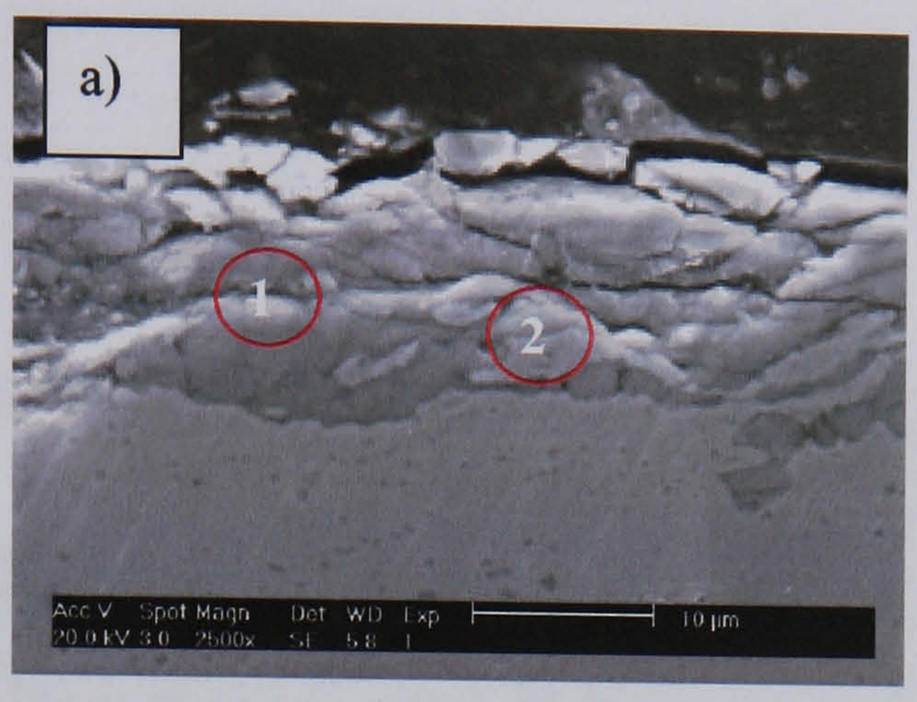

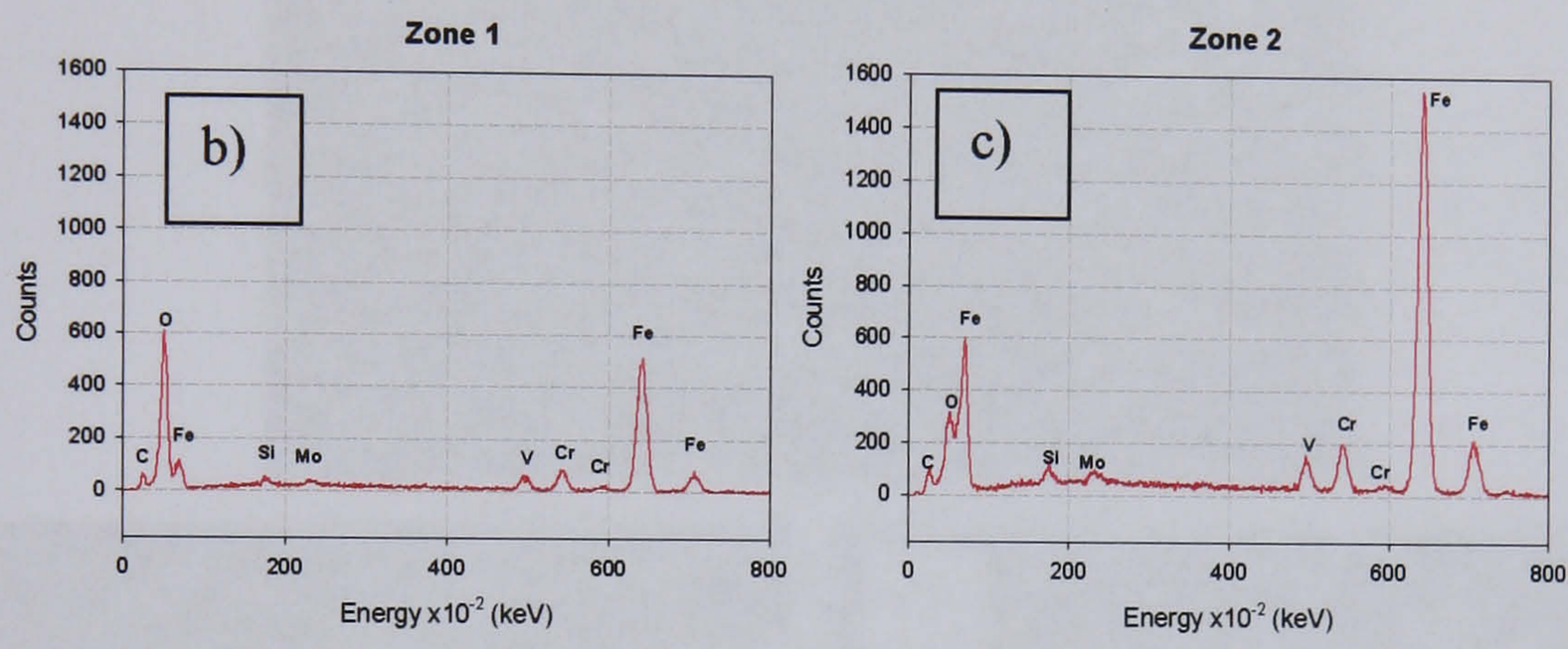

Fig.4.114. EDX area analysis of the characteristics zones found in the sample b) Zone 1, the oxide layer. c) Zone 2, the steel substrate.

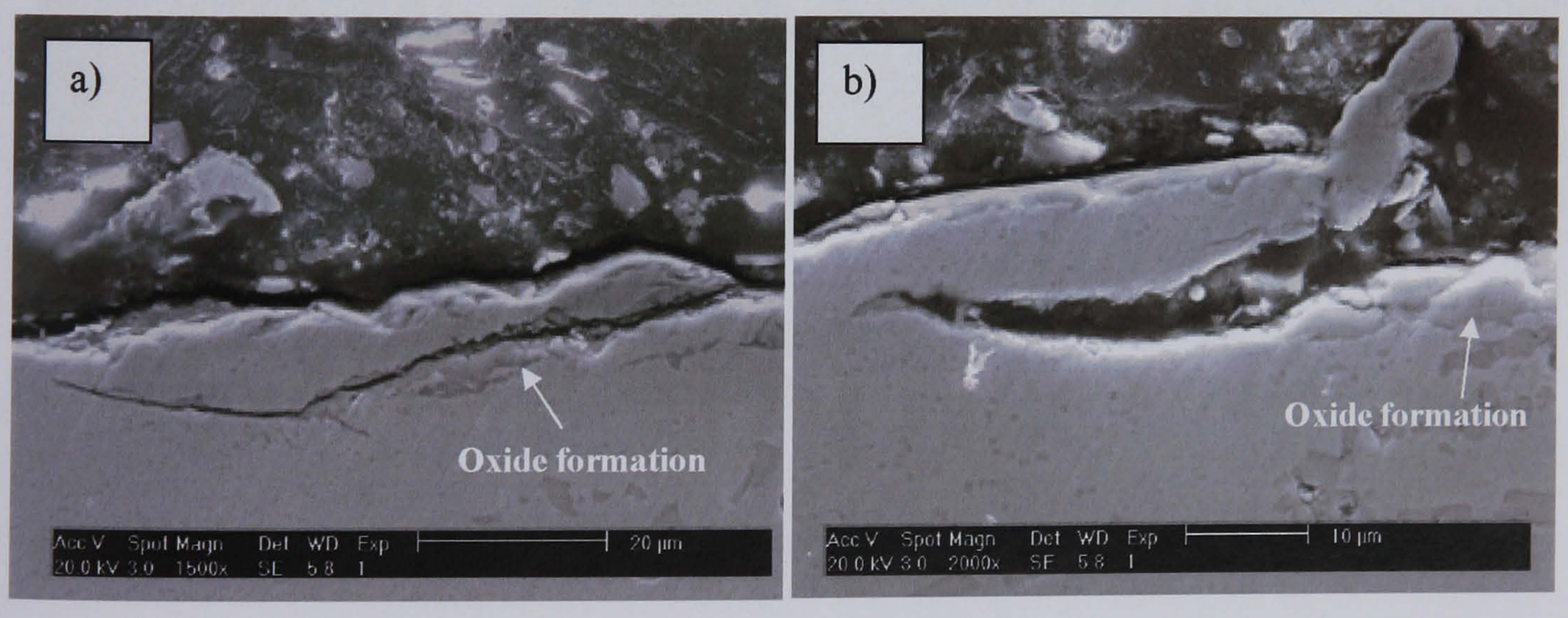

Fig.4.115. a) Separation of metal due to subsurface crack formation and oxidation within the crack. b) Severe fracture of a section of the disc.

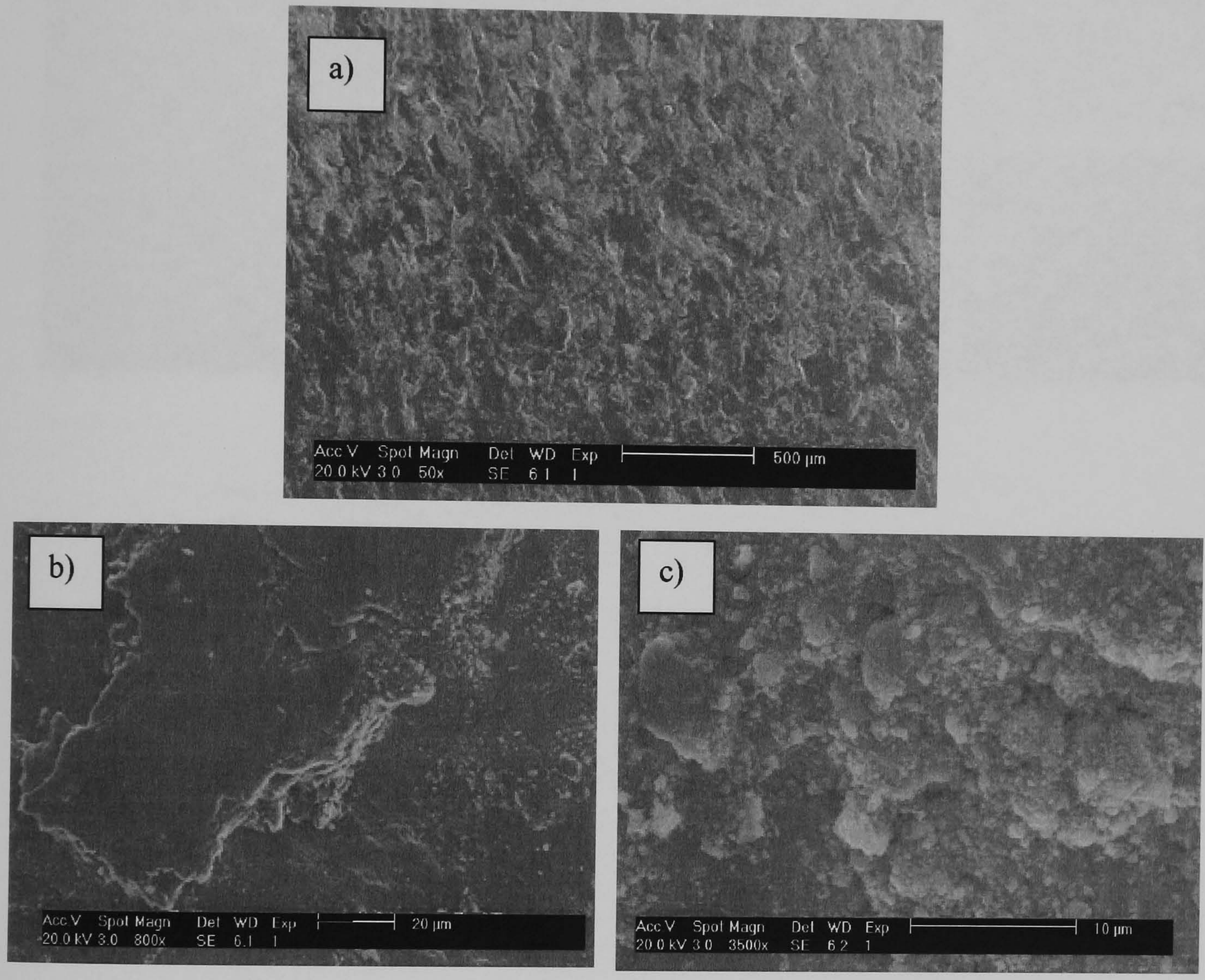

Fig.4.116. Characteristic zones found on the surface of the disc tested at **500°C** in dry air. b) Big oxide cluster and abraded zone with exposed steel. c) Wear debris.

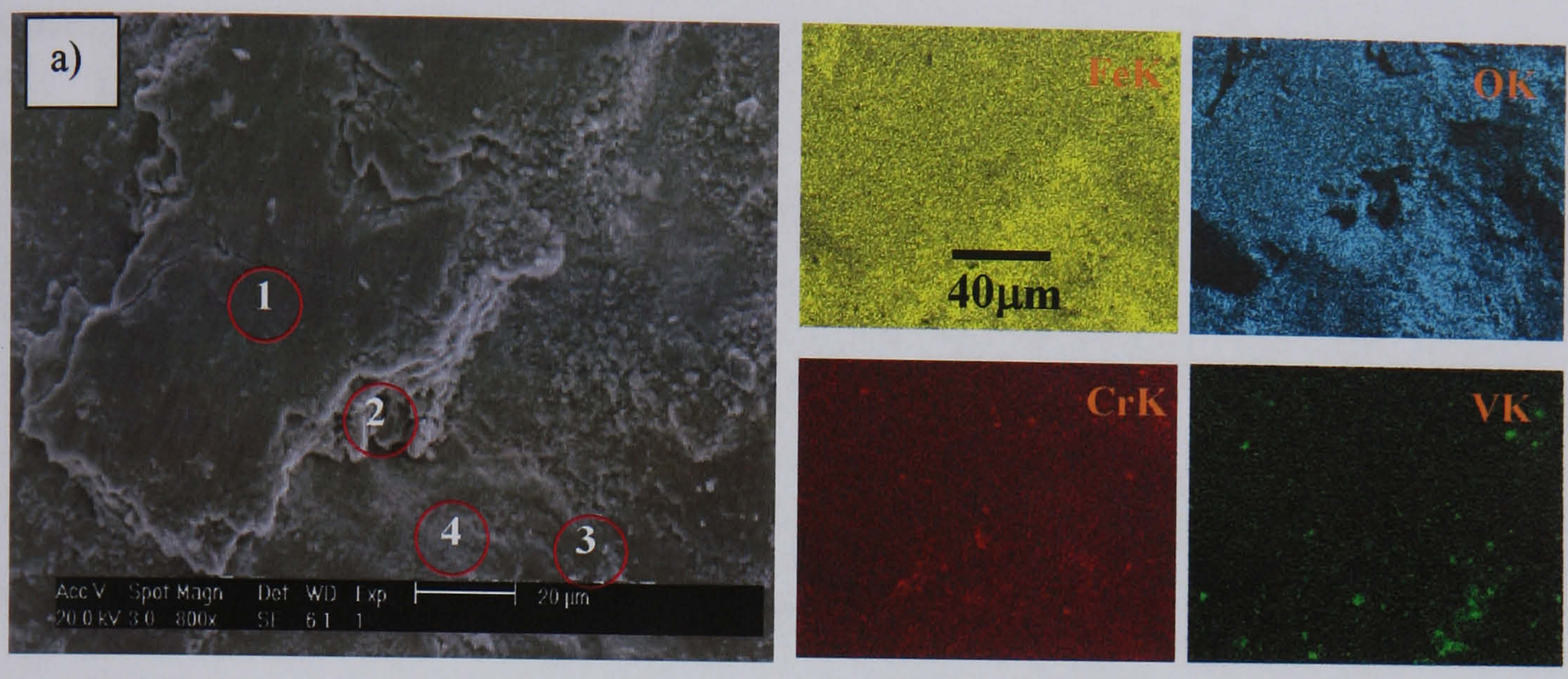

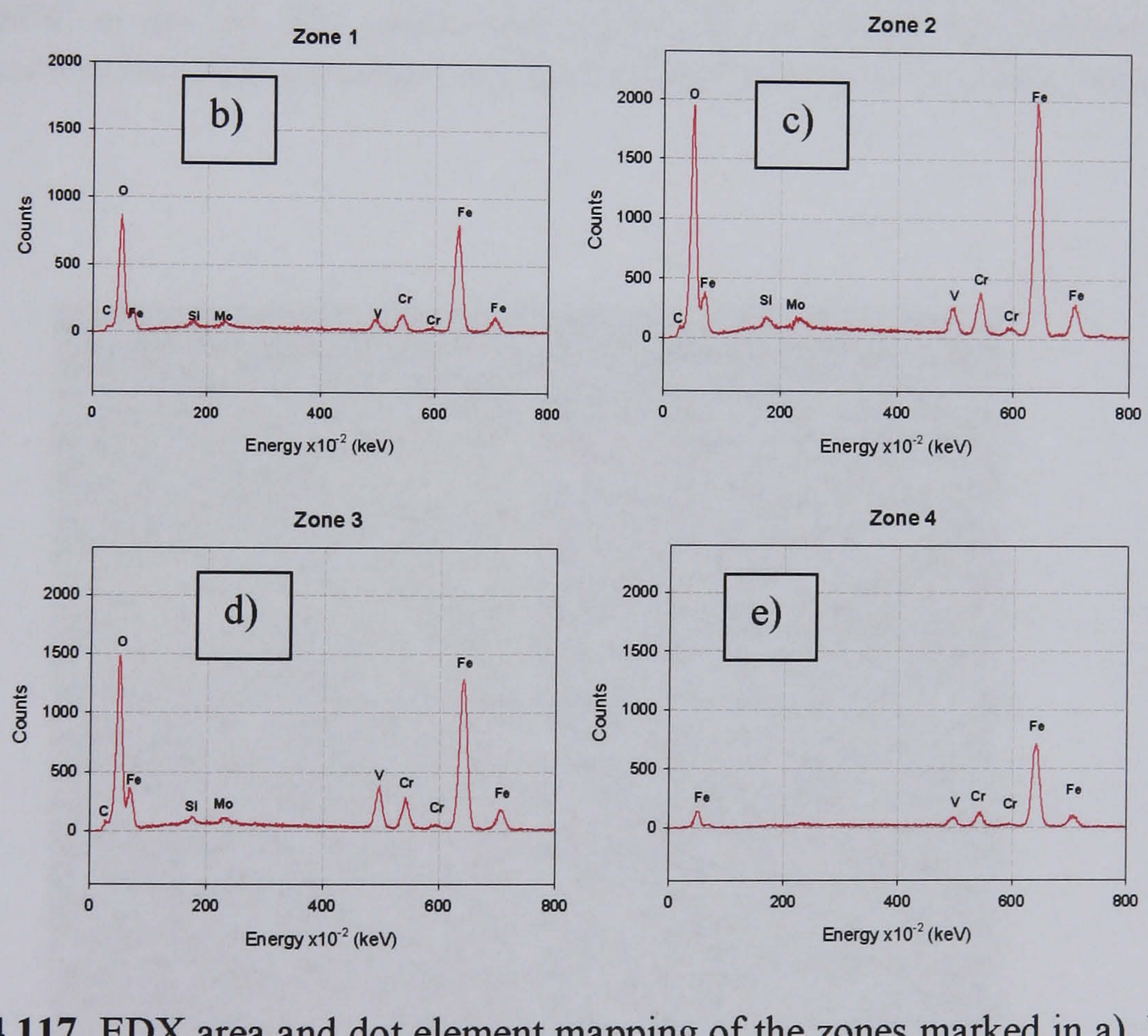

Fig.4.117. EDX area and dot element mapping of the zones marked in a). b) and c) Peaks corresponding to the oxide cluster. d) High vanadium concentration detected, related to the oxidation of a MC carbide and e) the exposed steel substrate.

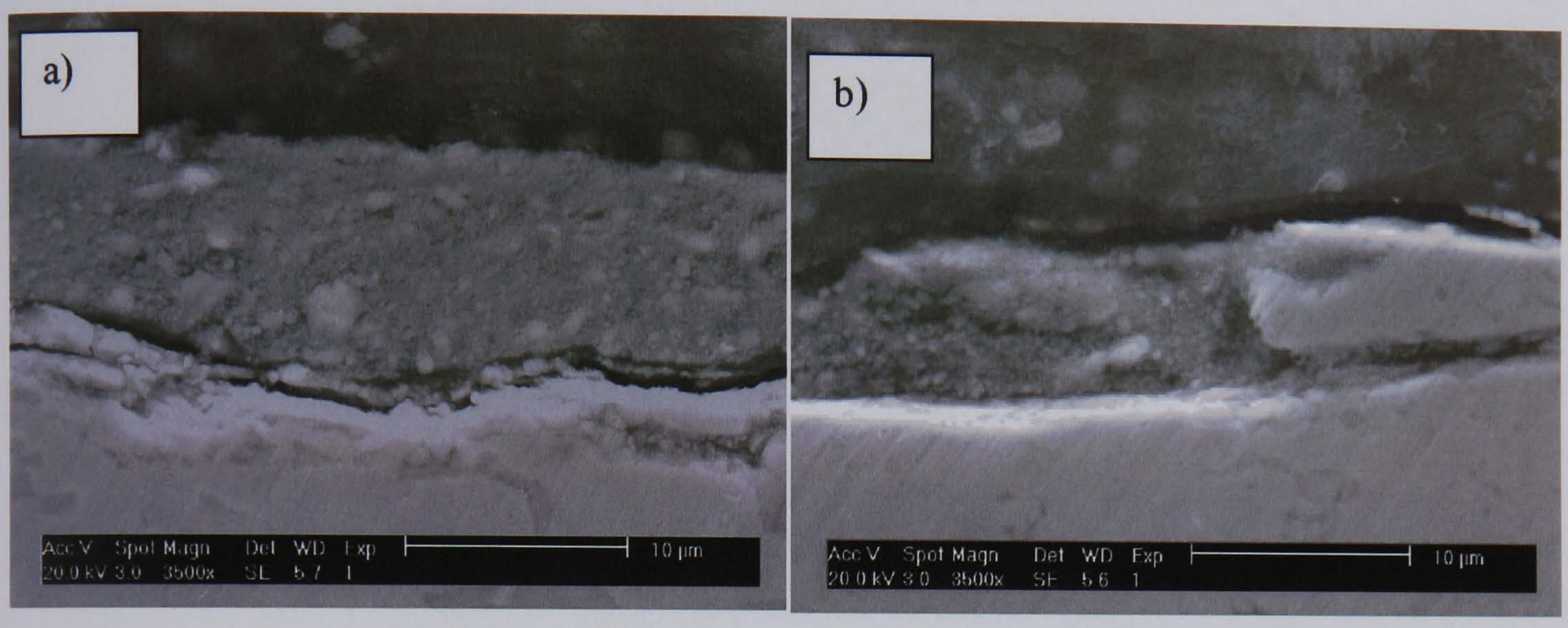

Fig.4.118. a) and b) Cross sections of the oxide scale formed on the surface of the disc tested at **500°C** in dry air. The oxide layer looks like an arrangement of mechanically mixed and compacted oxide particles in a). Subsurface formation of oxide is evident.

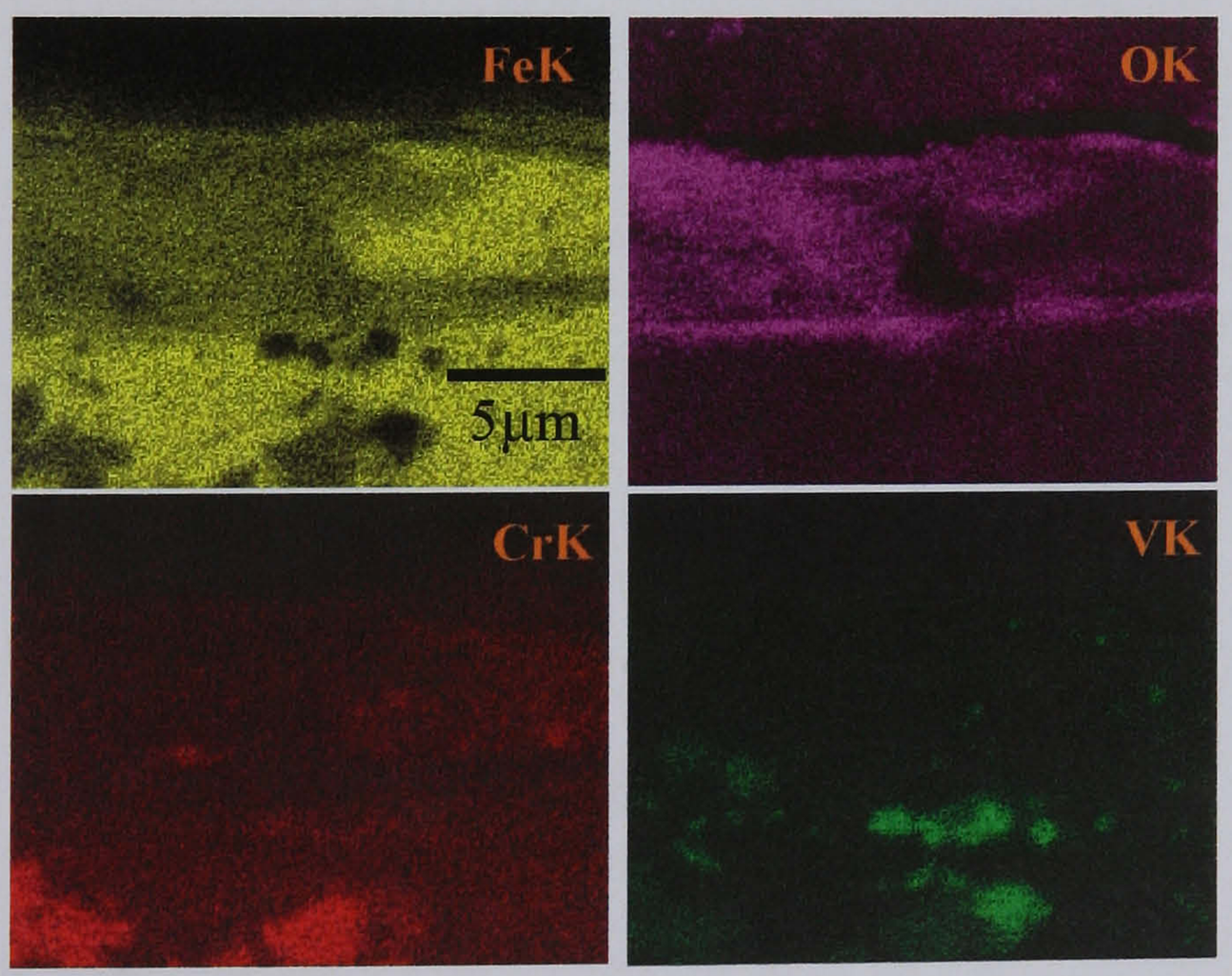

Fig.4.119. EDX dot maps of the elements present in oxide scale shown in picture b) of Fig.4.118. The presence of chromium in the oxide layer suggests that this layer is formed predominantly by spinel M_3O_4. Non oxidized and fractured steel is also evident in the iron map.

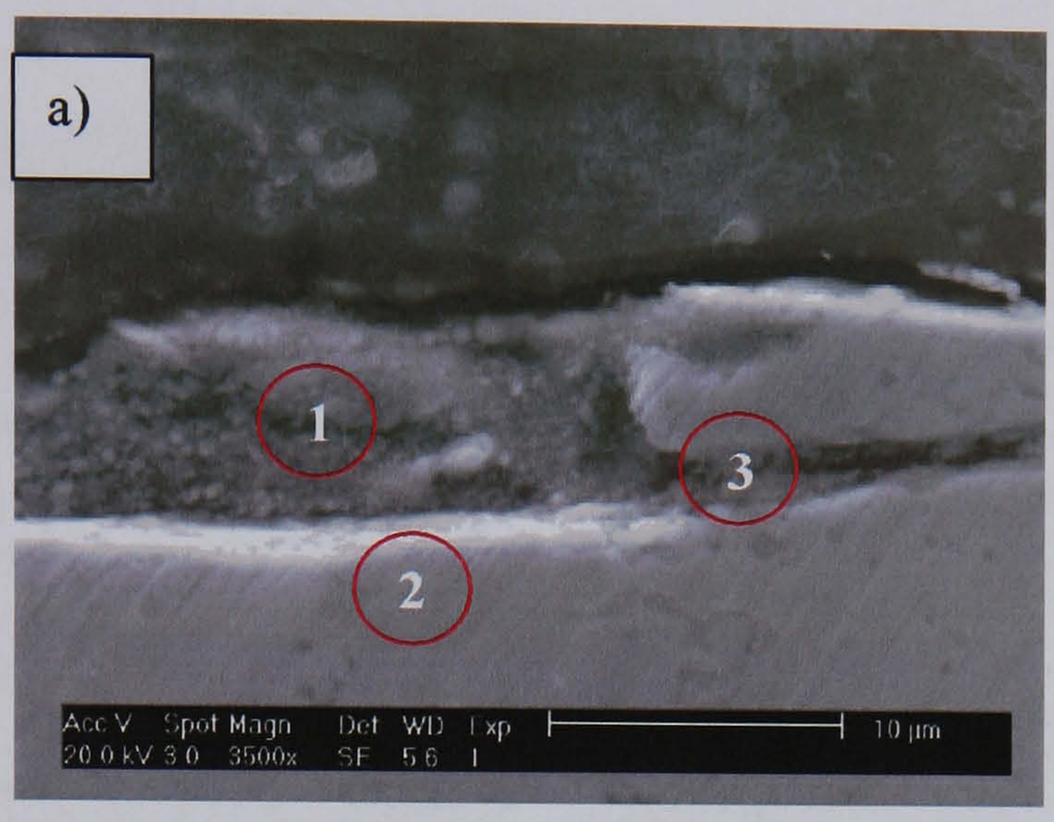

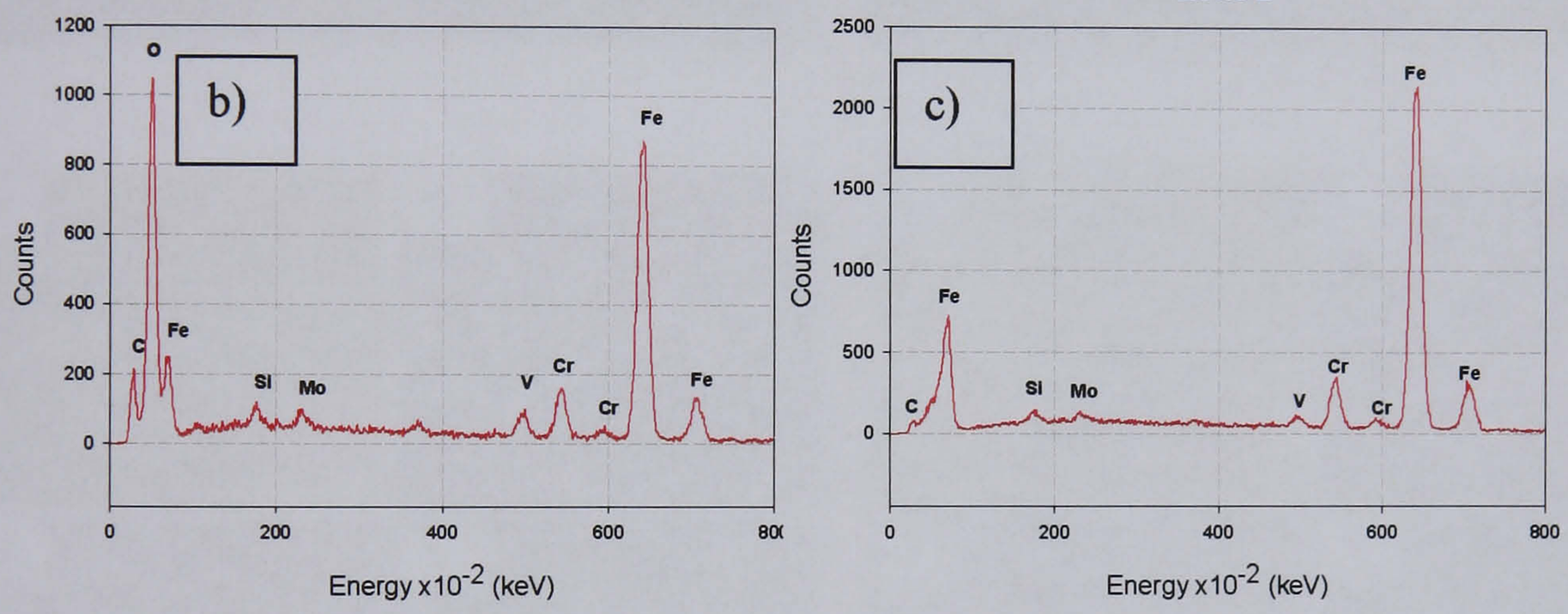

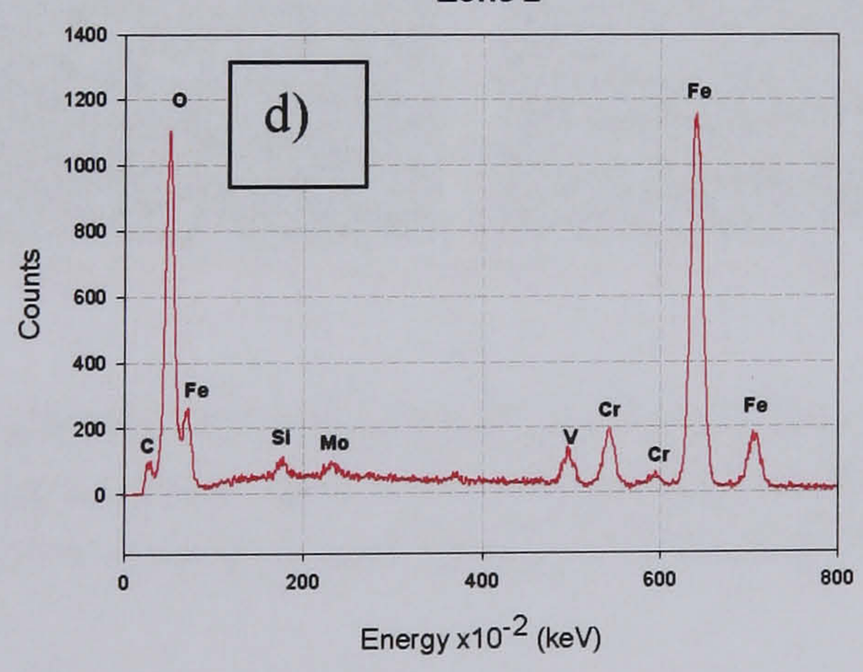

Fig.4.120. EDX area analyses of the points marked in a). b) Zone 1, the oxide layer, c) Zone 2 the steel substrate and d) the subsurface oxide formation.

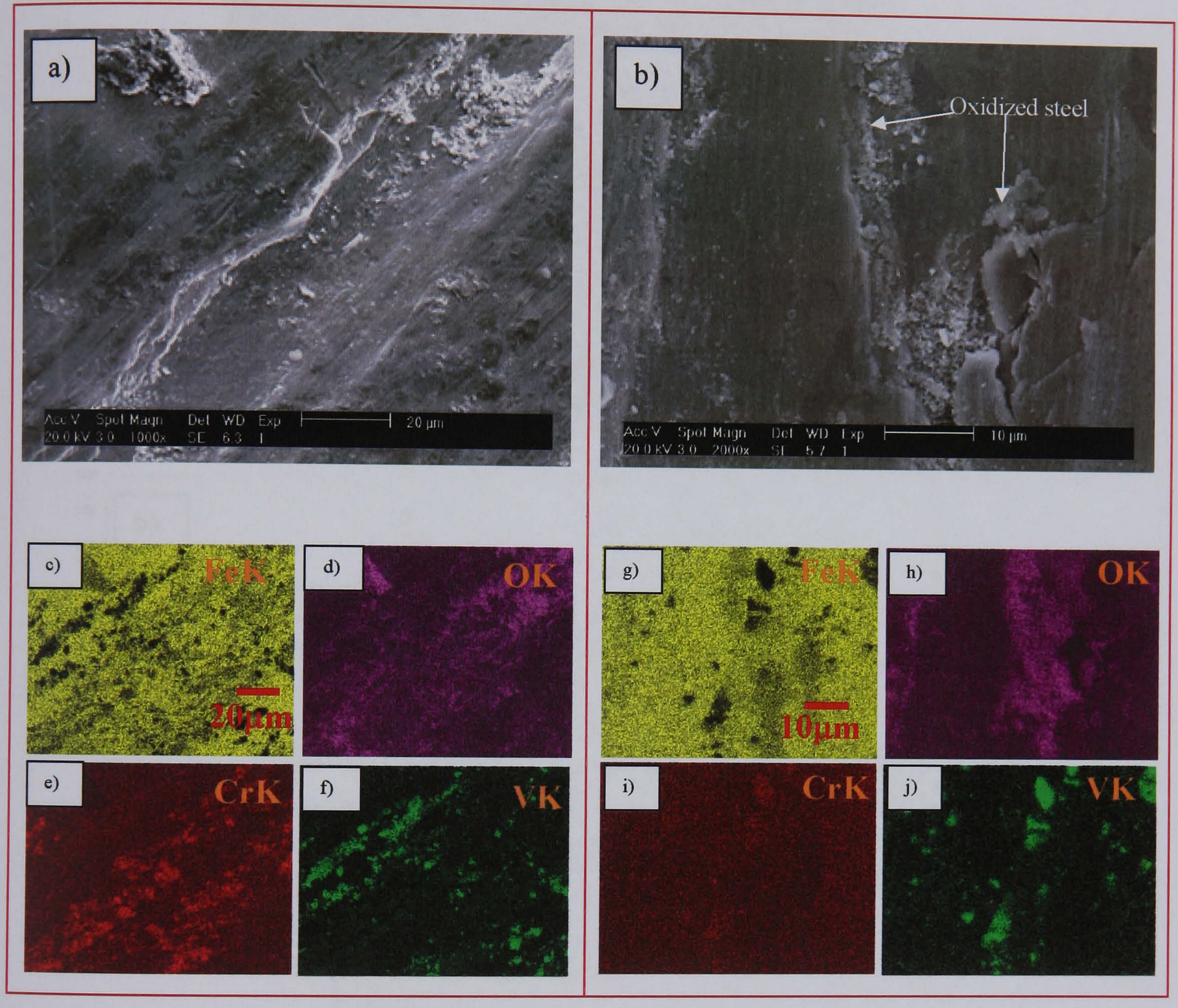

Fig.4.121. a) and b) Characteristic zones found on the surface of the disc tested at **400°C** in dry air, where severe plastic deformation is evident. MC carbides were oxidized during the test as suggested in figures d) and f) and h) and j) for zones the found in figures a) and b) respectively.

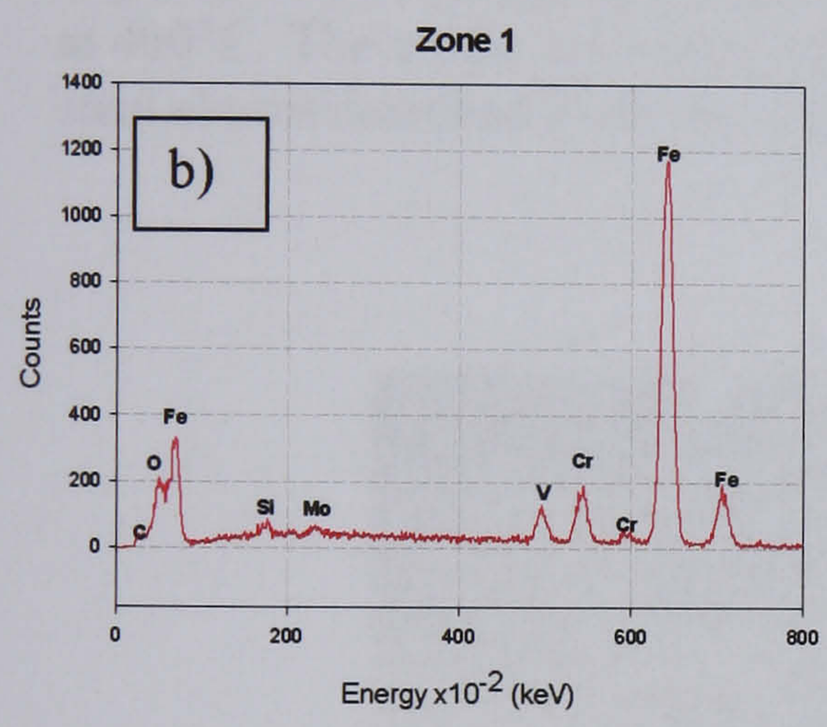

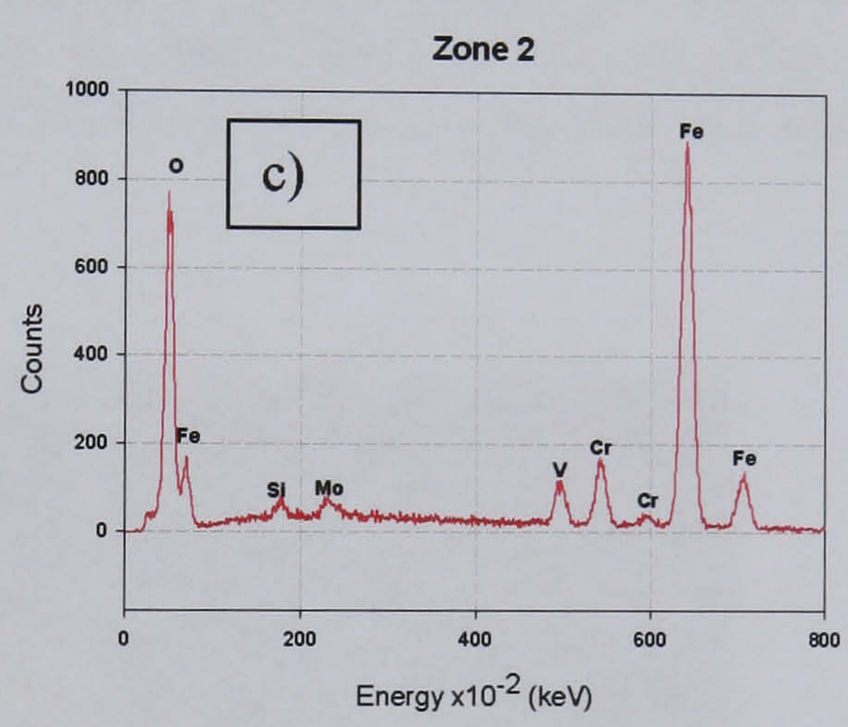

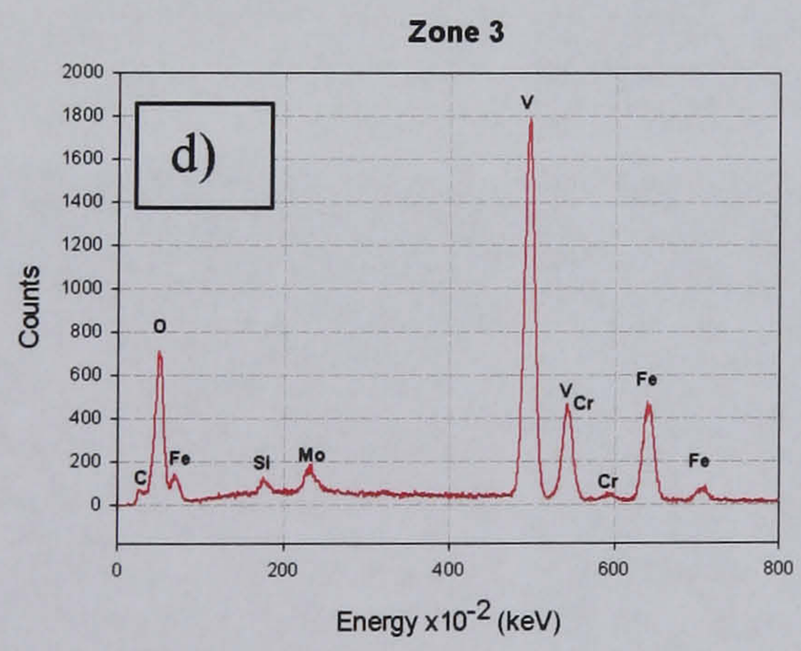

Fig.4.122. EDX area analysis of the zones found in picture a). b) Zone 1 in image a), the steel substrate containing oxygen dissolved. c) Zone 2 in image a), the wear debris and d) zone 3. a) Oxide formation in a MC vanadium rich carbide.

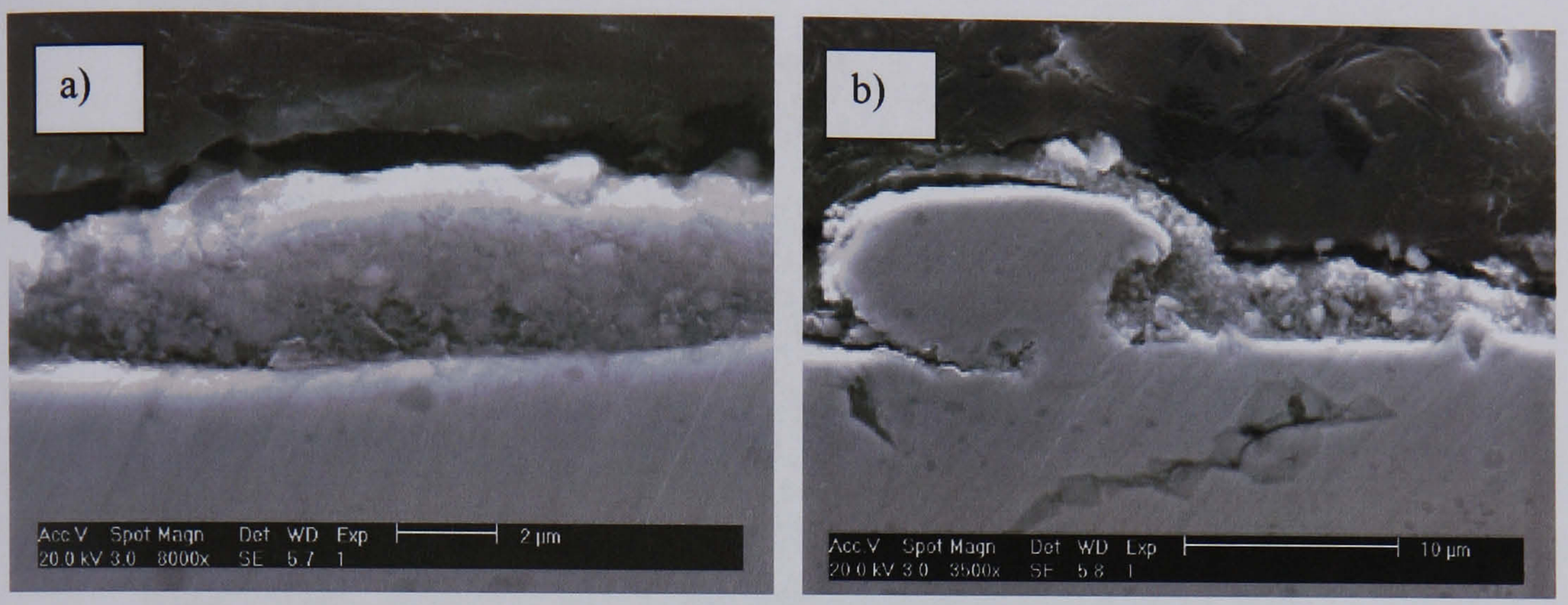

Fig.4.123. a) Cross section of the oxide clusters formed on the surface of the discs tested at **400°C**. The oxide layer is an agglomerate of fine oxide particles. b) Oxide layer and steel almost detached from the surface, the fracture of a MC carbide is also evident.

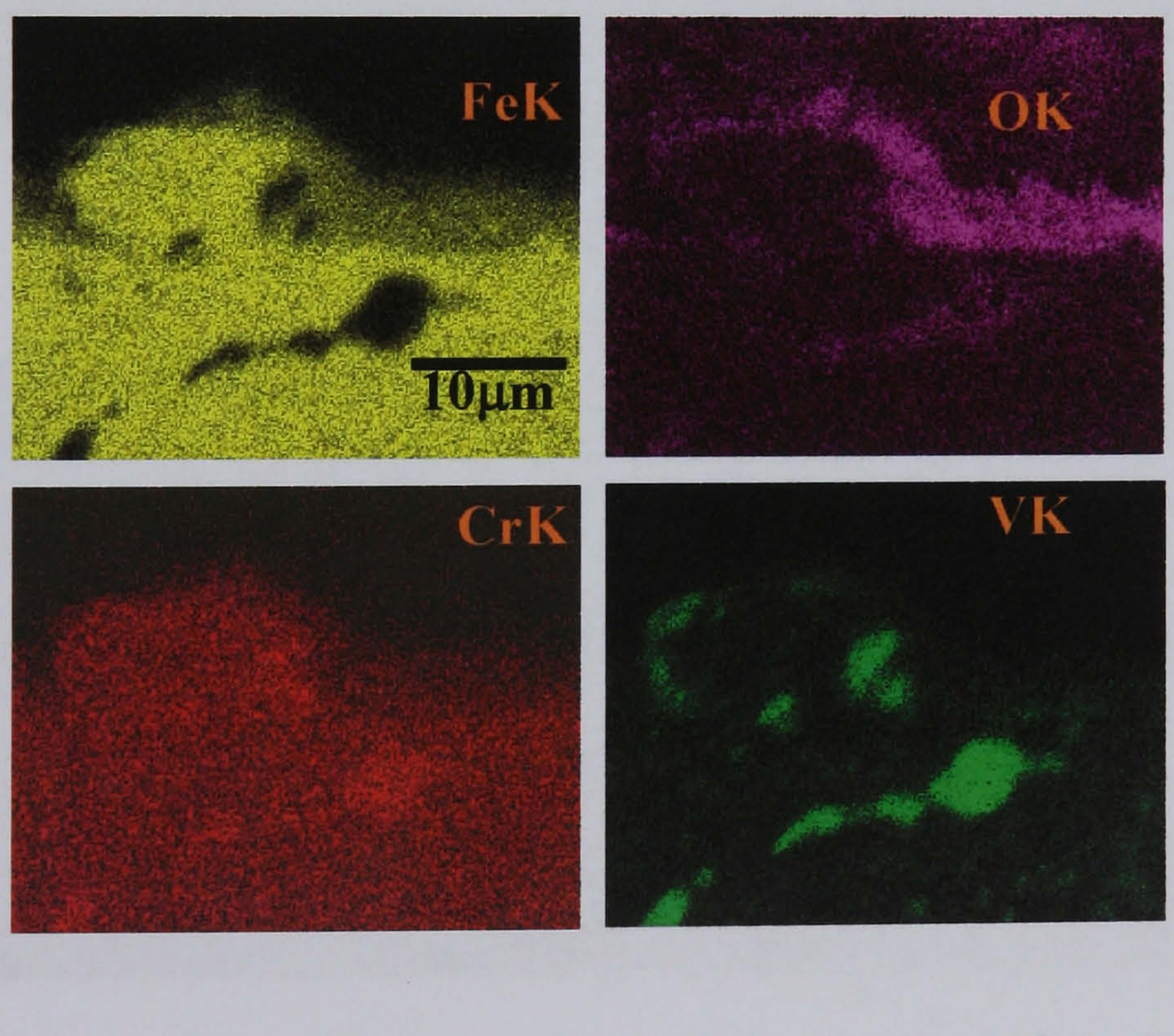

Fig.4.124. EDX maps of the elements present in the oxide layer of Fig.4.123 b).

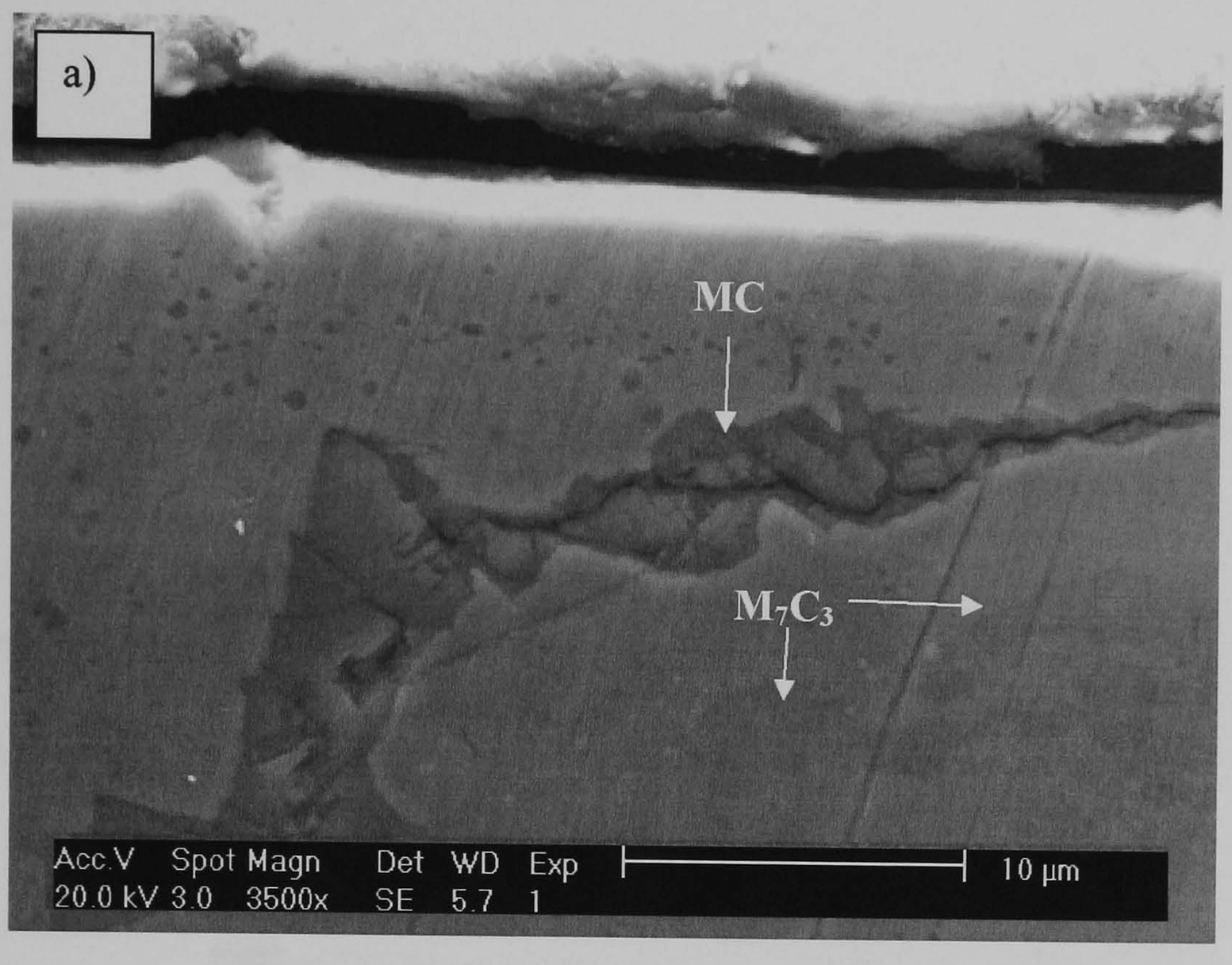

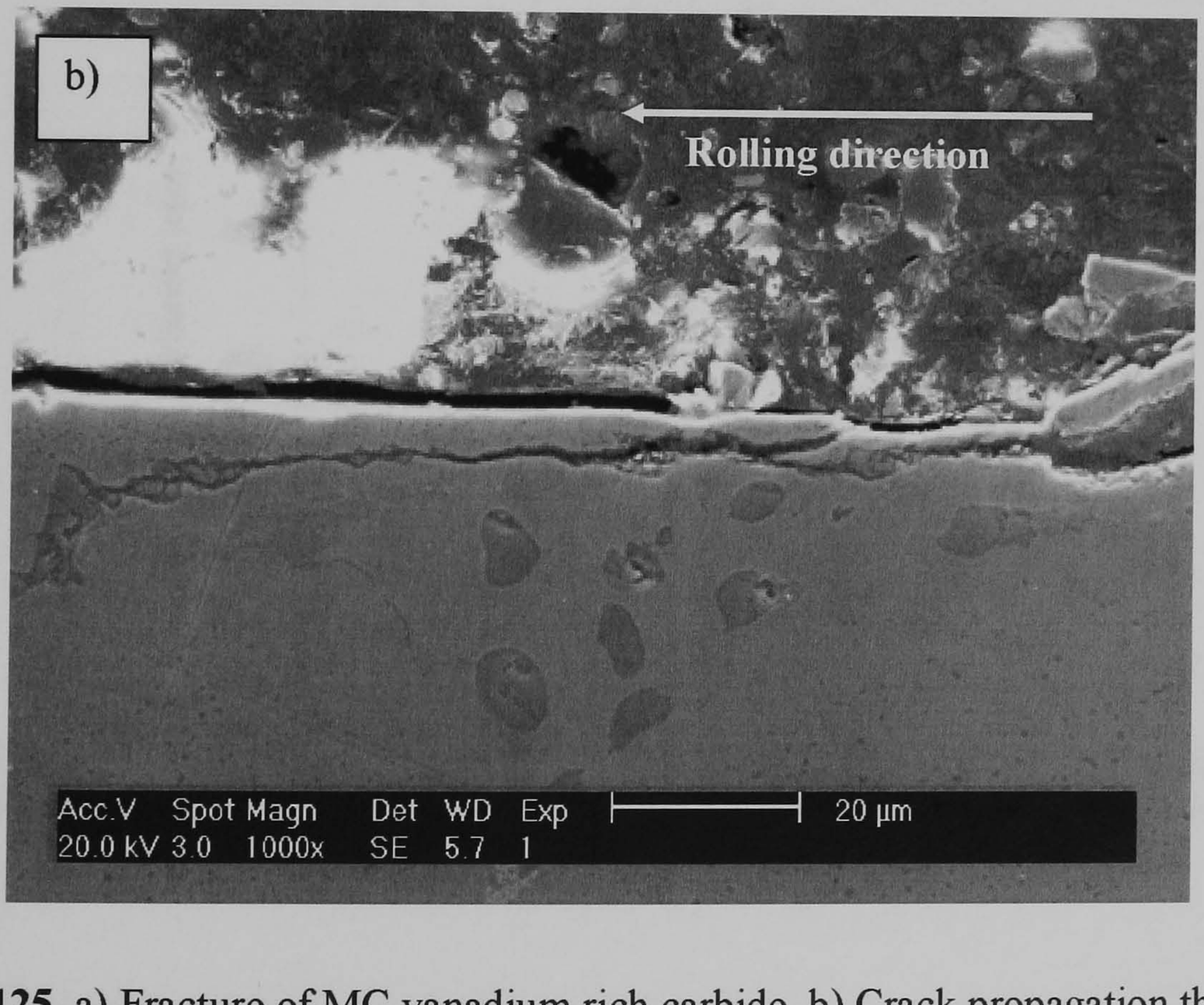

Fig.4.125. a) Fracture of MC vanadium rich carbide. b) Crack propagation through the steel.

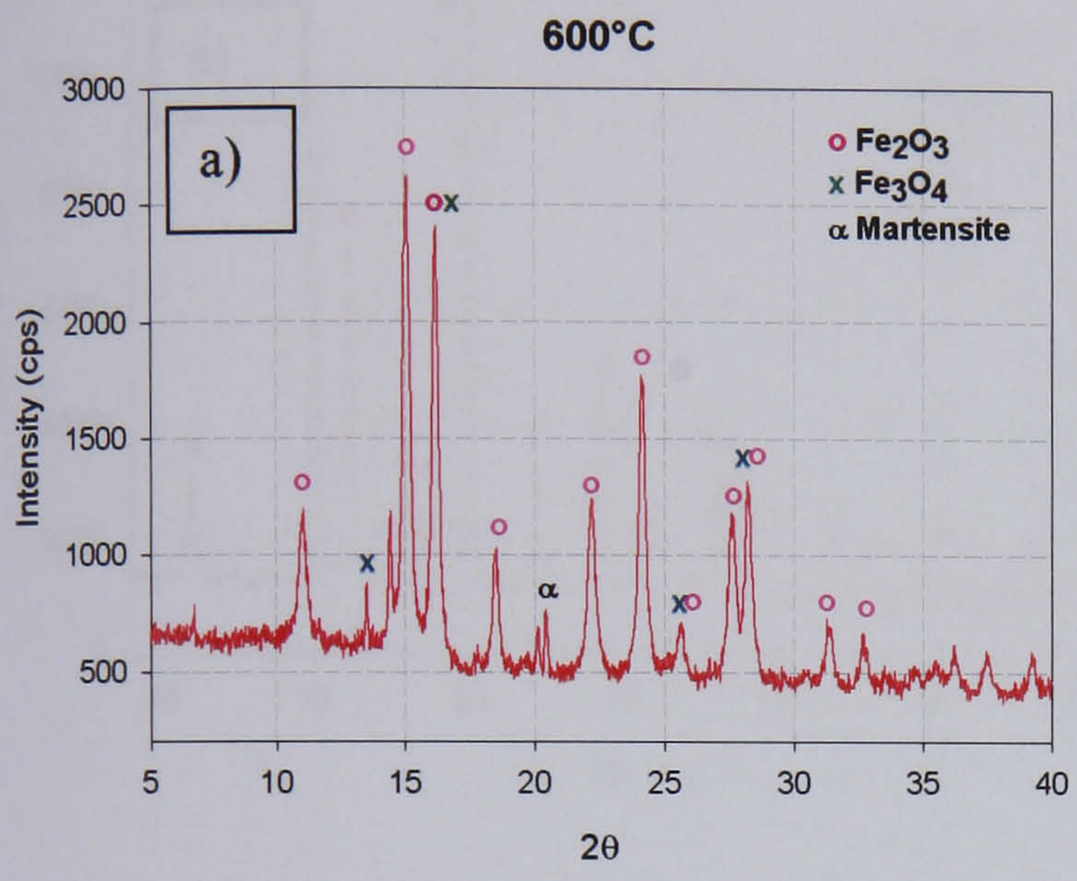

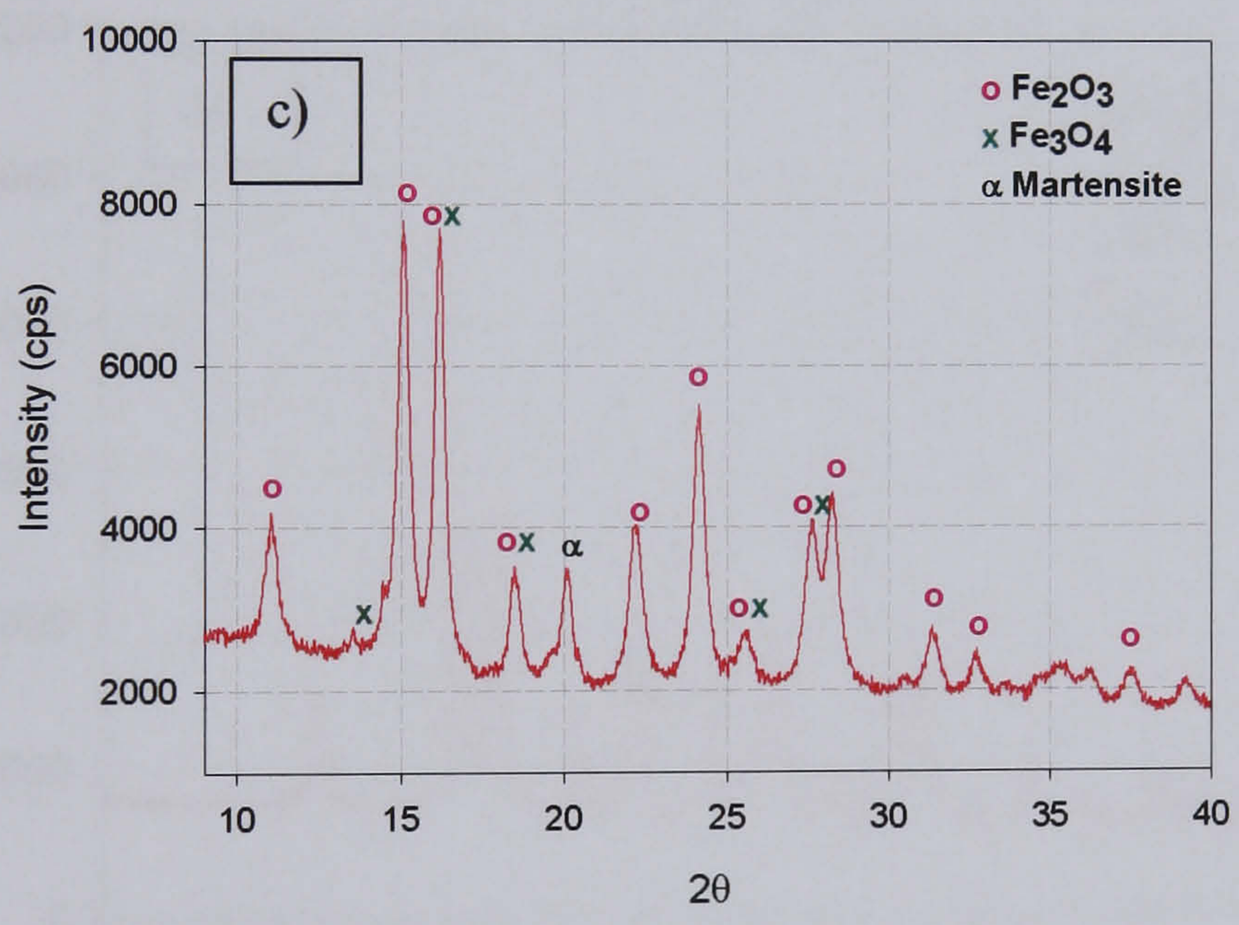

Fig.4.126 XRD diffraction patterns of the wear debris generated during the sliding tests at different temperatures under the presence of water. a) 600°C, b) 500°C, c) 400 °C.

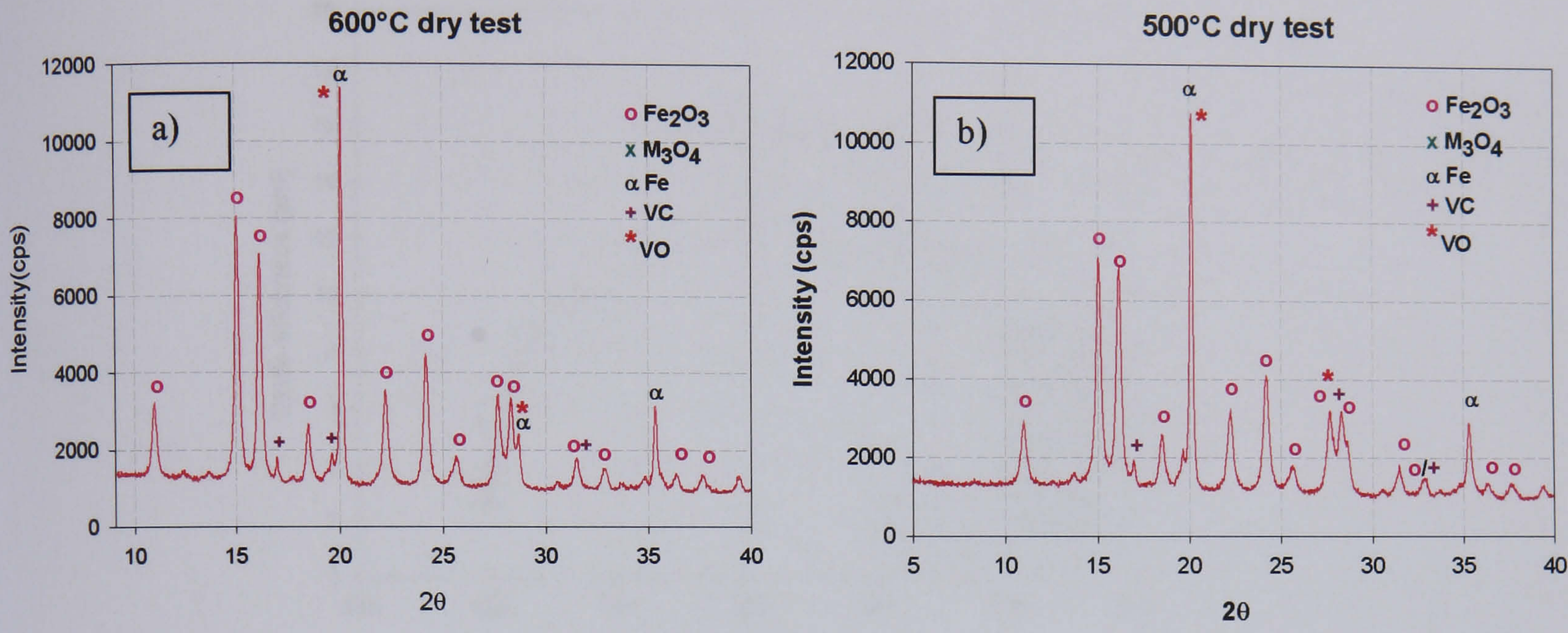

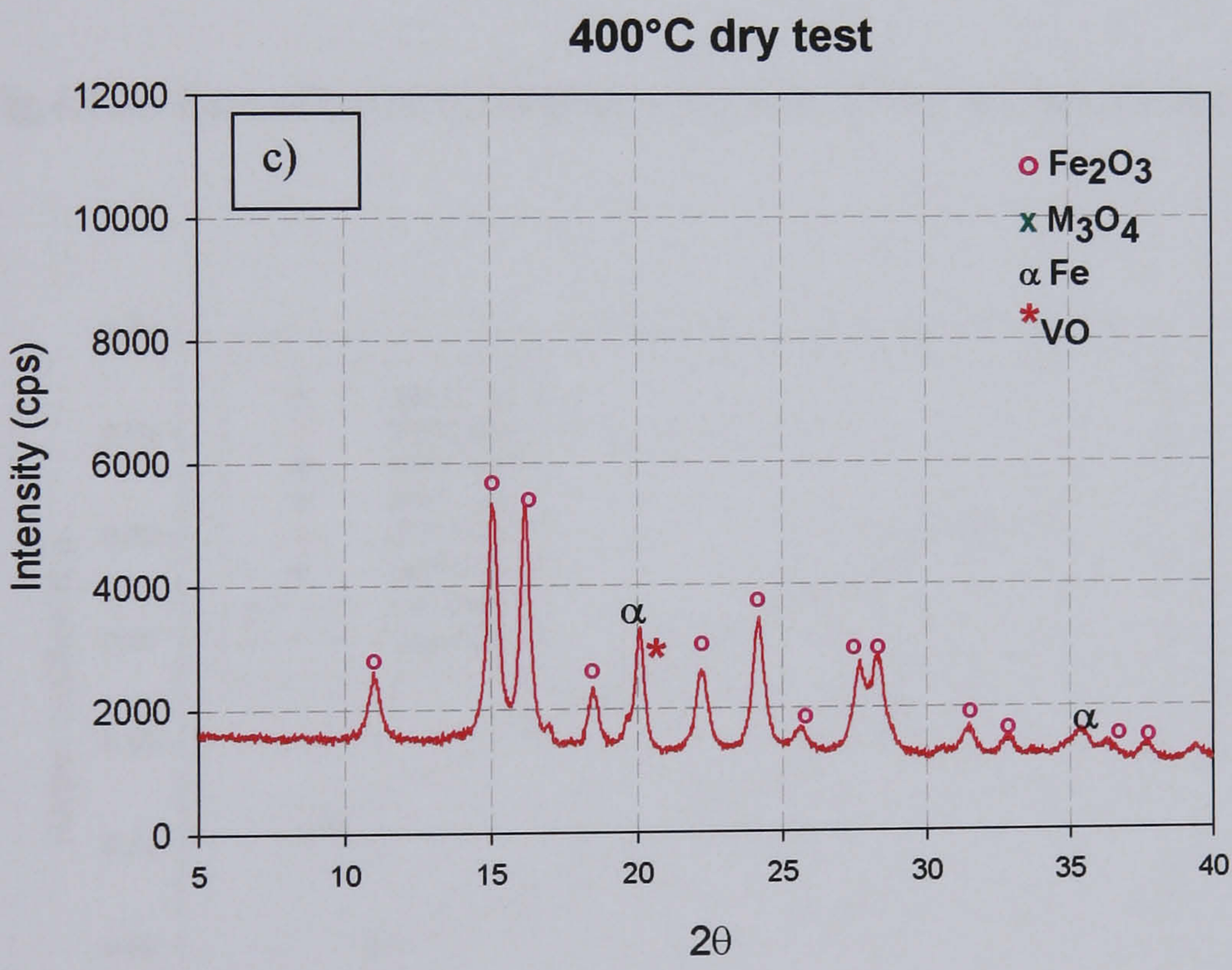

Fig.4.127. XRD diffraction patterns of the wear debris generated during the sliding tests at different temperatures in dry air. a) 600°C, b) 500°C, c) 400 °C.

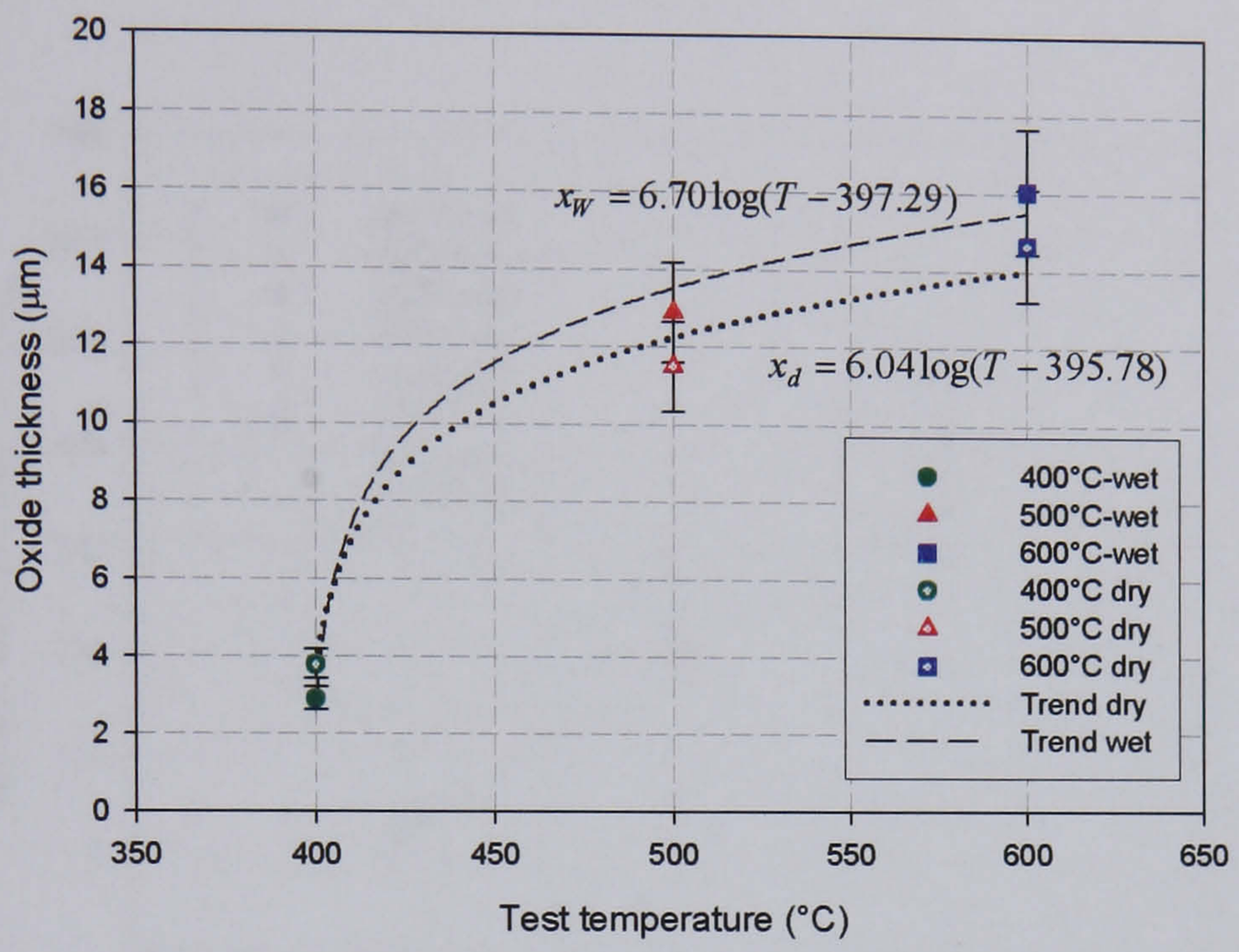

Fig.4.128. Rate of oxide build up as a function of the test temperature.

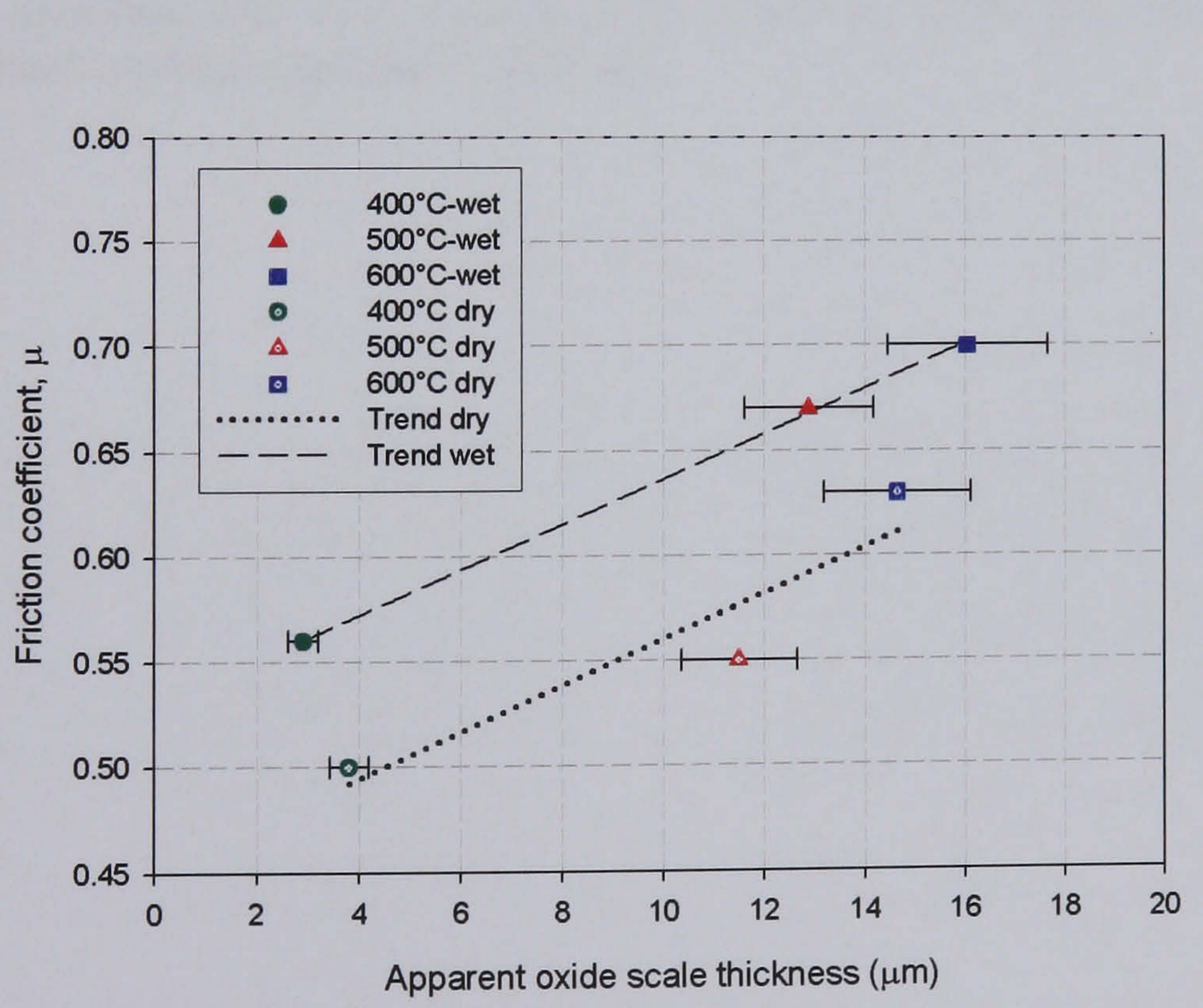

Fig.4.129. Variation of the friction coefficient as a function of the thickness oxide scale measured for each testing condition.

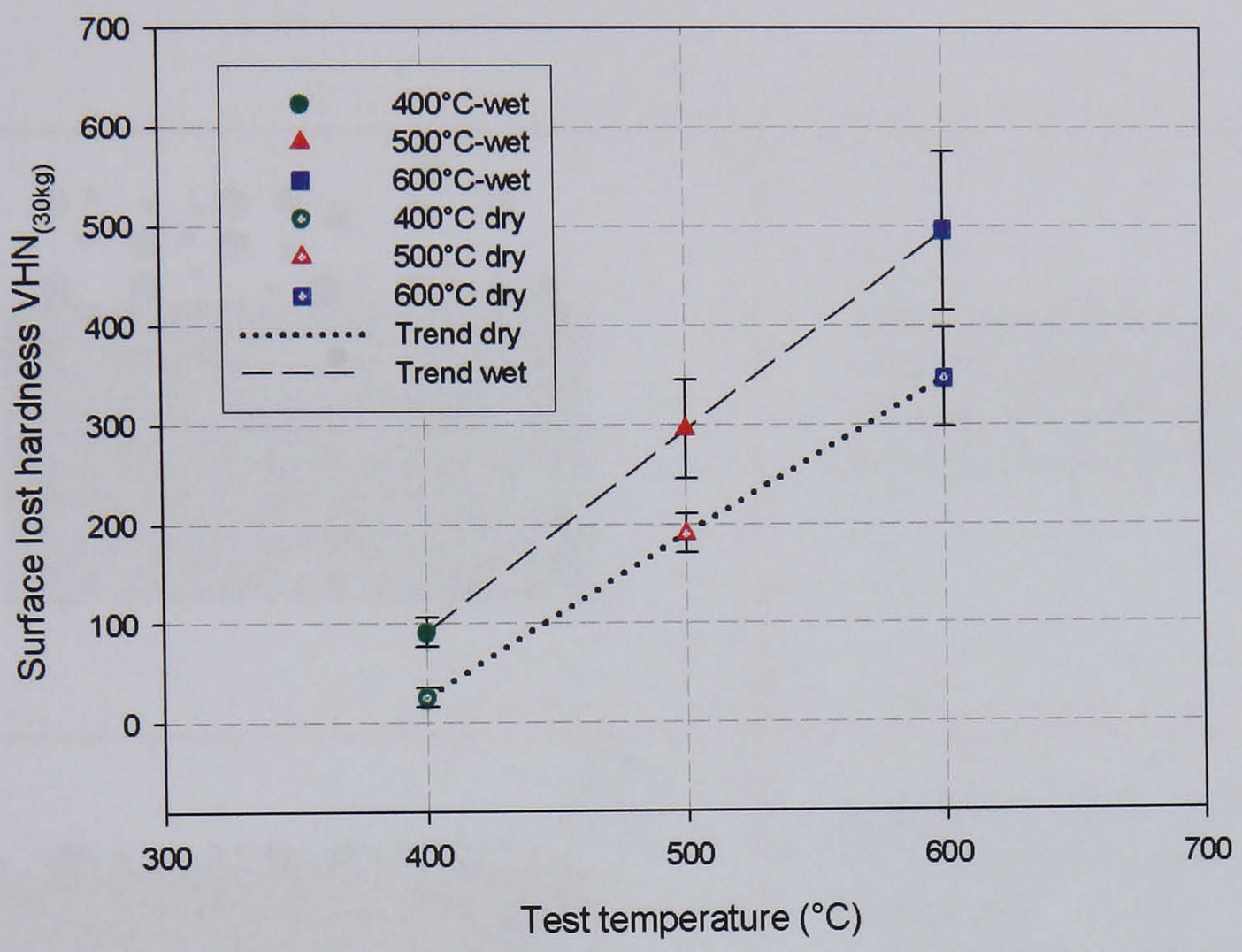

Fig.4.130. Hardness lost of the test discs as a function of the temperature and the environmental conditions present in each trial.

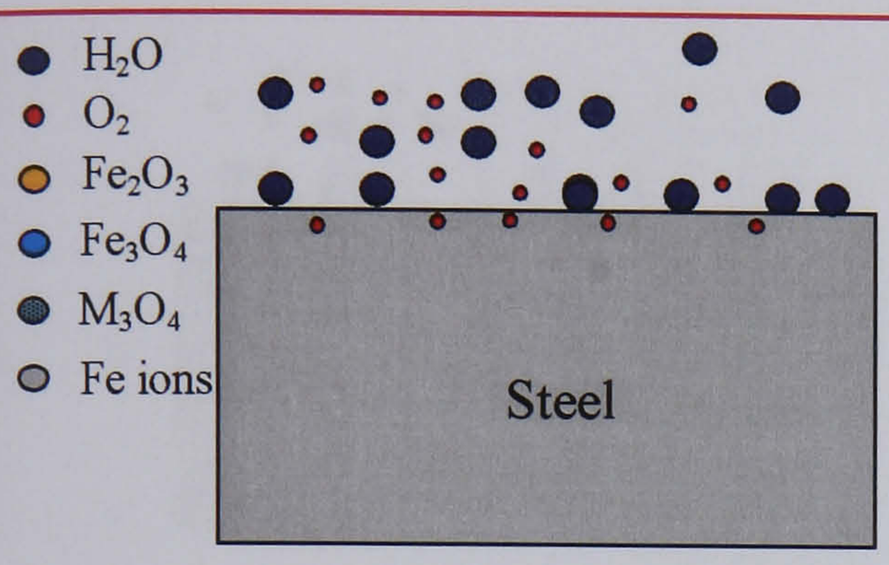

The atmosphere is saturated with water vapour so that pO_2 is reduced. Initial stages of oxide formation, showing the adsorption of oxygen ions into the steel.

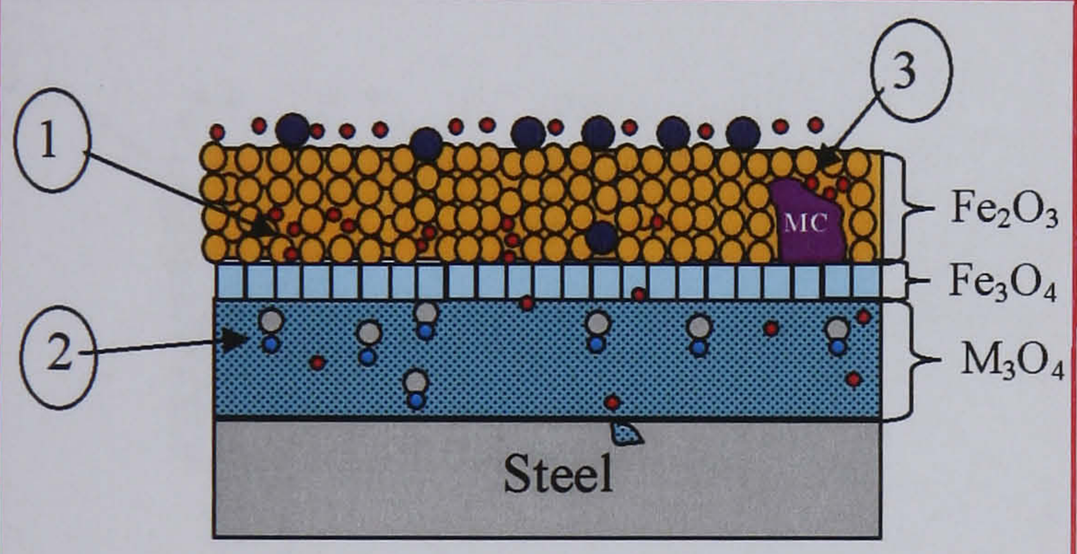

Rapid formation of Fe_2O_3 and Fe_3O_4. The rate of reaction is reduced by the closed morphology of the top layer that complicates the diffusion of oxygen ions (1). Iron ions leave their positions in the Fe_3O_4 layer and chromium ions from the matrix occupy these sites (2). Carbides are covered by the oxide layer (3).

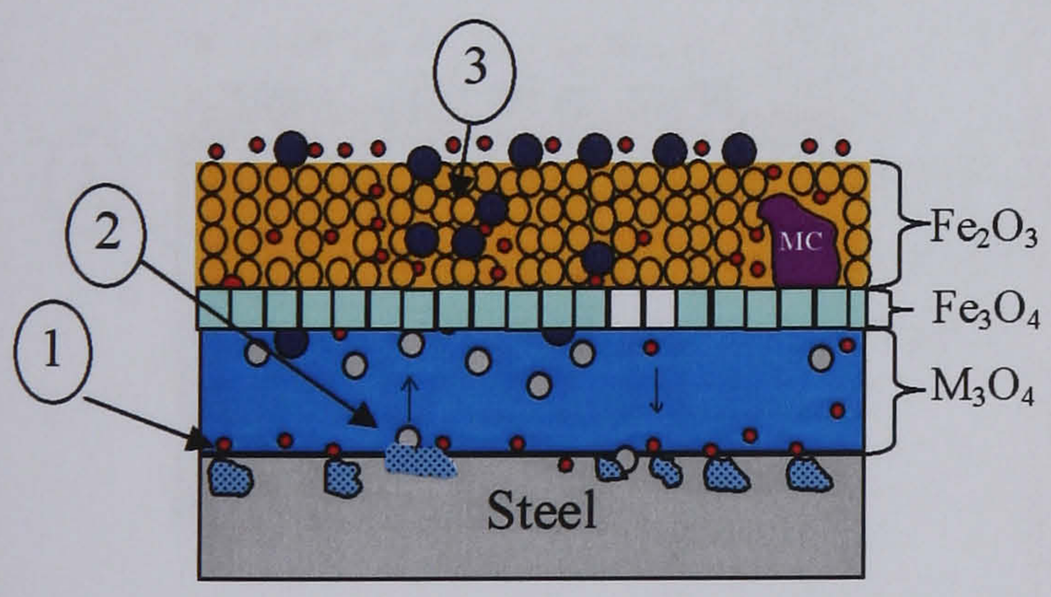

Oxygen ions accumulated across the Fe_2O_3 layer reach the substrate and react to form Fe_3O_4 (1) that is rapidly transformed into a M_3O_4 layer as iron ions leave their positions to produce more Fe_2O_3 at the hematite-magnetite interface (2) increasing the oxidation rate of the steel. The plasticity of the oxide layer increased as more water molecules were dissolved in Fe_2O_3, facilitating the ionic flux across the scale. The M_3O_4 spinel is now a stable phase.

Fig.5.1.Oxidation mechanism experienced under condition 1.

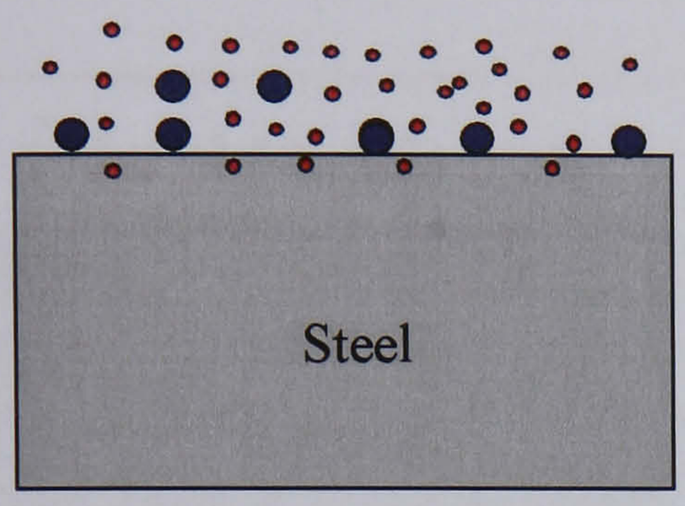

The atmosphere under this condition is 30 less saturated with water vapour than in condition 1 and therefore more oxygen is present in the oxidant atmosphere than the amount contained in condition 1. The formation of Fe_3O_4 is a limited process because the amount of sites where equation 5.3 is developed are also reduced and the oxidation process is slower under this condition during the early stages.

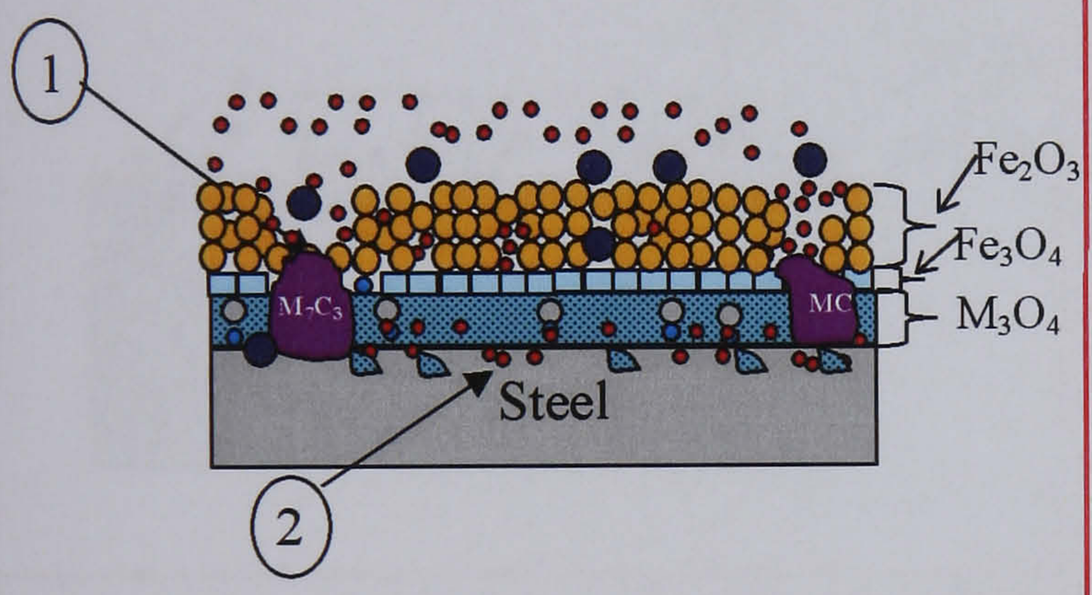

The oxide layer grows faster in the matrix but fails to cover the carbides (1) this allows more oxygen and water molecules to reach the substrate and react at these locations increasing the oxidation rate (2).

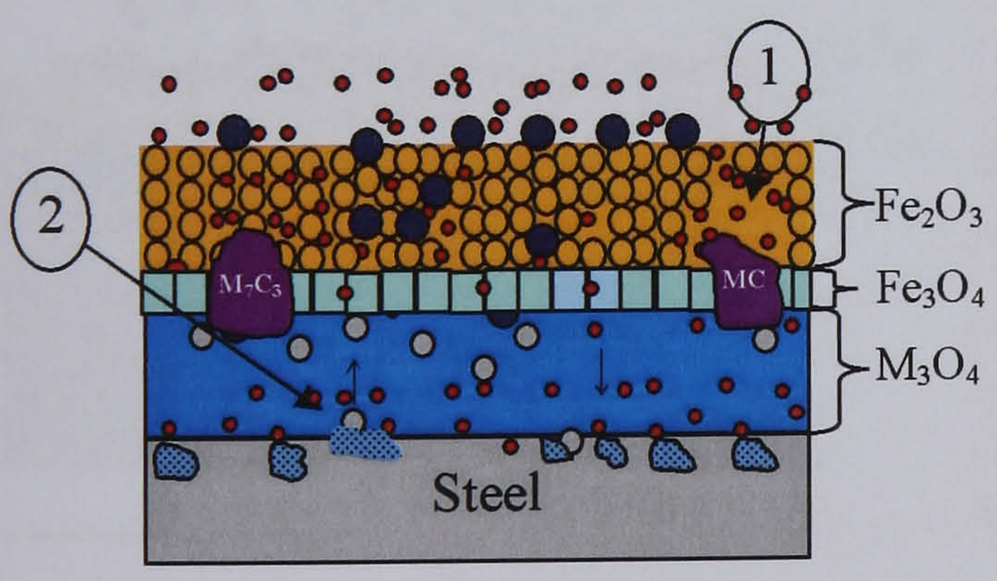

The oxide layer now covers the carbides but trapped oxygen (1) travels across the oxide layer to reach the steel substrate to form the spinel M_3O_4 layer (2). The growth of Fe_2O_3 is also favoured by the oxygen molecules trapped in this layer. Water molecules promote the plasticity of the oxide layer so that pores are closed either by lateral covering of the oxide or by new oxide growth, favouring the diffusion of ions.

Fig.5.2. Oxidation mechanism experienced under condition 2.

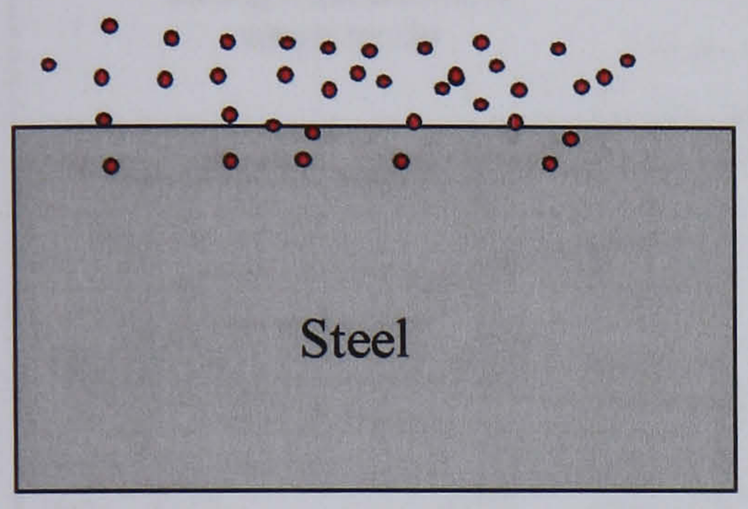

In this condition adsorption of oxygen is a limited process, and only reactions of equation 5.1 and 5.2 assisted the oxidation process.

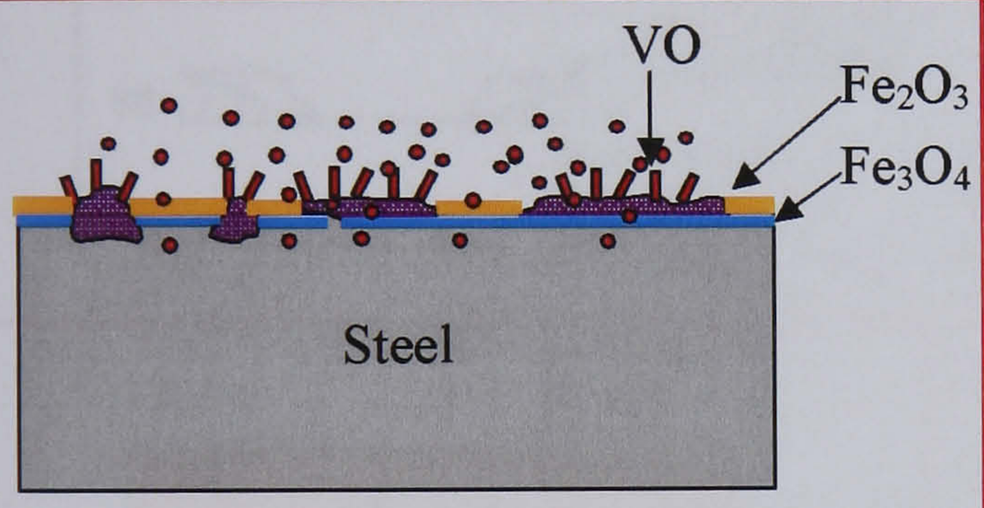

As oxygen adsorption was limited and water vapour was not present the growth of Fe_3O_4 and M_3O_4 was not favoured and preferably a thin layer was formed. Fe_2O_3 grew on the surface as well as vanadium oxide VO grew on MC carbides

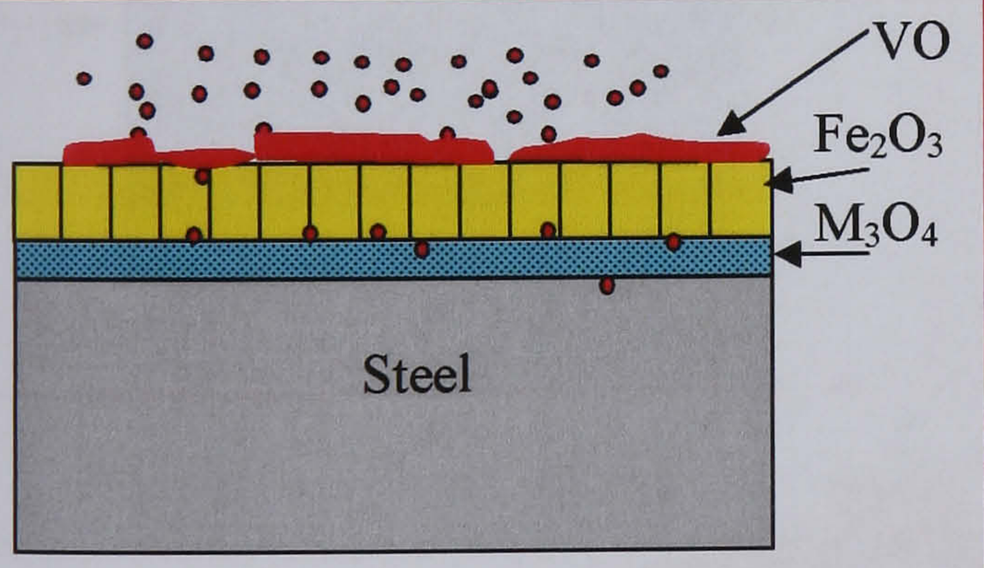

A vanadium oxide layer is formed at the top of the hematite layer. This layer is not uniform given the dispersion of MC vanadium carbides in the matrix. Diffusion of ions through this layer could be a difficult process that also accounted for the reduction in the oxidation rate of the steel

Fig.5.3. Oxidation mechanism experienced under condition 3.

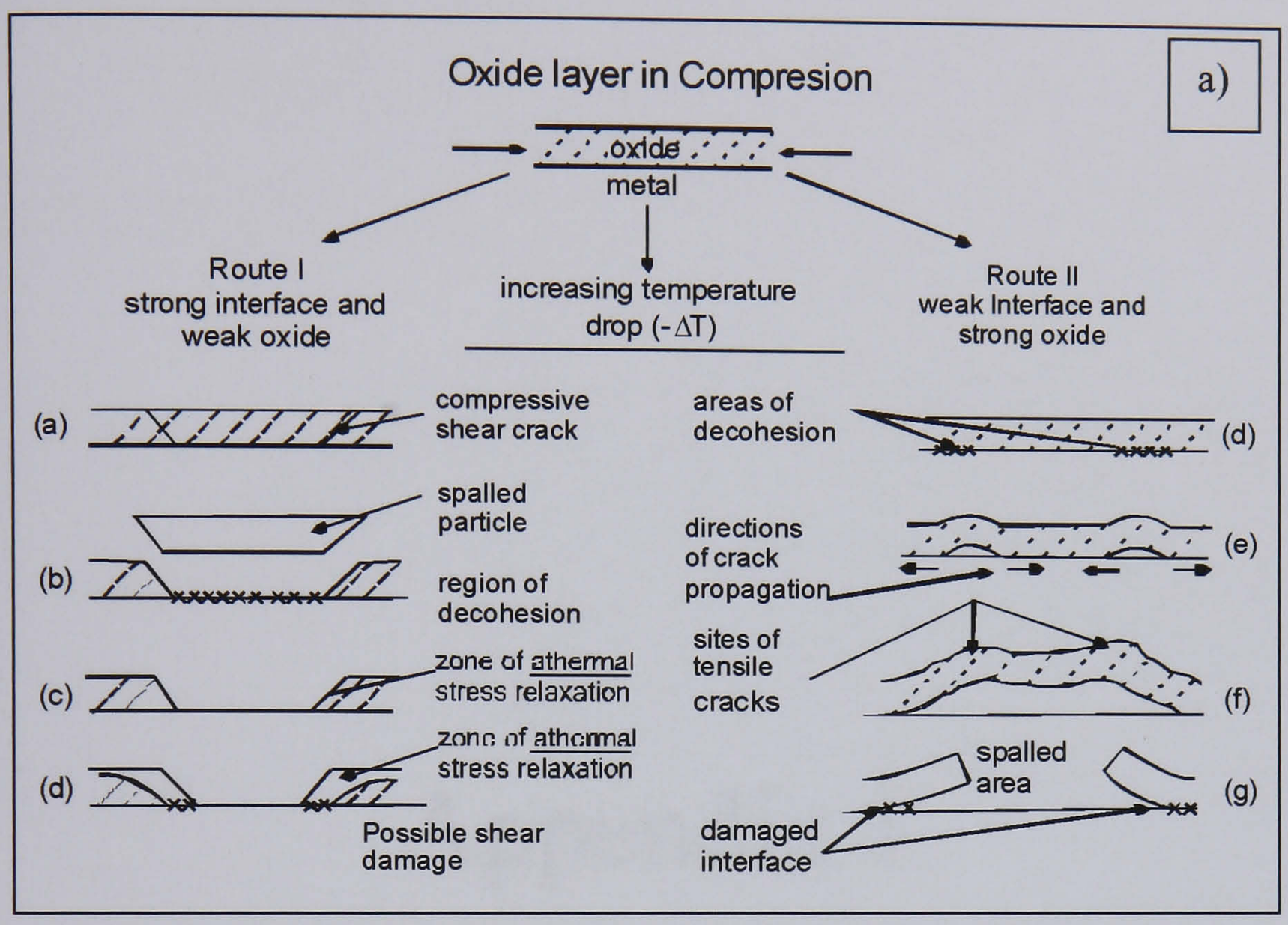

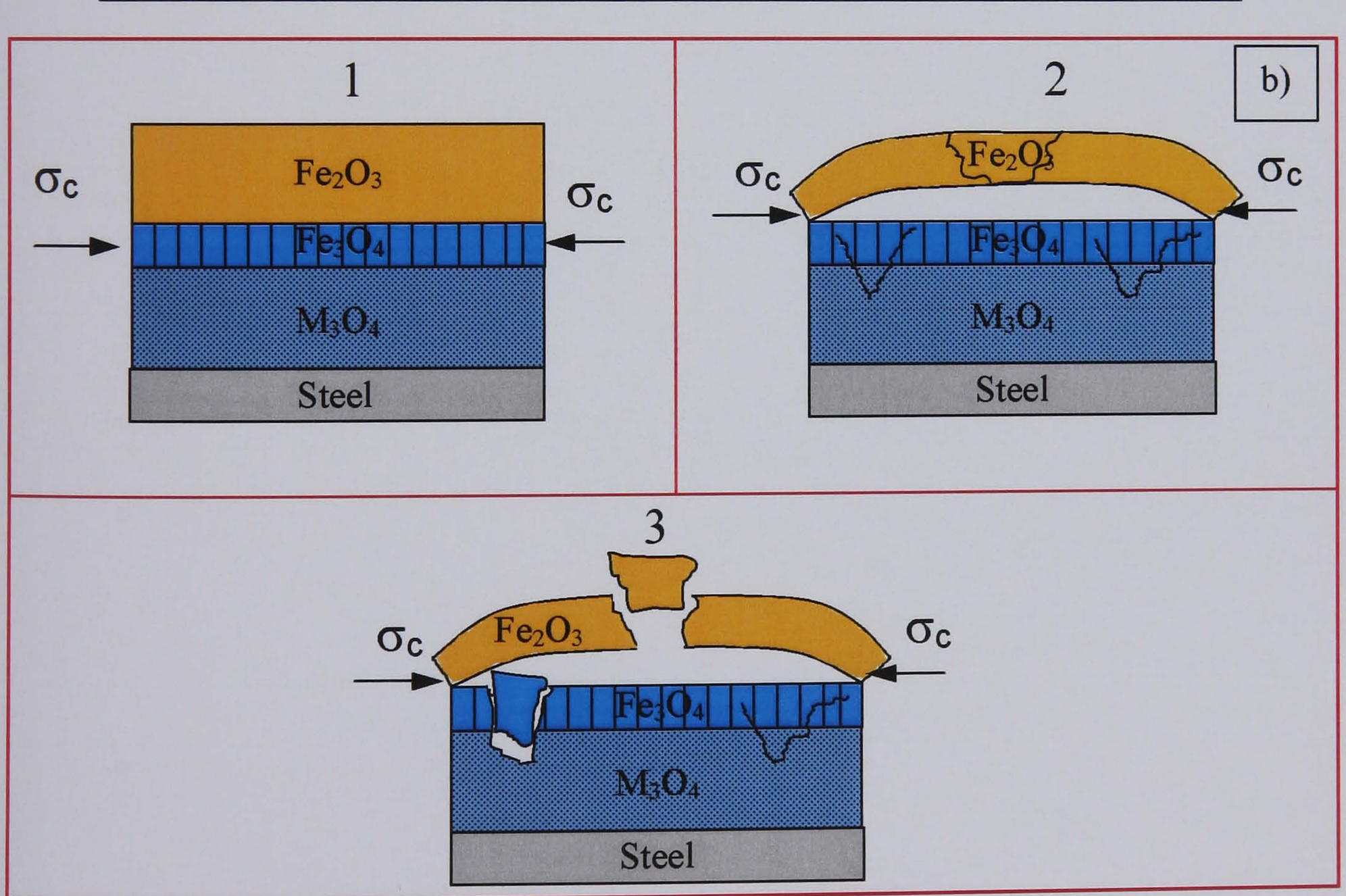

Fig.5.4. a) Spallation mechanisms proposed by Evans, (1995). b) Failure mechanisms of the oxide layer during the low frequency cycling. 1) Stress generation on cooling. 2) Crack development and, 3) Spallation by buckling in Fe_2O_3 and by wedging in Fe_3O_4 and M_3O_4 layers.

Appendix 1

Samples for the isothermal oxidation tests

PLANT VIEW

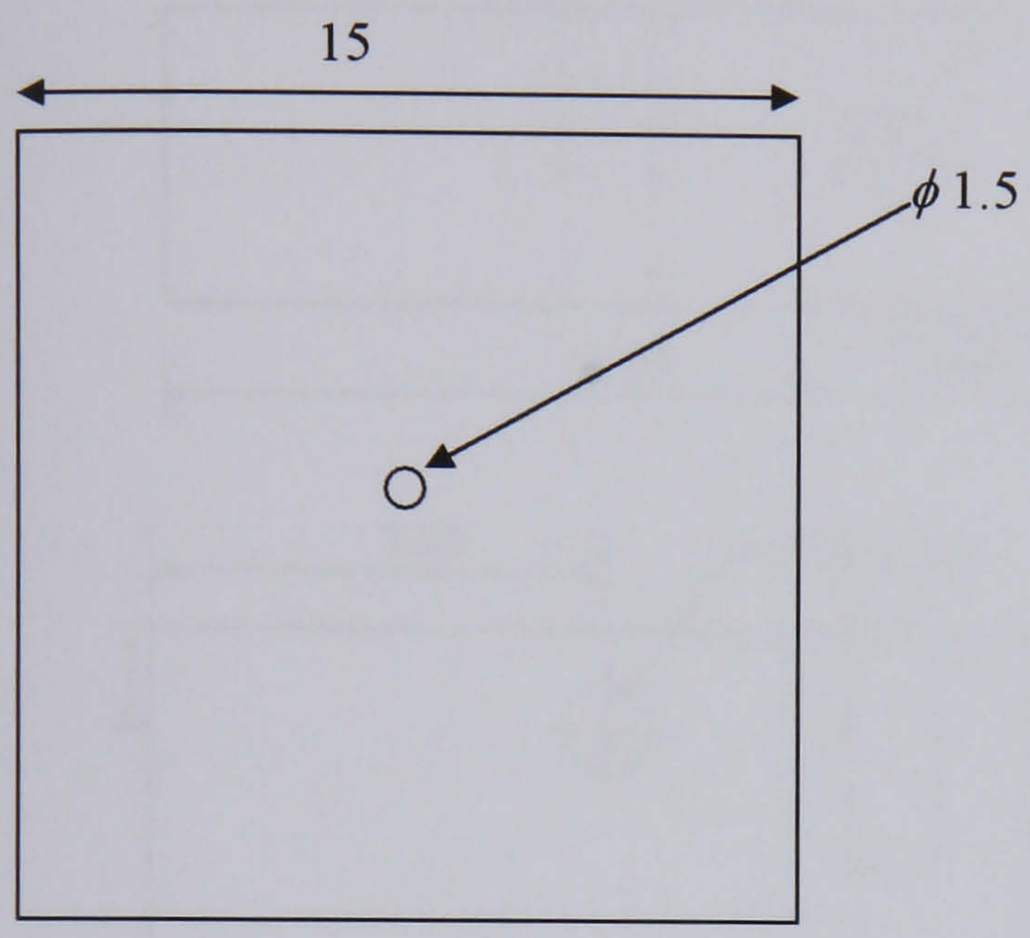

ISOMETRIC

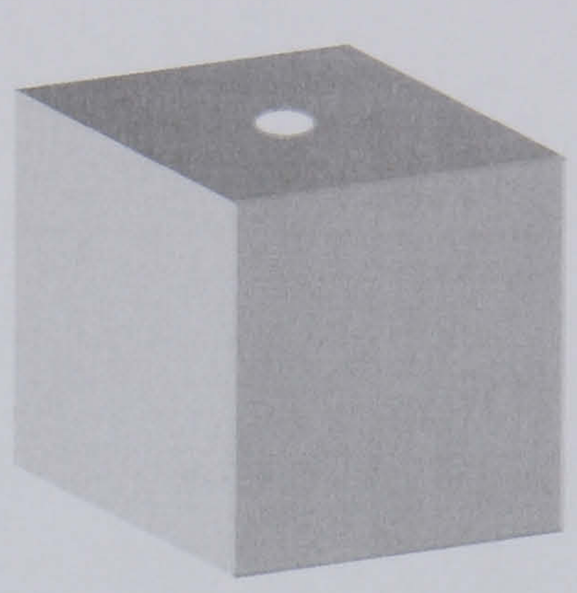

FRONTAL VIEW

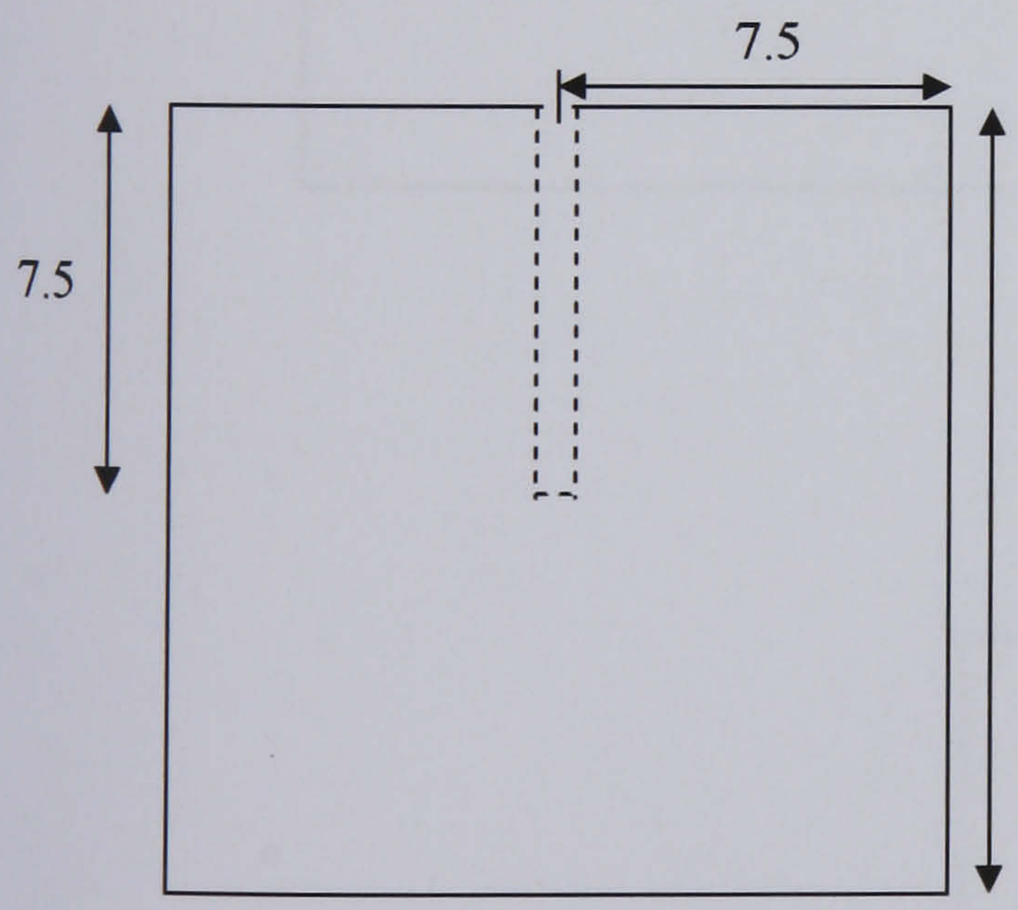

Sample for isothermal oxidation experiments
Material: High Speed Steel
All dimensions are in mm
Drawing not to scale

Nelson Garza-Montes
IMMPETUS
Department of Engineering Materials
The University of Sheffield
Tel: 222-5459
Fax: 222-5943
E-mail: mtp04ng@sheffield.ac.uk

Samples for the high and low frequency cyclic oxidation tests

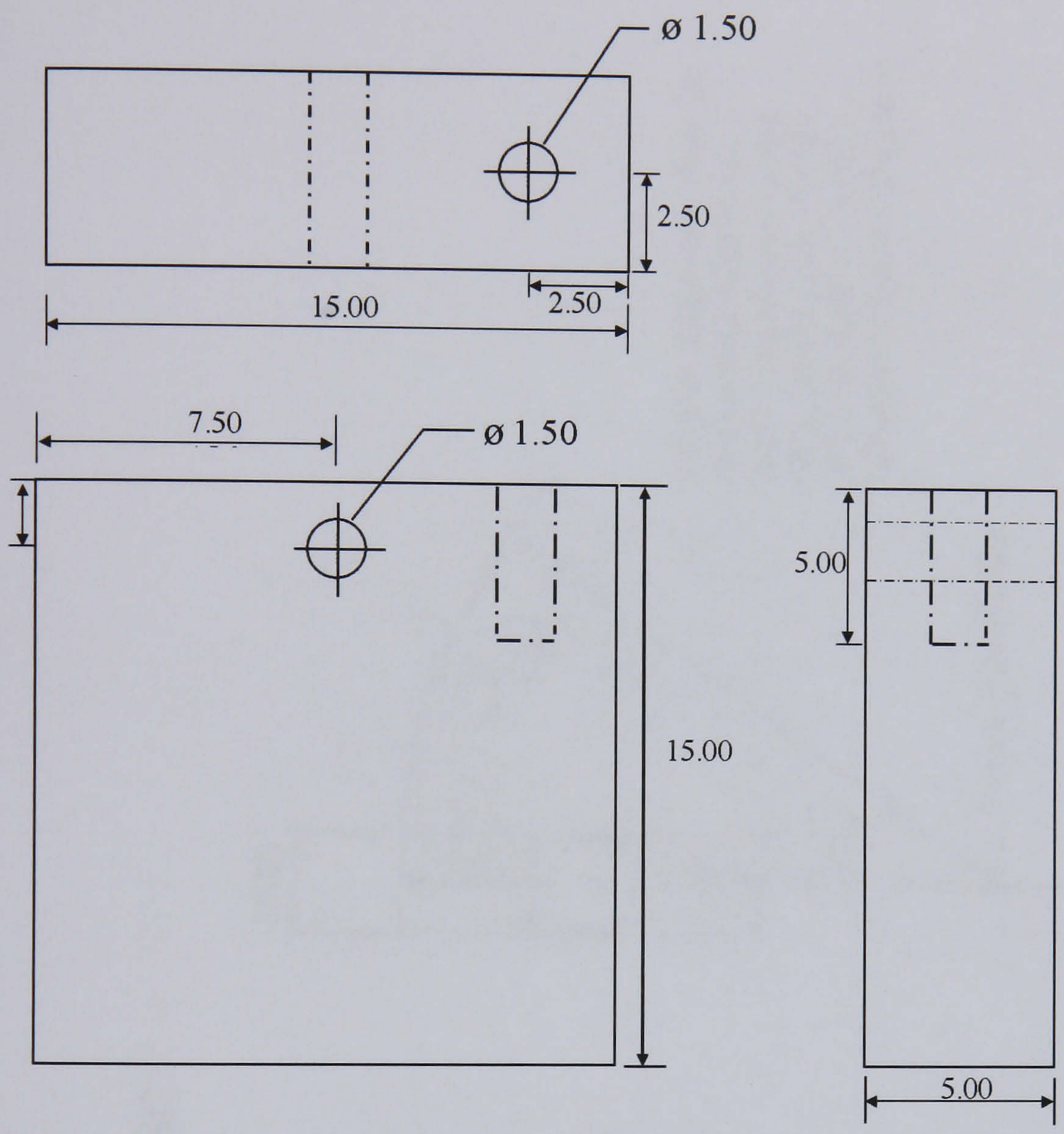

Sample for cyclic oxidation experiments
Material: High Speed Steel
All dimensions are in mm
Drawing not to scale

Nelson Garza-Montes
IMMPETUS
Department of Engineering Materials
The University of Sheffield
Tel: 222-5459
Fax: 222-5943
E-mail: mtp04ng@sheffield.ac.uk

Counterdisc engineering drawing

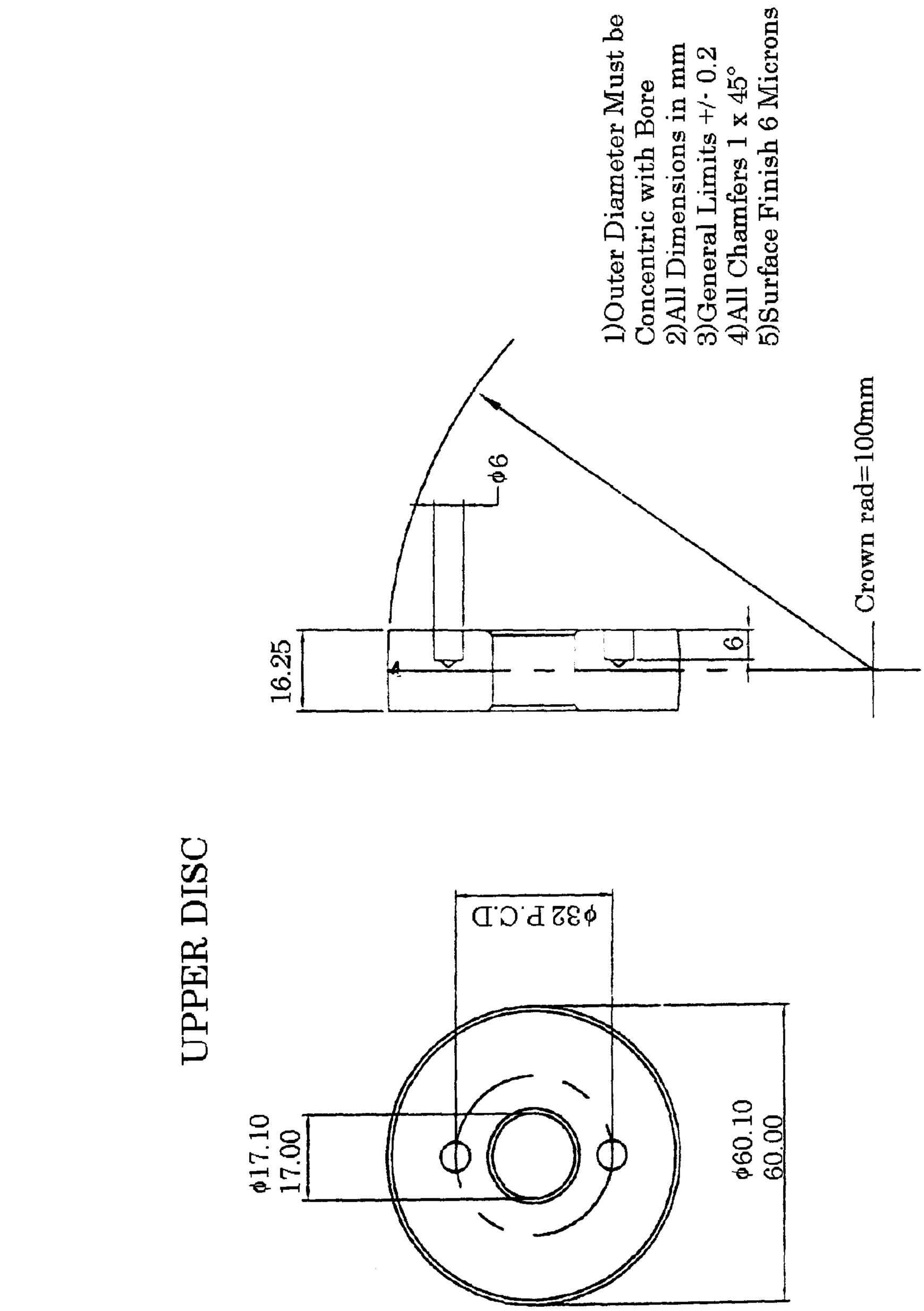

Test disc engineering drawing

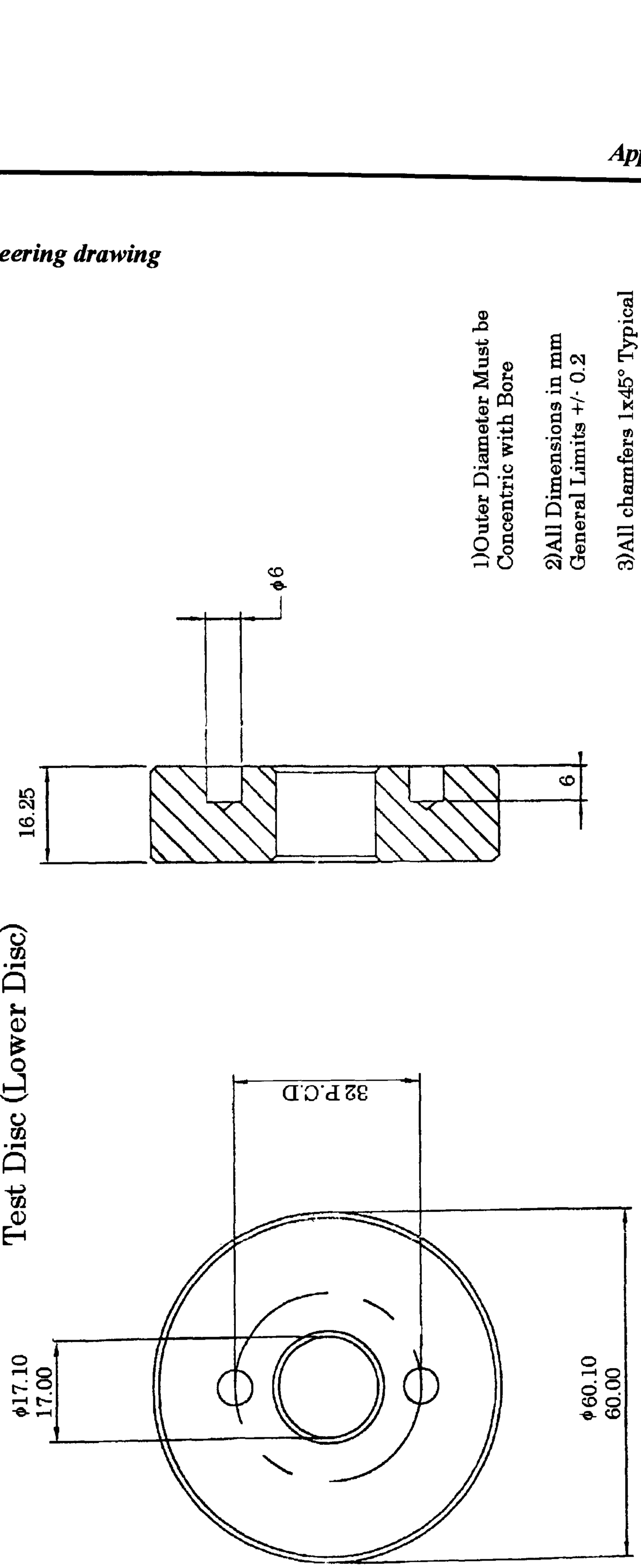

Appendix 2

Example of test disc roughness measured after the tests

Tests carried out at 600°C under the presence of water and water vapour

After test 1

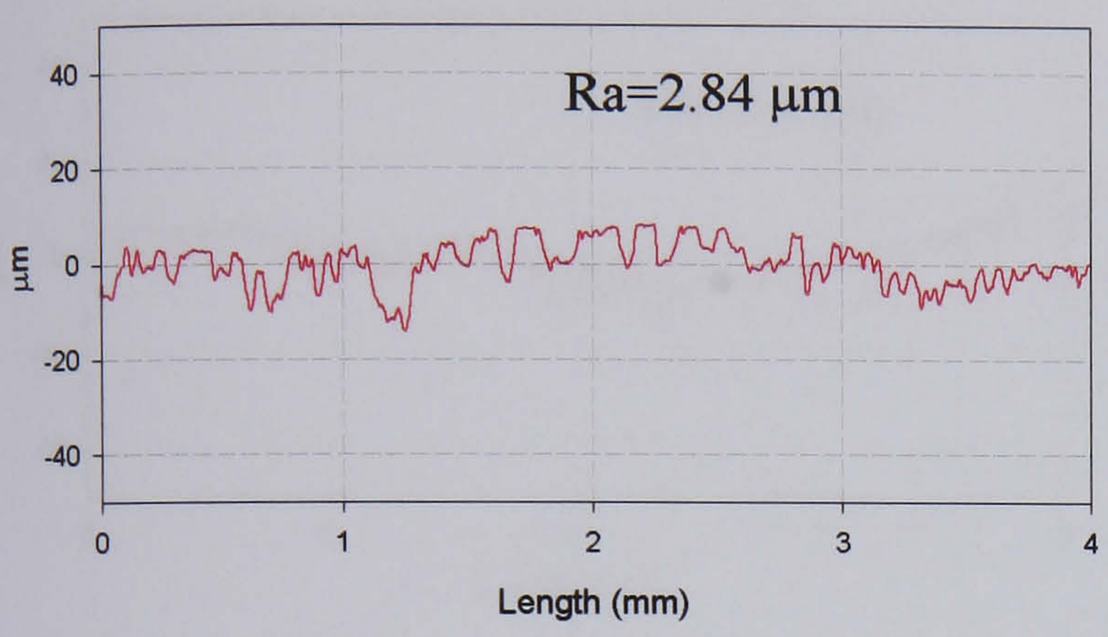

After test 2

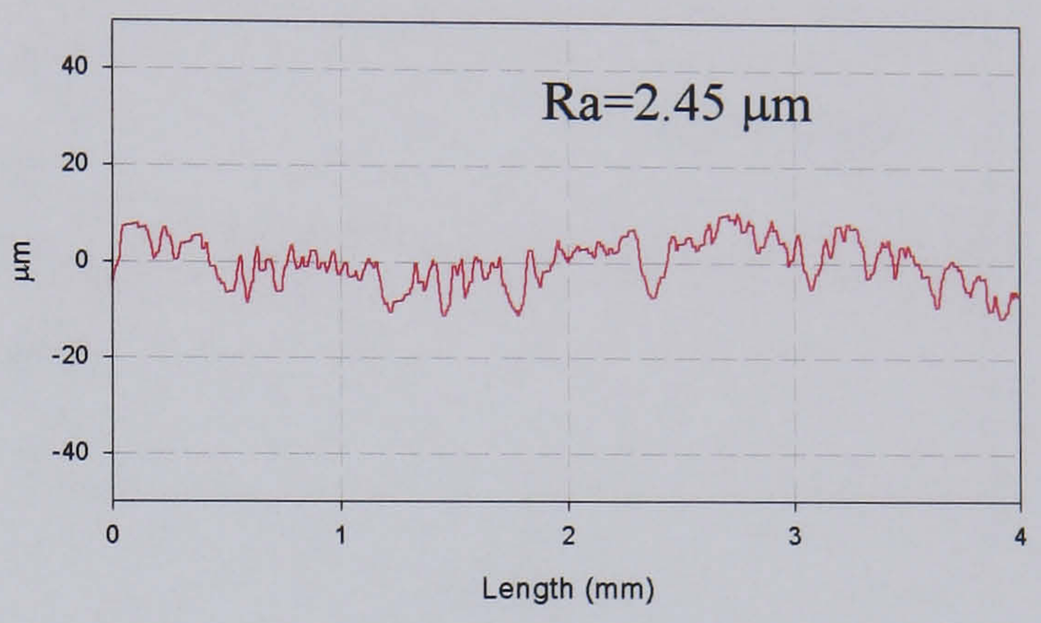

After test 3

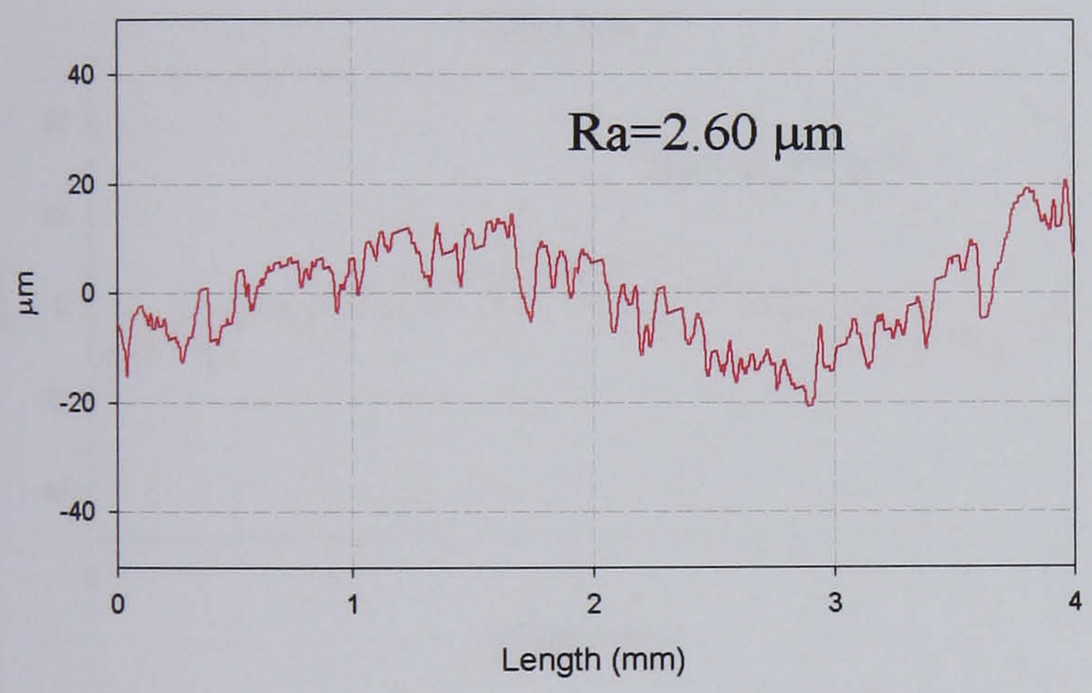

After test 4

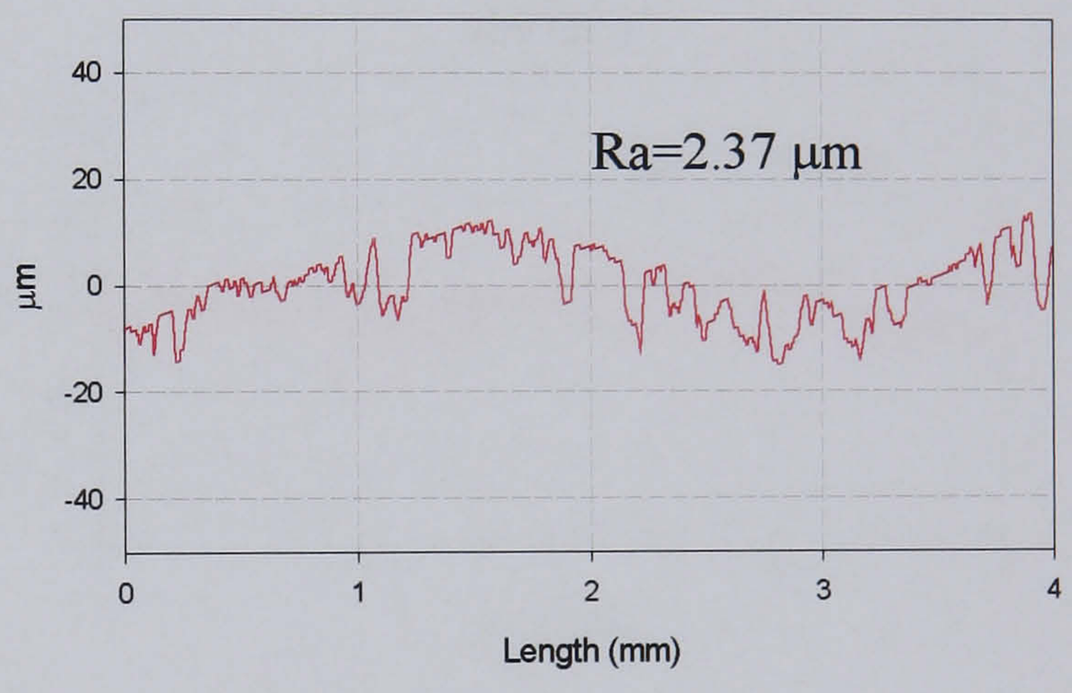

After test 5

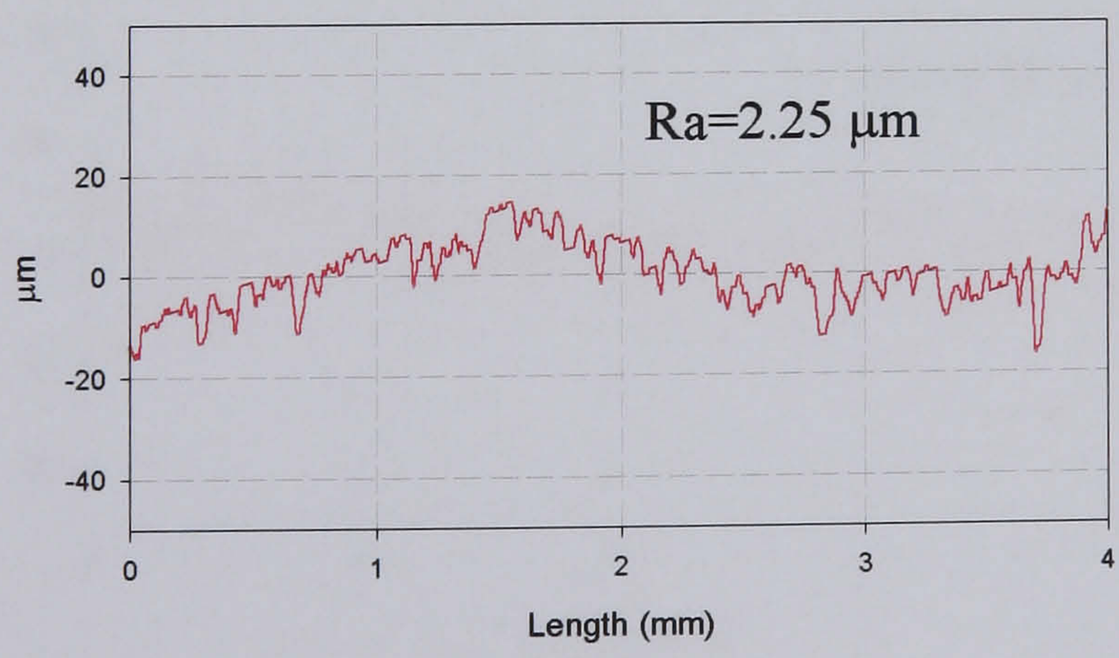

Tests carried out at 500°C under the presence of water and water vapour

After test 1

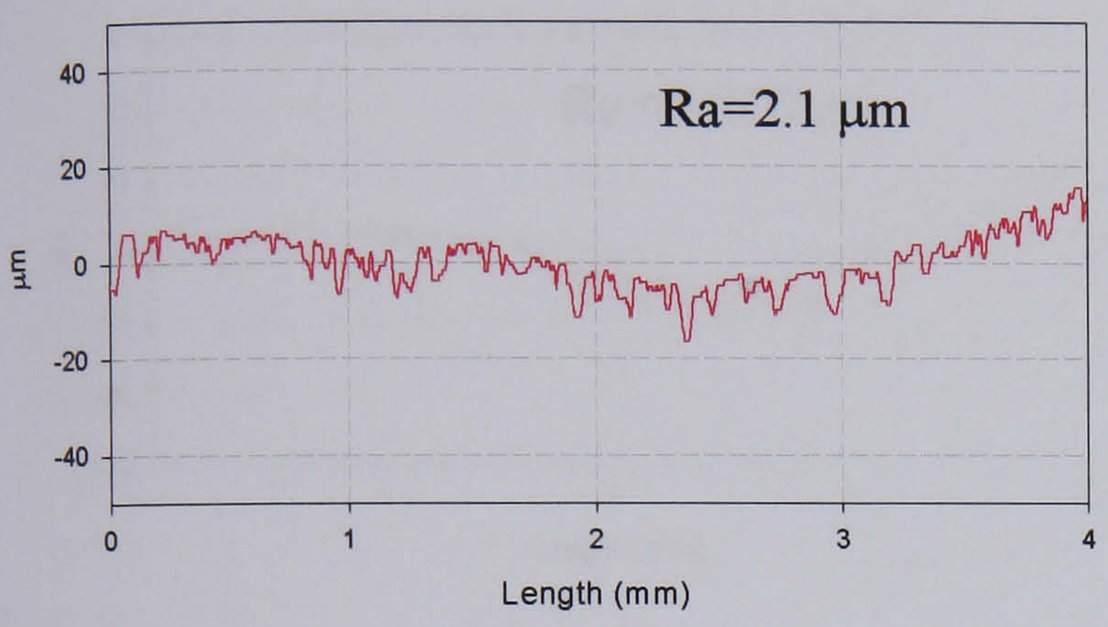

After test 2

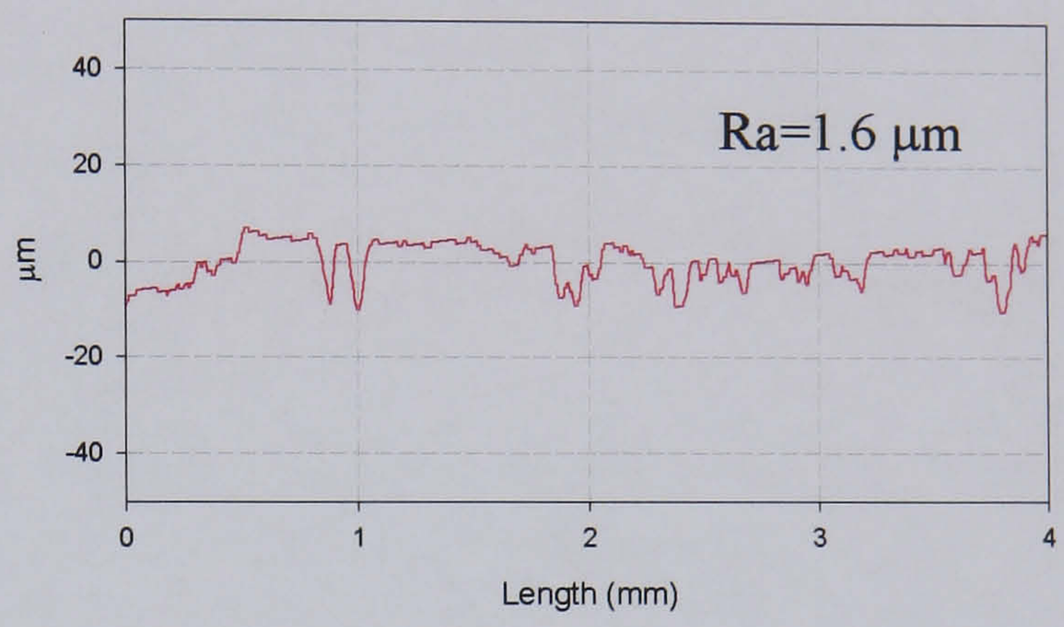

After test 3

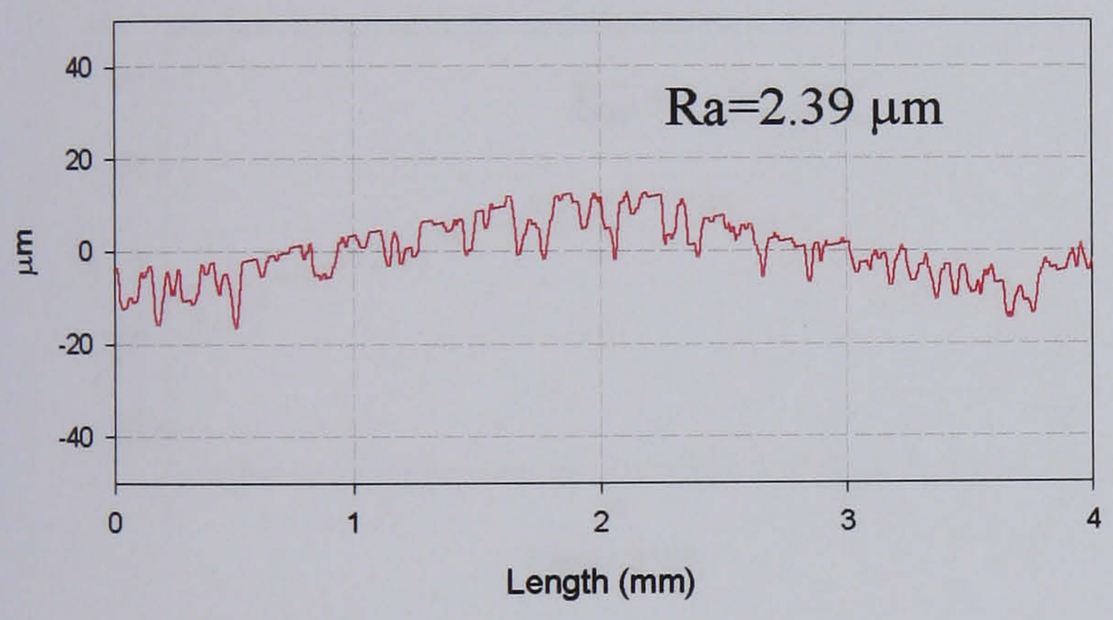

After test 4

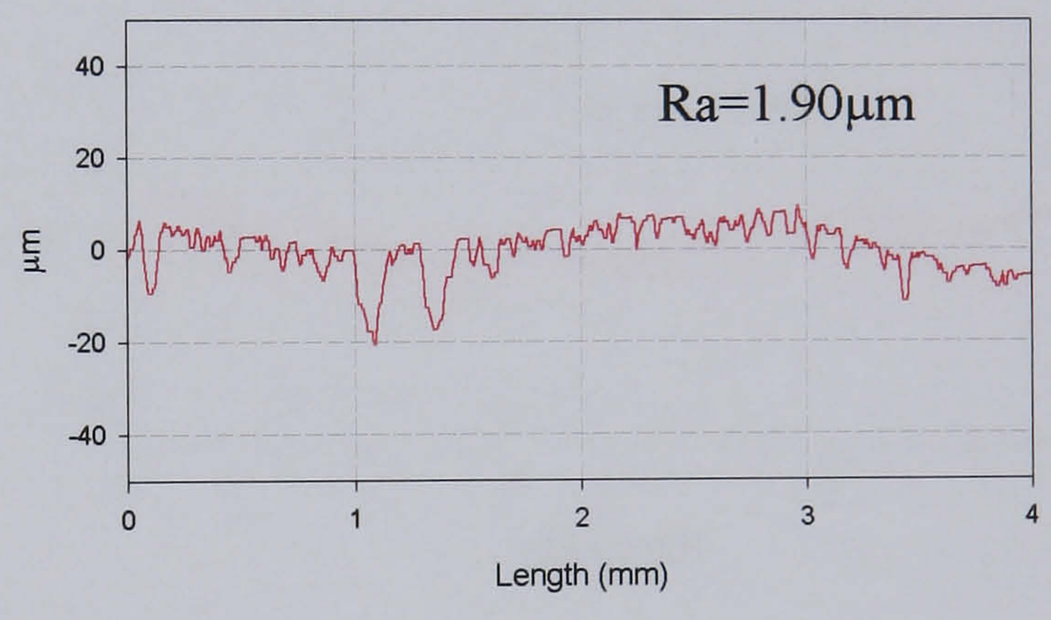

After test 5

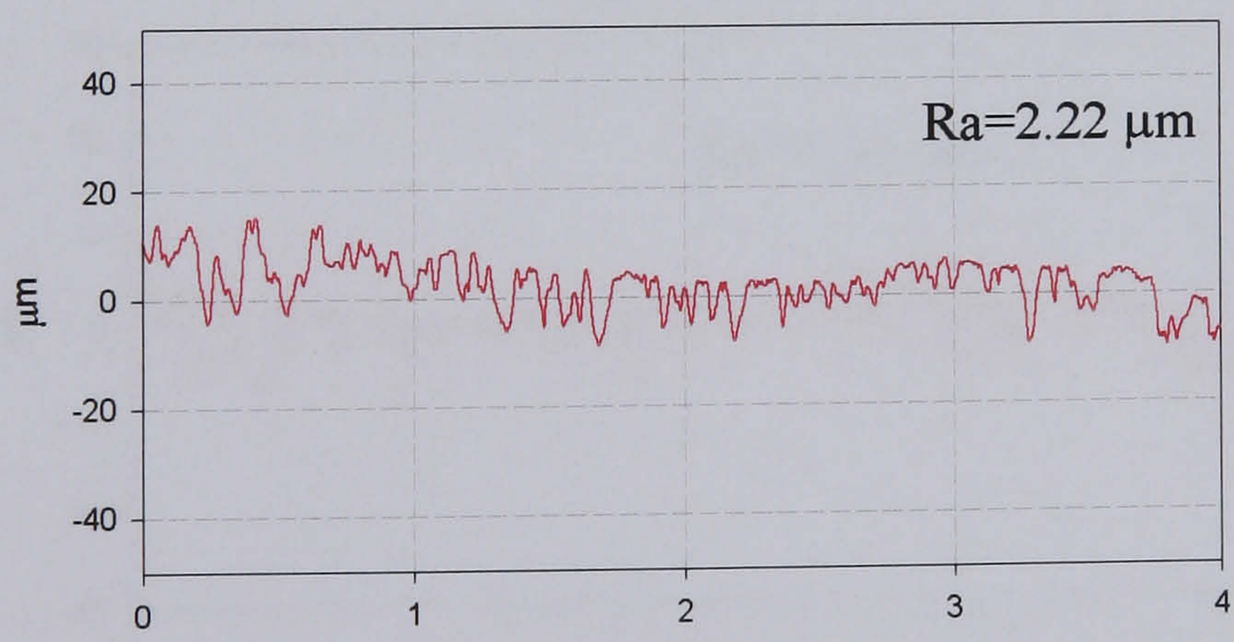

Tests carried out at 400°C under the presence of water and water vapour

After test 1

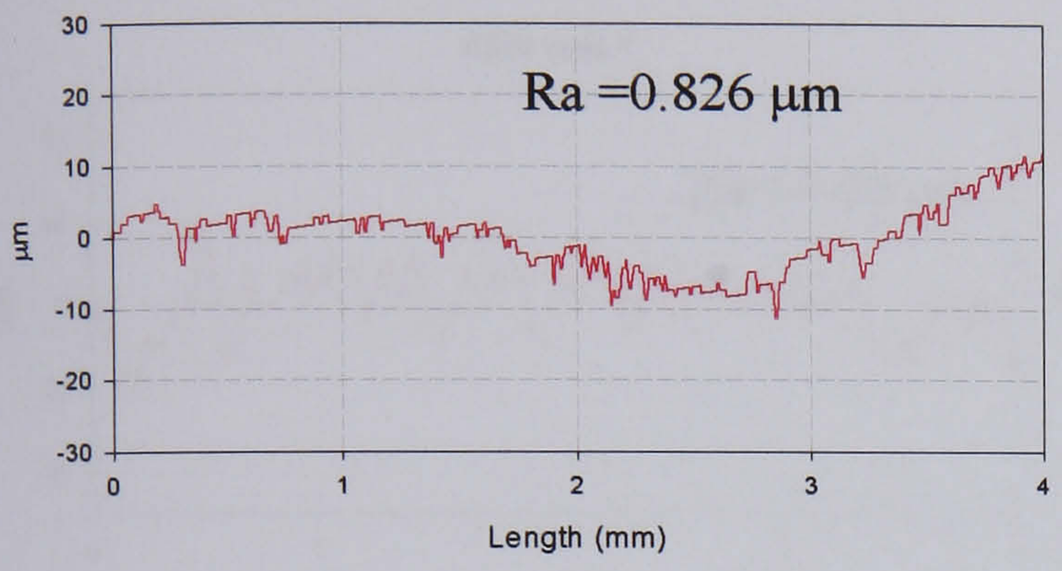

After test 2

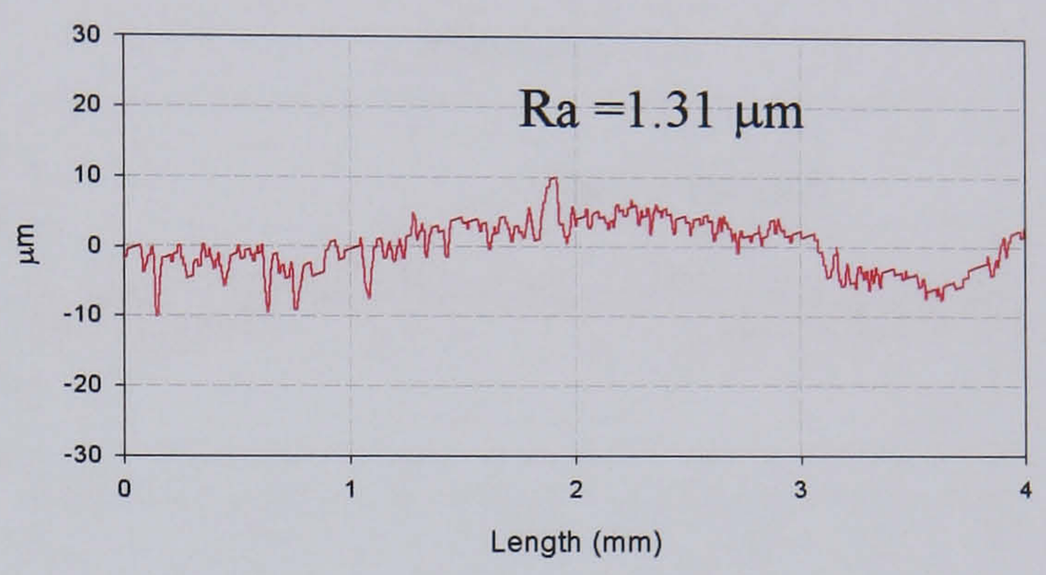

After test 3

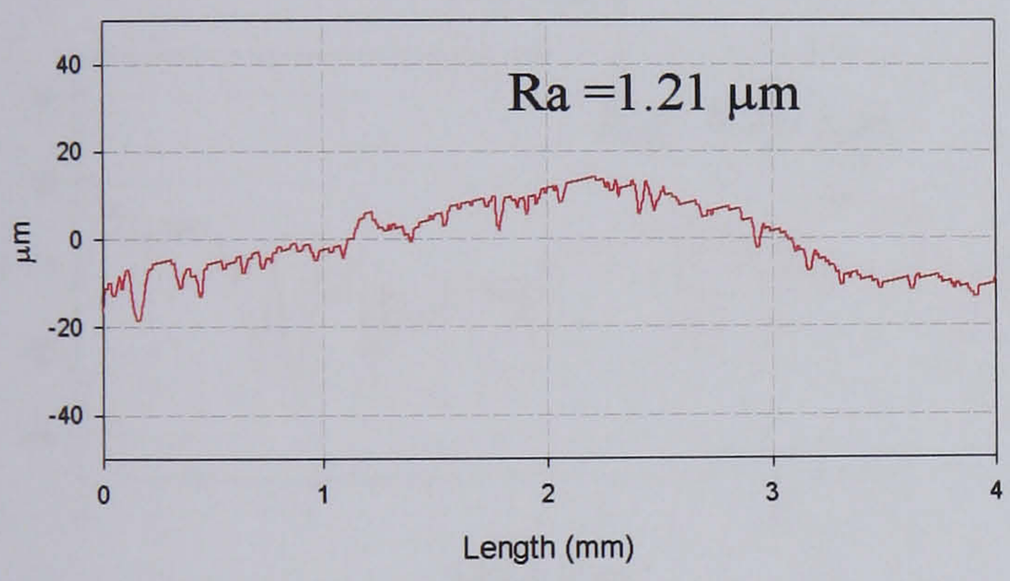

After test 4

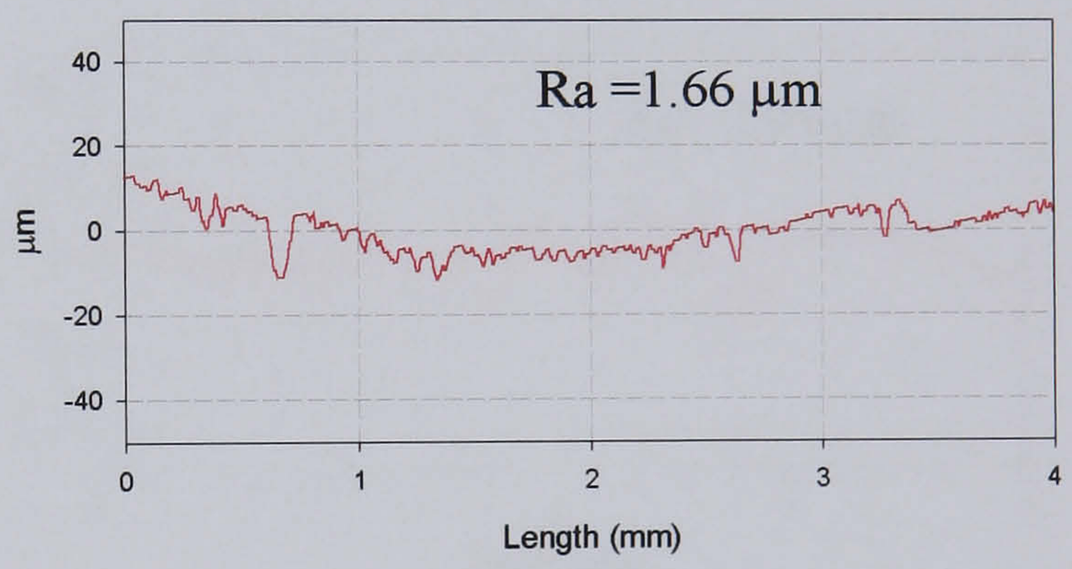

After test 5

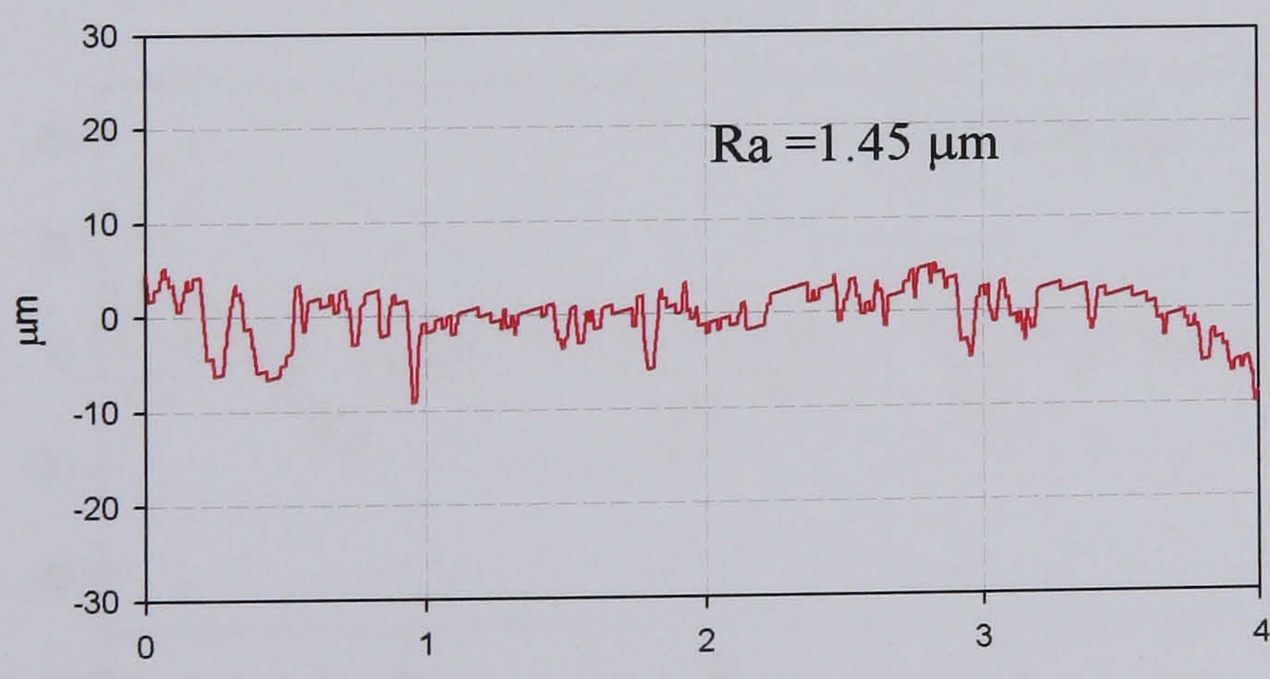

Example of test disc roughness measured after the tests

Tests carried out at 600°C in dry air

After test 1

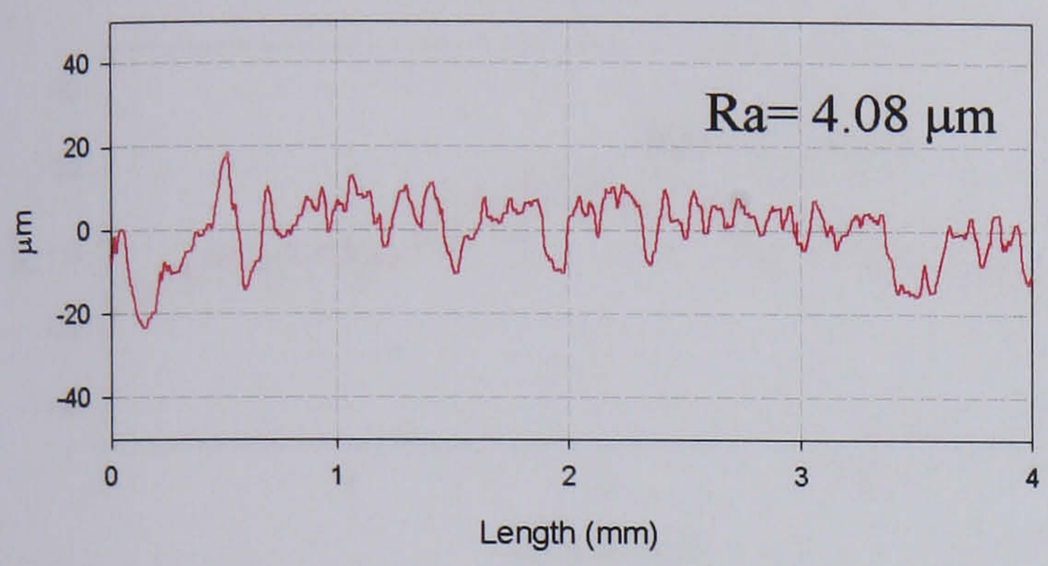

After test 2

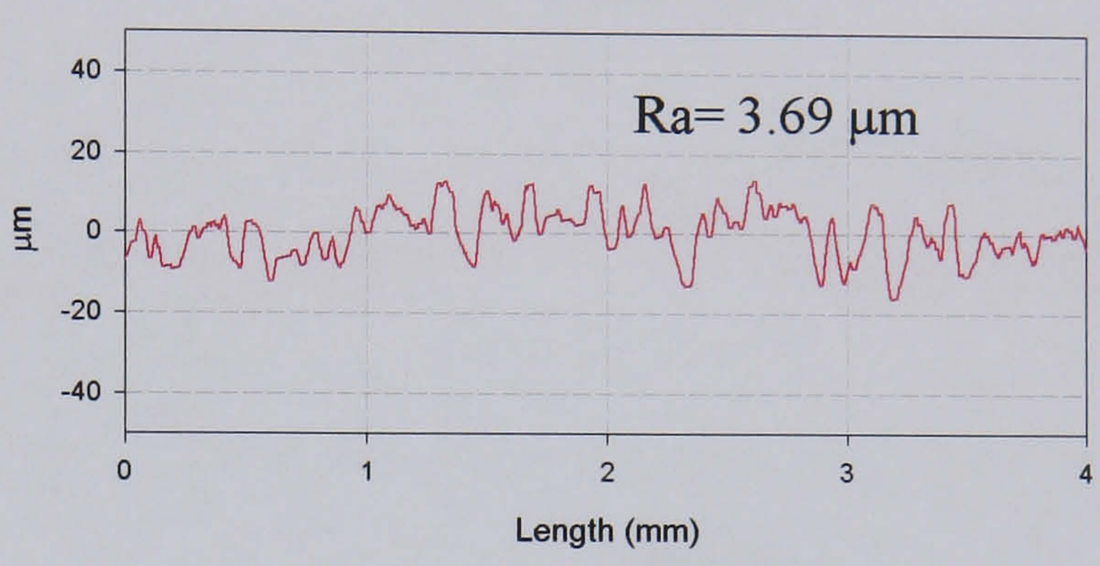

After test 3

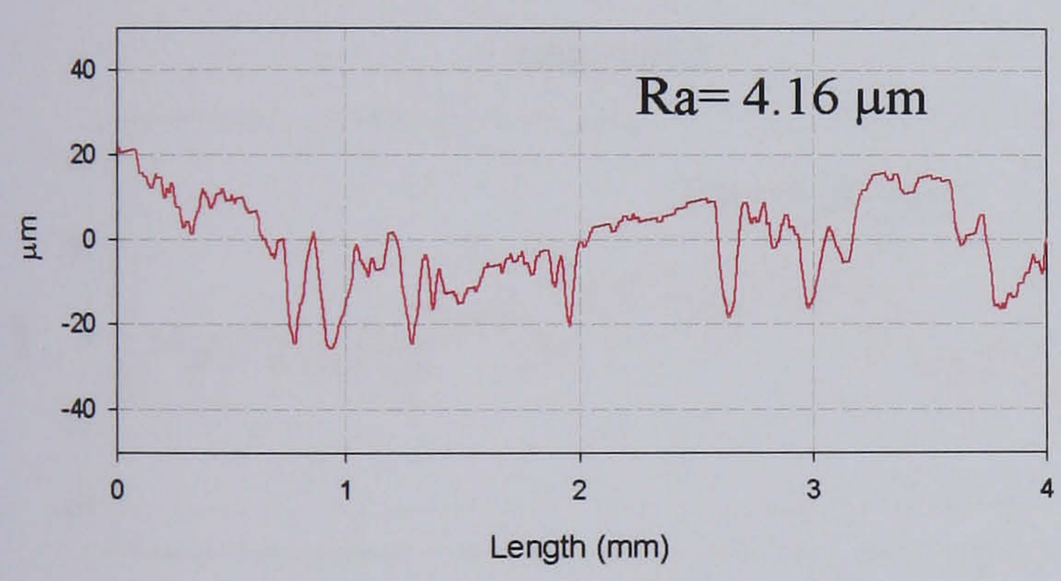

After test 4

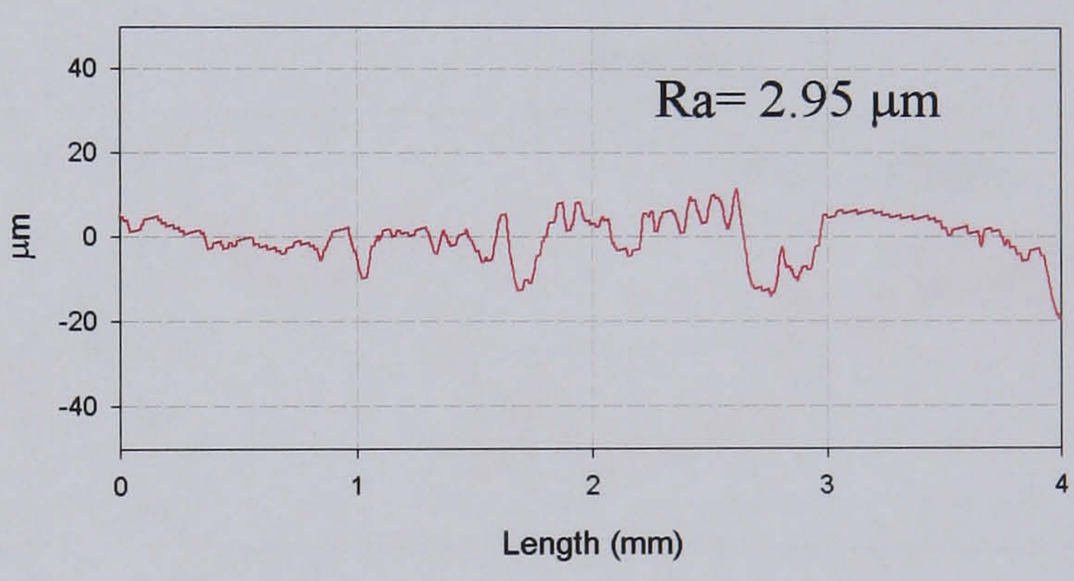

After test 5

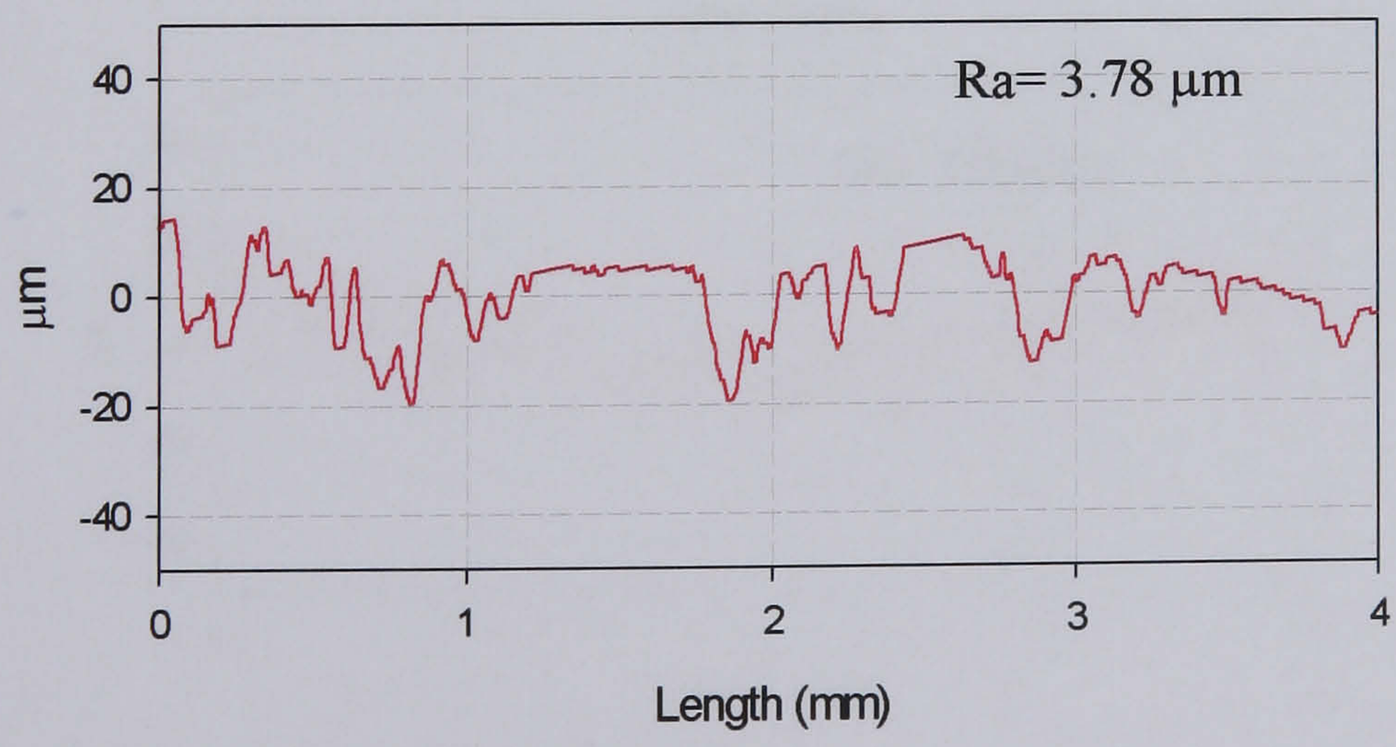

Test carried out in dry air at 500°C

After test 1

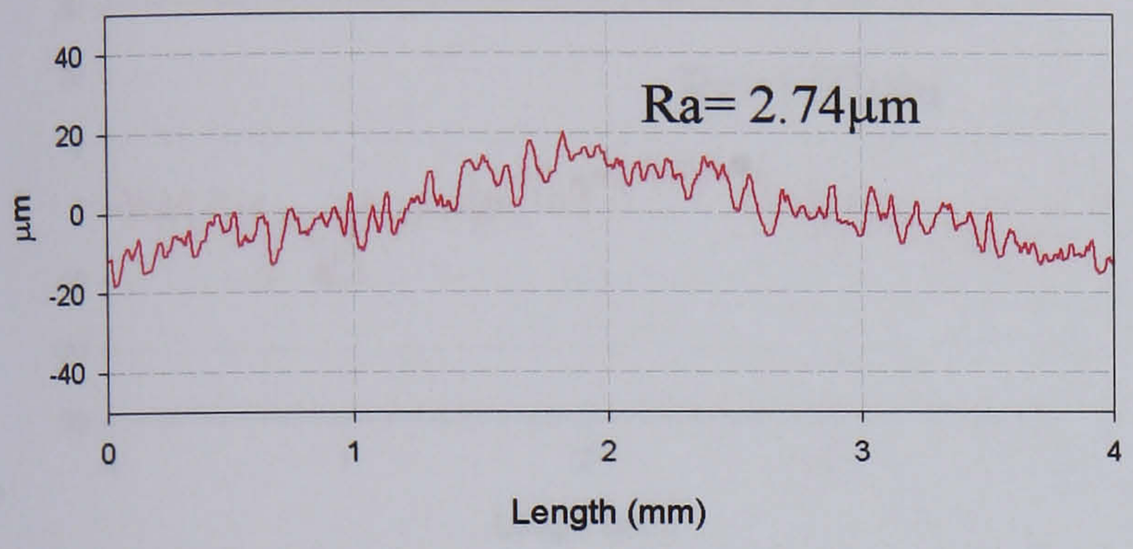

After test 2

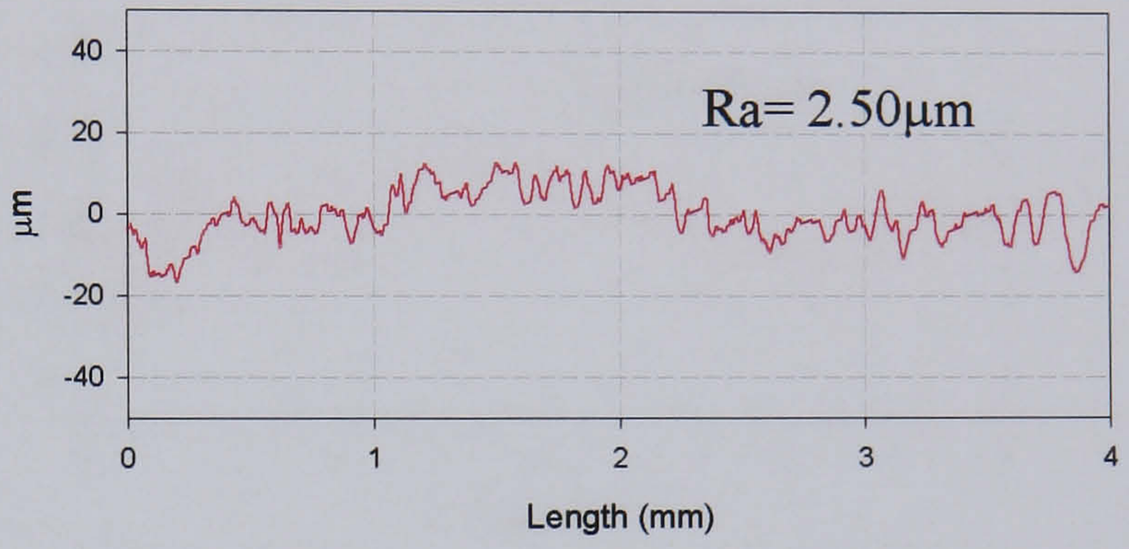

After test 3

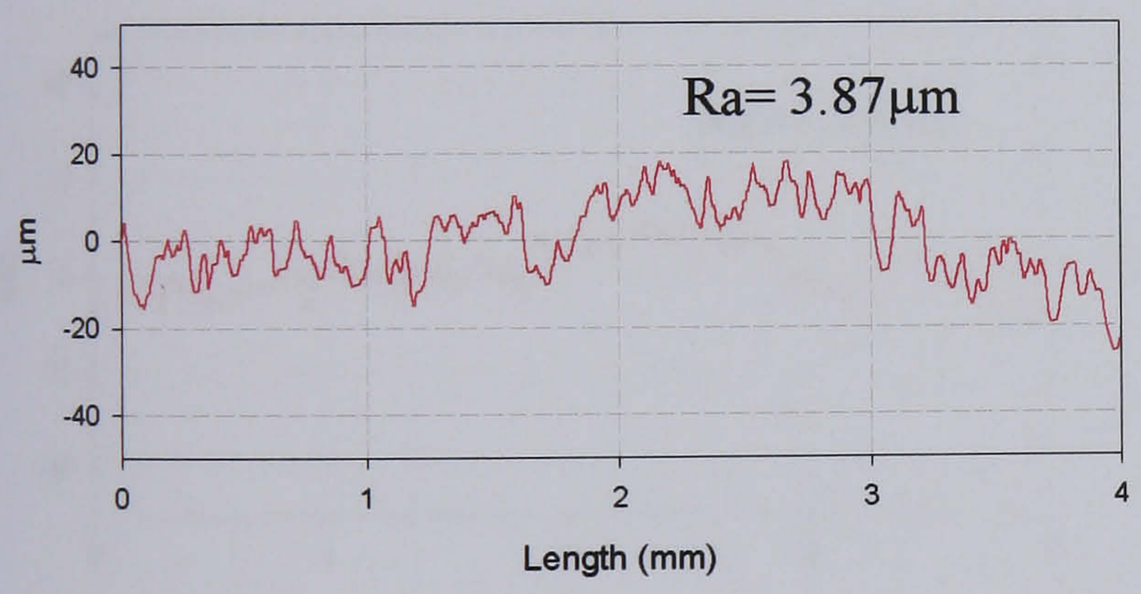

After test 4

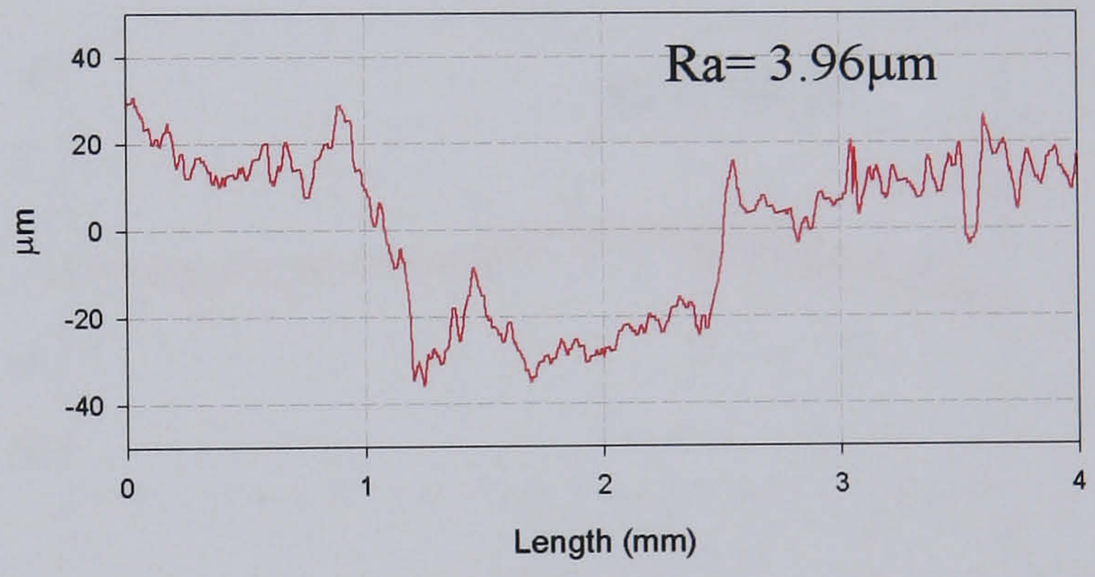

After test 5

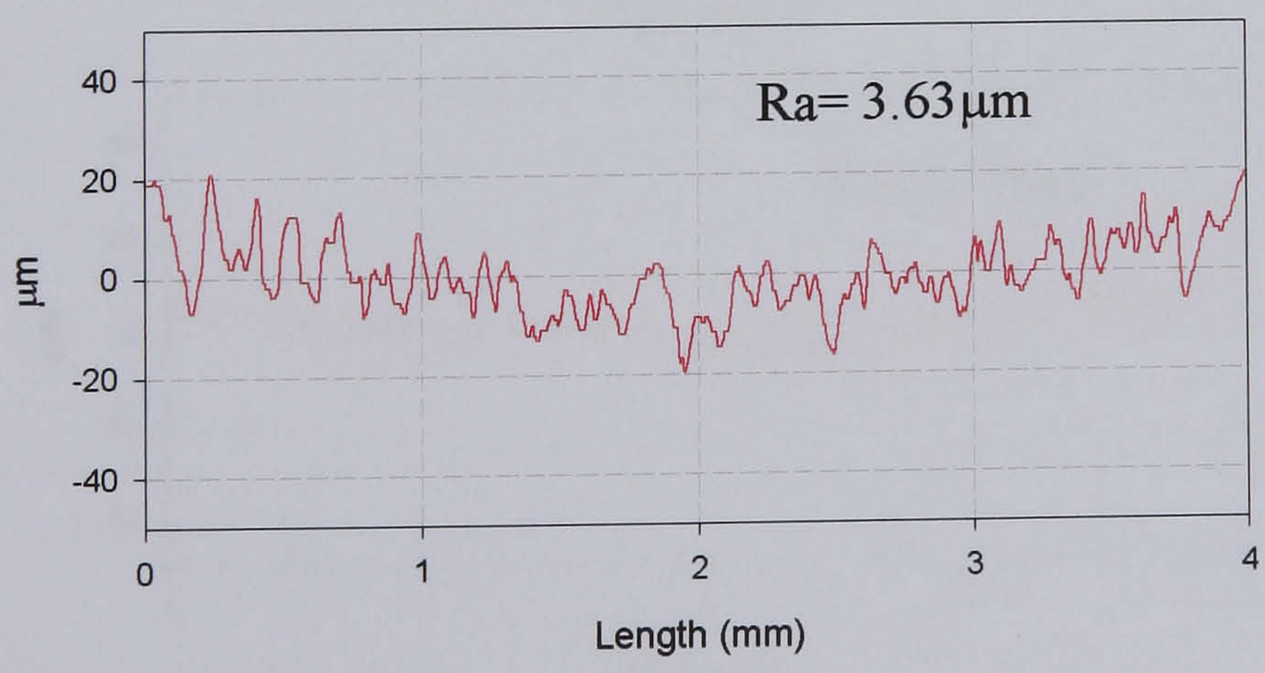

Tests carried out at 400°C in dry air

After test 1

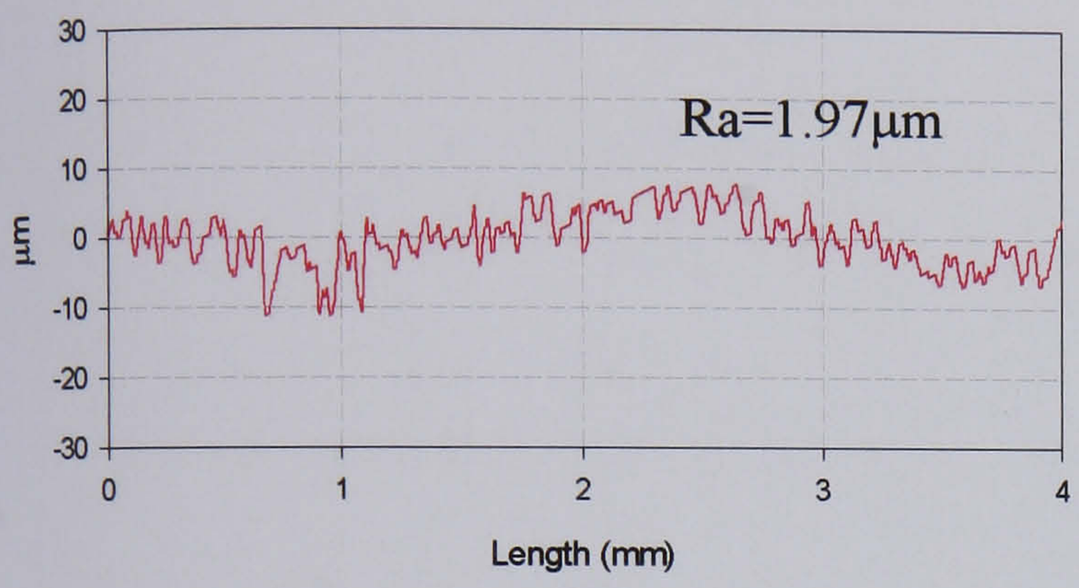

After test 2

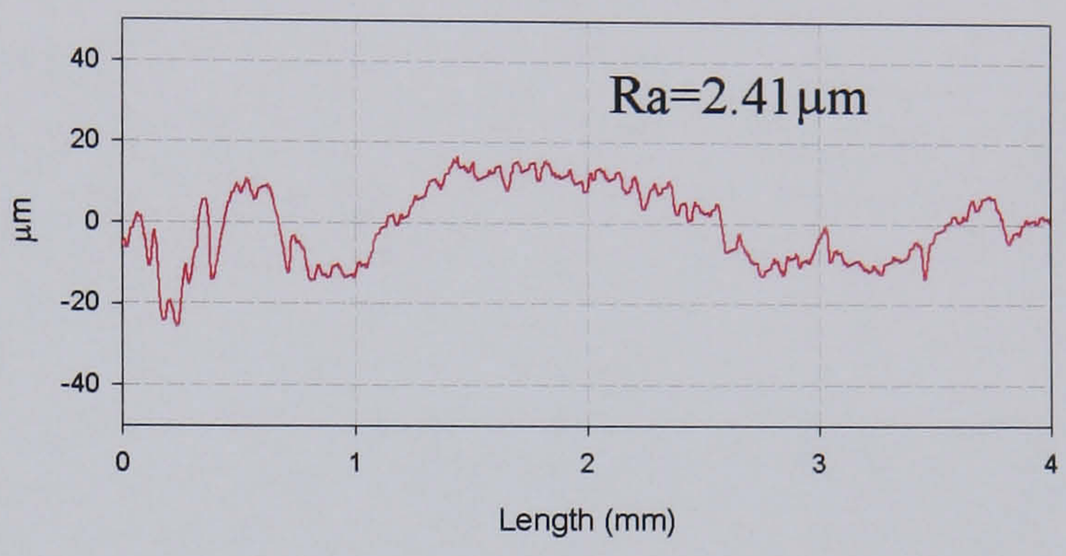

After test 3

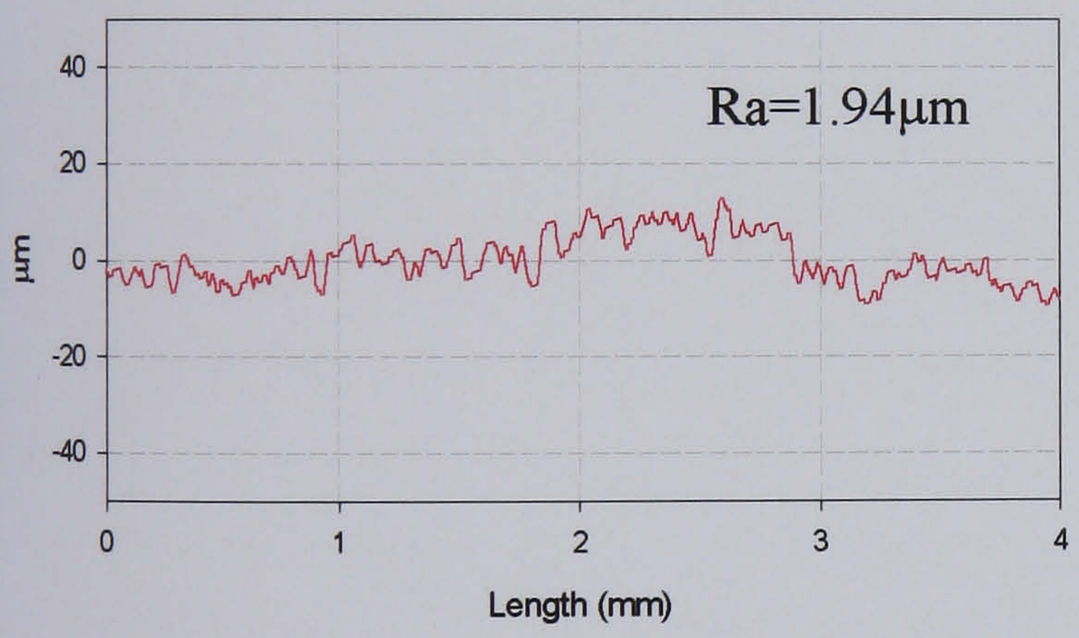

After test 4

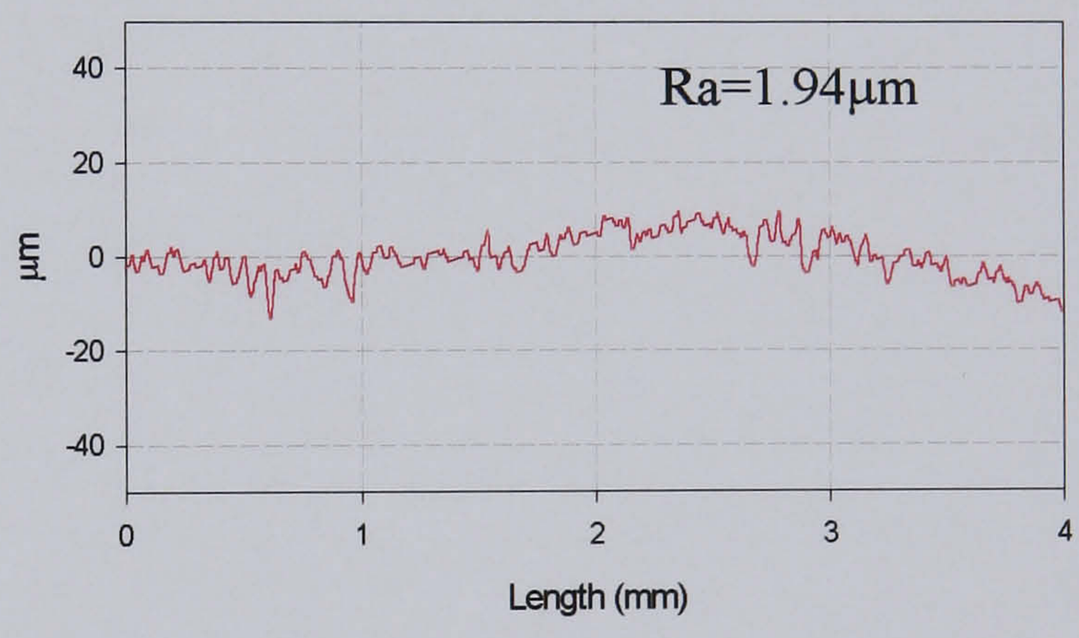

After test 5

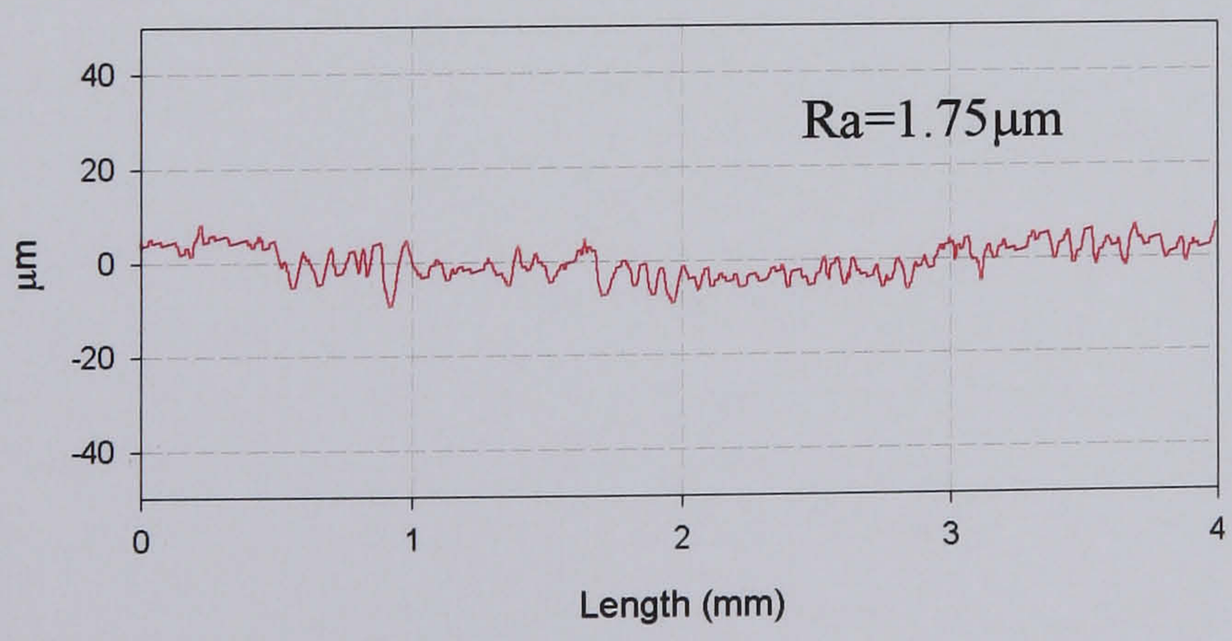

Appendix 3

Calculation of the initial contact pressure of the disc on disc configuration used during the rolling-sliding tests.

Considering that when the discs are brought into contact the point of contact is deformed so that the contact is described having an elliptical shape of major axis with radius a and minor axis with radius b as:

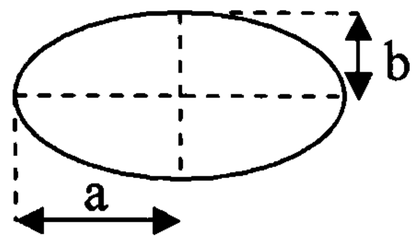

The values of radius a and b are obtained by

$$a = \sqrt[3]{\frac{3k^2 \mathrm{E} PR'}{\pi E^*}} \tag{3.1}$$

and

$$b = \sqrt[3]{\frac{3 \mathrm{E} PR'}{\pi k E^*}} \tag{3.2}$$

Where E* is the effective elastic modulus of the contact calculated from the elastic modulus E_1 and E_2 of the discs and R' the equivalent radius of the contact given by the equations:

$$\frac{1}{E^*} = \frac{1}{2}\left(\frac{1-\upsilon_1{}^2}{E_1} + \frac{1-\upsilon_2{}^2}{E_2}\right) \tag{3.3}$$

and

$$\frac{1}{R'} = \frac{1}{R_x} + \frac{1}{R_y} \tag{3.4}$$

where R_x and R_y are the radius of curvature of the bodies given by:

$$\frac{1}{R_x} = \frac{1}{R_{1x}} + \frac{1}{R_{2x}}$$

$$\frac{1}{R_y} = \frac{1}{R_{1y}} + \frac{1}{R_{2y}} \tag{3.5}$$

The constant E is called the ellipse integral and the constant k is obtained from tables or empirical relations like:

$$\mathrm{E} = 1.0003 + \frac{0.5968 R_x}{R_y} \tag{3.6}$$

and

$$k = 1.0339 \left(\frac{R_x}{R_y} \right)^{0.6360} \tag{3.7}$$

The value of the contact pressures is given by:

$$p_o = \frac{3P}{2\pi ab} \tag{3.8}$$

Lewis. R, "Tribology of machine elements, lecture notes". The University of Sheffield, Department of Mechanical Engineering, 2005.

Acknowledgments

First of all I would like to express my most sincere gratitude to Conacyt and the Mexican government for the scholarship given to me for my Ph.D studies.

Undoubtedly, I want to say THANK YOU to my supervisor Professor W. Mark Rainforth first for undertaking the supervision of my studies when I did not have a supervisor and then for his guidance, unconditional support and PATIENCE to complete this work. Thank you Mark for believing in me.

I also want to thank my family, first my parents Federico y Maricela who have always shown support and love to me and also taught me with the good examples of hard work and being a good person (...which I think I am). I also want to thank my sister Lissette and my brother Gerardo who made a big effort to care of things in Mexico while I was not there. Maricela, Zeferino and baby Matias thank you for your continuous support in the difficult moments that I had. This work is for you all. I think the difficult times are slowly passing by. Thank you also to my grandmother Conchita and my grandfather Ezequiel (+) you have been a BIG inspiration to me....love you.

I want to say thank you to my dear friend Dr. Jesus Talamantes for always being a good friend to me and for his continuous advice and support.

I want to express my sincere gratitude to my friends in office D1 both the old guard (Rich, Mike, John, Matt, Pete, Sam, Magda and Conny) and the new guard (Both Mohamed's, Rob, Nima, Moi, Rahul, Jodie, Lin and Oliver). Guys I did enjoyed my time with you there and I want to apologize for both: not playing Quake or worms and my "beautiful" singing of Mexican folk music in stressful moments.

I also want to say thank you to the guys in office H6 (Akemi, Jorge, my good friends Amit and Le Ma, Super Sam, Vishwa, Hasan, and Shingo) and also to Dr. Ian Ross and Dr. Zhaoxia Zhou for being good friends and colleagues of work. Thank you very much guys and also sorry for my singing.

My gratitude is also expressed to the guys in the foundry department Ian (my Dad in Sheffield), Dean (uncle 1), Stu (uncle2) and Mel without whom this work could not be finished. Thank also to Phil in the preparation lab.

I also want to say thank you to the Mexican gang, Viko and Rosy, Adriana and Omar, Sabino, Juan but specially to Ezequiel who has been always supporting me. Thank you for the nice moments we had in Sheffield.

If you read this and find out that your name is not here, please do not feel bad, for some reason I forgot it but for sure you are in my thoughts and in my heart. I never forget good moments.

I also want to deeply thank Beata for being with me in a very difficult moment of my life and for her BIG effort of drawing a smile on my face everyday in order for me to finish this work. Thank you very much!

Finally I want to express my love and gratitude to God, who undoubtedly has been present with me during my WHOLE life and blessed me with a good but sometimes troubled brain and MANY opportunities of living. Dear friend, this work represents something very important to me and I dedicate it to you..... I hope you like it.